

Multiscale Modeling and Simulation of Transport Processes in Porous Media

Vom Stuttgart Center for Simulation Science
und der Fakultät Bau- und Umweltingenieurwissenschaften
der Universität Stuttgart genehmigte Habilitationsschrift

vorgelegt von
Carina Bringedal, Ph.D.
aus
Haugesund

Hauptberichter: Prof. Dr.-Ing. Rainer Helmig
1. Mitberichter: Prof. Dr. Guido Schneider
2. Mitberichter: Prof. Dr. Peter Knabner
3. Mitberichter: Prof. Dr. Helge Dahle

Tag der mündlichen Prüfung: 07.12.2022

Institut für Wasser- und Umweltsystemmodellierung
Lehrstuhl für Hydromechanik und Hydrosystemmodellierung

2022

Acknowledgements

This habilitation thesis is based on work that was carried out between the years 2017 and 2022, mainly at the Department of Hydromechanics and Modelling of Hydrosystems (LH2), Institute for Modelling Hydraulic and Environmental Systems (IWS), University of Stuttgart. Here I have been employed as Junior Professor in “Advanced Methods in Porous Media”, and I have been associated to the Stuttgart Center for Simulation Science (SC SimTech). Through this position I have gotten the opportunity to be part of the collaborative research center SFB1313 and the SimTech excellence cluster. Hence, I would like to thank University of Stuttgart for giving me the opportunity to develop as researcher, research leader and as lecturer through the juniorprofessorship.

Furthermore, I would like to thank those that have influenced my scientific life over the last years. First of all, I want to thank Prof. Dr. Rainer Helmig. He was largely involved in the creation of the juniorprofessorship, and also encouraged me to apply. He has also taken great care in integrating me in research activities in and outside LH2. His positive and supportive attitude has made it a pleasure to work with him, and his ability to find solutions to both research and practical problems never stops to amaze me. Secondly, I want to thank Prof. Dr. Iuliu Sorin Pop at Hasselt University. His belief in me already from my early research stages has helped me arrive where I am today, and his support during (and after) my postdoctoral position with him has greatly shaped my academic path, which I am very thankful for. Several of the publications in this thesis have appeared through our collaboration and through our “children”.

At the University of Stuttgart I would also like to thank the ones I have collaborated with, or who have somehow helped or supported me through the daily academic life. Especially I would like to thank Prof. Dr. Andrea Barth, Prof. Dr. Andrea Beck, Prof. Dr. Thomas Ertl, Prof. Dr. Bernd Flemisch, Dr. Maren Paul, Prof. Dr. Christian Rohde, Jun. Prof. Dr. Benjamin Uekermann, and Dr. Lars von Wolff. At LH2 in particular, I want to thank everyone who makes the chair a pleasant place to work, and especially the secretariat consisting of Stefanie Siegert and Beate Spinner, and the system administrator David Werner. I want to thank my international collaborators Prof. Dr. Florin A. Radu and Prof. Dr. Kundan Kumar at University of Bergen, Prof. Dr. Cornelis Johannes van Duijn at Technical University of Eindhoven, Prof. Dr. Peter Knabner and Dr. Nadja Ray at FAU Erlangen-Nürnberg, and Prof. Dr. Jochen Schütz at Hasselt University, for previous and ongoing collaborations, and always useful discussions. In particular I would like to thank my doctoral supervisor Prof. Dr. Inga Berre at University of Bergen for always being a great source of inspiration and for providing helpful advice.

Finally, I thank Alexander for always being supportive, for offering help and distraction, and for always being a good discussion partner independent of topic.

Bergen, February 2023

Carina Bringedal

Contents

Acknowledgements	iii
Deutsche Zusammenfassung	vii
Summary	xv
1 Introduction	1
1.1 Why use multiscale models and simulations for transport processes in porous media?	6
1.2 Overview of model equations at pore and Darcy scale	12
1.2.1 Pore scale	12
1.2.2 Darcy scale	21
1.3 Multiscale approaches	24
1.3.1 Transversal averaging	26
1.3.2 Boundary-layer methods	29
1.3.3 Homogenization	33
1.3.4 Heterogeneous multiscale methods	41
1.4 Structure of thesis	44
1.4.1 Part A: Multiscale parabolic problems	44
1.4.2 Part B: Two-phase porous-media flow	48
1.4.3 Part C: Reactive transport with heterogeneous reactions	51
1.4.4 Part D: Evaporation from porous media	54
A Multiscale parabolic problems	57
2 Numerical homogenization of parabolic problems	61
3 Effective heat transport in thin porous media	81
4 Effective heat transport near clogging	115
B Two-phase porous-media flow	141
5 Layered two-phase flow in a thin strip	145
6 Dynamic contact angle in a thin strip	165
7 Two-phase flow in a periodic porous medium	209

C	Reactive transport with heterogeneous reactions	233
8	Pore-scale and two-scale model for mineral precipitation and dissolution	237
9	Two-scale simulation of mineral precipitation and dissolution	275
10	Comparison of level-set and phase-field models for three-phase systems	299
D	Evaporation from porous media	327
11	Stability analysis of evaporation-induced density instabilities	331
12	Conclusion and outlook	377
	Bibliography	385

Deutsche Zusammenfassung

Strömungs- und Transportprozesse in porösen Medien sind für eine Vielzahl technischer, geologischer und biologischer Systeme von großer Bedeutung. Die Modellierung und Simulation dieser Prozesse stellt eine große Herausforderung für die Forschung im Bereich der Ingenieurwissenschaften, Mathematik und Informatik dar. Ein Grund dafür ist die Tatsache, dass Strömungs- und Transportprozesse in porösen Medien in der Regel miteinander gekoppelte Prozesse sind. Die daraus resultierenden Interaktionen zwischen dem strömendem Fluid (oder den strömenden Fluiden) und dem porösen Medium führen zu hochgradig gekoppelten Problemen, die die Simulation solch gekoppelter Systeme äußerst herausfordernd machen. Ein anderer Grund sind die inhärent großen Skalenunterschiede dieser Probleme und innerhalb des porösen Mediums. Die Kopplungen und Interaktionen auf einer Längenskala können sich von den Kopplungen und Interaktionen auf einer anderen Längenskala stark unterscheiden. Deshalb ist es unumgänglich zu verstehen, welche Prozesse auf der für eine Anwendung relevanten Skala von Bedeutung sind, wenn man sich mit der Modellierung und Simulation von Transportprozessen in porösen Medien beschäftigt.

Die beschriebenen Eigenschaften motivieren die Verwendung von mehrskaligen Ansätzen für die Modellierung und Simulation dieser Transportprozesse. In dieser Habilitationsschrift werden verschiedene Mehrskalmethoden und -ansätze angewandt, um das Verhalten innerhalb poröser Medien zu analysieren und um die Interaktionen zwischen den verschiedenen Skalen des porösen Mediums zu verstehen. Die Mehrskalansätze, die in dieser Arbeit betrachtet werden, können in vier Kategorien unterteilt werden:

- Transversale Mittelung, die verwendet wird, wenn man mit langen aber dünnen Gebieten arbeitet, um ein dimensionsreduziertes Modell für das wirksame Verhalten herzuleiten.
- Grenzschichtmethoden, die verwendet werden, um das wirksame Verhalten nahe und weit entfernt von Singularitäten oder Diskontinuitäten zu adressieren.
- Homogenisierung, die bei lokal-periodischen Problemen verwendet wird, um das wirksame Verhalten auf einer größeren Skala zu bestimmen.
- Heterogene Mehrskalmethoden, die verwendet werden, um numerische Lösungsverfahren für Modelle, die über zwei (oder mehr) Skalen miteinander gekoppelt sind, zu entwerfen.

Um die Anwendungen dieser Mehrskalansätze im Kontext von Transportprozessen in porösen Medien zu demonstrieren, betrachten wir drei typische Arten von Transportverhalten, die alle eine wichtige Rolle in den Umweltwissenschaften, der Energieerzeugung und den Materialwissenschaften spielen. Dabei handelt es sich um mehrskalige parabolische Probleme (Diffusions- bzw. Wärmeleitungsprozesse), Zweiphasenströmungen in porösen Medien und reaktive Transportprozesse mit heterogenen Reaktionen. Diese drei Arten von

Strömung und Transport repräsentieren verschiedene physikalische Prozesse und Interaktionen innerhalb des porösen Mediums und sie treten, abhängig von der betrachteten Skala, auf verschiedene Art und Weise auf. Wenn wir die mehrskaligen parabolischen Probleme betrachten, dann interessieren wir uns hauptsächlich für die Bestimmung des wirksamen Diffusions-/Wärmeleitungskoeffizienten auf der großen Skala. Dies erlaubt es, großskalige Anwendungen zu modellieren und zu simulieren, ohne den Einfluss feinskaliger Prozesse zu vernachlässigen. Die Modellgleichungen, die die Zweiphasenströmung beschreiben, unterscheiden sich gravierend, abhängig davon ob die fein- oder großskaligen (bzw. wirksamen) Prozesse berücksichtigt werden. Im Allgemeinen ist der Zusammenhang dieser zwei Skalen unbekannt. Im Fall der reaktiven Transportprozesse mit heterogenen Reaktionen interagieren die Strömung und der Transportprozess des gelösten Stoffs mit dem Festkörper des porösen Mediums. Dies resultiert in einem sich (zeitlich) verändernden porösen Medium. Wie diese Veränderung auf der Porenskala und deren Einfluss auf die große Skala modelliert werden, sind große Herausforderungen.

Die Unterschiede zwischen den Prozessen und die damit verbundenen Herausforderungen motivieren die Betrachtung der folgenden vier Themen in jeweils eigenen Teilen in dieser Arbeit:

- A Mehrskalige parabolische Probleme
- B Zweiphasenströmung in porösen Medien
- C Reaktiver Transport mit heterogenen Reaktionen
- D Verdunstung aus porösen Medien

Die ersten drei Teile bestehen aus jeweils drei Publikationen, die jeweils verschiedene mehrskalige Aspekte des betreffenden Prozesses betrachten. Der vierte Teil ist insofern besonders, dass er auf einer einzigen Publikation basiert, bei der die mehrskaligen Aspekte nicht explizit betrachtet werden. Stattdessen werden Prozesse betrachtet, die in den ersten drei Teilen behandelt werden, und motiviert so die Verwendung von Mehrskalensätzen im Kontext der Verdunstung aus porösen Medien, um den Verdunstungsprozess besser zu verstehen. Dies wird in der Zusammenfassung und Ausblick weiter diskutiert, s. Kapitel 12. Alle Publikationen, die in dieser Arbeit inkludiert sind, sind Originalpublikationen. Die jeweils veröffentlichenden Fachzeitschriften haben der Wiederverwendung der veröffentlichten Publikationen in der vorliegenden Arbeit zugestimmt.

Der Teil A beschäftigt sich mit dem wirksamen Verhalten von parabolischen Problemen, die die Druckverteilung, Diffusion oder Wärmeleitung in porösen Medien beschreiben und basiert auf den folgenden Publikationen:

- M. Bastidas, C. Bringedal, I. S. Pop, and F. A. Radu. *Numerical homogenization of non-linear parabolic problems on adaptive meshes*. *Journal of Computational Physics* 425 (2021), p. 109903. doi: 10.1016/j.jcp.2020.109903.
- L. Scholz and C. Bringedal. *A Three-Dimensional Homogenization Approach for Effective Heat Transport in Thin Porous Media*. *Transport in Porous Media* 141.3 (2022), pp. 737–769. doi: 10.1007/s11242-022-01746-y.
- C. Bringedal and K. Kumar. *Effective Behavior Near Clogging in Upscaled Equations for Non-isothermal Reactive Porous Media Flow*. *Transport in Porous Media* 120.3 (2017), pp. 553–577. doi: 10.1007/s11242-017-0940-y.

In der ersten Publikation, s. Kapitel 2, betrachten wir eine nichtlineare parabolische Gleichung. Diese Gleichung könnte den Druck eines ungesättigten Fluids bei Modellierung von Strömungen mittels der Richards-Gleichung nach Anwendung der Kirchhoff-Transformation beschreiben. Andererseits könnte die Gleichung, insbesondere im linearisierten Fall, ebenfalls ein typisches Diffusions- oder Wärmeleitungsproblem beschreiben. Das Hauptziel dieses Kapitels ist es, ein effizientes und genaues numerisches Verfahren zu entwickeln, indem adaptive Gitter verwendet werden. Die Gitteradaptivität wird durch einen lokalen Fehlerschätzer gesteuert. Allerdings ist es durch die Verwendung von feinen und groben Gittern notwendig, den wirksamen Diffusionskoeffizienten (bzw. die Permeabilität im Kontext der Richards-Gleichung) auf den Längenskalen dieser Gitter zu bestimmen. Der Startpunkt sind bekannte Informationen auf der feinen Skala und Homogenisierung zusammen mit einem Algorithmus, der auf heterogenen Mehrskalmethoden basiert, um das numerische Lösungsverfahren zu konstruieren. Eine erwähnenswerter Punkt ist die Tatsache, dass Homogenisierung im Allgemeinen lokale Periodizität voraussetzt, aber die Anwendung der Homogenisierung auf Probleme ohne diese Eigenschaft dennoch sinnvolle Ergebnisse liefert, wenn man sie mit lokalen Fehlerschätzern und adaptiver Gitterverfeinerung kombiniert.

In der zweiten Publikation, s. Kapitel 3, betrachten wir Wärmeleitung in einem dünnen porösen Medium. Der Startpunkt ist ein Modell auf der Porenskala bei dem Wärmeleitung im sättigenden Fluid mit Wärmetransport durch die festen Körner gekoppelt wird. Eine solch detaillierte Geometrie numerisch darzustellen, würde sehr feine Rechengitter benötigen, während es unser Ziel ist, Gleichungen herzuleiten, die das wirksame Verhalten auf der Darcy-Skala beschreiben. Da das poröse Medium dünn ist, wird eine Homogenisierungsstrategie mit transversaler Mittelung kombiniert, um das Modell auf der Darcy-Skala herzuleiten. Dies führt zu einem dimensionsreduzierten Modell auf der Darcy-Skala. Diese angepasste Homogenisierungsprozedur resultiert in Zellproblemen, die gelöst werden können, um den wirksamen Wärmeleitungskoeffizienten des porösen Mediums zu bestimmen. Die Randbedingungen auf der Ober- und Unterseite des dünnen porösen Mediums treten auch in den Zellproblemen auf und beeinflussen so den wirksamen Wärmeleitungskoeffizienten. In diesem Kapitel wird mittels eines numerischen Beispiels ebenfalls demonstriert, wie gut die Ergebnisse des Modells, das das wirksame Verhalten beschreibt, den Mittelwert der Ergebnisse auf der Porenskala repräsentieren.

Die dritte Publikation in diesem Teil, s. Kapitel 4, beschäftigt sich mit dem wirksamen Verhalten innerhalb eines porösen Mediums, das sich durch heterogene chemische Reaktionen verändern. Somit kombiniert dieses Kapitel Aspekte aus Teil A und Teil C. Da das Hauptaugenmerk dieses Kapitels auf den wirksamen Parametern Permeabilität, Wärmeleitungskoeffizient und Diffusionskoeffizient liegt, ist dieses Kapitel dennoch Teil von Teil A. Das Kapitel baut auf einem bereits hergeleiteten Zweiskalenmodell auf, das durch Homogenisierung hergeleitet wurde. Das Zweiskalenmodell koppelt Strömung, Wärmetransport und den Transport gelöster Stoffe auf der Darcy-Skala mit Zellproblemen auf der Porenskala, die die zeitliche Veränderung der Porengeometrie durch Mineralausfällung und -auflösung berücksichtigen. Dadurch können die Veränderungen der Permeabilität, des wirksamen Wärmeleitungskoeffizienten und des wirksamen Diffusionskoeffizienten auf der Darcy-Skala berücksichtigt werden. Das Ziel dieses Kapitels ist die Untersuchung dieser wirksamen Parameter unter besonderer Berücksichtigung von porösen Medien die aufgrund der Mineralausfällung nahe dem Zustand der Selbstdichtung sind. Für simple Kornformen, wie kreisförmige Körner, können die wirksamen Parameter in Form eines parametrisierten Ausdrucks bestimmt werden. Dies vereinfacht Simulationen

auf der Darcy-Skala signifikant. Wenn solche parametrisierten Ausdrücke anwendbar sind, kann auf die Verwendung einer heterogenen Mehrskalenmethode verzichtet werden.

Teil B fokussiert sich auf die Bestimmung wirksamer Parameter für Zweiphasenströmungen in porösen Medien bei der die Interaktion zwischen den zwei Fluiden auf der Porenskala berücksichtigt wird. Dieser Teil basiert auf den folgenden Publikationen

- S. Sharmin, C. Bringedal, and I. S. Pop. *On upscaling pore-scale models for two-phase flow with evolving interfaces*. *Advances in Water Resources* 142 (2020), p. 103646. doi: 10.1016/j.advwatres.2020.103646.
- S. B. Lunowa, C. Bringedal, and I. S. Pop. *On an averaged model for immiscible two-phase flow with surface tension and dynamic contact angle in a thin strip*. *Studies in Applied Mathematics* 147.1 (2021), pp. 84–126. doi: 10.1111/sapm.12376.
- S. Sharmin, M. Bastidas, C. Bringedal, and I. S. Pop. *Upscaling a Navier-Stokes-Cahn-Hilliard model for two-phase porous-media flow with solute-dependent surface tension effects*. *Applicable Analysis* (2022), doi: 10.1080/00036811.2022.2052858.

Die erste Publikation dieses Teils, s. Kapitel 5, beschäftigt sich mit Zweiphasenströmung in einem dünnen Streifen. Solch ein dünner Streifen kann eine einzelne Pore eines porösen Mediums repräsentieren, aber ist ebenfalls für die Strömung durch Rohre relevant oder als Grenzfläche zwischen zwei Gebieten. Die zwei Fluide haben eine geschichtete Struktur, d.h. es wird angenommen, dass sich die Grenzfläche zwischen den zwei Fluiden über die gesamte Länge des Streifens erstreckt. Die Fluid-Fluid-Grenzfläche darf sich durch die Strömung und die Oberflächenspannung zwischen den zwei Fluiden verändern. Aufgrund der langen aber dünnen Struktur des betrachteten Gebiets wird das wirksame Verhalten mittels transversaler Mittelung entlang des Streifens bestimmt. Die hergeleiteten wirksamen Modelle sind dementsprechend dimensionsreduziert, da nur die Veränderungen entlang des Streifens explizit aufgelöst werden müssen. Das Ziel dieses Kapitels ist die Herleitung verschiedener Modelle für das wirksame Verhalten, bei der die Größenordnung der betrachteten Kapillarzah und das Verhältnis der Viskositäten der Fluide berücksichtigt werden. Durch die Berücksichtigung der veränderlichen Fluid-Fluid-Grenzfläche sind die hergeleiteten wirksamen Modelle ähnlich zum erweiterten Darcy-Gesetz, die allerdings von der Standardform des Darcy-Gesetzes abweichen. Numerische Experimente, die das ursprüngliche zweidimensionale Gebiet auflösen, zeigen, dass das hergeleitete Modell das transversal gemittelte Verhalten wiedergibt, wenn der Streifen länger und dünner wird.

In der zweiten Publikation, s. Kapitel 6, werden ebenfalls Zweiphasenströmungen in einem dünnen Streifen betrachtet. In diesem Fall kann eines der Fluide das andere verdrängen, was dem Fall einer Fluid-Fluid-Grenzfläche quer zum Streifen entspricht. Um den Fluid-Fluid-Festkörper-Kontaktpunkt zu modellieren, wird ein dynamischer Kontaktwinkel verwendet. Das wirksame Verhalten kann mittels transversaler Mittelung ausschließlich in ausreichender Entfernung von der Fluid-Fluid-Grenzfläche bestimmt werden. Da die Grenzfläche in diesem Kapitel eine Diskontinuität darstellt und das Verhalten dort stark abweicht, verwenden wir Grenzschichtmethoden um diese Interaktionen zu berücksichtigen. Das Ziel dieses Kapitels ist die Herleitung eines geschlossenen dimensionsreduzierten Modells für die Strömung durch den dünnen Streifen, das die Wechselwirkungen zwischen den Fluiden bei der Verdrängung des einen durch das andere berücksichtigt. Dies wird durch die Kombination der transversalen Mittelung und der Grenzschichtmethode erreicht. Wie in Kapitel 5 finden wir ein wirksames Modell das ähnlich zu dem erweiterten

Darcy-Gesetz ist, aber von der Standardform abweicht. Mit Hilfe des daraus resultierenden wirksamen Modells werden wirksame wohlbekannte Eigenschaften wie der dynamische Kapillardruck oder Hystereseffekte untersucht.

Die dritte Publikation dieses Teils, s. Kapitel 7, berücksichtigt Zweiphasenströmungen in einem periodischen porösen Medium. Da keine besonderen Anforderungen an das Auftreten der Fluid-Fluid-Grenzfläche gestellt werden, wird die Grenzfläche mittels eines Phasenfeldmodells auf der Porenskala modelliert. Die Periodizität auf der Porenskala ermöglicht die Herleitung eines Modells für das wirksame Verhalten auf der Darcy-Skala mittels Homogenisierung. Ziel dieses Kapitels ist die Herleitung eines Zweiskalenmodells, bei dem das Modell für die Zweiphasenströmung auf der Darcy-Skala von den Zellproblemen auf der Porenskala zur Bestimmung der wirksamen Parameter abhängt. Wir sind insbesondere an dem Fall interessiert, bei dem die sich verändernde Fluid-Fluid-Grenzfläche von einer variierenden Oberflächenspannung zwischen den zwei Fluiden beeinflusst wird. Das hergeleitete Modell auf der Darcy-Skala hat Ähnlichkeiten mit dem Standardmodell für Zweiphasenströmungen in porösen Medien ohne Kapillardruck. Allerdings unterscheidet es sich von dem Standardmodell durch die Berechnung der wirksamen Parameter durch die Zellprobleme auf der Porenskala. Die veränderliche Fluid-Fluid-Grenzfläche wird in diesen Zellproblemen aufgelöst und berücksichtigt so den Einfluss der variierenden Oberflächenspannung. Ein von den Ideen der heterogenen Mehrskalenmethoden inspiriertes explizites numerisches Lösungsverfahren für das Zweiskalenmodell wird verwendet, um den Effekt der variierenden Oberflächenspannung auf der Darcy-Skala zu zeigen.

Teil C befasst sich mit der Modellierung auf der Porenskala, dem Finden des wirksamen Verhaltens und Zweiskalensimulationen von reaktiven Transportprozessen in porösen Medien. Dabei wird die Veränderung der Porengeometrie aufgrund von Mineralausfällung und -auflösung berücksichtigt. Der Teil basiert auf den folgenden Publikationen:

- C. Bringedal, L. von Wolff, and I. S. Pop. *Phase Field Modeling of Precipitation and Dissolution Processes in Porous Media: Upscaling and Numerical Experiments*. Multiscale Modeling & Simulation 18.2 (2020), pp. 1076–1112. doi: 10.1137/19M1239003.
- M. Bastidas Olivares, C. Bringedal, and I. S. Pop. *A two-scale iterative scheme for a phase-field model for precipitation and dissolution in porous media*. Applied Mathematics and Computation 396 (2021), p. 125933. doi: 10.1016/j.amc.2020.125933.
- M. Kelm, S. Gärttner, C. Bringedal, B. Flemisch, P. Knabner, N. Ray. *Comparison study of phase-field and level-set method for three-phase systems including two minerals*. Computational Geosciences (2022). doi: 10.1007/s10596-022-10142-w

Die erste Publikation dieses Teils, s. Kapitel 8, beschäftigt sich mit reaktiven Transportprozessen bei denen das gelöste Mineral das Fluid verlassen und so zu einem Feststoff ausfallen kann. Gleichzeitig ist das feste Mineral in dem Fluid löslich und kann so gelöstes Mineral an das Fluid abgeben. Die veränderliche Fluid-Festkörper-Grenzfläche wird mittels eines Phasenfeldmodell auf der Porenskala modelliert. Es wird ein neues Phasenfeldmodell, das die Fluidströmung in Kombination mit Mineralausfällung und -auflösung erlaubt, formuliert. Die Verifikation erfolgt mittels numerischer Experimente und dem Vergleich mit dem Grenzzustand mit infinitesimaler Grenzflächendicke des Phasenfeldmodell. Durch die Verwendung von Grenzsichtmethoden wird gezeigt, dass sich das hergeleitete Modell für den Grenzzustand größtenteils zu dem erwarteten physikalische Modell vereinfacht.

Es bleibt nur die zusätzliche induzierte Bewegung durch die Krümmung des Phasenfeldmodells erhalten, die ein inhärenter Bestandteil von Phasenfeldmodellen ist. Anschließend wird das Phasenfeldmodell für ein periodisches Gebiet auf der Porenskala formuliert, um Homogenisierung anwenden zu können. Das Ziel dieses Kapitels ist nicht nur die Formulierung und Untersuchung des neuen Phasenfeldmodells für reaktive Transportprozesse, sondern ebenfalls die Herleitung eines Zweiskalenmodells bei dem das wirksame Modell für den reaktiven Transportprozess auf der Darcy-Skala die geometrischen Veränderungen durch Mineralausfällung und -auflösung auf der Porenskala berücksichtigen kann. Das resultierende Modell hat die gewünschte zweiskalige Struktur, bei der die Zellprobleme auf der Porenskala die sich verändernde Porengeometrie auflösen, so dass damit die wirksamen Parameter für das Modell auf der Darcy-Skala bestimmt werden können.

In der zweiten Publikation, s. Kapitel 9, wird das Zweiskalenmodell aus Kapitel 8 mittels einer heterogenen Mehrskalenmethode implementiert. Das Ziel ist die Konstruktion eines effizienten, robusten und genauen numerischen Lösungsverfahrens, welches das Verhalten auf der Darcy-Skala auflöst und dabei die Informationen von der Porenskala über die Lösung der in Kapitel 8 hergeleiteten Zellprobleme berücksichtigt. Dies wird durch die Verwendung eines iterativen Verfahrens mit zwei Arten von Adaptivität sichergestellt. Die Zellprobleme auf der Porenskala und das Problem auf der Darcy-Skala hängen voneinander ab, aber werden mittels eines partitionierten iterativen Ansatzes gelöst. Der Konvergenzbeweis des Verfahrens zeigt, dass die Konvergenz ausschließlich milde Bedingungen an die verwendete Zeitschrittweite und die verwendeten Parameter des Phasenfeldmodells hat. Zur Effizienzsteigerung wird Gitteradaptivität auf der Porenskala verwendet und gleichzeitig wird adaptiv entschieden, welche der Zellprobleme in einem Zeitschritt gelöst werden müssen. Die zweite Art der Adaptivität führt zu großen Einsparungen bezogen auf die benötigte Rechenzeit bei nur geringer Abnahme der Simulationsgenauigkeit.

Die dritte Publikation dieses Teils, s. Kapitel 10, berücksichtigt die Modellierung und Simulation von reaktiven Transportprozessen bei dem sich zwei verschiedene Mineralien auflösen und ausfällen können. Dies entspricht einem Dreiphasenproblem bei dem die numerische Simulation sehr anspruchsvoll ist. Das Ziel dieses Kapitels ist der Vergleich von zwei verschiedenen Ansätzen zum Lösen dieses anspruchsvollen Problems: Level-Sets und Phasenfelder. Beide Ansätze müssen an das Problem angepasst werden, um dreiphasige Probleme behandeln zu können. Um die drei Phasen und die zugehörigen Grenzflächen unterscheiden zu können, wird die Level-Set Gleichung mit Indikatorfunktionen gekoppelt. Das Phasenfeldmodell verwendet einen ternären Phasenfeldansatz bei dem drei Phasenfeldgleichungen (je eine für jede Phase) miteinander gekoppelt werden. Durch die Verwendung von Grenzschichtmethoden wird gezeigt, dass sich das Phasenfeldmodell für den Grenzzustand mit infinitesimaler Grenzflächendicke zu dem erwarteten physikalischen Modell vereinfacht. Es bleibt nur die zusätzliche induzierte Bewegung durch die Krümmung des Phasenfelds. Obwohl das Phasenfeldmodell eine höhere Effizienz bezogen auf den Rechenaufwand hat und masseerhaltend ist, leidet die Qualität der Approximation der korrekten zeitlichen Veränderung der drei Phasen aufgrund der durch die Krümmung induzierten Bewegung. Insbesondere die korrekte Repräsentation von Kanten ist schwierig. Die Berechnung von wirksamen Koeffizienten wie den Diffusionskoeffizienten oder der Permeabilität auf der Darcy-Skala mittels Homogenisierung zeigen, dass die effektiven Parameter für beide Ansätze gut miteinander übereinstimmen.

Teil D beschäftigt sich mit der Verdunstung von salzhaltigem Wasser aus einem porösen Medium, bei dem der Gradient der Salzkonzentration durch die Verdunstung zu Dichtestabilitäten führt. Dieser Teil basiert auf der folgenden Publikation:

- C. Bringedal, T. Schollenberger, G. J. M. Pieters, C. J. van Duijn, R. Helmig. *Evaporation-Driven Density Instabilities in Saturated Porous Media*. Transport in Porous Media (2022). doi: 10.1007/s11242-022-01772-w.

Diese Publikation, s. Kapitel 11, ist durch Versalzung und deren potentiell großen Umwelteinfluss motiviert. Bei Böden, die mit salzhaltigem Wasser gesättigt sind, induziert die Verdunstung von Wasser eine Ansammlung von Salz in den oberen Erdschichten, da das Salz bei der Verdunstung im Boden verbleibt. Wenn der Salzgehalt in diesen Schichten wächst, dann wird die Löslichkeitsgrenze von Salz in Wasser unvermeidlich erreicht und es bildet sich eine Salzkruste an der Oberfläche und der Boden versalzt. Allerdings ist der Zustand mit salzhaltigerem Wasser an der Oberfläche gravitationsbedingt instabil, da das salzhaltigere Wasser eine höhere Dichte hat als das restliche Wasser. Dies kann wiederum zu Dichteinstabilitäten führen. Diese Dichteinstabilitäten können zu einem Transport von Salz weg von der Oberfläche in tiefere Erdschichten verursachen, wodurch die Salzkonzentration an der Oberfläche insgesamt abnimmt und somit die Salzausfällung an der Oberfläche verhindert wird. Das Ziel dieses Kapitels ist die Untersuchung der Anfangszeiten zu denen die Dichteinstabilitäten beginnen aufzutreten und zu analysieren, ob diese Instabilitäten die Salzausfällung verhindern. Dies wird mittels einer linearen Stabilitätsanalyse und numerischen Simulationen erreicht. Die Anfangszeiten liegen bei realistischer Wahl der Parameter je nach Permeabilität im Bereich von Stunden bis Tagen, während das Salz auch bei Instabilitäten noch ausfallen kann, da sich die Instabilitäten nur langsam entwickeln, was deren Stärke betrifft. Es wird in diesem Kapitel eine vereinfachte Analyse auf der Darcy-Skala durchgeführt. Nichtsdestotrotz sind die Prozesse auf der Porenskala für die Interaktion zwischen Wasser (flüssig) und Luft (gasförmig) auf der Porenskala des porösen Mediums und für die Veränderung der Porengeometrie durch die Salzausfällung auf der Porenskala relevant. Wie man die Analyse durch die Integration von Mehrskalensätzen weiter verbessern kann, wird in Kapitel 12 vorgestellt.

Im abschließenden Kapitel dieser Arbeit, s. Kapitel 12, werden die wichtigsten Erkenntnisse zusammengefasst und weitere Ideen für weiterführende Forschung für alle Problemtypen und Mehrskalensätze, die in dieser Arbeit diskutiert werden, vorgestellt.

Bevor die jeweiligen Publikationen in den folgenden Kapiteln im Detail vorgestellt werden, wird zunächst in Kapitel 1 ein Überblick über die verschiedenen Anwendungen, die verschiedenen Skalen und die zugehörigen Modelle dieser Arbeit gegeben. Außerdem werden die verwendeten Mehrskalensätze erläutert und die Verbindungen zwischen den verschiedenen Kapiteln im Bezug auf den Inhalt und die Bedeutung der dort verwendeten Mehrskalensätzen erläutert.

Summary

Flow and transport processes in porous media are important for several technical, geological and biological systems. Modeling and simulation of such processes pose many challenges for research in the fields of engineering, mathematics and computer science. One reason for this is that flow and transport processes in porous media are generally coupled processes, where the interactions between the flowing fluid (or fluids) and the porous medium give rise to highly coupled problems. Another reason is the large difference in scales inherent in these processes and in the porous medium itself. Couplings and interactions at one scale can be different than at another scale. Hence, understanding which processes are relevant at the scale of interest is a vital question when dealing with modeling and simulation of transport processes in porous media.

These aspects motivate the use of multiscale approaches for modeling and simulating these transport processes. In this habilitation thesis, several types of multiscale methods and approaches are applied to analyze behavior within the porous medium and to understand the interaction between different scales of the porous medium. The multiscale approaches considered in this thesis can be divided into four categories:

- Transversal averaging, which is applied when dealing with long and thin domains to find a dimensionally reduced model for effective behavior.
- Boundary-layer methods, which are applied to address effective behavior close to and far away from a singularity or discontinuity.
- Homogenization, which is applied to locally periodic problems to find the effective behavior at a larger scale.
- Heterogeneous multiscale methods, which are applied to design numerical schemes for models coupled over two (or more) scales.

To be able to demonstrate the application of these method in the context of transport processes in porous media, we consider three main types of transport behavior, that all play an important role in environmental sciences, energy supply and material sciences. These are multiscale parabolic problems (diffusion/conduction processes), two-phase porous-media flow, and reactive transport with heterogeneous reactions. These three forms of flow and transport represent different physics and interactions within the porous medium, and they manifests themselves differently depending on the scale in question. For the multiscale parabolic problems, we are mainly concerned with finding effective diffusion/conduction coefficients that are valid at larger scales in order to be able to model and simulate large-scale applications, while still accounting for the influence from small-scale processes. Two-phase flow problems rely on completely different model equations depending on whether the smaller pore scale or a larger, effective scale is considered, and the connection between these scales is generally not clear nor well understood. In the case of reactive transport with heterogeneous reactions, the fluid flow and transport of solute interact with the solid part of the porous medium, resulting in an evolving porous medium. How to model this evolution at the pore scale and its influence on the larger scale are challenging tasks.

These differences in processes and connected challenges motivate the consideration of the following parts of the thesis:

- A Multiscale parabolic problems
- B Two-phase porous-media flow
- C Reactive transport with heterogeneous reactions
- D Evaporation from porous media

The first three parts consist of three publications each, all addressing various multiscale aspects of the process in question. The fourth part stands out as only containing one publication and by not considering any multiscale aspects explicitly. However, this last part addresses processes treated in all the three first parts, which motivates the use of multiscale approaches also for this context for increased understanding. These aspects are further discussed in the Conclusion and outlook of this thesis, which is found in Chapter 12. All publications included in this thesis are the original publications, where the respective journals have granted permission to re-use the published work in this thesis.

Part A focuses on effective behavior of parabolic problems, representing pressure distribution, diffusion or heat conduction in porous media. This part is based on the publications

- M. Bastidas, C. Bringedal, I. S. Pop, and F. A. Radu. *Numerical homogenization of non-linear parabolic problems on adaptive meshes*. *Journal of Computational Physics* 425 (2021), p. 109903. doi: 10.1016/j.jcp.2020.109903.
- L. Scholz and C. Bringedal. *A Three-Dimensional Homogenization Approach for Effective Heat Transport in Thin Porous Media*. *Transport in Porous Media* 141.3 (2022), pp. 737–769. doi: 10.1007/s11242-022-01746-y.
- C. Bringedal and K. Kumar. *Effective Behavior Near Clogging in Upscaled Equations for Non-isothermal Reactive Porous Media Flow*. *Transport in Porous Media* 120.3 (2017), pp. 553–577. doi: 10.1007/s11242-017-0940-y.

In the first publication, corresponding to Chapter 2 of this thesis, we consider a non-linear parabolic equation. This equation could represent the fluid pressure in the context of modeling unsaturated flow with Richards equation, after applying the Kirchhoff transformation. However, the equation can, in particular in the linearized case, also represent a standard diffusion or heat conduction problem. The main goal of this chapter is to design an efficient and accurate numerical scheme by using adaptive meshes. The mesh adaptivity is based on a local error estimate. However, the use of coarse and fine meshes raises the need to find the effective diffusion coefficient (or permeability, in the context of Richards equation) on the scales represented by these meshes. The starting point is known fine-scale information, and homogenization together with an algorithm based on heterogeneous multiscale methods are used to design the numerical algorithm. An interesting point is that, although homogenization generally relies on local periodicity, applying it to problems not having this property is still found to give reasonable results when combined with local error estimates and mesh adaptivity.

In the second publication, corresponding to Chapter 3 of this thesis, we consider heat transport through a thin porous medium. The starting point is a pore-scale model, where heat transport in the saturating fluid is coupled with heat transport through the solid

grains. To discretize such a detailed geometry to perform numerical simulations, would require very fine meshes. The goal of this chapter is to instead derive effective equations allowing a description of the heat transport on the Darcy scale. Since the porous medium is thin, a homogenization strategy combined with transversal averaging is applied to derive the Darcy-scale model. Hence, a dimensionally reduced Darcy-scale model is found. This adapted homogenization procedure results in cell problems that can be solved to find the effective heat conductivity of the porous medium. The boundary conditions of the top and bottom boundary of the thin porous medium appear in the cell problems, and hence influence the effective heat conductivity. This chapter also shows how well the results of the effective model represents the average of the results from the original pore-scale model through a numerical example.

The third publication in this part, found in Chapter 4, concerns effective behavior in a porous medium that is evolving due to heterogeneous chemical reactions, and hence combines aspects found in Part A and in Part C. Since the main focus of this chapter is on the behavior of the effective parameters permeability, solute diffusion and heat conductivity, the chapter is still placed in Part A. The chapter builds on a previously derived two-scale model which has been found by homogenization. The two-scale model couples Darcy-scale flow, solute transport and heat transport, with pore-scale cell problems accounting for the evolution of the pore-scale geometry due to mineral precipitation and dissolution, which results in changes of the permeability, effective diffusion coefficient and effective heat conductivity at Darcy scale. The goal of this chapter is to investigate the behavior of these effective parameters, in particular in the case when the porous medium is close to clogging due to mineral precipitation. For simple grain shapes, for example circular, the effective parameters can be found in terms of parametrized expressions, which highly simplifies numerical simulations at the Darcy scale. When such parametrized expressions are applicable, a heterogeneous multiscale scheme is not needed.

Part B focuses on finding effective behavior of two-phase flow, where the interaction between the two fluids at the pore scale is accounted for. This part is based on the publications

- S. Sharmin, C. Bringedal, and I. S. Pop. *On upscaling pore-scale models for two-phase flow with evolving interfaces*. Advances in Water Resources 142 (2020), p. 103646. doi: 10.1016/j.advwatres.2020.103646.
- S. B. Lunowa, C. Bringedal, and I. S. Pop. *On an averaged model for immiscible two-phase flow with surface tension and dynamic contact angle in a thin strip*. Studies in Applied Mathematics 147.1 (2021), pp. 84–126. doi: 10.1111/sapm.12376.
- S. Sharmin, M. Bastidas, C. Bringedal, and I. S. Pop. *Upscaling a Navier-Stokes-Cahn-Hilliard model for two-phase porous-media flow with solute-dependent surface tension effects*. Applicable Analysis (2022), doi: 10.1080/00036811.2022.2052858.

The first publication of this part, corresponding to Chapter 5, addresses two-phase flow in a thin strip. Such a thin strip can represent a single pore in a porous medium, but is also relevant for flow through pipes or as an interface layer between two compartments. The two fluids have a layered structure, which means that interface between the two fluids is assumed to be stretching along the strip. The fluid-fluid interface is still allowed to evolve due to the flow and surface tension between the two fluids. The goal of this chapter is to derive different effective models depending on which regime in terms of capillary number

and viscosity ratio between the fluids is considered. Since the domain is a long, thin structure, transversal averaging across the strip is used to find the effective behavior. The derived effective models are hence dimensionally reduced as only variability along the strip has to be explicitly resolved. Due to the incorporation of the evolving fluid-fluid interface, the derived effective models are similar to extended Darcy's law for two-phase flow, but with a non-standard form. Numerical experiments resolving the original two-dimensional geometry show that the effective models can capture the transversally averaged behavior as the strip becomes thinner and longer.

In the second publication, corresponding to Chapter 6, two-phase flow in a thin strip is again considered. In this case, one fluid phase displaces the other, which corresponds to the fluid-fluid interface is stretching across the strip. As before, the fluid-fluid interface can evolve due to the flow and surface tension. A dynamic contact angle is used to model the fluid-fluid-solid contact point. Transversal averaging can only be applied to derive the effective behavior in regions away from the fluid-fluid interface. Since the interface here represents a discontinuity in the system and quite different behavior is found near the interface, boundary-layer methods are applied to handle these interactions. The goal of this chapter is to find a closed, dimensionally reduced model for the flow through the thin strip, accounting for the interactions between the fluids as one displaces the other. This is achieved by combining transversal averaging with boundary-layer methods. As in Chapter 5, an effective model similar to an extended Darcy's law is found, but with a non-standard form. The resulting effective model is used to investigate effective properties that are well-known for two-phase porous-media flow, like dynamic capillary pressure and hysteretic effects.

The third publication of this part, corresponding to Chapter 7, considers two-phase flow in a periodic porous medium. Here, no special restrictions are placed on the appearance of the fluid-fluid interface and is therefore modeled with a phase-field equation on the pore scale. The periodicity of the pore-scale structure allows to use homogenization to derive a model for the effective behavior at Darcy scale. The goal of this chapter is to derive a two-scale model, where the Darcy-scale model equations for the two-phase porous-medium flow rely on local pore-scale cell problems to calculate effective parameters. In particular, we are here interested in the case when the evolving fluid-fluid interface is influenced by a varying surface tension between the two fluids. The derived Darcy-scale equations show similarities with standard two-phase porous-medium flow models without capillary pressure, but separates by calculating effective parameters via pore-scale cell problems. In these cell problems, the evolving fluid-fluid interface is resolved, capturing the influence of the varying surface tension. An explicit numerical scheme of the two-scale model, inspired by the ideas of heterogeneous multiscale methods, is applied to show the effect of the varying surface tension at the Darcy scale.

Part C focuses on pore-scale modeling, finding effective behavior, and two-scale simulations of reactive transport in porous media, where the pore-scale geometry evolves due to mineral precipitation and dissolution. This part is based on the publications

- C. Bringedal, L. von Wolff, and I. S. Pop. *Phase Field Modeling of Precipitation and Dissolution Processes in Porous Media: Upscaling and Numerical Experiments*. Multiscale Modeling & Simulation 18.2 (2020), pp. 1076–1112. doi: 10.1137/19M1239003.
- M. Bastidas Olivares, C. Bringedal, and I. S. Pop. *A two-scale iterative scheme for*

a phase-field model for precipitation and dissolution in porous media. Applied Mathematics and Computation 396 (2021), p. 125933. doi: 10.1016/j.amc.2020.125933.

- M. Kelm, S. Gärttner, C. Bringedal, B. Flemisch, P. Knabner, N. Ray. *Comparison study of phase-field and level-set method for three-phase systems including two minerals*. Computational Geosciences (2022). doi: 10.1007/s10596-022-10142-w

The first publication in this part, corresponding to Chapter 8, addresses reactive transport, where solute transported in the fluid can leave the fluid and precipitate as solid mineral, and mineral can dissolve and hence release solute to the fluid. The evolving fluid-solid interface is modeled with a phase-field equation at the pore scale. A new phase-field model allowing for fluid flow in combination with mineral precipitation and dissolution is formulated. The model is verified against its sharp-interface limit, and numerically by comparing with available benchmarks. By applying boundary-layer methods, the sharp-interface limit is found to reduce to the expected sharp-interface physics, with the exception of curvature-driven motion. The presence of such curvature-driven motion is an inherent part of phase-field models. The phase-field model is then formulated in a pore-scale domain, which is periodic. Then, homogenization can be applied. The goal of this chapter is not only to formulate and investigate a new phase-field model for reactive transport, but also to find a two-scale model where the effective Darcy-scale model for reactive transport can incorporate the pore-scale geometrical changes due to the mineral precipitation and dissolution. The resulting model derived by homogenization has this desired two-scale structure, where pore-scale cell problems resolve the evolving pore-scale geometry and provide effective parameters to the Darcy-scale model equations.

In the second publication, corresponding to Chapter 9, the two-scale model from Chapter 8 is implemented using a heterogeneous multiscale method. The goal is to obtain an efficient, robust and accurate numerical algorithm that resolves the Darcy-scale behavior by incorporating information from the pore scale through the solutions of the derived cell problems from Chapter 8. This is achieved by applying an iterative scheme with two forms of adaptivity. The pore-scale cell problems and Darcy-scale model equations depend on each other, but are solved using a partitioned, iterative approach. The convergence of the scheme is proved with only mild restrictions on the time-step size and on the phase-field parameters. For increased efficiency, mesh adaptivity at the pore scale is applied, and also adaptivity in terms of which cell problems are to be solved. The latter adaptivity offers a large gain in terms of reduced computational costs, with only relatively minor loss of accuracy.

The third publication of this part, corresponding to Chapter 10, considers modeling and simulation of reactive transport where two different minerals can dissolve and precipitate. This corresponds to a three-phase problem, which is challenging to simulate. The goal of this chapter is to compare two possible approaches for this challenging setting, namely level sets and phase fields. Both approaches need adaptations to handle such a three-phase setting. To be able to separate the different phases and interfaces, the level-set equation is coupled with indicator functions. The phase-field model is using a ternary phase-field approach, where three phase-field equations (one for each phase) are coupled to each other. Using boundary layer methods, the sharp-interface limit of the phase-field model reduces to the expected sharp-interface physics, but with additional curvature-driven motion. Although the phase-field model is computationally more efficient and is also mass conservative, it struggles to capture the correct evolution of the phases due to this curvature-driven motion. Especially corners are difficult to represent properly. By applying homogenization, effective

properties as Darcy-scale diffusion and permeability, are found to still compare well between the two approaches.

Part D concerns evaporation of saline waters from porous media, where density instabilities develop due to the gradient in solute concentration, which is caused by the evaporation. This part is based on the publication

- C. Bringedal, T. Schollenberger, G. J. M. Pieters, C. J. van Duijn, R. Helmig. *Evaporation-Driven Density Instabilities in Saturated Porous Media*. Transport in Porous Media (2022). doi: 10.1007/s11242-022-01772-w.

This publication, which corresponds to Chapter 11, is motivated by soil salinization, which has a potentially large environmental impact. For soils saturated with saline water, evaporation of the water induces accumulation of salt near the upper parts of the soil as salts stay behind during the evaporation. If the salt concentration continues to build up, the solubility limit will eventually be reached, causing a salt crust and soil salinization. However, as this setting is also gravitationally unstable with saltier, denser waters on top of less dense water, density instabilities can develop. These density instabilities have the potential to give a net downwards transport of salt, avoiding salt to precipitate. The goal of this chapter is to investigate the onset times for when density instabilities can start to develop, and whether they can hinder salt precipitation. This is achieved by applying linear stability analysis and numerical simulations. Onset times are for realistic parameter choices found to be in the range of hours to days depending on the permeability, while salt is found to still potentially precipitate even if instabilities occur, as the instabilities develop slowly in terms of strength. In this chapter, a simplified Darcy-scale analysis is performed. However, pore-scale processes are relevant - both in terms of the interaction between water and air phases on the pore scale of the porous medium, and in terms of the evolution of the pore-scale geometry due to salt precipitation. How to further improve this analysis by integrating multiscale approaches is discussed in Chapter 12.

In the final chapter of this thesis, Chapter 12, we summarize the main findings and discuss directions of further research for all the types of problems and multiscale approaches addressed in this thesis.

Before we present the different publications to more detail in the following chapters, we first give in Chapter 1 an overview of the applications addressed by this thesis, as well as the considered scales and model equations. Furthermore, we explain the multiscale approaches that are applied in the respective chapters, and it is shown how the different parts and chapters are connected in terms of content and the role of the multiscale approaches.

1 Introduction

Porous media appear inside fuel cells, in the subsurface and in the human body. Flow and transport processes in porous media therefore play a role for several technical, biological, environmental and everyday applications - from medical treatment to enhanced oil recovery and development of renewable energies. Especially in the subsurface, transport processes through porous media are important, see Figure 1.1. In this figure, several applications are highlighted, where transport of heat, solutes and fluids through the subsurface plays a role. Some of these applications will be addressed to greater detail in this thesis. We will especially focus on geothermal energy (point 6 in Figure 1.1) and soil salinization, which is related to groundwater flow (point 7 in Figure 1.1).

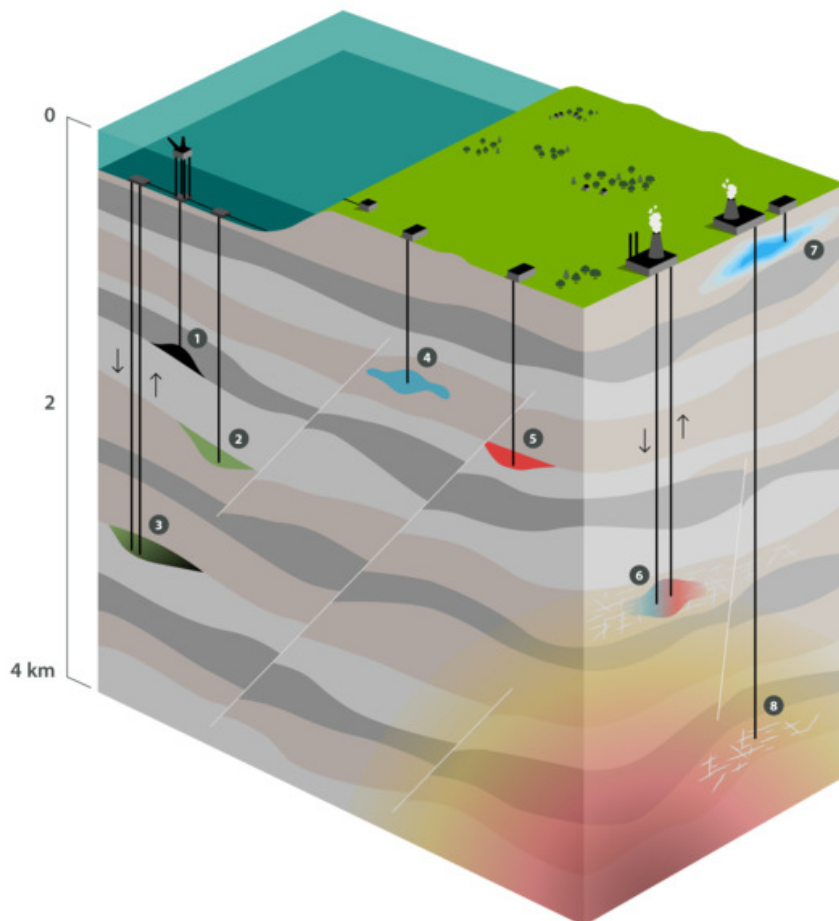


Figure 1.1: Sketch of subsurface applications, where transport processes in porous media are relevant. The following applications are highlighted: 1. Oil and gas production. 2. CO₂ storage. 3. CO₂ utilization and storage. 4. Wastewater disposal. 5. Hydrogen, methane and energy storage. 6. Geothermal energy production. 7. Groundwater flow. 8. Supercritical geothermal energy. Figure by Center for Modeling of Coupled Subsurface Dynamics (CSD).

In the following, we highlight challenges and possibilities for three different applications all depending on transport through porous media: geothermal energy, soil salinization, and fuel cells.

Geothermal energy Geothermal energy is an environmentally friendly energy which utilizes the thermal energy stored in the earth's crust. The subsurface becomes gradually warmer with depth, which is quantified through the geothermal gradient. There are several ways to utilize this thermal energy, and we highlight here energy production by using two wells: one injection well where cold water is injected, and one production well where warm water is produced, as highlighted in point 6 in Figure 1.1. The temperature difference between the injected and produced water corresponds to an energy gain, which can be converted to electricity or used directly for heating purposes. Geothermal energy can be produced independent of weather conditions and is associated with low emissions per produced kWh compared to natural gas, oil and coal [39]. According to [14], the total installed capacity of geothermal used for electricity in 2015 was 12.7 GW, with a forecasted capacity of 21.4 GW for 2020 (numbers from 2016). The reported long-term targets add up to 140 GW in 2050, which is estimated to be 8.3% of the total world electricity production [14]. The main part of the production is located in hotspots, with Philippines, New Zealand, USA, Mexico, Italy, Iceland and Kenya being the largest producers. Although much of the production occurs near continental rift zones where the geothermal gradient is larger than average, geothermal energy can also be utilized in other regions by drilling deeper or by enhanced geothermal systems [97].

In order to quantify the potential heat production of a geothermal reservoir, understanding the fluid flow and heat transport processes in the subsurface porous medium is vital. Mathematical and numerical modeling of the interaction between flow and heat transport are therefore important in geothermal energy research. In particular, when cold fluid is injected into the subsurface, and is gradually heated as it flows through the porous domain towards the production well, chemical reactions play a role. Precipitation and dissolution of minerals as anhydrite, calcite, silica and quartz are known to cause the porosity and permeability of the geothermal reservoir to change [74, 96, 109, 113, 117]. See Figure 1.2 for an illustration. The mineral precipitation and dissolution are to a large extent caused by the solubility of these minerals being temperature-dependent [81]. Hence, there is an interaction between the fluid flow, heat transfer and chemical reactions within geothermal reservoirs. Understanding these processes and especially their large-scale influence on the flow and transport through geothermal reservoirs is essential within geothermal energy research.

Soil salinization Groundwater in the subsurface is usually located near the upper parts of the underground, see point 7 in Figure 1.1. The groundwater can be saline, which can be due to marine influence in coastal regions, or due to natural or anthropogenic terrestrial reasons [106]. The latter types are typical in regions with climatic conditions supporting large evaporation rates, but low amount of groundwater flushing (e.g. low amount of rain and horizontal groundwater flow) that could transport salts dissolved in the groundwater away [118]. As water evaporates to the atmosphere, salts accumulate near the top of the porous medium as they stay behind during evaporation. See Figure 1.3 for an illustration of involved processes that can influence soil salinization and salt precipitation. In soils, soil salinization has a large environmental impact as it hampers plant growth and affects

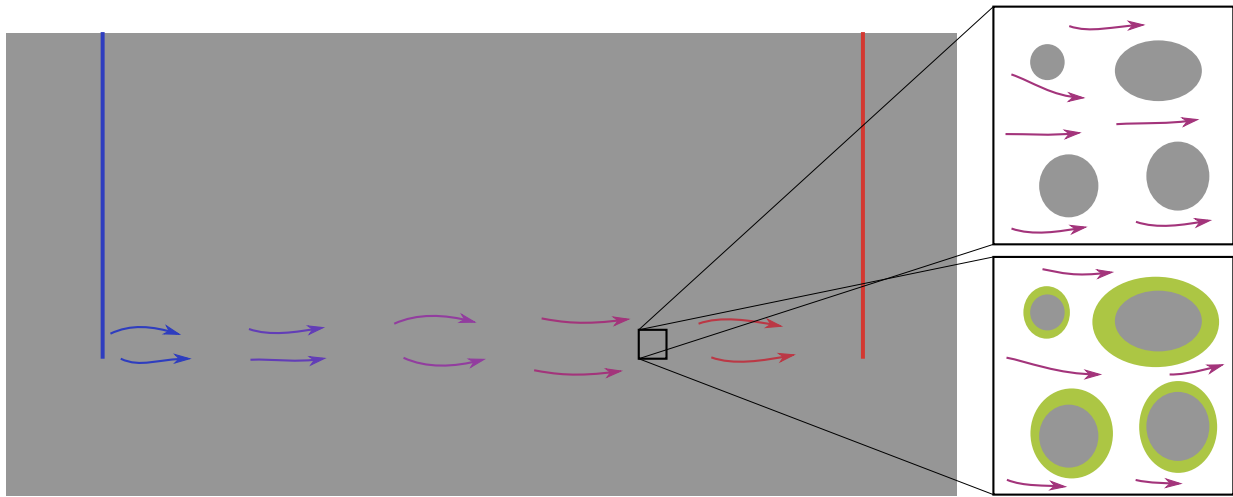


Figure 1.2: Illustration of flow (arrows) through a geothermal field from the cold injection well (blue line) to the warmer production well (red line). The injected fluid gradually heats up as it flows, but replaces fluid that was initially warmer. The inlets at the right show a zoomed-in view of how mineral (in green) can change the pore-scale porous geometry as it precipitates or dissolves.

biological activities [29]. High salinity in the water can also affect the photosynthesis of plants as the salinity causes stress for the plants [25].

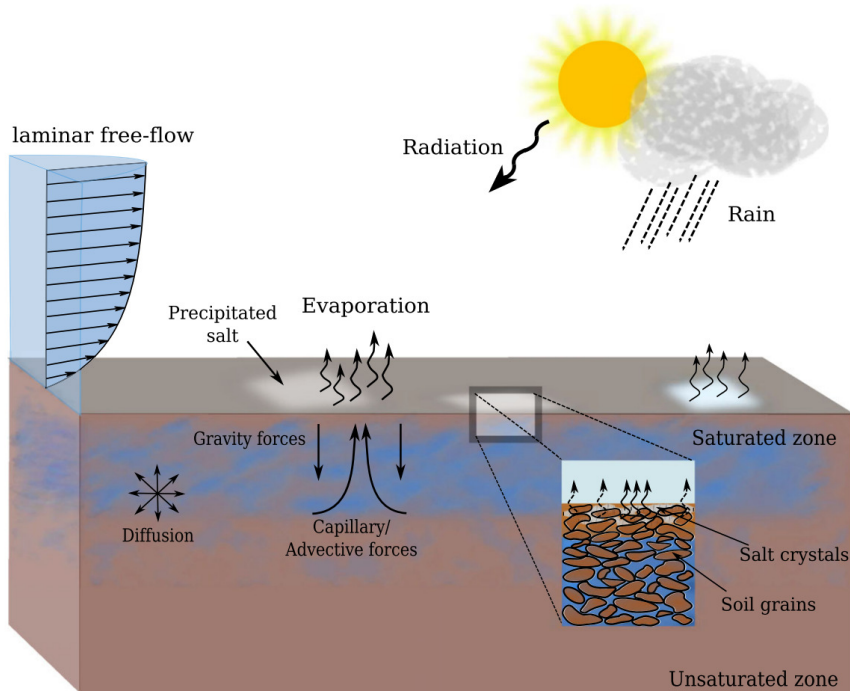


Figure 1.3: Illustration of involved processes for evaporation causing soil salinization and salt precipitation in the upper part of soil. Figure from [54]. Reprinted with permission from Springer.

In arid regions, soil salinization has a major impact on agricultural activities [68, 92]. According to [106], 24 030 million km² around the globe have a significant likelihood of

groundwater salinity at shallow and intermediate depths, where evaporation of shallow groundwater is a cause for around 20% of these. To analyze such processes in the subsurface, one has to model the interplay between the groundwater flow and connected salt transport by the groundwater. Due to the evaporation, also air (and vapor) flows through the upper parts of the porous medium, influencing the groundwater flow. In this case, the flow is unsaturated [95]. Also, as the water evaporates and causes the salt concentration to increase, the salt can eventually reach its solubility limit and precipitate. The salt precipitation can create a salt crust at the top of the soil, creating a barrier to the atmosphere as the soil is clogged [54], see Figure 1.4. However, the setting with saltier water located above water that is less salty, is gravitational unstable. Hence, density instabilities in the form of fingers can be triggered and potentially cause a net downwards transport of salt [114, 115]. Hence, behind the process of soil salinization, there are several coupled porous-media transport processes that influence each other.

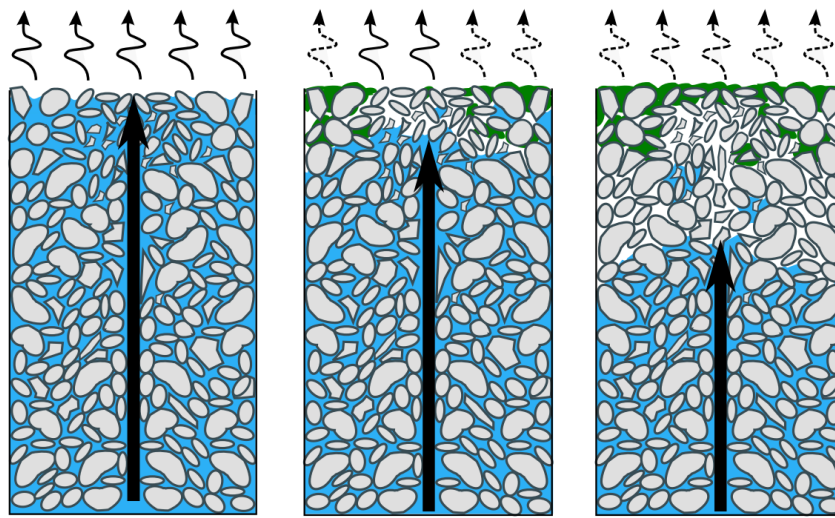


Figure 1.4: Illustration of how salt (green) precipitates at the top of the soil due to evaporation. Figure from [54]. Reprinted with permission from Springer.

Fuel cells A significant amount of global CO_2 emissions come from traffic. Hence, finding alternative power technologies with less emissions can have a large, positive impact. One possibility is the use of fuel cells. Fuel cells operating on hydrogen do not generate any CO_2 emissions as the only exhaust products are air and water. Hydrogen still needs to be produced, which comes with some emissions [10]. However, the overall CO_2 emissions from hydrogen fuel cells compared to traditionally fueled cars and trucks are very low [53]. There are different types of fuel cell technologies. They all rely on letting hydrogen react with oxygen to create electricity (and water), but operate under different conditions, affecting their efficiency but also applicability. We here focus on Proton Exchange Membrane (PEM) fuel cells, which operate at temperatures of $60\text{-}100^\circ\text{C}$, are less efficient than other fuel cell technologies, but they can vary the generated power quickly and are hence amendable for transportation purposes [88]. Inside a PEM fuel cell, hydrogen and oxygen from air react in a two-step reaction. In the anode, hydrogen (H_2) splits into two H^+ cations, which are also known as protons, and two electrons. The protons can go through the membrane, while the electrons have to go around, generating a current. On the cathode side, oxygen (O_2) reacts

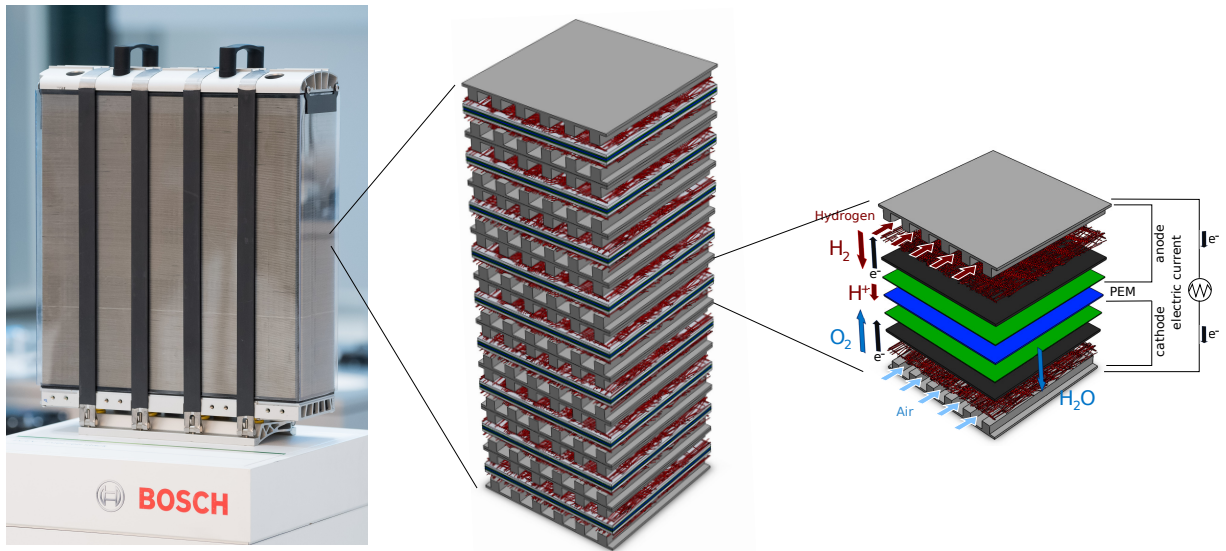


Figure 1.5: PEM fuel cells. Left: example of larger fuel cell stack, consisting of several towers of fuel cells on top of each other (middle). Right: one single PEM fuel cell, where oxygen (via air) and hydrogen are supplied via gas channels (blue and red horizontal arrows). On the anode side, H^+ cations can go through the membrane (blue layer), while electrons go around. On the cathode side, they react with oxygen to create water, which then has to be transported away in the air gas channel. Figure from Bosch, with support from C. Michalkowski.

with four H^+ cations and four electrons, to create water (H_2O), which is in liquid form. See Figure 1.5. On the cathode side, oxygen (typically in the form of air) has to be supplied, while liquid water has to be removed. This takes place in the same gas channel, which is connected to the cathode through a porous medium, known as the gas diffusion layer. See Figure 1.6 for a sketch. Water has to be removed fast enough to not flood the fuel cell and cut off air supply. Hence, we have a two-phase flow problem both in the porous medium, and in the gas channel [8]. The water management of PEM fuel cells is quite essential for their performance and much effort is placed in the design of the porous medium and the gas channel for optimal water management [66, 78]. However, especially inside the porous medium, the behavior of this two-phase flow is sensitive to the description of wettability

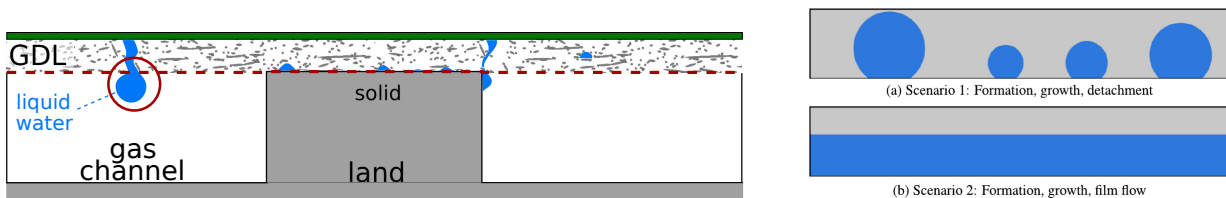


Figure 1.6: Two-phase flow processes in the gas channel on the cathode side. Left: water droplets emerging in the gas channel from the gas diffusion layer (GDL), which is connected to the cathode (green). Figure adapted from [71] with support from C. Michalkowski. Right: two possible two-phase flow scenarios in the connected gas channel, where an increased amount of water (blue) appears in the form of droplets, alternatively as a layer. Figure from [3].

and capillary pressure [4, 71]. In the gas channel, one has two-phase flow in a long, narrow domain, which is also challenging to model [3, 70].

These applications motivate the study of transport processes in porous media. The focus of this thesis is mainly on multiscale aspects of such processes. This introductory chapter presents an overview of the modeling and multiscale concepts used in this thesis. We first discuss why multiscale models and simulations are beneficial when addressing porous-media transport processes in Section 1.1. Then, an overview of the model equations at the considered scales are presented in Section 1.2. Afterwards we present the multiscale approaches that are applied in this thesis to bridge the gap between the various scales in a porous medium in Section 1.3. Finally, in Section 1.4 a detailed overview of the structure of the thesis is given. Here, we describe the main motivation, approach and contribution of the publications included in the thesis.

1.1 Why use multiscale models and simulations for transport processes in porous media?

We are in this thesis concerned with the flow of one or several fluids filling a porous medium, and the transport of chemical components and heat through the porous medium. This thesis addresses the following three main forms of flow and transport through porous media:

- Diffusive/conductive transport, which can be modeled by a parabolic problem.
- Two-phase flow, where two immiscible fluids interact with each other.
- Reactive transport, where a fluid transports one or more chemically reactive solutes which can cause the structure of the porous medium to change.

These different types of transport processes come with different challenges, and we are here mainly concerned with multiscale aspects to model and simulate such processes. Before going further into detail of these three transport processes, we first discuss some general aspects of scales in porous media.

A porous medium is inherently scale dependent. A porous medium can, in the simple case, be characterized as a medium consisting of solid space and void space, where the void space in our case will be filled with one or more fluids. However, the behavior of these processes differ depending on which scale one considers. We will mainly address the pore scale and the so-called Darcy scale, and we will in the following explain what is meant with these two scales. The pore scale considers a detailed view of the porous medium, meaning that one considers and models the detailed geometric structure where the solid and fluid-filled void space can be separated and hence be seen as separate domains. Transport processes occurring in each domain (e.g. within fluid and solid, or within each of the fluids for two-phase flow) can be formulated using partial differential equations defined on the different domains. The pore scale hence allows for highly detailed models, and therefore highly detailed simulations of the relevant processes. Typical length scales at the pore scale are in the order of magnitude $10^{-6} - 10^{-3}$ m, see Figure 1.7 for an overview. However, this also means that a very fine grid is needed to resolve the detailed processes at the pore scale. The inlets at the right part of Figure 1.2 and of Figure 1.3, and the illustration in

1.1 Why use multiscale models and simulations for transport processes in porous media?

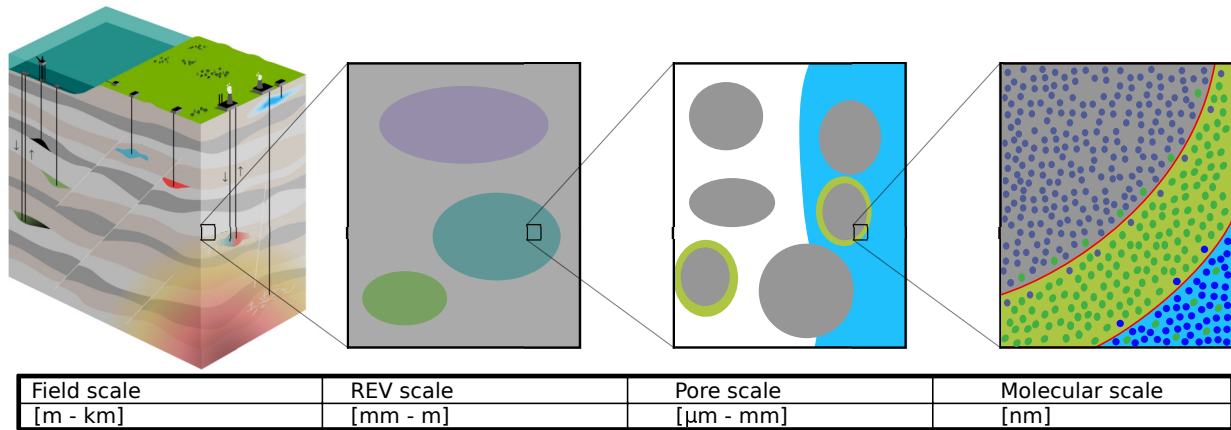


Figure 1.7: Overview of scales and related length scales. The field and REV scale will be commonly called Darcy scale. In this thesis we are mainly concerned with Darcy and pore scale. Figure inspired by [50].

Figure 1.4 are both examples of pore-scale domains, since the fluid and solid domains are explicitly separated. Also the gas channels in Figure 1.6 can be seen as a form of pore scale in the sense that void and solid space are explicitly separated.

Unfortunately, for most practical applications, simulating a pore-scale model for the entire domain of interest is not feasible due to the large computational costs. In stead one can use models that rather take an averaged approach. The idea is that behavior at the pore scale can be averaged over an *representative elementary volume* (REV). This gives rise to the name REV scale, which is the scale where such averages can be defined in a meaningful manner. Since only averages are used, detailed behavior from the pore scale is no longer available. The porous medium at REV scale can hence not be separated into solid and void space explicitly, but can only be described through averaged quantities such as the void fraction within an REV; the porosity. Variables are also only available as averaged quantities, e.g. the average fluid velocity through the REV. Hence, at REV scale one deals with one averaged domain representing both fluid(s) and solid space within the REV. Processes at REV scale are formulated using partial differential equations for the averaged variables using averaged parameters. How large an REV is, and hence what a typical length scale on the REV scale is, depends on the structure of the porous medium and the considered process. Typical length scale are around 10^{-3} m to 1 m, as highlighted in Figure 1.7. This means that for a simulation at the REV scale, a much coarser grid compared to the pore scale can be applied. However, this comes with the cost of not being able to resolve detailed information anymore as only averaged behavior can be found. If averaging over the inlets of Figure 1.2 or Figure 1.3, or over each of the three columns in Figure 1.4, an REV is obtained. That means, in a REV-scale simulation, each of these REV's are represented as one grid cell, where one porosity and one averaged velocity are used to represent the behavior within it.

Although the REV scale can be up to meters, one would in certain applications - typically for subsurface applications like geothermal energy and groundwater flow - be interested in domains ranging for several kilometers. In this case, averaged approaches for even larger scales are to be considered. This larger scale is called field scale when stretching beyond meters, as highlighted in Figure 1.7. In Figure 1.1, Figure 1.2 and Figure 1.3, a field-scale view is taken as the domains in question typically range several kilometers. The field scale

is similar to the REV scale in the sense that averaged behavior is sought. But where the REV scale typically addresses the smallest possible scale where an averaged behavior can be defined, the focus of the field scale is to use a scale amenable for simulations of large-scale applications. However, the model equations at the REV and field scales would generally be the same, but with different values for averaged parameters to model the averaged behavior at their scale. For single-phase fluid flow, both would apply Darcy's law for the average flow rate through the porous medium. In Darcy's law, the average flow rate is proportional to the average pressure gradient, where the proportionality constant is equal to the porous medium's permeability divided by the fluid viscosity. The permeability is a measure of the porous medium's ability to transmit fluid. Hence, the value of the permeability would typically vary between the REV scale and the field scale. At the field scale, averaged permeabilities at a coarser grid are used. However, since Darcy's law can be applied at both scales, the REV and field scales are often commonly called the Darcy scale. In this thesis, we will generally use the phrase Darcy scale when we refer to a porous domain where an averaged view is taken and Darcy's law can be applied to describe the flow. Hence, Darcy scale can refer to either the REV scale or the field scale depending on the considered length scale.

The Darcy scale is much more amenable for modeling and simulating practical applications compared to the pore scale, due to its efficiency by considering averaged quantities and variables. However, detailed information about the pore-scale processes is potentially lost when considering a pure Darcy-scale model. This can lead to inaccurate or wrong models and simulation results when pore-scale processes affect the Darcy-scale behavior. How that can happen for the above-mentioned transport processes, we will highlight in the following.

Parabolic problems Diffusive or conductive transport processes are relevant in a wide range of applications in porous media [12]. Such processes can describe the diffusive redistribution of temperature or a solute concentration as described by the traditional heat equation [48], but can also model the pressure distribution at the Darcy scale in the case of single-phase and multi-phase flow [46]. The common factor between these different applications and processes is that they can be described with a (linear or non-linear) parabolic equation. The overarching question is what a suitable value for the effective diffusion (or, equivalently, conduction) coefficient is.

The case of Darcy-scale single-phase or multi-phase fluid flow can be modeled through a parabolic equation with the (averaged) fluid pressure as variable. In this parabolic equation, the diffusion coefficient is the permeability tensor. The permeability itself depends on the local pore-scale geometry, where wider, well-connected pore channels typically lead to larger permeabilities than narrow channels. When considering subsurface flow, we can use a permeability field to model the flow at Darcy scale. Due to heterogeneities in the subsurface, the resulting permeability fields are typically highly varying, see Figure 1.8 for an example.

Due to the fine-scale information in the permeability field, a very fine grid is needed to resolve it. However, to consider larger Darcy-scale domains, one would want to find permeabilities of larger batches of the porous medium and rather use a coarser grid. This corresponds to taking the step from REV to field scale, and is relevant for understanding the large-scale flow in e.g. geothermal and groundwater applications (cf. Figure 1.1). Finding a suitable averaged permeability at a larger scale or grid becomes the problem that we

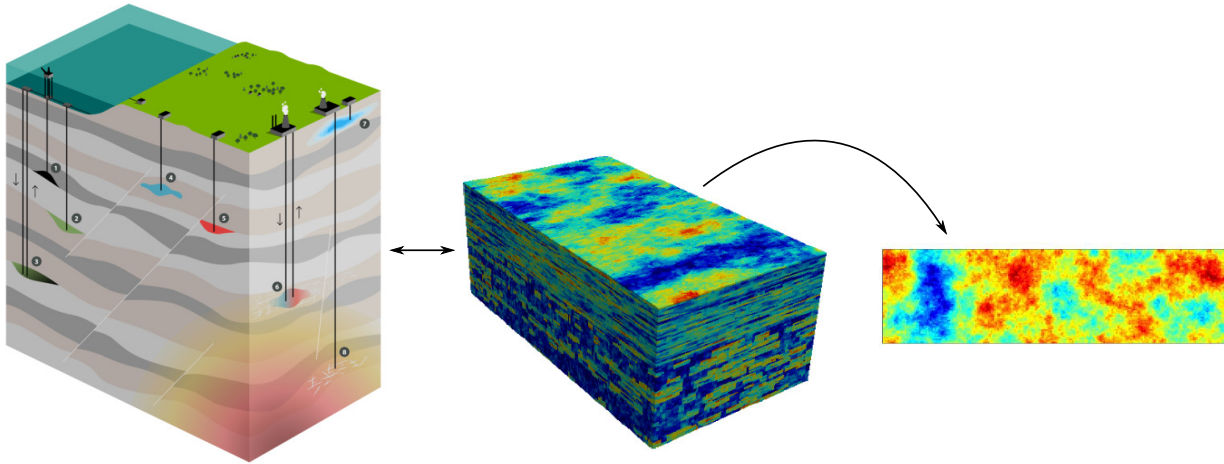


Figure 1.8: The subsurface (left) can be represented by a highly varying permeability field (center and right). The permeability fields shown here are from the SPE tenth comparative solution project [26].

here wish to address. Hence, which permeability represents the averaged flow well, when considering larger domains and coarser grids? This problem of *upscaling* permeabilities is a common problem for many reservoir simulators and has hence resulted in many approaches for estimating these [112]. A typical benchmark for upscaling permeabilities is found in the SPE tenth comparative solution project [26], which is the permeability field shown in Figure 1.8.

These types of questions for finding parameters at larger scales are not only relevant in the context of highly varying permeability fields, but also for heterogeneous materials where the diffusion coefficient is highly varying. The role of both the permeability and the diffusion coefficient is that they appear in a diffusive term of parabolic equations, and therefore similar strategies can be used to find their averaged counterparts at a larger scale. In both cases, the goal of the averaging is to find an averaged diffusion parameter that allows simulation on a coarser grid.

In the case of heat conduction at the pore scale, one typically has a given heat conductivity of the saturating fluid, and a given heat conductivity of the solid grains. At the interfaces between fluid and grain, there is a discontinuity in the heat conductivity, but continuity of the heat flux and also typically of temperature. The temperature gradient is hence discontinuous at the pore scale, leading to an overall complex behavior of the temperature inside the porous medium. To simulate such a system, a very fine grid resolving all fluid-solid interfaces would be necessary, e.g. as shown in the inlets at the right part of Figure 1.2. If one is mainly interested in the overall heat conductivity of a larger part of the porous medium, it is more beneficial to rather consider an averaged approach and hence rely on coarser grids. In this case, one would consider an effective heat conductivity of the porous medium, and correspondingly an averaged temperature as variable. Hence, for an inlet in Figure 1.2, only one temperature and one effective heat conductivity would be used to model the heat transport for that batch of domain. Ideally, the average of the complexly varying pore-scale temperature corresponds to the one found through an averaged approach using an effective heat conductivity. This however depends on how well the effective heat conductivity represents the averaged behavior of the pore-scale conductive processes. If a good choice of effective heat conductivity can be found, this allows for fast

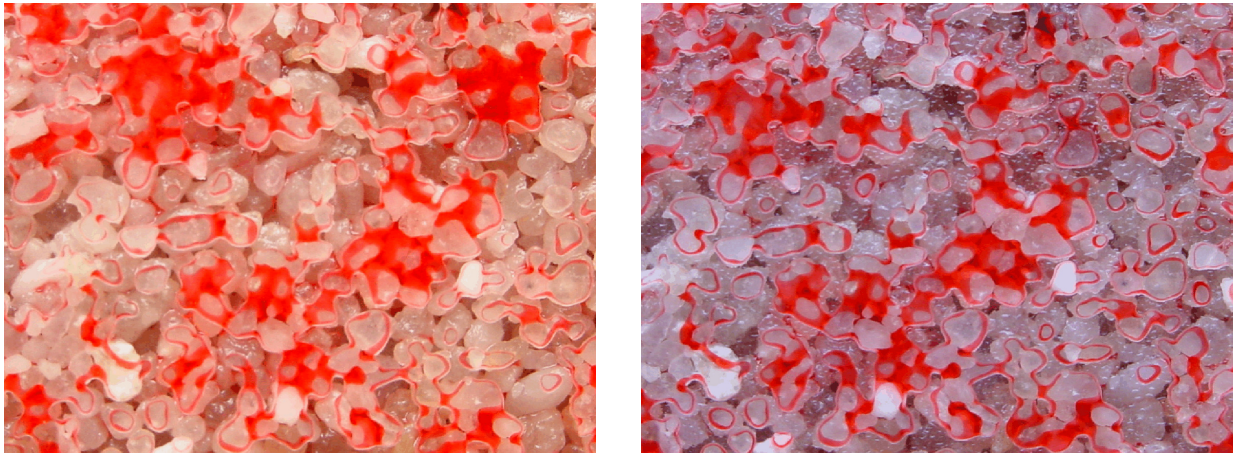


Figure 1.9: Two-phase flow in a pore-scale geometry. Solid glass beads are shown in white, while one fluid is red and the other fluid is transparent. Note that these two snapshots are from the same location in the porous medium but due to the flow, the fluid-fluid interfaces move locations.

simulations of larger domains as a much coarser grid can be considered, see e.g. discussion in [75, Chapter 2].

Two-phase flow Two-phase porous-media flow is relevant for applications as enhanced oil recovery (water or gas displaces oil), CO_2 storage (CO_2 injected into brine), and fuel cells (water and air on the cathode side) [4, 48]. Here, a clear difference in the behavior at pore and Darcy scale can be found. At the pore scale, one can identify and explicitly describe the fluid-fluid interface separating the two fluids, as seen in Figure 1.9. Also in Figure 1.4, two-phase flow at the pore scale is seen, as air penetrates the porous medium while water evaporates. In Figure 1.6, two-phase flow at the pore scale of the porous GDL is found, and there is two-phase flow in the gas channel. As the fluids flow, the fluid-fluid interface deforms due to the flow itself and due to the surface tension between the fluids. This results in a highly coupled process where the flow of the two fluids interacts not only with the solid pore walls, but also with each other. These processes are generally well understood at the pore scale, and can be modeled with well-known partial differential equations in evolving domains, with coupling conditions on the evolving fluid-fluid interface. However, simulations of such models are extremely expensive, especially due to the need of resolving the evolving fluid-fluid interface.

At the Darcy scale, one has no information about the location or behavior of the fluid-fluid interface and hence has no means to describe it nor its influence on the flow. Instead, one has to rely on averaged quantities and variables, which in the case of two-phase flow is mainly the saturation; the volume fraction of one of the fluids inside the REV or within the field-scale grid cell. Typically, one relies on models describing the relative permeability and the capillary pressure as functions of the saturation. The relative permeability and capillary pressure are averaged quantities that should represent the averaged behavior as the fluids flow through the porous medium. However, finding these averaged quantities is not straightforward, and it is not clear whether they are suitable to describe the averaged behavior [11]. However, when a suitable Darcy-scale model can be found, it is possible to perform simulations on much coarser grids, hence one is able to cover much larger domains. That means, for e.g. field-scale CO_2 storage (cf. Figure 1.1) and evaporation of groundwater

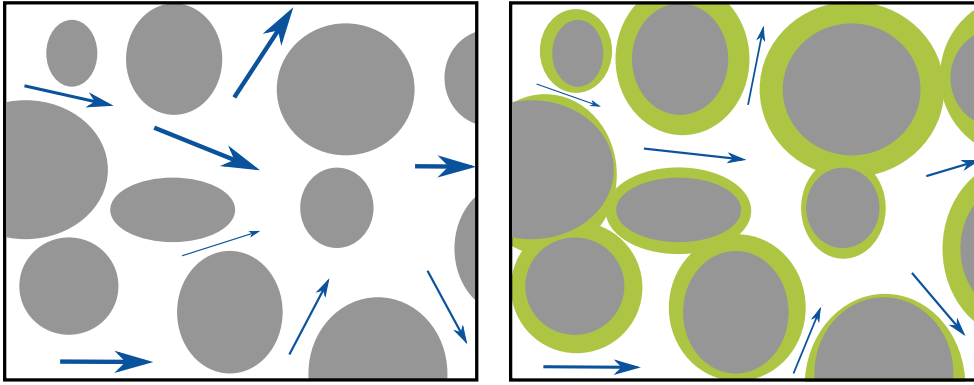


Figure 1.10: Sketch of flow through pore-scale geometries, where precipitated mineral (in green, right) changes the possible flow paths.

where air penetrates the soil (cf. Figure 1.3), large-scale simulations can be made when a Darcy-scale approach can be applied.

Reactive transport The transport of solutes through porous media appears in many applications, for example within contaminant transport and groundwater management, geothermal energy and CO₂ storage [48]. We are here particularly interested in settings where the solutes can react with each other and precipitate in form of solid minerals [32], which in turn can also dissolve to release solutes back to the fluid. Reactive transport with mineral precipitation and dissolution is common where large concentrations of solute in the saturating liquid are present (e.g. due to evaporation from porous media as highlighted in Figure 1.4), or where temperature variability affects the solubility of the minerals (e.g. during geothermal energy production as highlighted in Figure 1.2).

As in the case of two-phase flow, one has a clear difference in the behavior at pore and Darcy scale, although this time due to an evolving fluid-solid interface. At the pore scale, the mineral precipitation or dissolution causes the location and amount of solid grains and fluid-filled void space to change with time. Hence, the interface between fluid and solid evolves as the mineral precipitates or dissolves. This corresponds to the available space for fluid to flow through changes with time. Flow paths can also clog or new can open, as illustrated in Figure 1.10. Such models are relatively well understood at the pore scale, although less straightforward due to the need to describe the mass transfer across the fluid-solid interface. Simulations can again be very expensive due to the need to resolve this evolving interface.

At the Darcy scale, the location or behavior of the evolving fluid-solid interface is not available, and one must again rely on averaged quantities and variables; in this case the porosity and absolute permeability of the porous medium. However, the porosity and permeability of the porous medium change with time as minerals precipitate and dissolve, in an a-priori unknown manner. As the porosity is mainly a volume balance, this one can easier be estimated through reaction rates. The permeability on the other hand depends also on the local pore-scale geometry. Empirical models to estimate the permeability from the porosity exist; see [50] for an overview, with the most popular one being the Kozeny-Carman relation [24, 57]. However, if not fitted based on measurements [94], this relation generally gives bad estimates of the actual permeability [108]. When a suitable Darcy-scale model can be found, simulations of larger porous domains are possible. That means,

simulations of geothermal reservoirs, incorporating the permeability changes (cf. Figure 1.2) and of salt crust formation in a larger groundwater reservoir (cf. Figure 1.3) are possible when a Darcy-scale approach can be applied.

As highlighted above, pore-scale processes can have a significant influence on the averaged Darcy-scale transport. Although the relevant processes can be described accurately at the pore scale, the use of pore-scale simulations for larger domains quickly becomes unfeasible. Although a Darcy-scale simulation is in this case to be preferred, there are two potential problems: (i) It is often not known what a suitable Darcy-scale model would be; (ii) It is simply not possible to use a Darcy-scale model only as pore-scale quantities and variables would still need to be resolved to capture the averaged behavior correctly. Both these aspects can be resolved through the use of multiscale approaches. For the first problem, an averaged description can be derived from the (known) pore-scale model equations by using averaging approaches such as transversal averaging, boundary-layer methods and homogenization. These methods have the ability to derive what the averaged or effective behavior is, and how the pore-scale processes influence this behavior. For the second problem, a model addressing both the Darcy and the pore scale needs to be considered. Such a model can be found through homogenization, and can be simulated by applying a heterogeneous multiscale method. By applying a heterogeneous multiscale method to simulate such a model, one gets both the benefit of having a fast simulation of the averaged behavior at the Darcy scale, but also the ability to incorporate relevant influence from the processes at the pore scale. These methods will be further explained in Section 1.3. First we give an overview of the mathematical background of the pore and Darcy scales, and the model equations describing the considered transport processes.

1.2 Overview of model equations at pore and Darcy scale

As discussed in the previous section and highlighted in Figure 1.7, there are several scales with different types of dominant behavior in a porous medium. In this thesis we are concerned with the pore and the Darcy scale, which are sketched in Figure 1.11. In the following, we mainly focus on describing the processes at the pore scale, which are generally well understood since the processes in the fluid and solid spaces can be described as separate domains. We also present standard Darcy-scale models and focus on their limitations in the context of single-phase and two-phase flow, reactive transport and heat transport.

1.2.1 Pore scale

In this section, we give an overview of pore-scale model equations to describe the transport processes considered in this theses. The model equations are organized in the categories fluid flow, reactive transport and heat transport, and approaches to model evolving fluid-fluid and fluid-solid interfaces. These model equations represent the starting point for multiscale approaches and will throughout this thesis be used to derive Darcy-scale or multiscale models that represent the averaged behavior. Since we are interested in processes that typically have low flow rates, assumptions to simplify the model equations will be made where relevant. For simplicity, we will neglect the presence of gravity in the presentation of the governing equations, but including the influence of gravity is generally straightforward.

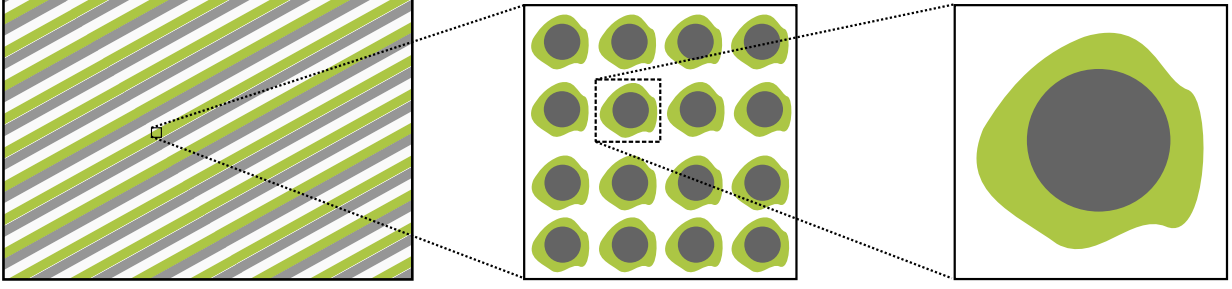


Figure 1.11: Sketch of porous medium. Left: Darcy scale, where an averaged view is taken and only averaged information can be obtained (here represented by stripes). Right: Pore scale, where a more detailed approach is possible, and solid and fluid phases can be separated and modeled explicitly.

With pore scale we mean the zoomed-in view of the porous medium, where fluid-filled void space and solid grain space can be explicitly separated and hence be considered as separate domains of the porous medium, as highlighted in the right part of Figure 1.11. Note that we still deal with a continuum scale, hence length scales should be significantly longer than those at molecular scale, as highlighted in Figure 1.7. Hence, we can use a continuum approach to describe processes within one fluid (or within several fluids in the case of two-phase flow) and within the solid grain separately, and also interactions between these phases in terms of boundary conditions between the various domains. We will throughout this section denote the fluid-filled void space Ω_f and the solid grain space Ω_s . In the case of reactive transport with mineral precipitation and dissolution, the locations of these domains will change with time and are hence time-dependent. The interface between void space and solid will be denoted Γ . In the case of two-phase flow, Ω_f is divided into two disjoint subdomains denoted $\Omega_f^{(1)}$ and $\Omega_f^{(2)}$, corresponding to each of the two fluid phases. In this case, the fluid-fluid interface between $\Omega_f^{(1)}$ and $\Omega_f^{(2)}$ is denoted Γ_f . See Figure 1.12 for an overview of these domains at the pore scale.

In the following we present the governing model equations to describe fluid flow, reactive transport and heat transport in the void space (and for heat transport also in the grain space). In the end, we discuss models for how to describe evolving fluid-fluid and fluid-solid interfaces.

Fluid flow

The flow of a Newtonian fluid is modeled by the Navier-Stokes equations, which describe the conservation of mass and momentum of the fluid:

$$\begin{aligned} \partial_t \rho_f + \nabla \cdot (\rho_f \mathbf{v}) &= 0 && \text{in } \Omega_f, \\ \partial_t (\rho_f \mathbf{v}) + \nabla \cdot (\rho_f \mathbf{v} \otimes \mathbf{v}) + \nabla \cdot (p \mathbf{I}) &= \nabla \cdot (\mu (\nabla \mathbf{v} + \nabla \mathbf{v}^T)) - \frac{2}{3} \nabla \cdot (\mu (\nabla \cdot \mathbf{v}) \mathbf{I}) && \text{in } \Omega_f. \end{aligned}$$

Here, \mathbf{v} is the fluid velocity, ρ_f and μ are the density and viscosity of the fluid, respectively, and p is the fluid pressure. We use \mathbf{I} to denote the identity matrix. Note that in the case of constant fluid density and viscosity, these equations can be simplified. Also, since one generally considers creeping flow, corresponding to low Reynolds numbers ($Re < 1$), the

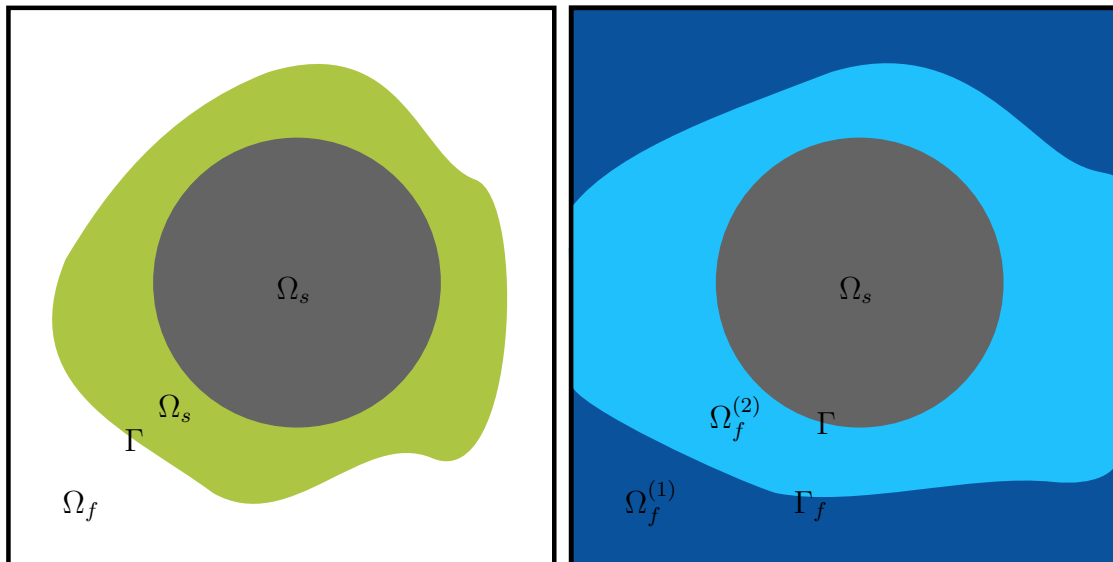


Figure 1.12: Notation used for domains at the pore scale. Left: Fluid-filled void space Ω_f in white, while solid space Ω_s is gray and green. Right: Fluid-filled void space is divided into two subdomains $\Omega_f^{(1)}$ in dark blue, and $\Omega_f^{(2)}$ in light blue, while solid space Ω_s is in gray.

momentum equation could be replaced with the Stokes equation. In this case,

$$\begin{aligned} \nabla \cdot \mathbf{v} &= 0 && \text{in } \Omega_f, \\ \nabla \cdot (p\mathbf{I}) &= \mu \nabla \cdot (\nabla \mathbf{v}) && \text{in } \Omega_f. \end{aligned}$$

Typically one uses no-slip boundary conditions at the fluid-solid interface. This corresponds to the tangential component of the fluid velocity being zero on Γ , but is often written as both tangential and normal components of the fluid velocity being zero. However, the latter corresponds to a no-penetration boundary condition. In the case of the fluid-solid interface moving (due to mineral precipitation and dissolution), the normal component of the fluid velocity is generally non-zero on Γ but depends on the normal velocity of the fluid-solid interface v_n^Γ and the difference in fluid and mineral densities [103]. Hence, for the fluid velocity we apply

$$\begin{aligned} \mathbf{v} \cdot \mathbf{t}^\Gamma &= 0 && \text{on } \Gamma, \\ \mathbf{v} \cdot \mathbf{n}^\Gamma &= 0 \text{ or } \mathbf{v} \cdot \mathbf{n}^\Gamma = v_n^\Gamma \frac{\rho_f - (n_1 + n_2)\rho_m}{\rho_f} && \text{on } \Gamma, \end{aligned}$$

where \mathbf{t}^Γ and \mathbf{n}^Γ represent the unit tangential and normal vectors of Γ , respectively, with \mathbf{n}^Γ pointing into the solid. Further, ρ_m is the mineral density, and n_1, n_2 are the number of cations and anions in one mineral molecule. This latter condition is a Rankine-Hugoniot jump condition and hence conserves the amount of mass as solutes leave the fluid phase to rather become part of the solid phase, or the other direction. However, if fluid velocities are larger than the normal velocity of the interface, this condition is often simplified to $\mathbf{v} \cdot \mathbf{n}^\Gamma = 0$. This corresponds to not accounting for the volume changes caused by the reaction [103].

In the case of two-phase flow, each of the two fluids can be modeled by the Navier-Stokes

equation in their respective domain. Using (i) with $i = 1, 2$ as superscript to denote the two fluids, and considering for simplicity incompressible flow and constant viscosities, we have:

$$\begin{aligned} \nabla \cdot \mathbf{v}^{(i)} &= 0 && \text{in } \Omega_f^{(i)}, \\ \rho_f^{(i)}(\partial_t \mathbf{v}^{(i)} + \mathbf{v}^{(i)} \cdot \nabla \mathbf{v}^{(i)}) + \nabla \cdot (p^{(i)} \mathbf{I}) &= \mu^{(i)} \nabla \cdot (\nabla \mathbf{v}^{(i)}) && \text{in } \Omega_f^{(i)}. \end{aligned}$$

For two-phase flow, the no-slip condition at the fluid-solid interface will lead to a singularity at the fluid-fluid-solid contact point. Hence, it is necessary to use a slip condition [52]:

$$\begin{aligned} (\mathbf{v}^{(i)} + \lambda_L (\nabla \mathbf{v}^{(i)} + \nabla \mathbf{v}^{(i)T}) \mathbf{n}^\Gamma) \cdot \mathbf{t}^\Gamma &= 0 && \text{on } \Gamma^{(i)}, \\ \mathbf{v}^{(i)} \cdot \mathbf{n}^\Gamma &= 0 && \text{on } \Gamma^{(i)}, \end{aligned} \quad (1.1)$$

in the case of no mineral precipitation and dissolution. Here $\Gamma^{(i)}$ denotes the part of Γ facing $\Omega_f^{(i)}$, and λ_L is a slip length. On the fluid-fluid interface, additional boundary conditions are needed. When not allowing any mass transfer between the two fluids (e.g. no evaporation), there is continuity of the velocity and of tangential stress, while the normal stress has a jump due to surface tension:

$$\mathbf{v}^{(1)} = \mathbf{v}^{(2)} \quad \text{on } \Gamma_f, \quad (1.2)$$

$$-(p^{(1)} - p^{(2)}) \mathbf{n}^f + (\mu^{(1)} (\nabla \mathbf{v}^{(1)} + \nabla \mathbf{v}^{(1)T}) - \mu^{(2)} (\nabla \mathbf{v}^{(2)} + \nabla \mathbf{v}^{(2)T})) \mathbf{n}^f = \sigma \kappa \mathbf{n}^f \quad \text{on } \Gamma_f, \quad (1.3)$$

where \mathbf{n}^f refers to the unit normal vector on the fluid-fluid interface, σ is the surface tension between the two fluids and κ is the local mean curvature of the interface. Note that the first condition implicitly means that the normal velocity of the fluid-fluid interface v_n^f coincides with the velocity of both fluids on this interface. Secondly, note that from the second condition one generally has that there is a pressure jump between the two fluids on the fluid-fluid interface, which is related to the curvature of the interface and the jump of the viscous stress. Such a pressure jump is sometimes referred to as a local/pore-scale capillary pressure. Additionally, a contact angle law is needed for the fluid-fluid-solid contact point, see Figure 1.13. A linear model arising from molecular kinetics theory relates the dynamic contact angle θ with a static dynamic contact angle θ_s [15]:

$$\cos(\theta(v_n^f)) = \cos(\theta_s) - \eta Ca v_n^f, \quad (1.4)$$

where v_n^f is the normal velocity of the fluid-fluid interface at the contact point to the solid, η is a dynamic parameter and Ca the capillary number. How to enforce the contact angle θ depends on the description of the evolving fluid-fluid interface and is therefore not specified here.

Reactive transport

The concentration of a solute c_j dissolved in a fluid is transported through advection and diffusion within the fluid:

$$\partial_t c_j + \nabla \cdot (c_j \mathbf{v}) = \nabla \cdot (D_j \nabla c_j) + R_j \quad \text{in } \Omega_f,$$

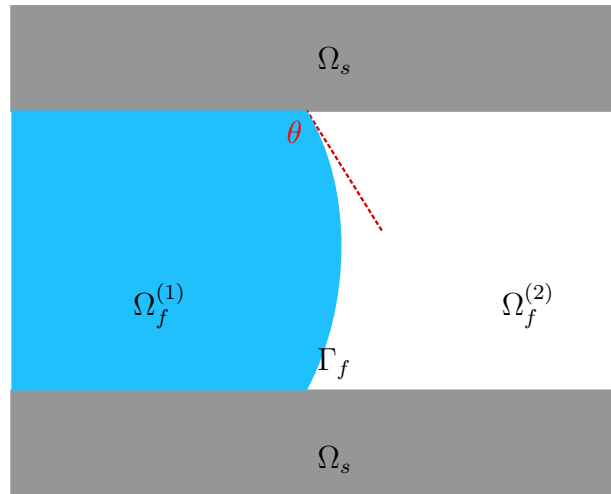
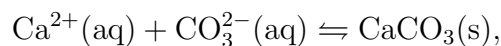


Figure 1.13: Illustration of contact angle θ at the fluid-fluid-solid contact point.

or correspondingly in $\Omega_f^{(i)}$ and using $\mathbf{v}^{(i)}$ in the case of two-phase flow and the solute is solvable in fluid phase i . Here, D_j is the diffusion coefficient of the solute, and R_j is a reaction rate for homogeneous reactions appearing within the fluid phase, which depends on the concentration of the other solutes appearing in the fluid. One needs to consider one of these advection-diffusion equation for each solute appearing in the fluid. We are here mainly concerned with reactions occurring on the interface between fluid and solid, which are called heterogeneous reactions as they concern two different phases. For these heterogeneous reactions, we focus on the case of single-phase flow only. In particular, we want to model mineral precipitation and dissolution, where solutes in the fluid are then either disappearing or released. For example, in the case of calcite precipitation and dissolution we have the reaction



where (ag) and (s) indicate dissolved in aqueous phase or as solid phase. In this reaction, one cation and one anion ($n_1 = n_2 = 1$) leave the liquid to form one solid mineral molecule, or the other direction. The mineral itself can be modeled by a constant mineral concentration:

$$\rho_m = \text{constant} \quad \text{in } \Omega_s.$$

Note that the amount of mineral is hence measured by the size of Ω_s , which changes with time. However, the concentration of the mineral itself is considered a constant as it is seen as an incompressible solid phase. Note that another approach to account for the amount of mineral is through surface concentrations, which then vary with the amount of mineral [99]. In this case, the fluid and solid spaces do not vary with time. Such models are suitable as long as the amount of mineral volume does not change significantly. Here we do account for the fluid and solid spaces varying with time, and we therefore account for the transfer of ions across the fluid-solid interface using a Rankine-Hugoniot boundary condition:

$$(c_j \mathbf{v} - D_j \nabla c_j) \cdot \mathbf{n}^\Gamma = (c_j - \rho_m) v_n^\Gamma \quad \text{on } \Gamma. \quad (1.5)$$

The normal velocity of the interface can be connected to the reaction rate of the mineral precipitation and dissolution reaction:

$$v_n^\Gamma = -\frac{1}{\rho_m} f(c_j) \quad \text{on } \Gamma, \quad (1.6)$$

where $f(c_j)$ is the net mineral precipitation rate and is hence negative if dissolution takes place. This reaction rate is connected to the solubility of the considered mineral; solute concentrations larger than the solubility limit lead to net precipitation, and concentrations below the solubility limit lead to net dissolution.

Heat transport

For the heat transport we here consider a simplified approach where temperature of the phase is sufficient to express the heat of the phase, through the density and specific heat capacity. This is valid when considering single-phase flow with low velocities and neglecting melting/freezing and evaporation/condensation [62]. In the fluid phase, the heat is then transported through advection and conduction:

$$\partial_t(\rho_f c_{p,f} T_f) + \nabla \cdot (\rho_f c_{p,f} T_f \mathbf{v}) = \nabla \cdot (k_f \nabla T_f) \quad \text{in } \Omega_f.$$

Here, $c_{p,f}$ and k_f are the specific heat capacity and heat conductivity of the fluid, respectively, while T_f denotes the temperature of the fluid phase. The specific heat capacity and heat conductivity are considered to be material constants. The solid phase can transport heat through heat conduction, hence

$$\partial_t(\rho_s c_{p,s} T_s) = \nabla \cdot (k_s \nabla T_s) \quad \text{in } \Omega_s.$$

Here, $c_{p,s}$ and k_s are the specific heat capacity and heat conductivity of the solid, respectively, while T_s denotes the temperature of the solid phase. We here use ρ_s to express the density of the solid phase, which is for simplicity considered to be the same as the mineral density ρ_m in the case of mineral precipitation and dissolution models. At the interface between fluid and solid, we consider continuity of the heat flux and local thermal equilibrium. The latter corresponds to temperatures T_f and T_s being the same on the interface Γ and is sometimes referred to as pore-scale thermal equilibrium. However, the continuity of heat flux must be expressed by a Rankine-Hugoniot boundary condition in the case of the fluid-solid interface moving due to mineral precipitation and dissolution. The two conditions are expressed as

$$\begin{aligned} (\rho_f c_{p,f} T_f \mathbf{v} - k_f \nabla T_f + k_s \nabla T_s) \cdot \mathbf{n}^\Gamma &= v_n^\Gamma (\rho_f c_{p,f} T_f - \rho_s c_{p,s} T_s) && \text{on } \Gamma, \\ T_f &= T_s && \text{on } \Gamma. \end{aligned}$$

Note that the first condition reduces to the usual continuity of the heat flux when $v_n^\Gamma = 0$, which corresponds to no mineral precipitation and dissolution. In either case, this condition ensures the conservation of heat as heat is transferred between the fluid and solid phases.

Evolving interfaces

To describe evolving fluid-fluid or fluid-solid interfaces there are two main approaches that are applied in this thesis: either the interfaces can be considered as sharp interfaces or as

diffuse transition zones. The model equations considered so far have implicitly assumed the evolving fluid-solid or fluid-fluid interfaces to be sharp; that is, there is an identifiable surface (in 3D) or line (in 2D) where interface conditions between the two domains are formulated. One typically has discontinuities at each side of the interface, e.g. in terms of material properties like heat conductivities or densities. In the case of diffuse interfaces, one has instead a smooth transition between the parameters and processes occurring at each side of the transition zone. Hence, discontinuities are smoothed out, and boundary conditions are incorporated into the model equations themselves. Hence, in the case of diffuse transition zones, one does not consider separate model equations for what happens at each side of the (diffuse) interface, but consider common model equations for the combined domain. In the case of two-phase flow, that means only one equation is used to describe the conservation of momentum for the mixture of the two fluids, defined in the combined domain $\Omega_f = \Omega_f^{(1)} \cup \Omega_f^{(2)} \cup \Gamma_f$, which is then not changing with time. Hence, the interface conditions on the evolving interface are also incorporated into the single model equation.

Although diffuse interfaces are physically meaningful at a molecular level, where one typically sees that the molecules of two phases mix in a transition zone, the diffuse interfaces considered in this thesis are only to be seen as a mathematical approximation. That is, the diffuse-interface width is too large to have a physical meaning. Such diffuse-interface models are approximations of the “real” sharp-interface physics. One typically requires that as the width of the diffuse transition zone approaches zero, one should be able to recover the corresponding sharp-interface model formulation. This can be done using matched asymptotic expansions, which are discussed in Section 1.3.2. The benefits of using a diffuse-interface model are twofold: First of all, by having a smooth interface, one avoids discontinuities which can be challenging to handle both in analysis and numerically. Secondly, by using model equations that are defined in domains that are not evolving in time, numerical implementation as well as homogenization (cf. Section 1.3.3) are simplified. However, by using a diffuse-interface model, one should keep in mind that the model equations are then approximations. Diffuse interfaces introduce curvature-driven motion of the evolving interface, which is not necessarily physical, as will be visible in particular in Chapters 8 and 10 of this thesis.

If formulating a sharp-interface model, one needs an equation for modeling the evolution of the interface. In the general case, this can be done with a level set L_S [77]. Then the interface is implicitly defined as the points where $L_S(t, \mathbf{x}) = 0$. Hence, in the case of the evolving fluid-fluid interface, one has

$$L_S(t, \mathbf{x}) = \begin{cases} < 0 & \text{if } \mathbf{x} \in \Omega_f^{(1)}(t), \\ 0 & \text{if } \mathbf{x} \in \Gamma_f(t), \\ > 0 & \text{if } \mathbf{x} \in \Omega_f^{(2)}(t). \end{cases}$$

The level set itself is defined in the entire domain and evolves according to the level-set equation

$$\partial_t L_S + v_n^f \|\nabla L_S\| = 0 \quad \text{in } \Omega_f.$$

The fluid-fluid interface velocity v_n^f corresponds to the fluid velocities at Γ_f and the level-set equation is hence coupled to the Navier-Stokes equations for the two fluids through equation

(1.2). A contact angle boundary condition at the solid wall can be included through [64]

$$\mathbf{n}^\Gamma \cdot \frac{\nabla L_S}{\|\nabla L_S\|} = -\cos\theta \quad \text{on } \Gamma.$$

Correspondingly, for an evolving fluid-solid interface, the level set is

$$L_S(t, \mathbf{x}) = \begin{cases} < 0 & \text{if } \mathbf{x} \in \Omega_f(t), \\ 0 & \text{if } \mathbf{x} \in \Gamma(t), \\ > 0 & \text{if } \mathbf{x} \in \Omega_s(t). \end{cases}$$

The evolution of the level set follows the same level-set equation as above, but this time defined in $\Omega = \Omega_f \cup \Omega_s \cup \Gamma$, which is fixed in time, and now using the fluid-solid interface normal velocity v_n^Γ . Here, v_n^Γ is connected to the reaction rate through equation (1.6) and is through this reaction rate coupled to the advection-diffusion equations of the solutes.

The level-set approach can in general model complex shapes, but can be challenging to implement and to incorporate in upscaling procedures. If one knows that the evolving interface follows a simpler evolution, special cases of the level set can instead be used to simplify the approach. For example, if the evolving interface is always circular, corresponding to having e.g. a mineral of a certain radius, one has (in 2D)

$$L_S(t, \mathbf{x}) = (R(t))^2 - x_1^2 - x_2^2.$$

Here, $\mathbf{x} = (x_1, x_2)$ and $R(t)$ is the radius. For a layer of a certain width $d(t, x_1)$, a level set corresponding to

$$L_S(t, \mathbf{x}) = d(t, x_1) - x_2 \tag{1.7}$$

can be used. In these cases, $R(t)$ or $d(t, x_1)$ is instead used as the unknown variable, and the level-set equation can be rewritten into an equation for this unknown.

For diffuse interfaces, we will consider two different types of phase-field equations: Allen-Cahn and Cahn-Hilliard. In both cases, the phase-field variable ϕ approaches a certain equilibrium value in one phase, and another in the other phase, but has a smooth transition between them, see Figure 1.14. The Allen-Cahn equation [7] is a second-order diffusion equation with a non-linear source term, which can be written

$$\partial_t \phi = -\frac{\gamma}{\lambda^2} P'(\phi) + \gamma \nabla^2 \phi.$$

Here, $P(\phi) = 8\phi^2(1 - \phi)^2$ is the double-well potential, ensuring that ϕ approaches the stable equilibria 0 and 1. The diffusion term ensures a smooth transition between these two. Further, λ and γ are phase-field parameters, where λ controls the width of the diffuse interface, and γ the equilibration time of the phase-field evolution. Note that the phase-field equation is defined in both domains it represents, and on the interface between them. In the case of a phase field representing fluid and solid, and chemical reactions influence the evolution of the fluid-solid interface, an additional source term is added:

$$\partial_t \phi = -\frac{\gamma}{\lambda^2} P'(\phi) + \gamma \nabla^2 \phi - \frac{4}{\lambda} \phi(1 - \phi) \frac{f(c_j)}{\rho_m} \quad \text{in } \Omega. \tag{1.8}$$

In this formulation, $\phi \rightarrow 1$ corresponds to fluid, and $\phi \rightarrow 0$ to mineral, while the reaction

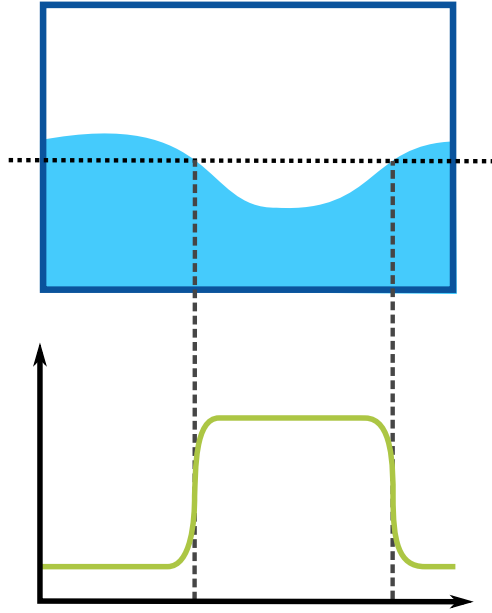


Figure 1.14: Illustration of phase-field variability (green line) as it crosses an interface between two phases (white and blue) along the black, dotted line.

rate either increases or decreases the amount of fluid/mineral depending on the sign of the reaction rate. Note that the factor $\frac{4}{\lambda}\phi(1-\phi)$ ensures that the reaction rate is only active in the transition zone for ϕ between 0 and 1, and is scaled such that the correct surface area is estimated.

The Cahn-Hilliard equation [23] is a fourth-order non-linear diffusion equation, which can be written

$$\partial_t \phi = m\lambda \nabla^2 \psi, \quad \psi = \hat{\sigma} \left(\frac{1}{\lambda} P'(\phi) - \lambda \nabla^2 \phi \right).$$

Here, ψ is known as the chemical potential, m as the mobility of the phase field, and $\hat{\sigma}$ is connected to the interfacial tension between the two phases. As before, λ controls the diffuse-interface width, and $P(\phi)$ is the double-well potential. If $P(\phi) = \frac{1}{4}(1-\phi^2)^2$ is applied, this corresponds to stable equilibria of -1 and $+1$. When using Cahn-Hilliard to model a fluid-fluid interface where the fluids can flow, the phase field should evolve with the velocity of the fluids. Hence, an advective term is added:

$$\partial_t \phi + \nabla \cdot (\phi \mathbf{v}) = m\lambda \nabla^2 \psi, \quad \psi = \hat{\sigma} \left(\frac{1}{\lambda} P'(\phi) - \lambda \nabla^2 \phi \right) \quad \text{in } \Omega_f. \quad (1.9)$$

Note that \mathbf{v} here represents the combined velocity of the mixture of the fluids. For phase fields, contact angle boundary conditions can be incorporated using

$$\mathbf{n}^\Gamma \cdot \nabla \phi = -g'(\phi) \cos \theta \quad \text{on } \Gamma,$$

where $g(\phi)$ is connected to the wall energy of the phase field [38].

Remark 1.1 *Note that a large range of different versions of the Allen-Cahn and Cahn-Hilliard equations exist. These versions differ in how scalings, double-well potentials and source terms are incorporated, and which equilibrium values are approached. Only versions close to the ones applied in the later chapters are presented here.*

1.2.2 Darcy scale

In this section, we give an overview of commonly used Darcy-scale models. These models are not necessarily applied in this thesis, but represents the “standard” approaches to model Darcy-scale fluid flow, reactive transport and heat transport in porous media. Since we are interested in settings with low flow rates, we focus on model equations covering this setting. Also here we will for simplicity neglect the influence of gravity when presenting the model equations.

With Darcy scale we mean the zoomed-out, averaged view of the porous medium, where void space and solid grain space cannot be explicitly separated anymore, as sketched in the left part of Figure 1.11. As mentioned in Section 1.1, the Darcy scale represents either the REV scale or the field scale, which both have in common that Darcy’s law can be applied to describe the average flow rate through the porous medium. At the Darcy scale, meaningful averages over REVs or of even larger batches of the porous domain can be defined for quantities like porosity and permeability. Since an averaged view is used, one always deals with only one domain which we here denote Ω , representing both the void and solid space. However, any local information about the pore-scale geometry is not accounted for and is generally not available. Instead only averaged quantities as saturation, porosity and permeability can be addressed in a meaningful way.

In the following we present the commonly used model equations to describe fluid flow, reactive transport and heat transport through a porous medium, and we discuss some limitations of these existing models.

Fluid flow

At the Darcy scale, single-phase flow is modeled using the volume-averaged flow rate $\bar{\mathbf{v}}$, which is called the Darcy velocity. The average is made over an REV or over an even larger part of the porous domain. Mass conservation can be formulated in terms of the Darcy velocity,

$$\partial_t(\Phi\rho_f) + \nabla \cdot (\rho_f\bar{\mathbf{v}}) = 0 \quad \text{in } \Omega,$$

where Φ is the porosity of the porous medium. The porosity represents the amount of (fluid-filled) void space per volume that is averaged over, and hence takes values between 0 and 1. In case of an incompressible fluid and porosity that is constant in time, this mass conservation equation reduces to a divergence-free Darcy velocity. When flow rates are low, so that flow within the porous medium can be considered as creeping flow (corresponding to low Reynolds number, $Re < 1$, as also considered in Section 1.2.1) the Darcy velocity is modeled through Darcy’s law [31]:

$$\bar{\mathbf{v}} = -\frac{\mathbf{K}}{\mu}\nabla\bar{p} \quad \text{in } \Omega.$$

Note that the pressure \bar{p} is to be understood as the fluid pressure averaged over the void space of the reference volume that is averaged over. Further, \mathbf{K} is the permeability matrix, which quantifies the ability of the porous medium to transmit fluid. This permeability can be found for samples of porous media through measurements or by numerical simulations. In both cases one applies a known pressure drop across each direction of the sample, and either measures the transmitted flow, or one numerically calculates the pore-scale velocities which are then averaged over the porous domain [108]. The permeability can be defined

for single REVs, but can also be defined for larger volumes of the porous domain. In the latter case, one has then an averaged permeability representing the medium's ability to transmit fluid at a larger scale. In general, the permeability can vary with location and flow direction. When the permeability is direction-independent (that is, isotropic), a scalar K ($\mathbf{K} = K\mathbf{I}$) can be used to model it.

For two-phase flow, the saturations $S^{(i)}$ of the two fluid phases are used as variables. A saturation $S^{(i)}$ is the fraction of the pore space occupied by the phase i within the considered reference volume, and hence lies between 0 and 1. For two-phase flow, we hence always have

$$S^{(1)} + S^{(2)} = 1 \quad \text{in } \Omega.$$

Due to this simple connection between the saturations, one can consider only one of the saturations as a variable, as the other one is immediately given by the first saturation. We consider in the following incompressible fluids and constant porosities only. The mass conservation of each phase is

$$\Phi \partial_t S^{(i)} + \nabla \cdot \bar{\mathbf{v}}^{(i)} = 0 \quad \text{in } \Omega, \quad (1.10)$$

where $\bar{\mathbf{v}}^{(i)}$ is the Darcy velocity of fluid i . These Darcy velocities are typically given by extended Darcy's laws [48]

$$\bar{\mathbf{v}}^{(i)} = -\frac{k_r^{(i)}}{\mu^{(i)}} \mathbf{K} \nabla \bar{p}^{(i)} \quad \text{in } \Omega, \quad (1.11)$$

where $k_r^{(i)}$ is known as the relative permeability of phase i . Here, the pressure $\bar{p}^{(i)}$ is to be understood as the pressure of phase i averaged intrinsically over the phase in the reference volume that is averaged over. Additional relations are needed to close the model equations. One typically assumes that the relative permeabilities can be expressed as functions of one of the saturations. Further, the pressure difference between the phases, usually called the (Darcy-scale) capillary pressure, is either assumed zero or to depend on a saturation [48]. In the case of high capillary number, the capillary pressure can be assumed zero, which corresponds to using the same pressure in both phases. When capillary effects have an influence, a capillary pressure-saturation relation is needed. Commonly used models for such relations are van Genuchten [101] and Brooks-Corey [21]. However, many experimental results show that such relations are not sufficient to describe the observed Darcy-scale behavior of two-phase flow [33]. Although extended models incorporating dynamic effects and hysteresis have been suggested and investigated [49], it still remains an open question what suitable model equations for Darcy-scale two-phase flow are, and whether parametrized expressions through saturation are sufficient to model the observed behavior.

The two-phase flow equations (1.10) and (1.11) can be simplified if one fluid phase is air and the other liquid. Due to the difference in viscosity, the dynamic influence of air on the liquid phase is negligible. Hence, the flow of air can be neglected, and its pressure can be considered constant. In this case one has unsaturated flow. Unsaturated flow at Darcy scale can be modeled with Richards equation [48, 87]

$$\Phi \partial_t S^{(l)} + \nabla \cdot \left(\frac{k_r^{(l)}}{\mu^{(l)}} \mathbf{K} \nabla \bar{p}_c \right) = 0 \quad \text{in } \Omega, \quad (1.12)$$

where we use superscript l to denote the liquid phase. Note that the gradient of the capillary pressure \bar{p}_c is related to the liquid pressure by $\nabla \bar{p}_c = -\nabla \bar{p}^{(l)}$. The capillary pressure \bar{p}_c is

still assumed to be a given relation of liquid saturation. When this is a monotone relation, it is also invertible and we can write $S^{(l)} = S^{(l)}(\bar{p}_c)$. By using the Kirchhoff transformation

$$\Psi(\bar{p}_c) = \int_0^{\bar{p}_c} \tilde{k}_r^{(l)}(\xi) d\xi, \quad (1.13)$$

where $\tilde{k}_r^{(l)}(\bar{p}_c) = k_r^{(l)}(S^{(l)}(\bar{p}_c))$, Richards equation (1.12) can be transformed to an equation in terms of Ψ :

$$\Phi \partial_t f(\Psi) + \nabla \cdot \left(\frac{\mathbf{K}}{\mu^{(l)}} \nabla \Psi \right) = 0 \quad \text{in } \Omega, \quad (1.14)$$

where $f(\Psi) = S^{(l)}(\bar{p}_c(\Psi))$. Note that we here use $\bar{p}_c(\Psi)$, namely the inverse of (1.13), which exists since the relative permeability is always positive. The transformed Richards equation is a non-linear parabolic equation. Both the original and the transformed versions of the Richards equation are considered challenging equations to solve numerically due to the non-linearities [37].

Reactive transport

The Darcy-scale concentration of a solute \bar{c}_j dissolved in a fluid is considered the average concentration over the void space in the reference volume that is averaged over, and is modeled by [12]

$$\partial_t(\Phi \bar{c}_j) + \nabla \cdot (\bar{c}_j \bar{\mathbf{v}}) = \nabla \cdot (\mathbf{D}_j \nabla \bar{c}_j) + R_j \quad \text{in } \Omega.$$

We only consider single-phase flow. Here, \mathbf{D}_j is the effective diffusion matrix of the solute. Since we consider generally low flow rates, dispersive effects are not accounted for. In the case of isotropic diffusion at Darcy scale, the diffusion matrix can be represented by a scalar \bar{D}_j , such that $\mathbf{D}_j = \bar{D}_j \mathbf{I}$. The reaction rate R_j is now accounting for both heterogeneous and homogeneous reactions involving solute \bar{c}_j inside the REV or larger volume that is averaged over. In the case of mineral precipitation and dissolution, the porosity Φ will change with time, and also the permeability \mathbf{K} and effective diffusion \mathbf{D}_j will be affected. The porosity changes can be connected to a volume balance of the precipitated mineral(s)

$$\partial_t \Phi = -\nu_m R_m \quad \text{in } \Omega,$$

where ν_m is the molar volume of the mineral, and R_m is the reaction rate for mineral precipitation/dissolution inside the volume that is averaged over, and is positive for net precipitation. The permeability \mathbf{K} and effective diffusion \mathbf{D}_j generally depend on the local pore-scale geometry. However, this information is not available at the Darcy scale. To express how permeability and effective diffusion changes as mineral precipitates and dissolves, parametrized expressions in terms of porosity are typically used [12]. A very common approach for permeability is to use the isotropic Kozeny-Carman relation [24, 57]

$$K(\Phi) = \frac{\Phi^3}{\tau(1 - \Phi)^2 s^2}, \quad (1.15)$$

where τ is the tortuosity and s the specific surface area of the porous medium. For a review of other (isotropic) $K(\Phi)$ relations, see [50]. The effective diffusion is usually considered to

be isotropic and scale linearly with porosity [12]

$$\overline{D}_j(\Phi) = \Phi D_j, \quad (1.16)$$

where D_j is the pore-scale diffusion coefficient. Although providing simple and closed model equations for reactive transport where mineral precipitates and dissolves, these parametrized expressions cannot account for any anisotropic effects. Typically, the tortuosity and specific surface area in the Kozeny-Carman relation (1.15) are not known, which means that the relation would need to be fitted to experimental or simulation data. The lacking feature of both expressions (1.15) and (1.16) is that they cannot properly account for any pore-scale information. However, at Darcy scale, pore-scale information is generally not available.

Heat transport

When still considering single-phase flow, low flow rates and limited temperature ranges, temperature can also at Darcy scale be used as variable to model heat transport. The Darcy-scale heat equations can be modeled as [48, 75]

$$\begin{aligned} \partial_t(\Phi \rho_f c_{p,f} \overline{T}_f) + \nabla \cdot (\rho_f c_{p,f} \overline{T}_f \overline{\mathbf{v}}) &= \nabla \cdot (\Phi k_f \nabla \overline{T}_f) + \alpha(\overline{T}_s - \overline{T}_f) && \text{in } \Omega, \\ \partial_t((1 - \Phi) \rho_s c_{p,s} \overline{T}_s) &= \nabla \cdot ((1 - \Phi) k_s \nabla \overline{T}_s) + \alpha(\overline{T}_f - \overline{T}_s) && \text{in } \Omega, \end{aligned}$$

where \overline{T}_f and \overline{T}_s are to be understood as the temperatures averaged over the respective phase within the REV or larger volume that is averaged over, and α is a (constant) coefficient accounting for the transfer between the fluid and solid phase. Especially in the case of low fluid velocities, it is usually assumed that one has (Darcy-scale) thermal equilibrium, which corresponds to $\overline{T}_s = \overline{T}_f = \overline{T}$, and we can use a single equation for the transport of heat [75]:

$$\partial_t((\rho c_p)_m \overline{T}) + \nabla \cdot (\rho_f c_{p,f} \overline{T} \overline{\mathbf{v}}) = \nabla \cdot (k_m \nabla \overline{T}) \quad \text{in } \Omega.$$

Here, $(\rho c_p)_m = \Phi \rho_f c_{p,f} + (1 - \Phi) \rho_s c_{p,s}$ and $k_m = \Phi k_f + (1 - \Phi) k_s$ represent the effective specific heat and effective heat conductivity of the porous medium, respectively. The effective heat conductivity is here a porosity-weighted arithmetic average of the heat conductivities found in the fluid and solid. However, this is found to not always represent well the actual effective heat conductivity of the porous medium. In [75] it is discussed whether porosity-weighted harmonic or geometric averages would be more suitable for the effective heat conductivity, depending on the pore-scale geometry. These would still give isotropic effective heat conductivities, but effective heat conductivities in anisotropic porous media would be better represented by a heat conductivity matrix [63]. Both in the case of scalar- and matrix-valued effective heat conductivities, it is not clear how the effective heat conductivity would change when the porosity (and pore-scale geometry) changes, for example due to mineral precipitation or dissolution.

1.3 Multiscale approaches

To bridge the scale gap between the known and generally well understood pore scale, and the (generally unknown or unclear) effective behavior at a larger scale, we will in this thesis apply several types of multiscale approaches. They can roughly be divided into four

categories:

- **Transversal averaging:** This technique is used when dealing with long and thin domains, for example a single pore which can be described as a thin strip (in 2D) or as a thin tube (in 3D). Here, the goal is to dimensionally reduce the model to find the effective behavior along the thin structure. This is done by determining the dominating behavior and averaging across the domain.
- **Boundary-layer methods:** These methods are used to address the behavior close to and away from some singularity or discontinuity that appears in the system, for example the fluid-fluid interface. This way one can find a (hopefully) simpler model describing the effective behavior away from the discontinuity, coupled to another model describing the effective behavior close to it. We will focus on the use of matched asymptotic expansions in this context.
- **Homogenization:** With homogenization we here mean the application of two-scale asymptotic expansions, which is sometimes also called periodic homogenization. This is used when finding the effective behavior at a larger scale by taking advantage of local periodicity. The influence of the smaller scale appears through local cell problems. Homogenization will in this thesis be used for finding Darcy-scale models based on pore-scale models, or finding effective parameters at a larger Darcy scale (e.g. from REV to field scale).
- **Heterogeneous multiscale methods:** This method is better described as an abstract framework for designing multiscale implementations. This framework will be applied to construct schemes to numerically simulate models where model equations at two different scales are coupled to each other (e.g. Darcy scale coupled to pore scale).

The first three approaches all have in common that they aim to derive new models for effective behavior. All of them depend on the appearance of a small number ε , which represents the scale separation in each of the three cases: For transversal averaging ε is the ratio between the width and the length of the domain, for boundary-layer methods ε describes the width of the region where an influence of the singularity can be found compared to the size of the full domain, while for homogenization ε is the length scale ratio between the smaller and larger scale - e.g. the pore and Darcy scale. All three methods let at some point $\varepsilon \rightarrow 0$ during the derivation of the effective behavior. In practice, ε is a fixed number given by the domain or physics in question, and letting $\varepsilon \rightarrow 0$ is hence only a mathematical exercise. However, how small or how large the physically given ε really is, can have an influence on how well the derived effective models describe the true effective behavior. A heterogeneous multiscale method (HMM) does not derive effective models, but relies on the presence of a given two-scale (or multiscale) description, which in our case is derived by homogenization. Here the focus is on constructing a numerical scheme honoring the coupling between the two scales. The difference in scales is taken advantage of as it is assumed that the model equations at the two scales can be discretized in a separated manner. In the following we go through the background and general ideas for these four multiscale approaches and explain how they can handle the type of multiscale problems discussed in Section 1.1.

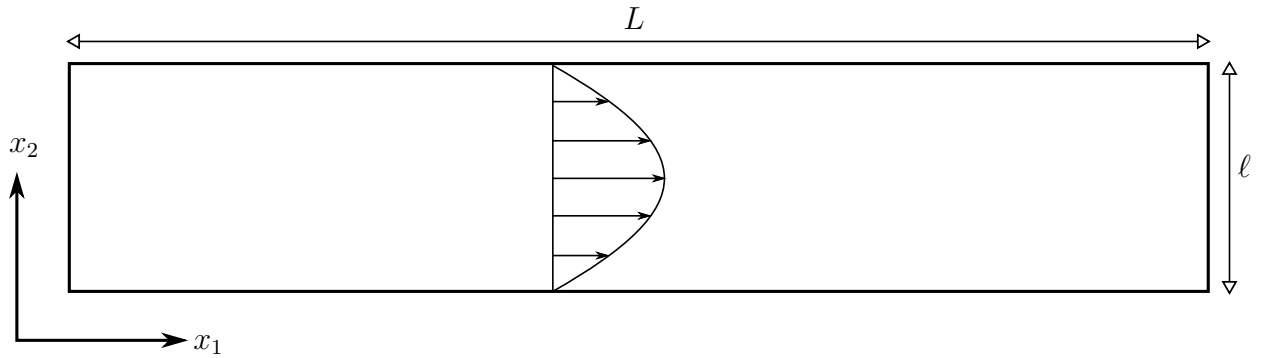


Figure 1.15: Domain depicting a thin strip, where $\ell \ll L$. Here, the domain corresponds to a channel, where there is flow along the channel, shown as a parabolic velocity profile.

1.3.1 Transversal averaging

We here consider a domain which is long and thin, for example a tube, channel or a layer located between parallel plates. This domain could represent a single pore in a porous medium, or a long channel as found for example in a fuel cell (cf. Figure 1.6). When considering a domain that is located between parallel plates, this domain can be seen as a two-dimensional domain, and is then denoted a thin strip. For simplicity, we use the thin strip in the following to exemplify and explain the idea of transversal averaging. This thin strip could correspond to the gas channel in Figure 1.6 if the channel is wide enough that the transport processes inside the channel are not affected by the sidewalls. If considering a two-dimensional porous medium, the thin strip can represent a single pore. Our considered thin strip is rectangular with length L and width ℓ , such that $\ell \ll L$. Hence, the scale separation $\varepsilon = \frac{\ell}{L} \ll 1$ can be identified. See Figure 1.15 for an illustration.

When applying transversal averaging, the goal is to obtain a dimensionally reduced model. For the thin strip, this means we obtain a one-dimensional model where only variability in the horizontal x_1 -direction is accounted for. Any variability in the transversal direction x_2 is incorporated through averages. The dimensionally reduced model is hence an effective model, and should generally be simpler than the original model. To easier isolate dominating behavior, model equations are cast to dimensionless form. We here use an example of single-phase Stokes flow through a channel (hence, flow along the thin strip) to illustrate the idea. We are hence searching for an effective model for

$$\left. \begin{aligned} \mu \nabla^2 \mathbf{v}^\varepsilon &= \nabla p^\varepsilon & (x_1, x_2) &\in (0, L) \times (0, \ell), \\ \nabla \cdot \mathbf{v}^\varepsilon &= 0 & (x_1, x_2) &\in (0, L) \times (0, \ell), \\ \mathbf{v}^\varepsilon &= \mathbf{0} & \text{on } x_2 &= 0, \ell, \\ p^\varepsilon(x_1 = 0) &= p_{\text{in}} & p^\varepsilon(x_1 = L) &= p_{\text{out}}. \end{aligned} \right\} (P^\varepsilon)$$

We here used a superscript ε to indicate that the variables depend on the scale separation ε . We non-dimensionalize the variables and spatial coordinates by

$$\hat{\mathbf{v}}^\varepsilon = \frac{\mathbf{v}^\varepsilon}{v_{\text{ref}}}, \quad \hat{p}^\varepsilon = \frac{p^\varepsilon - p_{\text{out}}}{p_{\text{ref}}}, \quad \hat{x}_1 = \frac{x_1}{L}, \quad \hat{x}_2 = \frac{x_2}{\ell},$$

where v_{ref} is some reference velocity and $p_{\text{ref}} = p_{\text{in}} - p_{\text{out}}$. Note that we use different length

scales for the horizontal and transversal direction. The non-dimensional version of (P^ε) is

$$\left. \begin{aligned} \frac{\mu v_{\text{ref}}}{L p_{\text{ref}}} \hat{\nabla}^2 \hat{\mathbf{v}}^\varepsilon &= \hat{\nabla} \hat{p}^\varepsilon & (\hat{x}_1, \hat{x}_2) \in (0, 1)^2, \\ \hat{\nabla} \cdot \hat{\mathbf{v}}^\varepsilon &= 0 & (\hat{x}_1, \hat{x}_2) \in (0, 1)^2, \\ \hat{\mathbf{v}}^\varepsilon &= \mathbf{0} & \text{on } \hat{x}_2 = 0, 1, \\ \hat{p}^\varepsilon(\hat{x}_1 = 0) &= 1 & \hat{p}^\varepsilon(\hat{x}_1 = 1) = 0. \end{aligned} \right\} \quad (\hat{P}^\varepsilon)$$

Here, the non-dimensional nabla operator is

$$\hat{\nabla} = \frac{\partial}{\partial \hat{x}_1} \mathbf{e}_1 + \frac{1}{\varepsilon} \frac{\partial}{\partial \hat{x}_2} \mathbf{e}_2$$

due to the difference in length scales in horizontal and transversal directions. We assume that the non-dimensional fraction $\frac{\mu v_{\text{ref}}}{L p_{\text{ref}}}$ is a small number, which corresponds to a low viscosity compared to the pressure drop. This is necessary to ensure non-trivial solutions of the flow and corresponds to the flow regime which is associated with the validity range of Darcy's law. More specifically, we assume

$$\frac{\mu v_{\text{ref}}}{L p_{\text{ref}}} = \varepsilon^2.$$

We then assume that the velocity and pressure have asymptotic expansions in terms of ε . That is,

$$\hat{p}^\varepsilon = \hat{p}_0 + \varepsilon \hat{p}_1 + \varepsilon^2 \hat{p}_2 + \dots,$$

and similar for each of the components of the velocity. This is used to find the dominating behavior as $\varepsilon \rightarrow 0$. In practice, we want to find new model equations in terms of the dominating terms \hat{p}_0 and $\hat{\mathbf{v}}_0$ only, but higher order approximations by incorporating first order (or even higher order) terms can be found correspondingly. These asymptotic expansions are then inserted into the model equations of (\hat{P}^ε) and sorted with respect to the order of ε . The Stokes equation becomes

$$\frac{\partial^2}{\partial \hat{x}_2^2} \hat{\mathbf{v}}_0 + \varepsilon \frac{\partial^2}{\partial \hat{x}_2^2} \hat{\mathbf{v}}_1 = \frac{1}{\varepsilon} \mathbf{e}_2 \frac{\partial \hat{p}_0}{\partial \hat{x}_2} + \left(\mathbf{e}_2 \frac{\partial \hat{p}_1}{\partial \hat{x}_2} + \mathbf{e}_1 \frac{\partial \hat{p}_0}{\partial \hat{x}_1} \right) + O(\varepsilon).$$

The dominating term here is of order $\frac{1}{\varepsilon}$. Hence, when $\varepsilon \rightarrow 0$, the only possibility is that

$$\frac{\partial \hat{p}_0}{\partial \hat{x}_2} = 0 \quad \implies \quad \hat{p}_0 = \hat{p}_0(\hat{x}_1).$$

This also means that the now dominating terms from the Stokes equation are of $O(\varepsilon^0)$. The mass conservation equation becomes

$$\frac{1}{\varepsilon} \frac{\partial \hat{\mathbf{v}}_{0,(2)}}{\partial \hat{x}_2} + \frac{\partial \hat{\mathbf{v}}_{1,(2)}}{\partial \hat{x}_2} + \frac{\partial \hat{\mathbf{v}}_{0,(1)}}{\partial \hat{x}_1} + O(\varepsilon) = 0,$$

where subscript (i) denotes velocity components. The boundary conditions at top and bottom can be written

$$\hat{\mathbf{v}}_0 + \varepsilon \hat{\mathbf{v}}_1 + \varepsilon^2 \hat{\mathbf{v}}_2 + O(\varepsilon^3) = 0 \quad \text{on } \hat{x}_2 = 0, 1.$$

The dominating terms of the mass conservation equation together with the boundary condition at top and bottom give

$$\hat{\mathbf{v}}_{0,(2)} = 0.$$

Hence, the dominating velocity is only in the horizontal direction. The horizontal component of the $O(\varepsilon^0)$ terms from the Stokes equation is

$$\frac{\partial^2 \hat{\mathbf{v}}_{0,(1)}}{\partial \hat{x}_2^2} = \frac{\partial \hat{p}_0}{\partial \hat{x}_1}.$$

Using that $\hat{p}_0 = \hat{p}_0(\hat{x}_1)$ and again the boundary condition for velocity at top and bottom, we arrive at

$$\hat{\mathbf{v}}_{0,(1)}(\hat{x}_1, \hat{x}_2) = \left(\frac{1}{2}(\hat{x}_2^2 - \hat{x}_2) \right) \frac{\partial \hat{p}_0}{\partial \hat{x}_1}(\hat{x}_1)$$

for the dominating, horizontal velocity. This is a parabolic velocity profile, as illustrated in Figure 1.15. Now, we finally transversally average this velocity in the \hat{x}_2 direction:

$$\hat{\bar{\mathbf{v}}}_{0,(1)}(\hat{x}_1) = \frac{1}{1} \int_0^1 \hat{\mathbf{v}}_{0,(1)}(\hat{x}_1, \hat{x}_2) d\hat{x}_2 = -\frac{1}{12} \frac{\partial \hat{p}_0}{\partial \hat{x}_1}(\hat{x}_1)$$

A second equation is obtained by averaging the $O(\varepsilon^0)$ -terms from the mass conservation in \hat{x}_2 :

$$0 = \frac{1}{1} \int_0^1 \left(\frac{\partial \hat{\mathbf{v}}_{1,(2)}}{\partial \hat{x}_2} + \frac{\partial \hat{\mathbf{v}}_{0,(1)}}{\partial \hat{x}_1} \right) d\hat{x}_2 = \frac{\partial \hat{\bar{\mathbf{v}}}_{0,(1)}}{\partial \hat{x}_1}(\hat{x}_1)$$

as $\hat{\mathbf{v}}_{1,(2)} = 0$ at $\hat{x}_2 = 0, 1$. We hence arrive at a one-dimensional, effective problem for $\hat{\bar{\mathbf{v}}}_{0,(1)}$ and \hat{p}_0 :

$$\left. \begin{aligned} \hat{\bar{\mathbf{v}}}_{0,(1)}(\hat{x}_1) &= -\frac{1}{12} \frac{\partial \hat{p}_0}{\partial \hat{x}_1}(\hat{x}_1) && \text{for } \hat{x}_1 \in (0, 1) \\ \frac{\partial \hat{\bar{\mathbf{v}}}_{0,(1)}}{\partial \hat{x}_1} &= 0 && \text{for } \hat{x}_1 \in (0, 1) \\ \hat{p}_0(\hat{x}_1 = 0) &= 1, && \hat{p}_0(\hat{x}_1 = 1) = 0. \end{aligned} \right\} (\hat{P}_0)$$

Hence, the averaged, horizontal velocity is proportional to the pressure drop, and is divergence-free (which in this one-dimensional setting corresponds to being constant). Note that the boundary conditions at the inlet and outlet never played a role, while the boundary conditions at the top and bottom boundaries influenced the derivation. If we re-dimensionalize the equations, we arrive at

$$\left. \begin{aligned} \bar{\mathbf{v}}_{0,(1)}(x_1) &= -\frac{1}{\mu} \frac{\ell^2}{12} \frac{\partial p_0}{\partial x}(x_1) && \text{for } x_1 \in (0, L) \\ \frac{\partial \bar{\mathbf{v}}_{0,(1)}}{\partial x_1} &= 0 && \text{for } x_1 \in (0, L) \\ p_0(x_1 = 0) &= p_{\text{in}}, && p_0(x_1 = L) = p_{\text{out}}. \end{aligned} \right\} (P_0)$$

We can identify the factor $\frac{\ell^2}{12}$ as the well-used permeability factor applied for fractures of aperture ℓ .

The concept of non-dimensionalizing, inserting asymptotic expansions and transversally averaging to find effective, dimensionally reduced equations can be applied also to much more complicated flow and transport processes than the one presented here. Especially when processes are changing along or across the domain, transversal averaging can be

useful. For example, in [103] single-phase flow with reactive transport in a thin strip was considered. Here, a mineral layer could precipitate or dissolve along the top and bottom boundaries. This corresponds to a free-boundary problem, but can be modeled using a layer width as variable. Since the layer width is a variable, Reynolds transport theorem (i.e. the Leibniz integral rule) has to be applied when doing the transversal averaging step. In this case, the resulting permeability and effective diffusion for the solute depend on the size of the mineral layer. Such settings have also been extended to be coupled to heat transport [17], incorporate biofilm growth [60, 105] and oscillating top and bottom boundaries [58] in thin strips. Transversal averaging can also be used to find the effective behavior in thin compartments between domains [3].

One important point when applying transversal averaging is that the non-dimensionalizing of the original model problem has an influence. When non-dimensionalizing and choosing the size of the appearing non-dimensional numbers (like $\frac{\mu v_{\text{ref}}}{L p_{\text{ref}}} = \varepsilon^2$), one chooses the regime the effective model is valid for. Different choices, corresponding to different regimes, will lead to different forms of the effective, dimensionally reduced models. For example, solute transport or heat transport with moderate Péclet numbers, lead to effective models having solute and heat transport due to both advection and diffusion in the effective model [17, 102]. However, a large Péclet number will lead to an effective hyperbolic model without diffusion when considering only the dominating terms, or a model with Taylor dispersion when including also next order terms [19, 59]. Hence, choosing the scaling of non-dimensional numbers and hence which regime is considered, is essential for deriving effective models using transversal averaging. However, it is not always possible to find a dimensionally reduced model for the effective behavior. There are regimes where the coupled behavior in the transversal direction is such that transversal averaging cannot be performed, or will not yield a closed effective model. This is for example the case if flow in turbulent regimes are considered. Note that we in this section derived a Darcy-like flow equation by starting with the Stokes equation. However, the same result would have been found if using the Navier-Stokes equations and assuming a sufficiently small Reynolds number.

In this thesis, effective models are derived by transversal averaging in Chapter 5 and in Chapter 6. In both these chapters, two-phase flow in a thin strip is considered, but with different assumptions on the flow morphology and on regimes. Both settings correspond to flow through a single pore in a porous medium and hence give dimensionally reduced models for the flow inside a small part of a porous medium. The settings could also represent the flow through a (wide) gas channel, as illustrated in Figure 1.6. In Chapter 3, ideas from transversal averaging are combined with homogenization to treat heat transport in a thin (and long) porous medium. This thin porous medium could represent the gas diffusion layer in a fuel cell (cf. Figure 1.6).

1.3.2 Boundary-layer methods

We are here concerned with models containing a region affected by a singularity or discontinuity - a boundary layer [90]. This boundary layer could occur due to the presence of an evolving fluid-fluid interface between two fluids in a two-phase flow setting, where surface tension between the two fluids give a different type of flow near the fluid-fluid interface compared to how the fluids are behaving further away from this interface. The fluid-fluid interface itself represents a discontinuity in the system since e.g. the densities, viscosities and the fluid pressures are typically discontinuous across the interface. Also an evolving

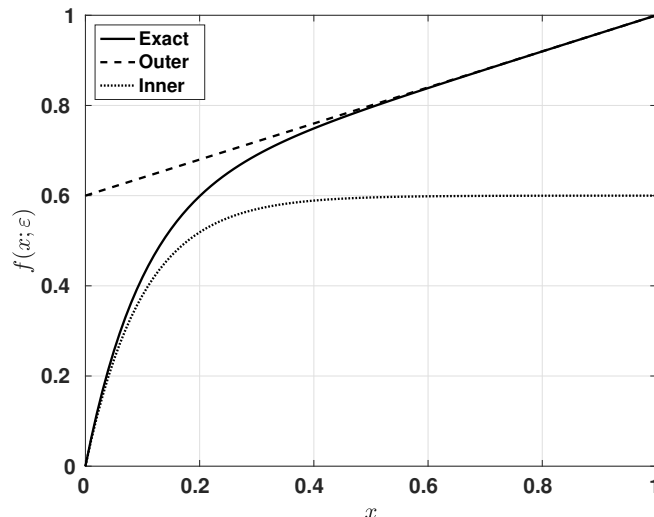


Figure 1.16: Exact solution (1.18) of (1.17), together with the outer (1.20) and inner (1.21) solutions.

fluid-solid interface in the case of mineral precipitation and dissolution can be seen as a discontinuity in the model, where also very different behavior is found at each side of the interface (i.e. flow in the fluid, stationary behavior in the solid mineral). Hence, different types of behavior can be found close to and far away from the singularity and can therefore be represented with different effective models. However, these different effective models should also be coupled to each other. We here consider the method of matched asymptotic expansions to find the dominating behavior in these two regions and to couple them. The idea is simple: We use *outer expansions* valid away from the singularity to find an *outer solution*, and *inner expansions* valid near the singularity to find an *inner solution*. These are then coupled together through *matching conditions*. These boundary-layer methods are relevant for understanding two-phase flow behavior and settings where single-phase flow interact with a solid through mineral precipitation and dissolution. Hence, boundary-layer methods are useful for understanding such processes at pore scale in a porous medium, e.g. for fuel cells and geothermal energy. However, these methods are relevant not only for processes in porous media, but are useful to understand and analyze effective behavior in many settings where a singularity or discontinuity occur.

We here use an example from [100] to illustrate the method of matched asymptotic expansions. The starting point is a one-dimensional two-point boundary-value problem, which includes a second-order, linear ODE:

$$\left. \begin{aligned} \varepsilon \frac{d^2 f}{dx^2} + \frac{df}{dx} &= a, \\ f(0) &= 0, \\ f(1) &= 1. \end{aligned} \right\} \quad (1.17)$$

Here, $\varepsilon > 0$ is a small number, $f(x; \varepsilon)$ is the unknown and a is a parameter. The analytical solution can then be found as

$$f(x; \varepsilon) = (1 - a) \frac{1 - e^{-x/\varepsilon}}{1 - e^{-1/\varepsilon}} + ax. \quad (1.18)$$

In Figure 1.16, the exact solution is plotted as a solid line. Note that a smaller value for ε corresponds to a narrower region near $x = 0$ where the curve is steeper. If $\varepsilon \rightarrow 0$, the original ODE reduces to a first order ODE

$$\frac{df}{dx} = a, \tag{1.19}$$

which can only fulfill one of the boundary conditions (unless $a = 1$). From the exact solution only $f(1) = 1$ is fulfilled when $\varepsilon \rightarrow 0$, while $f(0) = 0$ acts as a singularity. Here, ε represents the width of the region influenced by the singularity. If one lets $\varepsilon \rightarrow 0$ in the exact solution (1.18), this leads to the approximate solution

$$f(x; \varepsilon \rightarrow 0) = (1 - a) + ax \tag{1.20}$$

which is valid for small ε , but only away from $x = 0$. This is denoted as the outer solution (see dashed line in Figure 1.16) and can be seen as a good approximation away from the singularity. The outer solution (1.20) could also have been found by solving (1.19) together with $f(1) = 1$. This would hence correspond to the outer problem. Near the singularity $x = 0$, x is small. Hence, $x = O(\varepsilon)$. A scaled (magnified) inner coordinate X can be used to account for the behavior near the singularity. Therefore, the expression

$$f(x; \varepsilon) = F(X; \varepsilon) \quad \text{where } X = \frac{x}{\varepsilon}.$$

is used to find the inner problem. By applying the chain rule to the ODE in (1.17), the inner problem can then be written as

$$\left. \begin{aligned} \frac{d^2 F}{dX^2} + \frac{dF}{dX} &= a\varepsilon, \\ F(0) &= 0, \\ F\left(\frac{1}{\varepsilon}\right) &= 1. \end{aligned} \right\}$$

Here, the second boundary condition does not really make sense to use, as one is interested in the behavior of small x . Letting $\varepsilon \rightarrow 0$ and giving up the second boundary condition, the inner problem is fulfilled for any solution on the form

$$F(X; 0) = c(1 - e^{-X}) \quad c \in \mathbb{R}, \tag{1.21}$$

which is the inner solution (see dotted line in Figure 1.16). The constant c is then determined by a matching condition between the inner and outer solutions:

$$\begin{aligned} \lim_{X \rightarrow \infty} F(X; 0) &= \lim_{x \rightarrow 0} f(x; 0) \\ &\Downarrow \\ c &= 1 - a. \end{aligned} \tag{1.22}$$

This matching condition can also be seen in Figure 1.16 with

$$\lim_{X \rightarrow \infty} F(X; 0) = 0.6 = \lim_{x \rightarrow 0} f(x; 0).$$

Hence, by solving two simpler problems, the approximate solutions away from and near

the singularity for $\varepsilon \rightarrow 0$ can be found as

$$f(x; \varepsilon) \approx \begin{cases} (1-a) + ax & \text{for } \varepsilon \rightarrow 0 \text{ and } x > 0, \\ (1-a)(1 - e^{-X}) & \text{for } \varepsilon \rightarrow 0 \text{ and } X = \frac{x}{\varepsilon}. \end{cases}$$

In this example, the outer and inner problems could be found directly by letting $\varepsilon \rightarrow 0$ in the original model equations and using the scaled inner coordinates. For more complicated problems, one instead applies inner and outer asymptotic expansions and searches for outer and inner problems for the dominating terms as $\varepsilon \rightarrow 0$, similar as was done in Section 1.3.1 before averaging. In general, we would assume

$$\begin{aligned} f(x; \varepsilon) &= f_0(x) + \varepsilon f_1(x) + \varepsilon^2 f_2(x) + \dots, \\ F(X; \varepsilon) &= F_0(X) + \varepsilon F_1(X) + \varepsilon^2 F_2(X) + \dots, \end{aligned}$$

where

$$f(x; \varepsilon) = F(X; \varepsilon),$$

with the stretched inner variable

$$X = \frac{x - \alpha}{\varepsilon},$$

when there is a singularity in $x = \alpha$. We hence search for outer and inner problems in terms of the dominating terms f_0 and F_0 , respectively. For the general case, one still relies on being able to identify the small number ε describing the relative width of the inner region, in order to be able to apply matched asymptotic expansions.

One typically cannot solve the outer and inner problems exactly, like here. However, one is normally only interested in finding the limit problems for f_0 and F_0 , and not the limit solutions themselves. The matching conditions hence give the connection between the two limit problems. The applied matching condition (1.22) can generally be read as

$$\begin{aligned} &\text{The outer limit of the inner limit solution} \\ &= \text{The inner limit of the outer limit solution} \end{aligned}$$

This matching condition can hence also apply to higher order terms of the inner and outer expansions (when needed).

Matched asymptotic expansions is used for a large variety of flow problems, see [90, 100] for an overview. One can for example apply them to the setting of turbulent flow interacting with a wall. Such flows could be described by the Navier-Stokes equations in the entire domain, but can be simplified through matched asymptotic expansions. Near the wall, friction dominates and one would have a layer of creeping flow which can be described with a parabolic flow profile. Away from the wall, the viscous-free Euler equations could be used to describe the flow. These two problems are then coupled via matching conditions [90].

For phase fields, matched asymptotic expansions can be used to investigate the sharp-interface limit of the phase-field model. In this case, the ratio between the diffuse-interface width and a longer length scale (e.g. size of domain) can be identified as ε . Then, the outer expansions are applied far away from the diffuse transition zone, and the inner expansions close to the it. Hence, the outer expansions should recover the model equations inside each of the phases, while the inner expansions should recover the boundary conditions at the (now) sharp interface as $\varepsilon \rightarrow 0$. The matching conditions ensure that these boundary conditions are indeed for the interface between the two phases [22]. This way, one can

ensure that the phase-field model indeed represents the expected sharp-interface model as the diffuse-interface width approaches zero. For phase-field models for two-phase flow, matched asymptotic expansions are applied to find the sharp-interface limit in [2], and extended to two-phase flow with varying surface tension effects in [43]. Sharp-interface limits for reactive transport phase-field models (without flow) have been considered in [86, 104]. Although matched asymptotic expansions can be used to validate a phase-field model towards its sharp-interface limit, there is still no guarantee that the phase-field model still behaves as expected when a non-zero diffuse-interface width is used in a numerical simulation. However, the results from the phase-field model is however expected to approach the results from the corresponding sharp-interface model when using a smaller value for the diffuse-interface width.

To be able to apply matched asymptotic expansions, one relies on being able to find a suitable value for ε , which describes the (relative) size of the region where the discontinuity influences the behavior of the system. In the above example, we then used ε to scale the inner coordinate, but depending on the behavior of the problem in questions, other types of scaling with respect to ε , e.g. $\varepsilon^{1/2}$, could be necessary. Which scaling is needed to be able to find and isolate the effective behavior away from and near the singularity or discontinuity, and to couple these, is not obvious in advance. It is also not always possible to isolate the behavior away from and near the discontinuity. See [100] for a discussion on this matter. In this thesis, however, standard scalings with respect to the identified ε could be applied to find the effective behavior away from and near the discontinuity, and to couple them.

In this thesis, boundary-layer methods in the form of matched asymptotic expansions will be applied in Chapter 6, 8 and 10. In Chapter 6, matched asymptotic expansions are combined with transversal averaging to a two-phase flow problem in a thin strip to investigate the effective behavior away from and near the fluid-fluid interface. Due to the influence of the fluid-fluid interface, the matched asymptotic expansions are needed to find the effective behavior of the two-phase flow as the thin strip becomes longer and thinner. In Chapter 8 and Chapter 10, matched asymptotic expansions are applied to derive the sharp-interface limit for phase-field models for reactive transport. Hence, they help us in validating the phase-field models, which are then used to model reactive transport at the pore scale of a porous medium, relevant for geothermal energy (cf. Figure 1.2) and salt precipitation (cf. Figure 1.4).

1.3.3 Homogenization

Homogenization (also known as periodic homogenization) will be used to derive effective equations at a larger scale, in the case that the equations or considered domain at the smaller scale has some local periodicity. This can for example be applied on periodic pore-scale geometries to find effective equations at the Darcy scale. Performing this homogenization step is vital when having a known pore-scale model and one wishes to find the effective behavior at the larger Darcy scale. Homogenization is hence an essential multiscale method for bridging scale gaps in porous media, cf. Figure 1.7. Making this step is relevant for e.g. geothermal energy, where the pore-scale geometry changes due to mineral precipitation and dissolution, as highlighted in Figure 1.2, and for soil salinization where salts can precipitate due to the evaporation, as highlighted in Figures 1.3 and 1.4. However, performing this step is also important when one wants to find effective parameters at a larger scale, e.g. when finding permeabilities at field scale from given REV-scale permeabilities, as discussed in Section 1.1. Homogenization relies on the assumption that the

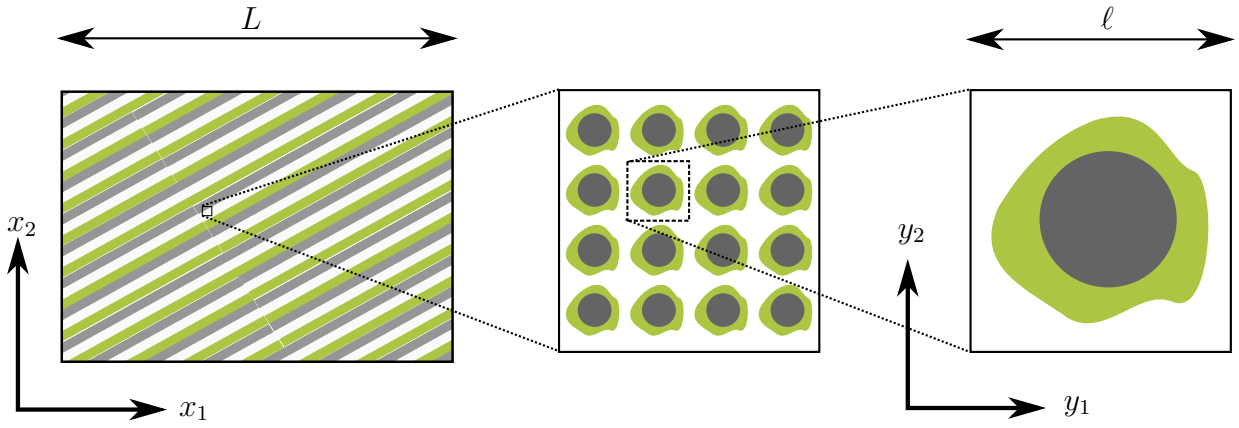


Figure 1.17: Porous medium with periodic pore-scale geometry. For the left part, a long length scale L can be identified for the averaged Darcy scale. For the rightmost part, a small length scale ℓ is found at the pore scale.

micro-scale (e.g. pore-scale) behavior can be described as locally periodic, and that there is a clear scale separation between the smaller and the larger scale. In a porous medium when going from pore to Darcy scale, this can be done by finding a typical pore-scale length scale ℓ , and a larger length scale L at the Darcy scale. See Figure 1.17 for an illustration. Hence, scale separation means that $\varepsilon = \frac{\ell}{L} \ll 1$.

When performing homogenization, one applies two-scale asymptotic expansions to the pore-scale model equations, and isolates dominating order terms at each scale, in order to arrive at Darcy-scale equations which are connected to local pore-scale problems giving effective parameters. These two-scale asymptotic expansions rely on the introduction of an extra coordinate system. One separates between macro-scale coordinates \mathbf{x} characterizing “slow” variability, and a local coordinate \mathbf{y} describing “fast” variability. These two coordinate systems are also sketched in Figure 1.17. Then, ε corresponds to the scaling factor between the two coordinate systems. Note that \mathbf{y} is to be understood as a local coordinate system: For every macro-scale point \mathbf{x} , one zooms in, and sees a local domain with its own local coordinate system through \mathbf{y} . Hence, \mathbf{x} itself will no longer be used to describe any small-scale variability, but only tell us where to zoom in, while the local variability is then resolved through \mathbf{y} . The local periodicity is hence required in the \mathbf{y} -coordinates.

Also here we need to cast the model equations to dimensionless form in order to apply homogenization. Similarly as in Section 1.3.1, we use ℓ to non-dimensionalize \mathbf{y} , and L for \mathbf{x} . Hence, the non-dimensional $\hat{\mathbf{y}}$ will therefore live in a unit square (or cube), $\hat{\mathbf{y}} \in Y = [0, 1]^d$, which will be called the unit cell. The periodicity in non-dimensional variables is then, for a variable $\hat{a}(\hat{\mathbf{y}})$

$$\hat{a}(\hat{\mathbf{y}}) = \hat{a}(\hat{\mathbf{y}} + \mathbf{e}_j), \quad j = 1, \dots, d.$$

This is called Y -periodicity. After non-dimensionalizing, we apply the *Homogenization Ansatz* to all variables, which is the assumption that all variables having both slow and fast variability can be described in terms of variability in the two coordinate systems $\hat{\mathbf{x}}$ and $\hat{\mathbf{y}}$ through two-scale asymptotic expansions:

$$\hat{a}^\varepsilon(\hat{\mathbf{x}}) = \hat{a}_0(\hat{\mathbf{x}}, \hat{\mathbf{y}}) + \varepsilon \hat{a}_1(\hat{\mathbf{x}}, \hat{\mathbf{y}}) + \varepsilon^2 \hat{a}_2(\hat{\mathbf{x}}, \hat{\mathbf{y}}) + \dots$$

where each \hat{a}_j is Y -periodic. Due to the introduction of the extra coordinate system and

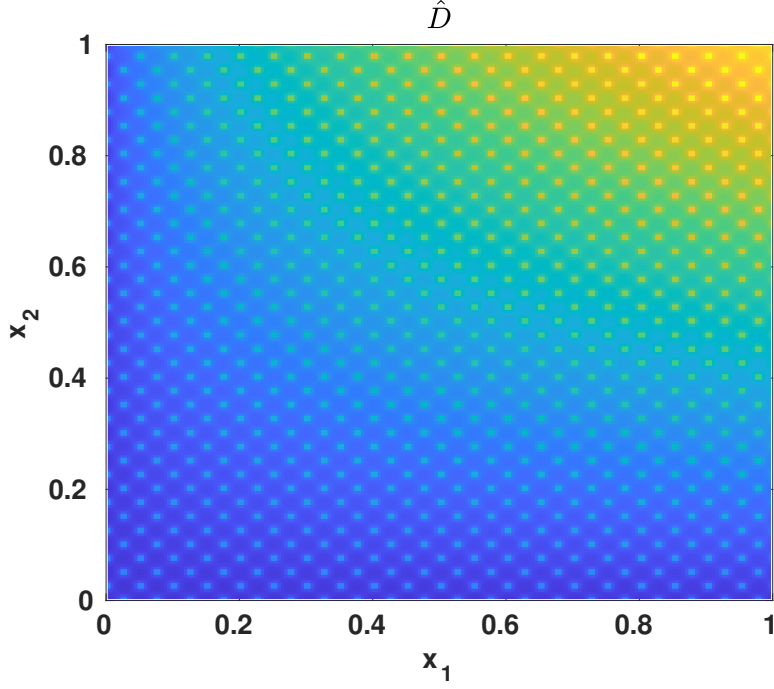


Figure 1.18: Highly oscillatory diffusion coefficient \hat{D} applied in equation (1.23).

the scaling difference between $\hat{\mathbf{x}}$ and $\hat{\mathbf{y}}$, gradients need to be rewritten according to

$$\hat{\nabla} \hat{a}^\varepsilon(\hat{\mathbf{x}}) = \left(\hat{\nabla}_{\hat{\mathbf{x}}} + \frac{1}{\varepsilon} \hat{\nabla}_{\hat{\mathbf{y}}} \right) \left(\hat{a}_0(\hat{\mathbf{x}}, \hat{\mathbf{y}}) + \varepsilon \hat{a}_1(\hat{\mathbf{x}}, \hat{\mathbf{y}}) + \varepsilon^2 \hat{a}_2(\hat{\mathbf{x}}, \hat{\mathbf{y}}) + \dots \right).$$

Then, by inserting the two-scale asymptotic expansions and rewriting accordingly, one isolates the dominating terms as $\varepsilon \rightarrow 0$. To illustrate the method, we consider a stationary diffusion problem with a highly oscillatory diffusion coefficient.

We here consider the non-dimensional diffusion problem

$$-\hat{\nabla} \cdot (\hat{D} \hat{\nabla} \hat{u}^\varepsilon) = \hat{f}, \quad \text{in } \Omega, \quad (1.23)$$

where \hat{D} is a given, but highly oscillatory, diffusion coefficient seen in Figure 1.18, \hat{f} is a given force, which is assumed to not be highly oscillatory, and \hat{u}^ε is the unknown. Assuming that the behavior of \hat{D} can be decomposed into slow and (locally periodic) fast variability, it can be written as

$$\hat{D} = \hat{D}(\hat{\mathbf{x}}, \hat{\mathbf{y}}). \quad (1.24)$$

Inserting the two-scale asymptotic expansions for \hat{u}^ε in (1.23) and sorting the terms after

increasing order with respect to ε , gives

$$\begin{aligned} & -\frac{1}{\varepsilon^2} \hat{\nabla}_{\hat{\mathbf{y}}} \cdot \left(\hat{D}(\hat{\mathbf{x}}, \hat{\mathbf{y}}) \hat{\nabla}_{\hat{\mathbf{y}}} \hat{u}_0(\hat{\mathbf{x}}, \hat{\mathbf{y}}) \right) \\ & -\frac{1}{\varepsilon} \left\{ \hat{\nabla}_{\hat{\mathbf{x}}} \cdot \left(\hat{D}(\hat{\mathbf{x}}, \hat{\mathbf{y}}) \hat{\nabla}_{\hat{\mathbf{y}}} \hat{u}_0(\hat{\mathbf{x}}, \hat{\mathbf{y}}) \right) \right. \\ & \quad \left. + \hat{\nabla}_{\hat{\mathbf{y}}} \cdot \left(\hat{D}(\hat{\mathbf{x}}, \hat{\mathbf{y}}) \left(\hat{\nabla}_{\hat{\mathbf{x}}} \hat{u}_0(\hat{\mathbf{x}}, \hat{\mathbf{y}}) + \hat{\nabla}_{\hat{\mathbf{y}}} \hat{u}_1(\hat{\mathbf{x}}, \hat{\mathbf{y}}) \right) \right) \right\} \\ & - \left\{ \hat{\nabla}_{\hat{\mathbf{x}}} \cdot \left(\hat{D}(\hat{\mathbf{x}}, \hat{\mathbf{y}}) \left(\hat{\nabla}_{\hat{\mathbf{x}}} \hat{u}_0(\hat{\mathbf{x}}, \hat{\mathbf{y}}) + \hat{\nabla}_{\hat{\mathbf{y}}} \hat{u}_1(\hat{\mathbf{x}}, \hat{\mathbf{y}}) \right) \right) \right. \\ & \quad \left. + \hat{\nabla}_{\hat{\mathbf{y}}} \cdot \left(\hat{D}(\hat{\mathbf{x}}, \hat{\mathbf{y}}) \left(\hat{\nabla}_{\hat{\mathbf{x}}} \hat{u}_1(\hat{\mathbf{x}}, \hat{\mathbf{y}}) + \hat{\nabla}_{\hat{\mathbf{y}}} \hat{u}_2(\hat{\mathbf{x}}, \hat{\mathbf{y}}) \right) \right) \right\} = \hat{f}(\hat{\mathbf{x}}) + O(\varepsilon). \end{aligned}$$

The dominating term as $\varepsilon \rightarrow 0$ is the $O(\varepsilon^{-2})$ -term. This leads to the following problem, for all $\hat{\mathbf{x}} \in \Omega$:

$$\left. \begin{aligned} \hat{\nabla}_{\hat{\mathbf{y}}} \cdot \left(\hat{D}(\hat{\mathbf{x}}, \hat{\mathbf{y}}) \hat{\nabla}_{\hat{\mathbf{y}}} \hat{u}_0(\hat{\mathbf{x}}, \hat{\mathbf{y}}) \right) &= 0 \quad \hat{\mathbf{y}} \in Y, \\ \hat{u}_0(\hat{\mathbf{x}}, \hat{\mathbf{y}}) &\text{ is } Y\text{-periodic.} \end{aligned} \right\} \quad (P^{-2})$$

The only possible solution of the (P^{-2}) -problem is

$$\hat{u}_0 = \hat{u}_0(\hat{\mathbf{x}}). \quad (1.25)$$

Therefore, \hat{u}_0 is constant with respect to $\hat{\mathbf{y}}$ and only contains “slow” variability.

Turning to terms of $O(\varepsilon^{-1})$, the following problem can be obtained for \hat{u}_1 , if \hat{u}_0 would be known, as

$$\left. \begin{aligned} \hat{\nabla}_{\hat{\mathbf{y}}} \cdot \left(\hat{D}(\hat{\mathbf{x}}, \hat{\mathbf{y}}) \left(\hat{\nabla}_{\hat{\mathbf{x}}} \hat{u}_0(\hat{\mathbf{x}}) + \hat{\nabla}_{\hat{\mathbf{y}}} \hat{u}_1(\hat{\mathbf{x}}, \hat{\mathbf{y}}) \right) \right) &= 0 \quad \hat{\mathbf{x}} \in \Omega, \hat{\mathbf{y}} \in Y \\ \hat{u}_1(\hat{\mathbf{x}}, \hat{\mathbf{y}}) &\text{ is } Y\text{-periodic.} \end{aligned} \right\} \quad (P^{-1})$$

To deal with (P^{-1}) , first observe that

$$\hat{\nabla}_{\hat{\mathbf{x}}} \hat{u}_0 = \sum_{j=1}^d \mathbf{e}_j \partial_{\hat{x}_j} \hat{u}_0. \quad (1.26)$$

From the linearity of (P^{-1}) , a linear response in \hat{u}_1 is expected if $\partial_{\hat{x}_j} \hat{u}_0$ changes. We hence expect

$$\hat{u}_1(\hat{\mathbf{x}}, \hat{\mathbf{y}}) = \tilde{u}_1(\hat{\mathbf{x}}) + \sum_{j=1}^d w_j(\hat{\mathbf{x}}, \hat{\mathbf{y}}) \partial_{\hat{x}_j} \hat{u}_0(\hat{\mathbf{x}}) \quad (1.27)$$

for some weights w_j . By inserting (1.27) and (1.26) in (P^{-1}) , the weights w_j are found to solve

$$\left. \begin{aligned} \hat{\nabla}_{\hat{\mathbf{y}}} \cdot \left(\hat{D}(\hat{\mathbf{x}}, \hat{\mathbf{y}}) \left(\mathbf{e}_j + \hat{\nabla}_{\hat{\mathbf{y}}} w_j(\hat{\mathbf{x}}, \hat{\mathbf{y}}) \right) \right) &= 0 \quad \hat{\mathbf{y}} \in Y \\ w_j(\hat{\mathbf{x}}, \hat{\mathbf{y}}) &\text{ is } Y\text{-periodic,} \\ \int_Y w_j(\hat{\mathbf{x}}, \hat{\mathbf{y}}) d\hat{\mathbf{y}} &= 0 \quad j = 1, \dots, d. \end{aligned} \right\} \quad (P_j^{-1})$$

The third equation is added to ensure uniqueness as the weights w_j would otherwise only be known up to a constant (with respect to $\hat{\mathbf{y}}$). With w_j known, also \hat{u}_1 is known (up to a constant).

Continuing with the $O(\varepsilon^0)$ -terms, we arrive at the following problem:

$$\left. \begin{aligned} & -\hat{\nabla}_{\hat{\mathbf{x}}} \cdot \left(\hat{D}(\hat{\mathbf{x}}, \hat{\mathbf{y}}) \left(\hat{\nabla}_{\hat{\mathbf{x}}} \hat{u}_0(\hat{\mathbf{x}}) + \hat{\nabla}_{\hat{\mathbf{y}}} \hat{u}_1(\hat{\mathbf{x}}, \hat{\mathbf{y}}) \right) \right) \\ & -\hat{\nabla}_{\hat{\mathbf{y}}} \cdot \left(\hat{D}(\hat{\mathbf{x}}, \hat{\mathbf{y}}) \left(\hat{\nabla}_{\hat{\mathbf{x}}} \hat{u}_1(\hat{\mathbf{x}}, \hat{\mathbf{y}}) + \hat{\nabla}_{\hat{\mathbf{y}}} \hat{u}_2(\hat{\mathbf{x}}, \hat{\mathbf{y}}) \right) \right) = \hat{f}(\hat{\mathbf{x}}) \quad \hat{\mathbf{x}} \in \Omega, \hat{\mathbf{y}} \in Y \\ & \hat{u}_2(\hat{\mathbf{x}}, \hat{\mathbf{y}}) \text{ is } Y\text{-periodic} . \end{aligned} \right\} \quad (P^0)$$

Averaging the equation over Y by integrating with respect to $\hat{\mathbf{y}}$ and using Gauss' theorem on the $\hat{\nabla}_{\hat{\mathbf{y}}} \cdot$ -term, leads to

$$\begin{aligned} & -\frac{1}{|Y|} \int_Y \hat{\nabla}_{\hat{\mathbf{x}}} \cdot \left(\hat{D}(\hat{\mathbf{x}}, \hat{\mathbf{y}}) \left(\hat{\nabla}_{\hat{\mathbf{x}}} \hat{u}_0(\hat{\mathbf{x}}) + \hat{\nabla}_{\hat{\mathbf{y}}} \hat{u}_1(\hat{\mathbf{x}}, \hat{\mathbf{y}}) \right) \right) d\hat{\mathbf{y}} \\ & - \frac{1}{|Y|} \int_{\partial Y} \left(\hat{D}(\hat{\mathbf{x}}, \hat{\mathbf{y}}) \left(\hat{\nabla}_{\hat{\mathbf{x}}} \hat{u}_1(\hat{\mathbf{x}}, \hat{\mathbf{y}}) + \hat{\nabla}_{\hat{\mathbf{y}}} \hat{u}_2(\hat{\mathbf{x}}, \hat{\mathbf{y}}) \right) \right) \cdot \mathbf{n} ds = \hat{f}(\hat{\mathbf{x}}) . \end{aligned}$$

Due to the Y -periodicity applied to \hat{u}_1 and \hat{u}_2 , the contributions from the various sides of the unit cell cancel each other. Hence, the net contribution from the integral along ∂Y is zero. Inserting (1.27), the above equation reformulates to

$$-\hat{\nabla}_{\hat{\mathbf{x}}} \cdot \left[\int_Y \hat{D}(\hat{\mathbf{x}}, \hat{\mathbf{y}}) \left(\hat{\nabla}_{\hat{\mathbf{x}}} \hat{u}_0(\hat{\mathbf{x}}) + \sum_{j=1}^d \hat{\nabla}_{\hat{\mathbf{y}}} w_j(\hat{\mathbf{x}}, \hat{\mathbf{y}}) \partial_{\hat{x}_j} \hat{u}_0(\hat{\mathbf{x}}) \right) d\hat{\mathbf{y}} \right] = \hat{f}(\hat{\mathbf{x}}) .$$

Using matrix notation, this can be rewritten as

$$-\hat{\nabla}_{\hat{\mathbf{x}}} \cdot \left(\hat{\mathbf{D}}(\hat{\mathbf{x}}) \hat{\nabla}_{\hat{\mathbf{x}}} \hat{u}_0(\hat{\mathbf{x}}) \right) = \hat{f}(\hat{\mathbf{x}}), \quad (1.28)$$

where the matrix $\hat{\mathbf{D}}$ has elements

$$\hat{\mathbf{D}}_{ij}(\hat{\mathbf{x}}) = \int_Y \hat{D}(\hat{\mathbf{x}}, \hat{\mathbf{y}}) (\delta_{ij} + \partial_{\hat{y}_i} w_j(\hat{\mathbf{x}}, \hat{\mathbf{y}})) d\hat{\mathbf{y}}, \quad (1.29)$$

and where the w_j are uniquely determined through the cell problems

$$\left. \begin{aligned} & \hat{\nabla}_{\hat{\mathbf{y}}} \cdot \left(\hat{D}(\hat{\mathbf{x}}, \hat{\mathbf{y}}) \left(\mathbf{e}_j + \hat{\nabla}_{\hat{\mathbf{y}}} w_j(\hat{\mathbf{x}}, \hat{\mathbf{y}}) \right) \right) = 0 \quad \hat{\mathbf{y}} \in Y \\ & w_j(\hat{\mathbf{x}}, \hat{\mathbf{y}}) \text{ is } Y\text{-periodic}, \\ & \int_Y w_j(\hat{\mathbf{x}}, \hat{\mathbf{y}}) d\hat{\mathbf{y}} = 0 \end{aligned} \right\} \quad (P_j^{-1}) \quad j = 1, \dots, d.$$

Note that (1.28) is an equation in $\hat{\mathbf{x}}$ only, and is hence the searched, effective equation. The parameter $\hat{\mathbf{D}}$ from (1.29) is called the effective diffusion matrix and includes local information through the cell problems (P_j^{-1}). The cell problems (P_j^{-1}) are equations that are only to be solved with respect to $\hat{\mathbf{y}}$, while $\hat{\mathbf{x}}$ only appears as a parameter. Variability in $\hat{\mathbf{x}}$ and $\hat{\mathbf{y}}$ are hence decoupled, as for each macroscale point $\hat{\mathbf{x}}$ the local cell problem in $\hat{\mathbf{y}}$ can be solved to determine $\hat{\mathbf{D}}(\hat{\mathbf{x}})$ in that point. Also note that it is not a problem that the weights w_j could only be determined up to a constant with respect to $\hat{\mathbf{y}}$, as only their derivatives with respect to \hat{y}_i are needed to calculate the effective diffusion matrix.

In Figure 1.19 the original, highly oscillatory diffusion coefficient \hat{D} can be seen together with the first component of the derived effective diffusion matrix $\hat{\mathbf{D}}$. The highly oscillatory diffusion coefficient is plotted on a 200×200 grid and contain oscillations with $\varepsilon = \frac{1}{20}$.

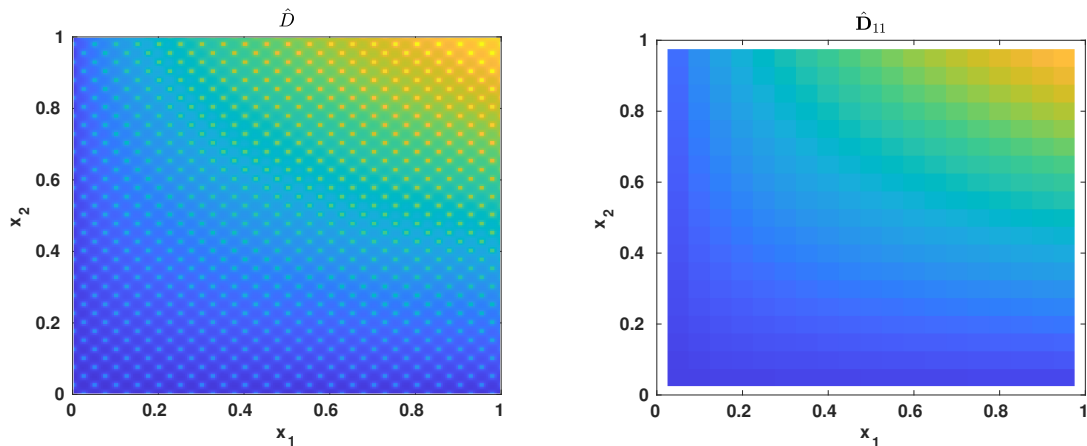


Figure 1.19: Diffusion coefficients. Left: original, highly oscillatory diffusion coefficient. Right: first component of derived effective diffusion matrix.

The element $\hat{\mathbf{D}}_{11}$ of the effective diffusion matrix was obtained by solving each local cell problem on a 20×20 grid. The component $\hat{\mathbf{D}}_{11}$ is in this example representative for the effective diffusion matrix, as $\hat{\mathbf{D}}_{11} \approx \hat{\mathbf{D}}_{22}$ and the off-diagonal components are almost zero. Hence, the effective diffusion matrix can be well represented by

$$\hat{\mathbf{D}} = \hat{\mathbf{D}}_{11} \mathbf{I}$$

in this case.

Solving the steady-state diffusion problem above with $\hat{f}(\hat{\mathbf{x}}) \equiv 1$ and using zero Dirichlet conditions on the boundary, the solutions of the original and of the effective model are obtained as seen in Figure 1.20. Here, the microscale solution \hat{u} (top left of Figure 1.20) was obtained by solving the original problem (1.23) with the highly oscillatory diffusion coefficient \hat{D} on a 200×200 grid. When averaging this solution on a 20×20 grid, the Figure 1.20 on the top right is obtained. This can then be compared to the effective solution \hat{u}_0 (bottom Figure 1.20), which was obtained by solving the effective model (1.28) on the coarser 20×20 grid. The relative L^2 -error between the averaged and effective solutions is $0.0451 = 4.51\%$. There is a clear gain in terms of computational costs, as solving many small problems on a coarser grid is cheaper than solving one huge problem on a fine grid. The loss in accuracy is however moderate.

As illustrated in this example, homogenization can be used not only for the transition from pore to Darcy scale, but also to find averaged coefficients of an oscillating parameter, e.g. for a diffusion problem. Finding averaged coefficients is relevant for porous media, where the permeability and (Darcy-scale) diffusion coefficients might be needed at larger scales (e.g. field scale). When applying homogenization to a pore-scale geometry, there are usually more steps needed for applying Gauss' theorem in (P^0) since there are internal boundaries, but the general idea and steps remain the same as presented above. The main challenge lies in finding relations like (1.27), which are needed to handle the appearance of the second-order terms. As also seen in the presented example, the assumption of local periodicity is essential. The periodicity both provides boundary conditions for the local cell problems, and also removes contributions along local boundary integrals when applying Gauss' theorem. The local periodicity ensures that each cell problem for effective quantities can be found independently of other cell problems (i.e. corresponding to other locations),

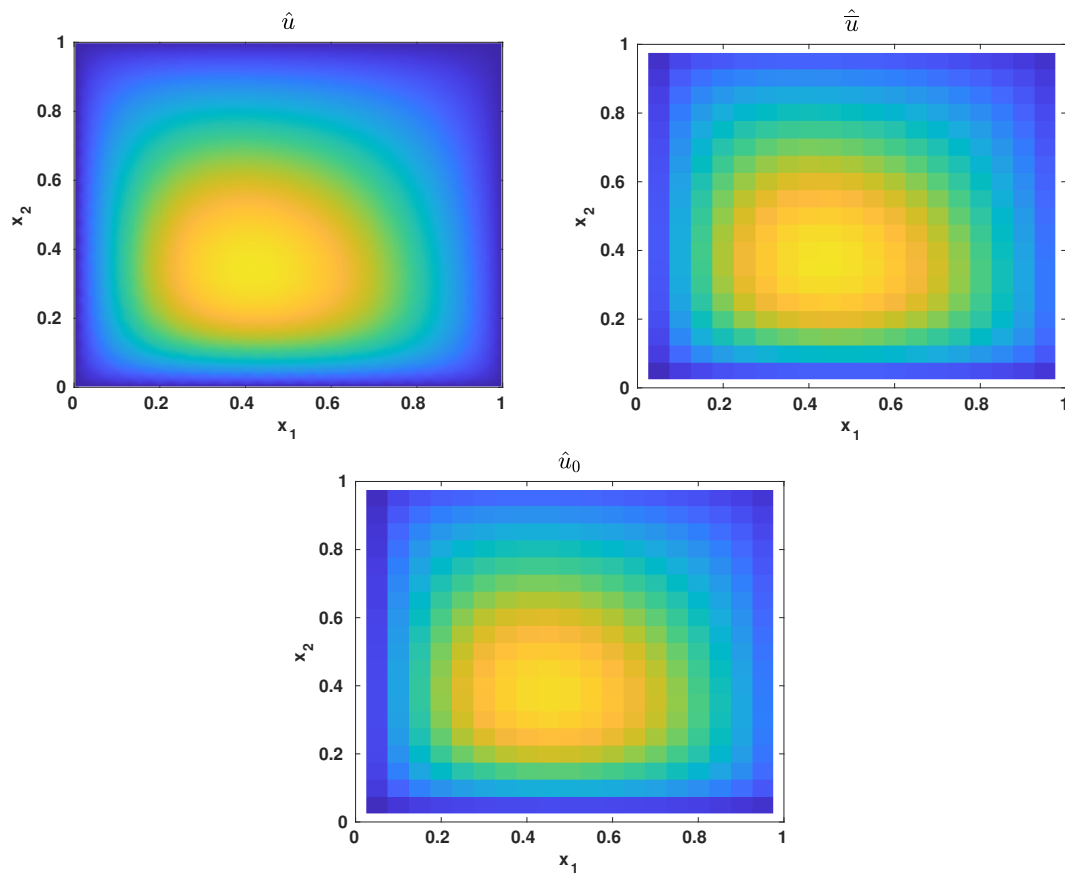


Figure 1.20: Various solutions of the diffusion problem. Top left: The solution \hat{u} of the original problem (1.23). Top right: The average of \hat{u} , $\hat{\hat{u}}$, on a coarser grid. Bottom: The solution \hat{u}_0 of the effective diffusion problem (1.28) on the same grid as for the averaged $\hat{\hat{u}}$.

since they do not rely on each other.

Homogenization has been applied to a wide range of porous-media problems, and we refer to [9, 27, 51] for books both explaining the method thoroughly and showing a wide range of applications. The challenges in applying homogenization come in particularly if considering evolving interfaces and/or coupled and non-linear processes. For the case of evolving, sharp interfaces (e.g. modeled by a level set), the separation of processes for each phase as well as the averaging over evolving domains are more technical and needs extra care since Reynold's transport theorem must be applied. In particular, boundary conditions at the evolving interface need to be incorporated in the homogenization steps. A procedure for applying homogenization to a reactive transport model with a level set was developed in [102], and this approach was later further adjusted and developed for more applications involving level sets, as coupled heat transport [18], colloid dynamics [83], drug release [84], and biofilm growth [93]. Applying homogenization to a phase-field model can be easier, as there is no need to separate processes at each side of the interface nor to incorporate boundary conditions at the evolving interface during homogenization. However, a phase-field model consists of tightly coupled equations, which can also cause difficulties. Also, the diffuse-interface width represents another length scale, and its size in relation to the pore-scale length scale must be clarified. Homogenization has been successfully applied to phase-field models for two-phase flow under various assumptions on the evolution dynamics of the phase field [30, 69, 91], for binary mixtures [35] and for reactive transport without flow [86].

Note that, as in the case of transversal averaging, homogenization is regime-dependent. Hence, the micro-scale model equations need to be cast in dimensionless form, and the size of appearing non-dimensional numbers need to be chosen large or small in comparison to the scale separator ε . These choices determine which regime the derived effective model will be valid for, and different choices will lead to different effective models. The validity of the derived effective model relies on several aspects. This validity could be addressed by comparing with pore-scale simulations, see e.g. [108]. Using two-scale convergence, the validity of the homogenization approach can be proven for simple, linear problems [5]. These proofs, however, can in general not be extended to more coupled and non-linear problems, as considered in this thesis. The assumption of local periodicity to apply homogenization can also be quite restrictive, as neither real pore-scale structures nor REV-scale permeabilities are usually periodic. However, as will be seen in Chapter 2, homogenization can still be applied also in a non-periodic case, but will generally have larger errors in regions where the actual behavior is not periodic. Hence, homogenization has the ability to provide useful information about the large-scale behavior also for more general settings, but at the cost of larger model errors.

In this thesis, homogenization is applied or plays a role in Chapters 2, 3, 4, 7, 8, 9 and 10. In Chapter 2, homogenization is combined with adaptive mesh refinement for a non-linear parabolic problem. Here, permeabilities at a larger scale are sought, as discussed in Section 1.1. In Chapter 3, homogenization and ideas from transversal averaging are applied to heat transport in a thin pore-scale domain, to find the effective Darcy-scale behavior. Chapter 3 as well as Chapter 4 investigate the behavior of the resulting effective parameters, in particular of heat conductivity, by solving cell problems arising from homogenization. Such investigations are useful to understand the Darcy-scale behavior for such effective parameters, which is relevant for especially geothermal energy (cf. Figure 1.2). In Chapter 7, homogenization is applied to a phase-field model for two-phase flow at the pore scale. Hence, a Darcy-scale model for the effective two-phase flow through the porous

medium is found, with effective parameters through local cell problems instead of relying on parametrized saturation expressions, as discussed in Section 1.2.2. A Darcy-scale model for reactive transport coupled to pore-scale cell problems is derived by homogenization in Chapter 8. The resulting two-scale model is implemented in Chapter 9, allowing effective simulations of porous-media problems where the pore-scale geometry changes due to mineral precipitation and dissolution, e.g. for geothermal energy (cf. Figure 1.2) or salt precipitation (cf. Figure 1.4). Effective properties from cell problems derived by homogenization for a level-set and a phase-field model for reactive transport are compared in Chapter 10. Hence, the influence of the interface description on Darcy-scale effective properties is in this way addressed.

1.3.4 Heterogeneous multiscale methods

The heterogeneous multiscale method (HMM) is not a discretization scheme that specifies how a discretized system of equations could be formulated, but is an abstract framework to design multiscale schemes. Some discretization scheme(s) still need to be applied to discretize the governing equations at the involved scales. HMM can be applied when model equations at two (or more) scales depend on each other. This is the case in porous media, e.g. as the field-scale permeability depends on the REV-scale permeability as discussed in Section 1.1, or that Darcy-scale model equations depend on effective parameters through pore-scale cell problems, as just discussed in Section 1.3.3. Hence, HMM are relevant for a large range of porous-media problems due to the dependence across scales (cf. Figure 1.7). We here present the main ideas of heterogeneous multiscale methods, based on the review [111] and book [110].

The starting point is a macroscale problem of the form

$$F(v_M, d_M) = 0,$$

which should be solved for the macroscale variable v_M , but where macroscale data d_M are missing. However, there is a connected microscale model

$$\mathcal{F}(v_m, d_m) = 0$$

for a microscale variable v_m that depends on (known) microscale data d_m . These microscale data might depend on v_m ($d_m = d_m(v_m)$). Both the macroscale and microscale model will typically be a PDE or a system of PDEs. After solving for v_m , a procedure to estimate the missing data d_M ($d_M = d_M(v_m)$) is applied. Hence, the two models and their data are coupled. The main idea of HMM is using a macroscopic solver to solve the macroscale problem, and designing procedures for estimating the missing data from the microscale model. That means, HMM keeps track of where and which macroscale data is needed, solves the microscale model under the necessary constraints, and processes the outcome to estimate the needed macroscale data.

Schematically, HMM can be depicted as seen in Figure 1.21. The macroscale variable v_M and microscale variable v_m could be connected to each other via compression and reconstruction operators. Concerning the models, the macroscale model F affects the microscale model \mathcal{F} through constraints, as the macroscale variable defines how the microscale model should be solved. This can for example be via initial or boundary conditions, or by influencing how some parameters d_m should be chosen. This ensures that the corresponding

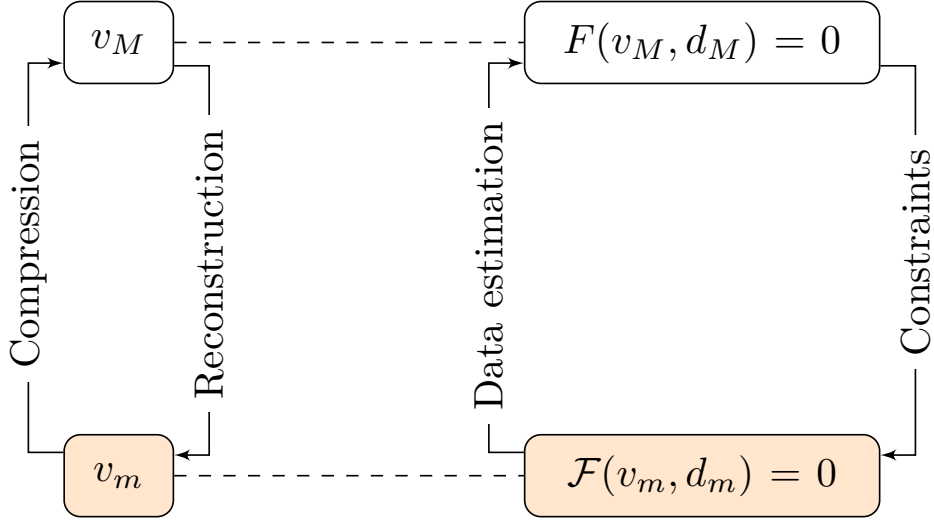


Figure 1.21: Schematics of HMM

or correct microscale model is solved. Once the microscale model is solved, the missing macroscale data can be estimated.

The design of the multiscale scheme depends on the coupling between the models and variables, and how time plays a role in the two scales. If both scales are time-dependent, with variability on the same time scale, a time-stepping procedure with same time-step size for the two models can be made. The microscale model is then updated first, using v_M from the previous time step to constrain the microscale data d_m . Using the updated microscale model solution found under this constraint, the macroscale variable can be time-stepped to the next time step. Such a procedure corresponds to an explicit approach, but can also be made iteratively. If the microscale model evolves much slower in time compared to the macroscale, the microscale model only has to be solved once in a while. Hence, one can reuse the estimated data for several time steps. If the microscale model evolves much faster in time than the macroscale model, a shorter time-step size for the microscale is needed and should ideally be time-stepped until a quasi-equilibrium is met. This is typical if the microscale model involves molecular dynamics. A last option is that the microscale data does not depend on the macroscale ($d_m \neq d_m(v_M)$). In this case, the microscale model can be solved a-priori and all needed data from the microscale model can be found before solving the macroscale model.

Applying HMM to the model derived in Section 1.3.3 would lead to a rather simple scheme as the microscale data does not depend on the macroscale variable and both problems are independent of time. Hence, only three steps are needed: first solve the microscale model, estimate the macroscale data, then solve the macroscale model. Although rather simple, we still use this example to illustrate the somewhat abstract concepts of HMM: Hence, the macroscale model corresponds to

$$\left. \begin{aligned} -\hat{\nabla}_{\hat{\mathbf{x}}} \cdot \left(\hat{\mathbf{D}}(\hat{\mathbf{x}}) \hat{\nabla}_{\hat{\mathbf{x}}} \hat{u}_0(\hat{\mathbf{x}}) \right) &= \hat{f}(\hat{\mathbf{x}}) & \hat{\mathbf{x}} \in \Omega \\ \hat{u}_0(\hat{\mathbf{x}}) &= 0 & \text{on } \partial\Omega. \end{aligned} \right\} \quad (F)$$

The macroscale variable is \hat{u}_0 , while the missing macroscale data is the effective diffusion

matrix $\hat{\mathbf{D}}$. To find this matrix, we have for every $\hat{\mathbf{x}} \in \Omega$ the microscale model

$$\left. \begin{aligned} \hat{\nabla}_{\hat{\mathbf{y}}} \cdot \left(\hat{D}(\hat{\mathbf{x}}, \hat{\mathbf{y}}) \left(\mathbf{e}_j + \hat{\nabla}_{\hat{\mathbf{y}}} w_j(\hat{\mathbf{x}}, \hat{\mathbf{y}}) \right) \right) &= 0 & \hat{\mathbf{y}} \in Y \\ w_j(\hat{\mathbf{x}}, \hat{\mathbf{y}}) &\text{ is } Y\text{-periodic,} \\ \int_Y w_j(\hat{\mathbf{x}}, \hat{\mathbf{y}}) d\hat{\mathbf{y}} &= 0 & j = 1, \dots, d. \end{aligned} \right\} \quad (\mathcal{F})$$

Hence, the microscale variables are the weights w_j . This problem depends on the highly oscillatory diffusion coefficient $\hat{D}(\hat{\mathbf{x}}, \hat{\mathbf{y}})$, but is considered to be unconstrained as it does not depend on \hat{u}_0 . We then have the data estimation through

$$\hat{\mathbf{D}}_{ij}(\hat{\mathbf{x}}) = \int_Y \hat{D}(\hat{\mathbf{x}}, \hat{\mathbf{y}}) (\delta_{ij} + \partial_{\hat{y}_i} w_j(\hat{\mathbf{x}}, \hat{\mathbf{y}})) d\hat{\mathbf{y}}.$$

Note that we do have a form of reconstruction and compression coming from the homogenization approach. We started with the Homogenization Ansatz, saying that

$$\hat{u}^\varepsilon(\hat{\mathbf{x}}) = \hat{u}_0(\hat{\mathbf{x}}, \hat{\mathbf{y}}) + \varepsilon \hat{u}_1(\hat{\mathbf{x}}, \hat{\mathbf{y}}) + O(\varepsilon),$$

and during the derivation in Section 1.3.3 we used that

$$\hat{u}_1(\hat{\mathbf{x}}, \hat{\mathbf{y}}) = \tilde{u}_1(\hat{\mathbf{x}}) + \sum_{j=1}^d w_j(\hat{\mathbf{x}}, \hat{\mathbf{y}}) \partial_{\hat{x}_j} \hat{u}_0(\hat{\mathbf{x}}).$$

Hence, finding w_j (and hence \hat{u}_1) could be seen as a reconstruction step (although only up to a constant), but is not needed in this HMM approach. The reconstruction and compression is normally only needed in the case of constrained approaches.

The strength of HMM appears in the case when the microscale model is constrained by the macroscale variable. This happens for example when the pore-scale geometry evolves due to mineral precipitation and dissolution [102]: Here, the microscale model is constrained by the macroscale solute concentration, which determines the reaction rate and therefore dictates how much mineral will precipitate or dissolve inside the local cell. Or, for two-phase flow where the microscale model for the fluid distribution is constrained by the macroscale saturation [69]. In these two cases, a HMM scheme would need a reconstruction step (to reconstruct the pore-scale geometry and fluid distribution) in order to solve the microscale model and estimate the needed macroscale data.

A HMM scheme is rather simple when the microscale model is not constrained by the macroscale variables as the needed data can be found a-priori. Also, if there is a very simple constraint coming from the macroscale variable, that could be parametrized, it would also be possible to solve the microscale model a-priori for an expected range of the constraint and parametrize the estimated data. For example, if one has mineral precipitation and dissolution, and the mineral is known to be circular, the needed permeability and effective diffusion coefficients could be found in terms of the radius, as done in [102]. Then, the macroscale model would solve for the mineral radii, and be coupled to the parametrized expression for permeability and effective diffusion. Parametrizations of permeability for more types of shapes are considered in [94]. In the case that simple parametrizations cannot be found, machine learning could also be applied to the microscale model in order to estimate the needed data a-priori [44].

Although applying a HMM scheme is useful for multiscale models, which occur frequently

in porous media, much information is still needed from the user in order to apply such a scheme. For example, HMM would only tell that a constraint is needed, but not what the constraint is. This, the user needs to know from the multiscale problem at hand. When applying HMM to a model coming from homogenization, the needed information is available as long the homogenization procedure led to a closed model. Applying HMM does not guarantee that the correct effective behavior is simulated, but the HMM framework comes with an error analysis to quantify the origin of the errors; see [110].

In this thesis, two-scale schemes resting on the framework of HMM will be applied in Chapters 2, 7 and 9. In Chapter 2, a scheme combining mesh adaptivity and ideas of HMM is applied to a multiscale parabolic problem for addressing the behavior of permeabilities at different scales (cf. Figure 1.7). In Chapter 7, an explicit two-scale scheme for two-phase porous-medium flow is implemented, coupling the Darcy-scale two-phase flow with pore-scale cell problems for effective Darcy-scale parameters. Hence, the interaction between the two fluids at the pore scale (cf. Figure 1.9) is incorporated in the simulation. Chapter 9 implements an iterative and adaptive two-scale scheme for reactive transport, and analyzes this scheme with respect to convergence. Here, pore-scale geometry changes are accounted for in the Darcy-scale flow, which is relevant for e.g. geothermal energy (cf. Figure 1.2). In Chapter 4, parametrized expressions for permeability and effective heat conductivity using simple solid shapes are found - so that one can avoid the computational effort of simulating a coupled multiscale scheme, but still incorporate the influence of pore-scale geometry changes at the Darcy scale as mineral precipitates or dissolves.

1.4 Structure of thesis

In the last part of the introduction, we turn to the different publications presented in this thesis. In particular, we outline the novel aspects concerning mathematical modeling, use of multiscale approaches, and numerical schemes. The thesis is divided into four parts, where the three first consider various multiscale aspects of parabolic problems, two-phase flow and reactive transport, respectively. The fourth part considers evaporation from porous media and stands out as being the only one addressing a pure Darcy-scale approach, but creates a starting point for further research as multiscale aspects from the first three parts can improve the approach of the fourth part. Note that the following chapters use similar, but not identical notation for parameters and variables as applied in this introductory chapter. However, each chapter defines its own notation which is used consistently throughout that chapter.

1.4.1 Part A: Multiscale parabolic problems

The first part of this thesis comprises three chapters, corresponding to three publications, which all deal with different aspects of multiscale parabolic problems, with a focus on finding and analyzing effective behavior at a larger scale. All three publications use or rely on homogenization, such that the larger-scale model equations depend on cell problems from the smaller scale for calculating effective parameters. The first publication, found in Chapter 2, considers a non-linear parabolic problem, where part of the challenge is to find the effective diffusion coefficients of this parabolic problem at larger scales. The main application of the non-linear parabolic problem is unsaturated flow, and in this case the diffusion coefficient is the permeability. The second publication, found in Chapter 3,

addresses heat transport through a thin porous medium. Heat transport both in the form of advection and conduction is included, but the main focus lies in investigating the role of the effective heat conductivity and how it is influenced by the pore-scale interactions. The third publication, found in Chapter 4, builds on the two-scale non-isothermal model for reactive transport derived through homogenization in [18], and analyzes the behavior of the effective parameters permeability, solute diffusivity and heat conductivity. Special attention is given to the case when the pore-scale geometry is about to clog. Although the model includes reactive transport, this publication is still included in Part A as the focus on finding effective parameters in parabolic equations aligns better with the type of challenges investigated in this part.

In Chapter 2, a non-linear parabolic problem is investigated. This problem could represent the transformed Richards equation (1.14) for unsaturated Darcy-scale flow, but can also be used to model other non-linear diffusion processes. This chapter hence focuses on the Darcy scale, where detailed information about the permeability is available. The permeability is here playing the role of the diffusion coefficient in the parabolic equation. The goal of this paper is to design an efficient numerical algorithm for the non-linear parabolic problem, by using a combination of coarse and fine meshes. This is to allow for large-scale simulations, where a larger domain has to be considered. The fine to coarse meshes hence represent the REV to field scale length scales (cf. Figure 1.7), respectively. Since the considered non-linear parabolic problem could be used to model unsaturated flow, this type of problem is relevant when considering groundwater flows, where the presence of air influences the flow of the groundwater. For large-scale groundwater applications, one cannot use a fine mesh everywhere as the computational costs would be too large. By using coarser meshes, larger domains can be considered, but with the potential loss of accuracy. Therefore, a strategy with combining fine and coarse meshes adaptively is sought.

In this chapter, an adaptive mesh refinement and coarsening strategy based on an error indicator is constructed. Using this error indicator, the mesh is either refined (where larger errors are indicated), coarsened (where lower errors are indicated) or left as is. The thresholds for refining and coarsening can easily be adjusted. The finest meshes that can be used is limited by the mesh of the given fine-scale permeability. However, when using coarser meshes, a permeability representing the effective permeability for the coarser mesh is needed. This is found through homogenization, similar as for the diffusion problem in Section 1.3.3. The strategy for incorporating permeability values coming from the solution of local cell problems at a smaller scale is inspired by the ideas in HMM (cf. Section 1.3.4). As discussed in Section 1.3.3, local periodicity is needed to apply homogenization, but the fine-scale permeabilities considered in Chapter 2 are generally not periodic. Permeabilities at the larger scale can still be found through homogenization by assuming periodicity, but these effective permeabilities are at best an approximation of the actual effective permeability. However, the applied error indicator is found to trigger mesh refinement in regions where non-periodic transitions happen, reducing the negative influence of the approximate permeabilities. The solutions found using adaptive meshes are compared to full fine-scale solutions to address the accuracy. Overall, the adaptive strategy is found to generally give low errors although much fewer grid cells are used.

The non-linear parabolic problem in Chapter 2 is discretized using mixed finite element methods (MFEM), ensuring a mass conservative scheme - also on the adaptive meshes. A challenging part of solving the discretized equations is the non-linearities, which is a well-known issue in particular for the Richards equation [37]. We here use backward Euler for discretizing time, which means that a non-linear system of equations needs to be solved

for every time step. Newton's method would offer second order convergence, but fails to converge unless a very small time-step size is chosen [65]. Another possible approach is the L-scheme, which formulates the non-linear iterations into contracting fixed-point iterations that are guaranteed to converge - but only linearly [65]. Therefore, a combination of these two methods is applied: First, L-scheme iterations are applied until a good starting point for Newton iterations is reached. Then, Newton iterations are performed until wanted accuracy is achieved. In this case, the non-linear solving steps are still fast, and without a severe restriction on the time-step size. Overall, this chapter provides a robust, accurate and efficient scheme for solving non-linear parabolic problems numerically - by applying homogenization in a mesh adaptivity strategy and by designing a robust solving strategy for the non-linearities.

In Chapter 3, heat transport in thin porous media is investigated. Thin porous media are important in many technical applications, for example in fuel cells, where a thin porous layer (the gas diffusion layer) is used to connect the gas channel with the anode and cathode. However, thin porous media are also relevant in the design of filters and composite materials used as membranes. The starting point of this chapter is a pore-scale model, where the heat transport in and between the fluid-filled void space and solid space are coupled, as described in Section 1.2.1. The goal of this paper is to derive a Darcy-scale model for the effective heat transport through the porous medium. Since the porous medium is thin, the homogenization strategy (cf. Section 1.3.3) borrows ideas from transversal averaging (cf. Section 1.3.1) to derive a Darcy-scale model. Hence, the derived Darcy-scale model is dimensionally reduced (from 3D to 2D), and relies at the same time on local cell problems for effective parameters. These cell problems still need to be solved in three-dimensional domains. As seen in Section 1.3.1, the boundary conditions at the top and bottom boundaries influence the transversal averaging, which is also found to be the case for the thin porous medium considered in Chapter 3. The cell problems derived by homogenization incorporate the boundary conditions applied at the top and bottom boundaries of the thin porous medium.

In this chapter, heat transport in the fluid by both advection and conduction is included. Upscaling flow in thin porous media has already been thoroughly investigated (see e.g. [36, 108]), hence the main focus of this chapter is on the effective heat conductivity. Since the boundary conditions at the top and bottom boundaries of the porous medium appear in the cell problems for the effective heat conductivity, different effective heat conductivities are found depending on which type of boundary conditions are applied. We here focus on the top and bottom boundaries being either perfectly conducting (i.e. Dirichlet boundary conditions) or transmitting a given heat flux (i.e. Neumann boundary conditions). The resulting cell problems are elliptic problems and solved by applying finite element methods (FEM). By solving the resulting cell problems in these two cases, it is found that the case of perfectly conducting top and bottom boundaries result in generally larger effective heat conductivities of the thin porous medium. However, the shape of the solid also has an influence on the effective heat conductivity. Hence, parametrizations of the effective heat conductivity in terms of e.g. porosity, would still need to be adapted to the actual pore-scale solid shape. This coincides with results for flow around different solid shapes for permeability [94].

The derived Darcy-scale model in this chapter is dimensionally reduced (2D instead of 3D), which already represents a potential large saving in terms of computational costs since only a two-dimensional domain has to be discretized. A rather coarse mesh can be used since the domain is at Darcy scale, and effective properties are found through the local cell

problems. These cell problems still need to be solved for three-dimensional domains, but can generally be solved on smaller batches of the original, thin porous medium. Hence, there is also a computational gain in rather solving many small problems instead of one very large problem. By comparing with the solution of conductive heat transport on the original, pore-scale domain, the derived Darcy-scale model is found to provide good results of the average behavior. One should however note that the derived Darcy-scale model can only resolve the average behavior - hence any detailed information concerning pore-scale variability is not available. However, the influence of the pore-scale geometry and processes at the pore scale are accounted for.

In Chapter 4, heat transport in a porous medium is investigated. The third spatial dimension is not included, which corresponds to this direction not having any influence (e.g. the porous medium stretches infinitely in the vertical direction and does not include any vertical variability). The investigated model was derived in [18] using homogenization. There, the starting point was a pore-scale model for coupled heat transport and reactive transport where a mineral could precipitate and dissolve. The motivation for this model comes from geothermal energy production, where the induced temperature variations can cause minerals to dissolve or precipitate depending on their solubility, which is generally temperature-dependent (cf. Figure 1.2). As the minerals dissolve or precipitate, the pore-scale geometry changes, influencing effective behavior at Darcy scale. In [18], a Darcy-scale model was derived using homogenization, such that effective parameters for permeability, solute diffusivity and heat conductivity could be found via local cell problems. These cell problems incorporate the local pore-scale geometry changes via a level-set equation. In this chapter, we investigate the properties of these resulting effective parameters, in particular for the case when the porous medium is about to clog; i.e., flow paths are about to close due to mineral precipitation.

Although Chapter 4 could fit into Part C since it considers reactive transport, it is placed in Part A since the main focus is on investigating the behavior of the effective permeability, solute diffusivity and heat conductivity. The derived two-scale model from [18] could be implemented with a heterogeneous multiscale method (cf. Section 1.3.4), where the Darcy-scale model equations are coupled to the pore-scale cell problems. Instead, a more efficient approach is sought by solving the cell problems a-priori for expected solid shapes and investigating the cell problem solutions. Such a strategy was already sought for reactive transport (without temperature dependence) in [102], by considering circular solids. In this chapter, we consider both circular and elliptic shapes and focus especially on the behavior close to clogging for the permeability. Close to clogging, the permeability changes several orders of magnitude for a very small addition of deposited mineral volume. To capture this behavior accurately, extra care is needed when finding a suitable parametrization. The effective heat conductivity depends on the solid shape (as also observed in Chapter 3). Further, comparing the cell problem solutions with the typical porosity-weighted means (arithmetic, geometric and harmonic [75]), shows that these means can generally not capture the overall behavior of the effective heat conductivity as the porosity changes. Similar results are found for the effective solute diffusion.

The found parametrizations for effective permeability, solute diffusion and heat conductivity make Darcy-scale simulations much easier, while still allowing to incorporate a dependence on the pore scale. If using for example the radius of the precipitated/dissolved mineral as variable, the reaction rate for mineral precipitation and dissolution will hence affect this radius. From the radius, the porosity can easily be calculated, and the effective permeability, solute diffusion and heat conductivity are found from the parametrizations in

terms of this radius. However, the parametrizations are found a-priori, hence the numerical scheme is only at the Darcy scale and active coupling to any pore-scale model equations is not needed during the simulation. Such a scheme is also demonstrated in this chapter for a case where mineral dissolves in one part of the domain and precipitates in a different part, where clogging therefore gradually occurs.

1.4.2 Part B: Two-phase porous-media flow

The second part of this thesis comprises three chapters, corresponding to three publications, which all deal with different aspects of finding effective behavior of two-phase flow. Two of the publications consider a thin strip and therefore rely on transversal averaging, while the third publication considers two-phase flow in a periodic porous medium and applies homogenization to derive the effective behavior. In the first publication, found in Chapter 5, it is assumed that the two fluid phases have a layered structure, such that a layer width can be used to describe the evolution of the fluid-fluid interface. In the second publication, found in Chapter 6, it is assumed that the fluid-fluid interface stretches across the thin strip and can hence be identified through its along-strip coordinate. Both of these models hence consider rather restrictive forms of the fluid-fluid interface, but still incorporate dynamically evolving interfaces due to flow and surface tension. Due to the simplicity of the models, it is possible to derive explicit expressions for the effective behavior through transversal averaging. The third publication, found in Chapter 7, considers a phase-field model in a periodic pore-scale geometry. Here, homogenization is applied to find the effective Darcy-scale model equations, which rely on pore-scale cell problems that need to be solved numerically to find effective parameters. These three publications all give valuable information about the effective behavior of two-phase flow through pores and porous media, which is relevant for e.g. water management in fuel cells.

In Chapter 5, two-phase flow in a thin strip is considered. The two fluids flow through the thin strip and interact with each other at the evolving fluid-fluid interface, as described in Section 1.2.1. The location of the fluid-fluid interface is assumed to be described with a layer width corresponding to (1.7), which means that the two fluids have a layered structure with one fluid on top of the other. The fluid-fluid interface still evolves due to the fluid flow, and due to the stresses of the fluids interacting through the surface tension, as described by (1.2) and (1.3). Hence, the layer width will dynamically evolve due to the interactions between the two fluids. The motivation for this setting is to consider the flow of two fluids through a single pore or channel, where one fluid is wetting and hence attaches to the walls. This can be the case of for example fuel cells, where the connected gas channel is hydrophilic (i.e., water-wetting) [71], as partly highlighted in Figure 1.6. The goal of this chapter is to find the effective behavior of this setting, which can be found by transversal averaging (cf. Section 1.3.1). The derived models are hence dimensionally reduced (from 2D to 1D), where only variability along the strip is explicitly solved for. Using a layer width to describe the evolution of the fluid-fluid interface strongly simplifies the transversal averaging steps compared to using a general level set. This setting also allows to find explicit expressions for the effective parameters, which are then easier to analyze. A similar setting was also considered in [3] where a thin layer was dimensionally reduced (from 3D to 2D), resulting in relative permeabilities for the two-phase flow in the thin layer.

Several different two-phase flow regimes are investigated in this chapter. The flow rates are always assumed low such that one is in the regime of Darcy's law (cf. the single-phase channel flow in Section 1.3.1), but different sizes of the capillary number and the viscosity

ratio between the two fluids are considered. These choices influence the interaction between the two fluids. In particular, if considering a large or moderate capillary number, corresponding to a weak to moderate surface tension between the fluids, the surface tension is found to not influence the effective behavior of the flow. In this case, there is no pressure jump between the fluids in the transversally averaged models. This corresponds to zero (Darcy-scale) capillary pressure. Only when the capillary number is very small, corresponding to a very large surface tension between the fluids, a pressure jump between the two fluids in the effective model equations can be found. Unlike typical Darcy-scale models, where the capillary pressure depends on the saturation of one fluid (cf. discussion in Section 1.2.2), the capillary pressure is here found to be connected to the second-order derivative (along the strip) of the layer width variable. The layer width could be interpreted as a measure of the saturation of one fluid, but is here relevant as it represents the curvature of the fluid-fluid interface along the strip. A similar setting is analyzed by volume averaging in [79], but differs from the effective models found in Chapter 5 as [79] only considered steady-state flow. In Chapter 5, the influence of Marangoni effects and large viscosity ratio between the fluids on the effective behavior is also investigated. In particular, by considering a large viscosity ratio between the two fluids, effective equations resembling unsaturated flow are derived through the transversal averaging. In this case, the derived model resembles the thin-film lubrication approximation [76].

The validity of the derived effective models in Chapter 5 is investigated by numerical experiments. Simulation results of the original thin strip with resolving the evolving interface through a level-set approach, are averaged and compared to numerical results of the effective models for the corresponding regime. It is found that the average of the original model results approach the results of the effective models as $\varepsilon \rightarrow 0$ (i.e., as the ratio between the width and length of the strip approaches zero). These results show that transversal averaging offers good approximations of the average behavior as the thin strip becomes longer and thinner.

Chapter 6 also considers two-phase flow in a thin strip, but investigates a different setup than Chapter 5. The main difference is that in Chapter 6, the fluid-fluid interface stretches across the thin strip instead of along it. The fluid-fluid interface can still evolve due to the flow itself and interactions between the two fluids as in Chapter 5. Hence, the starting point is the same model equations for two-phase flow as in Chapter 5 (cf. Section 1.2.1), except that now a contact angle model (1.4) is also needed, and slip conditions (1.1) at the solid wall are applied to avoid the singularity on the fluid-fluid-solid contact point. The location of the fluid-fluid interface is parametrized through its along-strip location, which is therefore used as an unknown in the model. The motivation for this setting is to consider the flow of two fluids through a single pore or channel, where one fluid displaces the other. This is a common setting in many two-phase flow problems, e.g. capillary rise [119], and also a common assumption in many pore-network models [28].

Due to the fluid-fluid interface stretching across the thin strip, transversal averaging as done in Section 1.3.1 cannot be applied in a straightforward manner to derive a model for the effective behavior in this case. The fluid-fluid interface represents a discontinuity in the model, and transversal averaging can only be applied in regions far away from the interface. To derive an effective model, transversal averaging is therefore combined with boundary-layer methods (cf. Section 1.3.2). By combining matched asymptotic expansions with transversal averaging, effective models valid away from the fluid-fluid interface as well as a model for the behavior near the fluid-fluid interface can be found. These models are connected by matching conditions. However, the resulting effective model is still a

dimensionally reduced model, where only variability along the strip is explicitly solved for.

Only the regime of moderately small capillary numbers is investigated in this chapter, as larger or even smaller capillary numbers would have lead to either trivial behavior or settings where an effective behavior cannot be derived. Instead, the focus of this chapter is to investigate the influence of a dynamic or hysteretic contact angle, slip length and viscosity ratio between the fluids. Especially the influence of dynamic or hysteretic contact angle is much discussed in the context of two-phase porous-media flow [49]. Due to the simplicity of the model, (semi-)explicit expressions for the dynamic capillarity can be found, allowing to quantify its influence. Numerical experiments of the effective model highlights the influence of a dynamic or hysteretic contact angle model. The results of this chapter have later been extended to cover the case of capillary rise by considering a tube and incorporating gravity. By comparing with experiments of capillary rise, the derived model shows that dynamic effects have an influence also in this setting [67].

In Chapter 7, two-phase flow in a periodic porous medium is investigated. The starting point is pore-scale model equations for two-phase flow as discussed in Section 1.2.1. Since no restrictions on the shape of the fluid-fluid interface are imposed (except periodicity), a phase-field model is applied to model the two-phase flow at the pore scale. In particular, the presence of a surfactant in one of the fluids is included, whose concentration influences the surface tension and hence the interaction between the two fluids. The motivation for including such surface-tension effects is that these surfactants play a role in many biological applications, and also in industrial applications such as enhanced oil recovery to re-mobilize oil [61]. In this chapter, an existing phase-field model based on the Cahn-Hilliard equation (1.9) incorporating soluble surfactants is considered [43]. The goal of this chapter is to find a Darcy-scale model including effective parameters through cell problems, by applying homogenization (cf. Section 1.3.3) to the phase-field model at the pore scale.

To perform homogenization on the phase-field model, special care is needed for in particular the parameters of the phase-field equation (1.9). Depending on which choices are made, one ends up with different behaviors for the phase-field equation in the derived cell problems. In both [30, 69], a faster time scale is introduced to resolve the phase field at the pore scale. In this chapter, we do not introduce a faster time scale. Instead, by choosing the arising non-dimensional parameters arising from the Cahn-Hilliard equation wisely, a steady-state form of the Cahn-Hilliard equation is arrived at as cell problem for the fluid-fluid interface evolution. This is in contrast to e.g. [69], which time-steps the faster time scale until a quasi-steady state is reached for the phase field. The steady-state cell problems for the phase field in Chapter 7 are instead solved under the constraint that a certain saturation (which can be related to an integral of the phase field over the local cell) should be fulfilled. This gives a distribution of the fluids that minimizes surface area and where one fluid is wetting. This fluid distribution is then used in the other cell problems, giving effective parameters corresponding to relative permeability and the influence of the surface tension in the Darcy-scale equations.

The two-scale model is implemented using an approach inspired by heterogenous multi-scale methods, cf. Section 1.3.4. In this context, the applied constraint for the saturation is the reconstruction step needed for the microscale simulation, as explained in Section 1.3.4. The applied HMM scheme is explicit; that is, iterations between the scales are not performed. Both the Darcy-scale and the pore-scale equations are implemented using MFEM. Using Darcy-scale solute concentration and pore-scale phase field from the previous time step, the pore-scale flow through local cell problems is found first. Then, from the averaged flow (the Darcy velocities), saturation and solute concentration at the Darcy scale

are updated. Finally, the local pore-scale phase fields are updated. This scheme allows to decouple the various pore-scale cell problems and Darcy-scale equations. Numerical experiments with constant and varying solute concentration show the influence of the varying surface tension on the effective Darcy-scale behavior. In particular, the fluid distribution on the pore scale (i.e. the solution of the phase field) is affected by the surface tension, which influences all the effective parameters.

1.4.3 Part C: Reactive transport with heterogeneous reactions

The third part of this thesis comprises three chapters, corresponding to three publications, which all deal with different aspects of modeling and simulating reactive transport at the pore and Darcy scale, where mineral precipitation and dissolution change the pore-scale geometry. All three publications use or rely on homogenization. The first publication, found in Chapter 8, develops a phase-field model that combines single-phase fluid flow with a solid structure evolving due to mineral precipitation and dissolution. This model is then formulated in a periodic pore-scale geometry, and its Darcy-scale counterpart is found by homogenization, such that effective parameters can be calculated through pore-scale cell problems. The second publication, found in Chapter 9, constructs an efficient and accurate two-scale scheme for the resulting model in the first publication, by using ideas from heterogeneous multiscale methods. The third publication, found in Chapter 10, considers a three-phase problem, where single-phase flow is combined with the precipitation and dissolution of two different minerals. Here, the numerical behavior and effective parameters for a level-set and a phase-field model are compared. These three publications all give valuable information for modeling and simulating reactive transport with heterogeneous reactions in a porous medium, relevant for geothermal energy (cf. Figure 1.2) and salt precipitation (cf. Figures 1.3 and 1.4), in particular when using diffuse interfaces to model the evolving fluid-solid interface.

In Chapter 8, a phase-field model for reactive transport with heterogeneous reactions is developed and investigated. The model combines single-phase flow and solute transport with mineral precipitation and dissolution, and hence builds on the sharp-interface equations presented in Section 1.2.1. An Allen-Cahn equation (1.8) is used to model the evolving fluid-solid interface. Compared to earlier phase-field models for reactive transport [86, 104, 116], flow of the fluid is now accounted for. The motivation for such a model is to be able to model the interaction between fluid flow and solute transport, where the available space for fluid to flow in dynamically changes due to the heterogeneous chemical reactions. Such processes are important in a large range in geological applications (e.g. geothermal energy, CO₂ storage, soil salinization) and technical applications (e.g. mineral deposits in pipes, corrosion). The goal of this paper is both to provide a phase-field model combining fluid flow with mineral precipitation and dissolution, and to find a model for the Darcy-scale behavior when these processes occur in a porous medium.

To formulate a phase-field model for the combined fluid flow, solute transport and mineral precipitation and dissolution, special care is needed to handle the flow equations. The phase-field model is defined in the combined domain of fluid, solid mineral and the interface between them. That means, the phase-field flow equations are also defined in the solid domain. To ensure that there is no flow inside the mineral, a penalizing term inspired by a phase-field model for shape optimization [42] is incorporated in the flow equations. The sharp-interface limit of the phase-field model is found by matched asymptotic expansion (cf. Section 1.3.2). The sharp-interface limit corresponds to the expected sharp-interface

model equations for fluid flow and reactive transport with a mass transfer across the interface following the Rankine-Hugonio jump condition (1.5). However, the sharp-interface limit includes also an additional curvature-driven motion for the normal velocity of the fluid-solid interface. This curvature-driven motion is an inherent part of Allen-Cahn phase-field models [7]. The phase-field model is implemented using finite volumes on a staggered grid. Comparisons to available benchmarks [72, 73] show that the curvature-driven motion causes an initially circular mineral to dissolve faster than expected.

By formulating the derived phase-field model in a periodic pore-scale geometry, homogenization is applied to derive a Darcy-scale model for the effective behavior, cf. Section 1.3.3. As in Chapter 7, special care is needed for the chosen size of non-dimensional phase-field parameters to perform the homogenization. However, for the Allen-Cahn phase-field equation in Chapter 8, a time-dependent phase-field evolution is obtained in the derived cell problem. The time scale for the phase-field evolution is the same as for the Darcy-scale time evolution. The derived Darcy-scale model couples Darcy-scale flow with solute transport, where the effective permeability and solute diffusion are found through pore-scale cell problems. These local cell problems incorporate the local evolution of the phase field, which depends on the Darcy-scale reaction rate. The effective permeability and solute diffusion hence also depend on the diffuse interface of the phase field. By comparing with the corresponding sharp-interface cell problems of [102], the diffuse interface is found to influence the value of the effective parameters slightly, but less when a smaller value for the diffuse-interface width is chosen. This shows that although phase-field models offer an easier approach to modeling and simulating reactive transport, there is an influence coming from the fact that phase-field models are indeed approximations of the sharp-interface physics.

In Chapter 9, the resulting two-scale model from Chapter 8 is implemented in an adaptive, iterative manner using a HMM-scheme, cf. Section 1.3.4. The goal of this chapter is to formulate and implement an efficient, robust and accurate scheme for the Darcy-scale behavior of reactive transport, while incorporating information from the pore scale. The scheme is also analyzed, in particular the convergence of the two-scale iterations is proven. Such an implementation allows to consider the influence of pore-scale geometric changes due to mineral precipitation and dissolution on the effective Darcy-scale behavior for larger domains, and hence for larger applications.

The starting point of this chapter is the derived two-scale model from Chapter 8. Both the Darcy-scale model for fluid flow and solute transport, and the local cell problems for resolving the phase field and calculating effective permeability and solute diffusion are implemented using MFEM in space, and implicit Euler in time. The two scales are coupled through the reaction rate and effective parameters, and an iterative HMM-scheme is formulated. That is, the pore-scale and Darcy-scale equations are solved in an iterative manner within each time step, until a sufficiently small change in the porosity (i.e., the integral of the phase field) is obtained. Here, the Darcy-scale reaction rate appears as a constraint for the pore-scale cell problem to reconstruct the local pore-scale geometry through the pore-scale phase-field equation. Since the two scales are solved separately, only one non-linear equation is to be solved: the Allen-Cahn equation (1.8). This non-linear equation is solved via L-scheme iterations, which converge for any initial guess. The resulting two-scale iterative scheme is proven to converge for a simplified case where flow is neglected. Restrictions on the time-step size and on the values of the phase-field parameters are needed in order to prove the convergence. The proof is done by introducing a regularization and showing that the resulting fixed-point iterations are a contraction.

This strategy is inspired by [55]. Hence, we have a robust scheme which is guaranteed to converge under relatively mild restrictions.

The efficiency of the two-scale scheme is improved by introducing two forms of adaptivity: Firstly, mesh adaptivity is applied for resolving the diffuse interface on the pore scale efficiently, using a predictor-corrector strategy from [47]. The motivation for the mesh adaptivity is that a fine grid is needed to resolve the diffuse transition zone, but a coarser grid can be applied further away. Secondly, adaptivity in terms of which Darcy-scale effective parameters should be calculated is applied. Here, a strategy from [85] is extended to account for heterogeneous pore-scale geometries. Only cell problems which are sufficiently different from other cell problems in terms of reaction rate and shape of the phase field are updated. The other cell problems instead copy the needed effective parameters from the most similar cell problem that was solved. The numerical examples highlight the influence of this Darcy-scale adaptivity. It is found that relatively small errors occur when only solving a smaller set of the cell problems, compared to solving all. Hence, the numerical scheme is therefore not only robust, but also efficient and accurate.

In Chapter 10, a three-phase problem for fluid flow and reactive transport is investigated. Here, single-phase fluid flow with solute transport is coupled to the precipitation and dissolution of two different minerals. One of the solutes is part of both minerals, hence the precipitation and dissolution of the minerals depend on each other. Such a setting is rather common, e.g. for geothermal energy, where the dissolution of one mineral can trigger precipitation of another, due to differences in solubility [120]. The starting point to formulate such a model is the single-phase fluid flow and solute transport equations in Section 1.2.1, but extended since two minerals and three solutes are considered. To model and simulate such a problem require extra care since three evolving and interacting phases are involved. The goal of this chapter is to formulate and implement both a sharp-interface model based on level sets, and a diffuse-interface model based on phase fields, and analyze and compare their behavior.

Both the level-set and phase-field models are formulated such that they allow solute diffusion and flow in the fluid phase. The phase-field model uses Allen-Cahn phase fields (1.8) as starting point, and the model is similar to the one in Chapter 8 when it comes to incorporating fluid flow. However, the model in Chapter 10 differs from the one in Chapter 8 by considering three phases. Three phases can be modeled by using a ternary phase-field model, and an approach similar as [86] is applied. The sharp-interface limit is found by matched asymptotic expansions (cf. Section 1.3.2) for each of the three phases/interfaces. The sharp-interface limit corresponds to the expected sharp-interface physics except for additional curvature-driven motion. The resulting phase-field model can be implemented by standard schemes, and is here implemented using a staggered finite volume scheme, which is conservative. The level-set model requires extra care when implementing. A Voronoi Implicit Interface Method is applied to handle the three interacting phases [89]. The level-set evolution is combined with indicator functions to separate the three phases. Instead of relying on the sign of the level-set function, a shifted version of an unsigned distance function for each interface is used. Finite differences are used to discretize the evolution of the interfaces. The resulting implementation is, unlike the phase-field implementation, not conservative.

The level-set and phase-field implementations are compared through a series of increasingly coupled problems. In all considered problems, the dissolution of one mineral triggers the precipitation of the other. The two approaches are found to differ in several ways: Firstly, the level-set implementation is not conservative and up to 2% of mass is lost dur-

ing the simulations, while the phase-field implementation is conservative up to machine precision. Secondly, the level-set implementation requires overall more unknowns than the phase-field implementation on the same grid, and also more Newton-iterations to solve the resulting non-linear system of equations. Thirdly, the level-set implementation can resolve the evolution of the fluid-solid-solid triple point, while the phase-field implementation struggles due to curvature-driven motion. Despite the differences between the two approaches, the evolution of the mineral volumes and surface areas are comparable. In particular, by calculating the effective permeability and diffusion coefficient using the corresponding cell problem formulations (cf. Section 1.3.3) for the two approaches, comparable evolutions of these effective parameters are found. Hence, both approaches are able to resolve geometrical changes in a three-phase system, and both can predict effective parameters if used as pore-scale model in a two-scale approach.

1.4.4 Part D: Evaporation from porous media

The last part of this thesis consists of one publication as well as the Conclusion and outlook. The publication, found in Chapter 11, analyzes evaporation from a porous medium. The motivation for this analysis is soil salinization [106], see Figure 1.3. This chapter addresses evaporation of water from the top of a porous medium, which is saturated with saline water. As the water evaporates, the salt stays behind. Due to the upwards fluid flow induced by the evaporation, salts will gradually accumulate near the top of the porous medium, causing increased salt concentrations. If the solubility limit of the salt is reached, salt will precipitate and create a salt crust [54], as highlighted in Figure 1.4. However, this setting is also gravitationally unstable as the water near the top of the porous medium will be heavier than the water found deeper down, due to the differences in salt concentration. Hence, density instabilities in the form of fingers can be triggered. These fingers can give a net downwards transport of salt. The goal of this chapter is to analyze these density instabilities to determine when or whether they occur, and whether they can hinder salt precipitation.

The starting point for the analysis is Darcy-scale model equations for single-phase fluid flow and solute transport, cf. Section 1.2.2. The evaporation rate is imposed as a boundary condition at the top boundary. Two approaches are used to analyze the onset of density instabilities in Chapter 11: linear stability analysis and numerical simulations. The linear stability analysis is applied to a simplified model setup by using a Boussinesq approximation. That means, the density variations of the fluid are neglected except when they occur together with gravity. In the linear stability analysis, the (instability-free) ground state is perturbed, in order to find criteria for when the perturbations can grow in strength. This results in an eigenvalue problem, which gives criteria for the onset of instabilities in the form of a critical Rayleigh number as a function of time. Hence, from this analysis, onset times for a given setting (e.g. given evaporation rate, permeability, initial salt concentration) can be found. Although considering a simplified model, the advantage of the linear stability analysis is that onset times can be found for a large range of parameter choices for very low computational costs. The linear stability analysis performed in Chapter 11 follows a rather standard procedure [75], but differs from other analyses in how the non-dimensionalization and incorporation of rather untypical boundary conditions are done.

The numerical simulations resolve the full Darcy-scale model equations using a finite-volume discretization, and are rather expensive to perform. However, where the linear stability analysis can only provide onset times, numerical simulations can also give infor-

mation about the further fate and development of the instabilities. The linear stability analysis also considers a more simplified setup, and the onset times between the two approaches are compared. In the numerical simulations, instabilities have to be triggered by adding a perturbation, and the two approaches compare well when the added perturbation resembles the perturbation from the linear stability analysis. After the instabilities are initiated, the numerical simulations show that the instabilities develop rather slowly with respect to strength. Hence, there is a longer time period where the instabilities gradually increase in strength before they cause a net downwards transport of salt. This means that salt could still precipitate despite instabilities being present. These findings provide vital information for understanding the interplay between flow, salt transport and salt precipitation in a saturated porous medium subject to evaporation.

The investigation performed in Chapter 11 differs from the publications in the other chapters of this thesis by not considering a multiscale approach. The linear stability analysis and numerical simulations are performed using Darcy-scale models only. However, questions regarding evaporation from porous media and soil salinization would benefit from an analysis incorporating pore-scale information, as visible in Figure 1.4. First of all, when salt precipitation occurs, the subsequent decrease of porosity and permeability depends on the changes of the pore-scale geometry. Secondly, as water evaporates from the top of the porous domain, air can also penetrate into the porous domain, which should be modeled as a two-phase or unsaturated flow. Hence, the evolving fluid-fluid interface at the pore scale influences the Darcy-scale flow of water.

The main findings of the research in this thesis are summarized in the Conclusion and outlook found in Chapter 12. Here, directions for further research, for both Chapter 11 and for the other chapters, are also discussed.

Part A

Multiscale parabolic problems

The first part of this thesis consists of three chapters that are based on three journal publications. Each publication addresses how to find effective parameters at a larger scale, in particular parameters appearing in the role as a diffusion coefficient in parabolic problems. Different applications and settings are targeted in the three chapters, but all approaches rely to some degree on homogenization. Homogenization is in particular useful for finding effective parameters, as the homogenization steps result in local cell problems for calculating such effective parameters.

Chapter 2: Numerical homogenization of parabolic problems In this chapter, a robust, accurate and efficient numerical strategy for a non-linear parabolic problem is developed. The main application of the considered parabolic problem is the Richards equation for Darcy-scale unsaturated flow in porous media. Given a fine-scale permeability, which in the non-linear parabolic problem appears as a diffusion coefficient, we develop a numerical scheme based on homogenization and heterogeneous multiscale methods. Based on an error indicator, the computational mesh is refined or coarsened. Homogenization together with ideas from heterogeneous multiscale methods are applied to estimate the effective permeability on the coarser meshes. The effective permeability on the coarser meshes are calculated by solving local cell problems, which are derived under the assumption of local periodic behavior, as explained in Section 1.3.3. The procedure is here applied to non-periodic permeabilities, which lead to inaccurate estimates of the true effective permeability. However, it is shown that by combining the procedure with the error indicator and local mesh refinement, profitable results are still obtained. This way, an accurate and efficient scheme is obtained. To solve the resulting non-linear discretized system of equations, we apply a combination of L-scheme iterations followed by Newton iterations. The L-scheme iterations, which are unconditionally - but only linear - convergent, are used to create a good starting point for the Newton iterations, which are second-order convergent. Hence, the resulting non-linear solving strategy is robust.

Chapter 3: Effective heat transport in thin porous media In this chapter, a dimensionally reduced Darcy-scale model for the effective heat transport through a thin porous medium is derived. Thin porous media appear in many technical applications as fuel cells and filters. Here, the starting point is a detailed pore-scale model for the heat transport through fluid and solid. Using a homogenization strategy with ideas from transversal averaging, an effective model for the Darcy-scale heat transport is obtained. This effective model is dimensionally reduced, and get effective parameters through local pore-scale cell problems. We are here in particular interested in the behavior of the effective heat conductivities. Due to the porous medium being thin, the boundary conditions at the top and bottom boundary of the porous medium appear in the local cell problems. Hence, the effective heat conductivity of the porous medium is influenced by which boundary conditions are applied. The shape of the solid is also found to influence the effective heat conductivity. It is demonstrated by numerical experiments of a steady-state heat conduction problem that the solution of the original pore-scale model is similar to the solution

of the derived effective model. However, the effective model cannot capture any detailed behavior. The computational costs for solving the original model are much larger than those of the effective model.

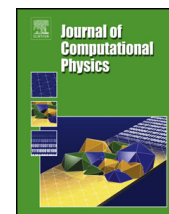
Chapter 4: Effective heat transport near clogging In the final chapter of Part A, we investigate the behavior of the effective parameters permeability, effective solute diffusivity and effective heat conductivity. These effective parameters are found through solving cell problems, which have been derived in an earlier publication [18] using homogenization. The model itself is motivated from coupled heat transport and heterogeneous reactions in geothermal reservoirs, where the temperature-dependent mineral solubilities cause the minerals to precipitate and dissolve due to the temperature variations. In this chapter, the behavior of these effective parameters are analyzed for different mineral shapes, in particular in the case when the porous medium is about to clog. Especially permeability can change several orders of magnitude close to clogging, and we find a suitable parametrization honoring this behavior. Also parametrizations for effective heat conductivity and solute diffusivity are found, and they are compared to porosity-dependent averages that are commonly used in literature. It is found that these porosity-dependent averages cannot accurately capture the overall behavior as the porosity changes due to mineral precipitation and dissolution.

2 Numerical homogenization of parabolic problems

The content of this chapter is based on the following original article:

M. Bastidas, C. Bringedal, I. S. Pop, and F. A. Radu. *Numerical homogenization of non-linear parabolic problems on adaptive meshes*. *Journal of Computational Physics* 425 (2021), p. 109903. doi: 10.1016/j.jcp.2020.109903.

Reprinted with courtesy of Elsevier.



Numerical homogenization of non-linear parabolic problems on adaptive meshes



Manuela Bastidas^{a,*}, Carina Bringedal^b, Iuliu Sorin Pop^{a,c}, Florin Adrian Radu^c

^a Faculty of Sciences, Hasselt University, Diepenbeek, Belgium

^b Institute for Modelling Hydraulic and Environmental Systems, University of Stuttgart, Stuttgart, Germany

^c Department of Mathematics, University of Bergen, Bergen, Norway

ARTICLE INFO

Article history:

Received 31 January 2020

Received in revised form 9 August 2020

Accepted 4 October 2020

Available online 7 October 2020

Keywords:

Flow in porous media

Homogenization

Mesh refinement

Non-linear solvers

MFEM

ABSTRACT

We propose an efficient numerical strategy for solving non-linear parabolic problems defined in a heterogeneous porous medium. This scheme is based on the classical homogenization theory and uses a locally mass-conservative formulation at different scales. In addition, we discuss some properties of the proposed non-linear solvers and use an error indicator to perform a local mesh refinement. The main idea is to compute the effective parameters in such a way that the computational complexity is reduced but preserving the accuracy. We illustrate the behavior of the homogenization scheme and of the non-linear solvers by performing two numerical tests. We consider both a quasi-periodic example and a problem involving strong heterogeneities in a non-periodic medium.

© 2020 Elsevier Inc. All rights reserved.

1. Introduction

Non-linear parabolic problems are encountered as mathematical models for several real-life applications. Examples in this sense are partially saturated flow in porous media, non-steady filtration, and reaction-diffusion systems. Realistic applications often involve heterogeneous domains, which translate into rapidly oscillating properties.

Letting Ω^ε be a bounded, possibly perforated domain in \mathbb{R}^d ($d = 2, 3$) with Lipschitz boundary $\partial\Omega^\varepsilon$ and $T > 0$ be a maximal time, we consider the non-linear parabolic equation

$$\partial_t b^\varepsilon(\mathbf{x}, p^\varepsilon(\mathbf{x}, t)) - \operatorname{div}(\mathbf{K}^\varepsilon(\mathbf{x}) \nabla p^\varepsilon(\mathbf{x}, t)) = f^\varepsilon(\mathbf{x}, t), \quad \text{in } \Omega^\varepsilon \times (0, T], \quad (1)$$

with suitable initial and boundary conditions. In this setting, ε is a positive small parameter and denotes the scale separation between the micro-scale (e.g., the scale of pores in a porous medium) and the macro-scale (e.g., the Darcy scale, the scale of simulation in case of heterogeneous media). With the superscript $0 < \varepsilon \ll 1$ we indicate that the medium is considered highly heterogeneous, which induces rapid oscillations in the parameters, in the non-linearities and consequently in the solution. Inspired by unsaturated fluid flow in a porous medium (1) can, for example, represent the non-dimensional Richards equation after applying the Kirchhoff transformation, without taking into account gravity effects (see [1]). In this case, the primary unknown $p^\varepsilon(\mathbf{x}, t)$ is the transformation of the fluid pressure. For simplicity $p^\varepsilon(\mathbf{x}, t)$ will be called *pressure* in what follows. The given data include the source f^ε , the absolute permeability matrix \mathbf{K}^ε and the volumetric fluid saturation b^ε , which is a given function of p^ε .

* Corresponding author.

E-mail address: manuela.bastidas@uhasselt.be (M. Bastidas).

The key issue in developing numerical methods capturing the interaction between scales is to avoid the high computational cost. The use of classical schemes over fine-scale meshes has often unreachable requirements. To capture the heterogeneities in the medium the required mesh size is smaller than ε . In this sense, standard numerical methods will either fail or become inefficient.

There are numerous numerical simulation techniques for processes that involve two or more scales in space and time. During the last years, approaches like the multi-scale finite-volume (MSFV), the algebraic dynamic multilevel (ADM), the heterogeneous multi-scale (HMM) and the multi-scale finite element (MsFEM) methods are becoming more and more relevant. Concretely, the MSFV and ADM methods proposed in [2,3] aim to solve problems involving different scales by incorporating the fine-scale variation into the coarse-scale operators. The multi-scale finite volume method (MSFV) in [3] includes a dynamic local grid refinement method to provide accurate and efficient simulations employing fine grids only where needed. A preliminary study comparing approaches based on ADM and numerical homogenization can be found in [4]. There the homogenization method is used to construct effective properties using a dynamic multilevel mesh.

On the other hand, the HMM (see [5,6]) relies on coupled macro and micro-scale solvers using homogenization (see [7]). This method takes advantage of the scale separation and is based on the numerical approximation of the macro-scale data. In [6,8,9] ideas on how to manage different scales in an efficient computational way are developed, using the standard finite element method (FEM). Further, the numerical computations using finite difference and discontinuous Galerkin method also demonstrate the potential of this framework in [5,10].

Improved multi-scale methods to simulate non-linear single-phase and multi-phase flow have been proposed in [11–15]. Specifically, the ideas of adaptive homogenization were applied in [15] for two-phase flow problems. An Enhanced Velocity Mixed Finite Element method is proposed in [13] to deal with non-matching, multi-block grids and couple micro and macro-scale domains. In the same line of research, [12] gives a computational strategy for the multi-scale dynamics over non-matching grids using mesh refinement and enriched multi-scale basis functions. In [11], the homogenization theory is combined with domain decomposition to obtain effective parameters and solve macro-scale problems. Further, the multi-scale finite element (MsFEM) method presented in [16–18] constructs a multi-scale mixed finite element space. This change of the discrete spaces allows the formal derivation of a-posteriori estimates to control the micro-scale error and its influence on the macro-scale.

In this paper, we develop a locally mass-conservative scheme that computes the homogenized permeability field of (1) over coarse meshes. In contrast with the papers mentioned before, we use an error indicator on the macro-scale solvers to localize the error and subsequently refine or coarsen the mesh accordingly. We propose a combination of techniques supported in the theoretical framework of the homogenization (see [7]) for non-linear parabolic equations. Our adaptive homogenization strategy builds on the ideas of the HMM method in [6,8,9] by using an efficient and robust non-linear solver and by considering important aspects as the conservation properties in multiple scales. We use the solution of certain micro-scale problems to calculate averaged parameters that are used in a macro-scale solver. The computation of the effective parameters can be parallelized and it is cheap to perform. The error induced by the calculation of the effective parameters can be dismissed when one applies a sufficiently accurate micro-scale solver. It is important to remark that, although periodicity is assumed in the classical homogenization theory, in the numerical examples we show that this upscaling technique can be also applied to problems involving non-periodic media.

We apply the backward Euler (BE) method for the time discretization and the mixed finite element method (MFEM) for the spatial discretization. We highlight that this strategy is not relying on a particular choice of basis functions or discretization method, and that the micro and macro-scale solvers are completely independent. In order to solve the fully discrete formulation of (1), non-linear solvers are required. We discuss the applicability of classical iterative solvers like Newton or Picard (see [19,20]) and we detail the formulation of a robust fixed-point method called L-scheme proposed in [21]. This linearization procedure has the advantage of being convergent independently of the initial guess, the spatial discretization and the mesh size. Nevertheless, the convergence rate of the L-scheme is only linear and therefore slower compared to the Newton scheme (see [22]). We mention the paper [23] for an approach combining the L and the Newton schemes in an optimized way. There, the L-scheme is applied to provide a suitable initial point for the Newton scheme. We use this strategy to improve the convergence of the scheme up to the quadratic convergence.

For time-dependent problems the idea of adaptive meshes is very useful to localize the changes in the solution between different time steps. On the other hand, reaching finer meshes becomes computationally expensive because it requires extra calculations of the macro-scale parameters. The finer the mesh for the upscaled model, the higher the computational effort as the effective parameters need to be computed in more points, thus more cell problems need to be solved. For this reason, we present an error indicator that specifies when the numerical solution and the effective parameters should be re-computed. With this strategy we aim to control the convergence rate of the numerical scheme and to avoid unnecessary computations of the local problems.

The paper is organized as follows. In Section 2 the details of the model, the geometry and the discrete formulation are given and the necessary assumptions are stated. Section 3 gives a summary of the standard procedure of the homogenization for a parabolic case in a periodic porous media. In Section 4 the mesh refinement and the coarsening strategy is stated and in Section 5 the linearization scheme is described. We discuss the numerical tests in Section 6, where the quasi-periodic and non-periodic cases are considered.

2. The model formulation and the spatial discretization

To construct a robust and locally conservative scheme we consider the mixed formulation of (1). Letting $\mathbf{u}^\varepsilon(\mathbf{x}, t)$ be the Darcy velocity, the unknowns $(p^\varepsilon, \mathbf{u}^\varepsilon)$ satisfy

$$\begin{aligned} \partial_t b^\varepsilon(\mathbf{x}, p^\varepsilon(\mathbf{x}, t)) + \operatorname{div}(\mathbf{u}^\varepsilon(\mathbf{x}, t)) &= f^\varepsilon(\mathbf{x}, t), & \text{in } \Omega_T^\varepsilon, \\ \mathbf{u}^\varepsilon(\mathbf{x}, t) &= -\mathbf{K}^\varepsilon(\mathbf{x}) \nabla p^\varepsilon(\mathbf{x}, t), & \text{in } \Omega_T^\varepsilon, \\ p^\varepsilon(\mathbf{x}, t) &= 0, & \text{on } \partial\Omega_T^\varepsilon, \\ p^\varepsilon(\mathbf{x}, 0) &= p_I, & \text{in } \Omega^\varepsilon. \end{aligned} \tag{2}$$

Here $\Omega_T^\varepsilon := \Omega^\varepsilon \times (0, T]$ and $\partial\Omega_T^\varepsilon := \partial\Omega^\varepsilon \times (0, T]$. As mentioned before, by using the superscript $\varepsilon > 0$ we emphasize that rapidly oscillating characteristics are involved. For example, the domain either involves characteristics changing within ε -sized regions, or it may include perforations.

We refer to [24] for the existence and uniqueness of a weak solution of (1) under the following assumptions:

(A1) The function $b^\varepsilon(\mathbf{x}, \cdot)$ is non-decreasing, $b^\varepsilon(\cdot, 0) = 0$ and locally Lipschitz continuous. There exists $L_b > 0$ such that

$$|b^\varepsilon(\mathbf{x}, p_1) - b^\varepsilon(\mathbf{x}, p_2)| \leq L_b |p_1 - p_2|,$$

for all $\mathbf{x} \in \Omega^\varepsilon$ and $p_1, p_2 \in \mathbb{R}$.

(A2) The permeability function $\mathbf{K}^\varepsilon : \Omega^\varepsilon \rightarrow \mathbb{R}^{d \times d}$ is symmetric for all $\mathbf{x} \in \Omega^\varepsilon$ and continuous. There exist $\beta, \lambda > 0$ such that

$$\beta \|\boldsymbol{\psi}\|^2 \leq \boldsymbol{\psi}^\top \mathbf{K}^\varepsilon(\mathbf{x}) \boldsymbol{\psi} \leq \lambda \|\boldsymbol{\psi}\|^2 \quad \text{for all } \boldsymbol{\psi} \in \mathbb{R}^d \text{ and } \mathbf{x} \in \Omega^\varepsilon.$$

(A3) The initial data p_I and the source term f^ε are essentially bounded uniformly w.r.t. ε .

In [25] the equivalence between the mixed and conformal weak formulations is proved in both continuous and semi-discrete cases.

2.1. The non-linear fully discrete problem

To define the discrete problem we let $\mathfrak{T}_{h^\varepsilon}$ be a triangular partition of the domain Ω^ε with elements \mathcal{T} of diameter $h_{\mathcal{T}}^\varepsilon$ and $h^\varepsilon := \max_{\mathcal{T} \in \mathfrak{T}_{h^\varepsilon}} h_{\mathcal{T}}^\varepsilon$ such that $h^\varepsilon \ll \varepsilon$.

Further, $0 = t_0 \leq t_1 \leq t_2 \leq \dots \leq t_N = T$, $N \in \mathbb{N}$ is a partition of the time interval $[0, T]$ with constant step size $\Delta t = t_{i+1} - t_i$, $i \geq 0$. For the discretization of the flux \mathbf{u}^ε we consider the lowest-order Raviart-Thomas space $V_{h^\varepsilon} := \mathcal{RT}_0(\mathfrak{T}_{h^\varepsilon})$ and for the pressure p^ε we use the discrete subspace of piecewise constant functions W_{h^ε} (see [26])

$$\begin{aligned} W_{h^\varepsilon} &:= \left\{ q \in L^2(\Omega^\varepsilon) \mid q \text{ is constant on each element } \mathcal{T} \in \mathfrak{T}_{h^\varepsilon} \right\}, \\ V_{h^\varepsilon} &:= \left\{ \mathbf{v} \in H(\operatorname{div}, \Omega^\varepsilon) \mid \mathbf{v}|_{\mathcal{T}} = \mathbf{a} + b\mathbf{x} \text{ for all } \mathcal{T} \in \mathfrak{T}_{h^\varepsilon}, \mathbf{a} \in \mathbb{R}^d, b \in \mathbb{R} \right\}, \end{aligned}$$

with $L^2(\Omega^\varepsilon)$ being the space of the square-integrable functions with the usual norm and $H(\operatorname{div}, \Omega^\varepsilon) := \{ \mathbf{v} \in [L^2(\Omega^\varepsilon)]^d \mid \operatorname{div}(\mathbf{v}) \in L^2(\Omega^\varepsilon) \}$. We let $\langle \cdot, \cdot \rangle$ represent the inner product on $L^2(\Omega^\varepsilon)$.

Problem $\mathbf{PM}_n^\varepsilon$. Let $n \geq 1$. Given $((p^\varepsilon)_{h^\varepsilon}^{n-1}, (\mathbf{u}^\varepsilon)_{h^\varepsilon}^{n-1}) \in W_{h^\varepsilon} \times V_{h^\varepsilon}$, find $(p^\varepsilon)_{h^\varepsilon}^n \in W_{h^\varepsilon}$ and $(\mathbf{u}^\varepsilon)_{h^\varepsilon}^n \in V_{h^\varepsilon}$ such that for any $q \in W_{h^\varepsilon}$ and $\mathbf{v} \in V_{h^\varepsilon}$ there holds

$$\begin{aligned} \left\langle b^\varepsilon(\cdot, (p^\varepsilon)_{h^\varepsilon}^n) - b^\varepsilon(\cdot, (p^\varepsilon)_{h^\varepsilon}^{n-1}), q \right\rangle + \Delta t \left\langle \operatorname{div}((\mathbf{u}^\varepsilon)_{h^\varepsilon}^n), q \right\rangle &= \Delta t \langle f^\varepsilon, q \rangle, \\ \left\langle [\mathbf{K}^\varepsilon]^{-1} (\mathbf{u}^\varepsilon)_{h^\varepsilon}^n, \mathbf{v} \right\rangle - \left\langle (p^\varepsilon)_{h^\varepsilon}^n, \operatorname{div}(\mathbf{v}) \right\rangle &= 0. \end{aligned}$$

We denote by $(p^\varepsilon)_{h^\varepsilon}^0$ the L^2 -projection of the initial condition p_I over the mesh $\mathfrak{T}_{h^\varepsilon}$. For simplicity, we omit writing the \mathbf{x} argument in $b^\varepsilon(\mathbf{x}, p^\varepsilon)$, which becomes now $b^\varepsilon(p^\varepsilon)$.

For details about the existence and uniqueness of the solution to problem $\mathbf{PM}_n^\varepsilon$ we refer to [25]. Note that the problem $\mathbf{PM}_n^\varepsilon$ is non-linear. Therefore a non-linear solver is needed. This is detailed in Section 5.

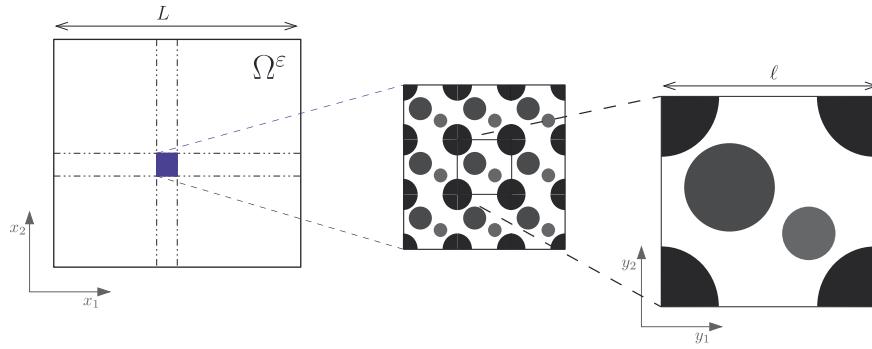


Fig. 1. The two-scale structure in \mathbb{R}^2 : the macro-scale domain (left), the complex structure (center) and the micro-scale (right). Note the typical length sizes L and ℓ .

3. The two-scale approach

We start the presentation for the case of a periodic medium. Building on this, we extend these ideas for non-periodic situations. The concept of coupling the scales through the calculation of effective parameters is used, among others, in [6,9,11]. Here we follow the ideas therein and enhance the strategy with adaptive mesh refinement and robust non-linear solvers.

We assume that the domain Ω^ϵ can be written as the finite union of *micro-scale* regions, namely Y , where the parameters change rapidly. In other words, the parameters and non-linearities take different values inside of Y (see Fig. 1). In the extreme case, the micro-scale Y can be viewed as a perforated region with a pore space and a solid grain (see, e.g., [7]). Here we give the ideas for non-perforated domains but this can be adapted straightforwardly to perforated ones.

At the micro-scale Y and the macro-scale Ω^ϵ we assume characteristic lengths ℓ and L respectively. The factor $\epsilon := \frac{\ell}{L}$ denotes the scale separation between the two scales. To identify the variations at the micro-scale we define a fast variable $\mathbf{y} := \frac{\mathbf{x}}{\epsilon}$. To each macro-scale point $\mathbf{x} \in \Omega^\epsilon$ corresponds one micro-scale cell Y that captures the fast changes in the parameters.

In the non-dimensional setting, the local cells are $Y := [0, 1]^d$ and we let $\vec{i} \in \mathbb{Z}^d$ and $\Omega^\epsilon = \cup \left\{ \epsilon(\vec{i} + Y) \mid \vec{i} \in \mathcal{I}_\epsilon \right\}$ for some set of vector indices \mathcal{I}_ϵ .

To formulate the homogenized problem, we make the following assumptions:

- (B1) There exists a function $b : \Omega^\epsilon \times \mathbb{R}^d \times \mathbb{R} \rightarrow \mathbb{R}$ such that $b^\epsilon(\mathbf{x}, p^\epsilon) := b(\mathbf{x}, \frac{\mathbf{x}}{\epsilon}, p^\epsilon)$ and $b(\mathbf{x}, \cdot, p^\epsilon)$ is Y -periodic.
- (B2) There exists a function $\mathbf{K} : \Omega^\epsilon \times \mathbb{R}^d \rightarrow \mathbb{R}^{d \times d}$ such that $\mathbf{K}^\epsilon(\mathbf{x}) := \mathbf{K}(\mathbf{x}, \frac{\mathbf{x}}{\epsilon})$ where $\mathbf{K}(\mathbf{x}, \mathbf{y})$ is symmetric and continuous for all $(\mathbf{x}, \mathbf{y}) \in \Omega^\epsilon \times Y$ and $\mathbf{K}(\mathbf{x}, \cdot)$ is Y -periodic.

3.1. The homogenization approach

A direct numerical approximation of the problem \mathbf{PM}_n^ϵ requires the usage of an extremely fine mesh to capture all the changes in the characteristics of the medium. We consider a homogenization-based approach and compute an effective model involving only the essential variations of the permeability matrix.

We restrict the presentation to the minimum needed for explaining the approach. We make use of the *homogenization ansatz* and refer to [7,27] for a detailed presentation of the method.

First, we assume that p^ϵ can be formally expanded as

$$p^\epsilon(\mathbf{x}, t) = p(\mathbf{x}, t) + \epsilon p_1(\mathbf{x}, \mathbf{y}, t) + \epsilon^2 p_2(\mathbf{x}, \mathbf{y}, t) + \dots, \tag{3}$$

where $\mathbf{y} = \frac{\mathbf{x}}{\epsilon}$ stands for the fast variable, \mathbf{x} is the slow variable and each function $p_i : \Omega^\epsilon \times Y \times (0, T] \rightarrow \mathbb{R}$ is Y -periodic w.r.t. \mathbf{y} . The function $p(\mathbf{x}, t)$ does not depend on \mathbf{y} and is in fact the *macro-scale approximation* of the pressure $p^\epsilon(\mathbf{x}, t)$.

Additionally, the two-scale gradient and divergence operators become

$$\nabla = \nabla_x + \frac{1}{\epsilon} \nabla_y \quad \text{and} \quad \text{div} = \text{div}_x + \frac{1}{\epsilon} \text{div}_y. \tag{4}$$

Using (3) and (4) in (2) and applying the Taylor expansion of $b(\cdot, \cdot, p)$ we obtain

$$\partial_t b - \left(\text{div}_x + \frac{1}{\epsilon} \text{div}_y \right) \left(\mathbf{K} \left(\nabla_x + \frac{1}{\epsilon} \nabla_y \right) \left(p + \epsilon p_1 + \epsilon^2 p_2 \right) \right) + \mathcal{O}(\epsilon) = f.$$

To determine p_1 as a function of p , for the terms of order $\mathcal{O}(\epsilon^{-1})$ we can write $p_1(\mathbf{x}, \mathbf{y}, t) = \hat{p}_1(\mathbf{x}, t) + \sum_{j=1}^d \frac{\partial p(\mathbf{x}, t)}{\partial x_j} \omega^j(\mathbf{x}, \mathbf{y})$ where the function \hat{p}_1 is an arbitrary function of \mathbf{x} , and ω^j are the solutions of the following mixed *micro-cell* problems

$$\begin{aligned} \operatorname{div}_y \boldsymbol{\xi}^j &= \operatorname{div}_y (\mathbf{K}(\mathbf{x}, \cdot) \mathbf{e}_j), & \text{in } Y, \\ \boldsymbol{\xi}^j &= -\mathbf{K}(\mathbf{x}, \cdot) \nabla_y \omega^j, & \text{in } Y, \\ \omega^j & \text{ is } Y \text{ - periodic.} \end{aligned} \tag{5}$$

Here $\{\mathbf{e}_j\}_{j=1}^d$ is the canonical basis of \mathbb{R}^d . To guarantee the uniqueness of the solution we assume that ω^j has the average 0 over the micro cells, that is, $\int_Y \omega^j(\mathbf{x}, \mathbf{y}) d\mathbf{y} = 0$ for all $\mathbf{x} \in \Omega^\varepsilon$.

To highlight that the homogenized domain does not contain heterogeneities, we use Ω instead of Ω^ε for the macro-scale domain and $\partial\Omega$ for its outer boundary. Following the homogenization, Ω does not contain any oscillatory behavior. Recalling the periodic boundary conditions and averaging over Y , one obtains the *homogenized* mixed formulation.

Letting $\mathbf{u}(\mathbf{x}, t)$ denote the upscaled Darcy velocity, the upscaled unknowns (p, \mathbf{u}) satisfy

$$\begin{aligned} \partial_t b^*(\mathbf{x}, p(\mathbf{x}, t)) + \operatorname{div}(\mathbf{u}(\mathbf{x}, t)) &= f^*(\mathbf{x}, t), & \text{in } \Omega_T \\ \mathbf{u}(\mathbf{x}, t) &= -\mathbf{K}^*(\mathbf{x}) \nabla p(\mathbf{x}, t), & \text{in } \Omega_T, \\ p(\mathbf{x}, t) &= 0, & \text{on } \partial\Omega_T, \\ p(\mathbf{x}, 0) &= p_I, & \text{in } \Omega. \end{aligned} \tag{6}$$

Here $\Omega_T := \Omega \times (0, T]$ and $\partial\Omega_T := \partial\Omega \times (0, T]$. The effective permeability $\mathbf{K}^* : \Omega \rightarrow \mathbb{R}^{d \times d}$ has the elements

$$\mathbf{K}_{i,j}^*(\mathbf{x}) = \int_Y \left(\mathbf{K}(\mathbf{x}, \mathbf{y}) \left(\mathbf{e}_j + \nabla_y \omega^j(\mathbf{x}, \mathbf{y}) \right) \right) \cdot \mathbf{e}_i d\mathbf{y}, \quad (i, j = 1, \dots, d). \tag{7}$$

The upscaled saturation and source terms are

$$b^*(\mathbf{x}, p) := \int_Y b(\mathbf{x}, \mathbf{y}, p) d\mathbf{y} \quad \text{and} \quad f^*(\mathbf{x}, t) := \int_Y f(\mathbf{x}, \mathbf{y}, t) d\mathbf{y}.$$

The difference between the solution of (2) and the solution of (6) is subtle. In the original problem, the main characteristics are present at all scales in a strongly coupled manner. Notice that a very fine mesh is needed to resolve all the variabilities in (2), leading to expensive numerical methods and oscillatory solutions. The *homogenized model* instead involves only essential variations at the macro-scale. The solution of (6) represents the average behavior of the solution of (2) and can be solved on much coarser meshes. However, to determine the value of the permeability tensor at a macro point $\mathbf{x} \in \Omega$, one has to solve d micro-cell problems (5) associated with that macro point. Note that these problems reflect the rapidly oscillating characteristics and are decoupled from the macro-scale variations. From a computational point of view, the importance of this decoupling becomes obvious. Instead of solving the full problem on a very fine mesh, one solves a collection of simpler problems. In general, analytic solutions are not available to compute the homogenized parameters. Then \mathbf{K}^* , b^* and f^* must usually be computed numerically and can therefore only be obtained at discrete points of the domain Ω .

If the original permeability \mathbf{K}^ε satisfies (A2) and (B2) then the effective tensor in (7) is also symmetric and positive definite. Nevertheless, even when the fine scale permeability is isotropic, the numerical approximation to the effective tensor can contain non-zero non-diagonal components or different diagonal components.

The non-linear discrete problem associated with the homogenized formulation (6) is defined in the following sections.

3.2. The non-linear fully discrete homogenized problem

Let \mathfrak{T}_H be a coarse, triangular partition of the domain Ω with coarse elements \mathcal{T} of diameter $H_{\mathcal{T}}$ and $H := \max_{\mathcal{T} \in \mathfrak{T}_H} H_{\mathcal{T}}$. For the discretization of the flux \mathbf{u} we consider the lowest-order Raviart-Thomas space $V_H := \mathcal{RT}_0(\mathfrak{T}_H)$ and for the pressure p we use the discrete subspace of piecewise constant functions W_H (see [26]).

Problem PH_n. For a given $p_H^{n-1} \in W_H$ and $n \geq 1$, find $p_H^n \in W_H$ and $\mathbf{u}_H^n \in V_H$ such that for any $q_H \in W_H$ and $\mathbf{v}_H \in V_H$ there holds

$$\begin{aligned} \langle b^*(\cdot, p_H^n) - b^*(\cdot, p_H^{n-1}), q_H \rangle + \Delta t \langle \operatorname{div}(\mathbf{u}_H^n), q_H \rangle &= \Delta t \langle f^*, q_H \rangle, \\ \langle [\mathbf{K}^*]^{-1} \mathbf{u}_H^n, \mathbf{v}_H \rangle - \langle p_H^n, \operatorname{div}(\mathbf{v}_H) \rangle &= 0. \end{aligned}$$

Again p_H^0 is the L^2 -projection of the initial p_I over the coarse mesh \mathfrak{T}_H . For simplicity, we omit writing the \mathbf{x} argument in $b^*(\mathbf{x}, p)$, which becomes now $b^*(p)$.

3.3. The micro-cell problems and the micro-scale discretization

As mentioned before, the effective parameters must be computed at each integration point on the coarse triangulation \mathfrak{T}_H . The effective tensor \mathbf{K}^* depends on the solution of the micro-cell problems (5). To solve (5) we use MFEM.

To approximate the solution of (5) we use a triangular decomposition \mathfrak{T}_h of the micro-scale domain Y with micro-scale mesh size h . For the discretization of the micro-scale unknowns we consider the lowest-order Raviart-Thomas space $V_h := \mathcal{RT}_0(\mathfrak{T}_h)$ and the discrete subspace of piecewise constant functions W_h . At each integration point $\mathbf{x} \in \mathcal{T}$ with $\mathcal{T} \in \mathfrak{T}_H$, the discrete micro-cell problem is

Problem \mathbf{Ph}_j . Find $(\omega_h^j, \xi_h^j) \in W_h \times V_h$ satisfying

$$\begin{aligned} \langle \operatorname{div} \xi_h^j, q_h \rangle &= \langle \nabla \cdot (\mathbf{K}(\mathbf{x}, \cdot) \mathbf{e}_j), q_h \rangle, \\ \langle [\mathbf{K}(\mathbf{x}, \cdot)]^{-1} \xi_h^j, \mathbf{v}_h \rangle - \langle \omega_h^j, \operatorname{div}(\mathbf{v}_h) \rangle &= 0, \\ \omega_h^j &\text{ is } Y\text{-periodic,} \\ \int_Y \omega_h^j(\mathbf{x}, \mathbf{y}) d\mathbf{y} &= 0, \end{aligned}$$

for all $q_h \in W_h$, $\mathbf{v}_h \in V_h$ and $j = 1, \dots, d$. After solving the problems \mathbf{Ph}_j , we use (7) to compute the discrete effective permeability and solve the discrete problem \mathbf{PH}_n . The cell problems \mathbf{Ph}_j are linear problems that only need to be solved initially, or when the mesh changes. The numerical cost of solving the micro-scale problems is minor compared to solving the original problem.

3.4. Non-periodic case

Until now the two-scale approach has been referenced by assuming periodicity of the permeability \mathbf{K}^ε . Nevertheless, we claim that the same strategy can be applied to non-periodic structures. When the permeability field \mathbf{K}^ε is non-periodic, the periodic boundary conditions in the problems \mathbf{Ph}_j are artificially imposed. However, the problems \mathbf{Ph}_j are well defined and will yield to one upscaled tensor \mathbf{K}^* . In other words, when one solves the micro-cell problems the resulting effective permeability field can systematically be considered an upscaled quantity obtained from the original data. The main issue is whether this upscaled permeability reflects the effective behavior at the macro-scale. Hence, we combine the numerical homogenization with mesh adaptivity to capture the local variability. In the numerical examples we show that the adaptive numerical homogenization applied to the non-periodic cases produces profitable results.

4. The two-scale discretization

In practical cases, one does not necessarily have any structure in the oscillations of the data. Nevertheless, the computation of macro-scale parameters remains a suitable idea. We propose to solve the micro-cell problems \mathbf{Ph}_j and compute the macro-scale parameters over a coarse mesh defined beforehand. This procedure consists of two steps:

- *The macro-scale partition:* Define a macro-scale division of the domain Ω with elements Q_k , ($k = 1, 2, \dots, M$), where M is the total number of coarse cells.
- *The micro-scale domains:* Solve the micro-cell problems \mathbf{Ph}_j and compute the constant effective permeability (7) over each coarse cell Q_k . Note that Q_k determines a micro-scale domain and there we define a micro-scale mesh size h . Moreover, at each micro-scale domain we impose periodic boundary conditions.

Based on this, one can first construct a coarse mesh for the macro-scale domain and inside each macro-scale element the effective parameters are obtained by solving the corresponding micro-scale cell problems. Subsequently, one can solve the homogenized problem \mathbf{PH}_n . It is important to highlight that over the coarse-scale partition we construct a uniform triangular mesh such that a constant effective permeability is assigned to each triangle. In Fig. 2, we show the configuration of the macro and micro-scale partition and the procedure described previously.

4.1. The error indicator

We propose a three-step strategy to adapt the macro-scale mesh to the evolution of the numerical solution of the homogenized problem. Our strategy is based on the idea of *error control based on averaging technique* introduced in [28,29]. The indicator of error uses a smoother approximation to the discrete solution \mathbf{u}_H^n . We define an average operator \mathfrak{A}_z

$$\mathfrak{A}_z \mathbf{u}_H^n(z) = \mathfrak{A}_z(\mathbf{u}_H^n) := \frac{1}{|w_z|} \int_{w_z} \mathbf{u}_H^n d\mathbf{x}$$

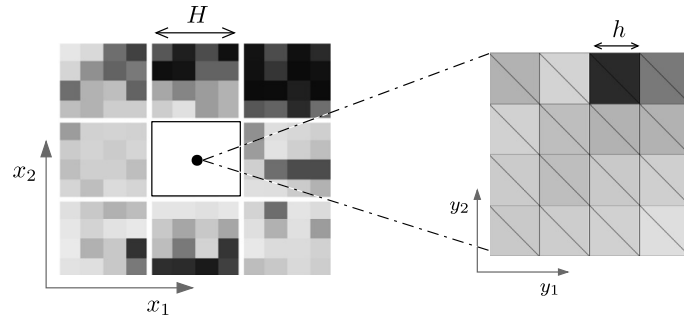


Fig. 2. The sketch of the macro-scale partition and the correspondent micro-scale discretization in a domain $\Omega \subset \mathbb{R}^2$. Different intensities represent different values of the permeability.

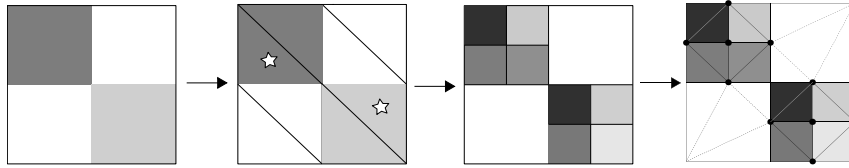


Fig. 3. The outline of the mesh refinement in \mathbb{R}^2 . (Left to right) Initial effective permeability. Initial triangulation and selected triangles to refine (\star). Refinement of the permeability field. Refinement of the triangular mesh such that each element corresponds to one and only one (effective) permeability.

where $w_z := \text{int}(\cup \{\mathcal{K} \in \mathfrak{T}_{H_n} : \mathcal{K} \cap \mathcal{T} \neq \emptyset, z \in \mathcal{T}\})$ is the patch corresponding to the point $z \in \Omega$.

With this choice of the error indicator we estimate the regions where the flux is changing substantially. Other indicators are possible and can be incorporated straightforwardly. For example, one could use estimators based on the changes in pressure, front capturing or aim to minimize the residual of the numerical solution (a posteriori estimators, e.g., [30]). We remark that by changing the error indicator one would not change the steps below, although different macro-scale meshes would be obtained by the procedure.

4.2. The macro-scale mesh refinement and coarsening

Our approach consists of the sequence: Solve - select the cells/triangles - refine/coarse the mesh. The mesh refining generates a sequence of triangular meshes (one mesh per time step).

- (S1) *Solve*: The starting point is an initial coarse mesh \mathfrak{T}_{H_0} and the approximation of the pressure and velocity (p_H^0, \mathbf{u}_H^0) that satisfy the discrete problem \mathbf{PH}_n in the first time step.
- (S2) *Select the cells/triangles*: Let the solution (p_H^n, \mathbf{u}_H^n) over \mathfrak{T}_{H_n} be given. Calculate the error indicator

$$\eta_{\mathcal{T}}^n := \|\mathbf{u}_H^n - \mathfrak{A}\mathbf{u}_H^n\|_{L^2(\mathcal{T})} \tag{8}$$

for all $\mathcal{T} \in \mathfrak{T}_{H_n}$. The elements marked to be refined are $\mathcal{T} \in \mathfrak{T}_{H_n}$ such that (see [31])

$$\eta_{\mathcal{T}}^n \geq \Theta_r \left(\max_{\mathcal{K} \in \mathfrak{T}_{H_n}} \eta_{\mathcal{K}}^n \right) \quad \text{with } \Theta_r \in (0, 1).$$

On the other hand, we select a set of triangles to be coarsened, i.e. $\mathcal{T} \in \mathfrak{T}_{H_n}$ such that

$$\eta_{\mathcal{T}}^n \leq \Theta_c \left(\min_{\mathcal{K} \in \mathfrak{T}_{H_n}} \eta_{\mathcal{K}}^n \right) \quad \text{with } \Theta_c \geq 1.$$

- (S3) *Adapt the mesh*: The last step of the adaptive procedure consists of including new elements, deleting the elements to be coarsened and re-meshing. Our strategy avoids nonconforming meshes. We refine each selected cell into four new cells to compute four new effective permeabilities, and the reverse process when coarsening is necessary. Inside of the new finer cells we re-mesh with the necessary triangles.

The outline of the steps (S1) to (S3) is presented in Figs. 3 and 4 for the 2D case. In Fig. 3 we sketch the situation when only refinement is encountered and in Fig. 4 we sketch the coarsening process. We will only consider 2D numerical examples, but in 3D the mesh refinement can be done as described in [32]. In Figs. 3 and 4 we highlight that at every time step it is necessary to ensure that in the new mesh each element corresponds only to one permeability value. That restriction forces us to also refine/coarsen neighboring elements. This is also evident in Fig. 5 in which we show three different steps of the mesh adaptivity.

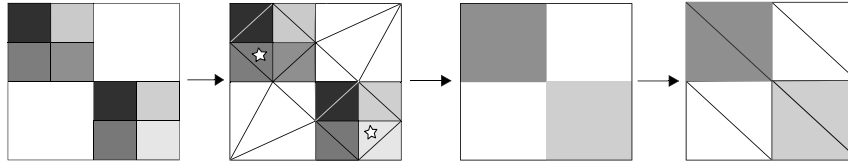


Fig. 4. The outline of the mesh coarsening in \mathbb{R}^2 . (Left to right) Refined effective permeability. Refined triangulation and selected triangles to coarsen (\star). Coarsened permeability field. Coarsened triangulation such that each element corresponds to one and only one (effective) permeability.

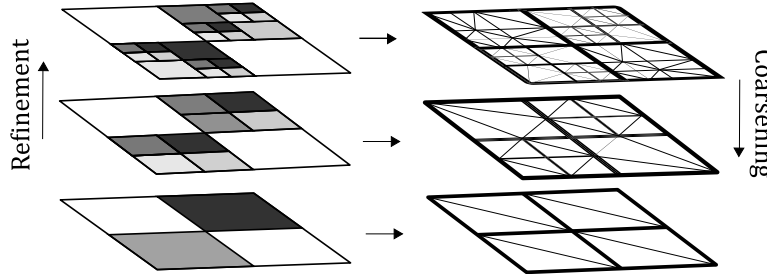


Fig. 5. The outline of the mesh adaptivity. (Left) Three different levels of the effective permeability refinement (bottom to top) or coarsening (top to bottom) and (right) three different levels of the mesh refinement (bottom to top) or coarsening (top to bottom).

With this strategy, we allow more than one level of refinement. However, the homogenization theory presented earlier is restricted to only two levels. In Fig. 5 we sketch the mesh adaptivity process when different levels are involved at one step. Note that the thresholds for the refinement can be chosen depending on the problem. Higher values of Θ_r and Θ_c lead to coarser meshes and less error control. We remark that the adaptive homogenization strategy does not depend on which error indicator is applied and can be changed without modifying the steps presented here.

5. The linearization scheme and the final algorithm

Since the time discrete problem \mathbf{PH}_n is non-linear, solving it then requires a linear iterative scheme. A popular choice is the Newton method (see [19]), which converges quadratically. However, we remark that the quadratic convergence is only achieved under certain restrictions. Specifically, the initial guess for the iterations must be close enough to the solution. For evolution equations, the solution computed at the previous time step is a natural choice for the initial guess. Therefore, the time step should be small enough and depending on the spatial discretization and the mesh size this often leads to impractical values (see [33,34]). We refer to [35–41] for several modifications of the Newton scheme leading to an improved convergence behavior. We remark that in these papers either the equation to solve involves a convex-concave first order term or a particular type of discretization is considered. None of these aspects are relevant for our setting. To avoid a time step restriction we apply the L-scheme, which is a contraction-based approach. Although it is only linearly convergent, the convergence is guaranteed regardless of the initial guess and on the spatial discretization. It does not involve any derivatives (see [21,23,42]).

Let $\mathcal{L} \geq L_b$ (see (A1)) be fixed and assume p_H^{n-1} given. With $i \in \mathbb{N}$, $i \geq 1$ being the iteration index, the next iteration in the L-scheme is the solution of the following linear problem.

Problem \mathbf{PH}_n^i . Find $p_H^{n,(i)} \in W_H$ and $\mathbf{u}_H^{n,(i)} \in V_H$ such that for any $q_H \in W_H$ and $\mathbf{v}_H \in V_H$ there holds

$$\begin{aligned} & \left\langle \mathcal{L} \left(p_H^{n,(i)} - p_H^{n,(i-1)} \right) + b^* \left(\cdot, p_H^{n,(i-1)} \right), q_H \right\rangle \\ & + \Delta t \left\langle \operatorname{div} \left(\mathbf{u}_H^{n,(i)} \right), q_H \right\rangle = \Delta t \left\langle f^*, q_H \right\rangle + \left\langle b^* \left(\cdot, p_H^{n-1} \right), q_H \right\rangle, \\ & \left\langle \mathbf{u}_H^{n,(i)}, \mathbf{v}_H \right\rangle - \left\langle \mathbf{K}^* p_H^{n,(i)}, \operatorname{div} \left(\mathbf{v}_H \right) \right\rangle = 0. \end{aligned}$$

As discussed, the natural choice for the initial iteration $p_H^{n,(0)}$ is p_H^{n-1} but the convergence of the scheme does not depend on this choice. In the non-linear solver the iterations take place until one reaches a prescribed threshold for the L^2 -norm of the difference between iterations, namely $\delta(p_H^{n,(i)}) := p_H^{n,(i)} - p_H^{n,(i-1)}$.

For the L-scheme the convergence rate is $\alpha = \frac{\mathcal{L}-m}{\mathcal{L}+C\Delta t}$ for some $C > 0$ and $m < \mathcal{L}$ (see [21]). Moreover, when using the L-scheme with $\mathcal{L} = L_b$ the discrete maximum principle is preserved if the spatial discretization also has this property. In particular, we use MFEM and the maximum principle is guaranteed for this method.

Finally, we combine the non-linear solver, the mesh adaptivity and the homogenization ideas in a simple algorithm presented below. For a better understanding of the stages in the proposed method, a flow chart is given in Fig. 6, presenting the steps in the algorithm.

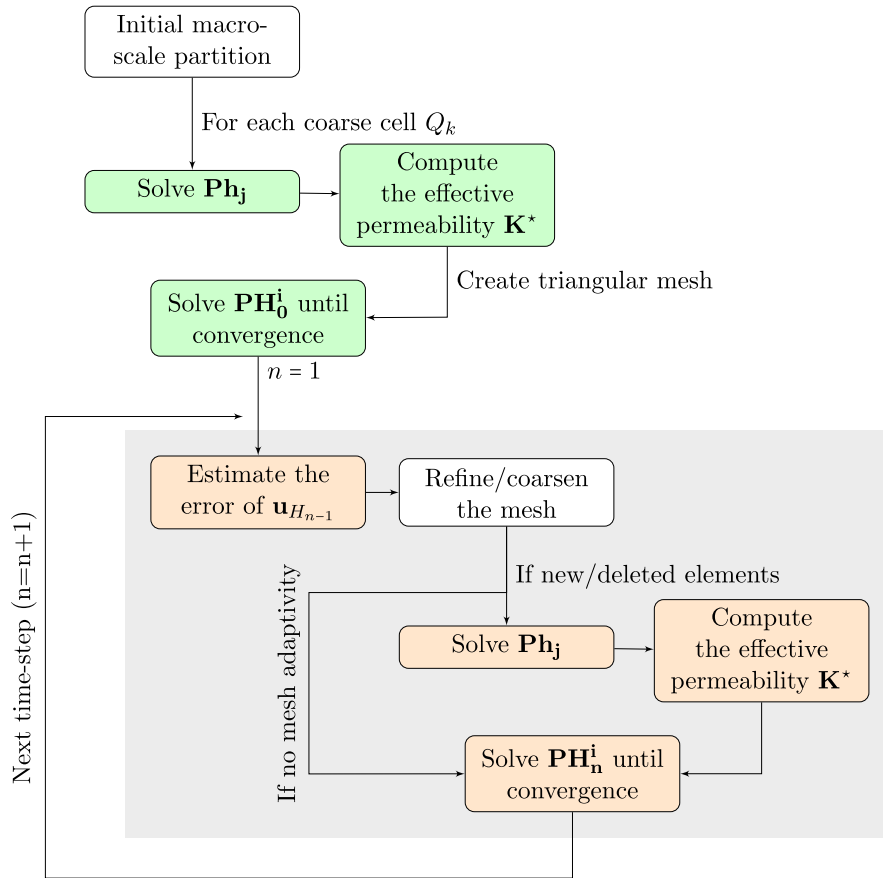


Fig. 6. The sketch of the adaptive numerical homogenization strategy.

Algorithm 1 Adaptive numerical homogenization.

Result: Pressure p_{H_N} and velocity \mathbf{u}_{H_N} over a refined mesh \mathfrak{T}_{H_N}
 Choose an initial coarse-mesh \mathfrak{T}_{H_0} and compute the coarse effective permeability \mathbf{K}^* (7).
for time step t_n **do**
 Estimate the error indicator (8) of the solution $\mathbf{u}_{H_{n-1}}$
 Refine/coarsen the mesh $\mathfrak{T}_{H_{n-1}}$
 if new/deleted elements **then**
 Solve the micro-cell problems \mathbf{Ph}_j
 Re-compute the effective parameter \mathbf{K}^* (7)
 end
 while $\|\delta(p_H^{n(i)})\| > tol$ **do**
 Compute the solutions $p_{H_n}^{n(i)}$ and $\mathbf{u}_{H_n}^{n(i)}$ by solving problem \mathbf{PH}_n^i over the new mesh \mathfrak{T}_{H_n}
 end
end

6. Numerical results

We present two numerical examples in \mathbb{R}^2 to illustrate the behavior of the proposed adaptive homogenization procedure. We first verify our numerical homogenization approach using a manufactured periodic and quasi-periodic media and subsequently use a non-periodic test case. Note that all parameters specified in the following examples are non-dimensional. The pressures are also shifted to lie between 0 and 1.

6.1. The periodic and quasi-periodic cases

Consider the macro-scale domain $\Omega^\varepsilon = (0, 1) \times (0, \frac{1}{2})$ with initial condition $p_0 = 0$. We impose the pressure to be 1 and 0 in the upper-right and the lower-left corners respectively, and we use no-flow boundary conditions elsewhere. The volumetric concentration is $b^\varepsilon(\mathbf{x}, p^\varepsilon) = \mathcal{R} \cdot (p^\varepsilon)^3$. Here \mathcal{R} is a non-dimensional constant and it is chosen to be $\mathcal{R} = 0.5E-1$.

Table 1

The error E_p for three values of ε and three macro-scale coarse meshes. No adaptivity is included.

	Mesh 1		Mesh 2		Mesh 3	
	H	#Elements	H	#Elements	H	#Elements
$\varepsilon = 1/8$	0.1768	64	0.0884	256	0.0442	1024
$\varepsilon = 1/16$		8.145E-2		2.549E-2		1.415E-2
$\varepsilon = 1/32$		6.616E-2		2.497E-2		1.349E-2
		5.594E-2		1.721E-2		1.128E-2

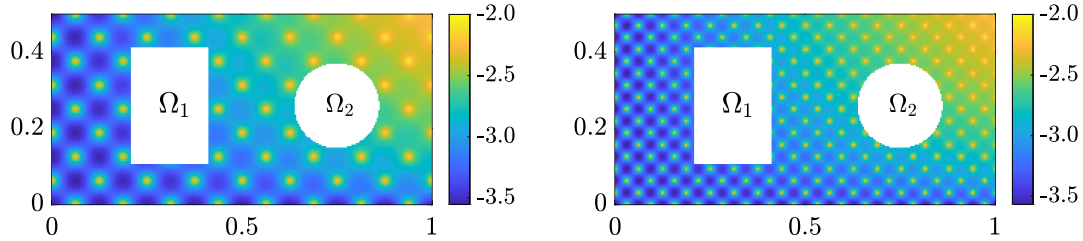


Fig. 7. The fine scale permeability field ($\mathbf{K}_{1,1}^\varepsilon$) (left) $\varepsilon = \frac{1}{8}$ and (right) $\varepsilon = \frac{1}{16}$ (Log_{10} scale).

This choice of \mathcal{R} is such that the dynamic behavior extends up to the reference time $T = 1$. Finally, we take $\Delta t = 0.1$ and the isotropic periodic permeability field is defined by $\mathbf{K}^\varepsilon(\mathbf{x}) = \kappa^\varepsilon(\mathbf{x})\mathbb{I}_{2 \times 2}$ with

$$\kappa^\varepsilon(\mathbf{x}) = \left(10x_1^2x_2 + \frac{1}{2 + 1.8 \cos(2\pi \frac{x_1}{\varepsilon}) \cos(2\pi \frac{x_2}{\varepsilon})} \right). \tag{9}$$

To solve the problem $\mathbf{PM}_h^\varepsilon$ with the necessary resolution to capture the oscillations over Ω^ε the mesh size is restricted to be $h^\varepsilon \ll \varepsilon$. We use a uniform mesh with 65536 elements and $h^\varepsilon = 5E-3$ to compute the fine-scale solutions $(p_{h^\varepsilon}, \mathbf{u}_{h^\varepsilon})$ when $\varepsilon = \frac{1}{8}, \frac{1}{16}$ and $\frac{1}{32}$. The reference solutions are computed using the same MFEM, backward Euler scheme and the L-scheme with $\mathcal{L} = 3\mathcal{R} \geq \max(3\mathcal{R} \cdot (p^\varepsilon)^2)$.

Table 1 shows the history of convergence of the error for different values of ε and three fixed and uniform coarse meshes \mathfrak{T}_H (without refinement) and $H \gg h^\varepsilon$. In other words, in Table 1 we evidence the behavior of the method on three different static coarse meshes for different values of ε . The L^2 -error of the upscaled pressure p_H is calculated as

$$E_p = \|\Pi_{h^\varepsilon}(p_H) - p_{h^\varepsilon}\|_{L^2([0,T];L^2(\mathfrak{T}_{h^\varepsilon}))}, \tag{10}$$

where $\Pi_{h^\varepsilon}(p_H)$ is the L^2 -projection of the upscaled solution in the fine mesh $\mathfrak{T}_{h^\varepsilon}$. With this result we show how the homogenized solution tends to the solution of the original problem when $H \rightarrow 0$ (rows) and also when $\varepsilon \rightarrow 0$ (columns).

As follows from Table 1, a finer mesh reduces the errors. However, the errors are not necessarily distributed uniformly. The domain can include regions where the errors are significantly larger than in other regions, and these regions may also change in time. With this example we motivate the use of an adaptive mesh refinement, combined with an error indicator to identify the regions where the errors are high.

6.1.1. The isotropic case

We use a modified permeability field to indicate that the assumption of periodicity is not essential. We include in the same domain Ω^ε a high permeability region Ω_1 and a low permeability region Ω_2 where the scalar permeability is $1E-2$ and $1E-7$ respectively.

$$\Omega_1 := [0.21, 0.41] \times [0.11, 0.41] \text{ and } \Omega_2 := \left\{ \mathbf{x} \in \Omega^\varepsilon \mid \|\mathbf{x} - [0.75, 0.26]\|_2 \leq 0.1^2 \right\}.$$

In Fig. 7 the normalized (quasi-periodic) permeability field is shown for two values of the scale parameter ε . The boundary conditions, the volumetric concentration, the source term and the time discretization remain the same as before.

Fig. 8 shows four levels of the first component of the effective permeability tensor ($\mathbf{K}_{1,1}^*$) with $\varepsilon = \frac{1}{16}$ starting with a coarse grid of 16×8 cells. Referring to the different levels of the effective permeabilities, it is important to remark that the coarse-scale permeabilities are computed in zones that not always match with the initial resolution or periodicity. Here one can notice the influence of neighbouring macro-cells in the numerical solution of the micro problems \mathbf{Ph}_j . This effect is evident at the boundary of the low permeability zone Ω_2 . To point out this behavior in the Fig. 8 we highlight with a dashed lines the original location of the low and high permeability areas.

To quantify the anisotropic deviation of \mathbf{K}^* we compute the following quantities

$$\tau_1 = \left(\frac{\int_\Omega \|\mathbf{K}_D^*(\mathbf{x}) - \mathbf{K}^*(\mathbf{x})\|_2^2 d\mathbf{x}}{\int_\Omega \|\mathbf{K}_D^*(\mathbf{x})\|_2^2 d\mathbf{x}} \right)^{\frac{1}{2}} \text{ and } \tau_2 = \left(\frac{\int_\Omega |\mathbf{K}_{1,1}^*(\mathbf{x}) - \mathbf{K}_{2,2}^*(\mathbf{x})|^2 d\mathbf{x}}{\int_\Omega \frac{\mathbf{K}_{1,1}^*(\mathbf{x})^2}{2} + \frac{\mathbf{K}_{2,2}^*(\mathbf{x})^2}{2} d\mathbf{x}} \right)^{\frac{1}{2}},$$

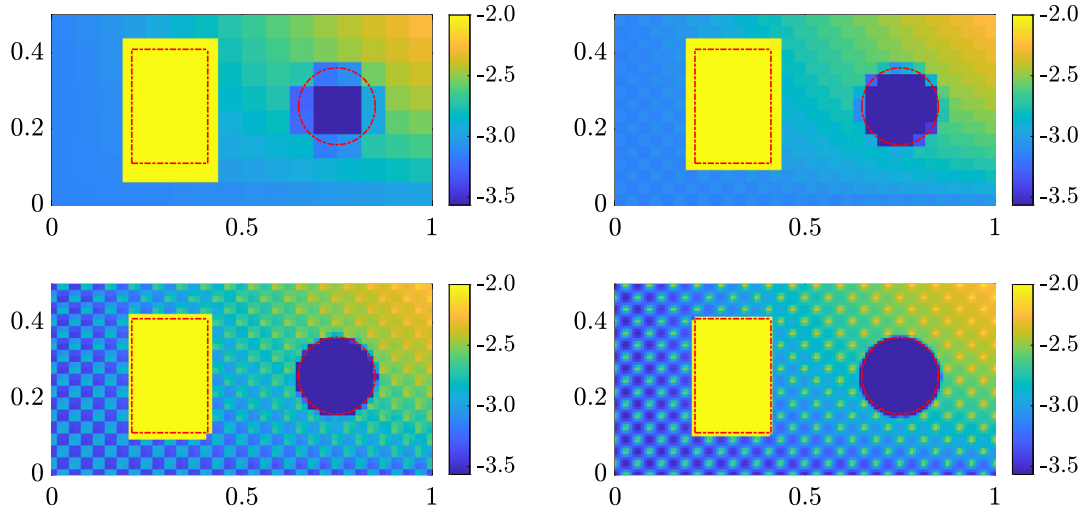


Fig. 8. The coarse-scale permeability distribution ($\mathbf{K}_{1,1}^*$) (Log_{10} scale) starting with a coarse grid of 16×8 cells. The red lines indicate the original location of the low permeability zone ($\mathbf{K}^e = 1\text{E-}7\mathbb{I}_{2 \times 2}$) and high permeability zone ($\mathbf{K}^e = 1\text{E-}2\mathbb{I}_{2 \times 2}$).

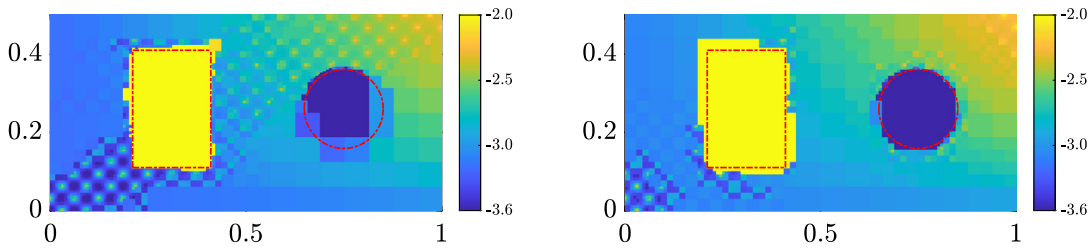


Fig. 9. The refined permeability field ($\mathbf{K}_{1,1}^*$) at $t = 1$ (Log_{10} scale) by using $\Theta_r = 0.3$ (left) and $\Theta_r = 0.5$ (right).

Table 2

The adaptivity results for $\Theta_c = 1$ and a varying refining parameter Θ_r . #Elements corresponds to the average number of elements during the simulation.

	Θ_r				
	0.2	0.3	0.5	0.7	0.8
#Elements	2755	1295	692	392	331
E_p	1.581E-2	1.664E-2	1.727E-2	1.8422E-2	1.901E-2

where \mathbf{K}_D^* is the diagonal matrix that contains the diagonal elements of \mathbf{K}^* .

The anisotropic deviation of the effective permeability tensor in the quasi-periodic case (see Fig. 8) corresponds to $9.65\text{E-}5 \leq \tau_1 \leq 3.18\text{E-}4$ and $3.57\text{E-}5 \leq \tau_2 \leq 8.06\text{E-}4$. With this we conclude that the non-diagonal components of \mathbf{K}^* can be neglected and due to the similarity between $\mathbf{K}_{1,1}^*$ and $\mathbf{K}_{2,2}^*$ in Figs. 8 and 9 we only show the first component ($\mathbf{K}_{1,1}^*$) of the effective parameter.

In Table 2 we present the results of the adaptive homogenization process when using different values of Θ_r . Given the parabolic nature of the problem the coarsening process is expected to be less relevant during the simulation. In Table 2 the upscaled solution is computed employing the mesh refinement described in Section 4 by using $\Theta_c = 1$, i.e., without coarsening the mesh. This allows studying the influence of the refinement parameter Θ_r only.

Furthermore, after the adaptivity process we obtain a refined version of the permeability field and Fig. 9 shows the result of the refined permeability at $t = 1$ for two different values of the refinement parameter. The numerical solution of the upscaled problem \mathbf{PH}_n when using $\Theta_r = 0.5$ is showed in Fig. 10. Notice that the results in Fig. 10 use only 1.06% of the original degrees of freedom used in the computation of the reference solution.

Concerning the behavior of the non-linear solver, our test case is an example where the convergence of the Newton method highly depends on the initial guess. To compute the homogenized solution using only the linear solver (L-scheme) an average of 50 iterations are needed until the threshold $\|\delta(p_H^{n,(i)})\|_2$ decays below $1\text{E-}8$. To improve the linear solver a mixed strategy is adopted (see [23]). The target is to construct an initial solution that suits a non-problematic starting point for the Newton method. In this case we use the L-scheme until $\|\delta(p_H^{n,(i)})\|_2 < 1\text{E-}2$ and then the classical Newton method until one reaches $\|\delta(p_H^{n,(i)})\|_2 < 1\text{E-}8$. In Fig. 11 we show the convergence of the non-linear solver for five time steps using the L-scheme and the Newton method afterwards. An average of 3 iterations are needed for the L-scheme to reach the threshold $\|\delta(p_H^{n,(i)})\|_2 < 1\text{E-}2$.

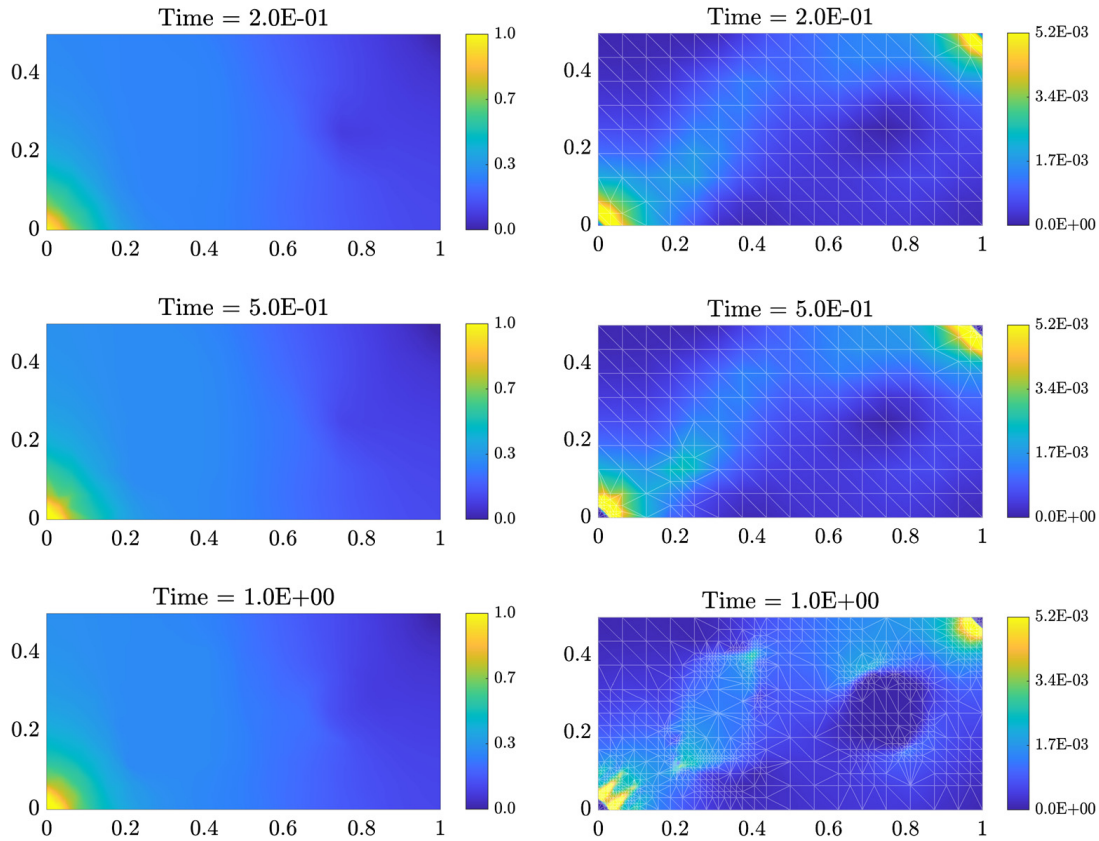


Fig. 10. The results when using adaptive homogenization at $t = 0.2$ (top), 0.5 (middle), 1 (bottom). The pressure p_{H_n} (left) and the magnitude of the velocity field $\|\mathbf{u}_{H_n}\|_2$ (right) are computed for $\Delta t = 0.1$ and by using $\Theta_r = 0.5$ and $\Theta_c = 1$.

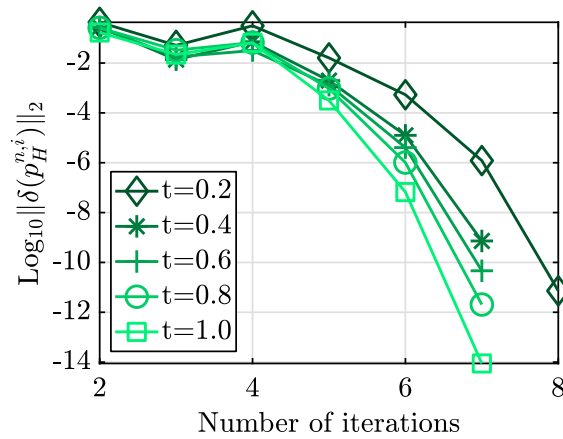


Fig. 11. The convergence of the non-linear solver. The results for five different times using the L-scheme until $\|\delta(p_H^{n,i})\|_2 < 1E-2$ and the Newton method afterwards.

6.1.2. The anisotropic case

One can also apply the adaptive homogenization strategy to anisotropic media. Consider the same macro-scale domain, the volumetric concentration, the initial and the boundary conditions as before. The anisotropic quasi-periodic permeability field is defined by

$$\mathbf{K}^\varepsilon(\mathbf{x}) = \kappa^\varepsilon(\mathbf{x}) \begin{pmatrix} \cos(\theta) & -\sin(\theta) \\ \sin(\theta) & \cos(\theta) \end{pmatrix} \begin{pmatrix} 1 & 0 \\ 0 & 1E-3 \end{pmatrix} \begin{pmatrix} \cos(\theta) & -\sin(\theta) \\ \sin(\theta) & \cos(\theta) \end{pmatrix}^{-1}$$

with $\kappa^\varepsilon(\mathbf{x})$ as in equation (9). Moreover $\kappa^\varepsilon(\mathbf{x}) = 1E-2$ in the sub-domain Ω_1 and $\kappa^\varepsilon(\mathbf{x}) = 1E-7$ in the sub-domain Ω_2 . We take the rotation angle $\theta = 30^\circ$.

In Fig. 12 we show the resulting permeability field when using $\Theta_c = 1$ and $\Theta_r = 0.3$. Fig. 13 shows the numerical solution of the upscaled problem \mathbf{PH}_n for the anisotropic test case.

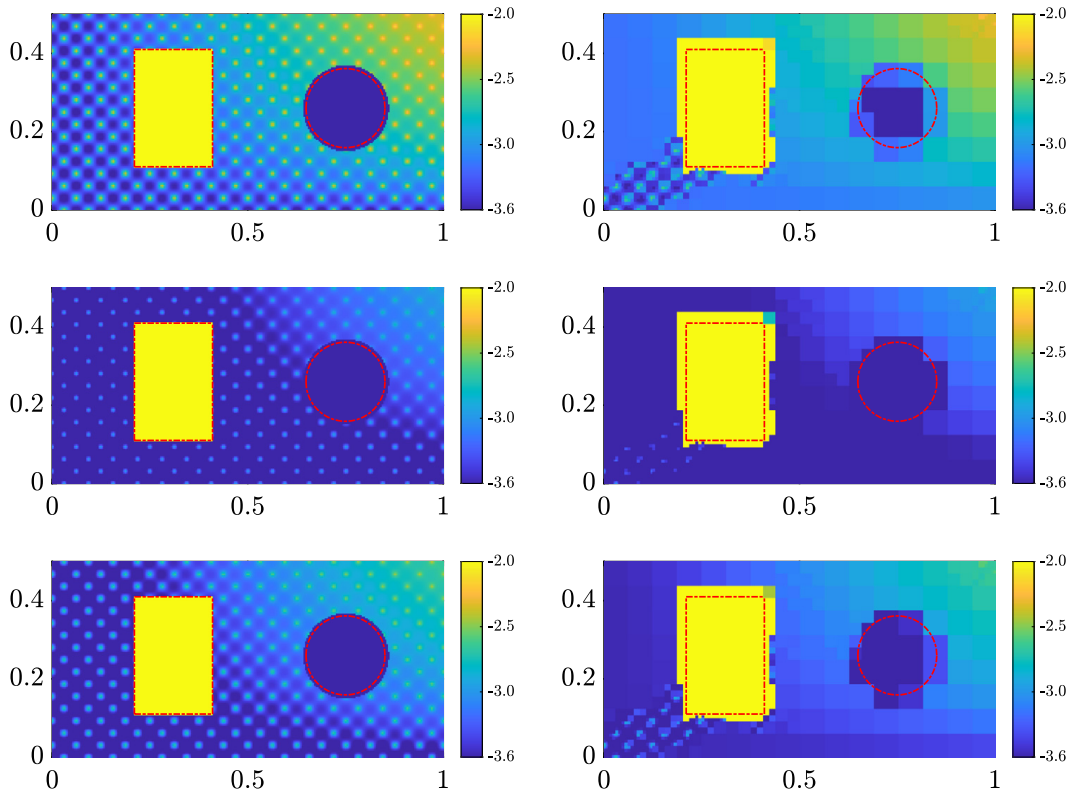


Fig. 12. The anisotropic permeability field (left) and the refined permeability (right) $\mathbf{K}_{1,1}^*$, $\mathbf{K}_{2,2}^*$ and $\mathbf{K}_{1,2}^* = \mathbf{K}_{2,1}^*$ (top to bottom) at $t = 1$ (Log_{10} scale) by using $\Theta_r = 0.3$ and $\Theta_c = 1$.

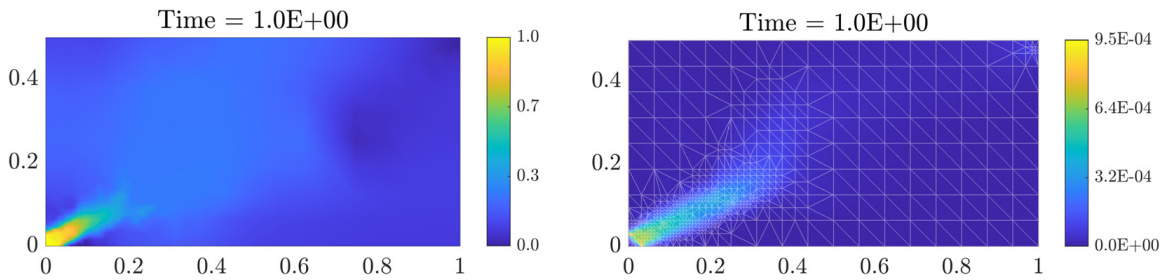


Fig. 13. The results when using adaptive homogenization at $t = 1$. The pressure p_{H_n} (left) and the magnitude of the velocity field $\|\mathbf{u}_{H_n}\|_2$ (right) by using $\Theta_r = 0.3$ and $\Theta_c = 1$.

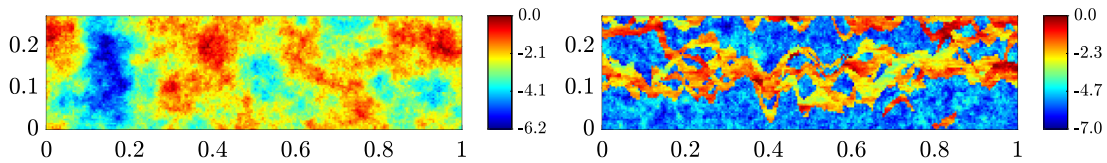


Fig. 14. The fine scale permeability distribution ($\mathbf{K}_{1,1}^e$) for the SPE10th-TopLayer (left) and SPE10th-38thLayer (right) of the SPE10th (Log_{10} scale).

The L^2 -error of the upscaled pressure p_H , calculated as in (10), is $E_p = 5.96\text{E-}2$ for the anisotropic case. Finally, we remark that the convergence of the non-linear solver is not affected by the anisotropy of the medium and remains as in Fig. 11.

6.2. The non-periodic case

Here we consider a highly heterogeneous and non-periodic medium. We utilize the data of the SPE Comparative Solution Projects [43]. This provides a vehicle for an independent comparison of methods and a recognized suite of test datasets for specific problems. We show simultaneously the results when using the isotropic permeability field \mathbf{K}^e defined by the top layer and the 38th-layer of the SPE10th data set (see Fig. 14).

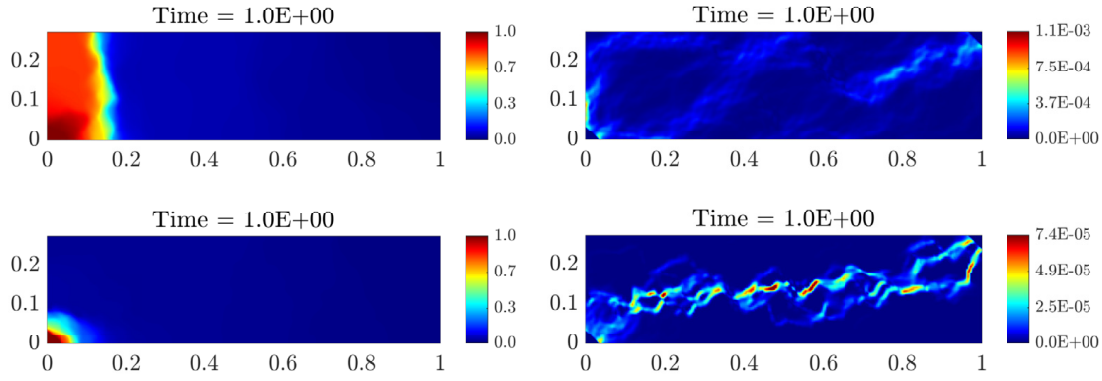


Fig. 15. The fine scale pressure p_h^ϵ (left) and (right) magnitude of the velocity field $\|\mathbf{u}_h^\epsilon\|_2$ for the SPE10th-TopLayer (top) and SPE10th-38thLayer (bottom).

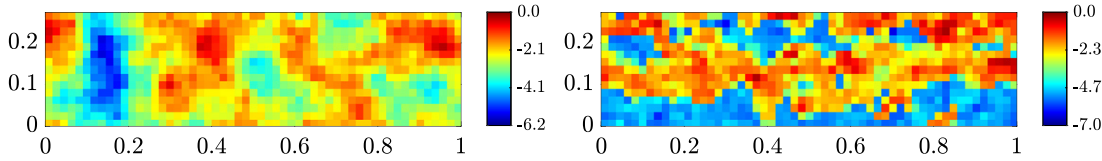


Fig. 16. The coarse-scale permeability distribution ($\mathbf{K}_{1,1}^*$) (Log_{10} scale) for the SPE10th-TopLayer (left) and SPE10th-38thLayer (right).

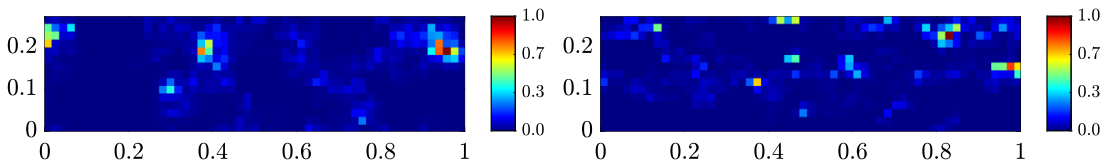


Fig. 17. The normalized difference between the coarse-scale effective permeabilities using homogenization vs harmonic average for the SPE10th-TopLayer (left) and SPE10th-38thLayer (right).

The macro-scale domain is a two-dimensional rectangle (see Fig. 14). We impose the pressure to be 1 and 0 in the upper-right and the lower-left corners, respectively and we use no-flow boundary conditions elsewhere. The volumetric concentration is $b^\epsilon(\mathbf{x}, p^\epsilon) = \mathcal{R} \cdot (p^\epsilon)^3$. Here \mathcal{R} is a non-dimensional constant and it is chosen to be $\mathcal{R} = 1\text{E-}4$ such that the dynamic behavior extends up to $T = 1$ and we choose $\Delta t = 0.1$. The parameter for the non-linear solver is $\mathcal{L} = 3\mathcal{R} \geq \max(3\mathcal{R} \cdot (p^\epsilon)^2)$.

To solve the problem (2) with the resolution of Fig. 14 we construct a grid with 26400 elements in a homogeneous triangular mesh \mathcal{T}_{h^ϵ} . In Fig. 15 we show the reference solution $(p_{h^\epsilon}, \mathbf{u}_{h^\epsilon})$ at the last time step.

Using a coarse grid of 55×15 squares we compute the first effective permeability field. This coarse grid corresponds to a macro-scale mesh with 1650 triangular elements, which is 6.25% of the number of elements used to compute the reference solution. In Fig. 16 we show the first component ($\mathbf{K}_{1,1}^*$) of the coarse-scale permeability fields.

When computing the solution of the problem \mathbf{PH}_n using the coarse-scale permeabilities displayed in Fig. 16 and without mesh adaptivity, the L^2 -error of the solution is $E_p = 5.956\text{E-}2$ for the top layer and $E_p = 6.227\text{E-}2$ for the 38th layer.

In Fig. 17 we show the difference between the effective permeabilities computed with homogenization and using the harmonic average. Such a strategy is used to calculate upscaled parameters, among others, in [44,45]. The difference between these strategies is higher in zones with high permeability. One can point out that the harmonic average underestimates the permeability. This is problematic because the high permeability regions are regions where one should increase the accuracy of the effective parameter in order to have better numerical solutions. When we compute the solution of the problem \mathbf{PH}_n using the coarse-scale permeabilities obtained by harmonic average and without mesh adaptivity the L^2 -error of the solution are $E_p = 7.542\text{E-}2$ and $E_p = 2.283\text{E-}1$ when using the SPE10th top layer and 38th layer, respectively.

In Table 3 and 4 we study the error when using different values of the parameters Θ_c and Θ_r for the dynamic mesh refinement. We remark that regardless of the choice of the coarsening parameter Θ_c the L^2 -error E_p (computed as in (10)) tends to decrease for smaller values of Θ_r . Nevertheless, due to the interplay of the parameters Θ_c and Θ_r one sees that for high values of the coarsening parameter the average number of elements does not change significantly and the difference in the errors is negligible. For these test cases and due to the choice of $b^\epsilon(\mathbf{x}, p^\epsilon)$, the refinement of the mesh plays a larger role in the error control compared to the coarsening process.

Using the adaptivity process we obtain a refined version of the permeability field. Fig. 18 shows the permeability fields after the mesh adaptivity when using $\Theta_r = 0.3$ and $\Theta_c = 5$.

Fig. 19 and 20 show the numerical solution of the upscaled problem \mathbf{PH}_n using the mesh adaptivity strategy described in Section 4.

Table 3

The adaptivity results for the SPE10th-TopLayer and different values of parameters Θ_c and Θ_r . #Elements indicates the average number of elements during the simulation.

$\Theta_c \backslash \Theta_r$		0.3	0.5	0.7
		1	#Elements	2176
	E_p	5.006E-2	5.146E-2	5.292E-2
5	#Elements	2110	1799	1723
	E_p	5.092E-2	5.393E-2	5.431E-2
10	#Elements	2051	1709	1716
	E_p	5.098E-2	5.460E-2	5.468E-2

Table 4

The adaptivity results for the SPE10th-38thLayer and different values of parameters Θ_c and Θ_r . #Elements indicates the average number of elements during the simulation.

$\Theta_c \backslash \Theta_r$		0.3	0.5	0.7
		1	#Elements	4088
	E_p	3.691E-2	4.398E-2	4.684E-2
5	#Elements	3586	2162	1873
	E_p	3.875E-2	4.549E-2	4.772E-2
10	#Elements	3603	2102	1793
	E_p	3.955E-2	4.821E-2	5.127E-2

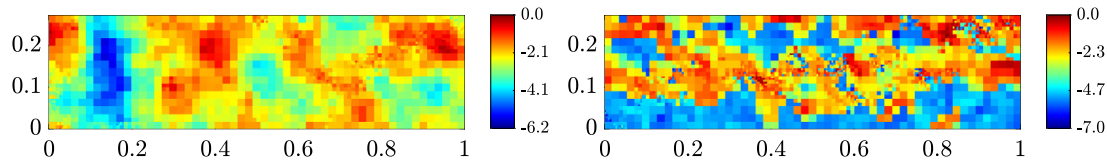


Fig. 18. The refined permeability field ($K_{1,1}^*$) at $t = 1$ (Log_{10} scale) for the SPE10th-TopLayer (left) and SPE10th-38thLayer (right) by using $\Theta_r = 0.3$ and $\Theta_c = 5$.

Notice that the results in Fig. 19 and 20 use respectively the 7.99% and 13.58% of the original degrees of freedom used in the reference solutions.

Finally, in Fig. 21 we show the convergence of the norm $\delta(p_H^{n,(i)})$ when one uses a combination of the L-scheme and Newton method. Here we use a mixed strategy (see [23]) to construct an initial solution that suits a non-problematic starting point for the Newton method. As in the previous example we use the L-scheme until $\|\delta(p_H^{n,(i)})\|_2 < 1E-2$ (typically 3 iterations) and then the classical Newton method until one reaches $\|\delta(p_H^{n,(i)})\|_2 < 1E-8$.

7. Conclusions

We have presented a numerical scheme based on homogenization to solve a non-linear parabolic equation defined in a heterogeneous porous medium. The discrete non-linear system is obtained by a backward Euler and the lowest order Raviart-Thomas mixed finite element discretization. Our approach proposes a local mesh adaptivity that leads to the computation of the effective parameters locally through decoupled cell problems. The mesh adaptivity is based on the idea that the upscaled parameters are updated only when necessary. Moreover, to illustrate the performance we have presented two general examples. First we considered a periodic case to show the history of convergence of the error when the scale separation tends to zero. Here we included an anisotropic case and also studied the effect of the anisotropic deviation caused by homogenization. Further we considered a non-periodic case based on a benchmark from the SPE10th project and we showed that the homogenization can be used also in more general non-periodic cases.

An advantage of this strategy is its flexibility. We showed in the numerical examples that the calculation of the effective parameters based on the solution of micro-cell problems is suitable also for non-periodic media. In all cases, the macro-scale problems are non-linear and to find the numerical solution we used a combined approach, in which a number of L-scheme iterations are used to provide a good starting point for the Newton scheme. This leads to a robust and efficient non-linear solver. Moreover, the convergence of the L-scheme is independent of the mesh and the discretization method.

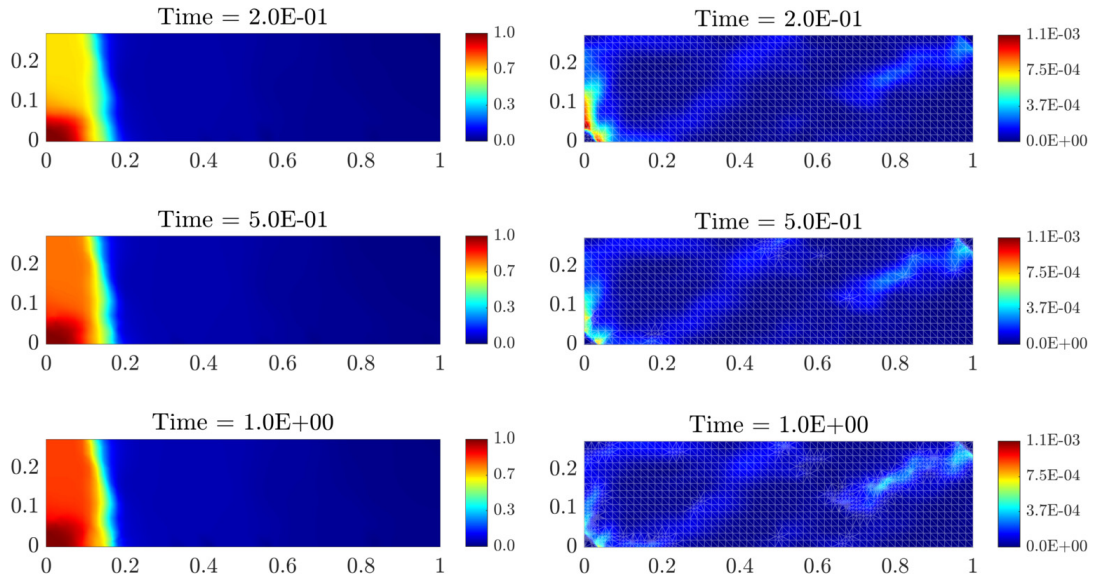


Fig. 19. The results of the adaptive homogenization for the SPE10th-TopLayer at $t = 0.2$ (top), 0.5 (middle), 1 (bottom). Pressure p_{H_n} (left) and magnitude of the velocity field $\|\mathbf{u}_{H_n}\|_2$ (right) are computed for $\Delta t = 0.1$ and by using $\Theta_r = 0.3$ and $\Theta_c = 5$.

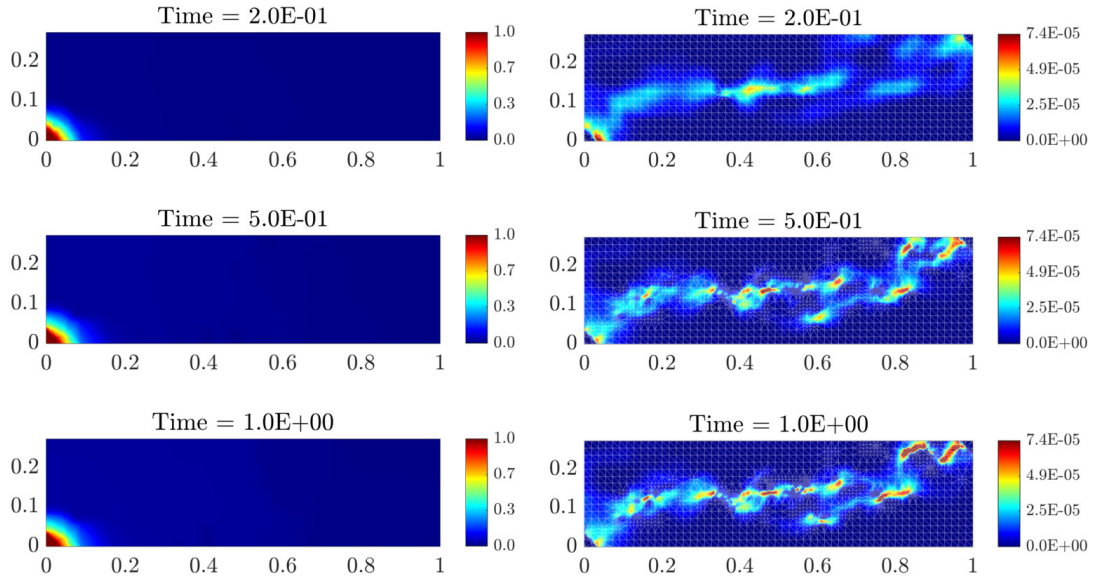


Fig. 20. The results of the adaptive homogenization for the SPE10th-38thLayer at $t = 0.2$ (top), 0.5 (middle), 1 (bottom). Pressure p_{H_n} (left) and magnitude of the velocity field $\|\mathbf{u}_{H_n}\|_2$ (right) are computed for $\Delta t = 0.1$ and by using $\Theta_r = 0.3$ and $\Theta_c = 5$.

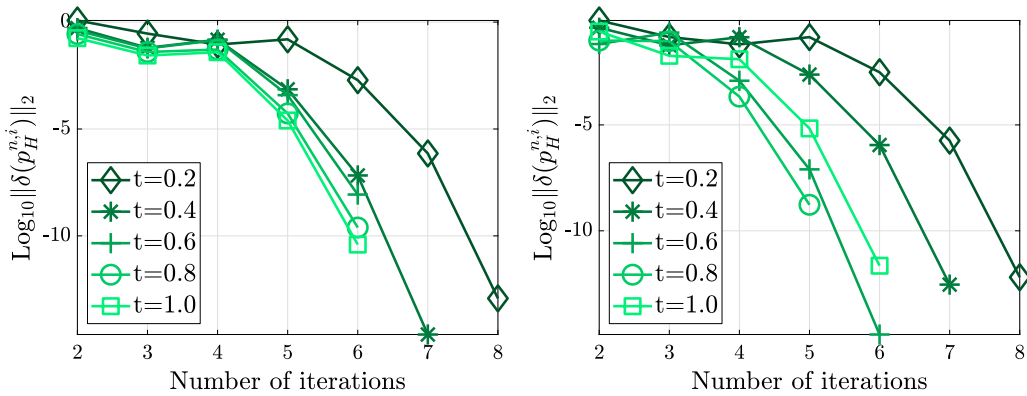


Fig. 21. The convergence of the non-linear solver for the SPE10th-TopLayer (left) and SPE10th-38thLayer (right). Results for five different times steps using the L-scheme until $\|\delta(p_H^{n,i})\|_2 < 1E-2$ and the Newton method afterwards.

Since the mesh adaptivity plays an important role in the multi-scale strategy, it is desirable that the changes in the mesh do not affect the converge of the non-linear solver.

We have studied the application of this adaptive homogenization technique to single-phase flow but the extension to other problems should be further investigated, e.g., the case of non-linear dependencies of the permeability tensor, or fractured media. By adapting the error indicator and the linearization scheme, we believe that this strategy can be applied to other models. This includes two-phase flow with or without capillary forces and complex micro-scale models, e.g., reactive transport with moving interfaces affecting the structure of the pore-scale geometry.

CRedit authorship contribution statement

Manuela Bastidas: Conceptualization, Software, Writing - original draft. **Carina Bringedal:** Methodology, Validation, Writing - review & editing. **Iuliu Sorin Pop:** Conceptualization, Funding acquisition, Methodology, Supervision, Writing - review & editing. **Florin Adrian Radu:** Conceptualization, Methodology, Writing - review & editing.

Declaration of competing interest

The authors declare that they have no known competing financial interests or personal relationships that could have appeared to influence the work reported in this paper.

Acknowledgements

The authors gratefully acknowledge financial support from the Research Foundation - Flanders (FWO) through the Odysseus programme (Project GOG1316N). In addition, we wish to thank Professor Mary F. Wheeler and Professor Ivan Yotov who made valuable suggestions or who have otherwise contributed to the ideas behind this manuscript. Part of this work was elaborated during the stay of the first author at the University of Bergen, supported by the Research Foundation - Flanders (FWO), through a travel grant for a short stay abroad. We thank the referees for their valuable comments that helped improving this work.

References

- [1] J. Bear, Y. Bachmat, Introduction to Modeling of Transport Phenomena in Porous Media, vol. 4, Springer Science & Business Media, 2012.
- [2] H. Hajibeygi, G. Bonfigli, M.A. Hesse, P. Jenny, Iterative multiscale finite-volume method, *J. Comput. Phys.* 227 (19) (2008) 8604–8621.
- [3] M. Cusini, C. van Kruijsdijk, H. Hajibeygi, Algebraic dynamic multilevel (ADM) method for fully implicit simulations of multiphase flow in porous media, *J. Comput. Phys.* 314 (2016) 60–79.
- [4] H. Hajibeygi, M.B. Olivares, M. HosseiniMehri, S. Pop, M. Wheeler, A benchmark study of the multiscale and homogenization methods for fully implicit multiphase flow simulations, *Adv. Water Resour.* 143 (2020) 103674.
- [5] W. E, B. Engquist, Z. Huang, Heterogeneous multiscale method: a general methodology for multiscale modeling, *Phys. Rev. B, Condens. Matter* 67 (9) (2003) 092101.
- [6] A. Abdulle, W. E, B. Engquist, E. Vanden-Eijnden, The heterogeneous multiscale method, *Acta Numer.* 21 (2012) 1–87.
- [7] U. Hornung, Homogenization and Porous Media, vol. 6, Springer Science & Business Media, 1997.
- [8] A. Abdulle, A. Nonnenmacher, A short and versatile finite element multiscale code for homogenization problems, *Comput. Methods Appl. Mech. Eng.* 198 (2009) 2839–2859.
- [9] A. Abdulle, A. Nonnenmacher, Adaptive finite element heterogeneous multiscale method for homogenization problems, *Comput. Methods Appl. Mech. Eng.* 200 (37–40) (2011) 2710–2726.
- [10] S. Chen, W. E, C.-W. Shu, The heterogeneous multiscale method based on the discontinuous Galerkin method for hyperbolic and parabolic problems, *Multiscale Model. Simul.* 3 (4) (2005) 871–894.
- [11] Y. Amanbek, G. Singh, M.F. Wheeler, H. van Duijn, Adaptive numerical homogenization for upscaling single phase flow and transport, *J. Comput. Phys.* 387 (2019) 117–133.
- [12] T. Arbogast, G. Pencheva, M.F. Wheeler, I. Yotov, A multiscale mortar mixed finite element method, *Multiscale Model. Simul.* 6 (1) (2007) 319–346.
- [13] J.A. Wheeler, M.F. Wheeler, I. Yotov, Enhanced velocity mixed finite element methods for flow in multiblock domains, *Comput. Geosci.* 6 (3–4) (2002) 315–332.
- [14] O. Møyner, K.-A. Lie, A multiscale restriction-smoothed basis method for high contrast porous media represented on unstructured grids, *J. Comput. Phys.* 304 (2016) 46–71.
- [15] G. Singh, Y. Amanbek, M.F. Wheeler, et al., Adaptive homogenization for upscaling heterogeneous porous medium, in: SPE Annual Technical Conference and Exhibition, Society of Petroleum Engineers, 2017.
- [16] F. Hellman, P. Henning, A. Malqvist, Multiscale mixed finite elements, arXiv preprint, arXiv:1501.05526, 2015.
- [17] P. Henning, M. Ohlberger, B. Schweizer, Adaptive heterogeneous multiscale methods for immiscible two-phase flow in porous media, *Comput. Geosci.* 19 (1) (2015) 99–114.
- [18] P. Henning, M. Ohlberger, B. Schweizer, An adaptive multiscale finite element method, *Multiscale Model. Simul.* 12 (3) (2014) 1078–1107.
- [19] L. Bergamaschi, M. Putti, Mixed finite elements and Newton-type linearizations for the solution of Richards' equation, *Int. J. Numer. Methods Eng.* 45 (8) (1999) 1025–1046.
- [20] M.A. Celia, E.T. Bouloutas, R.L. Zarba, A general mass-conservative numerical solution for the unsaturated flow equation, *Water Resour. Res.* 26 (7) (1990) 1483–1496.
- [21] I.S. Pop, F. Radu, P. Knabner, Mixed finite elements for the Richards' equation: linearization procedure, *J. Comput. Appl. Math.* 168 (1–2) (2004) 365–373.
- [22] F.A. Radu, K. Kumar, J.M. Nordbotten, I.S. Pop, A robust, mass conservative scheme for two-phase flow in porous media including Hölder continuous nonlinearities, *IMA J. Numer. Anal.* 38 (2) (2017) 884–920.
- [23] F. List, F.A. Radu, A study on iterative methods for solving Richards' equation, *Comput. Geosci.* 20 (2) (2016) 341–353.
- [24] H.W. Alt, S. Luckhaus, Quasilinear elliptic-parabolic differential equations, *Math. Z.* 183 (3) (1983) 311–341.

- [25] F.A. Radu, I.S. Pop, P. Knabner, Error estimates for a mixed finite element discretization of some degenerate parabolic equations, *Numer. Math.* 109 (2) (2008) 285–311.
- [26] F. Brezzi, M. Fortin, *Mixed and Hybrid Finite Element Methods*, vol. 15, Springer Science & Business Media, 2012.
- [27] D. Cioranescu, P. Donato, *An Introduction to Homogenization*, vol. 17, Oxford University Press, Oxford, 1999.
- [28] C. Carstensen, All first-order averaging techniques for a posteriori finite element error control on unstructured grids are efficient and reliable, *Math. Comput.* 73 (247) (2004) 1153–1165.
- [29] C. Carstensen, S.A. Funken, A posteriori error control in low-order finite element discretisations of incompressible stationary flow problems, *Math. Comput.* 70 (1999) 1353–1381.
- [30] C. Cancès, I. Pop, M. Vohralík, An a posteriori error estimate for vertex-centered finite volume discretizations of immiscible incompressible two-phase flow, *Math. Comput.* 83 (285) (2014) 153–188.
- [31] C. Carstensen, R. Hoppe, Error reduction and convergence for an adaptive mixed finite element method, *Math. Comput.* 75 (255) (2006) 1033–1042.
- [32] N. Golias, R. Dutton, Delaunay triangulation and 3D adaptive mesh generation, *Finite Elem. Anal. Des.* 25 (3) (1997) 331–341.
- [33] F.A. Radu, I.S. Pop, P. Knabner, Newton-type methods for the mixed finite element discretization of some degenerate parabolic equations, in: A.B. de Castro, D. Gómez, P. Quintela, P. Salgado (Eds.), *Numerical Mathematics and Advanced Applications*, Springer, Berlin, Heidelberg, 2006, pp. 1192–1200.
- [34] K. Brenner, C. Cancès, Improving Newton's method performance by parametrization: the case of the Richards equation, *SIAM J. Numer. Anal.* 55 (4) (2017) 1760–1785.
- [35] J.E. Jones, C.S. Woodward, Newton–Krylov-multigrid solvers for large-scale, highly heterogeneous, variably saturated flow problems, *Adv. Water Resour.* 24 (7) (2001) 763–774.
- [36] D.A. Knoll, D.E. Keyes, Jacobian-free Newton–Krylov methods: a survey of approaches and applications, *J. Comput. Phys.* 193 (2) (2004) 357–397.
- [37] X. Wang, H.A. Tchelepi, Trust-region based solver for nonlinear transport in heterogeneous porous media, *J. Comput. Phys.* 253 (2013) 114–137.
- [38] F.P. Hamon, B.T. Mallison, H.A. Tchelepi, Implicit hybrid upwinding for two-phase flow in heterogeneous porous media with buoyancy and capillarity, *Comput. Methods Appl. Mech. Eng.* 331 (2018) 701–727.
- [39] S. Lee, Y. Efendiev, Hybrid discretization of multi-phase flow in porous media in the presence of viscous, gravitational, and capillary forces, *Comput. Geosci.* 22 (5) (2018) 1403–1421.
- [40] R. Younis, H.A. Tchelepi, K. Aziz, et al., Adaptively localized continuation-Newton method–nonlinear solvers that converge all the time, *SPE J.* 15 (02) (2010) 526–544.
- [41] P. Jenny, H.A. Tchelepi, S.H. Lee, Unconditionally convergent nonlinear solver for hyperbolic conservation laws with s-shaped flux functions, *J. Comput. Phys.* 228 (20) (2009) 7497–7512.
- [42] M. Slodicka, A robust and efficient linearization scheme for doubly nonlinear and degenerate parabolic problems arising in flow in porous media, *SIAM J. Sci. Comput.* 23 (5) (2002) 1593–1614.
- [43] M.A. Christie, M.J. Blunt, *Tenth SPE Comparative Solution Project: A Comparison of Upscaling Techniques*, Society of Petroleum Engineers, 2001.
- [44] P. Renard, G. De Marsily, Calculating equivalent permeability: a review, *Adv. Water Resour.* 20 (5–6) (1997) 253–278.
- [45] K.-A. Lie, *An Introduction to Reservoir Simulation Using MATLAB/GNU Octave: User Guide for the MATLAB Reservoir Simulation Toolbox (MRST)*, Cambridge University Press, 2019.

3 Effective heat transport in thin porous media

The content of this chapter is based on the following original article:

L. Scholz and C. Bringedal. *A Three-Dimensional Homogenization Approach for Effective Heat Transport in Thin Porous Media*. *Transport in Porous Media* 141.3 (2022), pp. 737–769. doi: 10.1007/s11242-022-01746-y.

This publication is an open access article and distributed under the Creative Commons CC BY license.



A Three-Dimensional Homogenization Approach for Effective Heat Transport in Thin Porous Media

Lena Scholz¹ · Carina Bringedal¹

Received: 14 June 2021 / Accepted: 13 January 2022
© The Author(s) 2022

Abstract

Heat transport through a porous medium depends on the local pore geometry and on the heat conductivities of the solid and the saturating fluid. Through upscaling using formal homogenization, the local pore geometry can be accounted for to derive effective heat conductivities to be used at the Darcy scale. We here consider thin porous media, where not only the local pore geometry plays a role for determining the effective heat conductivity, but also the boundary conditions applied at the top and the bottom of the porous medium. Assuming scale separation and using two-scale asymptotic expansions, we derive cell problems determining the effective heat conductivity, which incorporates also the effect of the boundary conditions. Through solving the cell problems, we show how the local grain shape, and in particular its surface area at the top and bottom boundary, affects the effective heat conductivity through the thin porous medium.

Keywords Upscaling · Heat transport · Thin porous media

1 Introduction

Heat conduction in porous media is a relevant process in applications ranging from geothermal engineering to various technical applications. Especially in the latter field, many porous components have a thin shape (see, e.g., Belgacem et al. 2016, Michaud 2016), where filters, fuel cells and membranes count among typical examples. A thin porous layer is often part of composite materials (see, e.g., Asbik et al. 2006). For a porous medium where grains and the saturating fluid are under local thermal equilibrium, the effective heat conductivity of the porous medium characterizes the medium's ability to transport heat via conduction. A better understanding of the heat transport in porous media, in particular finding the medium's effective heat conductivity, can help to not only predict the heat transport in a certain setup, but also to design porous materials according to the needs of industrial applications. In this context, the detailed properties of the considered porous medium are necessary to investigate (see, e.g., Ranut and Nobile 2014).

✉ Carina Bringedal
carina.bringedal@iws.uni-stuttgart.de

¹ Institute of Modelling Hydraulic and Environmental Systems, University of Stuttgart, Pfaffenwaldring 5a, 70569 Stuttgart, Germany

When investigating heat transport in porous media, completely pore-scale resolved models (see, e.g., Koch et al. 2021) are often not feasible for large domains due to their computational complexity. Because of that, we will determine the effective heat conductivity of the porous medium at the Darcy scale. While simple approaches like a porosity-weighted averaging are suitable to approximate the effective heat conductivity of layered media, as shown in Bringedal and Kumar (2017), they are not applicable to more complex pore structures as also the pore and grain shapes themselves, for example through surface area, affect the effective heat conductivity. We aim at capturing pore-scale effects by incorporating them into a model at the Darcy scale. This is done by deriving the effective heat conductivity. Two of the most common approaches are the method of volume averaging, and the theory of homogenization. When using volume averaging, effective quantities are obtained based on closure relations (Whitaker 1999). Applications to heat transport in porous media can be found in Hsu (1999) and Quintard et al. (1997). However, in the present work we consider the approach of formal homogenization to obtain effective heat conductivities (Auriault et al. 2009; Hornung 1997). Formal homogenization allows to derive upscaled equations and corresponding effective quantities following suitable assumptions. Within this framework, the effective properties of the porous medium are obtained by solving so-called cell problems at the pore scale. If a porous medium exhibits local periodicity in its structure, we can obtain accurate results for general grain shapes using the theory of homogenization (Auriault 1983). Then, representative sections of the porous medium need to be considered at the pore scale and are the basis for deriving upscaled equations with corresponding effective quantities.

In the following, thin porous media are considered. With a thin porous medium, we mean a porous medium where the thickness of the porous medium is of the same order of magnitude as the length of a representative elementary volume at the pore scale. This corresponds to the proportionally thin porous medium (PTPM) considered in Fabricius et al. (2016). Note that different types of thin porous media are also discussed in that paper, in the context of fluid flow. For thin porous media, the boundary conditions applied at the top and bottom boundaries will have an influence on the overall effective behavior and hence on the effective quantities of the porous medium.

The presence of thin layers embedded in a surrounding porous medium and their effect on effective quantities have been analyzed by homogenization in the context of diffusion–reaction systems (Bhattacharya et al. 2020; Gahn et al. 2021, 2017, 2018; Neuss-Radu and Jäger 2007) and for unsaturated flow (Kumar et al. 2020; List et al. 2020). In these works, the focus has been in particular on transmission conditions across the thin layer and the interaction with the surrounding porous medium as the width of the layer approaches zero. Homogenization techniques can also be applied to free-standing thin structures. By considering a thin strip as a simplified representation of a porous medium, effective equations have been found by combining asymptotic expansions and transversal averaging for reactive transport (van Noorden 2009), heat transport (Bringedal et al. 2015), biofilm growth (van Noorden et al. 2010) and two-phase flow (Lunowa et al. 2021; Sharmin et al. 2020). However, in these works the thin strip is in practice a channel and does not contain a porous structure. On the other hand, when considering a thin porous medium, both the porous structure as well as the boundary conditions at top and bottom boundaries influence the effective behavior.

Much work has been done considering flow in thin porous media. Laminar as well as turbulent single-phase flow in thin porous media have been investigated for example in Chen and Papathanasiou (2008), Fabricius et al. (2016), Hellström et al. (2010), Koch and Ladd (1997) and Wagner et al. (2021). A benchmark comparison for a homogenization-based

approach applied to flow through thin porous media in Wagner et al. (2021) shows a good agreement between the results of three-dimensional homogenization and pore-scale resolved models as well as experimental findings. In this paper, we extend the formal homogenization approach applied to fluid flow in thin porous media in Fabricius et al. (2016) by incorporating heat transport and focus in particular on the role of the arising effective heat conductivity.

This work is also related to Bringedal and Kumar (2017), which takes a similar approach to investigate the influence of chemical reactions on effective heat conductivities in two-dimensional periodic porous media. In Bringedal and Kumar (2017), the focus is, however, on the impact of the evolving pore structure on the effective quantities. Here, we will not explicitly account for reactive transport and subsequent evolving pore geometries, but we will investigate the effect of different grain shapes and sizes. Moreover, we consider a fully three-dimensional approach. As a consequence, since the porous medium is thin, the type of boundary conditions applied in the third spatial dimension will impact the results. Although we will not explicitly account for any evolution of the grains in this paper, the resulting models for effective heat conductivity found in this paper would under suitable assumptions be the same if allowing the grains to evolve, and complementing the model by an appropriate evolution equation. As shown in Bringedal et al. (2016), the influence of the evolving grains appears in the derived Darcy-scale model, while the effective quantities only depend on the grain shape at a given time (Bringedal et al. 2016; Bringedal and Kumar 2017). Hence, extensions to porous media evolving due to mineral precipitation and dissolution reactions can be formulated and included in the upscaling procedure by considering, e.g., a level-set formulation as in Bringedal et al. (2016).

In the following, we first introduce the model formulation for a thin, periodic porous medium in Sect. 2. The two-scale asymptotic expansions of the formal homogenization approach are introduced in Sect. 3. In Sect. 4, we obtain the respective cell problems at the pore scale. Upscaled equations valid at the Darcy scale are derived in Sect. 5. The Darcy-scale equations rely on effective quantities, which are found through solving the corresponding cell problem. We continue with a discussion on the impact of different boundary conditions and grain shapes on the derived effective heat conductivity as well as the impact of the upscaling procedure itself in Sect. 6, before we end with some concluding remarks.

2 Model Formulation

2.1 Structure of Porous Medium

The modeled porous medium Ω^ε consists of void space Ω_f^ε that is occupied by fluid, and grain space Ω_g^ε such that $\Omega^\varepsilon = \Omega_f^\varepsilon \cup \Omega_g^\varepsilon \cup S_\Omega^\varepsilon$, where S_Ω^ε denotes the internal boundaries between void and grain space. The porous medium Ω^ε is characterized by a coordinate system (x_1, x_2, z) , and we assume that $x_1, x_2 \in [0, L]$ and $z \in [0, H]$, with $H \ll L$ since we are dealing with a proportionally thin porous medium. We introduce the parameter

$$\varepsilon = \frac{l}{L} \ll 1$$

to separate Darcy and pore scale. The quantity l describes the horizontal extent of the chosen pore-scale reference domain and defines the length size of the pore scale. Hence, we

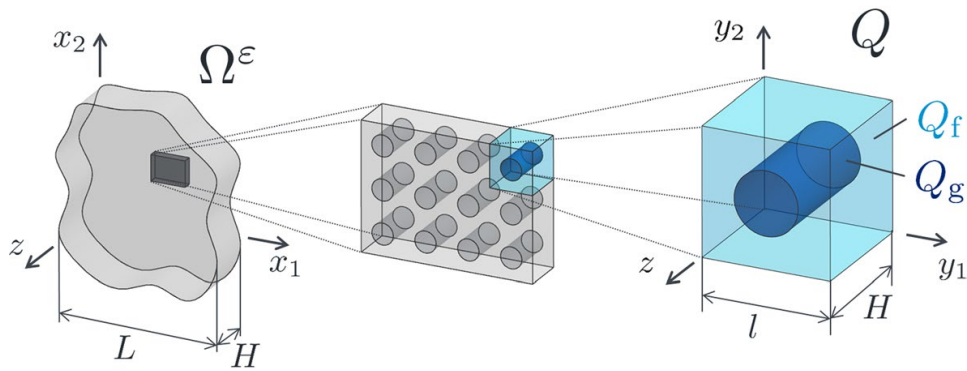


Fig. 1 Darcy and pore scale with cell Q . Note that we consider the z -direction as the *vertical* direction, but is for simplicity depicted as pointing out of the paper in figure

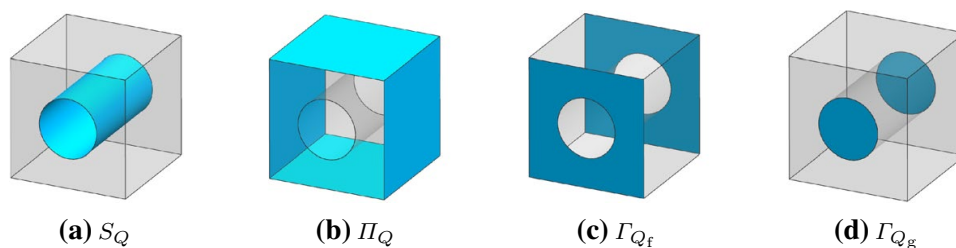


Fig. 2 Surfaces of the pore-scale cell Q

can model the periodically oscillating domain at the pore scale by introducing the local variable

$$\mathbf{y} = \frac{1}{\varepsilon} \mathbf{x}.$$

For a given point $(\mathbf{x}, z) \in \Omega^\varepsilon$, we then have $(\mathbf{y}, z) \in Q := [0, l]^2 \times [0, H]$. We use the superscript ε to stress that the domain Ω^ε contains highly oscillatory structures.

A so-called cell Q , as shown in Fig. 1, consists of void space Q_f , which is occupied by fluid, and grain space Q_g . The internal surface between Q_f and Q_g is denoted with S_Q . Furthermore, we introduce Π_Q for the internal sidewalls as well as Γ_Q for top and bottom of the cell as visualized in Fig. 2. We have that $\Gamma_Q = \Gamma_{Q_f} \cup \Gamma_{Q_g}$, where Γ_{Q_f} and Γ_{Q_g} are the fluid and grain part of the top and bottom surfaces, respectively. Hence, we define the boundary of the void space as $\partial Q_f = \Gamma_{Q_f} \cup S_Q \cup \Pi_Q$ and of the grain space as $\partial Q_g = \Gamma_{Q_g} \cup S_Q$. For simplicity, we here assume that the internal sidewalls Π_Q are occupied by fluid, but allowing grains to touch these sidewalls represents no practical difference for the presented model as long the void space remains connected. Note that S_{Q_f} and S_{Q_g} indicate the same surface but with opposite orientation. Altogether, we have the surface of the whole cell to be given as $\partial Q = \Gamma_Q \cup \Pi_Q$. We consider Q to be a zoomed-in view for a given \mathbf{x} and in Sect. 3 we assume that functions defined on Q are periodic in \mathbf{y} . Hence, Ω^ε is built up through several cells Q . Note that these cells do not need to be identical as, e.g., grain shape could vary, but all cells follow the structure as described above. Different grain shapes correspond to the pore-scale geometry varying with \mathbf{x} . However, since we will rely on local periodicity in \mathbf{y} , two nearby-lying cells Q should not be too different from each other.

The whole porous medium Ω^ε is defined as the union of all pore-scale cells Q , meaning $\Omega^\varepsilon = \bigcup Q$. Accordingly, we obtain $\Omega_f^\varepsilon = \bigcup Q_f$ and $\Omega_g^\varepsilon = \bigcup Q_g$. Similarly, the union of all boundaries is defined by $\Gamma_{\Omega_f}^\varepsilon = \bigcup \Gamma_{Q_f}^\varepsilon$, $\Gamma_{\Omega_g}^\varepsilon = \bigcup \Gamma_{Q_g}^\varepsilon$ and $S_\Omega^\varepsilon = \bigcup S_Q$.

2.2 Equation Set and Boundary Conditions

To model fluid flow and heat transport on the pore scale of the porous medium, we formulate corresponding conservation equations and boundary conditions. We consider the conservation of mass and the conservation of momentum by using the Stokes equations

$$\partial_t \rho_f + \nabla \cdot (\rho_f \mathbf{u}) = 0 \quad \text{in } \Omega_f^\varepsilon, \tag{1}$$

$$\nabla p = \nabla \cdot (\nu \nabla \mathbf{u}) \quad \text{in } \Omega_f^\varepsilon, \tag{2}$$

where $\rho_f(T_f)$ denotes the density of the fluid, \mathbf{u} the velocity, p the pressure and $\nu(T_f)$ the viscosity of the fluid. The fluid density and viscosity are assumed to depend smoothly on fluid temperature. We use here the Stokes equations instead of the more general Navier–Stokes equations as we in the upscaling only consider the creeping flow regime to be in the range of Darcy’s law. However, with suitable assumptions on the Reynolds number, Darcy’s law can also be derived from the Navier–Stokes equations (see, e.g., Bringedal et al. 2016).

To describe the conservation of energy in the system, we consider a simplified system. Since we are considering creeping flow in a porous medium, fluid velocities will generally be low. Further, we consider temperature ranges such that no phase change occurs. In this case, energy conservation can be formulated in terms of temperature (Landau and Lifshitz 1987). We introduce the two temperatures T_f defined in the void space Ω_f^ε , and T_g defined in the grain space Ω_g^ε . In the fluid, heat transport is due to advection and conduction, while any internal heat production due to friction is neglected. The heat transport in the grain space only occurs through conduction:

$$\partial_t (\rho_f c_f T_f) = \nabla \cdot (k_f \nabla T_f - \rho_f c_f \mathbf{u} T_f) \quad \text{in } \Omega_f^\varepsilon, \tag{3}$$

$$\partial_t (\rho_g c_g T_g) = \nabla \cdot (k_g \nabla T_g) \quad \text{in } \Omega_g^\varepsilon. \tag{4}$$

The quantities k_f and k_g denote the heat conductivities of the fluid and the grain, whereas c_f and c_g are the specific heats. They are all assumed to be material constants. Finally, $\rho_g(T_g)$ is the density of the grain, which is assumed to depend smoothly on the grain temperature. Note that the equations (1–4) are strongly coupled as the fluid flow and temperatures jointly affect each other through the advective term, and since the densities and viscosity are temperature dependent.

Note that although we here consider relatively simple energy equations (3), (4), extending the model by including, e.g., temperature-dependent specific heats in the upscaling is straightforward as long as they depend smoothly on temperature. However, due to the special role of heat conduction, allowing the heat conductivities to depend on temperature would affect the upscaling procedure as higher-order effects for this process play a role. Hence, we are limited to consider moderate temperature ranges and fluids and solids such that the assumptions behind (3), (4) remain valid.

To close the model, boundary conditions at all boundaries as well as initial conditions for the variables are needed. Since the upscaling only depends on boundary conditions on $\Gamma_\Omega^\varepsilon$ and S_Ω^ε , only these will be specified in the following. Regarding the flow, we assume no-slip

boundary conditions on the grain surface and on the top and bottom boundaries of the porous medium:

$$\mathbf{u} = \mathbf{0} \quad \text{on } \Gamma_{\Omega_f}^\varepsilon \cup S_{\Omega}^\varepsilon. \quad (5)$$

No-slip conditions are commonly used for porous-media flows and ensure that the fluid flow remains in the creeping regime. For completeness, we mention that extensions with slip also exist (Lasseux and Valdés-Parada 2017; Lunowa et al. 2021). The impact of Neumann as well as Dirichlet boundary conditions on the top and bottom boundaries of the domain for the energy conservation will be considered:

$$k_f \nabla T_f \cdot \mathbf{e}_z = \psi(\mathbf{x}, t) \quad \text{on } \Gamma_{\Omega_f}^\varepsilon \quad (6a)$$

$$\text{or } T_f = \theta(\mathbf{x}, t) \quad \text{on } \Gamma_{\Omega_f}^\varepsilon, \quad (6b)$$

$$k_g \nabla T_g \cdot \mathbf{e}_z = \psi(\mathbf{x}, t) \quad \text{on } \Gamma_{\Omega_g}^\varepsilon \quad (7a)$$

$$\text{or } T_g = \theta(\mathbf{x}, t) \quad \text{on } \Gamma_{\Omega_g}^\varepsilon. \quad (7b)$$

Hence, we will use either (6a) and (7a), or (6b) and (7b). Here, \mathbf{e}_z denotes the basis vector in z -direction. Further, we have introduced the heat flux ψ and the temperature θ that are specified on top and bottom boundaries of the cell Q . The Neumann boundary conditions correspond to an applied heat flux ψ at the top and bottom boundaries. Applying Dirichlet boundary conditions corresponds to assuming that the top and bottom boundaries are perfectly heat conducting and hence adopts the applied temperature θ imposed here. These two types of boundary conditions represent the two complementary cases of the top and bottom boundaries either transmitting a given heat flux or being perfectly heat conducting. Combinations of these two cases can be formulated through Robin boundary conditions, but are outside the scope of this work. Note that the heat flux ψ or the temperature θ could themselves come from a heat transport model for an adjacent medium, which is why they could in the general case vary with time and space. We are interested in how the two different types of coupling to the thin porous medium affect the heat transport. Note that the boundary conditions are for consistency assumed to be the same on the top and bottom boundaries. Furthermore, they are assumed to not depend on the local variable \mathbf{y} , meaning that they cannot be highly oscillating in space. We also assume that they are not highly oscillating with time. The latter two assumptions are needed to enable a separation of scales when upscaling the model.

On the interface between fluid and grain, we assume local thermodynamic equilibrium:

$$T_f = T_g \quad \text{on } S_{\Omega}^\varepsilon, \quad (8)$$

which is a reasonable assumption in the creeping flow regime. Alternatively one can apply a contact conductivity model, and we refer to Auriault et al. (2009)[Chapter 4.3] for the influence of such boundary conditions. To conserve the energy, the heat flux from fluid to grain is the same as from grain to fluid:

$$\mathbf{n} \cdot (k_f \nabla T_f) = \mathbf{n} \cdot (k_g \nabla T_g) \quad \text{on } S_{\Omega}^\varepsilon, \quad (9)$$

where \mathbf{n} denotes the normal vector on S_{Ω}^ε .

2.3 Non-Dimensionalization

The equations and boundary conditions (1) - (9) are non-dimensionalized by introducing the following reference quantities to define non-dimensional variables and quantities:

$$\begin{aligned}
 \tilde{x} &= \frac{x}{L}, & \tilde{\rho}_f &= \frac{\rho_f}{\rho_{\text{ref}}}, & \tilde{v} &= \frac{v}{v_{\text{ref}}}, \\
 \tilde{y} &= \frac{y}{l}, & \tilde{\rho}_g &= \frac{\rho_g}{\rho_{\text{ref}}}, & \tilde{T}_f &= \frac{T_f}{T_{\text{ref}}}, \\
 \tilde{z} &= \frac{z}{l}, & \tilde{u} &= \frac{u}{u_{\text{ref}}}, & \tilde{T}_g &= \frac{T_g}{T_{\text{ref}}}, \\
 \tilde{t} &= \frac{t}{t_{\text{ref}}}, & \tilde{p} &= \frac{p}{p_{\text{ref}}}, & &
 \end{aligned} \tag{10}$$

Since we consider thin porous media, we assume that H , which is the length of the domain in z -direction, is of the same order as the length l of the previously defined cell. This leads to $\tilde{H} := H/l = O(\epsilon^0)$, where the non-dimensional height \tilde{H} does not depend on ϵ . We use the horizontal length scale l to non-dimensionalize the vertical direction to emphasize their same order in size. Our assumption corresponds to the case 'Proportionally Thin Porous Medium' introduced in Fabricius et al. (2016). The non-dimensionalization of the spatial variables in (10) allows us to introduce the non-dimensional domains $\tilde{Q} = \{(\tilde{y}_1, \tilde{y}_2, \tilde{z}) : \tilde{y} \in [0, 1]^2, \tilde{z} \in [0, \tilde{H}]\}$ and $\tilde{\Omega}^\epsilon \subset \{(\tilde{x}_1, \tilde{x}_2, \tilde{z}) : \tilde{x} \in [0, 1]^2, \tilde{z} \in [0, \tilde{H}]\}$. Due to the different scalings used for \tilde{x} and \tilde{y} , both pore-scale and Darcy-scale domains appear as unit sized domains. Note that $\tilde{\nabla}$ denotes the non-dimensionalized nabla operator in the following.

By inserting the non-dimensionalized definitions (10), all model equations and boundary conditions can be rewritten in terms of non-dimensional variables and characteristic non-dimensional numbers. From dimensional analysis, we expect 5 independent non-dimensional numbers in addition to the length scale ratio ϵ . These 5 non-dimensional numbers are described and chosen below. The conservation of mass (1) and momentum (2) result in

$$\partial_{\tilde{t}} \tilde{\rho}_f + \tilde{\nabla} \cdot (\tilde{u} \tilde{\rho}_f) = 0 \quad \text{in } \tilde{\Omega}_f^\epsilon, \tag{11}$$

$$\text{ReEu} \tilde{\nabla} \tilde{p} = \tilde{\nabla} \cdot (\tilde{v} \tilde{\nabla} \tilde{u}) \quad \text{in } \tilde{\Omega}_f^\epsilon, \tag{12}$$

where we have introduced the Euler number $\text{Eu} = p_{\text{ref}}/u_{\text{ref}}^2 \rho_{\text{ref}}$ and the Reynolds number $\text{Re} = \rho_{\text{ref}} u_{\text{ref}} L / \nu_{\text{ref}}$. Note that for the mass conservation equation we have assumed that the reference time t_{ref} is equal to the advective time scale; $t_{\text{ref}} = L/u_{\text{ref}}$, which corresponds to choosing one non-dimensional number ($t_{\text{ref}} u_{\text{ref}} / L = 1$). Since we use Stokes equations, it is implicitly assumed that the Reynolds number is small. In order to ensure that we are in the creeping flow regime where Darcy's law is valid, we assume $\text{ReEu} = O(\epsilon^{-2})$. Hence, we write $\text{ReEu} = k_{\text{flow}} \epsilon^{-2}$, where k_{flow} is a non-dimensional constant not depending on ϵ .

The equations describing the heat transport in the void (3) as well as the grain space (4) are rewritten in the following way

$$\partial_{\tilde{t}} (\tilde{\rho}_f \tilde{T}_f) = \tilde{\nabla} \cdot (\kappa_f \tilde{\nabla} \tilde{T}_f - \tilde{\rho}_f \tilde{u} \tilde{T}_f) \quad \text{in } \tilde{\Omega}_f^\epsilon, \tag{13}$$

$$\partial_{\tilde{t}}(\tilde{\rho}_g \tilde{T}_g) = \tilde{\nabla} \cdot (\kappa_g \tilde{\nabla} \tilde{T}_g) \quad \text{in } \tilde{\Omega}_g^\varepsilon, \quad (14)$$

with $\kappa_f = k_f / Lu_{\text{ref}} \rho_{\text{ref}} c_f = 1 / \text{Pe}_f$ and $\kappa_g = k_g / Lu_{\text{ref}} \rho_{\text{ref}} c_g = 1 / \text{Pe}_g$. Here, Pe_f and Pe_g are the thermal Péclet numbers for fluid and grain, and hence, our last two independent non-dimensional numbers. We assume $\text{Pe}_f, \text{Pe}_g = O(\varepsilon^0)$, which means that the time scales for heat conduction and heat advection are the same. Our assumption implies that heat transport by conduction and advection are equally important at the macroscopic scale, and both will appear in the resulting upscaled model. Different assumptions on the Péclet number would lead to either only conduction (low Péclet number) or only advection (high Péclet number) to be dominating at the macro-scale. Note that our assumption also implies that the ratio between k_f and c_f has to be the same order of magnitude as the ratio between k_g and c_g . For the influence of large differences between the heat conductivities, we refer to Auriault et al. (2009)[Chapter 4.2]. In the following, we denote with κ_f and κ_g the non-dimensional heat conductivities of fluid and grain, respectively.

The non-dimensionalized boundary conditions are:

$$\tilde{\mathbf{u}} = \mathbf{0} \quad \text{on } \tilde{\Gamma}_{\Omega_f}^\varepsilon \cup \tilde{S}_{\Omega}^\varepsilon, \quad (15)$$

$$\tilde{T}_f = \tilde{T}_g \quad \text{on } \tilde{S}_{\Omega}^\varepsilon, \quad (16)$$

$$\kappa_f \tilde{\nabla} \tilde{T}_f = \kappa_g \tilde{\nabla} \tilde{T}_g \quad \text{on } \tilde{S}_{\Omega}^\varepsilon, \quad (17)$$

$$\kappa_f \tilde{\nabla} \tilde{T}_f \cdot \mathbf{e}_{\tilde{z}} = \tilde{\psi} \quad \text{on } \tilde{\Gamma}_{\Omega_f}^\varepsilon, \quad (18a)$$

$$\text{or } \tilde{T}_f = \tilde{\theta} \quad \text{on } \tilde{\Gamma}_{\Omega_f}^\varepsilon, \quad (18b)$$

$$\kappa_g \tilde{\nabla} \tilde{T}_g \cdot \mathbf{e}_{\tilde{z}} = \tilde{\psi} \quad \text{on } \tilde{\Gamma}_{\Omega_g}^\varepsilon, \quad (19a)$$

$$\text{or } \tilde{T}_g = \tilde{\theta} \quad \text{on } \tilde{\Gamma}_{\Omega_g}^\varepsilon. \quad (19b)$$

Note that we have introduced $\tilde{\psi} = \psi / u_{\text{ref}} \rho_{\text{ref}} c_f T_{\text{ref}}$ and $\tilde{\theta} = \theta / T_{\text{ref}}$. Since we will only consider the non-dimensional variables in the following, we skip the tilde.

3 Two-Scale Asymptotic Expansions

To incorporate the dependence on the local variable \mathbf{y} , we introduce two-scale asymptotic expansions for the velocity, the pressure as well as the temperatures in the fluid and the grain. For $\varphi \in \{\mathbf{u}, p, T_f, T_g\}$ we assume

$$\varphi(\mathbf{x}, z, t) = \varphi_0(\mathbf{x}, \mathbf{y}, z, t) + \varepsilon \varphi_1(\mathbf{x}, \mathbf{y}, z, t) + \varepsilon^2 \varphi_2(\mathbf{x}, \mathbf{y}, z, t) + \dots$$

We hence have that these functions φ_i are periodic in \mathbf{y} , meaning that

$$\varphi_i(\mathbf{x}, (y_1, y_2), z, t) = \varphi_i(\mathbf{x}, (y_1 + 1, y_2), z, t) = \varphi_i(\mathbf{x}, (y_1, y_2 + 1), z, t)$$

for all $(y_1, y_2, z) \in Q$. Due to the difference in scaling for \mathbf{x} , \mathbf{y} and z , the non-dimensional nabla operator is

$$\nabla[\cdot] = \nabla_x[\cdot] + \frac{1}{\varepsilon} \nabla_y[\cdot] + \frac{1}{\varepsilon} \nabla_z[\cdot]$$

where

$$\begin{aligned} \nabla_x &= (\partial_{x_1}, \partial_{x_2}, 0)^T, \\ \nabla_y &= (\partial_{y_1}, \partial_{y_2}, 0)^T, \\ \nabla_z &= (0, 0, \partial_z)^T. \end{aligned}$$

For the non-dimensional Laplace operator $\Delta[\cdot] = \nabla \cdot \nabla[\cdot]$, we introduce

$$\begin{aligned} \Delta_x &= \partial_{x_1}^2 + \partial_{x_2}^2, \\ \Delta_y &= \partial_{y_1}^2 + \partial_{y_2}^2, \\ \Delta_z &= \partial_z^2. \end{aligned}$$

Furthermore, we introduce for convenience the short-hand notation

$$\begin{aligned} \nabla_{y+z} &:= \nabla_y + \nabla_z, \\ \Delta_{y+z} &:= \Delta_y + \Delta_z. \end{aligned}$$

Recall that the densities and the viscosity are assumed to depend smoothly on the temperature. By inserting the asymptotic expansions for the temperatures and applying the Taylor expansion, we get

$$\begin{aligned} \rho_f(T_f) &= \rho_f(T_{f0} + \varepsilon T_{f1} + \dots) \\ &= \rho_f(T_{f0}) + (\varepsilon T_{f1} + O(\varepsilon^2)) \rho'_f(T_{f0}) + O(\varepsilon^2) \\ &= \underbrace{\rho_f(T_{f0})}_{=: \rho_{f0}} + \varepsilon \underbrace{T_{f1} \rho'_f(T_{f0})}_{=: \rho_{f1}} + O(\varepsilon^2), \end{aligned} \tag{20}$$

$$\rho_g(T_g) = \rho_g(T_{g0}) + \varepsilon T_{g1} \rho'_g(T_{g0}) + O(\varepsilon^2) = : \rho_{g0} + \varepsilon \rho_{g1} + O(\varepsilon^2), \tag{21}$$

$$\nu(T_f) = \nu(T_f) + \varepsilon T_{f1} \nu'(T_{f0}) + O(\varepsilon^2) = : \nu_0 + \varepsilon \nu_1 + O(\varepsilon^2), \tag{22}$$

where we have introduced the short-hand notations ρ_{f0} , ρ_{f1} , ρ_{g0} , ρ_{g1} , ν_0 and ν_1 to describe the temperature-dependence as indicated in (20)-(22). We are interested in the limit as $\varepsilon \rightarrow 0$ and analyze which terms of the model equations are then dominating. By inserting the asymptotic expansions into the model equations and sorting the terms after increasing order in terms of ε , we can isolate those terms.

When the asymptotic expansions of the velocity and fluid temperature are inserted into the conservation of mass (11), the terms for the two lowest orders in ε are:

$$\varepsilon^0 : 0 = \nabla_{y+z} \cdot (\mathbf{u}_0 \rho_{f0}) \quad \text{in } \Omega_f^\varepsilon, \quad (23)$$

$$\varepsilon^1 : 0 = \partial_t \rho_{f0} + \nabla_x \cdot (\mathbf{u}_0 \rho_{f0}) + \nabla_{y+z} \cdot (\mathbf{u}_0 \rho_{f1} + \mathbf{u}_1 \rho_{f0}) \quad \text{in } \Omega_f^\varepsilon. \quad (24)$$

Similarly, the conservation of momentum (12) results in

$$\varepsilon^{-1} : 0 = -\nabla_{y+z} p_0 \quad \text{in } \Omega_f^\varepsilon, \quad (25)$$

$$\varepsilon^0 : 0 = -k_{\text{flow}}(\nabla_x p_0 + \nabla_{y+z} p_1) + \nabla_{y+z} \cdot (v_0 \nabla_{y+z} \mathbf{u}_0) \quad \text{in } \Omega_f^\varepsilon. \quad (26)$$

For the conservation of energy within the void space (13), we insert asymptotic expansions for the velocity as well as the fluid temperature and get

$$\varepsilon^{-2} : 0 = \nabla_{y+z} \cdot (\kappa_f \nabla_{y+z} T_{f0}) \quad \text{in } \Omega_f^\varepsilon, \quad (27)$$

$$\begin{aligned} \varepsilon^{-1} : 0 = & \nabla_x \cdot (\kappa_f (\nabla_{y+z} T_{f0})) \\ & + \nabla_{y+z} \cdot (\kappa_f (\nabla_x T_{f0} + \nabla_{y+z} T_{f1}) - \rho_{f0} \mathbf{u}_0 T_{f0}) \quad \text{in } \Omega_f^\varepsilon, \end{aligned} \quad (28)$$

$$\begin{aligned} \varepsilon^0 : \partial_t (\rho_{f0} T_{f0}) = & \nabla_x \cdot (\kappa_f (\nabla_x T_{f0} + \nabla_{y+z} T_{f1}) - \rho_{f0} \mathbf{u}_0 T_{f0}) \\ & + \nabla_{y+z} \cdot (\kappa_f (\nabla_x T_{f1} + \nabla_{y+z} T_{f2}) \\ & - \rho_{f0} (\mathbf{u}_0 T_{f1} + \mathbf{u}_1 T_{f0}) - \rho_{f1} \mathbf{u}_0 T_{f0}) \quad \text{in } \Omega_f^\varepsilon. \end{aligned} \quad (29)$$

Using the respective asymptotic expansions in the non-dimensionalized conservation of energy in the grain space (14), yields

$$\varepsilon^{-2} : 0 = \nabla_{y+z} \cdot (\kappa_g \nabla_{y+z} T_{g0}) \quad \text{in } \Omega_g^\varepsilon, \quad (30)$$

$$\begin{aligned} \varepsilon^{-1} : 0 = & \nabla_x \cdot (\kappa_g \nabla_{y+z} T_{g0}) \\ & + \nabla_{y+z} \cdot (\kappa_g (\nabla_x T_{g0} + \nabla_{y+z} T_{g1})) \quad \text{in } \Omega_g^\varepsilon, \end{aligned} \quad (31)$$

$$\begin{aligned} \varepsilon^0 : \partial_t (\rho_{g0} T_{g0}) = & \nabla_x \cdot (\kappa_g (\nabla_x T_{g0} + \nabla_{y+z} T_{g1})) \\ & + \nabla_{y+z} \cdot (\kappa_g (\nabla_x T_{g1} + \nabla_{y+z} T_{g2})) \quad \text{in } \Omega_g^\varepsilon. \end{aligned} \quad (32)$$

The two lowest orders of the velocity's no-slip boundary are obtained by inserting the asymptotic expansions of the velocity into the non-dimensionalized boundary condition (15):

$$\varepsilon^0 : \mathbf{u}_0 = \mathbf{0} \quad \text{on } \Gamma_{\Omega_f}^\varepsilon \cup S_{\Omega}^\varepsilon, \quad (33)$$

$$\varepsilon^1 : \mathbf{u}_1 = \mathbf{0} \quad \text{on } \Gamma_{\Omega_f}^\varepsilon \cup S_{\Omega}^\varepsilon. \quad (34)$$

Analogously, the Neumann and Dirichlet boundary conditions for the temperature on the top and bottom boundary of the void and grain space (18) and (19) result in

$$\varepsilon^{-1} : \partial_z T_{f0} = 0 \text{ on } \Gamma_{\Omega_f}^\varepsilon, \tag{35a}$$

$$\text{or } T_{f0} = \theta \text{ on } \Gamma_{\Omega_f}^\varepsilon, \tag{35b}$$

$$\partial_z T_{g0} = 0 \text{ on } \Gamma_{\Omega_g}^\varepsilon, \tag{36a}$$

$$\text{or } T_{g0} = \theta \text{ on } \Gamma_{\Omega_g}^\varepsilon, \tag{36b}$$

$$\varepsilon^0 : \kappa_f \partial_z T_{f1} = \psi \text{ on } \Gamma_{\Omega_f}^\varepsilon, \tag{37a}$$

$$\text{or } T_{f1} = 0 \text{ on } \Gamma_{\Omega_f}^\varepsilon, \tag{37b}$$

$$\kappa_g \partial_z T_{g1} = \psi \text{ on } \Gamma_{\Omega_g}^\varepsilon, \tag{38a}$$

$$\text{or } T_{g1} = 0 \text{ on } \Gamma_{\Omega_g}^\varepsilon, \tag{38b}$$

$$\varepsilon^1 : \partial_z T_{f2} = 0 \text{ on } \Gamma_{\Omega_f}^\varepsilon, \tag{39a}$$

$$\text{or } T_{f2} = 0 \text{ on } \Gamma_{\Omega_f}^\varepsilon, \tag{39b}$$

$$\partial_z T_{g2} = 0 \text{ on } \Gamma_{\Omega_g}^\varepsilon, \tag{40a}$$

$$\text{or } T_{g2} = 0 \text{ on } \Gamma_{\Omega_g}^\varepsilon, \tag{40b}$$

where we for convenience have multiplied the Dirichlet conditions (18b) and (19b) with ε^{-1} .

The internal boundary condition for the temperature in void and grain space (16) holds in a similar way for the different orders as well:

$$\varepsilon^0 : T_{f0} = T_{g0} \text{ on } S_\Omega^\varepsilon, \tag{41}$$

$$\varepsilon^1 : T_{f1} = T_{g1} \text{ on } S_\Omega^\varepsilon. \tag{42}$$

By inserting the asymptotic expansions for the temperatures into the internal flux boundary (17), we get

$$\varepsilon^{-1} : \mathbf{n} \cdot (\kappa_f \nabla_y T_{f0}) = \mathbf{n} \cdot (\kappa_g \nabla_y T_{g0}) \text{ on } S_\Omega^\varepsilon, \tag{43}$$

$$\varepsilon^0 : \mathbf{n} \cdot (\kappa_f (\nabla_x T_{f0} + \nabla_y T_{f1})) = \mathbf{n} \cdot (\kappa_g (\nabla_x T_{g0} + \nabla_y T_{g1})) \text{ on } S_\Omega^\varepsilon, \tag{44}$$

$$\varepsilon^1 : \quad \mathbf{n} \cdot (\kappa_f(\nabla_x T_{f1} + \nabla_y T_{f2})) = \mathbf{n} \cdot (\kappa_g(\nabla_x T_{g1} + \nabla_y T_{g2})) \quad \text{on } S_\Omega^\varepsilon. \quad (45)$$

3.1 Dominating Order Behavior

Based on the dominating term in the momentum equation (25), we can conclude that

$$p_0 = p_0(\mathbf{x}, t), \quad (46)$$

which means that p_0 does not depend on \mathbf{y} and z . Equivalent results for T_{f0} and T_{g0} follow from the dominating terms in the conservation of energy (27) and (30), and the respective top and bottom boundaries (35a) - (36b) as well as the interface condition (43). Hence, T_{f0} and T_{g0} are constant within a cell and fulfill

$$T_{f0}(\mathbf{x}, t) = T_{g0}(\mathbf{x}, t) = :T_0(\mathbf{x}, t) \quad (47)$$

because of the continuity condition on the interface (41). Moreover, since v_0 , ρ_{f0} and ρ_{g0} only depend on T_{f0} and T_{g0} , respectively, this leads to

$$\rho_{f0}(T_{f0}) = \rho_{f0}(\mathbf{x}, t), \quad \rho_{g0}(T_{g0}) = \rho_{g0}(\mathbf{x}, t), \quad v_0(T_{f0}) = v_0(\mathbf{x}, t). \quad (48)$$

Hence, these variables remain constant within the respective cell for a given \mathbf{x} at the Darcy scale.

4 Cell Problems

The equations corresponding to a fixed order with respect to ε from the previous section are now used to derive so-called cell problems which describe the variations at the pore scale. We first consider the conservation of mass and momentum which results in a cell problem for the flow. The corresponding derivation for the upscaled flow in a porous medium can be found, e.g., in section 1.4 of Hornung (1997) or for the proportionally thin porous medium in Fabricius et al. (2016), and is only included for completeness here. Our main focus is on the conservation of energy and the corresponding cell problems for heat transport which are discussed afterwards.

4.1 Conservation of Mass and Momentum

Due to the linearity of the terms of order ε^0 in the conservation of momentum (26), we can rewrite $p_1 = p_1(\mathbf{x}, \mathbf{y}, z, t)$ and $\mathbf{u}_0 = \mathbf{u}_0(\mathbf{x}, \mathbf{y}, z, t)$ as linear combinations of $\partial_{x_j} p_0$

$$p_1(\mathbf{x}, \mathbf{y}, z, t) = \sum_{j=1}^2 r_j(\mathbf{x}, \mathbf{y}, z) \partial_{x_j} p_0(\mathbf{x}, t), \quad (49)$$

$$\mathbf{u}_0(\mathbf{x}, \mathbf{y}, z, t) = -\frac{k_{\text{flow}}}{v_0} \sum_{j=1}^2 s_j(\mathbf{x}, \mathbf{y}, z) \partial_{x_j} p_0(\mathbf{x}, t) \quad (50)$$

for some unknown weights r_j and s_j . In order to ensure the periodicity of p_1 and \mathbf{u}_0 , we require periodicity of r_j and s_j in \mathbf{y} .

We insert the linear combinations (49) and (50) into the second lowest order terms of the conservation of momentum (26) as well as the lowest order terms of mass conservation (23) and the second lowest order terms of the no-slip boundaries (34). By making use of the dependencies of density and viscosity in (48), we obtain the following cell problems to determine r_j and s_j for $j = 1, 2$:

$$\left. \begin{aligned} \mathbf{0} &= \mathbf{e}_j + \nabla_{\mathbf{y}+\mathbf{z}} r_j + \Delta_{\mathbf{y}+\mathbf{z}} s_j && \text{in } Q_f, \\ 0 &= \nabla_{\mathbf{y}+\mathbf{z}} \cdot s_j && \text{in } Q_f, \\ \mathbf{0} &= s_j && \text{on } \Gamma_{Q_f} \cup S_{Q_f}, \\ s_j, r_j &\text{ are periodic in } \mathbf{y}, \end{aligned} \right\} (P^{\text{flow}}(\mathbf{x}))$$

where \mathbf{e}_j denotes the unit vector in x_j -direction. As mentioned before, s_j and r_j are periodic on Π_Q . We add the constraint

$$\int_{Q_f} r_j \, d(\mathbf{y}, z) = \text{constant}$$

to ensure the uniqueness of the solution. One should note that this cell problem only needs to be solved in \mathbf{y} and z . The effect of \mathbf{x} comes in as a parameter accounting for the chosen pore geometry at a position \mathbf{x} at the Darcy scale. Hence, the cell problem accounts for the local flow at the pore scale and will later be used to define the permeability of the porous medium. By solving for r_j and s_j in $(P^{\text{flow}}(\mathbf{x}))$, we can obtain p_1 and \mathbf{u}_0 as functions of $\nabla_x p_0$ through (49) and (50).

4.2 Conservation of Energy

Next, we apply a similar approach to the conservation of energy: The linearity of the terms (28) and (31) of order ε^{-1} indicates that T_{fl} and T_{gl} can be represented as linear combinations of $\partial_{x_j} T_0$, factorizing the dependencies on \mathbf{x} and \mathbf{y} . Since the following steps depend on which boundary conditions are used on the top and bottom boundary Γ_Q , we divide our approach into two cases: We first consider Neumann boundary conditions, and then, the results for Dirichlet boundary conditions are presented. For a clear distinction between the two cases, we use the superscript 'N' or 'D', respectively, to indicate the considered boundary conditions.

4.2.1 Neumann Boundary Conditions on Top and Bottom Boundary Γ_Q

Due to the linearity of the problem, we choose the following expressions in order to satisfy the boundary conditions at the top and bottom boundaries:

$$T_{\text{fl}}(\mathbf{x}, \mathbf{y}, z, t) = \sum_{j=1}^2 v_j^{\text{N}}(\mathbf{x}, \mathbf{y}, z) \partial_{x_j} T_0(\mathbf{x}, t) + \frac{\psi(\mathbf{x}, t)}{\kappa_f} z, \tag{51a}$$

$$T_{g1}(\mathbf{x}, \mathbf{y}, z, t) = \sum_{j=1}^2 w_j^N(\mathbf{x}, \mathbf{y}, z) \partial_{x_j} T_0(\mathbf{x}, t) + \frac{\psi(\mathbf{x}, t)}{\kappa_g} z, \tag{51b}$$

where v_j^N and w_j^N ($j = 1, 2$) are weights that are to be determined. Note that the last term in (51a) and (51b) ensures that the Neumann boundary conditions (37a) and (38a) are fulfilled. In the case of homogeneous Neumann boundary conditions, the last term is zero. By inserting the linear combination (51a) into the second lowest order terms of the energy conservation (28) and using the dependencies of T_{f0} in (47) as well as the lowest order terms of the mass conservation (23), we get

$$0 = \Delta_{y+z} v_j^N \quad \text{for } j = 1, 2 \quad \text{in } Q_f. \tag{52}$$

For the grain space, a similar expression can be derived when the linear combination (51b) and the respective equation for energy conservation (31) are used:

$$0 = \Delta_{y+z} w_j^N \quad \text{for } j = 1, 2 \quad \text{in } Q_g. \tag{53}$$

Suitable boundary conditions result from inserting the linear combinations into the second lowest order terms of the existing boundary conditions (37a), (38a), (41) and (44):

$$0 = \partial_z v_j^N \quad \text{for } j = 1, 2 \quad \text{on } \Gamma_{Q_f}, \tag{54}$$

$$0 = \partial_z w_j^N \quad \text{for } j = 1, 2 \quad \text{on } \Gamma_{Q_g}, \tag{55}$$

$$v_j^N = w_j^N \quad \text{for } j = 1, 2 \quad \text{on } S_Q, \tag{56}$$

$$\mathbf{n} \cdot (\kappa_f(\mathbf{e}_j + \nabla_{y+z} v_j^N)) = \mathbf{n} \cdot (\kappa_g(\mathbf{e}_j + \nabla_{y+z} w_j^N)) \quad \text{for } j = 1, 2 \quad \text{on } S_Q. \tag{57}$$

By combining the derived equations (52) - (57), we get two coupled cell problems, for $j = 1, 2$:

$$\left. \begin{aligned} 0 &= \Delta_{y+z} v_j^N && \text{in } Q_f, \\ 0 &= \Delta_{y+z} w_j^N && \text{in } Q_g, \\ 0 &= \partial_z v_j^N && \text{on } \Gamma_{Q_f}, \\ 0 &= \partial_z w_j^N && \text{on } \Gamma_{Q_g}, \\ v_j^N &= w_j^N && \text{on } S_Q, \\ \mathbf{n} \cdot (\kappa_f(\mathbf{e}_j + \nabla_{y+z} v_j^N)) &= \mathbf{n} \cdot (\kappa_g(\mathbf{e}_j + \nabla_{y+z} w_j^N)) && \text{on } S_Q, \\ v_j^N, w_j^N &\text{ are periodic in } \mathbf{y}. \end{aligned} \right\} (P^{\text{heat}, N}(\mathbf{x}))$$

The weights v_j^N and w_j^N are required to be periodic in \mathbf{y} due to the periodicity of T_{f1} and T_{g1} . We add the uniqueness constraint

$$\int_{Q_f} v_j^N d(\mathbf{y}, z) + \int_{Q_g} w_j^N d(\mathbf{y}, z) = \text{constant} \quad \text{for } j = 1, 2 \tag{58}$$

with an arbitrary constant. Note that since we added the inhomogeneous Neumann boundary condition as part of the series expansions (51), we obtain a cell problem which is independent of the heat flux applied at the top and bottom boundaries. Hence, $(P^{\text{heat}, N}(\mathbf{x}))$ is used both for homogeneous and inhomogeneous Neumann boundary conditions.

Dimensionality of the Cell Problem If we consider a pore geometry that is constant with respect to z , we find that

$$\partial_z v_j^N(\mathbf{x}, \mathbf{y}, z) = 0 \quad \text{in } Q_f, \tag{59}$$

$$\partial_z w_j^N(\mathbf{x}, \mathbf{y}, z) = 0 \quad \text{in } Q_g, \tag{60}$$

which means that we can reduce the three-dimensional cell problem to two spatial dimensions and still obtain the same results. To see this, we start by rewriting

$$\begin{aligned} v_j^N(\mathbf{y}, z) &= m_f^j(\mathbf{y}) \cdot o_f^j(z), \\ w_j^N(\mathbf{y}, z) &= m_g^j(\mathbf{y}) \cdot o_g^j(z), \end{aligned}$$

where we have omitted writing the dependence on \mathbf{x} to simplify the notation. Consequently, we can rewrite the cell problem, namely the Laplace equation in Q_f (52) as well as the Neumann boundary condition (54), based on the separation of the variables \mathbf{y} and z , as

$$\begin{aligned} \Delta_{\mathbf{y}+z} v_j^N &= o_f^j \Delta_{\mathbf{y}} m_f^j + m_f^j \Delta_z o_f^j \stackrel{!}{=} 0 && \text{in } Q_f \\ \Rightarrow \frac{1}{m_f^j} \Delta_{\mathbf{y}} m_f^j &= -\frac{1}{o_f^j} \Delta_z o_f^j = \lambda = \text{constant} && \text{in } Q_f, \end{aligned} \tag{61}$$

$$\begin{aligned} \partial_z v_j^N(\mathbf{y}, z) &= m_f^j(\mathbf{y}) \cdot \partial_z o_f^j(z) \stackrel{!}{=} 0 && \text{on } \Gamma_{Q_f} \\ \Rightarrow \partial_z o_f^j(z) &= 0 && \text{on } \Gamma_{Q_f}. \end{aligned} \tag{62}$$

Hence, we have derived two equations that involve either only \mathbf{y} or z :

$$\begin{aligned} \Delta_{\mathbf{y}} m_f^j(\mathbf{y}) &= m_f^j(\mathbf{y}) \lambda, \\ \Delta_z o_f^j(z) &= -o_f^j(z) \lambda. \end{aligned} \tag{63}$$

There exist only two types of solutions for $o_f^j(z)$ that fulfill the z -dependent equation (63) as well as the Neumann boundary condition in (62):

$$o_f^j(z) = \text{constant} \quad \text{in } [0, H], \text{ or} \tag{64}$$

$$o_f^j(z) = d \cdot \cos\left(\frac{\pi c}{H} z\right) \quad \text{in } [0, H], \text{ for } c \in \mathbb{N}, d \in \mathbb{R}. \tag{65}$$

Note that since (65) leads to a constant solution in case of $c = 0$, we only consider $c \neq 0$ here. Using same arguments for Q_g and Γ_{Q_g} , we find that $o_g^j(z)$ has a form corresponding to (64) or (65). In case of a constant solution (64), it is trivial that this solution does not

depend on z and satisfies (62). Hence, we now show that (65) cannot be a solution of our problem.

As mentioned above, v_j^N and w_j^N need to satisfy a uniqueness condition as given in (58) for an arbitrary constant. In the following, we set the constant to one. If we incorporate the separation approach (61), we get

$$\int_{Q_f} m_f^j(\mathbf{y}) \cdot \sigma_f^j(z) \, d(\mathbf{y}, z) + \int_{Q_g} m_g^j(\mathbf{y}) \cdot \sigma_g^j(z) \, d(\mathbf{y}, z) = 1.$$

However, the first term can be rewritten into

$$\begin{aligned} \int_{Q_f} m_f^j(\mathbf{y}) \cdot \sigma_f^j(z) \, d(\mathbf{y}, z) &= \int_{Q_{f,2D}} m_f^j(\mathbf{y}) \, d\mathbf{y} \int_0^H \sigma_f^j(z) \, dz \\ &= \int_{Q_{f,2D}} m_f^j(\mathbf{y}) \, d\mathbf{y} \left[\frac{dH}{\pi c} (\sin(\pi c) - \sin(0)) \right] = 0, \end{aligned}$$

where $Q_{f,2D}$ is a two-dimensional cross section of the fluid domain in the cell. Note that this separation can only be done since the geometry does not vary with z . Similarly, we rewrite the integral of w_j^N . The uniqueness condition is calculated as

$$\int_{Q_f} m_f^j(\mathbf{y}) \cdot \sigma_f^j(z) \, d(\mathbf{y}, z) + \int_{Q_g} m_g^j(\mathbf{y}) \cdot \sigma_g^j(z) \, d(\mathbf{y}, z) = 0 + 0 \neq 1 \quad (66)$$

which is a contradiction. Hence, $\sigma_f^j(z)$ as well as $\sigma_g^j(z)$ have to be constant functions as stated in (64). The three-dimensional cell problem can therefore be reduced to a two-dimensional problem if the geometry does not depend on z . Note that we still obtain three-dimensional solutions for the cell problem that cannot be reduced to two-dimensional cell problems, if the grain shape changes along the z -axis.

4.2.2 Dirichlet Boundary Conditions on Top and Bottom Boundary Γ_Q

To satisfy the Dirichlet boundary conditions on Γ_Q , we can use a similar linear combination as for zero-Neumann boundary conditions:

$$T_{f1}(\mathbf{x}, \mathbf{y}, z, t) = \sum_{j=1}^2 v_j^D(\mathbf{x}, \mathbf{y}, z) \partial_{x_j} T_0(\mathbf{x}, t), \quad (67a)$$

$$T_{g1}(\mathbf{x}, \mathbf{y}, z, t) = \sum_{j=1}^2 w_j^D(\mathbf{x}, \mathbf{y}, z) \partial_{x_j} T_0(\mathbf{x}, t), \quad (67b)$$

where v_j^D and w_j^D ($j = 1, 2$) are weights that are to be determined. We insert the linear combinations in the respective equations following similar steps as before and obtain the following coupled cell problem for $j = 1, 2$:

$$\left. \begin{aligned}
 0 &= \Delta_{y+z} v_j^D && \text{in } Q_f, \\
 0 &= \Delta_{y+z} w_j^D && \text{in } Q_g, \\
 0 &= v_j^D && \text{on } \Gamma_{Q_f}, \\
 0 &= w_j^D && \text{on } \Gamma_{Q_g}, \\
 v_j^D &= w_j^D && \text{on } S_Q, \\
 \mathbf{n} \cdot (\kappa_f(\mathbf{e}_j + \nabla_{y+z} v_j^D)) &= \mathbf{n} \cdot (\kappa_g(\mathbf{e}_j + \nabla_{y+z} w_j^D)) && \text{on } S_Q, \\
 v_j^D, w_j^D &\text{ are periodic in } \mathbf{y}.
 \end{aligned} \right\} (P^{\text{heat}, D}(\mathbf{x}))$$

This cell problem differs from the previous case of Neumann boundary conditions in the boundary conditions on Γ_{Q_f} and Γ_{Q_g} . Note that due to the Dirichlet boundary conditions, these cell problems cannot be reduced to two-dimensional even if the geometry is not depending on z .

5 Darcy-Scale Equations

In the following, we integrate the flow equation (50) over its domain Q_f . Further, the next order terms with respect to ε from the mass (24) and energy conservation (29) and (32) are integrated over the respective domains within Q . This is done in order to obtain equations at the Darcy scale, while including effects from the pore scale through effective quantities.

5.1 Effective Flow

The derivation of the effective flow, meaning Darcy’s law, can be found in the literature (e.g., in Sect. 1.4 of Hornung (1997) in the case of constant viscosity and density, and Bringedal et al. (2016) with temperature-dependent viscosity and density) and is again only shown for completeness. For the effective flow $\bar{\mathbf{u}}_0$ in the porous medium, the definition of \mathbf{u}_0 as stated in (50) is integrated

$$\bar{\mathbf{u}}_0 = \frac{1}{|Q|} \int_{Q_f} \mathbf{u}_0(\mathbf{x}, \mathbf{y}, z, t) \, d(\mathbf{y}, z) = -\frac{1}{\nu_0} \mathbf{K} \nabla_x p_0 \tag{68}$$

where the components of \mathbf{K} are

$$K_{ij}(\mathbf{x}) = \frac{k_{\text{flow}}}{|Q|} \int_{Q_f} s_{j,i}(\mathbf{x}, \mathbf{y}, z) \, d(\mathbf{y}, z) \quad i, j = 1, 2 \tag{69}$$

and the viscosity follows the dependency in (48). The components $s_{j,i}$ follow from solving the local, three-dimensional cell problem ($P^{\text{flow}}(\mathbf{x})$). The averaged equation (68) is Darcy’s law, where \mathbf{K} is the permeability of the porous medium. The matrix \mathbf{K} is symmetric and positive definite and we refer to Lemma 4.2 in Sect. 1.4 in Hornung (1997) for a detailed proof. Note that the permeability in our case is a 2×2 matrix, although the cell problem is solved in a three-dimensional domain. In Fabricius et al. (2016) and Wagner et al. (2021), the authors discuss the applicability of approximate, two-dimensional forms of the cell problem, accounting for the porous medium being thin. Hence, under suitable assumptions, the resulting permeability for thin porous media can be found more cheaply.

By integrating the second lowest order terms of the mass conservation (24) over the volume and using Gauss' theorem, the following equation is derived:

$$0 = |\mathcal{Q}_f| \partial_t \rho_{f0} + \int_{\mathcal{Q}_f} \nabla_x \cdot (\mathbf{u}_0 \rho_{f0}) \, d(\mathbf{y}, z) + \int_{\partial \mathcal{Q}_f} (\mathbf{u}_0 \rho_{f1} + \mathbf{u}_1 \rho_{f0}) \cdot \mathbf{n} \, d\sigma. \quad (70)$$

Note that the boundary of the void space was previously defined as $\partial \mathcal{Q}_f = \Gamma_{\mathcal{Q}_f} \cup S_{\mathcal{Q}_f} \cup \Pi_{\mathcal{Q}}$. The integral over $\Pi_{\mathcal{Q}}$ is zero due to the periodicity of \mathbf{u}_0 and \mathbf{u}_1 . In addition to that, the integral over $\Gamma_{\mathcal{Q}_f}$ and $S_{\mathcal{Q}_f}$ disappears because we assumed no-slip boundaries in (34). The upscaled equation (70) can be rewritten based on the definition of $\bar{\mathbf{u}}_0$ in (68) as

$$\phi \partial_t \rho_{f0} + \nabla_x \cdot (\bar{\mathbf{u}}_0 \rho_{f0}) = 0 \quad (71)$$

where $\phi := |\mathcal{Q}_f|/|\mathcal{Q}|$ is the porosity.

5.2 Effective Energy Conservation

To describe the conservation of energy in the void as well as the grain space at the Darcy scale, the third lowest order terms in void and grain space (29) and (32) are used. If we integrate them over their respective domains, add them up, divide by $|\mathcal{Q}|$ and apply Gauss' theorem as well as the definition of the effective flow (68), we obtain

$$\begin{aligned} \phi \partial_t (\rho_{f0} T_0) + (1 - \phi) \partial_t (\rho_{g0} T_0) &= \underbrace{\frac{1}{|\mathcal{Q}|} \int_{\mathcal{Q}_f} \nabla_x \cdot (\kappa_f (\nabla_x T_0 + \nabla_{y+z} T_{f1})) \, d(\mathbf{y}, z)}_{=: A_1} \\ &+ \underbrace{\frac{1}{|\mathcal{Q}|} \int_{\mathcal{Q}_g} \nabla_x \cdot (\kappa_g (\nabla_x T_0 + \nabla_{y+z} T_{g1})) \, d(\mathbf{y}, z)}_{=: A_2} \\ &+ \underbrace{\frac{1}{|\mathcal{Q}|} \left(\int_{\partial \mathcal{Q}_f} \kappa_f (\nabla_x T_{f1} + \nabla_{y+z} T_{f2}) \cdot \mathbf{n} \, d\sigma + \int_{\partial \mathcal{Q}_g} \kappa_g (\nabla_x T_{g1} + \nabla_{y+z} T_{g2}) \cdot \mathbf{n} \, d\sigma \right)}_{=: B} \\ &- \underbrace{\frac{1}{|\mathcal{Q}|} \int_{\partial \mathcal{Q}_f} (\rho_{f1} (\mathbf{u}_0 T_{f1} + \mathbf{u}_1 T_0)) \cdot \mathbf{n} \, d\sigma}_{=: C} - \nabla_x \cdot (\rho_{f0} T_0 \bar{\mathbf{u}}_0). \end{aligned} \quad (72)$$

Considering the composition of $\partial \mathcal{Q}_f = \Gamma_{\mathcal{Q}_f} \cup S_{\mathcal{Q}_f} \cup \Pi_{\mathcal{Q}}$ and $\partial \mathcal{Q}_g = \Gamma_{\mathcal{Q}_g} \cup S_{\mathcal{Q}_g}$, we first show that term C vanishes: For the integrals over $\Gamma_{\mathcal{Q}_f} \cup S_{\mathcal{Q}_f}$, we make use of the no-slip boundary conditions (33) and (34) again. Since all functions within the integral are periodic in \mathbf{y} , the contributions of the different parts of $\Pi_{\mathcal{Q}}$ cancel each other.

Note that $\partial \mathcal{Q}_f \cap \partial \mathcal{Q}_g = S_{\mathcal{Q}}$, while the respective normal vectors on this domain point in opposite directions for the fluid ($S_{\mathcal{Q}_f}$) and the grain component ($S_{\mathcal{Q}_g}$). Due to the continuity condition (45), the contributions from $S_{\mathcal{Q}}$ in term B cancel each other. The integral over $\Pi_{\mathcal{Q}}$ is zero due to periodicity. Hence, term B results in

$$\begin{aligned}
B &= \int_{\Gamma_{Q_f}} \frac{\kappa_f}{|Q|} (\nabla_x T_{f1} + \nabla_{y+z} T_{f2}) \cdot \mathbf{n} \, d\sigma + \int_{\Gamma_{Q_g}} \frac{\kappa_g}{|Q|} (\nabla_x T_{g1} + \nabla_{y+z} T_{g2}) \cdot \mathbf{n} \, d\sigma \\
&= \int_{\Gamma_{Q_f}} \frac{\kappa_f}{|Q|} \partial_z T_{f2} n_3 \, d\sigma + \int_{\Gamma_{Q_g}} \frac{\kappa_g}{|Q|} \partial_z T_{g2} n_3 \, d\sigma,
\end{aligned} \tag{73}$$

where we have introduced $n_3 = \pm 1$ to denote the third component of the normal vector on Γ_{Q_f} and Γ_{Q_g} , respectively. The following steps depend on the top and bottom boundary of the domain. Hence, we consider the case of Neumann boundary conditions first before moving on to Dirichlet boundary conditions.

5.2.1 Neumann Boundary Conditions on Top and Bottom Boundary Γ_Q

In this case, the contributions of the integrals over Γ_{Q_f} and Γ_{Q_g} in term B as given in (73) disappear according to the Neumann boundary conditions (39a) and (40a). Therefore, term B is zero.

To simplify the terms A_1 and A_2 , we insert the linear combinations (51a) for T_{f1} and (51b) for T_{g1} and use that T_{f0} as well as T_{g0} do not depend on \mathbf{y} and z :

$$\begin{aligned}
A_1 + A_2 &= \kappa_f \nabla_x \cdot \left(\mathbf{V}^N \nabla_x T_0 + \frac{\psi_f}{\kappa_f} \mathbf{e}_z \right) + \kappa_g \nabla_x \cdot \left(\mathbf{W}^N \nabla_x T_0 + \frac{\psi_g}{\kappa_g} \mathbf{e}_z \right) \\
&= \kappa_f \nabla_x \cdot (\mathbf{V}^N \nabla_x T_0) + \kappa_g \nabla_x \cdot (\mathbf{W}^N \nabla_x T_0),
\end{aligned}$$

with components

$$V_{ij}^N = \delta_{ij} \phi + \frac{1}{|Q|} \int_{Q_f} \partial_{y_i} v_j^N \, d(\mathbf{y}, z) \quad i, j = 1, 2, \tag{74}$$

$$W_{ij}^N = \delta_{ij} (1 - \phi) + \frac{1}{|Q|} \int_{Q_g} \partial_{y_i} w_j^N \, d(\mathbf{y}, z) \quad i, j = 1, 2. \tag{75}$$

We can further simplify these expressions by using the following relation:

$$\int_{Q_f} \partial_{y_i} v_j^N \, d(\mathbf{y}, z) = - \int_{Q_g} \partial_{y_i} w_j^N \, d(\mathbf{y}, z) \quad i, j = 1, 2. \tag{76}$$

This relation is obtained by rewriting the left-hand side of the equation and applying the Gauss' theorem:

$$\begin{aligned}
\int_{Q_f} \partial_{y_i} v_j^N \, d(\mathbf{y}, z) &= \int_{Q_f} \nabla_{y+z} \cdot (v_j^N \mathbf{e}_i) \, d(\mathbf{y}, z) = \int_{\partial Q_f} (v_j^N \mathbf{e}_i) \cdot \mathbf{n} \, d\sigma \\
&= \int_{\Gamma_{Q_f} \cup S_{Q_f} \cup \Pi_Q} v_j^N n_i \, d\sigma.
\end{aligned}$$

The integral over Π_Q vanishes due to periodicity of v_j^N , and on Γ_{Q_f} the normal component n_i is zero since the respective normal vector is parallel to the z -axis. If we use the continuity condition (56) of the cell problem, we get

$$\int_{S_{Q_f}} v_j^N n_i \, d\sigma = \int_{S_{Q_f}} w_j^N n_i \, d\sigma = - \int_{S_{Q_g}} w_j^N n_i \, d\sigma,$$

because S_{Q_f} and S_{Q_g} denote the same surface but with opposite orientation. When applying the previous steps in inverse order, we end up with

$$- \int_{S_{Q_g}} w_j^N n_i \, d\sigma = - \int_{Q_g} \nabla_{y+z} \cdot (w_j^N \mathbf{e}_i) \, d(\mathbf{y}, z) = - \int_{Q_g} \partial_{y_i} w_j^N \, d(\mathbf{y}, z).$$

Hence, we have (76).

Making use of the relation between the integrals (76) and the quantities \mathbf{V}^N and \mathbf{W}^N in (74) and (75), the upscaled effective heat conductivity is given as

$$\mathbf{S}^N = \kappa_f \mathbf{V}^N + \kappa_g \mathbf{W}^N$$

with components $i, j = 1, 2$

$$S_{ij}^N = \delta_{ij}(\kappa_f \phi + \kappa_g(1 - \phi)) + \frac{\kappa_f - \kappa_g}{|Q|} \int_{Q_f} \partial_{y_i} v_j^N \, d(\mathbf{y}, z). \quad (77)$$

Note that the first term represents the volume-weighted average of the heat conductivities in fluid and grain. The second term accounts for the internal structure of the heat transport within the cell problem and the interaction with the top and bottom boundaries, which are not accounted for by the volume-weighted averages.

If we insert all derived expressions above into (72), we obtain the upscaled form of conservation of energy:

$$\partial_t(\phi \rho_{f0} T_0 + (1 - \phi) \rho_{g0} T_0) = \nabla_x \cdot (\mathbf{S}^N \nabla_x T_0 - \rho_{f0} T_0 \bar{\mathbf{u}}_0). \quad (78)$$

5.2.2 Dirichlet Boundary Conditions on Top and Bottom Boundary Γ_Q

We first consider the simplified form of term B as stated in (73): If we assume that T_{f2} and T_{g2} are symmetric with respect to z , term B is zero since the remaining integrals sum up to zero. This assumption is reasonable due to the symmetric boundary conditions and since the setup of the discussed problem yields a symmetric behavior.

As done for the case of Neumann boundary conditions, we also insert the respective linear combinations (67a) and (67b) into the terms A_1 and A_2 . This results in:

$$A_1 + A_2 = \kappa_f \nabla_x \cdot (\mathbf{V}^D \nabla_x T_0) + \kappa_g \nabla_x \cdot (\mathbf{W}^D \nabla_x T_0).$$

The components of \mathbf{V}^D and \mathbf{W}^D are given by:

$$\begin{aligned} V_{ij}^D &= \delta_{ij} \phi + \frac{1}{|Q|} \int_{Q_f} \partial_{y_i} v_j^D \, d(\mathbf{y}, z) & i, j = 1, 2, \\ W_{ij}^D &= \delta_{ij} (1 - \phi) + \frac{1}{|Q|} \int_{Q_g} \partial_{y_i} w_j^D \, d(\mathbf{y}, z) & i, j = 1, 2. \end{aligned}$$

Note that the integrals of $\partial_{y_i} v_j^D$ over Q_f and of $\partial_{y_i} w_j^D$ over Q_g satisfy

$$\int_{Q_f} \partial_{y_i} v_j^D d(\mathbf{y}, z) = - \int_{Q_g} \partial_{y_i} w_j^D d(\mathbf{y}, z) \quad i, j = 1, 2.$$

The relation can be derived analogously to the case of Neumann boundary conditions (see (76)). By using this relation as well as the definitions of V^D and W^D , we define the effective heat conductivity

$$S^D = \kappa_f V^D + \kappa_g W^D$$

with components $i, j = 1, 2$

$$S_{ij}^D = \delta_{ij}(\kappa_f \phi + \kappa_g(1 - \phi)) + \frac{\kappa_f - \kappa_g}{|Q|} \int_{Q_f} \partial_{y_i} v_j^D d(\mathbf{y}, z). \tag{79}$$

As in (77), we see that the effective heat conductivity can be written as the sum of the volume-weighted average of the heat conductivities, and of a part accounting for the internal structure of the heat transport and interactions with top and bottom boundaries. Hence, we obtain the following Darcy-scale equation for the heat transport:

$$\partial_i(\phi \rho_{f0} T_0 + (1 - \phi) \rho_{g0} T_0) = \nabla_x \cdot (S^D \nabla_x T_0 - \rho_{f0} T_0 \bar{\mathbf{u}}_0). \tag{80}$$

5.2.3 Remarks Regarding the Effective Heat Conductivities

If we compare the effective heat conductivities S^N in (77) for Neumann boundary conditions and S^D in (79) for Dirichlet boundary conditions on the top and bottom boundary, one finds that they have the same structure. However, they depend on the solution of the respective cell problems ($P^{\text{heat}, N}(\mathbf{x})$) and ($P^{\text{heat}, D}(\mathbf{x})$), which are not the same. Hence, we obtain different effective heat conductivities depending on the type of boundary conditions.

The effective heat conductivities S^N in (77) and S^D in (79) are both symmetric and positive definite, as one also finds for two- or three-dimensional porous media where the top and bottom boundary conditions do not have an influence Auriault (1983). To see this, one considers the weak form of the cell problems ($P^{\text{heat}, N}(\mathbf{x})$) and ($P^{\text{heat}, D}(\mathbf{x})$). Using test functions that also fulfill the top and bottom boundary conditions, the weak form for ($P^{\text{heat}, N}(\mathbf{x})$) is

$$\begin{aligned} \int_{Q_f} \kappa_f \nabla_{y+z} v_j^N \cdot \nabla_{y+z} \omega d(\mathbf{y}, z) + \int_{Q_g} \kappa_g \nabla_{y+z} w_j^N \cdot \nabla_{y+z} \omega d(\mathbf{y}, z) \\ = \int_{S_Q} \psi(\kappa_g - \kappa_f) \mathbf{e}_j \cdot \mathbf{n} d\sigma \end{aligned}$$

for all sufficiently smooth ω that are periodic in \mathbf{y} and fulfilling $\partial_z \omega = 0$ on Γ_Q . Choosing ω equal to v_j^N in Q_f and to w_j^N in Q_g , and using (76) together with Gauss' theorem, we obtain

$$\int_{Q_f} \kappa_f \nabla_{y+z} v_i^N \cdot (\nabla_{y+z} v_j^N + \mathbf{e}_j) d(\mathbf{y}, z) + \int_{Q_g} \kappa_g \nabla_{y+z} w_i^N \cdot (\nabla_{y+z} w_j^N + \mathbf{e}_j) d(\mathbf{y}, z) = 0.$$

This identity can be used to rewrite the components S_{ij}^N to

$$S_{ij}^N = \int_{Q_t} \kappa_f (\nabla_{y+z} v_j^N + \mathbf{e}_j) \cdot (\nabla_{y+z} v_i^N + \mathbf{e}_i) d(\mathbf{y}, z) \\ + \int_{Q_g} \kappa_f (\nabla_{y+z} w_j^N + \mathbf{e}_j) \cdot (\nabla_{y+z} w_i^N + \mathbf{e}_i) d(\mathbf{y}, z)$$

which is obviously symmetric, and can be seen to be positive definite by considering the sum $\sum_{i,j=1}^2 \alpha_i S_{ij}^N \alpha_j$ for real numbers α_i (see also Proposition 3.2 for a diffusion problem in Hornung 1997). For the cell problem with Dirichlet boundary conditions ($P^{\text{heat}, D}(\mathbf{x})$), the argument follows similar steps, but using test functions ω fulfilling $\omega = 0$ on Γ_Q . The corresponding weak form and components of S_{ij}^D can be written the same way as for the Neumann boundary conditions case, using v_j^D, w_j^D instead of v_j^N, w_j^N .

Note that although the cell problems ($P^{\text{heat}, N}(\mathbf{x})$) and ($P^{\text{heat}, D}(\mathbf{x})$) generally need to be solved in three-dimensional domains, the resulting effective matrices $S^N(\mathbf{x})$ and $S^D(\mathbf{x})$ only vary in the horizontal directions, meaning along $\mathbf{x} = (x_1, x_2)$. A z -dependence of the effective heat conductivity would appear if higher order terms from the conservation of energy in (13) and (14) would be included, which would correspond to a better approximation of the original problem. The presented effective model is based on terms up to the order $O(\varepsilon^0)$. In the expressions for $A_1 + A_2$, the divergence with respect to \mathbf{x} is zero in the third component. Therefore, the third row and column of the effective heat conductivity are zero and we only need to consider $S \in \mathbb{R}^{2 \times 2}$.

Hence, in a thin porous medium, the resulting effective heat conductivity for the horizontal heat transfer depends on the three-dimensional structure of the pore scale and on the boundary conditions applied to the top and bottom boundaries of the thin porous medium.

5.3 Summary of Upscaled Model

The derived upscaled model consists of Darcy's law (68) and upscaled mass conservation (71), together with an upscaled equation for the effective heat transport (78) or (80) depending on the choice of boundary conditions on the top and bottom boundary:

$$\bar{\mathbf{u}}_0 = -\frac{1}{\nu_0} \mathbf{K} \nabla_x p_0 \\ \phi \partial_t \rho_{f0} + \nabla_x \cdot (\bar{\mathbf{u}}_0 \rho_{f0}) = 0 \\ \partial_t (\phi \rho_{f0} T_0 + (1 - \phi) \rho_{g0} T_0) = \nabla_x \cdot (S \nabla_x T_0 - \rho_{f0} T_0 \bar{\mathbf{u}}_0),$$

where $S = S^N$ in the case of Neumann boundary conditions on the top and bottom boundaries, and $S = S^D$ in the case of Dirichlet boundary conditions. Equations of state describing how the fluid and grain densities and fluid viscosity depend on temperature must also be included to close the system. Note that these equations are all defined on two-dimensional domains, as the vertical (thin) direction does not need to be resolved. Hence, the effective matrices \mathbf{K}, S are 2×2 matrices. The components of the permeability matrix \mathbf{K} are determined by (69), where the solution of the corresponding cell problems is given through ($P^{\text{flow}}(\mathbf{x})$). The components of the effective heat conductivity S^N and S^D are given by (77) and (79), which depend on the corresponding cell problems ($P^{\text{heat}, N}(\mathbf{x})$) and ($P^{\text{heat}, D}(\mathbf{x})$), respectively. Note that the cell problems are defined on three-dimensional domains, which are small portions of the original domain. Despite the strong coupling between the original model equations, the cell problems can be solved independently of each other.

The upscaled model is valid under the assumptions on the original pore-scale model equations stated in Sect. 2.2, and under the assumption of the non-dimensional numbers as explained in Sect. 2.3. Note that the (scaled) non-dimensional numbers still appear in the resulting upscaled model through the effective quantities \mathbf{K}, \mathbf{S} and through the cell problems $(P^{\text{heat}, \text{N}}(\mathbf{x}))$ and $(P^{\text{heat}, \text{D}}(\mathbf{x}))$.

6 Effective Heat Conductivity Behavior Based on Cell Problems

In the following, we analyze the effective heat conductivities that are calculated based on the solutions of the cell problems $(P^{\text{heat}, \text{N}}(\mathbf{x}))$ and $(P^{\text{heat}, \text{D}}(\mathbf{x}))$. For the numerical results below, we have used Netgen for mesh generation and the finite element software NGSolve to solve the weak form of the cell problems (see Schöberl 2014). Note that the cell problems $(P^{\text{heat}, \text{N}}(\mathbf{x}))$ and $(P^{\text{heat}, \text{D}}(\mathbf{x}))$ are elliptic. To generate the mesh in Netgen, we specify the domain and location of the inner boundary and give the maximum mesh size h_{\max} . However, Netgen generally employs smaller grid cells near inner boundaries. To discretize the cell problems on these meshes, we use subspaces of H^1 , using polynomials up to third order as basis functions. The remaining computations to obtain the effective heat conductivities according to (77) and (79) have been performed using NGSolve, as the needed solution derivatives are directly available through NGSolve. As mentioned above, the cell problem can be reduced to two dimensions whenever we apply Neumann boundary conditions on the top and bottom boundary Γ_Q and consider a setup where the grain shape does not change along the z -axis. By reducing h_{\max} , larger accuracy is obtained. We found that four significant digits in the cell problem solution and in the effective quantity was obtained already by $h_{\max} = 0.1$. The number of used grid cells was in this case for the cell problems in Sect. 6.1–6.3 in the range 180–400 for two-dimensional cell problems, and 6 000–144 000 for three-dimensional cell problems. The largest amount of grid cell were needed for ellipsoid-shaped grains.

The provided code Scholz and Bringedal (2021) calculates all components of the effective heat conductivities \mathbf{S}^{N} and \mathbf{S}^{D} . We will limit our attention to isotropic grain shapes. In this case, the off-diagonal components S_{ij}^{N} and S_{ij}^{D} ($i \neq j$) are close to zero and $S_{11}^{\text{N}} = S_{22}^{\text{N}}$ as well as $S_{11}^{\text{D}} = S_{22}^{\text{D}}$. Therefore, we only present and discuss the first diagonal component in the following.

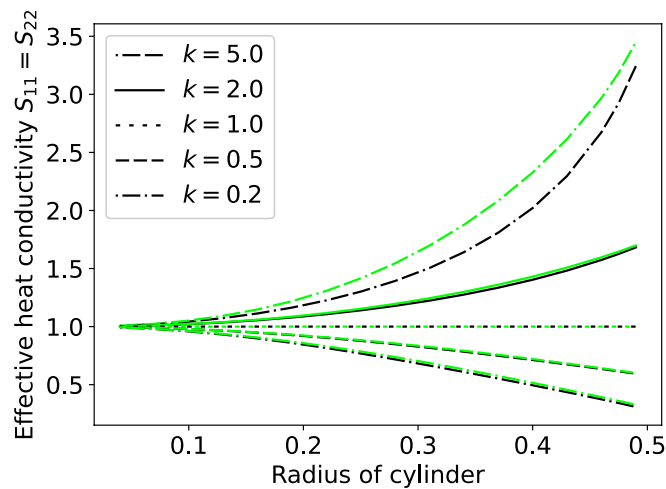
We are interested in which way the use of Neumann or Dirichlet boundary conditions on the top and bottom boundary Γ_Q as well as different grain shapes affect the effective heat conductivity. Besides that, different ratios of the heat conductivity of the grain κ_g and the fluid κ_f count among the parameters of interest. To simplify the comparison, we set $\kappa_f = 1$ and consider different values for $k = \kappa_g/\kappa_f = \kappa_g$. Note that it follows from assumptions on Pe_f and Pe_g that κ_f and κ_g are the same order of magnitude. Hence, with $\kappa_f = 1$, κ_g have to be close to 1 as well. In the following, we consider k between 0.2 and 5.

6.1 Effect of Boundary Conditions on Top and Bottom Boundary Γ_Q

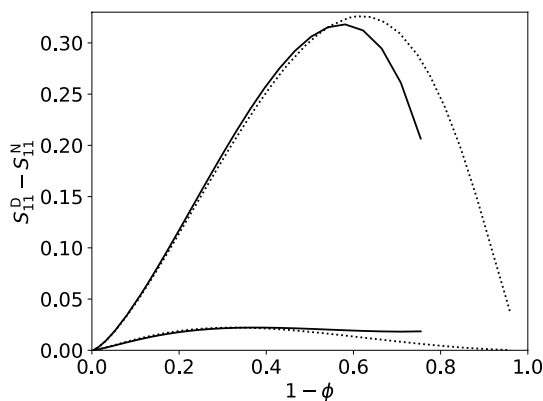
As shown in Sections 4.3 - 4.4, the cell problems for effective heat conductivities in case of Neumann and Dirichlet boundary conditions on Γ_Q differ. Despite the similar structure of the equations as given in (77) and (79), the respective cell problems $(P^{\text{heat}, \text{N}}(\mathbf{x}))$ and $(P^{\text{heat}, \text{D}}(\mathbf{x}))$ apply different boundary conditions. In the following, we consider circular

cylinder-shaped grains of different radii and compare the results for the two boundary condition types on Γ_Q . The resulting effective heat conductivities are shown in Fig. 3a.

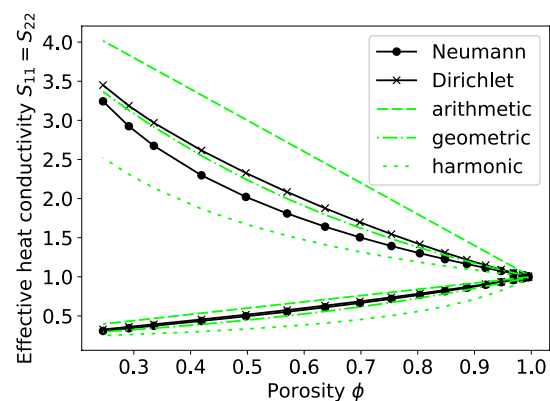
The results for Neumann boundary conditions are consistent with the ones presented and discussed in Bringedal and Kumar (2017), where two-dimensional cell problems without the effect of boundary conditions were considered. However, this is due to fact that the grain shapes do not vary along the vertical axis in this case. For Dirichlet boundary conditions, we obtain a similar behavior with respect to varying the size of the grain, but overall larger effective heat conductivities. In the trivial case of $k = 1$, fluid and grain have the same heat conductivity and we obtain the same constant effective heat conductivity for Neumann and Dirichlet boundary conditions. However, for $k \neq 1$ the effective heat



(a) Results for Neumann (dark-colored) and Dirichlet (light-colored) boundary conditions in case of a cylinder-shaped grain



(b) Difference $S_{11}^D - S_{11}^N$ for a cylinder-shaped grain and a cuboid-shaped grain (dotted line) for comparison. Upper lines are based on $k = 5.0$, bottom lines on $k = 0.2$. Note that the minimum porosity for cylinder-shaped grains is 0.2, while cuboid-shaped grains can approach 0



(c) Results for $k = 5$ (top curves) and $k = 0.2$ (bottom curves) together with porosity-weighted averages for cylinder-shaped grains as a function of porosity

Fig. 3 Comparison of the effective heat conductivities ($S_{11}^D = S_{22}^D$ and $S_{11}^N = S_{22}^N$) for Neumann and Dirichlet boundary conditions on the top and bottom boundary Γ_Q

conductivity is always larger in case of Dirichlet boundary conditions than for Neumann boundary conditions on Γ_Q . This positive impact of Dirichlet boundary conditions is due to them representing perfect heat conduction on Γ_Q . If we consider the respective difference in detail for a cylinder and a cuboid, as shown in Fig. 3b, we observe that for $\phi \rightarrow 0$ and $\phi \rightarrow 1$, meaning the grain fills almost all of the void space or its size is negligible, this difference goes down to zero. This is the case because the local domain is almost homogeneous and therefore equally heat conductive, independently of the boundary conditions. For porosities that are neither close to zero nor close to one the choice of Dirichlet boundary conditions has a strong, positive effect on the effective heat conductivity.

Note that the surface area between fluid and grain is proportional to the radius when considering cylinder-shaped grain. Hence, Fig. 3a can be read as effective heat conductivity as a function of fluid-grain surface area when scaling the horizontal axis with a factor $2\pi H = 2\pi$ for this setup. Hence, when one knows that the grains are cylinder-shaped, the effective heat conductivity can be determined by the cylinder radius, correspondingly the fluid-grain surface area.

Since effective heat conductivities for porous media are often calculated in terms of porosity-weighted averages of the individual heat conductivities found in fluid and grain (see, e.g., Nield and Bejan 2017), we compare in Fig. 3c the effective heat conductivities found through the cell problems with such averages. The averages are calculated through

$$\begin{aligned}
 S_{\text{arithmetic}} &= \kappa_f \phi + \kappa_g (1 - \phi), \\
 S_{\text{geometric}} &= \kappa_f^\phi + \kappa_g^{1-\phi}, \\
 S_{\text{harmonic}} &= \frac{1}{\frac{\phi}{\kappa_f} + \frac{1-\phi}{\kappa_g}}.
 \end{aligned}$$

As seen in Fig. 3c, and as pointed out earlier in Bringedal and Kumar (2017) for two-dimensional porous media without the influence of top and bottom boundary conditions, these porosity-weighted averages offer approximate values for the effective heat conductivity, but cannot predict the detailed behavior as the porosity varies.

6.2 Effect of Different Grain Shapes

We are interested in understanding to which extent the effective heat conductivity is affected by changes within the cross-sectional shape of the grain along the z -axis. The resulting equations for the effective heat conductivities (77) and (79) directly indicate the impact of the porosity on the effective heat conductivity. Therefore, we compare different grain shapes but always using the same grain volume $|Q_g^{\text{ref}}|$ in order to account for effects of the detailed shape. Since we consider the same porosity, any porosity-weighted average would always give the same value (for fixed κ_f and κ_g) independent of the shape. All considered shapes are rotationally symmetric with respect to the z -axis. Hence, we can introduce $r(z) : [0, 1] \rightarrow [0, 0.5]$ to describe the grain radius perpendicular to the axis for different values of z . Further, the minimum and maximum radius of a grain are given by

$$r_{\min} = \min_{z \in [0,1]} r(z), \quad r_{\max} = \max_{z \in [0,1]} r(z).$$

As grain reference volume $|Q_g^{\text{ref}}|$, we use a cylinder with radius $r^{\text{cyl}}(z) = 0.25$. In addition to the cylinder, we construct a cone-shaped as well as an ellipsoid-shaped grain which have the same volume as our reference grain. They are defined by

$$r^{\text{con}}(z) = (r_{\text{min}}^{\text{con}} - r_{\text{max}}^{\text{con}})z + r_{\text{max}}^{\text{con}},$$

$$r^{\text{ell}}(z) = \sqrt{(r_{\text{max}}^{\text{ell}})^2 - 4[(r_{\text{max}}^{\text{ell}})^2 - (r_{\text{min}}^{\text{ell}})^2]\left(z - \frac{1}{2}\right)^2}.$$

In order to ensure that all grains are of the same volume $|Q_g^{\text{ref}}|$, we obtain the following restrictions on the minimum and maximum radii of the cone and the ellipsoid for $r_{\text{min}}/r_{\text{max}} \rightarrow 0$:

$$|Q_g^{\text{ref}}| \stackrel{!}{=} \frac{\pi}{3}(r_{\text{max}}^{\text{con}} + r_{\text{min}}^{\text{con}})^2 \quad \Rightarrow r_{\text{max}}^{\text{con}} \rightarrow \frac{\sqrt{3}}{4} \approx 0.433 \text{ for } r_{\text{min}}^{\text{con}} \rightarrow 0,$$

$$|Q_g^{\text{ref}}| \stackrel{!}{=} \frac{\pi}{3}(2(r_{\text{max}}^{\text{ell}})^2 - (r_{\text{min}}^{\text{ell}})^2) \quad \Rightarrow r_{\text{max}}^{\text{ell}} \rightarrow \frac{\sqrt{6}}{8} \approx 0.306 \text{ for } r_{\text{min}}^{\text{ell}} \rightarrow 0.$$

In case of the limit $r_{\text{min}}/r_{\text{max}} \rightarrow 1$, the shapes of ellipsoid and cone approach the shape of the reference cylinder. The detailed setup is sketched in Fig. 4. The minimum and maximum radius of the different shapes satisfy $r_{\text{min}}^{\text{con}} \leq r_{\text{min}}^{\text{ell}} \leq r^{\text{cyl}}$ and $r^{\text{cyl}} \leq r_{\text{max}}^{\text{ell}} \leq r_{\text{max}}^{\text{con}}$ for any given ratio of the radii.

In the following, we compare the effective heat conductivities for different conductivity ratios k and Neumann as well as Dirichlet boundary conditions on the top and bottom boundary Γ_Q . In Fig. 5, we show how the results vary with the ratio $r_{\text{min}}/r_{\text{max}}$, the fluid-grain interfacial area and the contact area between top and bottom boundary and the more conductive phase. We do not show how the results vary with porosity as in Fig. 3, since the porosity is kept constant. Note that since only one cylinder is considered here, the results for the cylinder are included either as a reference line or as a reference point.

Neumann Boundary Conditions on Top and Bottom Boundary Γ_Q The dependence of the effective heat conductivity on the grain shape and the corresponding maximum and minimum radius is clearly visible: A variation of the grain shape causes larger effective heat conductivities. For $k < 1$ (Fig. 5a), the grain is less conductive than the fluid and therefore hinders the overall conduction of heat. Hence, decreasing the minimum radius of the grain causes a better connectivity of the fluid which increases the effective heat conductivity. Recall that in case of an ellipsoid- or cone-shaped grain, the minimum radius is smaller than for the reference cylinder. That is why we observe significant changes in the effective heat conductivity for the ellipsoid and the cone compared to the effective heat conductivity of the reference cylinder for small ratios, especially in the case of a cone-shaped grain, where the smaller minimum radius is found.

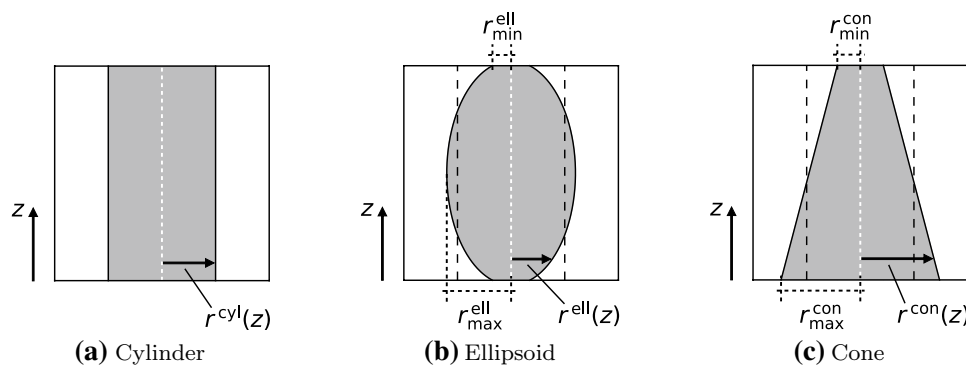
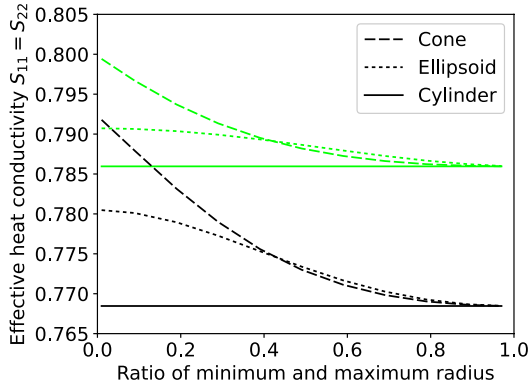
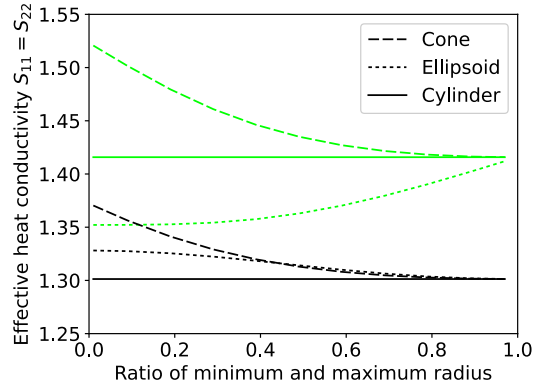


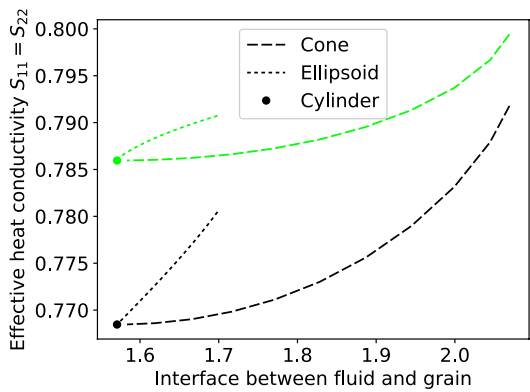
Fig. 4 Setup of the different grain shapes. All are rotationally symmetric with respect to the z -axis. The ratio $r_{\text{min}}/r_{\text{max}}$ for ellipsoid and cone in these figures is approximately 0.3



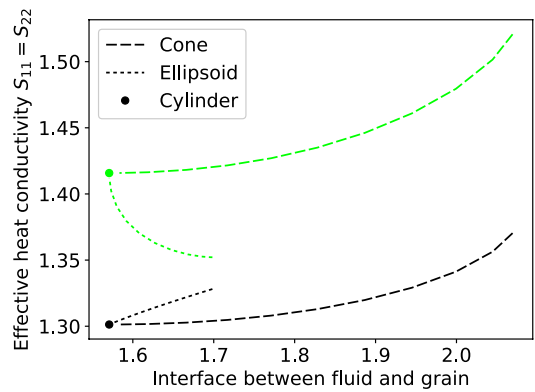
(a) Results for $k = 0.2$ as a function of the ratio r_{\min}/r_{\max}



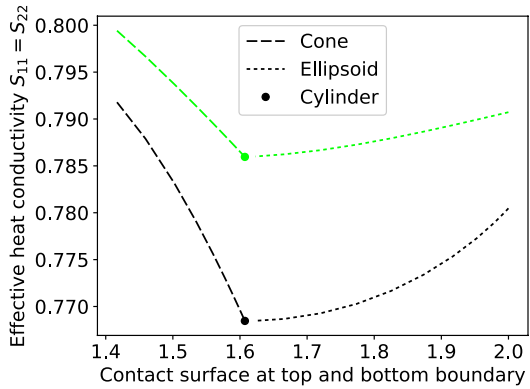
(b) Results for $k = 5.0$ as a function of the ratio r_{\min}/r_{\max}



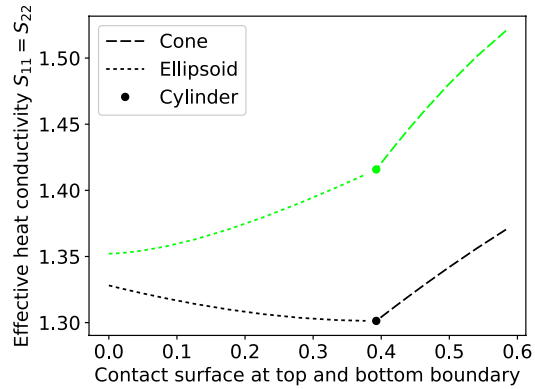
(c) Results for $k = 0.2$ as a function of the fluid-grain surface area



(d) Results for $k = 5.0$ as a function of the fluid-grain surface area



(e) Results for $k = 0.2$ as a function of the fluid contact area with top and bottom boundary



(f) Results for $k = 5.0$ as a function of the grain contact area with top and bottom boundary

Fig. 5 Comparison of the effective heat conductivities for grains with a volume of $|Q_g^{\text{ref}}| = \pi \cdot (0.25)^2$ and different shapes based on the ratio r_{\min}/r_{\max} . The curves represent the results for Neumann (dark-colored) and Dirichlet (light-colored) boundary conditions on the top and bottom boundary Γ_Q . Results for the respective cylinder are given as reference

For $k > 1$ (Fig. 5b), the grain is more conductive than the fluid. Consequently, having better connected grains, meaning a smaller distance between neighboring grains, increases the effective heat conductivity. This is obtained when the maximum radius of the grains

is increased. As mentioned above, the cone and the ellipsoid are characterized by a larger maximum radius compared to the cylinder, which indicates a better connection between the grains in neighboring cells. Therefore, we obtain larger effective heat conductivities also in this case when varying the grain shape, in particular for the cone where a larger maximum radius is found.

The increasing eccentricity of the cone- and ellipsoid-shaped grains corresponds to larger interfacial area between fluid and grain. Hence, for the Neumann boundary conditions, the effective heat conductivities generally increase with increasing surface area between fluid and grain, as seen in Fig. 5c and 5d. However, the interfacial area and value of k alone are not sufficient to determine the effective heat conductivity, and knowledge about the shape (cone or ellipsoid in this case) is also necessary. As seen from Fig. 5e and 5f, although the effective heat conductivity varies with the contact area between top and bottom and the more conductive phase, no specific trend can be determined when using Neumann boundary conditions.

Dirichlet Boundary Conditions on Top and Bottom Boundary Γ_Q By changing the boundary conditions on Γ_Q , we expect the effective heat conductivities to increase due to the positive impact of Dirichlet boundary conditions as discussed in the previous Sect. 6.1. However, the magnitude and overall importance of the positive impact of Dirichlet boundary conditions depends on the surface area of the fluid (for $k < 1$) or the grain (for $k > 1$), respectively, toward Γ_Q . In case of $k < 1$, the grain hinders the conduction of heat. Hence, the impact of Dirichlet boundary conditions is expected to be larger if the fluid has a larger surface area toward Γ_Q . This corresponds to $r(z)$ being smaller on Γ_Q . For $k > 1$, the opposite holds: A larger surface area of the grains toward Γ_Q increases the effective conductivities under Dirichlet boundary conditions. That is achieved by a larger radius $r(z)$.

We observe the same behavior for $k < 1$ (Fig. 5a) as in the corresponding case of Neumann boundary conditions but with the mentioned general increase based on the different boundary conditions. However, the interplay between increased fluid-grain interface area and the contact area between fluid and top and bottom is not straightforward. In Fig. 5c and 5e, we see how the ellipsoid generally shows an increasing trend with both interfacial area and contact area to top and bottom, while the cone is dominated by the increased interfacial area.

For $k > 1$ (Fig. 5b), the effective heat conductivities are still always larger than in the corresponding case of Neumann boundary conditions on Γ_Q . However, the values for an ellipsoid-shaped grain are now significantly smaller than for the reference cylinder. An ellipsoid-shaped grain has less surface area toward Γ_Q , especially for small ratios and therefore small r_{\min}^{ell} . In case of a cylinder, the grains exhibit a larger surface area toward Γ_Q since $r^{\text{cyl}} \geq r_{\min}^{\text{ell}}$. The results for a cone-shaped grain remain above the ones for the cylinder since the cone-shaped grain has a large surface area to the bottom boundary. This is visible in Fig. 5d and 5f. The effective heat conductivities for the cone- and ellipsoid-shaped grains are dominated by the increased contact area between grain and top and bottom boundaries. Here, the ellipsoid's effective heat conductivity therefore decreases with increased fluid-grain interfacial area.

Summary and Implications for Effective Heat Conductivities Both in the case of Dirichlet and Neumann boundary conditions at the top and bottom boundaries, information about the fluid-grain surface area and/or contact area to the top and bottom boundaries and porosity are not sufficient to determine the effective heat conductivity. Knowledge of the grain shape is also needed. Depending on the shape, different trends or dependencies on these surface areas are expected. As observed in Sect. 6.1 for circular cylinders, common porosity-weighted averages of the fluid and grain give at best an approximation of the overall effective heat

conductivity and cannot account for different shapes nor boundary conditions. Hence, if accurate knowledge of the effective heat conductivity is required, solutions of the cell problems ($P^{\text{heat, N}}(\mathbf{x})$) and ($P^{\text{heat, D}}(\mathbf{x})$) are necessary.

6.3 Comparison Between the Original and Upscaled Model

We here address the influence of the upscaling procedure by comparing the results from the original pore-scale model on an oscillating three-dimensional domain with the upscaled model on an effective two-dimensional domain using the estimated effective heat conductivity. Since we want to focus on the effective heat conductivity, we design a simplified setup employing heat conduction only. Comparison between pore-scale and upscaled approaches for flow can be found, e.g., in Wagner et al. (2021). The domains for the original pore-scale and upscaled models are shown in Fig. 6. The full pore-scale domain consists of 14×10 cylinders, with radius 0.2 and 0.4 in the left and right half of the domain, respectively. This domain corresponds to $\varepsilon = 0.1$.

We consider steady-state heat conduction, hence we solve

$$\begin{aligned} \nabla \cdot (\kappa_f \nabla T_f) &= 0 \text{ in } \Omega_f^\varepsilon, \\ \nabla \cdot (\kappa_g \nabla T_g) &= 0 \text{ in } \Omega_g^\varepsilon, \\ \kappa_f \nabla T_f &= \kappa_g \nabla T_g \text{ on } S_\Omega^\varepsilon, \\ T_f &= T_g \text{ on } S_\Omega^\varepsilon, \end{aligned}$$

on the three-dimensional pore-scale domain (Fig. 6a), and

$$\nabla_x \cdot (\mathbf{S} \nabla_x T) = 0$$

on the two-dimensional upscaled domain (Fig. 6b). The temperatures T_f and T_g from the pore-scale model will give the full variability, including any local oscillations, while the effective temperature T from the upscaled model can only account for the average behavior. For the left and right boundaries, we apply Dirichlet boundary conditions, using $T_1 = 0$ and

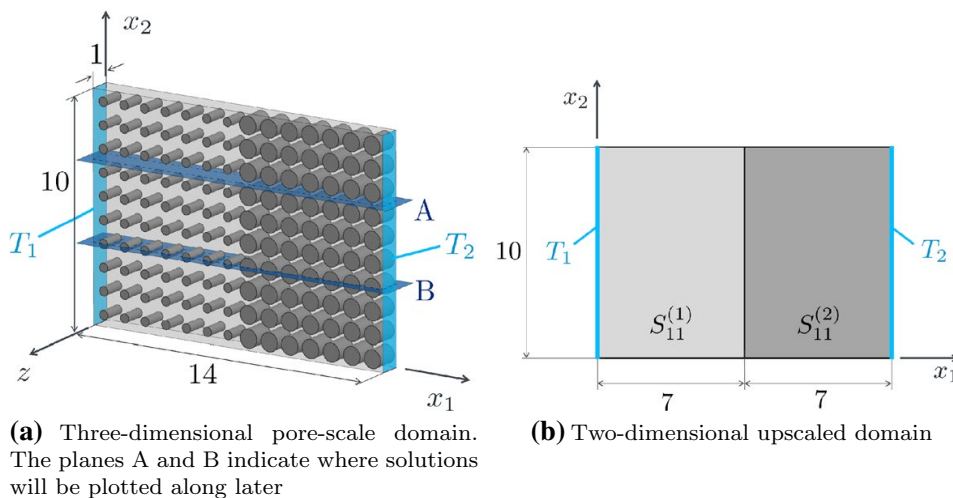
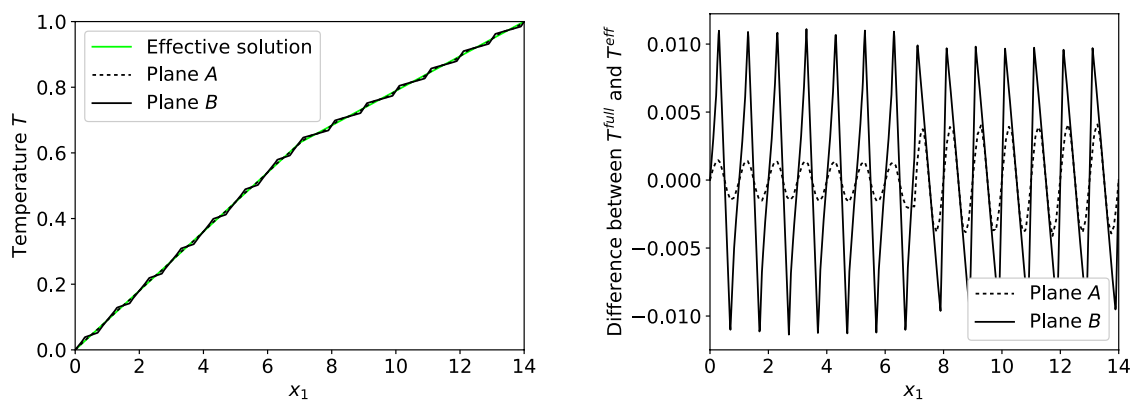


Fig. 6 Computational domains for the pore-scale (left) and upscaled (right) models. The pore-scale domain consists of 14×10 cylinders, with two different radii. The upscaled domain hence has two different effective heat conductivities, denoted $S_{11}^{(1)}$ and $S_{11}^{(2)}$. The left and right boundaries have Dirichlet boundary conditions, using $T_1 = 0$ and $T_2 = 1$. The other boundaries have homogeneous Neumann boundary conditions

$T_2 = 1$ (see Fig. 6), while the long-sides boundaries have homogeneous Neumann boundary conditions. For the pore-scale domain, the top and bottom boundaries fulfill homogeneous Neumann boundary conditions. We set $\kappa_f = 1$ and $\kappa_g = 5$, which is also used to find the effective heat conductivity in the two halves of the upscaled domain through $(P^{\text{heat}, N}(\mathbf{x}))$ and (77). Since the upscaled heat conductivities are isotropic tensors, we only need the first component and we have that $S_{11}^{(1)} = 1.183$ and $S_{11}^{(2)} = 2.021$ for the left and right halves of the upscaled domain, respectively. Both domains are meshed using Netgen and solved with finite elements through third order subspaces of H^1 using NGSolve. Since $h_{\max} = 0.1$ was found to be sufficient for the accuracy of the cell problems, we employ that here for the full pore-scale domain. This leads to a total of 782 201 grid cells as many internal boundaries need to be resolved by the mesh. The upscaled domain is two-dimensional and meshed with 318 grid cells. By comparing with (upscaled) solutions on finer meshes, we estimate the accuracy of the upscaled model to be five significant digits on this coarse mesh.

Since the temperatures in the pore-scale domain do not vary with the vertical direction (but with both horizontal directions), we can plot the solution along the planes A and B (marked in Fig. 6a) as lines. The effective temperature in the upscaled model does not vary in the x_2 -direction. The full solutions along the planes A and B and the effective solution from the upscaled model along the x_1 -direction are shown in Fig. 7. The temperatures are found to match very well, although small-scale oscillations are found in the full solution which are not captured by the upscaled model. This is expected since we use a nonzero value of ε . From the difference plot in Fig. 7b, the changes are found to be larger when considering a plane crossing through both fluid and grains in the pore-scale domain (plane B). However, the average of the deviations for each unit cell is close to zero, showing that the upscaled model captures the average behavior almost perfectly. Increased deviations near the external boundaries and near the transition at $x_1 = 7$ are not observed. Comparing the heat flux in the x_1 -direction (not shown) gives a similar deviation between the full pore-scale solution and the effective solution as shown in Fig. 7b, with maximum deviation around 0.08.

Note in particular that for the same estimated accuracy, the full pore-scale domain needed over 780 000 grid cells, while the upscaled domain was discretized using only 318 grid cells. To find the effective heat conductivities, we have to solve local cell problems as well. For this setup, the cell problems were discretized using 218 and 184 grid cells. Here,



(a) Temperature across respective domains from the upscaled model and along two planes in the full pore-scale model

(b) Difference between the full pore-scale solution and the effective solution from the upscaled model

Fig. 7 Effective solution from upscaled model and full solution from pore-scale model

only two different pore-scale geometries had to be accounted for, but even if more types of different (three-dimensional) geometries are used, the computational gain of rather solving several small, local problems followed by the upscaled problem is significant compared to solving the full pore-scale problem.

7 Conclusion

In this paper, effective heat transport through thin porous media has been considered. Starting with a pore-scale description, upscaled equations at the Darcy scale have been derived using formal homogenization, while accounting for the porous medium being thin. The Darcy-scale equations rely on the effective permeability as well as the effective heat conductivity of the porous medium which are found through solving local cell problems at the pore scale. These quantities account for the pore geometry as well as the boundary conditions on the top and bottom boundaries of the porous domain.

As a consequence, the effective heat conductivity can be used as an assessment tool for a material's local heat conduction properties without requiring to solve the whole model at the Darcy scale nor at the pore scale. Instead, only small local cell problems need to be solved. Since the cell problems are generally solved on smaller portions of the original domain, they are cheap to solve compared to discretizing and solving the full pore-scale domain. Also, the original pore-scale model is highly coupled, while the cell problems can be solved independently of each other. For homogeneous media, the cell problem solutions and hence effective parameters can be reused, while for heterogeneous media, many cell problems need to be solved. However, solving many small problems is generally cheaper than solving one larger problem from a computational perspective. Furthermore, the cell problems can be straightforwardly solved in parallel. The corresponding upscaled problem is two-dimensional and can be solved on a much coarser grid than the original pore-scale domain. In addition, we have shown that under certain assumptions, the three-dimensional cell problems can be reduced to two-dimensional ones. Hence, the computational costs of solving the cell problems can be further decreased in those cases.

The derived formulation emphasizes the dependence of the effective heat conductivity on the individual heat conductivities of fluid and grain, on the detailed pore geometry as well as on the boundary conditions on the top and bottom boundary. If the grains in a porous medium have a higher heat conductivity than the fluid occupying the void space, we can increase the effective heat conductivity either by decreasing the porosity or, for a constant porosity, by decreasing the minimum distance between the grains, i.e., establishing a better connection of the grains. Furthermore, the application of Dirichlet boundary conditions on the top and bottom boundary has a positive impact on the effective heat conductivities compared to Neumann boundary conditions. This positive impact is in particular strong when the surface area of the more conductive grains toward the top and bottom boundary remains large. However, the effective heat conductivity also depends on the grain shapes and cannot be quantified exclusively by simple parameters such as surface area and porosity.

Hence, to assess the effective heat conductivity of thin porous materials based on their properties at the pore scale, the derived strategy offers equations for determining such effective heat conductivities. These equations are cheap to solve and provide the effective heat conductivity locally, while incorporating the effect from the top and bottom boundary conditions and the pore-scale geometry.

Funding Open Access funding enabled and organized by Projekt DEAL. Funded by Deutsche Forschungsgemeinschaft (DFG, German Research Foundation) - Project Number 327154368 - SFB 1313. We thank the DFG for supporting this work by funding - EXC2075 - 390740016 under Germany's Excellence Strategy. We acknowledge the support by the Stuttgart Center for Simulation Science (SimTech).

Data availability Available through doi.org/10.18419/darus-2026.

Declarations

Conflicts of interest The authors declare that they have no conflict of interest.

Open Access This article is licensed under a Creative Commons Attribution 4.0 International License, which permits use, sharing, adaptation, distribution and reproduction in any medium or format, as long as you give appropriate credit to the original author(s) and the source, provide a link to the Creative Commons licence, and indicate if changes were made. The images or other third party material in this article are included in the article's Creative Commons licence, unless indicated otherwise in a credit line to the material. If material is not included in the article's Creative Commons licence and your intended use is not permitted by statutory regulation or exceeds the permitted use, you will need to obtain permission directly from the copyright holder. To view a copy of this licence, visit <http://creativecommons.org/licenses/by/4.0/>.

References

- Asbik, M., Zeghamati, B., Louahlia-Gualous, H., Yan, W.M.: The effect of thermal dispersion on free convection film condensation on a vertical plate with a thin porous layer. *Transp. Porous Media* **67**(3), 335 (2006)
- Auriault, J.-L., Boutin, C., Geindreau, C.: *Homogenization of coupled phenomena in heterogeneous media*. Wiley, Hoboken (2009)
- Auriault, J.L.: Effective macroscopic description for heat conduction in periodic composites. *Int. J. Heat Mass Transf.* **26**(6), 861–869 (1983)
- Belgacem, N., Agaësse, T., Pauchet, J., Prat, M.: Liquid invasion from multiple inlet sources and optimal gas access in a two-layer thin porous medium. *Transp. Porous Media* **115**(3), 449–472 (2016)
- Bhattacharya, A., Gahn, M., Neuss-Radu, M.: Effective transmission conditions for reaction-diffusion processes in domains separated by thin channels. *Appl. Anal.* 1–15 (2020)
- Bringedal, C., Berre, I., Pop, I.S., Radu, F.A.: A model for non-isothermal flow and mineral precipitation and dissolution in a thin strip. *J. Comput. Appl. Math.* **289**, 346–355 (2015). (Sixth international conference on advanced computational methods in engineering (ACOMEN 2014))
- Bringedal, C., Berre, I., Pop, I.S., Radu, F.A.: Upscaling of non-isothermal reactive porous media flow with changing porosity. *Trans. Porous Media.* **114**(2), 371–93 (2016)
- Bringedal, C., Kumar, K.: Effective behavior near clogging in upscaled equations for non-isothermal reactive porous media flow. *Transp. Porous Media* **120**(3), 553–577 (2017)
- Chen, X., Papathanasiou, T.D.: The transverse permeability of disordered fiber arrays: a statistical correlation in terms of the mean nearest interfiber spacing. *Transp. Porous Media* **71**(2), 233–251 (2008)
- Fabricius, J., Hellström, J.G.I., Lundström, T.S., Miroshnikova, E., Wall, P.: Darcy's law for flow in a periodic thin porous medium confined between two parallel plates. *Transp. Porous Media* **115**(3), 473–493 (2016)
- Gahn, M., Jäger, W., Neuss-Radu, M.: Correctors and error estimates for reaction-diffusion processes through thin heterogeneous layers in case of homogenized equations with interface diffusion. *J. Comput. Appl. Math.* **383**, 13126 (2021)
- Gahn, M., Neuss-Radu, M., Knabner, P.: Derivation of effective transmission conditions for domains separated by a membrane for different scaling of membrane diffusivity. *Disc. Contin. Dyn. Syst.- S* **10**(4), 773–797 (2017)
- Gahn, M., Neuss-Radu, M., Knabner, P.: Effective interface conditions for processes through thin heterogeneous layers with nonlinear transmission at the microscopic bulk-layer interface. *Netw. Heterog. Media* **13**(4), 609–640 (2018)
- Hellström, J.G.I., Jonsson, P.J.P., Lundström, S.: Laminar and turbulent flow through an array of cylinders. *J. Porous Media* **13**(12), 1073–1085 (2010)

- Hornung, U. (ed.): Homogenization and porous media. Springer-Verlag, Berlin, Heidelberg (1997)
- Hsu, C.T.: A closure model for transient heat conduction in porous media. *J. Heat Transfer* **121**(3), 733–739 (1999)
- Schöberl, J.: C++11 Implementation of finite elements in NGSolve. Technical Report ASC Report 30/2014, Institute for Analysis and Scientific Computing, Vienna University of Technology, Sep (2014). <https://www.asc.tuwien.ac.at/schoeberl/wiki/publications/ngs-cpp11.pdf>
- Koch, D.L., Ladd, A.J.C.: Moderate Reynolds number flows through periodic and random arrays of aligned cylinders. *J. Fluid Mech.* **349**, 31–66 (1997)
- Kumar, K., List, F., Pop, I.S., Radu, F.A.: Formal upscaling and numerical validation of unsaturated flow models in fractured porous media. *J. Comput. Phys.* **407**, 109138 (2020)
- Landau, L.D., Lifshitz, E.M.: Fluid mechanics, volume 6 of Course of Theoretical Physics. Pergamon Press, : Translated from the Russian by J. B. Sykes and W. H. Reid (1987)
- Lasseux, D., Valdés-Parada, F.J.: On the developments of Darcy’s law to include inertial and slip effects. *Comptes Rendus Mécanique* **345**(9), 660–669 (2017)
- Scholz, L., Bringedal, C.: Code for effective heat conductivity in thin porous media (2021). <https://doi.org/10.18419/darus-2026>
- List, F., Kumar, K., Pop, I. S., Radu, F. A.: Rigorous upscaling of unsaturated flow in fractured porous media. *SIAM J. Math. Anal.* **52**(1), 239–276 (2020)
- Lunowa, S.B., Bringedal, C., Pop, I.S.: On an averaged model for immiscible two-phase flow with surface tension and dynamic contact angle in a thin strip. *Stud. Appl. Math* **147**(1), 84–126 (2021)
- Michaud, V.: A review of non-saturated resin flow in liquid composite moulding processes. *Transp. Porous Media* **115**(3), 581–601 (2016)
- Neuss-Radu, M., Jäger, W.: Effective transmission conditions for reaction-diffusion processes in domains separated by an interface. *SIAM J. Math. Anal.* **39**(3), 687–720 (2007)
- Nield, D.A., Bejan, A.: Convection in porous media. Springer, Cham (2017)
- Quintard, M., Kaviany, M., Whitaker, S.: Two-medium treatment of heat transfer in porous media: numerical results for effective properties. *Adv. Water Resour.* **20**(2), 77–94 (1997)
- Ranut, P., Nobile, E.: On the effective thermal conductivity of metal foams. *J. Phys: Conf. Ser.* **547**, 012021 (2014)
- Sharmin, S., Bringedal, C., Pop, I.S.: On upscaling pore-scale models for two-phase flow with evolving interfaces. *Adv. Water Resour.* **142**, 103646 (2020)
- Koch, T., Weishaupt, K., Müller, J., Weigand, B., Helmig, R.: A (dual) network model for heat transfer in porous media. *Transp. Porous Media* **140**, 107–141 (2021)
- van Noorden, T.L.: Crystal precipitation and dissolution in a thin strip. *Eur. J. Appl. Math.* **20**(1), 69–91 (2009)
- van Noorden, T.L., Pop, I.S., Ebigbo, A., Helmig, R.: An upscaled model for biofilm growth in a thin strip. *Water Resour. Res.* **46**(6), 6 (2010)
- Wagner, A., Eggenweiler, E., Weinhardt, F., Trivedi, Z., Krach, D., Lohrmann, C., Jain, K., Karadimitriou, N., Bringedal, C., Volland, P., Holm, C., Class, H., Steeb, H., Rybak, I.: Permeability estimation of regular porous structures: a benchmark for comparison of methods. *Transp. Porous Media* **138**(1), 1–23 (2021)
- Whitaker, S.: The method of volume averaging. Springer, Netherlands, Dordrecht (1999)

Publisher’s Note Springer Nature remains neutral with regard to jurisdictional claims in published maps and institutional affiliations.

4 Effective heat transport near clogging

The content of this chapter is based on the following original article:

C. Bringedal and K. Kumar. *Effective Behavior Near Clogging in Upscaled Equations for Non-isothermal Reactive Porous Media Flow*. *Transport in Porous Media* 120.3 (2017), pp. 553–577. doi: 10.1007/s11242-017-0940-y.

Reprinted by permission from Springer.

Effective Behavior Near Clogging in Upscaled Equations for Non-isothermal Reactive Porous Media Flow

Carina Bringedal^{1,3}  · Kundan Kumar²

Received: 12 June 2017 / Accepted: 21 September 2017 / Published online: 9 October 2017
© Springer Science+Business Media B.V. 2017

Abstract For a non-isothermal reactive flow process, effective properties such as permeability and heat conductivity change as the underlying pore structure evolves. We investigate changes of the effective properties for a two-dimensional periodic porous medium as the grain geometry changes. We consider specific grain shapes and study the evolution by solving the cell problems numerically for an upscaled model derived in Bringedal et al. (Transp Porous Media 114(2):371–393, 2016. doi:[10.1007/s11242-015-0530-9](https://doi.org/10.1007/s11242-015-0530-9)). In particular, we focus on the limit behavior near clogging. The effective heat conductivities are compared to common porosity-weighted volume averaging approximations, and we find that geometric averages perform better than arithmetic and harmonic for isotropic media, while the optimal choice for anisotropic media depends on the degree and direction of the anisotropy. An approximate analytical expression is found to perform well for the isotropic effective heat conductivity. The permeability is compared to some commonly used approaches focusing on the limiting behavior near clogging, where a fitted power law is found to behave reasonably well. The resulting macroscale equations are tested on a case where the geochemical reactions cause pore clogging and a corresponding change in the flow and transport behavior at Darcy scale. As pores clog the flow paths shift away, while heat conduction increases in regions with lower porosity.

Keywords Upscaling · Homogenization · Free boundary · Periodic porous medium · Clogging · Reactive flow

Carina Bringedal
carina.bringedal@uib.no; carina.bringedal@uhasselt.be

Kundan Kumar
kundan.kumar@uib.no

¹ Geophysical Institute, University of Bergen, PO Box 7803, 5020 Bergen, Norway

² Department of Mathematics, University of Bergen, PO Box 7803, 5020 Bergen, Norway

³ Faculty of Sciences, University of Hasselt, Campus Diepenbeek, Agoralaan building D, BE3590 Diepenbeek, Belgium

1 Introduction

Geothermal reservoirs may encounter porosity changes induced by geochemical reactions in the pores. The injected water and the in situ brine have different temperatures and chemical composition, triggering mineral precipitation and/or dissolution. These chemical reactions cause reservoir rock properties to develop dynamically with time due to the porosity changes. When porosity is altered, the flow conditions are affected and the permeability of the medium will change. Also, as the volume contribution of fluid and rock change, effective properties such as heat conductivity are affected. For a geothermal reservoir, where subsurface heat transport and fluid flow are of high importance for the heat production performance, changes in such properties are important to model accurately to account for their possible impacts on operating conditions.

As reported from field studies and simulations, porosity and permeability changes due to precipitation and dissolution of minerals as silica, quartz, anhydrite, gypsum and calcite can occur when exploiting geothermal reservoirs (Libbey and Williams-Jones 2016; McNamara et al. 2016; Mielke et al. 2015; Mroczek et al. 2000; Pape et al. 2005; Sonnenthal et al. 2005; Taron and Elsworth 2009; Wagner et al. 2005; White and Mroczek 1998; Xu et al. 2009). These fluid–rock interactions can alter and possibly clog flow paths, potentially affecting the performance of the geothermal plant significantly. Modeling of the mineral precipitation and dissolution is important to understand the processes and to better estimate to which extent the chemical reactions can affect the permeability and other effective properties of the porous medium. However, reactive transport affecting flow properties and heat transport can be particularly challenging to model due to the processes jointly affecting each other.

When investigating porosity and permeability changes, understanding the underlying processes at the pore scale is essential for highly coupled problems. The pore geometry affects the reaction rates as the reactive surface develops, while the permeability depends on how the geometry changes. Also, ion diffusivity and heat conductivity can be affected by the grain shape and can be anisotropic. Hence, using a Darcy scale model based on an upscaled pore-scale model can give a better representation of the effective properties than common porosity-weighted average approaches. Pore-scale models incorporating mineral precipitation and dissolution have been studied earlier in van Duijn and Pop (2004) and van Noorden et al. (2007), and the corresponding Darcy scale models have been investigated both analytically and numerically further in van Duijn and Knabner (1997), Knabner et al. (1995), Kumar et al. (2013a, 2014). The rigorous derivation of upscaled model starting from the pore-scale model in van Duijn and Pop (2004) has been performed in Kumar et al. (2016) using two-scale convergence framework. These papers assume the pore geometry to be fixed, which is a valid assumption if the mineral layer is not changed much compared to the pore aperture. Upscaled pore-scale models honoring porosity changes are found in Kumar et al. (2011, 2013b), van Noorden (2009a, b). In these papers, the position of the interface between grain and void space is tracked, giving a problem with a free boundary. Similar models can also be obtained for biofilm growth (van Noorden 2010), for drug release from collagen matrices (Ray et al. 2013), and on an evolving microstructure (Peter 2009). These models do not include any temperature dependence in the reaction rates nor any heat transfer.

The present work builds on the pore-scale model for coupled heat transport and reactive transport in a thin strip first formulated by Bringedal et al. (2015). Later, this model was formulated for a periodic porous medium and upscaled to Darcy scale by Bringedal et al. (2016). The freely moving interface between the mineral layer and the void space is modeled through a level set function at the pore scale. The authors derive two-dimensional effective

equations honoring the pore-scale dependence through cell problems. The geometry is the same as considered by van Noorden (2009a), where Bringedal et al. (2016) also include heat transport as well as temperature effects in the fluid flow and in the chemical reactions. Including heat transport introduced a coupled cell problem at the pore scale with energy conservation in the void space and in the grain space, allowing for a more realistic transport of the conductive heat transfer through the pore. For geothermal systems, modeling the temperature dependences and heat transport correctly is crucial. We will build upon the upscaled model derived in Bringedal et al. (2016) by solving the cell problems and investigate the behavior of the resulting effective properties. Further, to test the model we consider an idealized case study where clogging occurs. The model by Bringedal et al. (2016) does not allow phase change, but we mention that (Duval et al. 2004) upscaled decoupled two-phase flow with phase change using volume averaging.

The effective model in Bringedal et al. (2016) is derived for a two-dimensional domain, but Schulz et al. (2016) recently derived an effective three-dimensional model for an isothermal reactive model without flow. The extension from two to three spatial dimensions could be performed by defining a tangent plane for the fluid–grain interface in the upscaling procedure, while the resulting effective model has the same appearance as in the two-dimensional case. The present paper deals only with the two-dimensional case, but a three-dimensional interpretation of the results is possible.

Our interest in this work stems from developing efficient computational techniques for deformable porous medium, in particular, in the limit case of clogging. As the upscaled equations in Bringedal et al. (2016) (see Sect. 2) show, the Darcy scale model is coupled to cell problems (pore-scale processes) via their coefficients depending upon the grain geometry. The latter is described by a level set and is in turn impacted by the Darcy scale variables such as pressure and temperature. In terms of discretization, in the upscaled two-scale model, there is a cell problem at each spatial mesh point. To obtain the effective parameters at the Darcy scale, the grain geometry at the cell problem needs to be updated at each time step and the corresponding problems need to be solved. Therefore, solving the upscaled model implies that *at each time step and at each spatial mesh point*, we need to solve as many cell problems as there are spatial mesh points to obtain the corresponding effective parameters. Assuming the Darcy scale domain to be a 2D domain, the upscaled model is a 4-dimensional model (2-dimensional for the cell problem and 2-dimensional for the Darcy scale domain). Even if these cell problems can be solved in parallel, the computational efforts involved are quite huge. Our approach here can be seen as a simplification of this full fledged approach. We assume that the geometry at the pore scale can be characterized by a single parameter and hence, the level set equation becomes an ordinary differential equation. Next, instead of solving the cell problems at each time step, we develop relationships (e.g., polynomial law) of the effective parameters based on the geometry parameter. As a result, solving the upscaled model requires simply using these fitted polynomials for the parameters drastically reducing the computational costs. Our approach should be contrasted with the prevalent approaches of treating porosity as an unknown, defining an ordinary differential equation for its evolution and using engineering correlations for the effective parameters such as permeability, heat conductivity, and diffusion coefficient (see, e.g., Chadam et al. 1986, 1991; Zhao 2014). In contrast to using the heuristic correlations, we use the homogenization approach to provide the polynomial fit. Moreover, even though we simplify the situation here by characterizing the geometry by only one unknown, this approach can be extended to include more parameters for characterizing the geometry and higher-order fits for the effective parameters.

Our contributions in this work are in studying the evolution of effective quantities, specially near the critical porosity limit, by solving the cell problems for certain grain geometries.

This work may also be interpreted as an extension of similar studies as (van Noorden 2009a) to a non-isothermal case and a focus on the near-clogging scenario. Additionally, we also provide an approximate closed form analytical solution for the cell problem and show its accuracy by comparing it to the detailed numerical simulations. In practice, there are several correlations used in engineering literature coupling porosity and effective quantities (see, e.g., Verma and Pruess 1988, Eq. 6 below). We enrich this study by comparing some of these correlations to homogenization approach for evolving geometry. The cell problem, as obtained from the homogenization theory, is solved to provide the effective parameters for the different geometries providing us plots for the effective parameters versus the geometry. We can interpret our approach as a derivation of these correlation-type relationships. Moreover, the changes in the geometry at the pore scale may not always be symmetric. Our approach allows the flexibility of characterizing the geometry in more than one variable and then studying this variation. Naturally, the more variables we take for characterizing the geometry at the pore scale, we get the flexibility of describing more complex geometries, but the offline computational costs increase. We also report a numerical study showing the impact of pore-scale geometry changes on the Darcy scale flow and transport.

The structure of this paper is as follows. In Sect. 2, we present the effective equations with corresponding cell problems, while in Sect. 3 we solve the cell problems numerically. Section 4 compares the numerical solution of the cell problems with analytical solution of approximate cell problems, before considering a macroscale case study with clogging in Sect. 5. The paper ends with a summary with some comments on applications together with some concluding remarks.

2 Effective Equations and Cell Problems

The non-dimensional upscaled model by Bringedal et al. (2016) considers coupled reactive flow with heat transport and varying porosity. We state here the resulting upscaled model and refer to Bringedal et al. (2016) for the derivation and underlying assumptions, and references therein for justification of model choices. In the general formulation, still using a level set function to describe the pore structure, the model consists of the five (non-dimensional) unknowns $S(x, y, t)$, $u(x, t)$, $T(x, t)$, $\bar{\mathbf{q}}(x, t)$ and $p(x, t)$, which are the level set function, macroscopic ion concentration, temperature, flow rate and pressure, respectively. All but the first depend only on time t and spatial variable x , which is defined for all $x = (x_1, x_2) \in \Omega$, Ω being the macroscopic, i.e., the Darcy scale, domain. The level set function $S(x, y, t)$ also depends on the microscopic variable $y = (y_1, y_2) \in [-\frac{1}{2}, \frac{1}{2}]^2$, where y is as a zoomed-in variable resolving the pore structure at a specific macroscopic point $x \in \Omega$. The five non-dimensional upscaled equations are ($x \in \Omega, t > 0$)

$$\begin{aligned} \partial_t \left(\rho S(x, y, t) \right) &= f(T, u, y) |\nabla_y S(x, y, t)|, \\ \partial_t \left(|Y_0(x, t)| u(x, t) + |G_0(x, t)| \rho \right) + \nabla_x \cdot \left(\bar{\mathbf{q}}(x, t) u(x, t) \right) \\ &= \nabla_x \cdot \left(D \mathcal{A}_u(x, t) \nabla_x u(x, t) \right), \\ \partial_t \left(|Y_0(x, t)| \rho_f(T) T(x, t) + |G_0(x, t)| \zeta \rho T(x, t) \right) + \nabla_x \cdot \left(\rho_f(T) \bar{\mathbf{q}}(x, t) T(x, t) \right) \\ &= \nabla_x \cdot \left(\kappa_f \mathcal{A}_f(x, t) \nabla_x T(x, t) + \kappa_g \mathcal{A}_g(x, t) \nabla_x T(x, t) \right), \end{aligned}$$

$$\partial_t \left(|Y_0(x, t)|\rho_f(T) + |G_0(x, t)|2\rho \right) + \nabla_x \cdot \left(\rho_f(T)\bar{\mathbf{q}}(x, t) \right) = 0,$$

$$\bar{\mathbf{q}}(x, t) = -\frac{1}{\mu_f(T)}\mathcal{K}(x, t)\nabla_x p(x, t).$$

In the above equations, ρ is the constant molecular density of the mineral, while ρ_f and μ_f are the molecular density and viscosity of the fluid and are allowed to depend on temperature. Further, D is the molecular diffusivity of the fluid, while κ_f and κ_g are the heat conductivities of fluid and grain, respectively. These are considered properties of the fluid/grain and are constant. The reaction rate f describes the mineral precipitation and dissolution and is given by

$$f(T, u, y) = ke^{-\alpha/T} \left(\frac{u^2}{K_m(T)} - w(\text{dist}(y, B), T, u) \right),$$

where k is the Damköhler number, and $\alpha = E/RT_{\text{ref}}$ where E is the activation energy, R the gas constant and T_{ref} a reference temperature. Further, $K_m(T)$ is the solubility of the mineral in question, and the function $w(\text{dist}(y, B), T, u)$ is defined by

$$w(d, T, u) = \begin{cases} 0 & \text{if } d < 0, \\ \min \left(\frac{u^2}{K_m(T)}, 1 \right) & \text{if } d = 0, \\ 1 & \text{if } d > 0, \end{cases} \tag{1}$$

where the distance corresponds to the width of the mineral layer. The spaces $G_0(x, t)$, $Y_0(x, t)$ and $\Gamma_0(x, t)$ refer to the microscopic grain space, void space and the interface between them, inside the unit cell $y \in [-\frac{1}{2}, \frac{1}{2}]^2$, see Fig. 1. These spaces are defined implicitly as where the level set function is positive, negative and zero, respectively. The notation $|\cdot|$ refers to the area (volume) of the space. The effective coefficients \mathcal{A}_u , \mathcal{A}_f , \mathcal{A}_g , and \mathcal{K} represent the porous medium’s ability to transmit ions through diffusion, heat through conduction in fluid/grain, and fluid through fluid flow. The effective coefficients are tensors with components

$$a_{ij}^u(x, t) = \int_{Y_0(x, t)} (\delta_{ij} + \partial_{y_i} v^j(y)) dy, \tag{2a}$$

$$a_{ij}^f(x, t) = \int_{Y_0(x, t)} (\delta_{ij} + \partial_{y_i} \Theta_f^j(y)) dy, \tag{2b}$$

$$a_{ij}^g(x, t) = \int_{G_0(x, t)} (\delta_{ij} + \partial_{y_i} \Theta_g^j(y)) dy, \tag{2c}$$

$$k_{ij}(x, t) = \int_{Y_0(x, t)} \omega_i^j(y) dy, \tag{2d}$$

respectively, for $i, j = 1, 2$. The functions $v^j(y)$, $\Theta_f^j(y)$, $\Theta_g^j(y)$ and $\omega^j(y)$ are solutions of the cell problems $(x \in \Omega, y \in [-\frac{1}{2}, \frac{1}{2}]^2, t > 0)$

$$\nabla_y^2 v^j(y) = 0 \text{ in } Y_0(x, t) \text{ and } \mathbf{n} \cdot (\mathbf{e}_j + \nabla_y v^j(y)) = 0 \text{ at } \Gamma_0(x, t), \tag{3a}$$

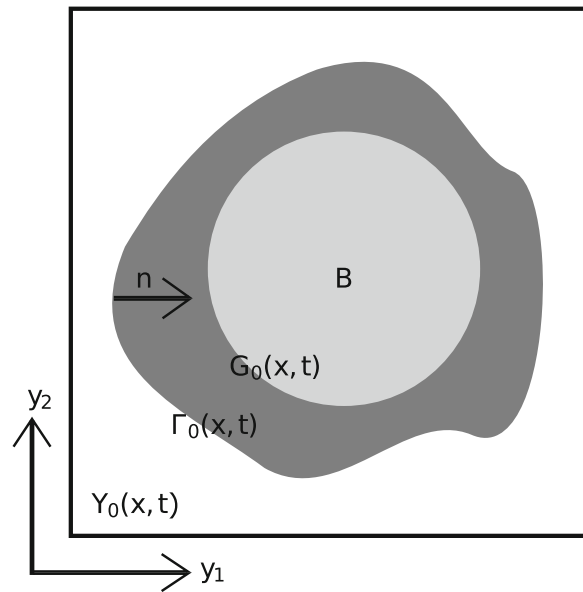
$$\nabla_y^2 \Theta_f^j(y) = 0 \text{ in } Y_0(x, t) \text{ and } \nabla_y^2 \Theta_g^j(y) = 0 \text{ in } G_0(x, t) \text{ where}$$

$$\kappa_f \mathbf{n}_0 \cdot (\mathbf{e}_j + \nabla_y \Theta_f^j(y)) = \kappa_g \mathbf{n}_0 \cdot (\mathbf{e}_j + \nabla_y \Theta_g^j(y))$$

$$\text{and } \Theta_f^j(y) = \Theta_g^j(y) \text{ at } \Gamma_0(x, t), \tag{3b}$$

$$\mathbf{e}_j + \nabla_y \Pi^j(y) = -\nabla_y^2 \omega^j(y) \text{ and } \nabla_y \cdot \omega^j(y) = 0 \text{ in } Y_0(x, t)$$

Fig. 1 Model of microscopic pore, with fluid space $Y_0(x, t)$, grain space $G_0(x, t)$ and the interface between them $\Gamma_0(x, t)$, which has unit normal \mathbf{n} pointing into the grain. Note that the grain consists of both a reactive mineral layer (dark gray) surrounding a non-reactive part B (light gray)



$$\text{and } \omega^j(y) = 0 \text{ at } \Gamma_0(x, t), \tag{3c}$$

together with the periodicity in y for $v^j(y)$, $\Theta_f^j(y)$, $\Pi^j(y)$ and $\omega^j(y)$, $j = 1, 2$. The periodicity assumption comes from the macroscopic domain being filled with microscopic cells, as the one seen in Fig. 1, lying adjacent to each other. Hence, the periodic boundary condition is due to the proximity of the neighboring cells. However, the neighboring cells do not have to be equal; hence, inhomogeneities are allowed.

We will consider a simplified version of this formulation by imposing constraints on the pore space geometry. By assuming the grains to have a specific shape described through a single variable, the level set equation can be replaced by an equation for that variable. Here, we show how the model equations change when using circular grains, but the approach is more general and can be used as long the grain shape can be described through one free parameter. For circular grains, we introduce the level set function $S(x, y, t) = R^2(x, t) - y_1^2 - y_2^2$, where $R(x, t)$ is the radius of the grains. Note that the grain radius is a function of position (and time) as the grain radius can vary between unit cells, allowing non-homogeneous media. The upscaled equations will depend on grain radius $R(x, t)$ instead of the level set function. This simplification was also made by van Noorden (2009a), but places severe constraints on the pore structure and should be interpreted as a choice made for visualization purposes. We mention that Frank et al. (2011) and Frank (2013) implemented other choices of the level set function for a Stokes–Nernst–Planck–Poisson system, and in the following section, we also solve the cell problems for elliptic grains to indicate the effect of anisotropy. Using the circular geometry, the Darcy scale model equations now become, for $(x \in \Omega, t > 0)$

$$\partial_t(\rho R(x, t)) = f(T, u, R), \tag{4a}$$

$$\begin{aligned} \partial_t((1 - \pi R^2(x, t))u(x, t) + \pi R^2(x, t)\rho) + \nabla_x \cdot (\bar{\mathbf{q}}(x, t)u(x, t)) \\ = \nabla_x \cdot (DA_u(R)\nabla_x u(x, t)), \end{aligned} \tag{4b}$$

$$\begin{aligned} \partial_t((1 - \pi R^2(x, t))\rho_f(T)T(x, t) + \pi R^2(x, t)\zeta\rho T(x, t)) + \nabla_x \cdot (\rho_f(T)\bar{\mathbf{q}}(x, t)T(x, t)) \\ = \nabla_x \cdot (\kappa_f A_f(R)\nabla_x T(x, t) + \kappa_g A_g(R)\nabla_x T(x, t)), \end{aligned} \tag{4c}$$

$$\partial_t \left((1 - \pi R^2(x, t)) \rho_f(T) + \pi R^2(x, t) 2\rho \right) + \nabla_x \cdot \left(\rho_f(T) \bar{\mathbf{q}}(x, t) \right) = 0, \tag{4d}$$

$$\bar{\mathbf{q}}(x, t) = -\frac{1}{\mu_f(T)} \mathcal{K}(R) \nabla_x p(x, t). \tag{4e}$$

The reaction rate f uses the distance between R and R_{\min} , where R_{\min} is the radius of the non-reactive solid, to calculate the width of the mineral layer. The matrices $\mathcal{A}_u, \mathcal{A}_f, \mathcal{A}_g$ and \mathcal{K} depend only on grain radius $R(x, t)$ as the integration area is determined by the radius alone. The cell problems are defined as before, but where the unit cell spaces are now defined using the grain radius. Hence, the pore space is $Y_0(x, t) = \{y \in [-\frac{1}{2}, \frac{1}{2}]^2 \mid y_1^2 + y_2^2 > R^2(x, t)\}$, grain space is $G_0(x, t) = \{y \in [-\frac{1}{2}, \frac{1}{2}]^2 \mid y_1^2 + y_2^2 < R^2(x, t)\}$ and the interface between them is $\Gamma_0(x, t) = \{y \in [-\frac{1}{2}, \frac{1}{2}]^2 \mid y_1^2 + y_2^2 = R^2(x, t)\}$. The tensors $\mathcal{A}_u, \mathcal{A}_f, \mathcal{A}_g$ and \mathcal{K} defined in Eq. (2) will now be cheaper to compute, and are due to the symmetric grain shape scalars.

3 Numerical Solution of Cell Problems

The cell problems are decoupled from the macroscale equations and solved beforehand. For various fixed values of grain radius R , the cell problems (3) can be solved, hence providing effective quantities $\mathcal{A}_u, \mathcal{A}_f, \mathcal{A}_g$ and \mathcal{K} that are functions of R . Note that the cell problems are second-order linear elliptic problems. The permeability and diffusion tensors cell problems are defined in the pore space with appropriate boundary conditions on the grain geometry, whereas the thermal problem is defined in the whole cell geometry together with interface conditions across the grain-pore space boundary. To solve these elliptic problems, we adopt standard approaches. We write down a weak formulation for these cell problems and use standard finite element techniques as implemented in the Finite Element package COMSOL multiphysics (COMSOL Inc. 2011). The coupled cell problems for effective heat conductivity coefficients \mathcal{A}_f and \mathcal{A}_g have not been considered earlier. We will in this paper focus on circular grains, which represents an isotropic medium. However, in this section we also solve the cell problems for elliptic grains to sketch the effect of anisotropy on the effective quantities. For solving these cell problems, we use Finite Element Method with triangular elements using P1-basis functions. Since we consider a sequence of pore-scale geometry, the corresponding mesh also changes. For example, as shown in Fig. 2, for the case of thermal conductivity computations, elliptic grain shape, with major axis diameter 0.4 and minor axis diameter of 0.1 (contrast of 4), the number of triangular elements is 1602. We use the automatic meshing and solution approach as implemented in COMSOL Inc. (2011). The post-processing of the solution to obtain the effective quantities is also performed using the available tools there. Note that the effective quantities are all non-dimensional according to the non-dimensionalization in Bringedal et al. (2016).

3.1 Circular Grains

As the resulting effective quantities $\mathcal{A}_u, \mathcal{A}_f, \mathcal{A}_g$ and \mathcal{K} are known to be scalars when the grains are circular due to isotropy, it is only necessary to solve Eqs. (2, 3) for $i = j = 1$. The resulting effective diffusion coefficient \mathcal{A}_u is identical as the one considered by van Noorden (2009a), and the results are not presented here.

The heat conductivity coefficients can be interpreted as a weighting of the relative importance of the void space and grain space, as a more accurate alternative to the usual porosity

Fig. 2 Mesh of a microscopic pore geometry with elliptic grain space with major axis 0.4 and minor axis of 0.1 (contrast of 4). Also, see Fig. 1 showing a representative unit cell geometry and Fig. 7 showing an elliptic grain geometry

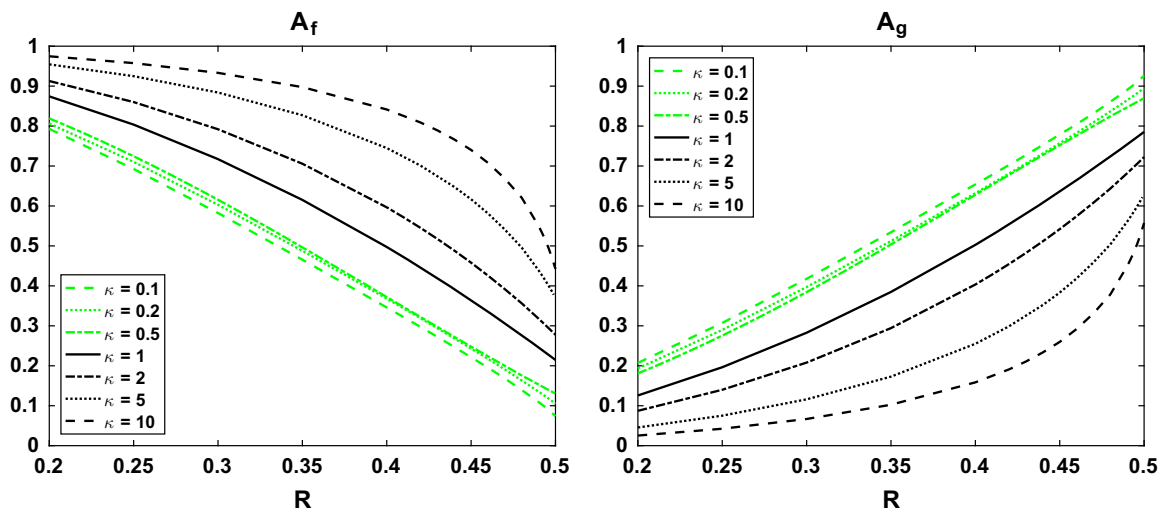
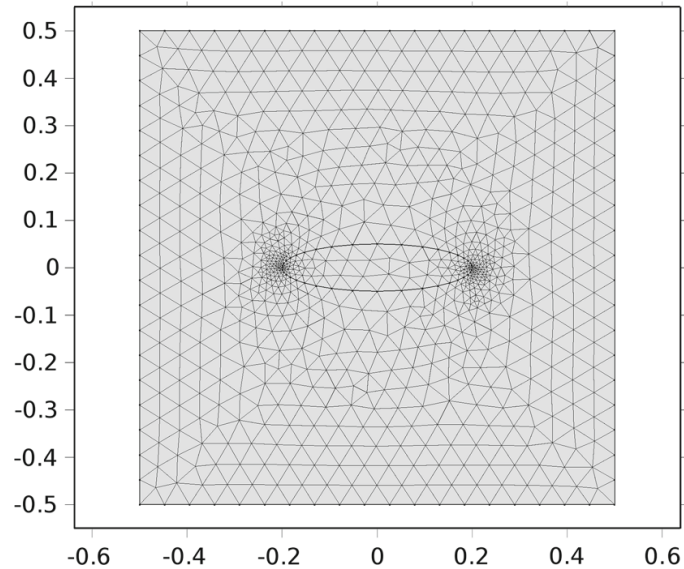


Fig. 3 Effective heat conductivity coefficients for fluid (left) and grain (right). Increasing grain radius R corresponds to less void space. When κ is larger than 1, the grain heat conductivity is larger than in the fluid

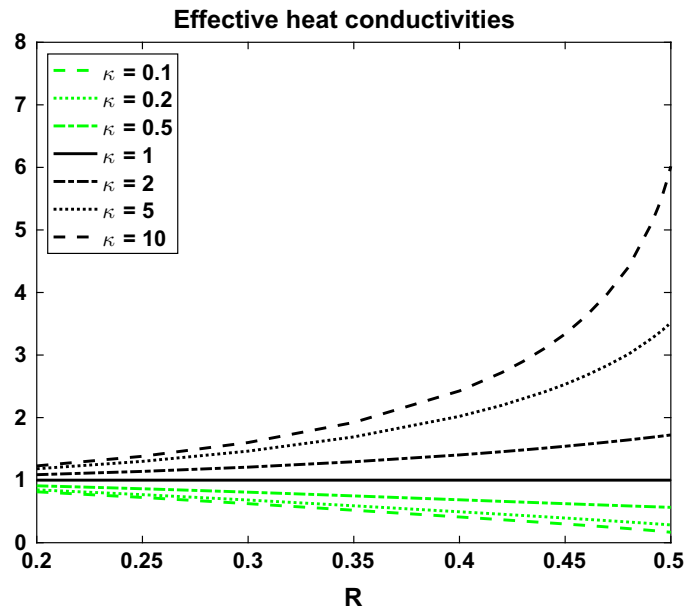
weighting since the actual heat transfer within and between fluid and grain is taken into account. The sum of \mathcal{A}_f and \mathcal{A}_g is always 1. Figure 3 shows the effective heat conductivity coefficients as a function of grain radius R , for various values of $\kappa = \kappa_g/\kappa_f$. The case $\kappa = 1$ corresponds to when the heat conductivities in fluid and grain are equal. In this case, the cell problem is trivial and $\mathcal{A}_f = \phi = 1 - \pi R^2$ and $\mathcal{A}_g = 1 - \phi = \pi R^2$, which corresponds to the usual porosity weighting. The figures only display values for radii between 0.2 and 0.5. A radius of 0.5 corresponds to the porous medium being clogged (although there is still void space caught between the circular grains), while we have not considered radii less than $R_{\min} = 0.2$ even though the cell problems are well defined for radii down to 0.

Figure 4 shows the effective heat conductivity of the medium that is defined as

$$\kappa_{\text{eff}} = \kappa_f \mathcal{A}_f + \kappa_g \mathcal{A}_g.$$

In Fig. 4 $\kappa_f = 1$, hence the value of $\kappa = \kappa_g/\kappa_f$ corresponds to the value of κ_g . Hence, all lines approach 1 if extending the plot to $R = 0$. Figure 5 compares two of the effective heat conductivities with the usual volume averaged heat conductivities

Fig. 4 Effective heat conductivities for the porous medium. In all cases, $\kappa_f = 1$, hence κ reflects the value of the heat conductivity in the grain κ_g



$$\kappa_{\text{eff,ar}} = \kappa_f(1 - \pi R^2) + \kappa_g \pi R^2, \tag{5a}$$

$$\kappa_{\text{eff,geo}} = \kappa_f^{(1-\pi R^2)} \kappa_g^{(\pi R^2)}, \tag{5b}$$

$$\kappa_{\text{eff,har}} = \frac{1}{\frac{1-\pi R^2}{\kappa_f} + \frac{\pi R^2}{\kappa_g}}, \tag{5c}$$

which are the arithmetic, geometric and harmonic averages, respectively. As seen in the figure, the effective heat conductivities calculated from the cell problems always give a smaller value than the arithmetic averaged value, which is the one usually employed for porous media (Nield and Bejan 2013). The overestimation of the effective heat conductivity by the arithmetic averaging can be understood as follows: Consider a case where the heat conductivity is much larger in grain than in fluid, corresponding to an extreme case of $\kappa = 2$ shown in Fig. 5. The unit cell would still experience a relatively low heat conductivity for low grain radii, as the grains are isolated from each other by the low-conductive fluid. However, when the grain radius is so high that the medium almost clogs and the distance between the highly conductive grains is smaller, the heat conductivity will increase substantially. This behavior is captured by the cell problem solutions, as illustrated by the line for $\kappa = 10$ in Fig. 4, while an arithmetic averaging based on porosity will not be able to capture such behavior and instead overestimates the importance of the highly conductive phase. The cell problem solution is best approximated by the geometric mean, which is the known as the more suitable solution for random porous media (Woodside and Messmer 1961). Also for such an extreme case of $\kappa = 10$, the geometric mean is the best choice (not shown). The case with $\kappa_f = \kappa_g$ is trivial and gives equal results for all methods.

The permeability \mathcal{K} is identical as the one found by van Noorden (2009a), and is displayed in Fig. 6. As grain radii close to 0.5 correspond to being close to clogging, the permeability quickly approaches zero for growing grain radius. From the logarithmic plot of the permeability, we can estimate that the permeability approaches zero as the grain radius approaches 0.5 with an inclination number corresponding to approximately $O((R - 0.5)^{5/2})$.

Fig. 5 Effective heat conductivities for the porous medium. The solid curves arise from the cell problem formulation, the dotted are the arithmetic means, the dashed are the geometric means, and the dashed-dotted are the harmonic means. The four top curves are for $\kappa = 2$, while the four lower are for $\kappa = 0.2$

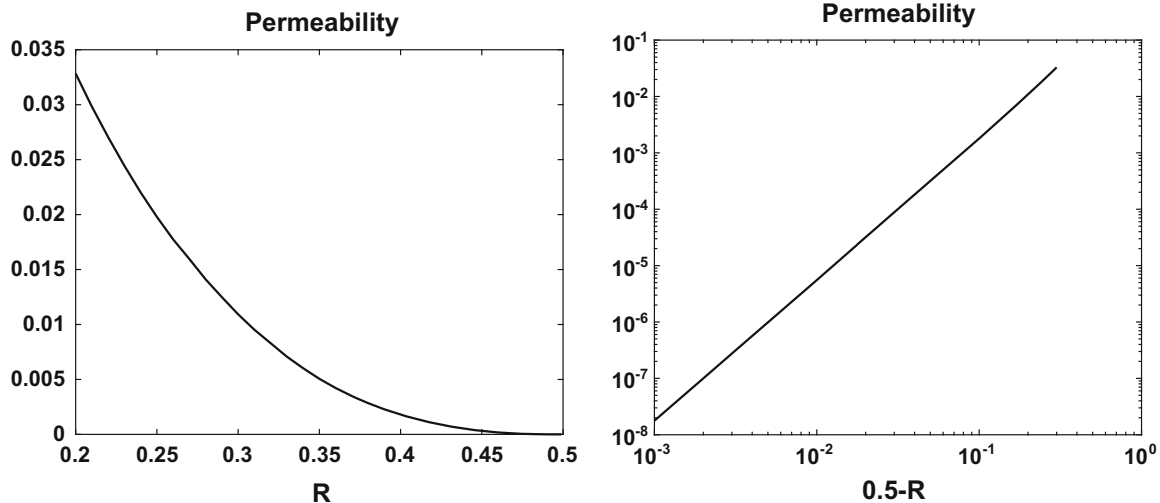
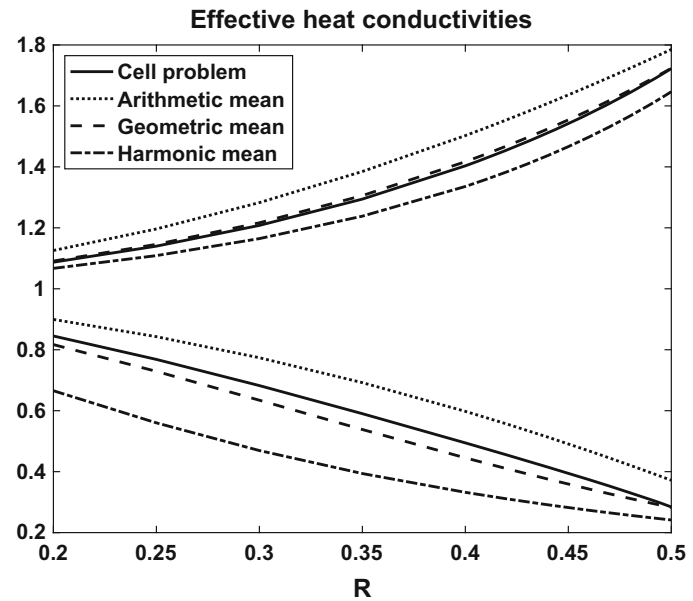


Fig. 6 Permeability of the porous medium. The right plot shows a log–log plot for the permeability as a function of $(0.5 - R)$, as the permeability approaches zero when the grain radius approaches 0.5. Note that the permeability values are non-dimensional, but dimensional (m^2) values can be obtained by scaling with l^2 , where l is the typical pore size, i.e., the scaling such that the cell in Fig. 1 has side lengths 1

3.2 Elliptic Grains

The level set formulation can also be applied to investigate other grain shapes than the isotropic circular shape, and we mention here the differences when going into an anisotropic regime using elliptic grains. We assume the grain in each unit cell being elliptic with a fixed ratio between the semi-major and semi-minor axis. When the grain grows and shrinks due to mineral precipitation and dissolution, the grain would not preserve its elliptic shape due to the underlying assumption of even growth/dissolution arising from the upscaling and derivation of the cell problem (Bringedal et al. 2016). However, making physical arguments through the grain shape itself locally allowing for higher or lower reaction rates, we could argue that the elliptic shape should be maintained, and hence the shape of the grain can at all times be explained through the parameter M , the length of the semi-major axis. See Fig. 7 for a sketch

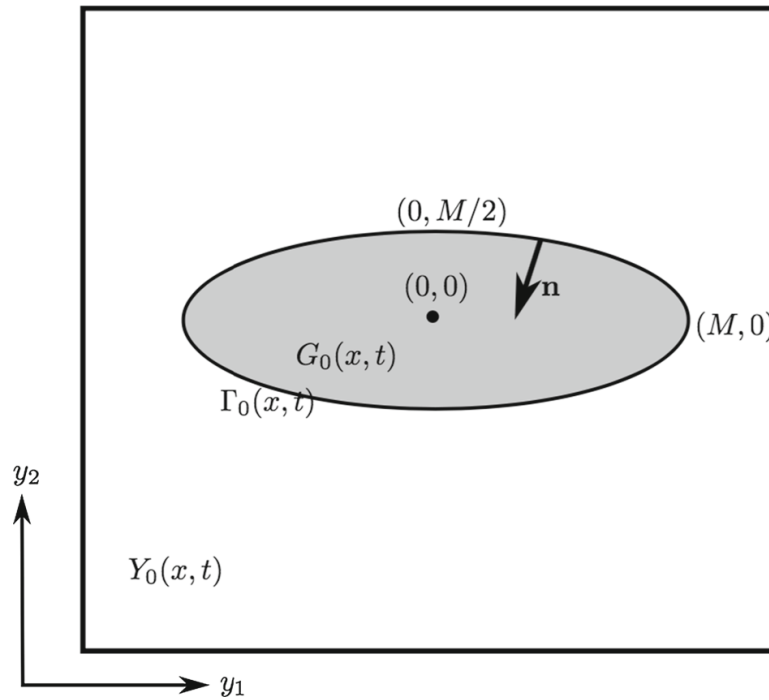


Fig. 7 Model of microscopic pore with elliptic shape with ratio of 2 between the semi-major and semi-minor axis. The unit cell has fluid space $Y_0(x, t)$, grain space $G_0(x, t)$ and the interface between them $\Gamma_0(x, t)$, which has unit normal \mathbf{n} pointing into the grain

of the unit cell, where the ratio between the semi-major and semi-minor axis of the grain is 2.

The formulation of the upscaled equations would be similar as in Eq. (4), replacing the radius $R(x, t)$ with the semi-major axis $M(x, t)$, and taking into account the fluid volumes and grain volumes changing. Now, $|Y_0(x, t)| = 1 - \pi M^2/2$ and $|G_0(x, t)| = \pi M^2/2$ when the ratio between semi-major and semi-minor axis is 2. As earlier, we assume there is some part of the grain that will not dissolve and choose this to be for $M_{\min} = 0.2$. This minimum choice of M corresponds to a different porosity than $R_{\min} = 0.2$. The maximum semi-major axis is $M = 0.5$, corresponding to clogging. Note, however, that $M = 0.5$ resembles a layered medium with no flow in the y_2 -direction, but still allowing flow in the y_1 -direction. The porosity is significantly higher than in the circular case with $R = 0.5$.

Due to the anisotropy of the grain shape, the resulting effective permeability, diffusivity and heat conductivities in Eq. (2) will no longer be scalars, but 2×2 matrices. The cell problems (3) are solved using elliptic grain shape with $M \in [0.2, 0.5)$ using COMSOL multiphysics (COMSOL Inc. 2011). For the heat conductivities, we only consider the two cases $\kappa = 0.2$ and $\kappa = 2$ as our goal is only to sketch the effect of anisotropy arising from the cell problem geometry. Although the cell problems provide 2×2 matrices, the off-diagonal terms are effectively zero due to the orientation of the grain shape; the anisotropy is aligned with the grid. Hence, we only focus on the diagonal terms. These diagonal values are also the eigenvalues of the matrices, which are important for characterizing the anisotropic medium.

Figure 8 shows the heat conductivity coefficients for the fluid and grain as a function of semi-major axis M , using $\kappa = \kappa_g/\kappa_f$ either equal to 0.2 or 2, and ratio between the semi-major and semi-minor axis being either 2 or 4. These plots should be compared to Fig. 3 for circular grains. There are several interesting findings for the anisotropic heat conductivities. Firstly, the differences between the y_1 - and y_2 -coefficients are significantly different already for a relatively small ratio between the semi-major and semi-minor axis, which becomes

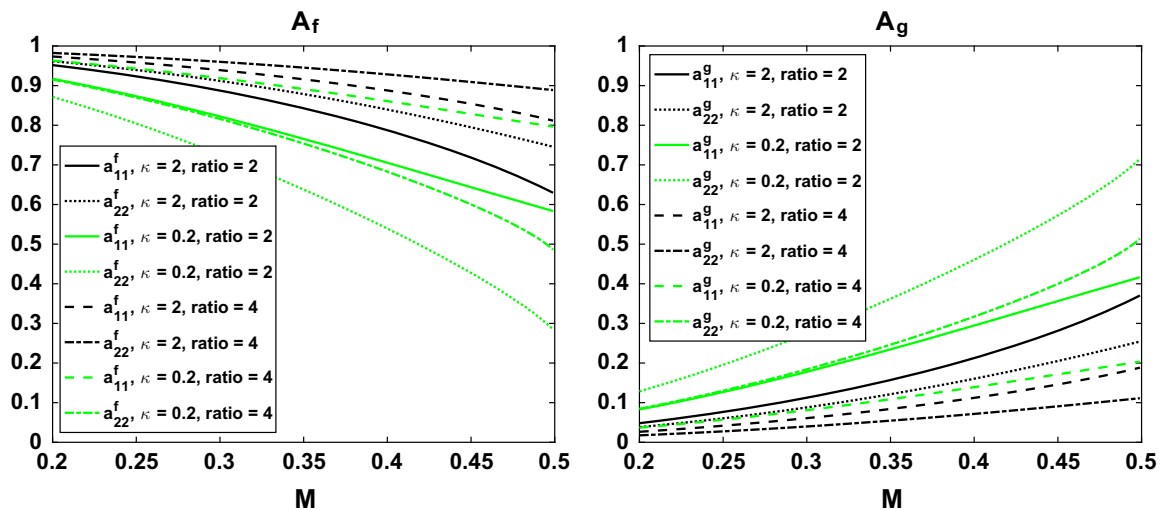


Fig. 8 Comparison of the effective heat conductivity coefficients for fluid (left) and grain (right). Increasing M corresponds to more grain space, while ‘ratio’ refers to the ratio between semi-major and semi-minor axis of the elliptic grain. When κ is larger than 1 (black lines), the grain heat conductivity is larger than in the fluid. Oppositely for κ smaller than 1 (green lines)

more visible when the grain is larger (corresponding to the anisotropic feature becoming more relevant), and these differences are important both for when heat conductivity is largest in the fluid and in the grain. Whether the heat conductivity coefficient is largest in the y_1 - or y_2 -direction depends on the value of κ , and phase: When $\kappa = 2$, the horizontally elongated shape of the grain makes the grain heat conductivity coefficient larger in the y_1 -direction than in the y_2 -direction, and oppositely for the fluid. Hence, the contribution from grain on heat conduction is more important for the y_1 -direction than in y_2 in this case, contributing to a larger medium heat conductivity in the y_1 -direction as the grain heat conductivity is larger than in the fluid. From Fig. 8, we see how the grain heat conductivity coefficient is larger in the y_2 -direction than in the y_1 -direction when $\kappa = 0.2$. Hence, the grain heat conductivity gives a larger contribution to the effective heat conductivity in the y_2 -direction than in the y_1 -direction. However, this contribution is a “negative” one as the heat conductivity in the grain is smaller than in fluid when $\kappa = 0.2$. Hence, the grain conductivity hampers the medium heat conductivity to a larger extent across the layers. The effective heat conductivities seen in Fig. 9 show how the heat conductivity is always larger in y_1 -direction for both values of κ . Hence, heat conductivity of the medium is always more efficient along the layers than across, independently of whether the fluid or grain has the largest conductivity.

Comparing the effective heat conductivities with corresponding arithmetic, geometric and harmonic averages based on (5) reveals some different behavior for the elliptic case as seen for the circular grains in Fig. 5. Figure 9 shows how the different effective behaviors in the y_1 - and y_2 -directions are approximated by the arithmetic, geometric and harmonic averages for the two choices of κ . While the circular grain effective heat conductivities were always closer to the geometric mean, the effective heat conductivity in the y_1 -direction (along layering) is best approximated by the arithmetic mean (low κ) or by the geometric mean (high κ and low M), and the effective heat conductivity in the y_2 -direction (across layering) is best approximated by the harmonic mean (high κ) or by the geometric mean (low κ and low M). These findings were to some extent expected as harmonic mean is known to be more suitable for series distributions and arithmetic mean for parallel distributions (Woodside and Messmer 1961). However, as seen from Fig. 9, the geometric averages can still be the best alternative for lower values of M and especially for small ratio between the semi-major and

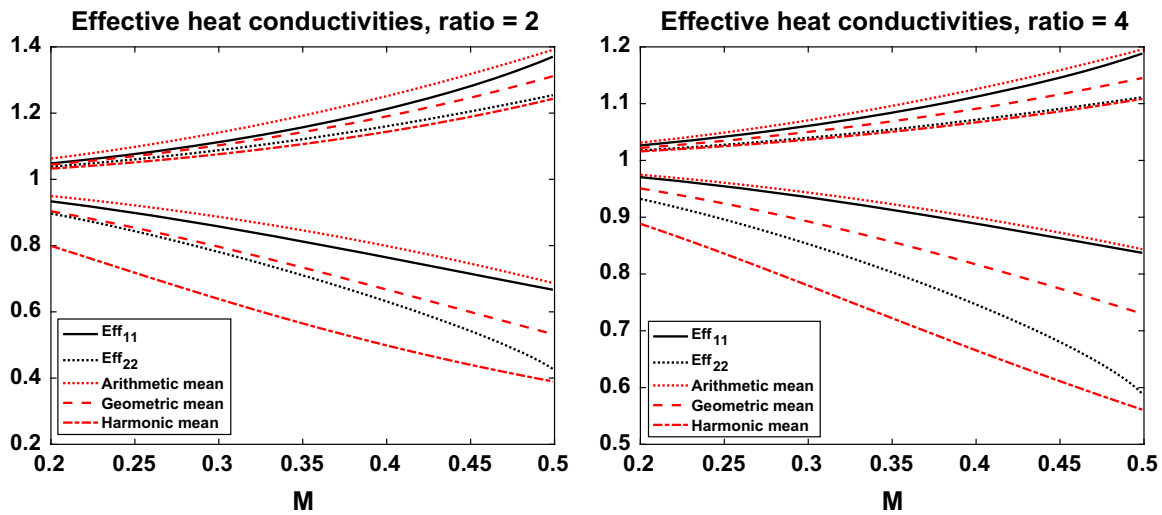
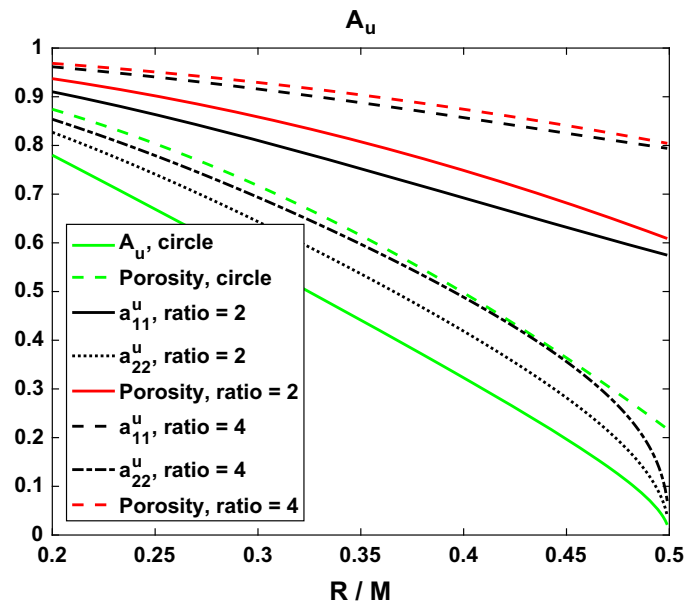


Fig. 9 Comparison of the effective heat conductivities for the porous medium for when the ratio between semi-major and semi-minor axis is 2 (left) and 4 (right). The five top curves are for $\kappa = 2$, while the five lower are for $\kappa = 0.2$

Fig. 10 Comparison of the effective ion diffusivity coefficients for circular and elliptic grains, as a function of either grain radius R or the semi-major axis M . Increasing R or M corresponds to more grain space, while ‘ratio’ refers to the ratio between semi-major and semi-minor axis of the elliptic grain



semi-minor axis, corresponding to when the anisotropic effect is not so strong. Hence, using arithmetic mean along the layering and harmonic mean across the layering is important when there are strong anisotropic effects in the porous medium.

For the ion diffusivity, the question of which type of averaging is not so relevant as the ion diffusivity in the grain is zero, and hence only the arithmetic mean would be applicable. In practice, the resulting diffusivity coefficient is then the porosity, which is often used when modeling diffusivities with varying porosity. However, as Fig. 10 shows, the porosity is a poor approximation for the effective diffusivity coefficient, even for circular geometries. The porosity approximates the diffusivity in the y_1 -direction (along layers) quite well, especially when anisotropic effects are strong, but gives a poor approximation for the y_2 -direction (across layers), which is zero when M is 0.5 due to clogging in the y_2 -direction, while the porosity is still large.

The permeability is also a tensor when considering elliptic grain shapes. The off-diagonal terms are effectively zero due to the orientation of the grain, and hence we only need to

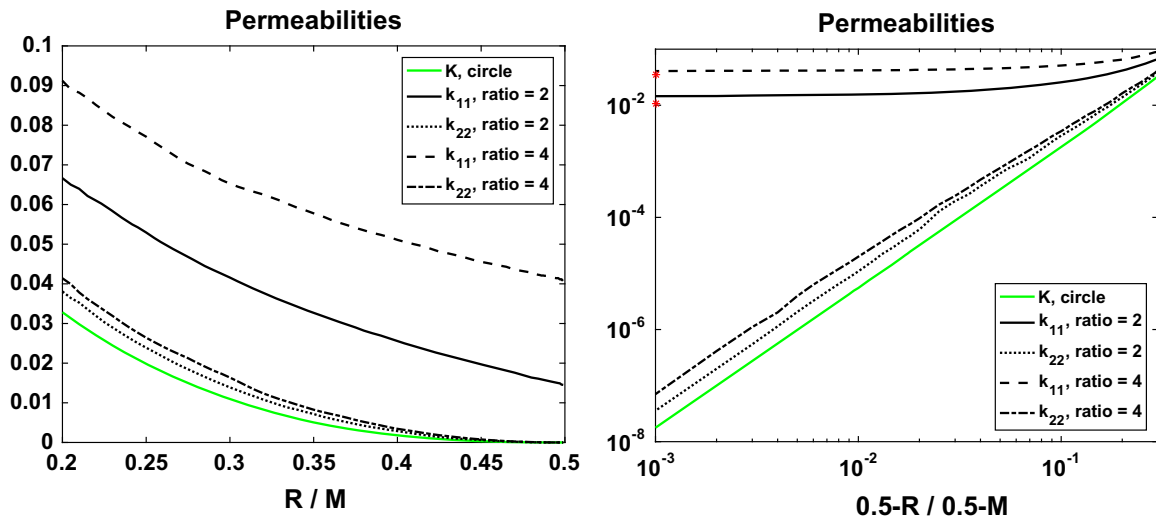


Fig. 11 Comparison of the permeabilities for the porous medium for circular and elliptic grains, as a function of either grain radius R or the semi-major axis M . The right plot shows a log–log plot of the permeabilities as a function of $(0.5 - R)$ or $(0.5 - M)$, as clogging occurs when R or M approaches 0.5. A ratio of 4 means that the grain is more elongated. The red stars in the right plot indicate the estimated permeability values based on an upscaled thin strip model (Bringedal et al. 2015)

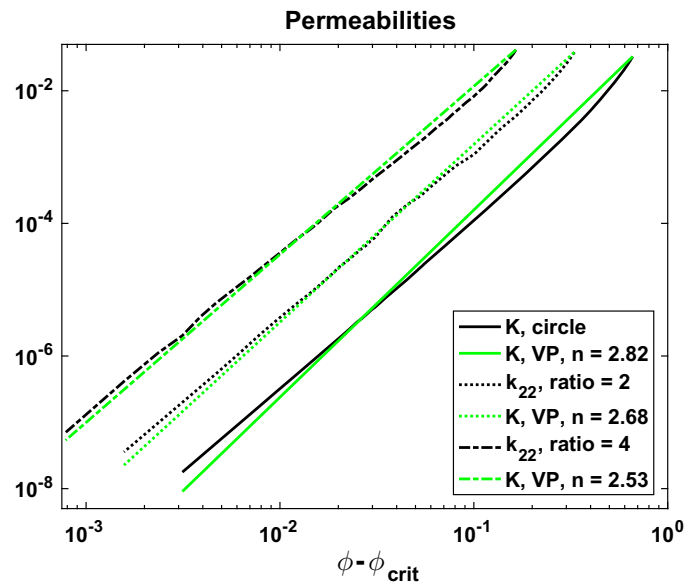
consider the two diagonal terms. Here, the y_2 -term will approach zero when M approaches 0.5 due to clogging, while the y_1 -term will still have a large permeability when M is 0.5. Figure 11 shows the diagonal components of the permeability tensor for the elliptic grain as a function of the semi-major axis M . For comparison, the circular grain permeability is also included.

As seen from Fig. 11, the permeabilities in the y_1 -direction do not approach zero when M approaches 0.5. Due to the elliptic grain shape, the medium is not blocked in the y_1 -direction but forms channels. For channels, it is shown earlier (Bringedal et al. 2015) that the non-dimensional permeability should behave as $K = d^3/12$ where d is the aperture. If we use the minimum distance between two adjacent grains as a measure of the aperture in the y_1 -direction of the channel-like medium, the cubic relationship estimates a (non-dimensional) permeability of $K = 0.0105$ and $K = 0.0352$ for when the ratio between the semi-major and semi-minor axis are 2 and 4, respectively. These two values are marked with red stars in the right part of Fig. 11. The k_{11} permeability values calculated from the cell problems when M is close to 0.5 are $k_{11} = 0.0145$ and $k_{11} = 0.0406$ for these two ratios. Hence, the cubic relationship slightly underestimates the calculated along-channel permeabilities, which is possibly due to the channel not being straight but is generally wider than the minimum value used here. Also, the cell problems are not solved for $M = 0.5$, as the flow cell problem is undefined in this case, and hence the comparison is made for $M = 0.499$.

The circular grain permeability and elliptic grain k_{22} -permeabilities all approach 0 when R or M approach 0.5, although at slightly different speeds. Due to the anisotropy, the clogging happens at different critical porosities. The critical porosity is defined as the remaining porosity when clogging (in the y_2 -direction) occurs and will be $\phi_{crit} = 1 - \pi 0.5^2$ for the circular grain, and $\phi_{crit} = 1 - \pi 0.5^2/2$ and $\phi_{crit} = 1 - \pi 0.5^2/4$ for the elliptic grain for ratio equal to 2 and 4, respectively. TOUGHREACT (Xu et al. 2012) incorporates a power law for the permeability based on Verma and Pruess (1988) when there is a known critical porosity, namely

$$K = K_0 \left(\frac{\phi - \phi_{crit}}{\phi_0 - \phi_{crit}} \right)^n, \tag{6}$$

Fig. 12 Comparison of the permeability, or permeability in the y_2 -direction when the porosity approaches the critical porosity. The green lines are the least-square fitted versions of Eq. (6) based on Verma and Pruess (1988)



where $K(\phi_0) = K_0$ at some other porosity $\phi_0 > \phi_{crit}$. The power n is, as the critical porosity, medium dependent and needs to be estimated. Using the permeabilities at R_{min} , $M_{min} = 0.2$ and the known critical porosities, we can estimate n through a least-square approach. We find $n = 2.82$ for the circular grain, while $n = 2.68$ and $n = 2.53$ are the powers best estimating the elliptic grain cases for when the ratio between semi-major and semi-minor axis is 2 and 4, respectively. See Fig. 12 for illustration of these three cases. Due to fitting of the entire interval, the resulting approximated permeabilities are slightly too steep when approaching the critical porosities, but do a fairly good job in capturing the behavior of the permeability near clogging.

4 Comparison with Approximate Solutions

The cell problems (3) can be solved numerically for discrete values of grain radius R , but when implementing the macroscale Eq. (4), it is more efficient if the effective quantities can be known through analytical expressions instead of solving the cell problems for each time step as the radius will vary with both time and space. One way to get around this is to solve the cell problems beforehand for a large number of discrete R values and create a lookup-table, but we here investigate the possibility of approximating the cell problem solutions with either solving a related cell problem analytically, or by solving the cell problems numerically for discrete values of R and use polynomial interpolation.

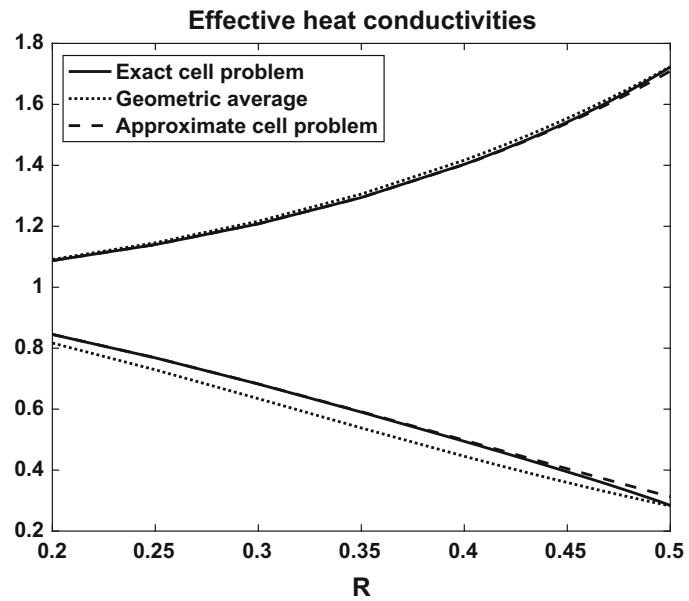
4.1 Approximate Heat Conductive Cell Problems

The cell problem (3b) used to calculate the heat conductivity coefficients \mathcal{A}_f and \mathcal{A}_g can be approximated by solving a related cell problem analytically. The cell problem is formulated through the unknown functions $\Theta_f(y_1, y_1)$ and $\Theta_g(y_1, y_2)$, that should fulfill Eq. (3b) together with periodicity across the external cell boundaries:

$$\Theta_f(y_1 = -1/2) = \Theta_f(y_1 = 1/2), \quad \Theta_f(y_2 = -1/2) = \Theta_f(y_2 = 1/2).$$

Our approach involves using polar coordinates and separation of variables; hence, we assume the solutions can be written on the form

Fig. 13 Comparison of the effective heat conductivities. The three lower curves are for $\kappa_f = 1, \kappa_g = 0.2$, while the three upper curves are for $\kappa_f = 1, \kappa_g = 2$



$$\Theta_f(r, \theta) = F_r(r)F_\theta(\theta), \quad \Theta_g(r, \theta) = G_r(r)G_\theta(\theta).$$

However, as shown in the “Appendix”, our assumption of separation of variables together with the resulting solution form in the azimuthal direction will lead to the periodicity requirement on the external boundary not being fulfilled. Instead, we search an approximate solution through alternative boundary conditions for the external boundary. We consider two alternatives: Either dropping the external boundary, allowing Θ_f to be defined for all $r > R$; or, keeping the boundary, but use other means to obtain a unique solution. Redefining the cell problem, makes it more similar to the conductive single-inclusion solutions handled by Torquato (2013). Torquato (2013) also shows how to expand these solutions to effective medium approximations of multiphase media. However, the two approaches lead to the same solution, namely:

$$\mathcal{A}_f = (1 - \pi R^2) \frac{1 + \kappa}{1 + \kappa + \pi R^2(1 - \kappa)}, \tag{7a}$$

$$\mathcal{A}_g = \pi R^2 \frac{2}{1 + \kappa + \pi R^2(1 - \kappa)}. \tag{7b}$$

The full derivation of the solution using the two approaches are found in the “Appendix”. Figure 13 compares the approximate effective heat conductivity from Eq. (7) with the exact solution found from the cell problem (3b) and the volume weighted geometric average (5b). The approximate cell problem does a better job than the volume averaging except for large values of R .

4.2 Approximate Polynomials for the Cell Problem Solutions

We here try to estimate the effective quantities $\mathcal{A}_u(R), \mathcal{A}_f(R), \mathcal{A}_g(R)$ and $\mathcal{K}(R)$ with approximate polynomials based on numerically found solutions of the cell problems (3), which have been obtained for discrete values of R within our interval of interest: $R \in [0.2, 0.5]$. As van Noorden (2009a), we use a polynomial with powers of $R^0, R^{1/2}, R^1, R^{3/2}$ and R^2 for the ion diffusivity coefficient and the heat conductivity coefficients. While van Noorden (2009a) could use that the polynomial for \mathcal{A}_u was 1 when $R = 0$ and 0 when $R = 0.5$, the latter is not the case for \mathcal{A}_f as there is still a large amount of conductive heat transfer in the fluid when

the porous medium is clogged. However, the polynomial for \mathcal{A}_g would be 0 for $R = 0$, and the polynomials approximating \mathcal{A}_f and \mathcal{A}_g should still fulfill that their sum is 1 for all R .

The polynomial found to approximate \mathcal{A}_u best in the least-square sense is

$$\mathcal{A}_u(R) \approx 0.7232(0.5 - R)^{1/2} - 0.2166(0.5 - R) + 4.8785(0.5 - R)^{3/2} - 3.9439(0.5 - R)^2.$$

The coefficients of this polynomial are quite different than the ones found by [van Noorden \(2009a\)](#), despite fitting within the same interval. The curves provide similar values. The maximal error in the fitting points was 10^{-3} for [van Noorden \(2009a\)](#), which is also the case here.

We approximate \mathcal{A}_f and \mathcal{A}_g with polynomials only for $\kappa = 2$ and $\kappa = 0.2$, to indicate the different behaviors for when κ is larger/smaller than 1. For $\kappa = 2$, the polynomials found to approximate \mathcal{A}_f and \mathcal{A}_g best in the least-square sense are

$$\mathcal{A}_f(R) \approx 3.3481R^{1/2} - 19.5551R + 38.2452R^{3/2} - 27.33065R^2 + 1.$$

$$\mathcal{A}_g(R) \approx -3.3433R^{1/2} + 19.5274R - 38.1923R^{3/2} + 27.2974R^2.$$

For $\kappa = 0.2$, the polynomials found to approximate \mathcal{A}_f and \mathcal{A}_g best in the least-square sense are

$$\mathcal{A}_f(R) \approx 1.0282R^{1/2} - 4.3256R + 3.8254R^{3/2} - 3.2395R^2 + 1.$$

$$\mathcal{A}_g(R) \approx -1.0317R^{1/2} + 4.3455R - 3.8638R^{3/2} + 3.2639R^2.$$

The polynomials for \mathcal{A}_f are assumed to have a constant factor of 1 as $\mathcal{A}_f(0) = 1$ and $\mathcal{A}_g(0) = 0$, but are otherwise only fitted within the interval of interest. Due to numerical roundoff error and as the least-square fitting have been done independently for the polynomials, the approximating polynomials do not sum up exactly to 1 for all R , but deviate from 1 with up to 10^{-4} . The maximum error for the fitting points is 10^{-3} for the effective heat conductivities in both cases. Plotting the effective heat conductivity calculated from the cell problems together with the approximate effective heat conductivity from the above polynomials, reveals the two curves being virtually equal. The two cases of high and low κ result in polynomials of similar structure, but the higher-order coefficients are of relative higher importance for R -values close to 0.5 when $\kappa = 2$, while the linear terms dominate for $\kappa = 0.2$. This behavior is due to the more curved shapes of the high κ curves near $R = 0.5$ seen in [Fig. 3](#).

The behavior of the permeability close to clogging is important to capture when modeling precipitation and clogging as the flow pattern can change significantly as pores close (and possibly reopen) and the relative permeability variations can vary within several orders of magnitude close to clogging. In [van Noorden \(2009a\)](#), the permeability was fitted with a sum of first-, second- and third-order powers of $(0.5 - R)$. Van Noorden did not focus on clogging and fitted with the factors that would capture the behavior over his whole region of interest. However, the sum of these three terms implies that the permeability should approach zero as $O(0.5 - R)$ as the first-order term will dominate the two others when R approaches 0.5. Investigating the permeability values when R is close to 0.5, as seen in the right part of [Fig. 6](#), reveals that the permeability does not approach zero linearly when close to clogging. The logarithmic plot indicates an inclination number of approximately 5/2 for R close to 0.5. This means that to capture the behavior close to clogging, the approximating polynomial should not contain terms with $(0.5 - R)$ -factors of power less than 5/2. The polynomial can, however, contain higher-order terms as these will not dominate close to clogging. A polynomial that is found to approximate the permeability values satisfactory, both away from clogging and close to clogging, is

$$\mathcal{K}(R) \approx 0.6191(0.5 - R)^{5/2} - 0.4892(0.5 - R)^3 + 1.0441(0.5 - R)^{7/2}.$$

The maximum error in the fitting points is 10^{-4} and is found for low values of R . The maximum relative error is 0.08 and occurs when the radius is close to clogging. Approximate polynomials with terms containing first-order $(0.5 - R)$ -terms are found to have a relative error larger than 1. An alternative approach to the above polynomial would be to approximate the behavior of the permeability with two polynomials: one valid for low values of R and one valid for R close to 0.5, and tie these two polynomials together with continuity constraints in some breaking point. This approach could, however, cause issues in a numerical implementation. As the logarithmic plot in Fig. 6 does not indicate any obvious breaking points, using the same polynomial for the whole fitting interval $[0.2, 0.5)$ should be feasible in this case.

5 Case Study: Clogging

To investigate the behavior of the upscaled effective Eq. (4) in a numerical implementation, we create a case study with initial and boundary conditions, mineral solubilities and rock properties such that clogging will occur at some distance away from the well. The Darcy scale domain is assumed to be filled with microscopic pores as Fig. 1 next to each other, in line with the periodic assumption in deriving the upscaled model in Bringedal et al. (2016). The microscopic cells are not explicitly visible in the Darcy scale domain, as they in the homogenization limit are assumed infinitesimally small, but contribute through the cell problem solution for effective quantities, e.g., permeability, at each macroscopic point in the domain. The goal of this case study is to see how the upscaled model equations behave close to clogging and how the heat transport is affected by the clogging.

5.1 Case Study Formulation and Implementation

Note that all parameters and numbers specified in the following are non-dimensional according to the non-dimensionalization given in Bringedal et al. (2016). Temperatures are also shifted to lie between 0 and 1. The macroscale domain is a two-dimensional square $x \in [0, 1]^2$ with injection and production wells operating at constant pressure. The injection well is located in $(x_1, x_2) = (0.2, 0.2)$, and the production well in $(x_1, x_2) = (0.8, 0.8)$. External boundaries are impermeable and insulated. The domain is initialized with a temperature of 1 and with an ion concentration such that the fluid is fully saturated with ions, in this case a concentration of $\sqrt{0.75}$. We mimic a reservoir with two types of rock that are such that the temperature drop due to injecting fluid of temperature 0 triggers mineral dissolution near the injection well and mineral precipitation further away. The two types of rocks meet along the line $x_1 = 0.5$. The injected fluid has the same ion concentration as the initial to resemble reinjection of produced fluid, but mineral dissolution will occur near the injection well due to the temperature drop. As fluid flows toward the production well, minerals start precipitating when crossing $x_1 = 0.5$, both due to the incoming fluid having a larger ion concentration from the upstream mineral dissolution, but also caused by the gradual temperature decrease.

The Darcy scale model Eq. (4) is modeled fully coupled with Euler forward in time and the control volume method on a square grid with two point flux approximation in space. The injection wells are handled through a mass conservative implementation as described in Bringedal et al. (2014). As clogging is a difficult process to model due to the degenerate nature of the transport equations, we use a time step constraint when one or more cells are close to clogging. Also, we consider a cell clogged when the grain radius exceeds $R = 0.4997$. When

a cell clogs, pressure is undefined in this cell and is no longer solved for. Heat conduction and chemical reactions are still solved for in the clogged cells, the latter to allow for any reopening at a later time. The dissolution rate, which has a discontinuity from (1), is regularized. We mention there are more sophisticated ways of dealing with both mineral dissolution (containing a discontinuous reaction term) and precipitation possibly leading to clogging, and refer to Agosti et al. (2015a, b) for details on event-driven implementation of this aspect. Despite using Euler forward for time stepping, the resulting system of equations is nonlinear due to the nonlinearities in the time derivatives. The nonlinear system of equations is solved with Newton iterations, using the solution from the previous time step as initial guess.

The effective quantities $\mathcal{A}_u(R)$, $\mathcal{A}_f(R)$, $\mathcal{A}_g(R)$ and $\mathcal{K}(R)$ arising from the cell problems are implemented with their approximating polynomials found in Sect. 4.2. Hence, the cell problems do not need to be solved at each mesh point at each time step, but pore-scale effects are included through the approximate polynomials of the effective quantities arising from cell problem solutions. We have used $\kappa_f = 1$ and $\kappa_g = 2$, which is a representative correspondence between heat conductivity in fluid and grain for many soils/rocks. The porous medium is initialized with $R = 0.3$, and the amount of minerals that cannot dissolve is chosen to correspond to $R_{\min} = 0.2$. Note that this choice of homogeneous initial condition (and minimum radius) for the rock is not a necessity for the model formulation and only chosen for convenience. Other parameters appearing in the model Eq. (4) are given by

$$D = 1, \quad \zeta = 1, \quad k = 1, \quad \alpha = 1, \quad \rho = 1, \\ \beta_\rho = 0.01, \quad \beta_\mu = 0.01, \quad \rho_0 = 2, \quad \mu_0 = 1,$$

where the fluid density is $\rho_f(T) = \rho_0 - \beta_\rho T$ and viscosity is $\mu(T) = \mu_0 - \beta_\mu T$. The injection pressure is 100, and production pressure is 0.5, which induces a pressure difference in the domain giving flow rates around 1 initially, and hence advective and diffusive processes occur at about the same time scale, which is one of the assumptions in the derivation of the upscaled model by Bringedal et al. (2016).

5.2 Numerical Results

When injection starts, the fluid flows toward the production well and brings along lower temperatures and larger ion concentrations as the minerals close to the injection well dissolves. Upon reaching the other rock type at $x_1 = 0.5$ minerals precipitate, resulting in gradually lower porosities and permeabilities behind this line. Also, as the minerals dissolves close to the injection well, the effective heat conductivity decreases due to κ_f being lower than κ_g . Although one would expect clogging to first occur in $(x_1, x_2) = (0.5, 0.2)$, this being the point closest to the injection well where clogging can occur; the clogging first occurs at $(x_1, x_2) = (0.5, 0)$. This is caused by the point $(x_1, x_2) = (0.5, 0)$ being cooled faster than $(x_1, x_2) = (0.5, 0.2)$, despite being further away from the injection point, triggering larger precipitation rates. The differences in cooling (and initiating of clogging) are small, but this faster cooling in $(0.5, 0)$ is a result of the heat conductivity being larger in regions where less minerals have dissolved. The convective cooling is (initially) focused mainly along the band between injection and production well, and hence conductive cooling dominates between the injection well and the line $x_1 = 0.5$ for low x_2 -values. As the dissolving occurs slower, along $x_2 = 0$ the heat conduction is faster than for $x_2 = 0.2$. The fact that clogging occurs first at $(x_1, x_2) = (0.5, 0)$ instead of in $(0.5, 0.2)$ is a nice example of the effect of the interplay between heat transfer and reactive transport. Clogging gradually occurs along increased values of x_2 as these cells are being cooled, and at the same time the flow is forced

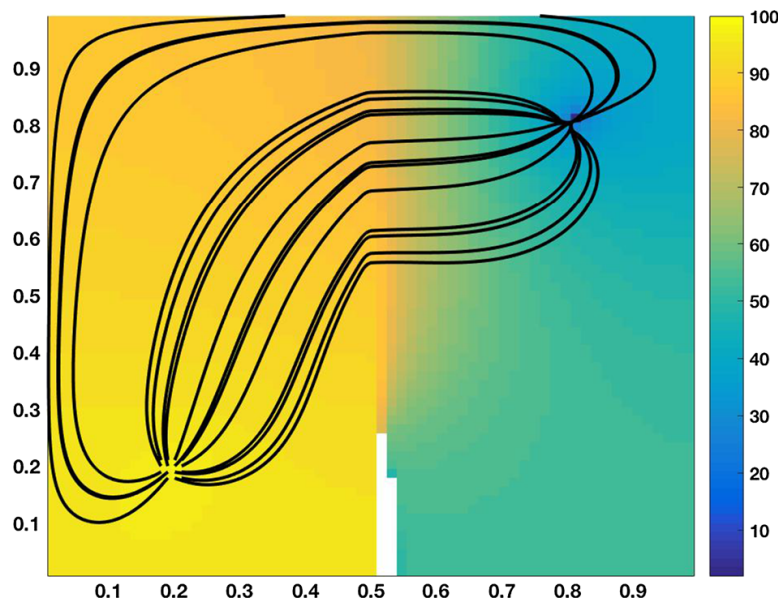


Fig. 14 Pressure distribution (colors) 1 time unit after injection starts. Clogged cells are marked as white as the pressure is undefined. Black lines are (instantaneous) stream lines. The flow trajectories are not smooth across $x_1 = 0.5$ as the grain radius R and hence also permeability \mathcal{K} are discontinuous here

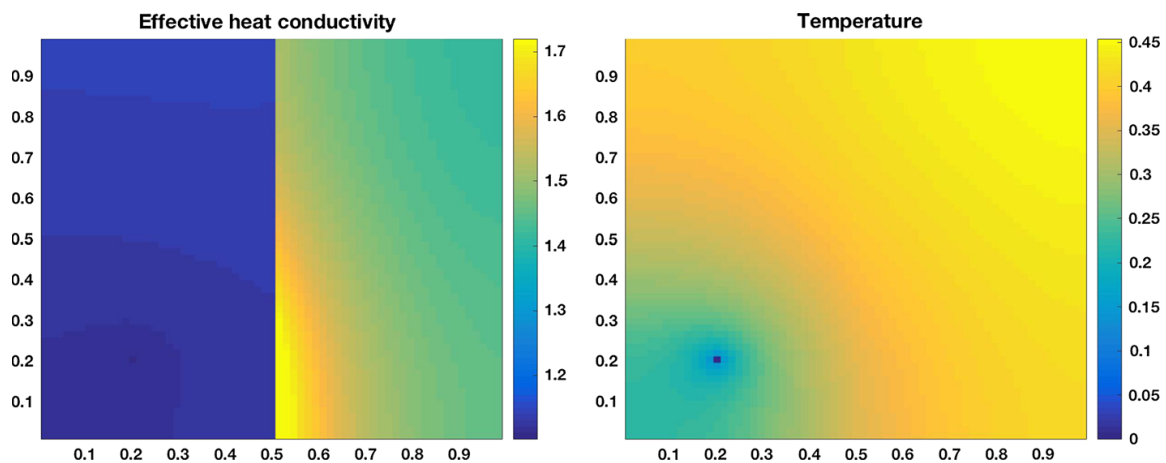


Fig. 15 Effective heat conductivity distribution (left) and temperature distribution (right) 1 time unit after injection starts. Temperature is still well defined in the clogged cell where the highest effective heat conductivity values are found. The increased heat conductivity is the reason for the relatively smooth temperature field despite flow paths being clogged

to follow trajectories further away from the clogged region. Due to heat conduction still playing a role in the blocked region, clogging still occurs behind the line $x_1 = 0.5$. Figure 14 shows the pressure distribution, and some flow trajectories some time after clogging have started near $(x_1, x_2) = (0.5, 0)$.

There is still heat conduction in the clogged cells. In fact, the clogged cells encounter an increased effective heat conductivity as the grain heat conductivity is larger than fluid heat conductivity. Hence, the temperature distribution is not strongly affected by the clogged flow paths in this case study. Figure 15 shows how the effective heat conductivity and temperature distributions are at the same time as the pressure distribution in Fig. 14.

6 Summary and Conclusion

In this paper, we have shown how the effective behavior of heat conductivity and permeability performs in a porous medium where porosity changes due to mineral precipitation and dissolution. The heat conductivity coefficients and permeability is calculated through cell problems derived from a pore-scale formulation based on [Bringedal et al. \(2016\)](#), using circular and elliptic grains as illustrative examples. We have shown how the effective behavior for the heat conductivity differs from the usually applied porosity-weighted averaging between fluid and grain, where the geometric averaging performs better in the isotropic case and harmonic, geometric or arithmetic averaging is the better approximation depending on degree of and direction of anisotropy.

We have solved the heat conductivity cell problems numerically, but approximate versions can be solved analytically. The resulting solutions for circular grains capture the effective behavior well and generally better than the geometric averaging. Hence, for practical use in simulators, one can either apply the approximate analytical solutions, or approximate polynomials based on least-square fitting of discretely solved cell problems. When doing least-square fitting for the cell problems, one has to decide which order terms to include in the polynomial, and this can potentially alter the behavior of the resulting effective parameters, especially near critical points as clogging represents. As the permeability can vary with several orders of magnitude near clogging, approximating with suitable terms and factors is especially important in this case.

As we are particularly interested in the behavior of the effective model near clogging, a case study where clogging would occur was designed. The case study mimics a geothermal reservoir where cold fluid is injected, and where composition of different rock types leads to mineral precipitation at some distance away from the well. The reduced permeability and gradual clogging of the medium lead to the injected water being forced through new flow paths further away from the production well, and at the same time increasing the effective heat conductivity through the medium.

Acknowledgements K. Kumar acknowledges the support by the Research Council of Norway under the project IMMENS no. 255426 and “EOR upscaling—from lab to field”, Petromaks 2 project. The authors would like to thank Nadja Ray and Raphael Schulz from FAU Erlangen-Nürnberg for their useful discussions supported by the Research Council of Norway (RCN) and German Academic Exchange Service (DAAD) Project No. 255773, “Upscaling Evolving Microstructures and its Applications”.

Appendix

Section 4.1 deals with analytical solutions of an approximate heat conductive cell problem, and we here give the derivation of these solutions. We seek the unknown functions $\Theta_f(y_1, y_1)$ and $\Theta_g(y_1, y_2)$ that should fulfill Eq. (3b) together with periodicity across the external cell boundary:

$$\Theta_f(y_1 = -1/2) = \Theta_f(y_1 = 1/2), \quad \Theta_f(y_2 = -1/2) = \Theta_f(y_2 = 1/2).$$

We use polar coordinates and assume separation of variables; hence, the solutions can be written

$$\Theta_f(r, \theta) = F_r(r)F_\theta(\theta), \quad \Theta_g(r, \theta) = G_r(r)G_\theta(\theta).$$

Then, the model equations from (3b) are

$$\begin{aligned} \frac{1}{r} \frac{d}{dr} \left(r \frac{dF_r}{dr} \right) F_\theta + \frac{1}{r^2} \frac{d^2 F_\theta}{d\theta^2} F_r &= 0, \quad y \in Y_0(x, t); \\ \frac{1}{r} \frac{d}{dr} \left(r \frac{dG_r}{dr} \right) G_\theta + \frac{1}{r^2} \frac{d^2 G_\theta}{d\theta^2} G_r &= 0, \quad y \in G_0(x, t), \end{aligned}$$

while the interior boundary conditions can be written as

$$\cos \theta + F'_r(R) F_\theta = \kappa \cos \theta + \kappa G'_r(R) G_\theta \text{ at } r = R, \quad (8a)$$

$$F_r(R) F_\theta = G_r(R) G_\theta \text{ at } r = R, \quad (8b)$$

and for all θ . The model equations for F_θ and G_θ reduce to $F''_\theta = -\lambda F_\theta$ for some number λ , which, together with the interior boundary condition (8a), suggest that

$$F_\theta(\theta) = G_\theta(\theta) = \cos \theta.$$

The model equations for F_r and G_r are then reduced to $r^2 F''_r + r F'_r - F_r = 0$, which have the general solutions

$$F_r(r) = b_1 r + b_2 \frac{1}{r}, \quad G_r(r) = b_3 r + b_4 \frac{1}{r},$$

where b_1, b_2, b_3, b_4 are integration constants. However, our assumption of separation of variables together with the solution in θ leads to the periodicity requirement on the external boundary not being fulfilled. There is periodicity across the horizontal boundaries, but periodicity across the vertical boundaries is not met. We instead search an approximate solution through alternative boundary conditions for the external boundary and consider two approaches: either dropping the external boundary and allowing Θ_f to be well defined for all $r > R$; or, keeping the boundary, but neglecting the boundary conditions and using other means to determine the constants b_1, b_2, b_3, b_4 .

Alternative I: Infinite Domain

We allow Θ_f to be defined for all $r > R$; hence, we require it to be finite as $r \rightarrow \infty$. Also, as Θ_g must be well defined as $r \rightarrow 0$, the general solutions in r are

$$F_r(r) = b_2 \frac{1}{r}, \quad G_r(r) = b_3 r.$$

Applying the internal boundary conditions (8) results in $b_2 = R^2(1 - \kappa)/(1 + \kappa)$ and $b_3 = (1 - \kappa)/(1 + \kappa)$. Hence, the solutions of the approximate cell problem are

$$\begin{aligned} \Theta_f(r, \theta) &= R^2 \frac{1 - \kappa}{1 + \kappa} \frac{1}{r} \cos \theta, \\ \Theta_g(r, \theta) &= \frac{1 - \kappa}{1 + \kappa} r \cos \theta. \end{aligned}$$

The approximate heat conductivity coefficients are then

$$\begin{aligned} \mathcal{A}_f &= \int_{Y_0(x,t)} (1 + \partial_x \Theta_f) dy = 1 - \pi R^2, \\ \mathcal{A}_g &= \int_{G_0(x,t)} (1 + \partial_x \Theta_g) dy = \pi R^2 \frac{2}{1 + \kappa}. \end{aligned}$$

Although Θ_f is now defined for all $r > R$, the original integration area for \mathcal{A}_f is used. As we made an error by allowing Θ_f to exist as $r \rightarrow \infty$, and as we know the sum of \mathcal{A}_f and \mathcal{A}_g should be 1 when in the finite pore space domain, our above approximation can be improved by scaling the above coefficients with the same number such that their sum is 1. Hence,

$$\mathcal{A}_f = (1 - \pi R^2) \frac{1 + \kappa}{(1 + \kappa)(1 - \pi R^2) + 2\pi R^2}, \tag{9a}$$

$$\mathcal{A}_g = \pi R^2 \frac{2}{(1 + \kappa)(1 - \pi R^2) + 2\pi R^2}. \tag{9b}$$

Alternative II: No Periodic Boundary Condition

In this approach, we keep the external boundary but do not require periodicity across it. We still require Θ_g to be well defined as $r \rightarrow 0$, and hence $b_4 = 0$ and the three remaining constants must be such that they fulfill the two internal boundary conditions (8):

$$1 + b_1 - \frac{b_2}{R^2} = \kappa + \kappa b_3,$$

$$1 + b_1 R + \frac{b_2}{R} = b_3 R.$$

Expressing b_2, b_3 as functions of b_1 leads to

$$b_2 = R^2 \frac{1 - \kappa}{1 + \kappa} (1 + b_1),$$

$$b_3 = \frac{1 - \kappa}{1 + \kappa} + \frac{2b_1}{1 + \kappa}.$$

The solutions of the (approximate) cell problem are then

$$\Theta_f(r, \theta) = \left(b_1 + \frac{R^2}{r^2} \frac{1 - \kappa}{1 + \kappa} (1 + b_1) \right) r \cos \theta,$$

$$\Theta_g(r, \theta) = \left(\frac{1 - \kappa}{1 + \kappa} + \frac{2b_1}{1 + \kappa} \right) r \cos \theta,$$

where the constant b_1 is to be determined later. The heat conductivities are then

$$\mathcal{A}_f = \int_{Y_0(x,t)} (1 + \partial_x \Theta_f) dy = (1 - \pi R^2)(1 + b_1),$$

$$\mathcal{A}_g = \int_{G_0(x,t)} (1 + \partial_x \Theta_g) dy = \pi R^2 \frac{2(1 + b_1)}{1 + \kappa}.$$

We now require the sum $\mathcal{A}_f + \mathcal{A}_g$ to be 1 and use this to determine b_1 . This way,

$$\mathcal{A}_f = (1 - \pi R^2) \frac{1 + \kappa}{1 + \kappa + \pi R^2(1 - \kappa)}, \tag{10a}$$

$$\mathcal{A}_g = \pi R^2 \frac{2}{1 + \kappa + \pi R^2(1 - \kappa)}. \tag{10b}$$

Although this derivation uses different assumptions than Alternative I, the resulting approximate heat conductivity coefficients \mathcal{A}_f and \mathcal{A}_g found in (9) and (10) are identical.

References

- Agosti, A., Formaggia, L., Scotti, A.: Analysis of a model for precipitation and dissolution coupled with a Darcy flux. *J. Math. Anal. Appl.* **431**, 752–781 (2015a). doi:[10.1016/j.jmaa.2015.06.003](https://doi.org/10.1016/j.jmaa.2015.06.003)
- Agosti, A., Formaggia, L., Giovanardi, B., Scotti, A.: MOX-report no. 08/2015, numerical simulation of geochemical compaction with discontinuous reactions. Tech. Rep., MOX, Politecnico di Milano (2015b)
- Bringedal, C., Berre, I., Radu, F.A.: An approach for investigation of geochemical rock-fluid interactions. In: Proceedings, Thirty-Ninth Workshop on Geothermal Reservoir Engineering, Stanford University (2014)
- Bringedal, C., Berre, I., Pop, I.S., Radu, F.A.: A model for non-isothermal flow and mineral precipitation and dissolution in a thin strip. *J. Comput. Appl. Math.* **289**, 346–355 (2015). doi:[10.1016/j.cam.2014.12.009](https://doi.org/10.1016/j.cam.2014.12.009)
- Bringedal, C., Berre, I., Pop, I.S., Radu, F.A.: Upscaling of non-isothermal reactive porous media flow with changing porosity. *Transp. Porous Media* **114**(2), 371–393 (2016). doi:[10.1007/s11242-015-0530-9](https://doi.org/10.1007/s11242-015-0530-9)
- Chadam, J., Hoff, D., Merino, E., Ortoleva, P., Sen, A.: Reactive infiltration instabilities. *IMA J. Appl. Math.* **36**(3), 207–221 (1986)
- Chadam, J., Peirce, A., Ortoleva, P.: Stability of reactive flows in porous media: coupled porosity and viscosity changes. *SIAM J. Appl. Math.* **51**(3), 684–692 (1991)
- COMSOL Inc. Version 4.2. <http://www.comsol.com> (2011)
- Duval, F., Fichot, F., Quintard, M.: A local thermal non-equilibrium model for two-phase flows with phase-change in porous media. *Int. J. Heat Mass Transf.* **47**(3), 613–639 (2004)
- Frank, F.: Numerical studies of models for elektrokinetic flow and charged solute transport in periodic porous media. Ph.D. thesis, Friedrich-Alexander-Universität Erlangen-Nürnberg (FAU) (2013)
- Frank, F., Ray, N., Knabner, P.: Numerical investigation of homogenized Stokes-Nernst-Planck-Poisson systems. *Comput. Vis. Sci.* **14**(8), 385–400 (2011)
- Knabner, P., van Duijn, C.J., Hengst, S.: An analysis of crystal dissolution fronts in flows through porous media. Part 1: compatible boundary conditions. *Adv. Water Resour.* **18**(3), 171–185 (1995)
- Kumar, K., van Noorden, T.L., Pop, I.S.: Effective dispersion equations for reactive flows involving free boundaries at the microscale. *Multiscale Model. Simul.* **9**(1), 29–58 (2011)
- Kumar, K., Pop, I.S., Radu, F.A.: Convergence analysis of mixed numerical schemes for reactive flow in a porous medium. *SIAM J. Numer. Anal.* **51**(4), 2283–2308 (2013a)
- Kumar, K., Wheeler, M.F., Wick, T.: Reactive flow and reaction-induced boundary movement in a thin channel. *SIAM J. Sci. Comput.* **35**(6), B1235–B1266 (2013b)
- Kumar, K., Pop, I.S., Radu, F.A.: Convergence analysis for a conformal discretization of a model for precipitation and dissolution in porous media. *Numer. Math.* **127**(4), 715–749 (2014)
- Kumar, K., Neuss-Radu, M., Pop, I.S.: Homogenization of a pore scale model for precipitation and dissolution in porous media. *IMA J. Appl. Math.* **81**(5), 877–897 (2016)
- Libbey, R.B., Williams-Jones, A.E.: Relating sulfide mineral zonation and trace element chemistry to subsurface processes in the Reykjanes geothermal system. *Iceland. J. Volcanol. Geotherm. Res.* **310**, 225–241 (2016)
- McNamara, D.D., Lister, A., Prior, A.J.: Calcite sealing in a fractured geothermal reservoir: insights from combined EBSD and chemistry mapping. *J. Volcanol. Geotherm. Res.* **323**, 38–52 (2016)
- Mielke, P., Nehler, M., Bignall, G., Sass, I.: Thermo-physical rock properties and the impact of advancing hydrothermal alteration—a case study from the Tauhara geothermal field. *New Zealand. J. Volcanol. Geotherm. Res.* **301**, 14–28 (2015)
- Mroczek, E.K., White, S.P., Graham, D.J.: Deposition of amorphous silica in porous packed beds predicting the lifetime of reinjection aquifers. *Geothermics* **29**(6), 737–757 (2000)
- Nield, D.A., Bejan, A.: *Convection in Porous Media*, 4th edn. Springer, Berlin (2013)
- Pape, H., Clauser, C., Iffland, J., Krug, R., Wagner, R.: Anhydrite cementation and compaction in geothermal reservoirs: interaction of pore-space structure with flow, transport, p-t conditions, and chemical reactions. *Int. J. Rock Mech. Min. Sci.* **42**(7), 1056–1069 (2005)
- Peter, M.A.: Coupled reaction-diffusion processes inducing an evolution of the microstructure: analysis and homogenization. *Nonlinear Anal. Theory Methods Appl.* **70**(2), 806–821 (2009)
- Ray, N., van Noorden, T.L., Radu, F.A., Friess, W., Knabner, P.: Drug release from collagen matrices including an evolving microstructure. *ZAMM J. Appl. Math. Mech.* **93**(10–11), 811–822 (2013)
- Schulz, R., Ray, N., Frank, F., Mahalo, H.S., Knabner, P.: Strong solvability up to clogging of an effective diffusion-precipitation model in an evolving porous medium. *Eur. J. Appl. Math.* **28**, 1–29 (2016)
- Sonnenthal, E., Ito, A., Spycher, N., Yui, M., Apps, J., Sugita, Y., Conrad, M., Kawakami, S.: Approaches to modeling coupled thermal, hydrological, and chemical processes in the drift scale heater test at yucca mountain. *Int. J. Rock Mech. Min. Sci.* **42**(5), 698–719 (2005)
- Taron, J., Elsworth, D.: Thermal-hydrologic-mechanical-chemical processes in the evolution of engineered geothermal reservoirs. *Int. J. Rock Mech. Min. Sci.* **46**, 654–855 (2009)

- Torquato, S.: Random Heterogeneous Materials: Microstructure and Macroscopic Properties. Springer, Berlin (2013)
- van Duijn, C.J., Knabner, P.: Travelling wave behavior of crystal dissolution in porous media flow. *Eur. J. Appl. Math.* **8**, 49–72 (1997)
- van Duijn, C.J., Pop, I.S.: Crystal dissolution and precipitation in porous media: pore scale analysis. *Journal für die reine und angewandte Mathematik* **577**, 171–211 (2004)
- van Noorden, T.L., Pop, I.S., Röger, M.: Crystal dissolution and precipitation in porous media: L1-contraction and uniqueness. In: *Discrete Contin. Dyn. Syst. (Dynamical Systems and Differential Equations. Proceedings of the 6th AIMS International Conference, Suppl.)*, pp. 1013–1020 (2007)
- van Noorden, T.L.: Crystal precipitation and dissolution in a porous medium: effective equations and numerical experiments. *Multiscale Model. Simul.* **7**(3), 1220–1236 (2009a)
- van Noorden, T.L.: Crystal precipitation and dissolution in a thin strip. *Eur. J. Appl. Math.* **20**, 69–91 (2009b)
- van Noorden, T.L., Pop, I.S., Ebigbo, A., Helmig, R.: An upscaled model for biofilm growth in a thin strip. *Water Resour. Res.* **46**(6) (2010). doi:[10.1029/2009WR008217](https://doi.org/10.1029/2009WR008217)
- Verma, A., Pruess, K.: Thermohydrological conditions and silica redistribution near high-level nuclear wastes emplaced in saturated geological formations. *J. Geophys. Res. Solid Earth (1978–2012)* **93**(B2), 1159–1173 (1988)
- Wagner, R., Kühn, M., Meyn, V., Pape, H., Vath, U., Clauser, C.: Numerical simulation of pore space clogging in geothermal reservoirs by precipitation of anhydrite. *Int. J. Rock Mech. Min. Sci.* **42**(7), 1070–1081 (2005)
- White, S.P., Mroczek, E.K.: Permeability changes during the evolution of a geothermal field due to the dissolution and precipitation of quartz. *Transp. Porous Media* **33**(1–2), 81–101 (1998)
- Woodside, W.M.J.H., Messmer, J.H.: Thermal conductivity of porous media. I. Unconsolidated sands. *J. Appl. Phys.* **32**, 1688–1699 (1961)
- Xu, T., Rose, P., Fayer, S., Pruess, K.: On modeling of chemical stimulation of an enhanced geothermal system using a high pH solution with chelating agent. *Geofluids* **9**, 167–177 (2009)
- Xu, T., Spycher, N., Sonnenthal, E., Zheng, L., Pruess, K.: TOUGHREACT user's guide: a simulation program for non-isothermal multiphase reactive transport in variably saturated geologic media, version 2.0. Earth Sciences Division, Lawrence Berkeley National Laboratory, Berkeley, USA (2012)
- Zhao, C.: Physical and Chemical Dissolution Front Instability in Porous Media: Theoretical Analyses and Computational Simulations. Springer, Berlin (2014)

Part B

Two-phase porous-media flow

The second part of this thesis consists of three chapters that are based on three journal publications. Each publication addresses derivation of effective behavior of two-phase flow from a pore-scale model. Different assumptions on domains and appearance of the evolving fluid-fluid interface are applied in the three chapters. Either homogenization or transversal averaging are used to derive the effective models. In all cases, the goal is to keep the influence of the evolving fluid-fluid interface in the derived model for the effective two-phase flow behavior.

Chapter 5: Layered two-phase flow in a thin strip In this chapter, a model for two-phase flow through a thin strip is the starting point. The fluid-fluid interface is assumed to be located along the strip, but can evolve due to the flow of the fluids and the surface tension between the fluids. The motivation behind such a setting is the flow of two fluids through a pore, channel or interface layer, where one fluid is wetting and therefore attaches to the walls. In this case, a layer width can be applied to model the location of the evolving fluid-fluid interface. Transversal averaging is applied to derive a dimensionally reduced (from 2D to 1D) model for the effective behavior of the two-phase flow. For different regimes with respect to the capillary number and viscosity ratio, different effective models are found. These effective models show some similarities with existing models for two-phase flow, but differ in how effective parameters for e.g. (Darcy-scale) capillary pressure behave. Numerical experiments of both the original, two-dimensional model using a level-set to describe the fluid-fluid interface, and of the derived effective models, show that the effective models approximate the transversal averaged behavior of the original model well as the thin strip becomes longer and thinner.

Chapter 6: Dynamic contact angle in a thin strip Also in the second chapter of Part B, two-phase flow in a thin strip is considered. The main difference from the setup in Chapter 5 is that now the fluid-fluid interface stretches across the strip. The same model equations for two-phase flow are however used as a starting point, except that also a contact angle and a slip condition now are incorporated, and a different approach to describe the evolving fluid-fluid interface is used. Transversal averaging is applied to derive a dimensionally reduced model for the effective behavior away from the fluid-fluid interface. The fluid-fluid interface itself appears as a discontinuity, hence the region near the interface must be handled in a different way. To couple the regions away from and near the fluid-fluid interface, matched asymptotic expansions are applied. The derived effective model for the entire thin strip is still a dimensionally reduced model, where the influence of a dynamic and hysteretic contact angle model is incorporated. In particular, the derived effective model is used to highlight the influence of such contact angles on the effective behavior.

Chapter 7: Two-phase flow in a periodic porous medium In the last chapter of this part, two-phase flow in a periodic porous medium is investigated. Here, a phase-field model for two-phase flow is used on the pore scale. In this chapter we are especially interested in the influence of a surfactant soluble in one of the fluid phases, which can alter the surface

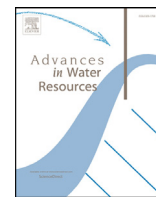
tension between the two fluids. This is modeled by adopting a special case of a phase-field model from [43]. By assuming that the pore-scale geometry is periodic, homogenization is applied to derive a Darcy-scale model for the effective behavior. The Darcy-scale model depends on local pore-scale cell problems for effective parameters, which are derived through the homogenization steps. The resulting two-scale model is implemented using a scheme inspired by heterogeneous multiscale methods. Numerical experiments with constant and varying surfactant concentration show the influence of the varying surface tension on the effective Darcy-scale behavior.

5 Layered two-phase flow in a thin strip

The content of this chapter is based on the following original article:

S. Sharmin, C. Bringedal, and I. S. Pop. *On upscaling pore-scale models for two-phase flow with evolving interfaces*. *Advances in Water Resources* 142 (2020), p. 103646. doi: 10.1016/j.advwatres.2020.103646.

With courtesy of Elsevier.



On upscaling pore-scale models for two-phase flow with evolving interfaces

Sohely Sharmin^{a,*}, Carina Bringedal^b, Iuliu Sorin Pop^a

^a Hasselt University, Campus Diepenbeek, Agoralaan Gebouw D, Diepenbeek 3590, Belgium

^b University of Stuttgart, Pfaffenwaldring 5a, Stuttgart 70569, Germany



ARTICLE INFO

Keywords:

Two-phase flow
Freely moving interface
Upscaled models
Marangoni effect
Capillary effect

ABSTRACT

The modelling and simulation of the unsaturated flow or the flow of two immiscible fluid phases in a porous medium is challenging as this flow takes place through the pores of the medium, which form a highly complex domain. Next to the complexity of the domain, a major challenge is to account for the interface separating the fluids, or the unsaturated fluid from the inert filling part, as the location of this interface is not known a-priori. The evolution of this interface depends on the flow of both fluids and of the surface tension. Moreover, the surface tension may depend on the concentration of a surfactant dissolved in one fluid phase. In this work, such aspects are taken into account, and effective, Darcy-scale models are derived based on the known physics at the pore scale. In this sense a thin strip is used as the representation of a single pore in the porous medium. The Darcy-scale models are derived for various regimes, accounting for different pore-scale processes. Numerical examples show that the upscaled models are a good approximation of the transversal average of the solution to the pore-scale models, as the ratio of the width and the length of the pore approaches zero.

1. Introduction

Two-phase flow in porous media is relevant for many industrial and environmental applications such as geological CO₂ sequestration, or oil recovery. Common for all these applications is the need to describe the flow at the Darcy scale (from now on the macro scale), the preferred scale for numerical simulations, where the grain and void space and the two (or more) fluid phases cannot be explicitly separated, but modelled through average quantities such as porosity and saturation. At the Darcy scale, the flow of each fluid phase is described with the help of Darcy-scale quantities like the absolute permeability, which depends strictly on the medium, and the fluid-specific relative permeability, which is a function of the fluid saturation.

The two-phase or, more general, the multi-phase and multi-component flow through a porous medium is inherently a process occurring at multiple scales, in which the processes at the pore scale do affect the overall flow on the Darcy scale. When considering the process at the scale of pores (here and below the micro scale), the fluids are assumed immiscible and they are separated by a fluid-fluid interface. The location of this interface gives directly the volume occupied by each of the two fluids within one pore, so it can be related directly to the saturation of the two fluids. The interface is evolving in an a-priori unknown manner, depending on the velocities of the two fluids and on the surface tension. This evolution has a high impact on the overall flow behaviour. Simply knowing the saturation of the two fluids is not sufficient for describing

the overall flow behaviour. We need to understand the processes affecting the fluid-fluid interface to be able to describe the flow.

One of the first mathematical models for the Darcy-scale flow in a porous medium was formulated by Henry Darcy (Darcy (1856)), based on experiments. In these experiments only one fluid phase was considered, occupying the entire pore space so the porous medium was fully saturated. The experiments showed a proportionality between the pressure gradient and the flow rate. Subsequent extensions, still based on experimental observations, have considered unsaturated media (Richards (1931), two-phase flow (Morrow and Harris (1965)), or reactive transport (Schechter and Gidley (1969)) in porous media. Traditionally, the flow models involve the mass balance for each phase, the Darcy law with a saturation-dependent (relative) permeability, and that the phase-pressure difference (the capillary pressure) is a nonlinear, monotone function of the saturation of the (say) wetting fluid. The relative permeability functions, and the one for the capillary pressure, are determined experimentally.

Although extensively used such models need improvements, as also motivated by experimental results. As shown in (Morrow and Harris (1965)), the capillary pressure - saturation function also depends on the process (infiltration or drainage). Also, the break-through curves determined in (Bottero et al. (2011)) for the phase-pressure difference, respectively for the saturation, reveal that the dependency of the former quantity on the latter is not necessarily monotone. Next to this, there is indirect evidence of the limited validity of assuming a nonlinear

* Corresponding author.

E-mail address: sohely.sharmin@uhasselt.be (S. Sharmin).

relationship dependency of the capillary pressure and the saturation. In this respect we mention that effects like saturation overshoot or finger formation, clearly evidenced in experiments reported e.g. in DiCarlo (2004); Pouloussis (1970); Shiozawa and Fujimaki (2004); Zhuang et al. (2019) and Glass et al. (1989); Rezaeezad et al. (2006), are ruled out by the mathematical models used traditionally.

To overcome these drawbacks, extensions of Darcy's law for unsaturated or two-phase flow in porous media have been proposed. In this sense we start by mentioning Abreu et al. (2019); Beliaev and Schotting (2001); Beliaev and Hassanizadeh (2001); van Duijn and Mitra (2018); Plohr et al. (2001), where different play-type hysteresis models are being proposed (an overview is provided in Schweizer (2017)), and Beliaev and Hassanizadeh (2001); Hassanizadeh and Gray (1993) for models incorporating dynamic effects in the capillary pressure - saturation dependency. Inspired by the thin film model proposed in Huppert (1982), a phase-field model involving the second-order spatial derivative of the saturation in the capillary pressure is proposed in Cueto-Felgueroso and Juanes (2008, 2009) for unsaturated flow in porous media (also see Armiti-Juber and Rohde (2020)). Finally, in Doster and Hilfer (2011) a model accounting for the differences between percolating and non-percolating parts of a fluid is discussed, whereas the interfacial area concept is incorporated in the porous media flow models discussed in Niessner and Hassanizadeh (2008); Hassanizadeh and Gray (1990); Pop et al. (2009).

The effectiveness of such extensions in capturing phenomena like saturation overshoot and fingering is evidenced in Zhuang et al. (2019); Cueto-Felgueroso and Juanes (2009); Chapwanya and Stockie (2010); van Duijn et al. (2013, 2018); Hilfer et al. (2012); Lamacz et al. (2011); Rätz and Schweizer (2014); Schneider et al. (2018); Zhang and Zegeling (2017). Two different major strategies can be observed in these papers. The first is to present numerical simulations for the extended models, aiming to reproduce the experimental results quantitatively. The second relies on mathematical analysis, and in particular on travelling waves, the focus being mainly on the qualitative behaviour of the solution, and in particular the dependence on the parameters appearing in the extended models.

The extended models discussed above are stated at the Darcy scale, where no distinction is being made between the pore space, where fluid flow takes place. These models are describing the averaged behaviour of the system by considering so-called representative elementary volumes, and without focussing on the detailed description of the processes inside each pore. Alternatively, one can consider the mathematical models valid at the scale of pores, which leads to models posed in an extremely complex domain consisting of the entire pore space of the porous medium. Such an approach allows to incorporate detailed pore-scale physics, which is generally better understood. There are various possibilities in this direction, like the smoothed particle hydrodynamics based simulations in Tartakovsky and Meakin (2006), the pore-network modelling in Joekar-Niasar and Hassanizadeh (2012) and we refer to Golparvar et al. (2018) for a review of such approaches. Closer to the present work are Mehmani and Tchelepi (2019) and Mehmani and Tchelepi (2018), where direct numerical simulations tools are developed to understand the flow and the interface dynamics at the scale of pores, and these tools are then incorporated in a multi-scale simulator. However, a numerical simulation at such detailed level and for the entire domain of interest remains simply infeasible for practical applications due to the computational complexity. To overcome the difficulties related to the complexity of the domain, one can apply upscaling techniques to derive Darcy-scale models. Such an approach is adopted in Mikelić (2003); Mikelić and Paoli (2000), by considering a simple pore geometry consisting of a long and thin pore, and for which transversal averaging is applied to derive a Darcy scale model. In this way, various model components and features can be included in a quite straightforward manner, and the corresponding Darcy-scale models can be derived in a rational manner. Recently Picchi and Battiato (2018) proposed an upscaling technique where they considered different flow distributions and de-

rived regime-specific upscaled model. To derive the upscaled models they assumed that the location of the fluid-fluid interface is known and stationary.

Here we follow the same approach as in Mikelić (2003); Mikelić and Paoli (2000) for deriving Darcy-scale models for two-phase or unsaturated, one-phase flow in porous media. In the former case a wetting and a non-wetting fluid are present, in the latter only a wetting fluid is present together with a fluid that has constant pressure (say, zero) and infinite mobility. The fluids are assumed incompressible and immiscible. The derived models also take into account the possibility that one fluid is transporting a solute, which has an impact on the surface tension coefficient. We start with formulating the relevant models at the pore scale and then derive upscaled (Darcy-scale) models based on reasonable assumptions on the underlying physics.

At the pore scale we assume that the flow of each fluid phase is modelled by the Navier-Stokes equations. When referring to two fluid phases (the unsaturated, one-phase case being similar), a peculiar aspect in this approach is in the fact that, since the fluids are assumed immiscible, at the pore scale they are separated by an interface having a location that is not known a-priori. This interface moves depending on the fluid velocities, and, if applicable, on the concentration of the solute at this interface. In mathematical terms, this interface represents a free boundary in the model. Jump conditions ensuring conservation of the involved quantities are used at the evolving interface, as well as kinematic conditions to model its evolution.

We consider here a single pore as a representative for the porous medium. The pore is long and thin, specifically a thin strip. Although this is a very simple geometry, upscaling thin-strip models in other contexts (e.g. biofilm growth van Noorden et al. (2010) and mineral precipitation van Noorden (2009b)) has shown that the upscaled models have the same structure as commonly accepted Darcy-scale models in general porous media (see van Noorden (2009a) and Schulz and Knabner (2017)). The advantage of using a single pore is that analytical expressions for the upscaled quantities are obtained. Inside the thin strip we assume that the two fluids have a layered structure. Hence, the location of the interface separating the two fluid phases can also uniquely describe the thickness of the wetting phase and hence the saturation. Such a fluid distribution is the same as the core-annular flow in Picchi and Battiato (2018) and the thin-film flow in Mikelić and Paoli (2000). In Picchi and Battiato (2018), upscaled models for core-annular flow and other fluid distributions are derived, but under steady-state conditions. Here we explicitly account for the evolving fluid-fluid interface by treating the width of the wetting phase as a variable. For more complicated situations, one can use e.g. a level-set approach Osher and Fedkiw (2001) to track the location of the interface. Alternatively, a diffuse-interface approach can be considered, using e.g. the phase-field model in Abels et al. (2012).

In any of these approaches, the resulting models can be used for deriving the upscaled, Darcy scale counterparts, which are more suited for numerical simulations. For the simplified situation here, we apply asymptotic expansion techniques and transversal averaging to derive the upscaled mathematical models. In doing so, we also include a solute-dependent surface tension, leading to so-called Marangoni effects in the upscaled equations.

An alternative to homogenization is the method of volume averaging, which has been successfully applied to upscaling two-phase flow in porous media in Whitaker (1986); Quintard and Whitaker (1988). The upscaled model in Quintard and Whitaker (1988) was explored numerically in Quintard and Whitaker (1990b) for stratified flows and compared to the dynamic setting in Quintard and Whitaker (1990a). The work from Quintard and Whitaker (1988) has been extended in Lasseux et al. (1996) to further investigate the resulting permeability tensors derived by the volume averaging.

This work is builds on Mikelić (2003); Mikelić and Paoli (2000), where mathematically rigorous upscaling results are obtained for two-phase flow in a single pore. Compared to Mikelić (2003); Mikelić and

Paoli (2000), here we consider more regimes with respect to the capillary number, and also include solute effects in the surface tension dependency. We also mention that, although not considering the flow in a porous medium, in Bresch (2009) a similar approach is used for deriving the shallow-water equations.

In this context, we mention that asymptotic homogenization methods in either a thin strip or in a periodic porous medium have been widely applied for many application in which evolving interfaces are encountered at the pore scale. Examples in this sense are the evolving fluid-solid interface due to mineral precipitation and dissolution van Noorden (2009b,a); Bringedal et al. (2015, 2016b, 2016a); Kumar et al. (2011); Schulz (2019b), or to biofilm growth or other biological processes van Noorden et al. (2010); Schulz and Knabner (2017); Landa-Marbán et al. (2020); Peszynska et al. (2016); Ray et al. (2013, 2012); Schulz (2019a). In all these cases, the derived Darcy-scale models were resembling well many of the models that are commonly accepted in the literature, but allow integrating additional effects in a rational manner.

The paper is organized as follows. In the next section the physical processes at the pore-scale and the corresponding mathematical models are introduced. With ϵ being a small parameter representing the ratio of the pore width and length, in Section 3, the pore-scale models are non-dimensionalized and their dependence on ϵ is derived. In Section 4 asymptotic expansion methods are applied to the pore-scale models and for various scaling regimes, and the corresponding upscaled are derived. In this sense, the cases in which the Marangoni effects do play a role at the Darcy scale are evidenced. Also, cases where the two upscaled fluid pressures are equal, or where the capillary pressure depends on the saturation in a non-standard way, resembling the models in Cueto-Felgueroso and Juanes (2008, 2009); Mikelić and Paoli (2000); Mikelić (2003). The results are summarized and discussed more closely in Section 5. In Section 6 provides some numerical examples that confirm the validity of the approach. Specifically, the numerical solutions to the original, pore-scale models are computed for different situations, and then their transversal averages are compared to the solutions to the upscaled models. These results support that, as ϵ approaches zero, the upscaled models are describing well the averaged behaviour of the considered pore-scale models. Finally, in Section 7 the different upscaled models are compared, highlighting the upscaled behaviour of the considered physical phenomena.

2. Mathematical model

A pore-scale model is considered for two-phase or unsaturated flow through a porous medium. For simplicity, we considered a thin two-dimensional strip to represent the local pore geometry. Two incompressible and immiscible fluids, where one is wetting and the other is non-wetting, are flowing through the strip. Densities and viscosities of the fluids are constant. The wetting phase is attached to the pore wall and the wetting layer has a thickness that changes with time and varies with the location of the wall. The two fluids are separated by a sharp interface with zero thickness which is changing with time. The movement is not known a-priori, hence we have a moving boundary at the fluid-fluid interface. The interface that separates the fluids moves because of the surface tension and of the flow/movement of the two fluids. There is a solute present only in the wetting fluid and the concentration of the solute will change subject to diffusion and transport. The surface tension is considered as a function of the solute concentration, which results in a tangential stress at the moving interface which is called the Marangoni stress. The gravity effects are neglected.

2.1. Geometric settings

The width and length of the thin strip are respectively $2l$ and L with $L \gg l$. For simplicity, we assume a symmetric case with respect to (w.r.t.) the x-axis. The lower half of the strip is shown in Fig. 1. Let

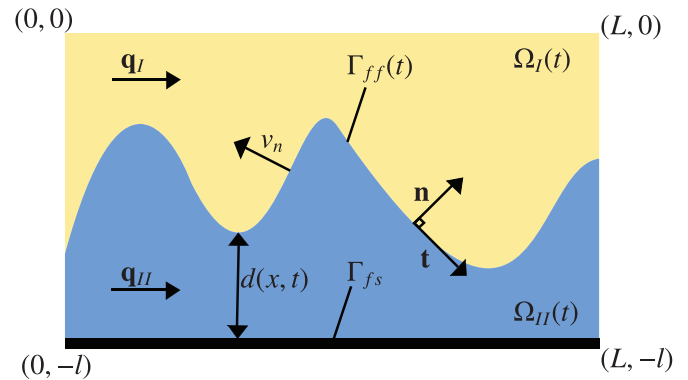


Fig. 1. Schematic representation of the lower half of a single pore.

$t > 0$ be the time variable. The thickness of the wetting fluid layer is denoted by $d(x, t)$, where $0 \leq d(x, t) \leq l$. The void space consists of two domains. The domain occupied by the non-wetting fluid (fluid-I) and by the wetting (fluid-II) fluid are denoted by respectively

$$\Omega_I(t) := \{(x, y) \in \mathbb{R}^2 | 0 < x < L, -l + d(x, t) < y < 0\},$$

$$\Omega_{II}(t) := \{(x, y) \in \mathbb{R}^2 | 0 < x < L, -l < y < -l + d(x, t)\}.$$

The fluid-fluid interface and the fluid-solid interface are respectively

$$\Gamma_{ff}(t) := \{(x, y) \in \mathbb{R}^2 | 0 < x < L, y = -l + d(x, t)\},$$

$$\Gamma_{fs} := \{(x, y) \in \mathbb{R}^2 | 0 < x < L, y = -l\}.$$

The velocity vectors are denoted by $\mathbf{q}_\alpha = (q_\alpha^{(1)}, q_\alpha^{(2)})$, where the index $\alpha = I, II$ is distinguishing between the non-wetting and the wetting fluid, respectively.

Since $d(x, t)$ gives the location of the fluid-fluid interface, the unit normal vector on the fluid-fluid interface pointing into fluid-I and the unit tangent vector are

$$\mathbf{n} := (-\partial_x d, 1)^T / \sqrt{1 + (\partial_x d)^2}, \text{ and } \mathbf{t} := (1, \partial_x d)^T / \sqrt{1 + (\partial_x d)^2}.$$

Given a point $(x, -l + d(x, t))$ on $\Gamma_{ff}(t)$, its normal velocity is

$$v_n := \partial_t d / \sqrt{1 + (\partial_x d)^2}. \quad (1)$$

2.2. Equations in the pore domain

We refer to Patankar (1980) and assume that the flow of the two fluids is governed by the Navier-Stokes equations

$$\begin{aligned} \rho_\alpha \partial_t \mathbf{q}_\alpha + \rho_\alpha (\mathbf{q}_\alpha \cdot \nabla) \mathbf{q}_\alpha &= -\nabla p_\alpha + \mu_\alpha \nabla^2 \mathbf{q}_\alpha, & \text{in } \Omega_\alpha(t) \ (\alpha = I, II), \\ \nabla \cdot \mathbf{q}_\alpha &= 0, & \text{in } \Omega_\alpha(t) \ (\alpha = I, II). \end{aligned}$$

where ρ_α and μ_α are respectively the constant viscosities and densities, and the pressures are p_α . For simplicity gravity effects are neglected.

We assume that one chemical species (solute) is present in fluid-II, its molar concentration being c . Additionally, there is no mass transfer of the solute from fluid-II to fluid-I, hence, the molar concentration of the solute in fluid-I is zero. The solute concentration changes both by diffusion and convection, resulting in

$$\partial_t c + \nabla \cdot (-D \nabla c + \mathbf{q}_{II} c) = 0, \text{ in } \Omega_{II}(t),$$

where D is the constant diffusion coefficient.

To complete the model above appropriate initial conditions, inflow and outflow boundary conditions can be added. However, as the upscaling procedure is independent of the choice of initial and external boundary conditions, these will not be specified here.

2.3. Boundary conditions at the fluid-fluid interface $\Gamma_{ff}(t)$

Here, we specify the boundary conditions at $\Gamma_{ff}(t)$. This means that all equations in this section are valid only at points at $\Gamma_{ff}(t)$. Firstly, we assume that the velocities of the two fluids are equal at $\Gamma_{ff}(t)$,

$$\mathbf{q}_I = \mathbf{q}_{II}.$$

Secondly, we assume that the normal velocity of $\Gamma_{ff}(t)$ as given in (1), equals the normal velocities of the two fluids,

$$\mathbf{q}_\alpha \cdot \mathbf{n} = v_n \quad (\alpha = I, II).$$

Further conditions at $\Gamma_{ff}(t)$ are involving the stress tensors

$$\mathbf{T}_\alpha := -p_\alpha \mathbf{I} + \mu_\alpha ((\nabla \mathbf{q}_\alpha) + (\nabla \mathbf{q}_\alpha)^T) \quad (\alpha = I, II),$$

the curvature of $\Gamma_{ff}(t)$

$$\nabla \cdot \mathbf{n} := -\partial_x \left(\frac{\partial_x d}{\sqrt{1 + (\partial_x d)^2}} \right),$$

and the surface tension γ . If γ is affected by the presence of the solute present in fluid-II, one has $\gamma = \gamma(c)$. For example, in [Smith and Gillham \(1999\)](#) the following law is proposed

$$\gamma(c) = \gamma_{ref} \left(1 - b \ln \left(\frac{c}{a c_{ref}} + 1 \right) \right), \quad (2)$$

where a , b are constants and γ_{ref} is the surface tension at reference concentration c_{ref} . Its tangential stress gradients is

$$\nabla_s \gamma(c) := \nabla \gamma(c) - \mathbf{n}(\mathbf{n} \cdot \nabla \gamma(c)).$$

With this, the third boundary condition at $\Gamma_{ff}(t)$ reads (see [Leal \(2007\)](#))

$$(\mathbf{T}_I - \mathbf{T}_{II}) \cdot \mathbf{n} = \gamma(c) (\nabla \cdot \mathbf{n}) \mathbf{n} - \nabla_s \gamma(c).$$

This jump can be written in terms of the normal and the tangential components. At $\Gamma_{ff}(t)$, for the normal component, one has

$$((\mathbf{T}_I - \mathbf{T}_{II}) \cdot \mathbf{n}) \cdot \mathbf{n} = \gamma(c) (\nabla \cdot \mathbf{n}),$$

while for the tangential component, also known as Marangoni stress, one gets

$$((\mathbf{T}_I - \mathbf{T}_{II}) \cdot \mathbf{n}) \cdot \mathbf{t} = -\mathbf{t} \cdot \nabla \gamma(c).$$

Finally, the mass balance for the solute at $\Gamma_{ff}(t)$ reads

$$(-D\nabla c + \mathbf{q}_{II}c) \cdot \mathbf{n} = v_n c.$$

2.4. Boundary conditions at the fluid-solid interface Γ_{fs}

As before, the equations hold only at the fluid-solid interface Γ_{fs} , where first no-slip is assumed,

$$\mathbf{q}_{II} = \mathbf{0}.$$

For the solute concentration, the normal flux into the solid matrix is zero,

$$(-D\nabla c + \mathbf{q}_{II}c) \cdot \mathbf{n} = 0.$$

2.5. Pore-scale model for the two-phase flow with solute-dependent surface tension

Recall that the sub-domain occupied by fluid α is time dependent, $\Omega_\alpha(t)$, and that the freely moving fluid-fluid interface is $\Gamma_{ff}(t)$ and considering the discussion above, one has

$$\rho_\alpha \partial_t \mathbf{q}_\alpha + \rho_\alpha (\mathbf{q}_\alpha \cdot \nabla) \mathbf{q}_\alpha = -\nabla p_\alpha + \mu_\alpha \nabla^2 \mathbf{q}_\alpha, \text{ in } \Omega_\alpha(t) \quad (\alpha = I, II), \quad (3)$$

$$\nabla \cdot \mathbf{q}_\alpha = 0, \text{ in } \Omega_\alpha(t) \quad (\alpha = I, II), \quad (4)$$

$$\partial_t c + \nabla \cdot (-D\nabla c + \mathbf{q}_{II}c) = 0, \text{ in } \Omega_{II}(t), \quad (5)$$

$$\mathbf{q}_I = \mathbf{q}_{II}, \text{ at } \Gamma_{ff}(t), \quad (6)$$

$$\mathbf{q}_\alpha \cdot \mathbf{n} = v_n, \text{ at } \Gamma_{ff}(t) \quad (\alpha = I, II), \quad (7)$$

$$((\mathbf{T}_I - \mathbf{T}_{II}) \cdot \mathbf{n}) \cdot \mathbf{n} = \gamma(c) (\nabla \cdot \mathbf{n}), \text{ at } \Gamma_{ff}(t), \quad (8)$$

$$((\mathbf{T}_I - \mathbf{T}_{II}) \cdot \mathbf{n}) \cdot \mathbf{t} = -\mathbf{t} \cdot \nabla \gamma(c), \text{ at } \Gamma_{ff}(t), \quad (9)$$

$$(-D\nabla c + \mathbf{q}_{II}c) \cdot \mathbf{n} = v_n c, \text{ at } \Gamma_{ff}(t), \quad (10)$$

$$\mathbf{q}_{II} = \mathbf{0}, \text{ at } \Gamma_{fs}, \quad (11)$$

$$(-D\nabla c + \mathbf{q}_{II}c) \cdot \mathbf{n} = 0, \text{ at } \Gamma_{fs}. \quad (12)$$

2.6. Pore-scale model for the two-phase flow with constant surface tension

Whenever the surface tension is constant, as happening e.g. in the absence of a solute in fluid-II or with a constant solute concentration, the tangential components of the normal stresses are equal at $\Gamma_{ff}(t)$. In this case, the pore-scale model is simpler, as (5), (10) and (12) become superfluous, while $\gamma(c) = \gamma$ in (8) and (9) reduces to

$$((\mathbf{T}_I - \mathbf{T}_{II}) \cdot \mathbf{n}) \cdot \mathbf{n} = \gamma (\nabla \cdot \mathbf{n}), \quad \text{at } \Gamma_{ff}(t),$$

$$((\mathbf{T}_I - \mathbf{T}_{II}) \cdot \mathbf{n}) \cdot \mathbf{t} = 0, \quad \text{at } \Gamma_{ff}(t).$$

The remaining equations are the same as in [Section 2.5](#).

2.7. Pore-scale model for the unsaturated flow with constant surface tension

A further simplification is to assume that the pressure in the fluid-I is constant and that its mobility is infinite. Essentially, this means that fluid-I plays no role for the flow of fluid-II. This situation appears e.g. if fluid-I is air and is connected to the atmosphere. Alternatively, this pore-scale model can be interpreted as a thin-film flow with an open surface where a liquid is attached to the wall of the pore and the middle domain is occupied by air. Then the number of variables reduces to those corresponding to fluid-II. Moreover, we assume the solute is absent in fluid-II, and the surface tension is constant. In this case, (5), (10) and (12) are excessive. Moreover, the model equations in [Section 2.5](#) are further simplified by giving up the equations for $\alpha = I$, reducing to the Navier-Stokes equations in $\Omega_{II}(t)$. At $\Gamma_{ff}(t)$, (7) is valid for $\alpha = II$, and (8), (9) shortens to

$$(\mathbf{T}_{II} \cdot \mathbf{n}) \cdot \mathbf{n} = -\gamma (\nabla \cdot \mathbf{n}), \quad \text{at } \Gamma_{ff}(t),$$

$$(\mathbf{T}_{II} \cdot \mathbf{n}) \cdot \mathbf{t} = 0, \quad \text{at } \Gamma_{ff}(t).$$

3. The non-dimensional model equations

To identify the model components that have a larger or smaller impact than others, we first bring the model to a non-dimensional form. To this aim, we use reference quantities and rescale the dimensional ones as specified in [Table 1](#). In particular, μ_{II} and ρ_{II} are taken as reference viscosity, respectively density. [Table 1](#) introduces two length scales, L and l . In a general porous medium, L would reflect the length scale of the entire medium, where l is the one of a pore. As we let a single pore represent the porous medium, we use the width and the length of the pore as described in [Section 2.1](#). In the same spirit, here we define the non-dimensional number $\epsilon := \frac{l}{L} > 0$, and assume that ϵ is small. Observe now that the x and y coordinates are scaled differently,

Table 1
Reference and non-dimensional quantities.

Variables	Reference values	Non-dimensional variables
time	t_{ref}	$\hat{t} = t/t_{ref}$
space	$x_{ref} = L, y_{ref} = l$	$\hat{x} = x/L, \hat{y} = y/l = y/(\epsilon L)$
depth of the wetting fluid		$\hat{d} = d/l = d/(\epsilon L)$
velocities	$q_{ref} = L/t_{ref}$	$\hat{\mathbf{q}}_I = \mathbf{q}_I/q_{ref}, \hat{\mathbf{q}}_{II} = \mathbf{q}_{II}/q_{ref}$
densities	$\rho_{ref} = \rho_{II}$	$\hat{\rho}_I = \rho_I/\rho_{II} = 1/N, \hat{\rho}_{II} = 1$
pressures	$p_{ref} = (L^4 \rho_{ref}) / (t_{ref}^2 l^2)$	$\hat{p}_I = p_I/p_{ref}, \hat{p}_{II} = p_{II}/p_{ref}$
kinematic viscosities	$\mu_{ref} = (l^2 \rho_{ref}) / (L q_{ref}) = \mu_{II}$	$\hat{\mu}_I = \mu_I/\mu_{II} = 1/M, \hat{\mu}_{II} = 1$
surface tension	γ_{ref}	$\hat{\gamma}(\hat{c}^\epsilon) = \gamma(c)/\gamma_{ref},$ $\hat{\gamma} = \gamma/\gamma_{ref} = 1, \text{ if } \gamma \text{ is constant}$
diffusion coefficient	$D_{ref} = L^2/t_{ref}$	$\hat{D} = D/D_{ref}$
molar concentration	c_{ref}	$\hat{c}^\epsilon = c/c_{ref}$
capillary number		$\text{Ca} = (\mu_{ref} q_{ref}) / \gamma_{ref}$

so that they become both of order 1, $\mathcal{O}(1)$. Based on this, the derivatives change into $\frac{\partial}{\partial \hat{x}} = L \frac{\partial}{\partial x}, \frac{\partial}{\partial \hat{y}} = \epsilon L \frac{\partial}{\partial y}$. The non-dimensional gradient is $\hat{\nabla} := \left(\partial_{\hat{x}}, \frac{1}{\epsilon} \partial_{\hat{y}} \right)$ due to the different scaling in x and y -direction.

Some assumptions are made in Table 1 by choosing the scaling for μ_{ref}, D_{ref} and p_{ref} . The ratio of the time scales for the diffusion and the convective transport, referred to as the Péclet number, $Pe = \frac{q_{ref} x_{ref}}{D_{ref}}$ is chosen moderate w.r.t ϵ . For simplicity, the Péclet number is taken equal to 1. However, in van Noorden et al. (2010); van Noorden (2009b,a); Schulz and Knabner (2017); Bringedal et al. (2015, 2016a); Schulz (2019b); Landa-Marbán et al. (2020); Peszynska et al. (2016); Ray et al. (2013, 2012) the case of moderate Péclet number (when diffusion dominates or is in balance with the transport) and in Bringedal et al. (2016b); Kumar et al. (2011); van Duijn et al. (2008); Mauri (2003) the case of high Péclet number (when the convective transport dominates the diffusion) are considered. Additionally, the scaling of the p_{ref} and μ_{ref} are chosen such that the Reynolds number, $Re = \frac{\rho_{ref} q_{ref} x_{ref}}{\mu_{ref}}$ is moderate, namely equal to 1 and the Euler number, $Eu = \frac{p_{ref}}{q_{ref}^2 \rho_{ref}}$, is equal to ϵ^{-2} . These choices ensure laminar flow and that the pressure drop dominates the flow, which are needed to ensure validity of Darcy's law on the macro scale.

Note that the dimensionless parameters M, N appearing in Table 1,

$$M := \mu_{II}/\mu_I, N := \rho_{II}/\rho_I,$$

may also depend on ϵ . In this respect, here we restrict to the case $N = 1$, while M is assumed first $\mathcal{O}(1)$, and later the limit $M \rightarrow \infty$ is considered to show that the two-phase model reduces to the unsaturated, single-phase one.

In the non-dimensional setting, the pore space occupied by the two fluids is

$$\hat{\Omega}_I^\epsilon(\hat{t}) := \{(\hat{x}, \hat{y}) \in \mathbb{R}^2 | 0 < \hat{x} < 1, -1 + \hat{d}^\epsilon(\hat{x}, \hat{t}) < \hat{y} < 0\}, \quad (13)$$

$$\hat{\Omega}_{II}^\epsilon(\hat{t}) := \{(\hat{x}, \hat{y}) \in \mathbb{R}^2 | 0 < \hat{x} < 1, -1 < \hat{y} < -1 + \hat{d}^\epsilon(\hat{x}, \hat{t})\}. \quad (14)$$

The fluid-fluid and fluid-solid interfaces become

$$\hat{\Gamma}_{ff}^\epsilon(\hat{t}) := \{(\hat{x}, \hat{y}) \in \mathbb{R}^2 | 0 < \hat{x} < 1, \hat{y} = -1 + \hat{d}^\epsilon(\hat{x}, \hat{t})\},$$

$$\hat{\Gamma}_{fs} := \{(\hat{x}, \hat{y}) \in \mathbb{R}^2 | 0 < \hat{x} < 1, \hat{y} = -1\}.$$

The normal and tangent unit vectors are, respectively

$$\hat{\mathbf{n}}^\epsilon := \frac{(-\epsilon \partial_{\hat{x}} \hat{d}^\epsilon, 1)}{\sqrt{1 + (\epsilon \partial_{\hat{x}} \hat{d}^\epsilon)^2}}, \text{ and } \hat{\mathbf{t}}^\epsilon := \frac{(1, \epsilon \partial_{\hat{x}} \hat{d}^\epsilon)}{\sqrt{1 + (\epsilon \partial_{\hat{x}} \hat{d}^\epsilon)^2}}.$$

The normal velocity becomes

$$\hat{v}_n^\epsilon := \frac{\epsilon \partial_{\hat{t}} \hat{d}^\epsilon}{\sqrt{1 + (\epsilon \partial_{\hat{x}} \hat{d}^\epsilon)^2}}.$$

The non-dimensional stress tensors are

$$\hat{\mathbf{T}}_I^\epsilon := -\hat{p}_I^\epsilon \mathbf{I} + \frac{\epsilon^2}{M} \{(\hat{\nabla} \hat{\mathbf{q}}_I^\epsilon) + (\hat{\nabla} \hat{\mathbf{q}}_I^\epsilon)^T\}, \hat{\mathbf{T}}_{II}^\epsilon := -\hat{p}_{II}^\epsilon \mathbf{I} + \epsilon^2 \{(\hat{\nabla} \hat{\mathbf{q}}_{II}^\epsilon) + (\hat{\nabla} \hat{\mathbf{q}}_{II}^\epsilon)^T\}$$

3.1. Non-dimensional model for the two-phase flow with solute-dependent surface tension

Substituting the non-dimensional variables into the pore-scale model in Section 2.5, for every $\hat{t} > 0$ the non-dimensional model equations for the two-phase flow model with solute-dependent surface tension become

$$\epsilon^2 \left(\partial_{\hat{t}} \hat{\mathbf{q}}_I^\epsilon + \left(\hat{\mathbf{q}}_I^\epsilon \cdot \hat{\nabla} \right) \hat{\mathbf{q}}_I^\epsilon \right) + \hat{\nabla} \hat{p}_I^\epsilon - \frac{\epsilon^2}{M} \hat{\nabla}^2 \hat{\mathbf{q}}_I^\epsilon = 0, \text{ in } \hat{\Omega}_I^\epsilon(\hat{t}), \quad (15)$$

$$\epsilon^2 \left(\partial_{\hat{t}} \hat{\mathbf{q}}_{II}^\epsilon + \left(\hat{\mathbf{q}}_{II}^\epsilon \cdot \hat{\nabla} \right) \hat{\mathbf{q}}_{II}^\epsilon \right) + \hat{\nabla} \hat{p}_{II}^\epsilon - \epsilon^2 \hat{\nabla}^2 \hat{\mathbf{q}}_{II}^\epsilon = 0, \text{ in } \hat{\Omega}_{II}^\epsilon(\hat{t}), \quad (16)$$

$$\hat{\nabla} \cdot \hat{\mathbf{q}}_\alpha^\epsilon = 0, \text{ in } \hat{\Omega}_\alpha^\epsilon(\hat{t}) \quad (\alpha = I, II), \quad (17)$$

$$\partial_{\hat{t}} \hat{c}^\epsilon - \hat{\nabla} \cdot (\hat{D} \hat{\nabla} \hat{c}^\epsilon - \hat{\mathbf{q}}_{II}^\epsilon \hat{c}^\epsilon) = 0, \text{ in } \hat{\Omega}_{II}^\epsilon(\hat{t}). \quad (18)$$

The boundary conditions at the fluid-fluid interface are

$$\hat{\mathbf{q}}_I^\epsilon = \hat{\mathbf{q}}_{II}^\epsilon, \text{ at } \hat{\Gamma}_{ff}^\epsilon(\hat{t}), \quad (19)$$

$$\hat{\mathbf{q}}_\alpha^\epsilon \cdot \hat{\mathbf{n}}^\epsilon = \hat{v}_n^\epsilon, \text{ at } \hat{\Gamma}_{ff}^\epsilon(\hat{t}) \quad (\alpha = I, II), \quad (20)$$

$$(-\hat{D} \hat{\nabla} \hat{c}^\epsilon + \hat{\mathbf{q}}_{II}^\epsilon \hat{c}^\epsilon) \cdot \hat{\mathbf{n}}^\epsilon = \hat{c}^\epsilon \hat{v}_n^\epsilon, \text{ at } \hat{\Gamma}_{ff}^\epsilon(\hat{t}), \quad (21)$$

$$((\hat{\mathbf{T}}_I^\epsilon - \hat{\mathbf{T}}_{II}^\epsilon) \cdot \hat{\mathbf{n}}^\epsilon) \cdot \hat{\mathbf{n}}^\epsilon = \frac{\epsilon^2}{\text{Ca}} \hat{\gamma}(\hat{c}^\epsilon) (\hat{\nabla} \cdot \hat{\mathbf{n}}^\epsilon), \text{ at } \hat{\Gamma}_{ff}^\epsilon(\hat{t}), \quad (22)$$

$$((\hat{\mathbf{T}}_I^\epsilon - \hat{\mathbf{T}}_{II}^\epsilon) \cdot \hat{\mathbf{n}}^\epsilon) \cdot \hat{\mathbf{t}}^\epsilon = -\frac{\epsilon^2}{\text{Ca}} (\hat{\mathbf{t}}^\epsilon \cdot \hat{\nabla} \hat{\gamma}(\hat{c}^\epsilon)), \text{ at } \hat{\Gamma}_{ff}^\epsilon(\hat{t}). \quad (23)$$

At the fluid-solid interface, the boundary conditions are

$$\hat{\mathbf{q}}_{II}^\epsilon = \mathbf{0}, \text{ at } \hat{\Gamma}_{fs}, \quad (24)$$

$$(-\hat{D} \hat{\nabla} \hat{c}^\epsilon + \hat{\mathbf{q}}_{II}^\epsilon \hat{c}^\epsilon) \cdot \hat{\mathbf{n}}^\epsilon = 0, \text{ at } \hat{\Gamma}_{fs}. \quad (25)$$

At $\hat{y} = 0$ we apply symmetry conditions for all variables.

3.2. Non-dimensional model for the two-phase flow with constant surface tension

Similar to Section 2.6, we consider the case without solute and γ being constant. With $\gamma_{ref} = \gamma$, one gets $\hat{\gamma} = 1$ and (22) and (23) become

$$((\hat{\mathbf{T}}_I^\epsilon - \hat{\mathbf{T}}_{II}^\epsilon) \cdot \hat{\mathbf{n}}^\epsilon) \cdot \hat{\mathbf{n}}^\epsilon = \frac{\epsilon^2}{\text{Ca}} \hat{\nabla} \cdot \hat{\mathbf{n}}^\epsilon, \text{ at } \hat{\Gamma}_{ff}^\epsilon(\hat{t}), \quad (26)$$

$$((\hat{\mathbf{T}}_I^\epsilon - \hat{\mathbf{T}}_{II}^\epsilon) \cdot \hat{\mathbf{n}}^\epsilon) \cdot \hat{\mathbf{t}}^\epsilon = 0, \text{ at } \hat{\Gamma}_{ff}^\epsilon(\hat{t}). \quad (27)$$

Further, (18), (21) and (25) are not needed anymore and the remaining equations are the same as in the above section.

3.3. Non-dimensional model for unsaturated flow with constant surface tension

Continuing as in Section 2.7, assuming that fluid-I does not influence the flow of fluid-II and in the absence of solute one ends up with (16), (17), (20) (for $\alpha = II$), (24) and

$$(\hat{\mathbf{T}}_{II}^\epsilon \cdot \hat{\mathbf{n}}^\epsilon) \cdot \hat{\mathbf{n}}^\epsilon = -\frac{\epsilon^2}{\text{Ca}} \hat{\mathbf{v}} \cdot \hat{\mathbf{n}}^\epsilon, \text{ at } \hat{\Gamma}_{ff}^\epsilon(\hat{t}), \quad (28)$$

$$(\hat{\mathbf{T}}_{II}^\epsilon \cdot \hat{\mathbf{n}}^\epsilon) \cdot \hat{\mathbf{t}}^\epsilon = 0, \text{ at } \hat{\Gamma}_{ff}^\epsilon(\hat{t}). \quad (29)$$

4. Asymptotic expansion

We use an asymptotic expansion w.r.t. ϵ to derive transversally averaged upscaled (effective) models at the Darcy scale. Since in this section only the non-dimensional variables are used, for the ease of presentation the hats are suppressed. We use the homogenization ansatz, namely that all variables can be expanded regularly w.r.t. ϵ . We assume that

$$p_\alpha^\epsilon(x, y, t) = p_{\alpha,0}(x, y, t) + \epsilon p_{\alpha,1}(x, y, t) + \mathcal{O}(\epsilon^2) \quad (\alpha = I, II),$$

$$q_{\alpha,0}^{(\epsilon^k)}(x, y, t) = q_{\alpha,0}^{(k)}(x, y, t) + \epsilon q_{\alpha,1}^{(k)}(x, y, t) + \mathcal{O}(\epsilon^2) \quad (\alpha = I, II, k = 1, 2),$$

$$c^\epsilon(x, y, t) = c_0(x, y, t) + \epsilon c_1(x, y, t) + \mathcal{O}(\epsilon^2),$$

$$d^\epsilon(x, t) = d_0(x, t) + \epsilon d_1(x, t) + \mathcal{O}(\epsilon^2). \quad (30)$$

where $p_{\alpha,j}(x, y, t), q_{\alpha,j}^{(k)}(x, y, t), c_j(x, y, t), d_j(x, t)$ are functions describing the $\mathcal{O}(\epsilon^j)$ order approximation (for $j = 1, 2, \dots$) of the corresponding variables. We will now insert these expansions in the model equations and equate terms of the same order in ϵ to find the transversally averaged equations. We do this for different regimes, and end up with different upscaled models.

4.1. Two-phase flow with solute-dependent surface tension

We start with the model for two-phase flow with solute-dependent surface tension (15)-(25). At this point we assume that M is $\mathcal{O}(1)$ w.r.t. ϵ .

4.1.1. Mass conservation

To derive an effective equation for the mass conservation, we follow the ideas in van Noorden (2009b); Bringedal et al. (2015); Kumar et al. (2011). Substituting the asymptotic expansion (30) in the mass conservation equation (17) and restricting the writing up to the $\mathcal{O}(\epsilon^0)$ terms gives

$$\frac{1}{\epsilon} \partial_y q_{\alpha,0}^{(2)} + \left(\partial_x q_{\alpha,0}^{(1)} + \partial_y q_{\alpha,1}^{(2)} \right) + \mathcal{O}(\epsilon) = 0, \text{ in } \Omega_\alpha^\epsilon(t). \quad (31)$$

To show that $q_{\alpha,0}^{(2)} = 0$ in $\Omega_\alpha^\epsilon(t)$, we use (30) in the kinematic conditions (20) and obtain

$$q_{\alpha,0}^{(2)} + \epsilon \left(q_{\alpha,1}^{(2)} - q_{\alpha,0}^{(1)} \partial_x d_0 - \partial_t d_0 \right) + \mathcal{O}(\epsilon^2) = 0, \text{ at } \Gamma_{ff}^\epsilon(t). \quad (32)$$

The lowest order terms in (31) - (32) give

$$\partial_y q_{\alpha,0}^{(2)} = 0, \text{ in } \Omega_\alpha^\epsilon(t), \text{ and } q_{\alpha,0}^{(2)} = 0, \text{ at } \Gamma_{ff}^\epsilon(t),$$

while (24) and the symmetry condition at $y = 0$ lead to

$$q_{\alpha,0}^{(2)} = 0, \text{ in } \Omega_\alpha^\epsilon(t). \quad (33)$$

To upscale the mass balance for the fluids, we consider a thin segment of the pore space, as sketched in Fig. 2. Let $Y_I := \{(x, y) | x_1 < x < x_1 + \delta x, 0 < y < -1 + d^\epsilon\}$ be the region in this segment that is occupied by fluid-I. By integrating (17) over Y_I , one obtains

$$\int_{Y_I} \nabla \cdot \mathbf{q}_I^\epsilon dV_I = 0.$$

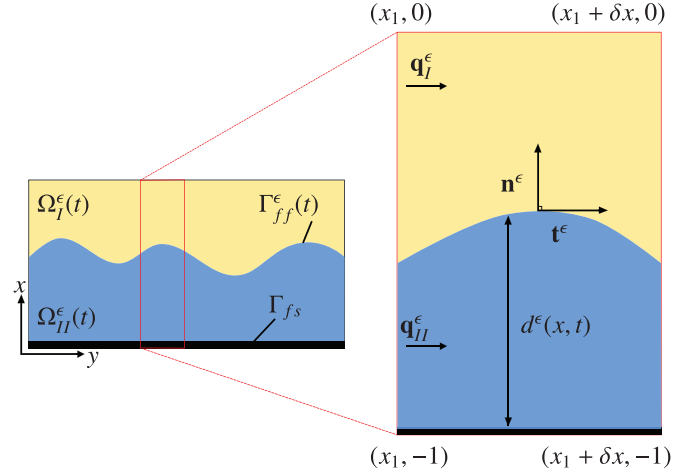


Fig. 2. Thin section of the pore space.

In the above equation, we apply the theorem of Gauss and divide all terms by δx , then using (20) and the asymptotic expansions (30) to get

$$\frac{1}{\delta x} \int_{-1+d_0}^0 q_{I,0}^{(1)} dy |_{x=x_1+\delta x} - \frac{1}{\delta x} \int_{-1+d_0}^0 q_{I,0}^{(1)} dy |_{x=x_1} + \frac{1}{\delta x} \int_{x_1}^{x_1+\delta x} q_{I,1}^{(2)} dx |_{y=0} - \frac{1}{\delta x} \int_{x_1}^{x_1+\delta x} \partial_t d_0 dx + \mathcal{O}(\epsilon) = 0.$$

Using the symmetry condition at $y = 0$ and equating the lowest order terms in the above gives

$$\frac{1}{\delta x} \int_{-1+d_0}^0 \left(q_{I,0}^{(1)} |_{x=x_1+\delta x} - q_{I,0}^{(1)} |_{x=x_1} \right) dy - \frac{1}{\delta x} \int_{x_1}^{x_1+\delta x} \partial_t d_0 dx = 0.$$

Defining the total flux of fluid-I as

$$\bar{q}_{I,0}^{(1)}(x, t) := \int_{-1+d_0}^0 q_{I,0}^{(1)}(x, y, t) dy, \quad (34)$$

and letting $\delta x \rightarrow 0$, one obtains

$$\partial_x \bar{q}_{I,0}^{(1)} - \partial_t d_0 = 0, \text{ for all } 0 < x < 1 \text{ and } t > 0. \quad (35)$$

Similarly using the fluid-II region $Y_{II} := \{(x, y) | x_1 < x < x_1 + \delta x, -1 + d^\epsilon < y < -1\}$, for

$$\bar{q}_{II,0}^{(1)}(x, t) := \int_{-1}^{-1+d_0} q_{II,0}^{(1)}(x, y, t) dy, \quad (36)$$

one obtains

$$\partial_x \bar{q}_{II,0}^{(1)} + \partial_t d_0 = 0, \text{ for all } 0 < x < 1 \text{ and } t > 0. \quad (37)$$

Remark 1. Recalling that the fluids are incompressible, observe that, since d_0 is the thickness of the wetting phase layer in the half-pore, it can be regarded as the saturation of the wetting fluid. In this sense (35) and (37) are the effective mass balance equations for the two fluid phases.

4.1.2. Solute transport

To upscale the solute transport, which is needed when considering the Marangoni effect, one uses the asymptotic expansion (30) in (18) to get

$$\partial_x c_0 - \left(\partial_x, \frac{1}{\epsilon} \partial_y \right) \cdot D \left(\partial_x, \frac{1}{\epsilon} \partial_y \right) (c_0 + \epsilon c_1 + \epsilon^2 c_2) + \left(\partial_x, \frac{1}{\epsilon} \partial_y \right) \cdot \left(q_{II,0}^{(1)}, q_{II,0}^{(2)} + \epsilon q_{II,1}^{(2)} \right) (c_0 + \epsilon c_1) + \mathcal{O}(\epsilon) = 0, \text{ in } \Omega_{II}^\epsilon(t). \quad (38)$$

First, we show that c_0 and c_1 do not depend on y . The ϵ^{-2} order Term in (38) is leading to

$$\partial_{yy} c_0 = 0, \text{ in } \Omega_{II}^\epsilon(t).$$

From the ϵ^{-1} order term in the boundary conditions (21) and (25), one obtains

$$\partial_y c_0 = 0, \text{ at } \Gamma_{ff}^\epsilon(t) \text{ and } \Gamma_{fs}.$$

This implies that c_0 does not depend on y ,

$$c_0 = c_0(x, t), \text{ in } \Omega_{II}^\epsilon(t).$$

In a similar fashion, using this, (33), the ϵ^{-1} order term in (38) and ϵ^0 order term in (21), (25), one obtains

$$c_1 = c_1(x, t), \text{ in } \Omega_{II}^\epsilon(t).$$

The non-dimensional equation describing the solute concentration (18) can be written as

$$\frac{1}{\epsilon^2} \partial_y (D \partial_y c^\epsilon) - \frac{1}{\epsilon} \partial_y (q_{II}^{(2)} c^\epsilon) - \partial_t c^\epsilon + \partial_x (D \partial_x c^\epsilon - q_{II}^{(1)} c^\epsilon) = 0.$$

We integrate the above equation w.r.t. y from $y = -1$ to $y = -1 + d^\epsilon$. Applying the Leibniz rule in the last two terms and taking into account that d^ϵ depends on x and t , one gets

$$\begin{aligned} & \left[\frac{1}{\epsilon^2} D \partial_y c^\epsilon - \frac{1}{\epsilon} q_{II}^{(2)} c^\epsilon \right]_{y=-1}^{y=-1+d^\epsilon} - \partial_t \left(\int_{-1}^{-1+d^\epsilon} c^\epsilon dy \right) + \partial_t d^\epsilon c^\epsilon|_{y=-1+d^\epsilon} \\ & + \partial_x \left(\int_{-1}^{-1+d^\epsilon} (D \partial_x c^\epsilon - q_{II}^{(1)} c^\epsilon) dy \right) - \partial_x d^\epsilon (D \partial_x c^\epsilon - q_{II}^{(1)} c^\epsilon)|_{y=-1+d^\epsilon} = 0. \end{aligned}$$

We insert the asymptotic expansion (30) in the above equation, recalling that c_0 and c_1 do not depend on y and that $\partial_y c_2 = 0$ and $q_{II,1}^{(2)} = 0$ at $y = -1$, since $q_{II,0}^{(2)} = 0$ in $\Omega_{II}^\epsilon(t)$, one obtains

$$\begin{aligned} & (D \partial_y c_2 - q_{II,1}^{(2)} c_0)|_{y=-1+d_0} - \partial_t \left(c_0 \int_{-1}^{-1+d_0} 1 dy \right) + \partial_t d_0 c_0|_{y=-1+d_0} \\ & + \partial_x \left(D \partial_x c_0 \left(\int_{-1}^{-1+d_0} 1 dy \right) - c_0 \left(\int_{-1}^{-1+d_0} q_{II,0}^{(1)} dy \right) \right) \\ & - \partial_x d_0 (D \partial_x c_0 - c_0 q_{II,0}^{(1)})|_{y=-1+d_0} + \mathcal{O}(\epsilon) = 0. \end{aligned}$$

Using (36) and the ϵ order terms from the boundary condition (21) at $y = -1 + d_0$, one obtains the effective equation for the solute transport

$$\partial_t (c_0 d_0) + \partial_x (c_0 \bar{q}_{II,0}^{(1)}) - \partial_x (D d_0 \partial_x c_0) = 0, \text{ for all } 0 < x < 1 \text{ and } t > 0. \tag{39}$$

4.1.3. Momentum conservation

We apply the asymptotic expansion (30) in the horizontal and vertical component of the momentum equation for fluid-II (16). Recalling that $q_{II,0}^{(2)} = 0$, in $\Omega_{II}^\epsilon(t)$, for all $t > 0$ one has

$$-\partial_{yy} q_{II,0}^{(1)} + \partial_x p_{II,0} - \epsilon \partial_{yy} q_{II,1}^{(1)} + \epsilon \partial_x p_{II,1} + \mathcal{O}(\epsilon^2) = 0, \tag{40}$$

$$\frac{1}{\epsilon} \partial_y p_{II,0} + \partial_y p_{II,1} + \epsilon \partial_y p_{II,2} - \epsilon \partial_{yy} q_{II,1}^{(2)} + \mathcal{O}(\epsilon^2) = 0. \tag{41}$$

Restricting to ϵ^{-1} order term in (41), for all $0 < x < 1$ and $t > 0$, one gets

$$p_{II,0} = p_{II,0}(x, t).$$

For all $t > 0$, the dominant terms in (40) give

$$\partial_{yy} q_{II,0}^{(1)} = \partial_x p_{II,0}, \text{ in } \Omega_{II}^\epsilon(t). \tag{42}$$

Integrating the above equation in y and taking into account that $p_{II,0}$ is independent of y , we obtain

$$\partial_y q_{II,0}^{(1)} = \partial_x p_{II,0} y + A_1(x, t), \text{ in } \Omega_{II}^\epsilon(t), \tag{43}$$

where $A_1(x, t)$ is an integrating constant that will be fixed using boundary condition for $q_{II,0}^{(1)}$. We now assume that the surface tension $\gamma = \gamma(c^\epsilon)$ depends smoothly on the solute concentration. Using (30) and expanding $\gamma(c^\epsilon)$ around c_0 gives

$$\gamma(c^\epsilon) = \gamma(c_0) + \epsilon c_1 \gamma'(c_0) + \mathcal{O}(\epsilon^2).$$

We apply the asymptotic expansion (30) in the boundary condition (23). Using the above equation and recalling that $q_{\alpha,0}^{(2)} = 0$ at $\Gamma_{ff}^\epsilon(t)$ and that c_0 is independent of y , we get

$$\begin{aligned} & \frac{1}{\epsilon} \left(\frac{1}{M} \partial_y q_{I,0}^{(1)} - \partial_y q_{II,0}^{(1)} \right) + \left(\frac{1}{M} \partial_y q_{I,1}^{(1)} - \partial_y q_{II,1}^{(1)} \right) + \epsilon \left(\frac{1}{M} \partial_y q_{I,2}^{(1)} - \partial_y q_{II,2}^{(1)} \right) \\ & + \epsilon \left(\frac{1}{M} \partial_x q_{I,1}^{(2)} - \partial_x q_{II,1}^{(2)} \right) + 2\epsilon \partial_x d_0 \left(\frac{1}{M} \partial_y q_{I,1}^{(2)} - \partial_y q_{II,1}^{(2)} \right) \\ & - 2\epsilon \partial_x d_0 \left(\frac{1}{M} \partial_x q_{I,0}^{(1)} - \partial_x q_{II,0}^{(1)} \right) - \epsilon (\partial_x d_0)^2 \left(\frac{1}{M} \partial_y q_{I,0}^{(1)} - \partial_y q_{II,0}^{(1)} \right) + \frac{1}{Ca} \partial_x \gamma(c_0) \\ & + \frac{\epsilon}{Ca} \partial_x (c_1 \gamma'(c_0)) + \mathcal{O}(\epsilon^2) = 0, \text{ at } \Gamma_{ff}^\epsilon(t). \end{aligned} \tag{44}$$

At this point, the upscaling depends on the capillary number Ca . We will discuss the cases with $Ca = \epsilon^\beta Ca$, for $0 \leq \beta \leq 3$, where $Ca = \mathcal{O}(1)$. We start by assuming $Ca = \mathcal{O}(1)$ thus $\beta = 0$. From (44), one gets the tangential stress boundary condition

$$\partial_y q_{I,0}^{(1)} = \frac{1}{M} \partial_y q_{II,0}^{(1)}, \text{ at } \Gamma_{ff}^\epsilon(t). \tag{45}$$

Using the above in (43) leads to

$$\frac{1}{M} \partial_y q_{II,0}^{(1)}|_{y=-1+d_0} = (-1 + d_0) \partial_x p_{II,0} + A_1(x, t), \text{ in } \Omega_{II}^\epsilon(t). \tag{46}$$

Applying the asymptotic expansion (30) into (15) and using (33), for all $t > 0$ one has

$$-\frac{1}{M} \partial_{yy} q_{I,0}^{(1)} + \partial_x p_{I,0} - \frac{\epsilon}{M} \partial_{yy} q_{I,1}^{(1)} + \epsilon \partial_x p_{I,1} + \mathcal{O}(\epsilon^2) = 0, \text{ in } \Omega_I^\epsilon(t), \tag{47}$$

$$\frac{1}{\epsilon} \partial_y p_{I,0} + \partial_y p_{I,1} + \epsilon \partial_y p_{I,2} - \frac{\epsilon}{M} \partial_{yy} q_{I,1}^{(2)} + \mathcal{O}(\epsilon^2) = 0, \text{ in } \Omega_I^\epsilon(t). \tag{48}$$

The lowest order term in (48) gives

$$p_{I,0} = p_{I,0}(x, t), \text{ for all } 0 < x < 1. \tag{49}$$

For all $t > 0$, the dominating terms in (47) satisfy

$$\partial_{yy} q_{I,0}^{(1)} = M \partial_x p_{I,0}, \text{ in } \Omega_I^\epsilon(t). \tag{50}$$

We integrate the above equation w.r.t. y . We use (49) and the symmetry condition $\partial_y q_{I,0}^{(1)}(x, y, t) = 0$ at $y = 0$, which leads to

$$\partial_y q_{I,0}^{(1)} = M \partial_x p_{I,0} y, \text{ in } \Omega_I^\epsilon(t). \tag{51}$$

We determine $A_1(x, t)$ from (46), by using (51) at $y = -1 + d_0$, one gets for all $t > 0$

$$\partial_y q_{I,0}^{(1)} = \partial_x p_{II,0} y + (-1 + d_0) (\partial_x p_{I,0} - \partial_x p_{II,0}), \text{ in } \Omega_{II}^\epsilon(t). \tag{52}$$

The lowest order terms in (24) imply that $q_{II,0}^{(1)} = 0$ at $y = -1$. Hence, integrating the above equation in y , one obtains

$$q_{II,0}^{(1)} = \frac{\partial_x p_{II,0} (y^2 - 1)}{2} + (-1 + d_0) (\partial_x p_{I,0} - \partial_x p_{II,0}) (y + 1), \text{ in } \Omega_{II}^\epsilon(t). \tag{53}$$

Integrating the above in y from $y = -1 + d_0$ to $y = -1$ and using (36), yields

$$\bar{q}_{II,0}^{(1)}(x, t) = -\frac{d_0^3}{3} \partial_x p_{II,0} - \frac{(1 - d_0) d_0^2}{2} \partial_x p_{I,0}, \text{ for all } 0 < x < 1 \text{ and } t > 0. \tag{54}$$

To derive an effective equation for the velocity of fluid-I, we integrate (51) twice w.r.t. y . To determine the integration constants we use the continuity of the velocity at the fluid-fluid interface. The lowest order terms in (19) imply $q_{I,0}^{(1)} = q_{II,0}^{(1)}$ and hence

$$\begin{aligned} \bar{q}_{I,0}^{(1)} = & -\left[\frac{M(1 - d_0)^3}{3} + d_0(1 - d_0)^2 \right] \partial_x p_{I,0} \\ & - \frac{(1 - d_0) d_0^2}{2} \partial_x p_{II,0}, \text{ for all } 0 < x < 1 \text{ and } t > 0. \end{aligned} \tag{55}$$

4.1.4. Effect of Ca

We recall that the boundary conditions coming from the normal (22) and the tangential (23) components of the jump in the normal stress depends on the capillary number, Ca. To complete the upscaled model representing the effective behaviour for two-phase flow, we still have to find a relationship between the pressure difference of the fluids (capillary pressure) and the saturation in the porous medium. To this aim, we rewrite (22) as

$$-\frac{1}{\epsilon^2} (p_I^\epsilon - p_{II}^\epsilon) + \frac{2}{\epsilon} \left(\partial_y q_I^{\epsilon,(2)} - M \partial_y q_{II}^{\epsilon,(2)} \right) - (\partial_x d^\epsilon)^2 (p_I^\epsilon - p_{II}^\epsilon) + 2 \partial_x d^\epsilon \left(\partial_y q_I^{\epsilon,(1)} - M \partial_y q_{II}^{\epsilon,(1)} \right) - 2 \epsilon \partial_x d^\epsilon \left(\partial_x q_I^{\epsilon,(2)} - M \partial_x q_{II}^{\epsilon,(2)} \right) + \frac{\epsilon \gamma(c^\epsilon) \partial_{xx} d^\epsilon}{Ca} + \mathcal{O}(\epsilon^2) = 0, \text{ at } \Gamma_{ff}^\epsilon(t). \tag{56}$$

Whenever $Ca = \mathcal{O}(1)$ thus $\beta = 0$, applying the asymptotic expansion (30) in the above equation and recalling (33) gives

$$p_{I,0} - p_{II,0} = 0, \text{ for all } 0 < x < 1 \text{ and } t > 0. \tag{57}$$

This means that in the upscaled model the pressures in both phases are equal. Since $p_{I,0} = p_{II,0}$ in the pressure relation (57), for simplicity, we set $p_0 = p_{\alpha,0}$ and the effective velocities (54) and (55) become, for all $0 < x < 1$ and $t > 0$

$$\bar{q}_{II,0}^{(1)} = -\frac{d_0^2 (3 - d_0)}{6} \partial_x p_0, \tag{58}$$

$$\bar{q}_{I,0}^{(1)} = -\left(\frac{M(1 - d_0)^3}{3} + \frac{d_0 (1 - d_0) (2 - d_0)}{2} \right) \partial_x p_0. \tag{59}$$

Thus, the upscaled model with $Ca = \mathcal{O}(1)$ is represented by the mass conservation equations (35), (37), the effective velocities (58), (59) and the solute transport (39). This can be expressed in terms of three primary variables, the saturation of the wetting fluid d_0 , the pressure p_0 (recall that the two fluid pressures are equal) and the concentration c_0 . Specifically, for all $0 < x < 1$ and $t > 0$ one has

$$\begin{aligned} \partial_t d_0 + \partial_x \left[\left(\frac{M(1 - d_0)^3}{3} + \frac{d_0 (1 - d_0) (2 - d_0)}{2} \right) \partial_x p_0 \right] &= 0, \\ \partial_t d_0 - \partial_x \left[\frac{d_0^2 (3 - d_0)}{6} \partial_x p_0 \right] &= 0, \\ \partial_t (c_0 d_0) + \partial_x \left[c_0 \left(\frac{d_0^2 (3 - d_0)}{6} \right) \partial_x p_0 \right] - \partial_x (D d_0 \partial_x c_0) &= 0. \end{aligned} \tag{60}$$

This means that the surface tension γ plays no role in the effective equations, and therefore the Marangoni effect is lost.

For regimes, where $Ca = \mathcal{O}(\epsilon^\beta) \bar{Ca}$ with $\beta > 0$, the Marangoni effect will play a role in the upscaled models. For example, if $Ca = \epsilon \bar{Ca}$ with $\bar{Ca} = \mathcal{O}(1)$, from (44), one gets the Marangoni stress boundary condition,

$$\partial_y q_{II,0}^{(1)} = \frac{\partial_y q_{I,0}^{(1)}}{M} + \frac{\partial_x \gamma(c_0)}{Ca}, \text{ at } \Gamma_{ff}^\epsilon(t). \tag{61}$$

Using this instead of (45) and repeating the same steps in Section 4.1.3, one gets for $0 < x < 1$ and $t > 0$,

$$\bar{q}_{I,0}^{(1)} = -\left(\frac{M(1 - d_0)^3}{3} + \frac{d_0 (1 - d_0) (2 - d_0)}{2} \right) \partial_x p_0 + \frac{(1 - d_0)d_0}{\bar{Ca}} \partial_x \gamma(c_0), \tag{62}$$

$$\bar{q}_{II,0}^{(1)} = -\frac{d_0^2 (3 - d_0)}{6} \partial_x p_0 + \frac{d_0^2}{2 Ca} \partial_x \gamma(c_0). \tag{63}$$

The upscaled model consists of the mass conservation equations (35), (37), effective velocities (62), (63) and the solute transport (39). The model can be expressed in terms of three primary variables, the water saturation d_0 , the pressure p_0 (recalling that the two fluid pressures are

equal) and the concentration c_0 . Specifically, for $0 < x < 1$ and $t > 0$ one has

$$\begin{aligned} \partial_t d_0 + \partial_x \left[\left(\frac{M(1 - d_0)^3}{3} + \frac{d_0 (1 - d_0) (2 - d_0)}{2} \right) \partial_x p_0 - \frac{(1 - d_0)d_0}{Ca} \partial_x \gamma(c_0) \right] &= 0, \\ \partial_t d_0 - \partial_x \left[\left(\frac{d_0^2 (3 - d_0)}{6} \right) \partial_x p_0 - \frac{d_0^2}{2 Ca} \partial_x \gamma(c_0) \right] &= 0, \\ \partial_t (c_0 d_0) + \partial_x \left[c_0 \left(\frac{d_0^2 (3 - d_0)}{6} \right) \partial_x p_0 \right] - \partial_x (D d_0 \partial_x c_0) &= 0. \end{aligned} \tag{64}$$

Assuming $Ca = \epsilon^\beta \bar{Ca}$, with $\beta = 2$ or 3 , will lead to different Marangoni stress condition than (61), involving the unknowns c_1, c_2 etc. In this case one needs to find an effective solute transport equation involving c_1, c_2 etc. This is beyond the scope of this paper.

4.2. Two-phase flow with constant surface tension

Now, we consider the pore-scale model in Section 3.2. We begin with the assumption that $M = \mathcal{O}(1)$. We recall that for a constant surface tension, the dynamic boundary conditions are now (26), (27).

4.2.1. Mass conservation

The derivation of the mass conservation equation in this section is identical to the one in Section 4.1.1. The mass conservation equation for the two-phase flow model with constant surface tension is the same as (35) and (37).

4.2.2. Momentum conservation

To derive the effective velocities for fluid-I and fluid-II we can follow the same steps discussed in Section 4.1.3. Since the surface tension γ is constant, we use the continuity in the tangential component of the normal stress (27). It is worth to mention that the capillary number Ca is absent in the tangential stress boundary condition. Applying asymptotic expansion (30) in the boundary condition (27), we get

$$\frac{1}{\epsilon} \left(\frac{1}{M} \partial_y q_{I,0}^{(1)} - \partial_y q_{II,0}^{(1)} \right) + \left(\frac{1}{M} \partial_y q_{I,1}^{(1)} - \partial_y q_{II,1}^{(1)} \right) + \mathcal{O}(\epsilon) = 0, \text{ at } \Gamma_{ff}^\epsilon(t).$$

The lowest order terms imply

$$\partial_y q_{II,0}^{(1)} = \frac{1}{M} \partial_y q_{I,0}^{(1)}, \text{ at } \Gamma_{ff}^\epsilon(t),$$

which is same as (45). Further as in Section 4.1.3, one obtains the same effective velocities, (54) and (55).

4.2.3. Effect of Ca

Assuming $Ca = \epsilon^\beta \bar{Ca}$ with $\beta < 3$ and applying asymptotic expansion (30) in (56) (recalling that here $\gamma(c^\epsilon) = 1$), the lowest order term implies the same pressure relation as in (57). The upscaled model for the two-phase flow with constant surface tension, large or moderate capillary number can be represented by the mass conservation equations (35), (37), by the effective velocities (59), (58) and the pressure relation (57). This can be expressed in terms of two primary variables, the water saturation d_0 and the pressure p_0 (recall that the two fluid pressures are equal). Specifically, for $0 < x < 1$ and $t > 0$ one has

$$\begin{aligned} \partial_t d_0 + \partial_x \left[\left(\frac{M(1 - d_0)^3}{3} + \frac{d_0 (1 - d_0) (2 - d_0)}{2} \right) \partial_x p_0 \right] &= 0, \\ \partial_t d_0 - \partial_x \left[\frac{d_0^2 (3 - d_0)}{6} \partial_x p_0 \right] &= 0 \end{aligned} \tag{65}$$

If the capillary number is $Ca = \epsilon^3 \bar{Ca}$, applying (30) in (56), we obtain

$$p_{I,0} - p_{II,0} = \frac{\partial_{xx} d_0}{Ca}. \tag{66}$$

In this case, the upscaled model for the two-phase flow with constant surface tension is given by the mass conservation equations (35), (37), the effective velocities (55), (54) and the capillary pressure relationship (66).

4.2.4. Effect of large viscosity ratio between the fluids

By now we assumed $M = \mathcal{O}(1)$, here we consider $M = \epsilon^{-1} \overline{M}$, where $\overline{M} = \mathcal{O}(1)$, which means that the viscosity of fluid-I is much smaller than that of fluid-II. We show that the first order terms when $M \rightarrow \infty$, up-scaling the equations in Section 4.2 will only include the fluid-II flow whereas the fluid-I flow component is vanishing, reducing the model to the unsaturated flow in Section 4.3. In this respect we first show that the pressure becomes constant (and set as reference value to 0) for fluid-I. Now, considering $M = \epsilon^{-1} \overline{M}$ with $\overline{M} = \mathcal{O}(1)$ in (47) and (48), for all $t > 0$ one has

$$\partial_x p_{I,0} + \epsilon \partial_x p_{I,1} - \frac{\epsilon}{M} \partial_{yy} q_{I,0}^{(1)} + \mathcal{O}(\epsilon^2) = 0, \text{ in } \Omega_f^\epsilon(t), \tag{67}$$

$$\frac{1}{\epsilon} \partial_y p_{I,0} + \partial_y p_{I,1} + \mathcal{O}(\epsilon) = 0, \text{ in } \Omega_f^\epsilon(t). \tag{68}$$

The lowest order terms in (67) and (68) give

$$\partial_x p_{I,0} = 0, \text{ and } \partial_y p_{I,0} = 0, \text{ in } \Omega_f^\epsilon(t).$$

Hence $p_{I,0}$ is constant in space. We assume it constant in time as well and set this value as a reference zero pressure, implying

$$p_{I,0} = 0, \text{ in } \Omega_f^\epsilon(t).$$

Considering the surface tension constant in (44) and $M = \epsilon^{-1} \overline{M}$, where $\overline{M} = \mathcal{O}(1)$, give

$$-\frac{1}{\epsilon} \partial_y q_{II,0}^{(1)} - \partial_y q_{II,1}^{(1)} + \frac{1}{M} \partial_y q_{I,0}^{(1)} + \mathcal{O}(\epsilon) = 0, \text{ at } \Gamma_{ff}^\epsilon(t).$$

The ϵ^{-1} order term in the above equation gives

$$\partial_y q_{II,0}^{(1)} = 0, \text{ at } \Gamma_{ff}^\epsilon(t). \tag{69}$$

To find the effective velocity for fluid-II we use (69) instead of (45) when integrating (42) in y . Recalling that γ is constant and $p_{I,0}$ is zero for fluid-I, we follow the same steps as in Section 4.1.3, which results in

$$q_{II,0}^{(1)} = \partial_x p_{I,0} \left(\frac{y^2}{2} + (1 - d_0) y + \left(\frac{1}{2} - d_0 \right) \right), \text{ in } \Omega_{II}^\epsilon(t). \tag{70}$$

Integrating (70) and using (36) gives the Darcy law

$$\overline{q}_{II,0}^{(1)} = -\frac{d_0^3}{3} \partial_x p_{II,0}, \text{ for all } 0 < x < 1 \text{ and } t > 0. \tag{71}$$

To find the pressure equation for fluid-II, we take $M = \epsilon^{-1} \overline{M}$ in Section 4.1.4 and we use the fact that the pressure for fluid-I is zero. Then the capillary pressure relation in (57) (for $\beta < 3$) changes into

$$p_{II,0} = 0, \text{ for all } 0 < x < 1 \text{ and } t > 0. \tag{72}$$

Remark 2. Since $p_{II,0} = 0$ in (72), the same holds for $\overline{q}_{II,0}^{(1)}$ in (71) and therefore the saturation is constant in space and time. This is a trivial situation corresponding to steady state.

Similarly, if $\beta = 3$, (66) becomes

$$p_{II,0} = -\frac{\partial_{xx} d_0}{Ca}, \text{ for all } 0 < x < 1 \text{ and } t > 0. \tag{73}$$

Note that fluid-I plays no role in the upscaled equations, which now reduces to the equations for fluid-II. Specially, the upscaled model consists of the mass conservation equation (37), the effective velocity (71) and the pressure equation (72) (for $\beta < 3$), respectively by (73) (for $\beta = 3$). Hence, in the limit when $M \rightarrow \infty$, only the flow of one phase is accounted for the lowest order and the upscaled model for two-phase flow reduces to the upscaled model for the unsaturated flow, as derived in Section 4.3.

4.3. Unsaturated flow with constant surface tension

We here now turn our attention to the model in Section 3.3.

4.3.1. Mass conservation

The derivation of the mass conservation equation in this section is identical to the one in Section 4.1.1. The mass conservation equation for the unsaturated flow model with constant surface tension is the same as (37).

4.3.2. Momentum conservation

We apply the asymptotic expansion (30) in the boundary condition (29) and recall that $q_{II,0}^{(2)} = 0$ at $\Gamma_{ff}^\epsilon(t)$, instead of (44), the boundary condition for unsaturated flow at $\Gamma_{ff}^\epsilon(t)$ reduces to

$$-\frac{1}{\epsilon} \partial_y q_{II,0}^{(1)} - \partial_y q_{II,1}^{(1)} + \mathcal{O}(\epsilon) = 0. \tag{74}$$

The ϵ^{-1} order gives

$$\partial_y q_{II,0}^{(1)} = 0, \text{ at } \Gamma_{ff}^\epsilon(t),$$

which is same as in (69). To find the effective velocity for fluid-II, we follow then the same steps as in Section 4.2.4, which results in (71), the same effective law for fluid-II as in Section 4.2.4.

4.3.3. Effects of Ca

In the unsaturated flow case, we disregard fluid-I in (56), which leads to

$$\begin{aligned} & -\frac{1}{\epsilon^2} p_{II}^\epsilon + \frac{2}{\epsilon} \partial_y q_{II}^{\epsilon(2)} - (\partial_x d^\epsilon)^2 p_{II}^\epsilon + 2 \partial_x d^\epsilon \partial_y q_{II}^{\epsilon(1)} - 2 \epsilon \partial_x d^\epsilon \partial_x q_{II}^{\epsilon(2)} \\ & - \frac{\epsilon \gamma(c^\epsilon) \partial_{xx} d^\epsilon}{Ca} + \mathcal{O}(\epsilon^3) = 0, \text{ at } \Gamma_{ff}^\epsilon(t). \end{aligned}$$

Applying (30) in the above equation and recalling $q_{II,0}^{(1)} = 0$ at $\Gamma_{ff}^\epsilon(t)$, we find the same capillary pressure relations as in Section 4.2.4. In particular, for $\beta < 3$, we get (72) and in this case the upscaled model is trivial (see Remark 2). The case $Ca = \epsilon^3 \overline{Ca}$ is more interesting as it gives the pressure relation (73). The upscaled model in this case is then represented by (35), (71) and (73).

5. Summary and discussion of upscaled models

We recall that in the upscaled models the width of the wetting fluid (fluid-II) d_0 can be seen as its saturation and therefore the saturation of the non-wetting fluid (fluid-I) is $(1 - d_0)$. The effective equations on the Darcy scale are now summarized and discussed in the sections below. These models are obtained in the limit situation when $\epsilon \rightarrow 0$. Practically, one has ϵ small but not zero. Therefore the upscaled models should be seen as an approximation of the pore-scale models, having a much simpler structure.

Assuming $Ca = \epsilon^\beta \overline{Ca}$, we have considered several regimes identified by the value of β , and derived different upscaled models. Table 2 is summarising these results, for $\beta = 1$ the Marangoni effects are relevant, and for $\beta < 3$ the phase pressures are equal but for $\beta = 3$ the difference of the phase pressures depends on the second order derivative of the saturation.

Table 2
Summary of the upscaled models obtained for different values of β in the capillary number $Ca = \epsilon^\beta \overline{Ca}$.

β	Marangoni effect	$p_{I,0} - p_{II,0}$
0	not present	constant
1	present	constant
2	-	constant
3	-	curvature dependent

5.1. Two-phase flow with solute-dependent surface tension

If $Ca = \mathcal{O}(1)$, then for all $0 < x < 1$ and $t > 0$, the upscaled model for the pore-scale model (15)-(25) becomes

$$\begin{aligned} \partial_t d_0 &= \partial_x \bar{q}_{I,0}^{(1)}, \\ \partial_t d_0 &= -\partial_x \bar{q}_{II,0}^{(1)}, \\ \bar{q}_{I,0}^{(1)} &= -\left(\frac{M(1-d_0)^3}{3} + \frac{d_0(1-d_0)(2-d_0)}{2}\right) \partial_x p_0, \\ \bar{q}_{II,0}^{(1)} &= -\frac{d_0^2(3-d_0)}{6} \partial_x p_0, \\ \partial_t(c_0 d_0) &= -\partial_x(c_0 \bar{q}_{II,0}^{(1)}) + \partial_x(D d_0 \partial_x c_0). \end{aligned} \quad (75)$$

If $Ca = \epsilon \bar{Ca}$, then for all $0 < x < 1$ and $t > 0$, the upscaled counterpart of the pore-scale model in Section 2.5 becomes

$$\begin{aligned} \partial_t d_0 &= \partial_x \bar{q}_{I,0}^{(1)}, \\ \partial_t d_0 &= -\partial_x \bar{q}_{II,0}^{(1)}, \\ \bar{q}_{I,0}^{(1)} &= -\left(\frac{M(1-d_0)^3}{3} + \frac{d_0(1-d_0)(2-d_0)}{2}\right) \partial_x p_0 + \frac{(1-d_0)d_0}{Ca} \partial_x \gamma(c_0), \\ \bar{q}_{II,0}^{(1)} &= -\frac{d_0^2(3-d_0)}{6} \partial_x p_0 + \frac{d_0^2}{2Ca} \partial_x \gamma(c_0), \\ \partial_t(c_0 d_0) &= -\partial_x(c_0 \bar{q}_{II,0}^{(1)}) + \partial_x(D d_0 \partial_x c_0). \end{aligned} \quad (76)$$

The upscaled models in (75) and (76) have a common structure. They include the mass balance for both fluid phases and the Darcy laws for the two fluid velocities. Finally, the last equation gives the mass balance for the solute.

One can recognize the effective velocities in (75) and (76) as Darcy-type laws for the two fluid phases. Since d_0 , respectively $(1-d_0)$ are the saturation of the two fluids, the factors multiplying the pressure gradients in these equations can be viewed as relative permeabilities of the two fluids. Compared to the effective velocities in (75), the influence of the surface tension gradient, namely the Marangoni effect, is visible in the effective velocities in (76).

The upscaled models in (75) and (76) are valid for the regimes where the capillary number is either moderate or large, which corresponds to very small surface tension. Hence the two phase pressures are equal, or, equivalently the capillary pressure is zero, as commonly assumed in petroleum reservoir simulation models Aziz and Settari (1979).

5.2. Two-phase flow with constant surface tension

If solute is not present in the fluid-II phase, the surface tension coefficient is constant. In this case the mass balance for solute is left out. Also, no Marangoni effect is encountered, which simplifies the models. Specifically, assuming $Ca = \epsilon^\beta \bar{Ca}$ for $\bar{Ca} = \mathcal{O}(1)$ and $\beta < 3$, the upscaled counterpart of the pore-scale model in Section 2.6 is

$$\begin{aligned} \partial_t d_0 &= \partial_x \bar{q}_{I,0}^{(1)}, \\ \partial_t d_0 &= -\partial_x \bar{q}_{II,0}^{(1)}, \\ \bar{q}_{I,0}^{(1)} &= -\left(\frac{M(1-d_0)^3}{3} + \frac{d_0(1-d_0)(2-d_0)}{2}\right) \partial_x p_0, \\ \bar{q}_{II,0}^{(1)} &= -\frac{d_0^2(3-d_0)}{6} \partial_x p_0, \end{aligned} \quad (77)$$

for all $0 < x < 1$ and $t > 0$. Here the upscaled model is valid in the flow regimes where the capillary number is moderate or large, which again implies that the pressures for the two fluid phases are same. Assuming,

$Ca = \epsilon^3 \bar{Ca}$ with $\bar{Ca} = \mathcal{O}(1)$, the upscaled model becomes

$$\begin{aligned} \partial_t d_0 &= \partial_x \bar{q}_{I,0}^{(1)}, \\ \partial_t d_0 &= -\partial_x \bar{q}_{II,0}^{(1)}, \\ \bar{q}_{I,0}^{(1)} &= -\left[\frac{M(1-d_0)^3}{3} + d_0(1-d_0)^2\right] \partial_x p_{I,0} - \frac{(1-d_0)d_0^2}{2} \partial_x p_{II,0}, \\ \bar{q}_{II,0}^{(1)} &= -\frac{d_0^3}{3} \partial_x p_{II,0} - \frac{(1-d_0)d_0^2}{2} \partial_x p_{I,0}, \\ p_{I,0} - p_{II,0} &= \frac{\partial_{xx} d_0}{Ca}, \end{aligned} \quad (78)$$

for all $0 < x < 1$ and $t > 0$. One can recognize the effective velocities in (77) and (78) as Darcy-type laws for the two fluid phases. Note that the effective velocities are depending on both pressure gradients from the two fluid phase. A similar case as considered here was also upscaled in Picchi and Battiato (2018). As Picchi and Battiato (2018) considered steady-state flow, the phase pressure difference there is different from what we obtained here.

Observe that compared to traditional two-phase flow models, in which the capillary pressure is a function of the saturation, here this involves second order derivative of the saturation. Here we emphasize the differences between the regimes $\beta < 3$ and $\beta = 3$ in the capillary pressure relation in (77) and (78). In the former, the pressures for both fluids are equal, which is similar to saying that the capillary pressure is zero. In the later case, one gets a model in which the commonly used pressure-saturation relation is replaced by a differential equation. Such a model is also derived in Mikelić (2003) and Mikelic and Paoli (2000) by homogenization techniques. Also, if the upscaled model derived here is reduced to a system of two equations, the capillary pressure relation in (78) would lead to a fourth order derivative term which is similar to the ones accounting for surface tension effects, as proposed in Huppert (1982) for the case of a thin fluid film flowing down a plane, and in Cueto-Felgueroso and Juanes (2008, 2009) for unsaturated, one-phase flow. However, when compared to Cueto-Felgueroso and Juanes (2008, 2009), here a nonlinear, algebraic function of the saturation is absent in the equation for the capillary pressure. This is due to the simple setting adopted here. On the other hand, as in Mikelić (2003); Mikelic and Paoli (2000) the models are derived by upscaling, whereas in Cueto-Felgueroso and Juanes (2008, 2009) they are formulated directly as upscaled models. One can explain the different results in the two (β depending) regimes starting by observing that γ is the reciprocal of Ca . Hence, in the first regime γ is much smaller than in the second one. As in the Young-Laplace equation, the pressure difference is proportional to γ . Whenever this is small, in the upscaled limit one obtains that the two pressure are equal.

5.3. Unsaturated flow with constant surface tension

Continuing in the same spirit as before, for the unsaturated case with constant surface tension in Section 2.7, the upscaled models are simplified. More precisely, assuming $Ca = \epsilon^\beta \bar{Ca}$ with $\bar{Ca} = \mathcal{O}(1)$, for $\beta < 3$ the upscaled fluid-II pressure becomes zero (as the one for fluid-I) and therefore the flow is vanishing as well. In this case, the saturation becomes constant in both space and time, which is actually steady state. In this case the upscaled model is trivial. For $\beta = 3$, the upscaled model becomes

$$\begin{aligned} \partial_t d_0 + \partial_x \bar{q}_{II,0}^{(1)} &= 0, \\ \bar{q}_{II,0}^{(1)} + \frac{d_0^3}{3} \partial_x p_{II,0} &= 0, \\ p_{II,0} &= -\frac{\partial_{xxx} d_0}{Ca} \end{aligned} \quad (79)$$

for all $0 < x < 1$ and $t > 0$. This can be expressed in terms of one primary variable, the water saturation d_0 . Specifically, for all $0 < x < 1$ and $t > 0$, one has

$$\partial_t d_0 + \partial_x \left(\frac{d_0^3}{3} \frac{\partial_{xxx} d_0}{Ca} \right) = 0, \quad (80)$$

This equation resembles the thin-film lubrication approximation Oron et al. (1997).

Similar to (78), the upscaled model in (79) is a non-standard model in the sense that the capillary pressure relation is given by the second derivative of the effective saturation. Also, for a large viscosity ratio, the pore-scale model for the two-phase flow in Section 3.2 reduces to the upscaled models in (79).

Remark 3. The Marangoni effect is only visible for the upscaled model (76). For (75), the Marangoni effect is lost and one immediately sees that (76) is equivalent to (75) for a constant surface tension. Additionally (76) is equivalent to (77) for a constant concentration and surface tension. Hence, for the numerical validation in Section 6, we will only consider the three upscaled models (76), (78) and (79), as these three models represent the different effective behaviours we have considered.

6. Model validation

In this section the upscaled models are validated by numerical experiments. Specifically, the full solutions (e.g. $p_\alpha^\epsilon, \mathbf{q}_\alpha^\epsilon, c^\epsilon, d^\epsilon$) of the two-dimensional pore-scale models, computed for pores having different width/length ratios (e.g. $\epsilon = 0.1, 0.07, 0.05, 0.01$), and for different capillary numbers ($\text{Ca} = \epsilon^\beta \overline{\text{Ca}}$ with $\overline{\text{Ca}} = \mathcal{O}(1)$, for $\beta = 1, 3$), are averaged in the transversal direction and compared to the approximate upscaled solutions (e.g. $p_{\alpha,0}, \mathbf{q}_{\alpha,0}, c_0, d_0$).

To compute the full solutions of the pore-scale models, we use COMSOL Multiphysics COM. For the simulations of the upscaled models, we use a simple finite difference scheme on an equidistant mesh, implemented in MATLAB. First and second order central differences are used for the space discretization. For the time discretization, an explicit method with fixed time-step size is used for (76), while for (78) and (79), an implicit method with fixed time-step size is used. We use harmonic averages for the relative permeabilities in the effective flow equations. For the advective flux in (76) we use an upwind approximation. We employ Newton’s method for solving the resulting non-linear system of equations.

We specify the pore geometry as in 13 and 14. For 13, we define the inflow and outflow boundaries as

$$\Gamma_{I,in}^\epsilon(t) := \{(x, y) \in \mathbb{R}^2 | x = 0, -1 + d^\epsilon(0, t) < y < 0\},$$

$$\Gamma_{I,out}^\epsilon(t) := \{(x, y) \in \mathbb{R}^2 | x = 1, -1 + d^\epsilon(1, t) < y < 0\}.$$

For 14, the inflow and outflow boundaries are given by

$$\Gamma_{II,in}^\epsilon(t) := \{(x, y) \in \mathbb{R}^2 | x = 0, -1 < y < -1 + d^\epsilon(0, t)\},$$

$$\Gamma_{II,out}^\epsilon(t) := \{(x, y) \in \mathbb{R}^2 | x = 1, -1 < y < -1 + d^\epsilon(1, t)\}.$$

In the following, all the presented numerical results are non-dimensional.

6.1. Two-phase flow with solute-dependent surface tension

Here we consider a numerical example of the pore-scale model in Section 3.1 where the regime is $\text{Ca} = \epsilon \overline{\text{Ca}}$ with $\overline{\text{Ca}} = 1$. At the fluid-fluid interface, the surface tension coefficient is chosen as (2) with $a = 1$ and $b = 1$, to include the Marangoni effect. The diffusion coefficient is chosen as $D = 1$ and the viscosity ratio as $M = 1$. The initial conditions are

$$d^\epsilon(x, t = 0) = 0.5, \text{ at } \Gamma_{ff}^\epsilon(t = 0), \quad c^\epsilon(x, y, t = 0) = 0.25, \text{ in } \Omega_{II}^\epsilon(t = 0),$$

$$\mathbf{q}_\alpha^\epsilon(x, y, t = 0) = \mathbf{0}, \text{ in } \Omega_\alpha^\epsilon(t = 0), \quad p_\alpha^\epsilon(x, y, t = 0) = 0, \text{ in } \Omega_\alpha^\epsilon(t = 0).$$

The inflow and outflow boundary conditions are

$$p_\alpha^\epsilon = 0.023 \text{ at } \Gamma_{\alpha,in}^\epsilon(t), \text{ and } p_\alpha^\epsilon = 0 \text{ at } \Gamma_{\alpha,out}^\epsilon(t),$$

$$c^\epsilon = 1 \text{ at } \Gamma_{II,in}^\epsilon(t), \text{ and } c^\epsilon = 0.25 \text{ at } \Gamma_{II,out}^\epsilon(t).$$

Compatible initial and boundary conditions are chosen by recalling the capillary pressure relation (57). To solve the upscaled model (76), the same initial and boundary conditions are chosen. We use homogeneous Neumann boundary conditions for d_0 at $x = 0$ and $x = 1$. The models are solved for a total time of $t = 0.1$.

In Fig. 3,4, Fig. 5, we have plotted the upscaled solutions of (76) together with the transversally averaged pore-scale solutions in Section 3.1 for four different ϵ . For decreasing ϵ , the averaged pore-scale solutions are converging to the upscaled solutions, which we also observe by calculating the L^2 -norm of the difference between the solutions in Table 3.

6.2. Two-phase flow with constant surface tension

Here we consider a numerical example of the pore-scale model in Section 3.2 where the regime is $\text{Ca} = \epsilon^3 \overline{\text{Ca}}$ with $\overline{\text{Ca}} = 1$. The viscosity ratio is chosen as $M = 1$. The initial conditions are

$$d^\epsilon(x, t = 0) = 0.5 - 1.2x + 1.2x^2, \text{ at } \Gamma_{ff}^\epsilon(t = 0),$$

$$\mathbf{q}_\alpha^\epsilon(x, y, t = 0) = \mathbf{0}, \text{ in } \Omega_\alpha^\epsilon(t = 0), \quad p_\alpha^\epsilon(x, y, t = 0) = 0, \text{ in } \Omega_\alpha^\epsilon(t = 0).$$

The inflow and outflow boundary conditions are

$$p_I^\epsilon = 0.023, \text{ at } \Gamma_{I,in}^\epsilon(t), \text{ and } p_I^\epsilon = 0 \text{ at } \Gamma_{I,out}^\epsilon(t),$$

$$p_{II}^\epsilon = -2.377, \text{ at } \Gamma_{II,in}^\epsilon(t), \text{ and } p_{II}^\epsilon = -2.4, \text{ at } \Gamma_{II,out}^\epsilon(t).$$

To avoid a non-smooth behaviour of the fluids, the values chosen above ensures that the initial and the boundary conditions are compatible. Moreover, the capillary pressure relation (66) is also satisfied for $t = 0$. To solve the upscaled model (78), the same initial and boundary conditions are chosen. We use homogeneous Neumann boundary conditions for d_0 at $x = 0$ and $x = 1$. The models are solved for a total time of $t = 1$.

In Fig. 6, 7, Fig. 8, we have plotted the upscaled solutions of (78) together with the averaged pore-scale solutions in Section 3.2 for various

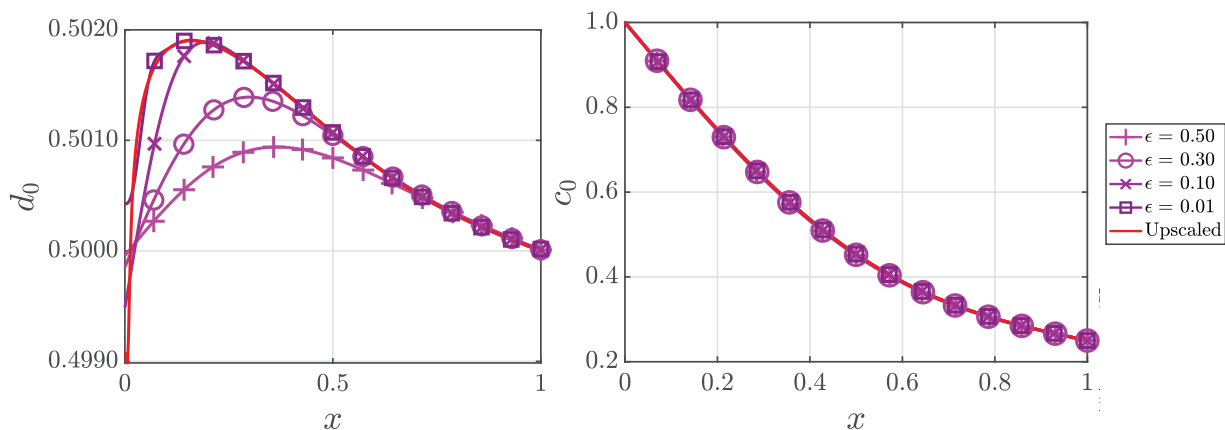


Fig. 3. Comparison of the saturation (left) and the concentration (right) of the upscaled model with the transversally averaged solutions of the pore-scale model for different ϵ at $t = 0.1$.

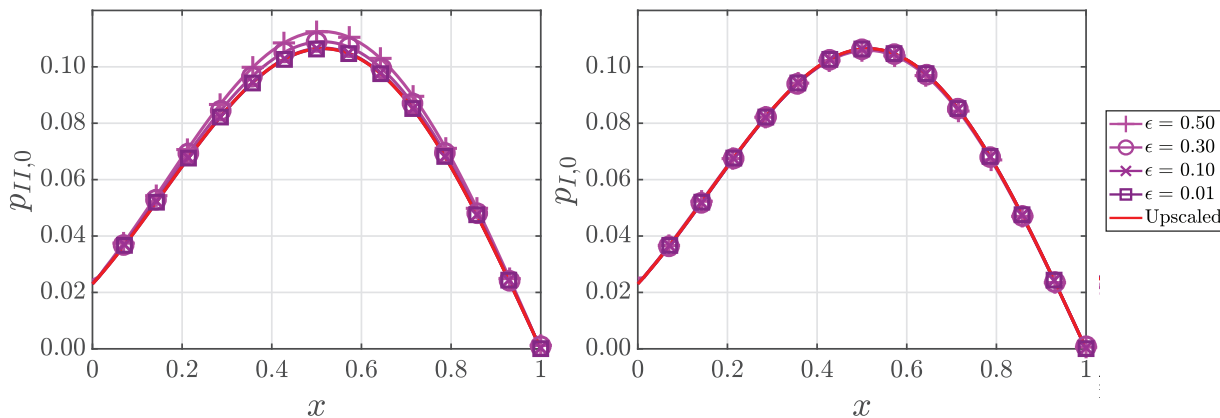


Fig. 4. Comparison of the pressures of the wetting (left) and the non-wetting fluid (right) of the upscaled model with the transversally averaged solutions of the pore-scale model for different ϵ at $t = 0.1$.

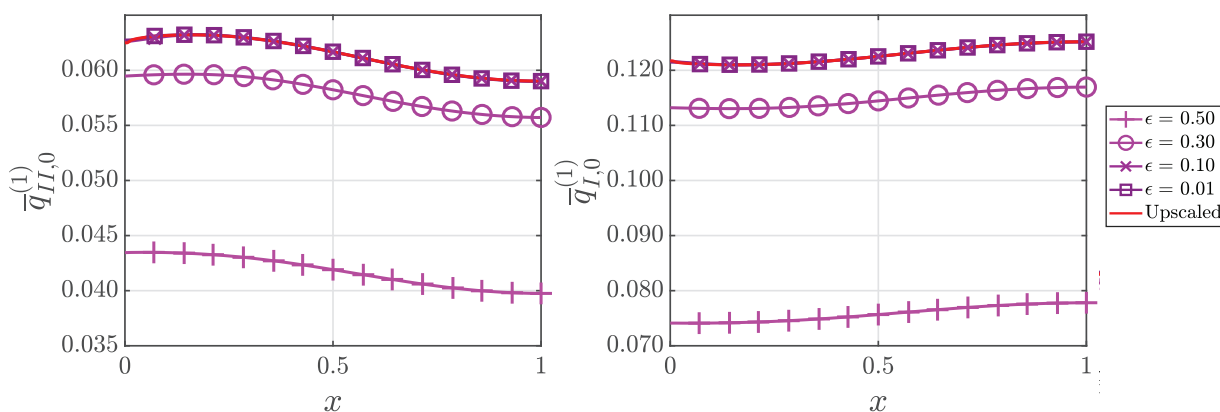


Fig. 5. Comparison of the fluxes of the wetting (left) and the non-wetting fluid (right) of the upscaled model with transversally averaged solutions of the pore-scale model for different ϵ at $t = 0.1$.

Table 3
 L^2 -norm of the difference between the upscaled quantities and the corresponding transversally averaged solutions of the pore-scale model for different ϵ at $t = 0.1$.

	$\epsilon = 0.5$	$\epsilon = 0.3$	$\epsilon = 0.1$	$\epsilon = 0.01$
$\ d_0 - d^\epsilon\ _{L^2(0,1)}$	$6.7 \cdot 10^{-4}$	$4.6 \cdot 10^{-4}$	$2.3 \cdot 10^{-4}$	$1.5 \cdot 10^{-4}$
$\ c_0 - c^\epsilon\ _{L^2(0,1)}$	$2.5 \cdot 10^{-3}$	$1.1 \cdot 10^{-3}$	$7.8 \cdot 10^{-5}$	$1.3 \cdot 10^{-4}$
$\ p_{II,0} - p_{II}^\epsilon\ _{L^2(0,1)}$	$4.2 \cdot 10^{-3}$	$1.7 \cdot 10^{-3}$	$1.7 \cdot 10^{-4}$	$8.0 \cdot 10^{-5}$
$\ p_{I,0} - p_I^\epsilon\ _{L^2(0,1)}$	$4.8 \cdot 10^{-4}$	$1.5 \cdot 10^{-4}$	$1.1 \cdot 10^{-4}$	$8.1 \cdot 10^{-5}$
$\ \bar{q}_{II,0}^{(1)} - \bar{q}_{II}^\epsilon\ _{L^2(0,1)}$	$2.0 \cdot 10^{-2}$	$3.4 \cdot 10^{-3}$	$4.5 \cdot 10^{-5}$	$3.2 \cdot 10^{-5}$
$\ \bar{q}_{I,0}^{(1)} - \bar{q}_I^\epsilon\ _{L^2(0,1)}$	$4.7 \cdot 10^{-2}$	$8.1 \cdot 10^{-3}$	$4.5 \cdot 10^{-5}$	$2.8 \cdot 10^{-5}$

Table 4
 L^2 -norm of the difference between the upscaled quantities and the corresponding transversally averaged solutions of the pore-scale model for different ϵ at $t = 1$.

	$\epsilon = 0.5$	$\epsilon = 0.3$	$\epsilon = 0.1$	$\epsilon = 0.01$
$\ d_0 - d^\epsilon\ _{L^2(0,1)}$	$1.7 \cdot 10^{-2}$	$2.2 \cdot 10^{-2}$	$5.9 \cdot 10^{-3}$	$2.2 \cdot 10^{-4}$
$\ p_{II,0} - p_{II}^\epsilon\ _{L^2(0,1)}$	$3.3 \cdot 10^{-1}$	$3.3 \cdot 10^{-1}$	$4.5 \cdot 10^{-2}$	$9.2 \cdot 10^{-4}$
$\ p_{I,0} - p_I^\epsilon\ _{L^2(0,1)}$	$1.2 \cdot 10^{-1}$	$1.9 \cdot 10^{-1}$	$2.8 \cdot 10^{-2}$	$1.6 \cdot 10^{-3}$
$\ \bar{q}_{II,0}^{(1)} - \bar{q}_{II}^\epsilon\ _{L^2(0,1)}$	$3.2 \cdot 10^{-2}$	$2.7 \cdot 10^{-2}$	$6.9 \cdot 10^{-3}$	$6.4 \cdot 10^{-4}$
$\ \bar{q}_{I,0}^{(1)} - \bar{q}_I^\epsilon\ _{L^2(0,1)}$	$5.3 \cdot 10^{-2}$	$4.0 \cdot 10^{-2}$	$1.5 \cdot 10^{-2}$	$4.0 \cdot 10^{-4}$

ϵ at $t = 1$. For decreasing ϵ , the averaged pore-scale solutions are converging to the upscaled solutions, which we also see by calculating the L^2 -norm of the difference between the solutions in Table 4.

6.3. Unsaturated flow with constant surface tension

The numerical computations of the pore-scale model in Section 3.3 are considered for the regime in $Ca = \epsilon^3 \overline{Ca}$ with $\overline{Ca} = \mathcal{O}(1)$.

The initial conditions are

$$d^\epsilon(x, t = 0) = 0.5 \text{ at } \Gamma_{ff}^\epsilon(t = 0),$$

$$\mathbf{q}_II^\epsilon(x, y, t = 0) = \mathbf{0} \text{ in } \Omega_{II}^\epsilon(t = 0), \quad p_{II}^\epsilon(x, y, t = 0) = 0 \text{ in } \Omega_{II}^\epsilon(t = 0).$$

The inflow and outflow boundary conditions are

$$p_{II}^\epsilon = 0.023 \text{ at } \Gamma_{II,in}^\epsilon(t) \text{ and } p_{II}^\epsilon = 0 \text{ at } \Gamma_{II,out}^\epsilon(t).$$

Table 5
 L^2 -norm of the difference between the upscaled quantities and the corresponding transversally averaged solutions of the pore-scale model for different ϵ at $t = 1$.

	$\epsilon = 0.5$	$\epsilon = 0.3$	$\epsilon = 0.1$	$\epsilon = 0.01$
$\ d_0 - d^\epsilon\ _{L^2(0,1)}$	$4.7 \cdot 10^{-3}$	$3.4 \cdot 10^{-3}$	$4.9 \cdot 10^{-4}$	$4.1 \cdot 10^{-6}$
$\ p_{I,0} - p_{II}^\epsilon\ _{L^2(0,1)}$	$9.1 \cdot 10^{-3}$	$6.1 \cdot 10^{-3}$	$7.3 \cdot 10^{-4}$	$1.9 \cdot 10^{-6}$
$\ \bar{q}_{\alpha,0}^{(1)} - \bar{q}_{II}^\epsilon\ _{L^2(0,1)}$	$1.4 \cdot 10^{-3}$	$1.0 \cdot 10^{-3}$	$1.4 \cdot 10^{-4}$	$4.4 \cdot 10^{-6}$

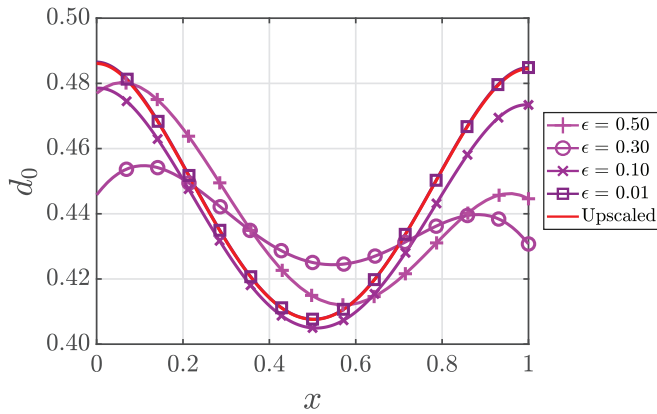


Fig. 6. Comparison of the saturation of the wetting fluid of the upscaled model with transversally averaged solutions of the pore-scale model for different ϵ at $t = 1$.

The initial conditions and the boundary conditions are same as for the pore-scale model. We use homogeneous Neumann boundary conditions for d_0 at $x = 0$ and $x = 1$. The models are solved for a total time of $t = 1$.

In Fig. 9 and Fig. 10, we have plotted the upscaled solutions of (79) together with the averaged pore-scale solutions in Section 3.3 for various ϵ at $t = 1$. For decreasing ϵ , the averaged pore-scale solutions are converging to the upscaled solutions, which we also see by calculating the L^2 -norm of the difference between the solutions in Table 5.

7. Model comparison

In Section 5, we have summarized all the upscaled models derived for different capillary regimes. The goal of this section is to numerically compare the upscaled models valid in the same capillary regime. The upscaled model (76) includes the Marangoni effect which reduces to

the upscaled model (77) of the two-phase flow model when the surface tension is constant or when the concentration of the solute is equally distributed. On the other hand when $M \rightarrow \infty$ the upscaled model (78) of the two-phase flow reduces to the unsaturated flow upscaled model (79). For this comparison we solve (78) for increasing values of M and then compare with (79).

7.1. Comparison of Marangoni flow and two-phase flow

Here we compare between the upscaled models in (76) and (77) where the regime is $Ca = \epsilon \overline{Ca}$ with $\overline{Ca} = 1$. The initial conditions are, for $0 < x < 1$,

$$d_0(x, 0) = 0.5, \quad c_0(x, 0) = 0.50,$$

$$\bar{q}_{\alpha,0}^{(1)}(x, 0) = 0, \quad p_{\alpha,0}(x, 0) = p_0(x, 0) = 0.$$

The inflow and outflow boundary conditions for the pressures are

$$p_{\alpha,0}(0, t) = 0.023, \quad \text{and} \quad p_{\alpha,0}(1, t) = 0.$$

Depending on the inflow boundary conditions for the concentration, we have tested three different cases to observe the Marangoni flow. Here the outflow boundary condition is set to the same value as the initial concentration. The three different cases are

- case(i): $c_0(0, t) = 0.25$, and $c_0(1, t) = 0.50$,
- case(ii): $c_0(0, t) = 0.50$, and $c_0(1, t) = 0.50$,
- case(iii): $c_0(0, t) = 1.00$, and $c_0(1, t) = 0.50$.

At the fluid-fluid interface, the surface tension coefficient is chosen as (2) with $a = 1$ and $b = 1$ to include the Marangoni effect. The diffusion coefficient is chosen as $D = 1$ and the viscosity ratio as $M = 1$. The models are solved for a total time of $t = 0.1$.

We see in Fig. 11 that case(ii) corresponds to a constant concentration and thus $\partial_x \gamma(c_0) = 0$. We want to emphasize that this is equivalent to the case of solving the upscaled model (77) for the two-phase flow with constant surface tension. This case will hence not include Marangoni

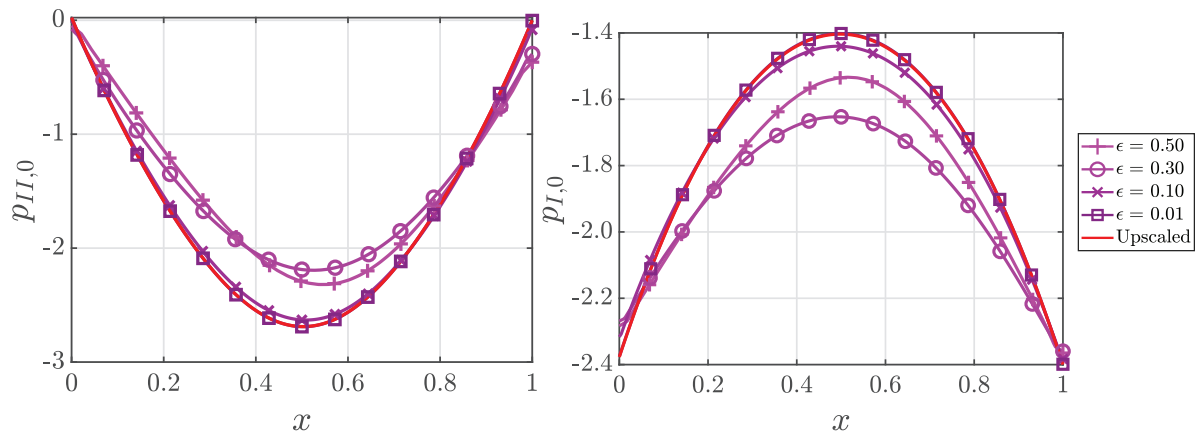


Fig. 7. Comparison of the pressures of the wetting (left) and the non-wetting fluid (right) of the upscaled model with transversally averaged solutions of the pore-scale model for different ϵ at $t = 1$.

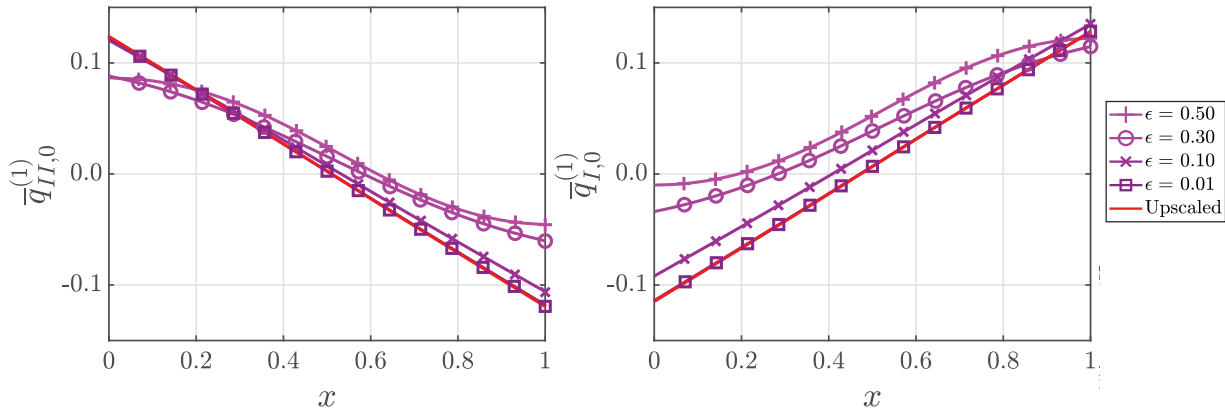


Fig. 8. Comparison of the fluxes of the wetting (left) and the non-wetting fluid (right) of the upscaled model with transversally averaged solutions of the pore-scale model for different ϵ at $t = 1$.

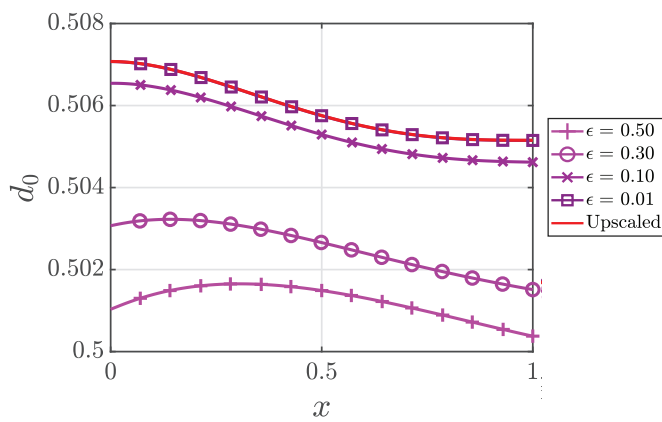


Fig. 9. Comparison of the saturation of the wetting fluid of the upscaled model with the transversally averaged solutions of the pore-scale model for different ϵ at time $t = 1$.

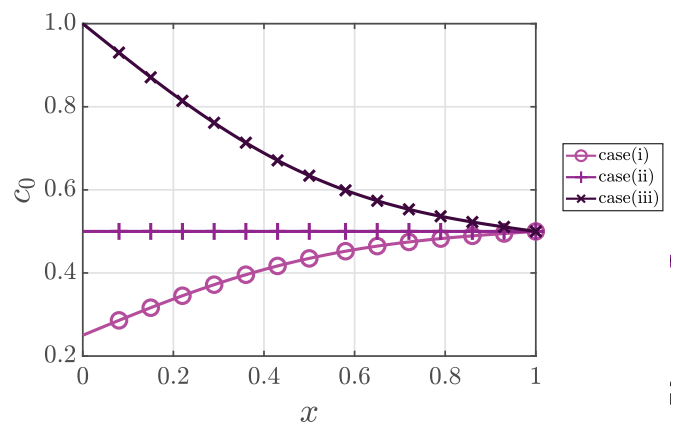


Fig. 11. Comparison of the concentration of the upscaled model (76) for the Marangoni flow for different test cases at $t = 0.1$.

effect. Due to the difference in inlet and outlet pressure, both fluid velocities are small but positive through the domain, accompanied by a linear pressure drop and a constant saturation as seen in Fig. 12 and Fig. 13.

For case(i) we see in Fig. 11 that this corresponds to $\partial_x c_0 > 0$, which implies $\partial_x \gamma(c_0) < 0$. Oppositely, case(iii) corresponds to $\partial_x \gamma(c_0) > 0$. The effect on the fluid velocities, pressures and saturations in Fig. 12 and

Fig. 13 is evident. For case(i) we see how the negative surface tension gradient along the strip results in overall negative velocities of both fluids through the strip. This is as expected from the Darcy-type laws in (76), and can be interpreted as the flow going towards the lower concentration of solute and hence towards the region of larger surface tension. In particular we see how the pressure distribution through the strip adjusts and hence is a convex function in case(i). Also, the saturation becomes slightly decreased near the inlet, which is due to the difference in

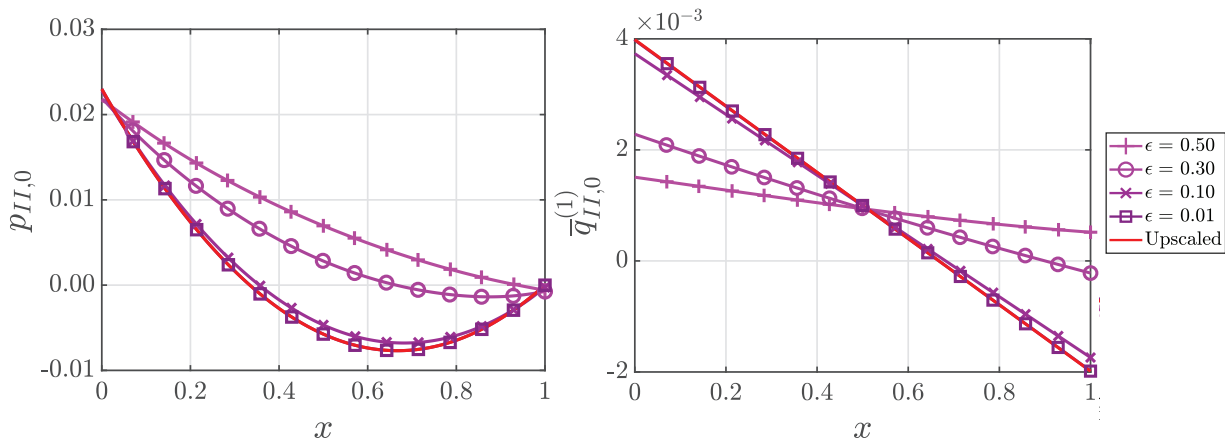


Fig. 10. Comparison of the pressure (left) and the flux (right) of the wetting fluid of the upscaled model with the transversally averaged solutions of the pore-scale model for different ϵ at time $t = 1$.

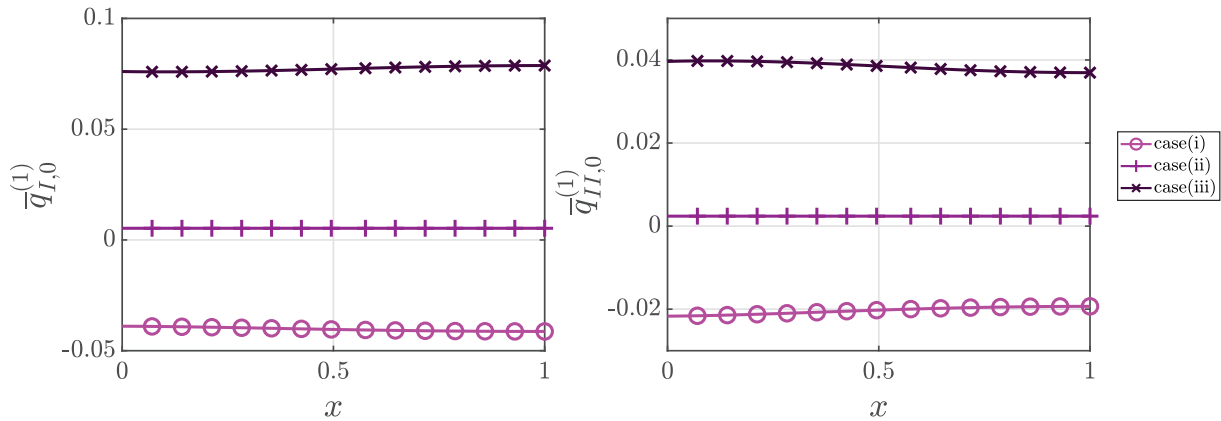


Fig. 12. Comparison of the fluxes of the non-wetting (left) and the wetting fluid (right) of the upscaled model (76) for the Marangoni flow for different test cases at $t = 0.1$.

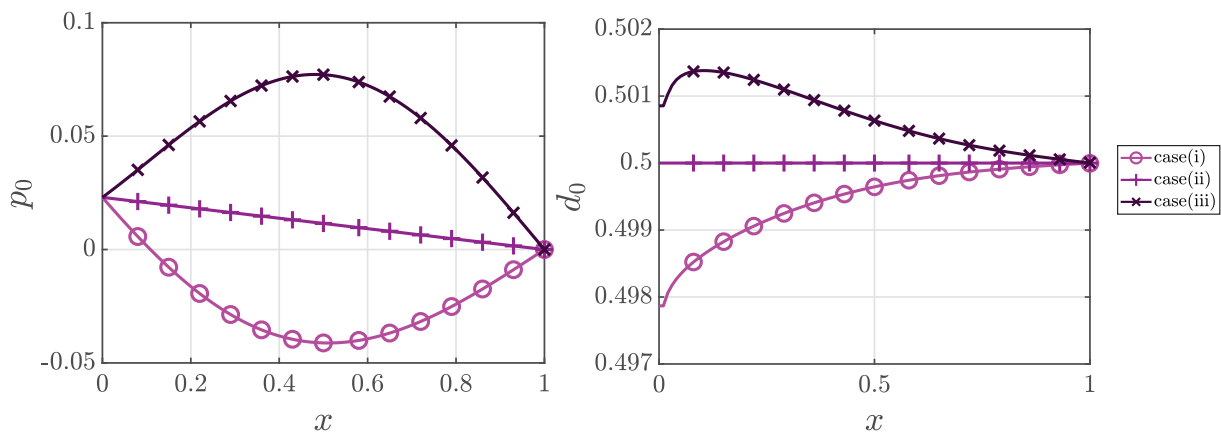


Fig. 13. Comparison of the pressure (left) and the saturation (right) of the upscaled model (76) for the Marangoni flow for different test cases at $t = 0.1$.

response of the two fluid velocities. The opposite behaviour is seen for case(iii). Here the negative solute concentration gradient, corresponding to a positive surface tension gradient, gives an increased flow in the positive direction through the strip. The pressure becomes concave, while the saturation near the inlet is seen to increase slightly due to the difference in fluid velocity.

This simple test case shows how the Marangoni effect can alter the flow and mass transfer through a pore due to processes at the fluid-fluid interface. We see how the flow is adjusted to be towards the region of larger surface tension, as is expected for Marangoni flow.

7.2. Comparison of two-phase flow and unsaturated flow

Here we compare between the upscaled models in (78) and (79) where the regime is $Ca = \epsilon^3 \overline{Ca}$ with $\overline{Ca} = 1$. The viscosity ratio is chosen as $M = 1, M = 5, M = 10$ and $M = 15$ in (78) and compared to (79) which corresponds to letting $M \rightarrow \infty$. The initial conditions are, for $0 < x < 1$

$$d_0(x, 0) = 0.5 - 1.2x + 1.2x^2, \quad \overline{q}_{\alpha,0}^{(1)}(x, 0) = 0, \quad p_{\alpha,0}(x, 0) = 0.$$

The inflow and outflow boundary conditions are

$$p_{I,0}(0, t) = 0.023, \text{ and } p_{I,0}(1, t) = 0, \\ p_{II,0}(0, t) = -2.377, \text{ and } p_{II,0}(1, t) = -2.4.$$

The models are solved for a total time of $t = 1$.

Fig. 14 and Fig. 15 show that the upscaled wetting phase quantities in the two-phase flow model are approaching the corresponding one in the unsaturated flow model as the viscosity ratio is increasing. This is confirmed in Table 6, presenting the L^2 -norm of the difference between

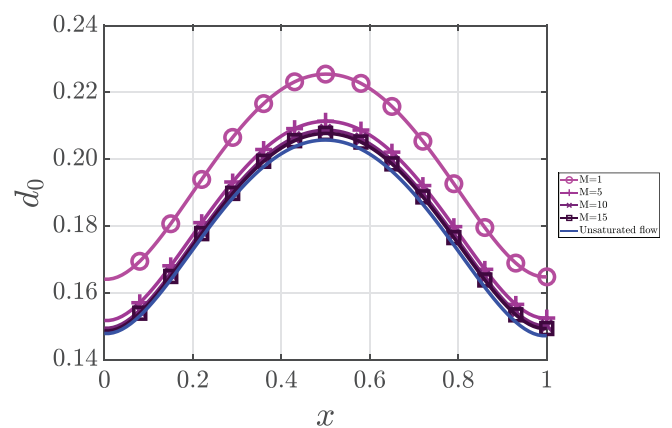


Fig. 14. Comparison of the saturation of the wetting fluid of the upscaled models at $t = 1$.

the wetting phase quantities in the two-phase flow model and the corresponding ones for the unsaturated flow, for different values of M at $t = 1$. Observe that the differences become smaller for larger viscosity ratios. We see that the behaviour of the wetting fluid is well approximated by the simpler unsaturated-flow model when the viscosity ratio increases. Hence, if the velocity and saturation of the wetting fluid is of main interest, one could use the unsaturated-flow model instead of the two-phase flow model already for relatively moderate viscosity ratios.

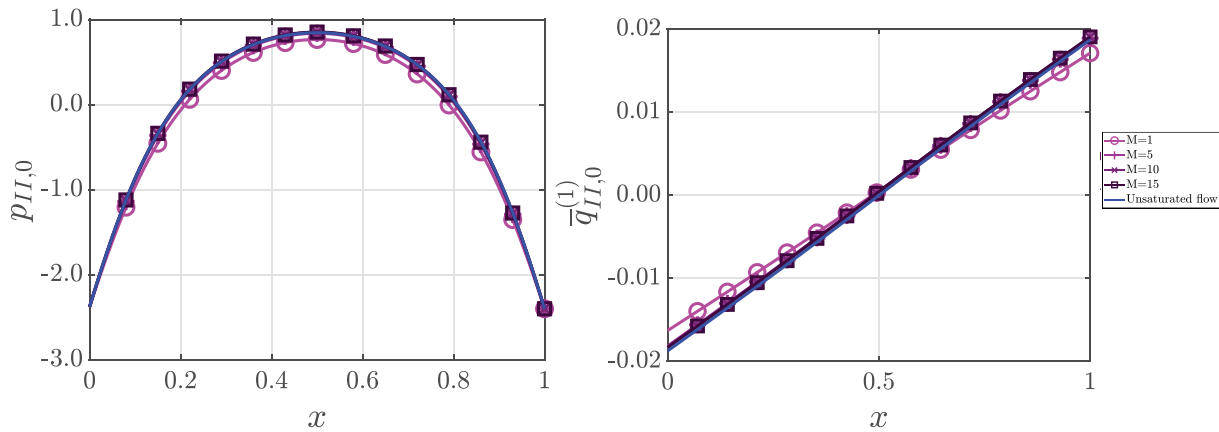


Fig. 15. Comparison of the pressure (left) and the flux (right) of the wetting fluid of the upscaled models at $t = 1$.

Table 6

L^2 -norm of the difference between the wetting phase quantities in the two-phase flow model and the corresponding ones for the unsaturated flow, for different values of M at $t = 1$.

	$M = 1$	$M = 5$	$M = 10$	$M = 15$
$\ d_0^U - d_0^M\ _{L^2(0,1)}$	$1.8 \cdot 10^{-2}$	$5.1 \cdot 10^{-3}$	$2.7 \cdot 10^{-3}$	$1.8 \cdot 10^{-3}$
$\ p_{II,0}^U - p_{II,0}^M\ _{L^2(0,1)}$	$9.7 \cdot 10^{-2}$	$1.7 \cdot 10^{-2}$	$5.2 \cdot 10^{-3}$	$4.6 \cdot 10^{-3}$
$\ \bar{q}_{II,0}^{(1)U} - \bar{q}_{II,0}^{(1)M}\ _{L^2(0,1)}$	$1.3 \cdot 10^{-3}$	$4.5 \cdot 10^{-4}$	$4.3 \cdot 10^{-4}$	$4.2 \cdot 10^{-4}$

8. Conclusion

We consider the flow of two immiscible and incompressible phases, respectively the unsaturated flow in a thin strip representing a porous medium. We account for the possible dependence of the surface tension on the solute transported by the wetting fluid. For the two-phase flow (the unsaturated, one-phase flow being similar) the starting point is the model at the pore scale, where the two fluids are separated by an interface having an a-priori unknown location but depending on the fluid velocities. The flow is described by the Navier-Stokes equations and the solute transport by the advection-diffusion equation. At the interface separating the two fluids, relevant interface conditions are imposed. In particular, the difference in the normal stress tensors depend on the surface tension, which may change depending on the solute. Considering a simplified situation, namely a thin strip representing a single pore, we have derived upscaled one-dimensional models describing the averaged behaviour of the system for different capillary regimes. We have validated our theoretical results with numerical experiments and we then compared the behaviour of the upscaled models. In doing so, different situations are considered, in which the capillary number and the viscosity ratio have a certain behaviour w.r.t. the ratio of the pore width and length. In particular, we see that the solute-dependent surface tension (the Marangoni effect) is relevant for the upscaled models only if the capillary number is small enough. In the case when the viscosity ratio becomes large, the two-phase flow model reduces to the unsaturated, one-phase model. One main conclusion is that for small capillary numbers instead of capillary pressure - saturation curve, we obtain capillary pressure - saturation dependency involving the second order derivative of the saturation, as also proposed in Cueto-Felgueroso and Juanes (2008, 2009); Mikelić (2003); Mikelić and Paoli (2000). Based on the numerical results, we emphasize that the presence of solute-dependent surface tension can strongly influence the flow.

Although considering a simple geometry, combining asymptotic expansions with various scaling of the non-dimensional parameters show which processes are important at the larger scale and which can be neglected. The upscaling procedure also shows how the capillary pressure depends on the saturation when the capillary pressure should be ac-

counted for. Allowing for other types of fluid displacement, such as a fluid-fluid-solid contact point, and more general geometries open for also other types of upscaled models.

Declaration of Competing Interest

The authors declare that they have no known competing financial-interestor personal relationships that could have appeared to influence the work reported in this paper.

CRediT authorship contribution statement

Sohely Sharmin: Conceptualization, Methodology, Software, Validation, Formal analysis, Writing - original draft. **Carina Bringedal:** Conceptualization, Methodology, Investigation, Resources, Writing - review & editing, Supervision. **Iuliu Sorin Pop:** Conceptualization, Methodology, Investigation, Resources, Writing - review & editing, Supervision.

Acknowledgement

The work was supported by the Research Foundation-Flanders (FWO), Belgium through the Odysseus programme (project G0G1316N). We thank the Deutsche Forschungsgemeinschaft (DFG, German Research Foundation) for supporting this work by funding SFB 1313, Project Number 327154368. We thank the reviewers for their valuable comments that helped improving this work.

References

Abels, H., Garcke, H., Grün, G., 2012. Thermodynamically consistent, frame indifferent diffuse interface models for incompressible two-phase flows with different densities. *Math. Models Methods Appl. Sci.* 22 (03), 1150013,40. <https://doi.org/10.1142/S0218202511500138>.

Abreu, E., Bustos, A., Ferraz, P., Lambert, W., 2019. A relaxation projection analytical-numerical approach in hysteretic two-phase flows in porous media. *J. Sci. Comput.* 79 (3), 1936–1980. <https://doi.org/10.1007/s10915-019-00923-4>.

Armiti-Juber, A., Rohde, C., 2020. On the well-posedness of a nonlinear fourth-order extension of Richards' equation. *J. Math. Anal. Appl.* 487 (2), 124005. <https://doi.org/10.1016/j.jmaa.2020.124005>.

Aziz, K., Settari, A., 1979. *Petroleum reservoir simulation*. Appl. Science. Publ. Ltd., London, UK.

- Beliaev, A., Hassanizadeh, S., 2001. A theoretical model of hysteresis and dynamic effects in the capillary relation for two-phase flow in porous media. *Transp. Porous Med.* 43 (3), 487–510. <https://doi.org/10.1023/A:1010736108256>.
- Beliaev, A.Y., Schotting, R.J., 2001. Analysis of a new model for unsaturated flow in porous media including hysteresis and dynamic effects. *Comput. Geosci.* 5 (4), 345–368.
- Bottero, S., Hassanizadeh, S.M., Kleingeld, P.J., Heimovaara, T.J., 2011. Nonequilibrium capillarity effects in two-phase flow through porous media at different scales. *Water Resour. Res.* 47. <https://doi.org/10.1029/2011WR010887>.
- Bresch, D., 2009. Shallow-water Equations and Related Topics. In: *Handbook of Differential Equations: Evolutionary Equations*. Elsevier/North-Holland, Amsterdam, pp. 1–104. [https://doi.org/10.1016/S1874-5717\(08\)00208-9](https://doi.org/10.1016/S1874-5717(08)00208-9).
- Bringedal, C., Berre, I., Pop, I.S., Radu, F.A., 2015. A model for non-isothermal flow and mineral precipitation and dissolution in a thin strip. *J. Comput. Appl. Math.* 289, 346–355. <https://doi.org/10.1016/j.cam.2014.12.009>.
- Bringedal, C., Berre, I., Pop, I.S., Radu, F.A., 2016. Upscaling of non-isothermal reactive porous media flow with changing porosity. *Transp. Porous Med.* 114 (2), 371–393. <https://doi.org/10.1007/s11242-015-0530-9>.
- Bringedal, C., Berre, I., Pop, I.S., Radu, F.A., 2016. Upscaling of nonisothermal reactive porous media flow under dominant pecllet number: the effect of changing porosity. *Multiscale Model. Simul.* 14 (1), 502–533. <https://doi.org/10.1137/15M1022781>.
- Chapwanya, M., Stockie, J.M., 2010. Numerical simulations of gravity-driven fingering in unsaturated porous media using a nonequilibrium model. *Water Resour. Res.* 46. <https://doi.org/10.1029/2009WR008583>.
- COMSOL Multiphysics® v. 5.4. www.comsol.com COMSOL AB, Stockholm, Sweden.
- Cueto-Felgueroso, L., Juanes, R., 2008. Nonlocal interface dynamics and pattern formation in gravity-driven unsaturated flow through porous media. *Phys. Rev. Lett.* 101 (24), 244504. <https://doi.org/10.1103/PhysRevLett.101.244504>.
- Cueto-Felgueroso, L., Juanes, R., 2009. A phase field model of unsaturated flow. *Water Resour. Res.* 45. <https://doi.org/10.1029/2009WR007945>.
- Darcy, H.P.G., 1856. *Les fontaines publiques de la ville de Dijon. Exposition et application des principes à suivre et des formules à employer dans les questions de distribution d'eau, etc.* V. Dalmon.
- DiCarlo, D.A., 2004. Experimental measurements of saturation overshoot on infiltration. *Water Resour. Res.* 40 (4). <https://doi.org/10.1029/2003WR002670>.
- Doster, F., Hilfer, R., 2011. Generalized buckley-leverett theory for two-phase flow in porous media. *New J. Phys.* 13. <https://doi.org/10.1088/1367-2630/13/12/123030>.
- van Duijn, C.J., Fan, Y., Peletier, L.A., Pop, I.S., 2013. Travelling wave solutions for degenerate pseudo-parabolic equations modelling two-phase flow in porous media. *Nonlinear Anal.-Real World Appl.* 14 (3), 1361–1383. <https://doi.org/10.1016/j.nonrwa.2012.10.002>.
- van Duijn, C.J., Mikelic, A., Pop, I.S., Rosier, C., 2008. Effective dispersion equations for reactive flows with dominant pecllet and damkohler numbers. *Adv. in Chem. Engrg.* 34, 1–45. [https://doi.org/10.1016/S0065-2377\(08\)00001-X](https://doi.org/10.1016/S0065-2377(08)00001-X).
- van Duijn, C.J., Mitra, K., 2018. Hysteresis and horizontal redistribution in porous media. *Transp. Porous Med.* 122 (2), 375–399. <https://doi.org/10.1007/s11242-018-1009-2>.
- Glass, R., Steenhuis, T., Parlange, J.-Y., 1989. Mechanism for finger persistence in homogeneous, unsaturated, porous media: theory and verification. *Soil Sci.* 148 (1), 60–70. <https://doi.org/10.1097/00010694-198907000-00007>.
- Golparvar, A., Zhou, Y., Wu, K., Ma, J., Yu, Z., 2018. A comprehensive review of pore scale modeling methodologies for multiphase flow in porous media. *Adv. Geo-Energy Res.* 2 (4), 418–440. <https://doi.org/10.26804/ager.2018.04.07>.
- Hassanizadeh, S.M., Gray, W.G., 1990. Mechanics and thermodynamics of multiphase flow in porous media including interphase boundaries. *Adv. Water Res.* 13 (4), 169–186. [https://doi.org/10.1016/0309-1708\(90\)90040-B](https://doi.org/10.1016/0309-1708(90)90040-B).
- Hassanizadeh, S.M., Gray, W.G., 1993. Thermodynamic basis of capillary pressure in porous media. *Water Resour. Res.* 29 (10), 3389–3405. <https://doi.org/10.1029/93WR01495>.
- Hilfer, R., Doster, F., Zegeling, P.A., 2012. Nonmonotone saturation profiles for hydrostatic equilibrium in homogeneous porous media. *Vadose Zone J.* 11 (3). <https://doi.org/10.2136/vzj2012.0021>.
- Huppert, H., 1982. Flow and instability of a viscous current down a slope. *Nature* 300 (5891), 427–429. <https://doi.org/10.1038/300427a0>.
- Joekar-Niasar, V., Hassanizadeh, S.M., 2012. Analysis of fundamentals of two-phase flow in porous media using dynamic pore-network models: a review. *Crit. Rev. Env. Sci. Tec.* 42 (18), 1895–1976. <https://doi.org/10.1080/10643389.2011.574101>.
- Kumar, K., Noorden, T.L.v., Pop, I.S., 2011. Effective dispersion equations for reactive flows involving free boundaries at the microscale. *Multiscale Model. Simul.* 9 (1), 29–58. <https://doi.org/10.1137/100804553>.
- Lamacz, A., Rätz, A., B., S., 2011. A well-posed hysteresis model for flows in porous media and applications to fingering effects. *Adv. Math. Sci. Appl.* 21, 33–64. <https://doi.org/10.17877/DE290R-6610>.
- Landa-Marbán, D., Bødtker, G., Kumar, K., Pop, I.S., Radu, F.A., 2020. An upscaled model for permeable biofilm in a thin channel and tube. *Transp. Porous Med.* 132 (1), 83–112. <https://doi.org/10.1007/s11242-020-01381-5>.
- Lasseux, D., Quintard, M., Whitaker, S., 1996. Determination of permeability tensors for two-phase flow in homogeneous porous media: theory. *Transp. Porous Med.* 24 (2), 107–137. <https://doi.org/10.1007/BF00139841>.
- Leal, L.G., 2007. *Advanced transport phenomena: Fluid mechanics and convective transport processes*, 7. Cambridge University Press.
- Mauri, R., 2003. Heat and mass transport in nonhomogeneous random velocity fields. *Phys. Rev. E* 68 (6), 066306. <https://doi.org/10.1103/PhysRevE.68.066306>.
- Mehmani, Y., Tchelepi, H., 2018. Multiscale computation of pore-scale fluid dynamics: single-phase flow. *J. Comput. Phys.* 375, 1469–1487. <https://doi.org/10.1016/j.jcp.2018.08.045>.
- Mehmani, Y., Tchelepi, H., 2019. Multiscale formulation of two-phase flow at the pore scale. *J. Comput. Phys.* 389, 164–188. <https://doi.org/10.1016/j.jcp.2019.03.035>.
- Mikelić, A., 2003. On an averaged model for the 2-fluid immiscible flow with surface tension in a thin cylindrical tube. *Comput. Geosci.* 7 (3), 183–196. <https://doi.org/10.1023/A:1025527716078>.
- Mikelić, A., Paoli, L., 2000. On the derivation of the buckley-leverett model from the two fluid navier-stokes equations in a thin domain. *Comput. Geosci.* 4 (1), 99–101. <https://doi.org/10.1023/A:1011503731330>.
- Morrow, N.R., Harris, C.C., 1965. Capillary equilibrium in porous materials. *SPE J.* 5 (1), 15–24. <https://doi.org/10.2118/1011-PA>.
- Niessner, J., Hassanizadeh, S.M., 2008. A model for two-phase flow in porous media including fluid-fluid interfacial area. *Water Resour. Res.* 44 (8). <https://doi.org/10.1029/2007WR006721>.
- van Noorden, T., Pop, I.S., Ebigo, A., Helmig, R., 2010. An upscaled model for biofilm growth in a thin strip. *Water Resour. Res.* 46. <https://doi.org/10.1029/2009WR008217>.
- van Duijn, C.J., Mitra, K., Pop, I.S., 2018. Travelling wave solutions for the Richards equation incorporating non-equilibrium effects in the capillarity pressure. *Nonlinear Anal.-Real World Appl.* 41, 232–268. <https://doi.org/10.1016/j.nonrwa.2017.10.015>.
- van Noorden, T.L., 2009. Crystal precipitation and dissolution in a porous medium: effective equations and numerical experiments. *Multiscale Model. Simul.* 7 (3), 1220–1236. <https://doi.org/10.1137/080722096>.
- van Noorden, T.L., 2009. Crystal precipitation and dissolution in a thin strip. *Eur. J. Appl. Math.* 20 (1), 69–91. <https://doi.org/10.1017/S0956792508007651>.
- Oron, A., Davis, S.H., Bankoff, S.G., 1997. Long-scale evolution of thin liquid films. *Rev. Mod. Phys.* 69 (3), 931. <https://doi.org/10.1103/RevModPhys.69.931>.
- Osher, S., Fedkiw, R.P., 2001. Level set methods: an overview and some recent results. *J. Comput. Phys.* 169 (2), 463–502. <https://doi.org/10.1006/jcph.2000.6636>.
- Patankar, S., 1980. *Numerical heat transfer and fluid flow*. CRC press.
- Peszynska, M., Trykozko, A., Iltis, G., Schlueter, S., Wildenschild, D., 2016. Biofilm growth in porous media: experiments, computational modeling at the porescale, and upscaling. *Adv. Water Res.* 95, 288–301. <https://doi.org/10.1016/j.advwatres.2015.07.008>.
- Picchi, D., Battiato, I., 2018. The impact of pore-scale flow regimes on upscaling of immiscible two-phase flow in porous media. *Water Resour. Res.* 54 (9), 6683–6707. <https://doi.org/10.1029/2018WR023172>.
- Plöhr, B., Marchesin, D., Bedrikovetsky, P., Krause, P., 2001. Modeling hysteresis in porous media flow via relaxation. *Comput. Geosci.* 5 (3), 225–256. <https://doi.org/10.1023/A:1013759420009>.
- Pop, I.S., van Duijn, C.J., Niessner, J., Hassanizadeh, S.M., 2009. Horizontal redistribution of fluids in a porous medium: the role of interfacial area in modeling hysteresis. *Adv. Water Res.* 32 (3), 383–390. <https://doi.org/10.1016/j.advwatres.2008.12.006>.
- Poulouvalis, A., 1970. Hysteresis of pore water in granular porous bodies. *Soil Sci.* 109 (1), 5–12. <https://doi.org/10.1097/00010694-197001000-00002>.
- Quintard, M., Whitaker, S., 1988. Two-phase flow in heterogeneous porous media: the method of large-scale averaging. *Transp. Porous Med.* 3 (4), 357–413. <https://doi.org/10.1007/BF00233177>.
- Quintard, M., Whitaker, S., 1990. Two-phase flow in heterogeneous porous media I: the influence of large spatial and temporal gradients. *Transp. Porous Med.* 5 (4), 341–379. <https://doi.org/10.1007/BF01141991>.
- Quintard, M., Whitaker, S., 1990. Two-phase flow in heterogeneous porous media ii: numerical experiments for flow perpendicular to a stratified system. *Transp. Porous Med.* 5 (5), 429–472. <https://doi.org/10.1007/BF01403477>.
- Rätz, A., Schweizer, B., 2014. Hysteresis models and gravity fingering in porous media. *ZAMM Z. Angew. Math. Mech.* 94 (7–8, SI), 645–654. <https://doi.org/10.1002/zamm.201200052>.
- Ray, N., van Noorden, T., Frank, F., Knabner, P., 2012. Multiscale modeling of colloid and fluid dynamics in porous media including an evolving microstructure. *Transp. Porous Med.* 95 (3), 669–696. <https://doi.org/10.1007/s11242-012-0068-z>.
- Ray, N., van Noorden, T., Radu, F.A., Friess, W., Knabner, P., 2013. Drug release from collagen matrices including an evolving microstructure. *ZAMM Z. Angew. Math. Mech.* 93 (1011), 811–822. <https://doi.org/10.1002/zamm.201200196>.
- Rezanezhad, F., Vogel, H.-J., Roth, K., 2006. Experimental study of fingered flow through initially dry sand. *Hydrol. Earth Syst. Sci. Discuss.* 3, 2595–2620. <https://doi.org/10.5194/hessd-3-2595-2006>.
- Richards, L.A., 1931. Capillary conduction of liquids through porous mediums. *Physics (College Park Md)* 1 (5), 318–333. <https://doi.org/10.1063/1.1745010>.
- Schechter, R.S., Gidley, J.L., 1969. The change in pore size distribution from surface reactions in porous media. *AIChE J.* 15 (3), 339–350. <https://doi.org/10.1002/aic.690150309>.
- Schneider, M., Koeppel, T., Helmig, R., Steinle, R., Hilfer, R., 2018. Stable propagation of saturation overshoots for two-phase flow in porous media. *Transp. Porous Med.* 121 (3), 621–641. <https://doi.org/10.1007/s11242-017-0977-y>.
- Schulz, R., 2019. Biofilm modeling in evolving porous media with beavers-joseph condition. *ZAMM Z. Angew. Math. Mech.* 99 (3). <https://doi.org/10.1002/zamm.201800123>.
- Schulz, R., 2019. Crystal precipitation and dissolution in a porous medium: evolving microstructure and perforated solid matrix. *Spec. Topic. Rev. Porous Media: An Int. J.* 10 (4), 305–321. <https://doi.org/10.1615/SpecialTopicsRevPorousMedia.2019029274>.
- Schulz, R., Knabner, P., 2017. An effective model for biofilm growth made by chemotactical bacteria in evolving porous media. *SIAM J. Appl. Math.* 77 (5), 1653–1677. <https://doi.org/10.1137/16M108817X>.
- Schweizer, B., 2017. Hysteresis in porous media: modelling and analysis. *Interface Free Bound.* 19 (3), 417–447. <https://doi.org/10.4171/IFB/388>.

- Shiozawa, S., Fujimaki, H., 2004. Unexpected water content profiles under flux-limited one-dimensional downward infiltration in initially dry granular media. *Water Resour. Res.* 40 (7). <https://doi.org/10.1029/2003WR002197>.
- Smith, J.E., Gillham, R.W., 1999. Effects of solute concentration-dependent surface tension on unsaturated flow: laboratory sand column experiments. *Water Resour. Res.* 35 (4), 973–982.
- Tartakovsky, A.M., Meakin, P., 2006. Pore scale modeling of immiscible and miscible fluid flows using smoothed particle hydrodynamics. *Adv. Water Res.* 29 (10), 1464–1478. <https://doi.org/10.1016/j.advwatres.2005.11.014>.
- Whitaker, S., 1986. Flow in porous media ii: the governing equations for immiscible, two-phase flow. *Transp. Porous Med.* 1 (2), 105–125. <https://doi.org/10.1007/BF00714688>.
- Zhang, H., Zegeling, P., 2017. A numerical study of two-phase flow models with dynamic capillary pressure and hysteresis. *Transp. Porous Med.* 116 (2), 825–846. <https://doi.org/10.1007/s11242-016-0802-z>.
- Zhuang, L., Hassanizadeh, S., van Duijn, C.J., Zimmermann, S., Zizina, I., Helmig, R., 2019. Experimental and numerical studies of saturation overshoot during infiltration into a dry soil. *Vadose Zone J.* 18 (1). <https://doi.org/10.2136/vzj2018.09.0167>.

6 Dynamic contact angle in a thin strip

The content of this chapter is based on the following original article:

S. B. Lunowa, C. Bringedal, and I. S. Pop. *On an averaged model for immiscible two-phase flow with surface tension and dynamic contact angle in a thin strip*. *Studies in Applied Mathematics* 147.1 (2021), pp. 84–126. doi: 10.1111/sapm.12376.

With courtesy from Wiley.

On an averaged model for immiscible two-phase flow with surface tension and dynamic contact angle in a thin strip

Stephan B. Lunowa¹  | Carina Bringedal²  | Iuliu Sorin Pop¹ 

¹ Computational Mathematics, UHasselt – Hasselt University, Diepenbeek, Belgium

² Institute for Modelling Hydraulic and Environmental Systems, University of Stuttgart, Stuttgart, Germany

Correspondence

Stephan B. Lunowa, UHasselt – Hasselt University, Computational Mathematics, Agoralaan, 3590 Diepenbeek, Belgium.
Email: stephan.lunowa@uhasselt.be

Funding information

Universiteit Hasselt, Grant/Award Number: BOF17NI01; Deutsche Forschungsgemeinschaft, Grant/Award Number: 327154368; Fonds Wetenschappelijk Onderzoek, Grant/Award Numbers: G051418N, G0G1316M

Abstract

We consider a model for the flow of two immiscible fluids in a two-dimensional thin strip of varying width. This represents an idealization of a pore in a porous medium. The interface separating the fluids forms a freely moving interface in contact with the wall and is driven by the fluid flow and surface tension. The contact-line model incorporates Navier-slip boundary conditions and a dynamic and possibly hysteretic contact angle law. We assume a scale separation between the typical width and the length of the thin strip. Based on asymptotic expansions, we derive effective models for the two-phase flow. These models form a system of differential algebraic equations for the interface position and the total flux. The result is Darcy-type equations for the flow, combined with a capillary pressure–saturation relationship involving dynamic effects. Finally, we provide some numerical examples to show the effect of a varying wall width, of the viscosity ratio, of the slip boundary condition as well as of having a dynamic contact angle law.

KEYWORDS

asymptotic expansions, dynamic contact angle, freely moving interface, thin strip, two-phase flow, upscaled models

1 | INTRODUCTION

Many industrial and environmental processes, such as oil recovery, geological CO₂ sequestration, or groundwater pollution, strongly depend on the flow in the respective porous medium. In all these applications, it is necessary to describe the flow of all involved fluid phases at a macroscopic scale to allow for efficient simulations in large domains. In particular, the complex pore structure and the exact distribution of fluids are simplified into a representation by averaged quantities such as the porosity and saturation. The relations between these macroscopic quantities must be expressed with the help of effective parameters, which should combine all pore-scale effects. However, in many state-of-the-art models these parameters are postulated and not derived from a pore-scale model.

One of the earliest models for the macroscale flow in a porous medium was proposed by Darcy.¹ Based on column experiments for fully saturated, single-phase flow in a porous medium, a proportionality between the pressure gradient and the velocity was observed, involving the medium's permeability as proportionality factor. Subsequently, further experiments by Richards² and by Morrow and Harris³ extended the theory to unsaturated and two-phase flow in porous media, respectively. The resulting flow models still include Darcy's law, with a then saturation-dependent permeability. However, they additionally involved the phase-pressure difference, also known as the capillary pressure, which appears due to surface tension between the phases.

Based on experiments at equilibrium conditions, nonlinear, but monotonic capillary pressure–saturation functions have been used for decades. However, already Morrow and Harris³ showed that this relation also depends on the process—imbibition or drainage. Besides this hysteresis, further dynamic effects were reported in many experiments,^{4–8} leading to a variety of nonmonotonic curves which cannot be combined into a simple capillary pressure–saturation function.

To overcome the mismatch between the experimental results and the mathematical models, several extensions of the capillary pressure–saturation relation have been proposed. Typically, dynamic effects and hysteresis are directly expressed in terms of spatial or temporal derivatives of the saturation leading to different capillary pressure models, for example, Refs. 9–12; for an overview, see Ref. 13. Alternatively, the interfacial area was introduced as an additional state variable leading to a capillary pressure–saturation–interfacial area relationship that implicitly models the dynamic and hysteretic effects via the change in interfacial area.^{14,15} Other hysteresis models are based on the concept of percolating/nonpercolating phases.^{16–18} These extended models are able to reproduce nonmonotonic phenomena such as saturation overshoot and fingering as shown in Refs. 19–21 by qualitative analysis using a traveling wave approach and in Refs. 22–27 by numerical simulations.

However, all models discussed above are considering the so-called Darcy scale, and thus describe the average behavior of the liquid phases disregarding the detailed pore structure and processes at the pore scale. It is crucial to understand the dependence of the effective parameters on the underlying pore structure. At the pore scale, the mathematical model can incorporate the detailed physical processes, but it is posed in the entire pore space, which is extremely complex, and needs to account for all interfaces between phases. Resolving the whole complicated pore space of realistic scenarios in direct numerical simulations is infeasible, so that further simplifications are necessary to link the properties of the different scales.

To approach this task, there exist a large variety of analytical upscaling techniques, see Ref. 28 for an overview. The volume averaging method has been used to derive effective equations for quantities at the level of a representative elementary volume, while restricting the form of constitutive equations using the second law of thermodynamics at the Darcy scale. This method has

been successfully applied to single-phase and two-phase flow in porous media in Refs. 29–31. However, the technique does only provide explicit expressions for the effective parameters in the constitutive equations via closure problems, when additional assumptions are made. Alternatively, the homogenization method is a (matched) asymptotic expansion approach for typically periodic systems, where there is a clear scale separation. The idea is to approximate the problem involving a small parameter ε (e.g., the ratio of an average pore diameter to a Darcy-scale length) by the limit problem and its solution as $\varepsilon \rightarrow 0$. For an introduction to this method, we mention Ref. 32 and the references therein. Many results for flow in porous media have been obtained by homogenization, see, for example, Refs. 33–39 leading either to explicit expressions or to so-called cell problems for the effective parameters. In both cases, knowledge of the underlying pore structure allows for the explicit computation of the effective parameters. Therefore, we apply the homogenization method to explicitly derive effective relations.

Here we consider a simplified geometry, namely, the flow through a single, long, and thin pore as a representative for the porous medium. Despite the very simplistic representation, the upscaling of thin-strip models typically leads to Darcy-scale models with the same structure as well-recognized Darcy-scale models in general porous media (see, e.g., Refs. 37–40). In addition, using a single pore allows for the explicit derivation of closed-form expressions for the upscaled quantities. We assume that the pore is filled by two incompressible and immiscible fluid phases. The interface separating the two fluids is traversal to the flow direction. The mathematical model consists of conservation laws for mass and momentum in time-dependent domains representing the fluids. Assuming a horizontal setting, we disregard gravity effects. The evolution of the interface separating the domains is not known a priori, but depends on the velocities of the fluids and on the surface tension between the fluids. Hence, the development of the boundary of the domains must be accounted for, and we have a free boundary problem.

While the fluid domains are assumed to be layered in Refs. 37–40, such that the fluid–fluid interface does not come into contact with the solid wall, we here consider the case when the interface is in contact with the pore walls. This requires a contact angle model, which is allowed to be dynamic or even hysteretic. In particular, this also implies that each fluid is only present either at the inlet or at the outlet. Note that the plug flow scenario considered in Ref. 40 has a similar fluid distribution, but the authors assume a fixed interface shape and a residual thin film, which yields dynamics that are very different from those generated by a variable interface with moving contact line. Furthermore, we allow for a slowly varying solid wall instead of a constant-width strip or tube used in Refs. 37–40.

Based on the discussed pore-scale model, we derive upscaled (Darcy-scale) models for two-phase or unsaturated single-phase flow in a porous medium under reasonable assumptions on the underlying physics. We follow the ideas in Refs. 37–39, where asymmetric expansions and transversal averaging is applied to obtain a macroscale model based on the simple, layered pore. We complement this with volume averages to account for the different geometry and fluid distribution. A similar strategy has been used to show that the upscaled models significantly differ for different flow regimes assuming stationary fluid–fluid interface shapes in Ref. 40, and in Ref. 39 when assuming a layered, parallel flow regime. In general, the thin-strip approach allows the derivation of explicit relations between the averaged quantities, while various additional features and processes can be easily incorporated (see, e.g., Refs. 39, 41–43).

This paper is organized as follows. In Section 2, we formulate the mathematical model for two-phase flow with evolving interface in a thin strip, which is then rescaled to obtain a nondimensional formulation. Next, we formally derive in Section 3 the effective models in the bulk domains and close to the interface when the ratio between the width and length of the thin strip approaches

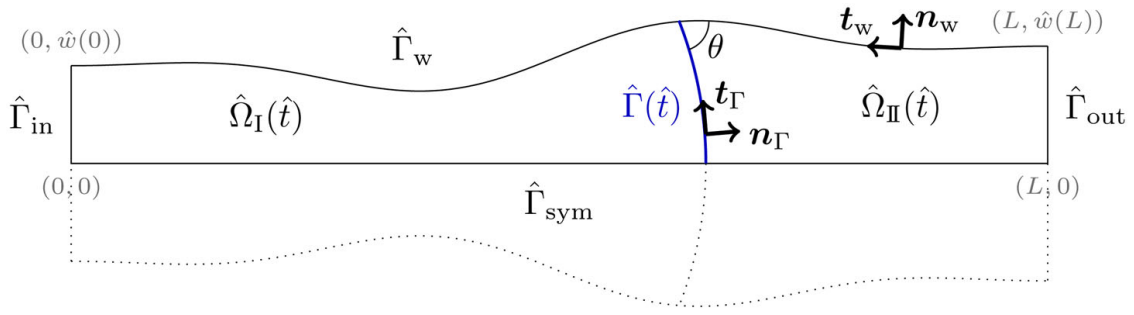


FIGURE 1 Sketch of the half thin strip $\hat{\Omega}$ filled by two fluids with interface $\hat{\Gamma}(\hat{t})$ at time \hat{t}

zero. These models form a system of differential algebraic equations for the interface position and the total flux. Based on the derived models, we discuss averaged and effective quantities and their relations in Section 4. In particular, there holds a Darcy-type equation for the flow and a capillary pressure–saturation relationship involving dynamic effects. Finally, Section 5 provides some numerical examples showing the behavior of the effective models for a constant as well as a varying wall width. The effect of the viscosity ratio, of the slip length, and of having a dynamic contact angle law is discussed in detail.

2 | MATHEMATICAL MODEL

We consider a two-dimensional thin strip of length $L > 0$, which is axisymmetric at $\hat{\Gamma}_{\text{sym}} := [0, L] \times \{0\}$. Let $\hat{w} : [0, L] \rightarrow (0, \infty)$ be a given smooth function (which is bounded away from zero), that describes the wall $\hat{\Gamma}_w := \{\hat{\mathbf{x}} \in (0, L) \times (0, \infty) \mid \hat{x}_2 = \hat{w}(\hat{x}_1)\}$. Here and in the following, the subscripts \cdot_1 and \cdot_2 denote the components of a vector. Then the domain of interest is $\hat{\Omega} := \{\hat{\mathbf{x}} \in (0, L) \times (0, \infty) \mid \hat{x}_2 < \hat{w}(\hat{x}_1)\}$. At each time $\hat{t} \in [0, \infty)$, the domain is partitioned into two sub-domains $\hat{\Omega}_I(\hat{t})$ and $\hat{\Omega}_{II}(\hat{t})$, which represent the parts occupied by the two fluids; one at the inlet boundary $\hat{\Gamma}_{\text{in}} := \{0\} \times [0, \hat{w}(0)]$ and the other at the outflow boundary $\hat{\Gamma}_{\text{out}} := \{L\} \times [0, \hat{w}(L)]$. Figure 1 illustrates the geometry.

We consider the particular case when the two fluids are separated by an axisymmetric fluid–fluid interface $\hat{\Gamma}(\hat{t}) := \partial\hat{\Omega}_I(\hat{t}) \cap \partial\hat{\Omega}_{II}(\hat{t})$, which is in contact with the solid wall $\hat{\Gamma}_w$. This interface has an a priori unknown location and shape, and therefore appears as a free boundary in the mathematical model. It is parameterized by $\hat{\gamma} : [0, \infty) \times [0, 1] \rightarrow \hat{\Omega}$, such that $\hat{\Gamma}(\hat{t}) = \{\hat{\gamma}(\hat{t}, s) \mid s \in [0, 1]\}$. The parameterization starts at the symmetry boundary and ends at the wall, that is,

$$\hat{\gamma}_2(\hat{t}, 0) = 0, \quad \hat{\gamma}_2(\hat{t}, 1) = \hat{w}(\hat{\gamma}_1(\hat{t}, 1)). \quad (1)$$

The point $\hat{\mathbf{x}}^*(\hat{t}) := \hat{\gamma}(\hat{t}, 1)$ is the so-called contact point.

At all boundaries of $\hat{\Omega}$, the outward normal and tangential unit vectors are denoted \mathbf{n} and \mathbf{t} with an index specifying the part of the boundary, for example, \mathbf{n}_{sym} for the normal vector at the symmetry boundary $\hat{\Gamma}_{\text{sym}}$. At the fluid–fluid interface $\hat{\Gamma}(\hat{t})$, the normal unit vector pointing from $\hat{\Omega}_I(\hat{t})$ into $\hat{\Omega}_{II}(\hat{t})$ is denoted by \mathbf{n}_Γ , while the tangential unit vector is \mathbf{t}_Γ . Therefore, these vectors are given by

$$\mathbf{t}_\Gamma = \frac{\partial_s \hat{\gamma}}{|\partial_s \hat{\gamma}|} = \frac{1}{\sqrt{(\partial_s \hat{\gamma}_1)^2 + (\partial_s \hat{\gamma}_2)^2}} \partial_s \hat{\gamma} \quad \mathbf{n}_\Gamma = \frac{\partial_s \mathbf{t}_\Gamma}{|\partial_s \mathbf{t}_\Gamma|} = \frac{1}{\sqrt{(\partial_s \hat{\gamma}_1)^2 + (\partial_s \hat{\gamma}_2)^2}} \begin{pmatrix} \partial_s \hat{\gamma}_2 \\ -\partial_s \hat{\gamma}_1 \end{pmatrix},$$

TABLE 1 Summary of all parameters (top), dimensionless numbers (center), and dimensional and dimensionless quantities and their respective scaling (bottom)

Parameter	Symbol	Dim.-less Number	Symbol	Value	
Length of the thin strip	L	Scale ratio	ε	$\hat{w}(0)/L$	
Characteristic velocity	U	Density ratio	R	$\rho_{\text{II}}/\rho_{\text{I}}$	
Density of fluid m	ρ_m	Viscosity ratio	M	$\mu_{\text{II}}/\mu_{\text{I}}$	
Viscosity of fluid m	μ_m	Reynolds number	Re	$\rho_{\text{I}}UL/\mu_{\text{I}}$	
Surface tension coefficient	σ	Capillary number	Ca	$\mu_{\text{I}}U/\sigma$	
		Eff. capillary number	$\overline{\text{Ca}}$	Ca/ε	
Quantity	Dimensional	Dim.-less	Scaling	Inner expansion	Scaling
Position	$\hat{\mathbf{x}}$	\mathbf{x}	$[L, \varepsilon L]$	\mathbf{X}	$[\varepsilon L, \varepsilon L]$
Time	\hat{t}	t	$[L/U]$	t	$[L/U]$
Velocity of fluid m	$\hat{\mathbf{u}}_m$	\mathbf{u}_m	$[U]$	\mathbf{U}_m	$[U]$
Pressure of fluid m	\hat{p}_m	p_m	$[\mu_{\text{I}}U/(\varepsilon^2L)]$	P_m	$[\mu_{\text{I}}U/(\varepsilon^2L)]$
Interface parameterization	$\hat{\boldsymbol{\gamma}}$	$\boldsymbol{\gamma}$	$[L, \varepsilon L]$	\mathbf{Y}	$[\varepsilon L, \varepsilon L]$
Interface curvature	$\hat{\kappa}$	κ	$[1/L]$	K	$[1/L]$
Slip length	$\hat{\lambda}$	λ	$[\varepsilon L]$	λ	$[\varepsilon L]$
Wall function (width)	\hat{w}	w	$[\varepsilon L]$	w	$[\varepsilon L]$
Contact angle law	$\hat{\theta}$	θ	$[1]$	θ	$[1]$

$$\mathbf{t}_w = -\frac{1}{\sqrt{1 + (\partial_{\hat{x}_1} \hat{w})^2}} \begin{pmatrix} 1 \\ \partial_{\hat{x}_1} \hat{w} \end{pmatrix} \quad \mathbf{n}_w = \frac{1}{\sqrt{1 + (\partial_{\hat{x}_1} \hat{w})^2}} \begin{pmatrix} -\partial_{\hat{x}_1} \hat{w} \\ 1 \end{pmatrix},$$

$$\mathbf{t}_{\text{sym}} = \begin{pmatrix} 1 \\ 0 \end{pmatrix} \quad \mathbf{n}_{\text{sym}} = \begin{pmatrix} 0 \\ -1 \end{pmatrix},$$

$$\mathbf{t}_{\text{in}} = \begin{pmatrix} 0 \\ -1 \end{pmatrix} \quad \mathbf{n}_{\text{in}} = \begin{pmatrix} -1 \\ 0 \end{pmatrix},$$

$$\mathbf{t}_{\text{out}} = \begin{pmatrix} 0 \\ 1 \end{pmatrix} \quad \mathbf{n}_{\text{out}} = \begin{pmatrix} 1 \\ 0 \end{pmatrix}.$$

In each subdomain $\hat{\Omega}_m(\hat{t})$, $m \in \{\text{I}, \text{II}\}$, we assume that the flow is modeled by the incompressible Navier–Stokes equations, which are written in dimensional form

$$\rho_m (\partial_{\hat{t}} \hat{\mathbf{u}}_m + (\hat{\mathbf{u}}_m \cdot \hat{\nabla}) \hat{\mathbf{u}}_m) + \hat{\nabla} \hat{p}_m = \mu_m \hat{\Delta} \hat{\mathbf{u}}_m \quad \text{in } \hat{\Omega}_m(\hat{t}), \quad (2)$$

$$\hat{\nabla} \cdot \hat{\mathbf{u}}_m = 0 \quad \text{in } \hat{\Omega}_m(\hat{t}), \quad (3)$$

where $\hat{\mathbf{u}}_m(\hat{t}, \hat{\mathbf{x}})$ and $\hat{p}_m(\hat{t}, \hat{\mathbf{x}})$ are the velocity and pressure of fluid m . The parameters ρ_m and μ_m denote the density and the dynamic viscosity of the fluid (Table 1 provides an overview of all parameters and quantities).

The symmetry conditions at $\hat{\Gamma}_{\text{sym},m}(\hat{t}) := \hat{\Gamma}_{\text{sym}} \cap \partial\hat{\Omega}_m(\hat{t})$ are

$$\hat{\mathbf{u}}_m \cdot \mathbf{n}_{\text{sym}} = 0, \mathbf{t}_{\text{sym}} \cdot \left(\hat{\nabla} \hat{\mathbf{u}}_m \mathbf{n}_{\text{sym}} \right) = 0 \quad \text{on } \hat{\Gamma}_{\text{sym},m}(\hat{t}), \quad (4)$$

$$\hat{\nabla} \hat{p}_m \cdot \mathbf{n}_{\text{sym}} = 0 \quad \text{on } \hat{\Gamma}_{\text{sym},m}(\hat{t}), \quad (5)$$

$$\mathbf{n}_{\Gamma} \cdot \mathbf{n}_{\text{sym}} = 0 \quad \text{at } s = 0. \quad (6)$$

The walls $\hat{\Gamma}_{w,m}(\hat{t}) := \hat{\Gamma}_w \cap \partial\hat{\Omega}_m(\hat{t})$ in contact with fluid $m \in \{\text{I}, \text{II}\}$ are assumed impermeable, such that there is no fluid flow in normal direction, that is,

$$\hat{\mathbf{u}}_m \cdot \mathbf{n}_w = 0 \quad \text{on } \hat{\Gamma}_{w,m}(\hat{t}). \quad (7)$$

Traditionally, this is complemented with the no-slip condition $\hat{\mathbf{u}}_m \cdot \mathbf{t}_w = 0$ under the assumption that the fluid adheres to the wall. However, the no-slip condition leads to a singularity in the pressure and in the shear stress at the contact point $\hat{\mathbf{x}}^*(\hat{t})$ between wall $\hat{\Gamma}_w$ and interface $\hat{\Gamma}(\hat{t})$.^{44–46} To overcome this issue, several alternative boundary conditions have been proposed for use close to the contact point (or contact line in three dimensions), see Refs. 47–49 and the references therein. Here, we consider the Navier-slip condition

$$\mathbf{t}_w \cdot \left(\hat{\mathbf{u}}_m + 2\hat{\lambda} \hat{\mathbf{D}}(\hat{\mathbf{u}}_m) \mathbf{n}_w \right) = 0 \quad \text{on } \hat{\Gamma}_{w,m}(\hat{t}), \quad (8)$$

where $\hat{\mathbf{D}}(\hat{\mathbf{u}}) := (\hat{\nabla} \hat{\mathbf{u}} + (\hat{\nabla} \hat{\mathbf{u}})^T)/2$ denotes the symmetric strain and $\hat{\lambda}$ is the slip length. This condition has been proposed originally by Huh and Scriven⁴⁴ to resolve the contact-line problem, and has been frequently used.^{50–55} Often, the Navier-slip condition is only applied close to the contact point. In this case, a variable slip length $\hat{\lambda}(\hat{x}_1)$ is adopted, decaying rapidly to zero away from the contact point $\hat{\mathbf{x}}^*(\hat{t})$ (see, e.g., Refs. 53, 56–58). This seems justified by molecular dynamics simulations showing that the no-slip boundary condition is only violated in a small region (up to some nm) around the contact point.^{59–63} In addition, surface wettability and roughness strongly affect the slip behavior (see, e.g., Refs. 64–67 for a mathematical analysis).

Remark 1. To be general, we will consider two cases here: a constant slip length $\hat{\lambda}$ on the whole wall $\hat{\Gamma}_w$, or a varying slip length $\hat{\lambda}(\hat{t}, \hat{x}_1) = \hat{\lambda}_e \exp(-c|\hat{x}_1 - \hat{x}_1^*(\hat{t})|)$ which decreases exponentially away from the contact point $\hat{\mathbf{x}}^*(\hat{t})$. Note that the overall dynamics of the two-phase system will be independent of the latter, local slip condition, and especially of the exact form used; only the flow field close to the interface will be affected (see Section 3). This is in accordance with the results in Refs. 46, 54. Furthermore, note that we consider for simplicity the same slip length $\hat{\lambda}$ for both fluids, although they could in principle differ. It is possible to extend the analysis below to incorporate fluid-dependent slip lengths.

At the contact point $\hat{\mathbf{x}}^*(\hat{t})$, the contact angle θ between the wall $\hat{\Gamma}_w(\hat{t})$ and the fluid interface $\hat{\Gamma}(\hat{t})$ must be prescribed. Minimization of the total surface energy yields the well-known Young's relation $\sigma_{\text{I}} - \sigma_{\text{II}} = \sigma \cos \theta_s$, where σ_{I} and σ_{II} denote the surface tension coefficients between the solid and the two fluids, and σ the interfacial tension between the two fluids. The angle θ_s is called the static contact angle and measured from the side of fluid II, as shown in Figure 1. Experiments per-

formed under dynamic conditions show a dynamic behavior of the contact angle. This is expressed as an apparent contact angle θ , and has a major influence on the overall flow dynamics.⁶⁸ In general, observations show increasing advancing angles, but decreasing receding angles, when the contact-line velocity U increases.^{46,69} The θ - U relation is essentially monotonic.

There are mainly two models to describe this phenomenon: the hydrodynamic theory and the molecular kinetic theory (for detailed reviews, see Refs. 48, 68, 70). The hydrodynamic theory emphasizes on dissipation due to viscous flow within the wedge of liquid near the moving contact line. The region close to the contact point is analyzed based on asymptotic expansions.^{46,50,52,57,71,72} For two-phase flow, this yields the well-known Cox law $g(\theta) = g(\theta_s) + C\mu U/\sigma$ for the dynamic contact angle θ , where U denotes the contact-line velocity, the constant C depends on the specific slip model, and g is an analytically derived function, which can be approximated by $g(\theta) \approx \theta^3$ for small angles.⁵⁷ The other approach is the molecular kinetic theory, where the dissipation is described due to the dynamic friction associated with the moving contact line. This yields the relation $U = C_1 \sinh(C_2 \sigma (\cos \theta_s - \cos \theta))$ with the constants C_1 and C_2 depending on molecular properties.^{69,73,74} After linearization for small differences in the angles, one obtains $U = C\sigma(\cos \theta_s - \cos \theta)$ for some constant C .⁶⁸

As for the slip length, the contact angle is strongly affected by surface wettability and roughness. In Refs. 68, 70, the resulting effects are made responsible for contact angle hysteresis, that is, that static contact angles can be achieved in the whole range $\theta_r < \theta_s < \theta_a$, where θ_a, θ_r denote the advancing and receding contact angles, respectively. Summarizing all the above results, we assume the contact angle θ to depend on the velocity $-\partial_t \hat{\mathbf{x}}^*(t) \cdot \mathbf{t}_w$ of the contact point parallel to the wall. Recall that $\hat{\mathbf{x}}^* = \hat{\boldsymbol{\gamma}}|_{s=1}$, so this contact angle condition is expressed as

$$\cos(\theta(-\partial_t \hat{\boldsymbol{\gamma}} \cdot \mathbf{t}_w|_{\hat{x}_1=\hat{\gamma}_1})) = \mathbf{t}_\Gamma \cdot \mathbf{t}_w|_{\hat{x}_1=\hat{\gamma}_1} \quad \text{at } s = 1, \quad (9)$$

where $\theta : \mathbb{R} \rightarrow (0, \pi)$ is a given dynamic contact angle model. Note that any dynamic contact angle model that satisfies assumption (A5) can be used. Specific relations for hysteretic θ and their effect on the behavior will be discussed in Subsection 3.4. Furthermore, to account for heterogeneities, the following analysis can be straightforwardly extended to the case when the contact angle also depends on the position $\hat{x}_1^*(t)$ of the contact point.

At the interface $\hat{\Gamma}(\hat{t})$, there holds continuity of the velocity and of the tangential stress, while the jump in the normal stress is caused by the surface tension

$$\hat{\mathbf{u}}_\Gamma = \hat{\mathbf{u}}_\Pi \quad \text{on } \hat{\Gamma}(\hat{t}), \quad (10)$$

$$-(\hat{p}_\Gamma - \hat{p}_\Pi)\mathbf{n}_\Gamma + 2(\mu_\Gamma \hat{\mathbf{D}}(\hat{\mathbf{u}}_\Gamma) - \mu_\Pi \hat{\mathbf{D}}(\hat{\mathbf{u}}_\Pi))\mathbf{n}_\Gamma = \sigma \hat{\kappa} \mathbf{n}_\Gamma \quad \text{on } \hat{\Gamma}(\hat{t}), \quad (11)$$

where $\hat{\kappa} = \det(\partial_s \boldsymbol{\gamma}, \partial_s^2 \boldsymbol{\gamma})/|\partial_s \boldsymbol{\gamma}|^3$ is the local mean curvature of the interface. Note that this curvature generalizes to $\hat{\nabla} \cdot \mathbf{n}_\Gamma$ for three-dimensional domains. The interface moves according to the normal velocity of the fluids,

$$\partial_{\hat{t}} \hat{\boldsymbol{\gamma}} \cdot \mathbf{n}_\Gamma = \hat{\mathbf{u}}_\Gamma \cdot \mathbf{n}_\Gamma \quad \text{on } \hat{\Gamma}(\hat{t}). \quad (12)$$

At the inlet boundary $\hat{\Gamma}_{\text{in}}$, either the pressure \hat{p}_{in} or the velocity $\hat{\mathbf{u}}$ in is given, namely, either

$$\hat{p}_\Gamma = \hat{p}_{\text{in}}, \quad \hat{\mathbf{u}}_\Gamma \cdot \mathbf{t}_{\text{in}} = 0 \quad \text{or} \quad \hat{\mathbf{u}}_\Gamma = \hat{\mathbf{u}}_{\text{in}} \quad \text{on } \hat{\Gamma}_{\text{in}}, \quad (13)$$

while an outflow boundary condition is applied at $\hat{\Gamma}_{\text{out}}$ (corresponding to $\hat{p}_{\text{out}} = 0$)

$$\hat{p}_{\text{II}} = 0, \quad \hat{\mathbf{u}}_{\text{II}} \cdot \mathbf{t}_{\text{out}} = 0 \quad \text{on } \hat{\Gamma}_{\text{out}}. \quad (14)$$

The problem is closed by the initial conditions $\hat{\gamma}|_{\hat{t}=0} = \hat{\gamma}_0$ for the position of the interface $\hat{\Gamma}(0)$ and $\hat{\mathbf{u}}_m|_{\hat{t}=0} = \hat{\mathbf{u}}_{m,0}$ for the velocity in $\hat{\Omega}_m(0)$. In the following, we will omit the initial conditions and implicitly require them to match the asymptotic solutions in Section 3 to avoid possible initial layer solutions for small times.

2.1 | Dimensionless formulation

To quantify the importance of the different terms of the model, we rewrite the equations in a dimensionless form. As we consider a single, thin pore, we introduce the small parameter $\varepsilon = \hat{w}(0)/L \ll 1$ which characterizes the ratio of the typical width to the length of the thin strip. Note that in a general porous medium, ε would reflect the ratio of the size of a pore to the length scale of a representative elementary volume. With this, we rescale the governing equations using the dimensionless quantities (Table 1)

$$\begin{aligned} x_1 &:= \frac{\hat{x}_1}{L}, & x_2 &:= \frac{\hat{x}_2}{\hat{w}(0)} = \frac{\hat{x}_2}{\varepsilon L}, & t &:= \frac{\hat{t}U}{L}, & \lambda^\varepsilon &:= \frac{\hat{\lambda}}{\hat{w}(0)} = \frac{\hat{\lambda}}{\varepsilon L}, \\ \gamma_1^\varepsilon(t, s) &:= \frac{\hat{\gamma}_1(\hat{t}, s)}{L}, & \gamma_2^\varepsilon(t, s) &:= \frac{\hat{\gamma}_2(\hat{t}, s)}{\hat{w}(0)} = \frac{\hat{\gamma}_2(\hat{t}, s)}{\varepsilon L}, & w^\varepsilon(x_1) &:= \frac{\hat{w}(\hat{x}_1)}{\hat{w}(0)} = \frac{\hat{w}(\hat{x}_1)}{\varepsilon L}, \\ \theta^\varepsilon(u) &:= \theta(uU), & \mathbf{u}_m^\varepsilon(t, \mathbf{x}) &:= \frac{\hat{\mathbf{u}}_m(\hat{t}, \hat{\mathbf{x}})}{U}, & p_m^\varepsilon(t, \mathbf{x}) &:= \frac{\hat{p}_m(\hat{t}, \hat{\mathbf{x}})\varepsilon^2 L}{\mu_1 U}, \end{aligned}$$

where $U > 0$ denotes a characteristic velocity. In particular, the pressure reference $\mu_1 U / (\varepsilon^2 L)$ is chosen such that pressure and viscous stress terms in Equation (2) are balanced. For moderate Reynolds number, this choice ensures laminar flow driven by the pressure gradients, which is crucial for the validity of Darcy's law on the Darcy scale. Note that the coordinates x_1 and x_2 are scaled differently to obtain a domain of order 1, $\mathcal{O}(\varepsilon^0)$. Hence, the nondimensional differential operators are

$$\nabla^\varepsilon = \begin{pmatrix} \partial_{x_1} \\ \varepsilon^{-1} \partial_{x_2} \end{pmatrix}, \quad \Delta^\varepsilon = \partial_{x_1}^2 + \varepsilon^{-2} \partial_{x_2}^2,$$

and the divergence changes accordingly. The nondimensional domains and boundaries become

$$\begin{aligned} \Gamma^\varepsilon(t) &= \{\gamma^\varepsilon(t, s) \mid s \in [0, 1]\}, & \Omega^\varepsilon &= \{\mathbf{x} \in (0, 1) \times (0, \infty) \mid x_2 < w^\varepsilon(x_1)\}, \\ \Gamma_{\text{in}}^\varepsilon &= \{0\} \times [0, 1], & \mathcal{M} &:= \{O \subset \Omega^\varepsilon \setminus \Gamma^\varepsilon(t) \mid O \cup \Gamma_{\text{in}}^\varepsilon \text{ is connected}\}, \\ \Omega_1^\varepsilon(t) &= \bigcup_{O \in \mathcal{M}} O, & \Omega_{\text{II}}^\varepsilon(t) &= \Omega^\varepsilon \setminus (\Gamma^\varepsilon(t) \cup \Omega_1^\varepsilon(t)), & \Gamma_{\text{out}}^\varepsilon &= \{1\} \times [0, w^\varepsilon(1)], \\ \Gamma_{\text{sym},m}^\varepsilon(t) &= \{\mathbf{x} \in \partial\Omega_m^\varepsilon(t) \mid x_2 = 0\}, & \Gamma_{w,m}^\varepsilon(t) &= \{\mathbf{x} \in \partial\Omega_m^\varepsilon(t) \mid x_2 = w^\varepsilon(x_1)\}. \end{aligned}$$

After the rescaling of Equations (1–14), the dimensionless equations read

$$\varepsilon^2 \text{Re}(\partial_t \mathbf{u}_I^\varepsilon + (\mathbf{u}_I^\varepsilon \cdot \nabla^\varepsilon) \mathbf{u}_I^\varepsilon) + \nabla^\varepsilon p_I^\varepsilon = \varepsilon^2 \Delta^\varepsilon \mathbf{u}_I^\varepsilon \quad \text{in } \Omega_I^\varepsilon(t), \quad (15)$$

$$\varepsilon^2 \text{RRe}(\partial_t \mathbf{u}_{II}^\varepsilon + (\mathbf{u}_{II}^\varepsilon \cdot \nabla^\varepsilon) \mathbf{u}_{II}^\varepsilon) + \nabla^\varepsilon p_{II}^\varepsilon = M \varepsilon^2 \Delta^\varepsilon \mathbf{u}_{II}^\varepsilon \quad \text{in } \Omega_{II}^\varepsilon(t), \quad (16)$$

$$\nabla^\varepsilon \cdot \mathbf{u}_m^\varepsilon = 0 \quad \text{in } \Omega_m^\varepsilon(t), \quad (17)$$

$$\mathbf{u}_m^\varepsilon \cdot \mathbf{n}_{\text{sym}} = 0, \quad \mathbf{t}_{\text{sym}} \cdot (\nabla^\varepsilon \mathbf{u}_m^\varepsilon \mathbf{n}_{\text{sym}}) = 0 \quad \text{on } \Gamma_{\text{sym},m}^\varepsilon(t), \quad (18)$$

$$\nabla^\varepsilon p_m^\varepsilon \cdot \mathbf{n}_{\text{sym}} = 0, \quad \text{on } \Gamma_{\text{sym},m}^\varepsilon(t), \quad (19)$$

$$\text{either } p_I^\varepsilon = p_{\text{in}}^\varepsilon, \quad \mathbf{u}_I^\varepsilon \cdot \mathbf{t}_{\text{in}} = 0, \quad \text{or } \mathbf{u}_I^\varepsilon = \mathbf{u}_{\text{in}}^\varepsilon \quad \text{on } \Gamma_{\text{in}}^\varepsilon, \quad (20)$$

$$p_{II}^\varepsilon = 0, \quad \mathbf{u}_{II}^\varepsilon \cdot \mathbf{t}_{\text{out}} = 0 \quad \text{on } \Gamma_{\text{out}}^\varepsilon, \quad (21)$$

$$\mathbf{t}_w^\varepsilon \cdot (\mathbf{u}_m^\varepsilon + 2\varepsilon \lambda^\varepsilon \mathbf{D}^\varepsilon(\mathbf{u}_m^\varepsilon) \mathbf{n}_w^\varepsilon) = 0, \quad \mathbf{u}_m^\varepsilon \cdot \mathbf{n}_w^\varepsilon = 0 \quad \text{on } \Gamma_{w,m}^\varepsilon(t), \quad (22)$$

$$\partial_t \begin{pmatrix} \gamma_1^\varepsilon \\ \varepsilon \gamma_2^\varepsilon \end{pmatrix} \cdot \mathbf{n}_\Gamma^\varepsilon = \mathbf{u}_I^\varepsilon \cdot \mathbf{n}_\Gamma^\varepsilon, \quad \mathbf{u}_I^\varepsilon = \mathbf{u}_{II}^\varepsilon \quad \text{on } \Gamma^\varepsilon(t), \quad (23)$$

$$-(p_I^\varepsilon - p_{II}^\varepsilon) \mathbf{n}_\Gamma^\varepsilon + 2\varepsilon^2 (\mathbf{D}^\varepsilon(\mathbf{u}_I^\varepsilon) - M \mathbf{D}^\varepsilon(\mathbf{u}_{II}^\varepsilon)) \mathbf{n}_\Gamma^\varepsilon = \frac{\varepsilon^2}{\text{Ca}} \kappa^\varepsilon \mathbf{n}_\Gamma^\varepsilon \quad \text{on } \Gamma^\varepsilon(t), \quad (24)$$

$$\mathbf{n}_\Gamma^\varepsilon \cdot \mathbf{n}_{\text{sym}} = 0 \quad \text{at } s = 0, \quad (25)$$

$$\cos(\theta^\varepsilon(-\partial_t \boldsymbol{\gamma}^\varepsilon \cdot \mathbf{t}_w^\varepsilon|_{x_1=\gamma_1^\varepsilon})) = \mathbf{t}_\Gamma^\varepsilon \cdot \mathbf{t}_w^\varepsilon|_{x_1=\gamma_1^\varepsilon} \quad \text{at } s = 1, \quad (26)$$

for $m \in \{I, II\}$, where the dimensionless numbers R, M, Re, and Ca are given in Table 1. The nondimensional strain is given by $\mathbf{D}^\varepsilon(\mathbf{u}^\varepsilon) = (\nabla^\varepsilon \mathbf{u}^\varepsilon + (\nabla^\varepsilon \mathbf{u}^\varepsilon)^T)/2$ and the transformed normal and tangential vectors are

$$\mathbf{t}_w^\varepsilon = -\frac{1}{\sqrt{1 + \varepsilon^2 (\partial_{x_1} w^\varepsilon)^2}} \begin{pmatrix} 1 \\ \varepsilon \partial_{x_1} w^\varepsilon \end{pmatrix}, \quad \mathbf{n}_w^\varepsilon = \frac{1}{\sqrt{1 + \varepsilon^2 (\partial_{x_1} w^\varepsilon)^2}} \begin{pmatrix} -\varepsilon \partial_{x_1} w^\varepsilon \\ 1 \end{pmatrix},$$

$$\mathbf{t}_\Gamma^\varepsilon = \frac{1}{\sqrt{(\partial_s \gamma_1^\varepsilon)^2 + \varepsilon^2 (\partial_s \gamma_2^\varepsilon)^2}} \begin{pmatrix} \partial_s \gamma_1^\varepsilon \\ \varepsilon \partial_s \gamma_2^\varepsilon \end{pmatrix}, \quad \mathbf{n}_\Gamma^\varepsilon = \frac{1}{\sqrt{(\partial_s \gamma_1^\varepsilon)^2 + \varepsilon^2 (\partial_s \gamma_2^\varepsilon)^2}} \begin{pmatrix} \varepsilon \partial_s \gamma_2^\varepsilon \\ -\partial_s \gamma_1^\varepsilon \end{pmatrix}.$$

Furthermore, the nondimensional curvature is given by

$$\kappa^\varepsilon = \frac{\varepsilon \det(\partial_s \boldsymbol{\gamma}^\varepsilon, \partial_s^2 \boldsymbol{\gamma}^\varepsilon)}{((\partial_s \gamma_1^\varepsilon)^2 + \varepsilon^2 (\partial_s \gamma_2^\varepsilon)^2)^{3/2}} = \frac{\varepsilon (\partial_s \gamma_1^\varepsilon \partial_s^2 \gamma_2^\varepsilon - \partial_s \gamma_2^\varepsilon \partial_s^2 \gamma_1^\varepsilon)}{((\partial_s \gamma_1^\varepsilon)^2 + \varepsilon^2 (\partial_s \gamma_2^\varepsilon)^2)^{3/2}}.$$

Remark 2. Integrating Equation (17) for $m = \text{I}$ over $V_a = \{\mathbf{x} \in \Omega_1^\varepsilon(t) \mid x_1 < a\}$ for any $a < \min_{s \in [0,1]} \gamma_1^\varepsilon(t, s)$ yields by the Gauss theorem and the boundary conditions Equations (18–22)

$$0 = \int_{V_a} \nabla^\varepsilon \cdot \mathbf{u}_1^\varepsilon d\mathbf{x} = \int_{\partial V_a} \mathbf{u}_1^\varepsilon \cdot \mathbf{n} ds = \int_0^{w^\varepsilon(a)} u_{1,1}^\varepsilon|_{x_1=a} dx_2 - \int_0^1 u_{1,1}^\varepsilon|_{x_1=0} dx_2.$$

Denoting the total flux into the half strip by $q^\varepsilon(t, 0) := \int_0^1 u_{1,1}^\varepsilon(t, \mathbf{x})|_{x_1=0} dx_2$, we obtain that for all $a < \min_{s \in [0,1]} \gamma_1^\varepsilon(t, s)$ the total flux $q^\varepsilon(t, a) := \int_0^{w^\varepsilon(a)} u_{1,1}^\varepsilon|_{x_1=a} dx_2 = q^\varepsilon(t, 0)$. Analogously, integrating Equation (17) for $m = \text{I}$ over $\Omega_1^\varepsilon(t)$ and for $m = \text{II}$ over $V_a = \{\mathbf{x} \in \Omega_{\text{II}}^\varepsilon \mid x_1 < a\}$ for any $a > \max_{s \in [0,1]} \gamma_1^\varepsilon(t, s)$ yields by the Gauss theorem, the boundary conditions, Equations (18–22), and the continuity of velocity at the interface, Equation (23), that

$$0 = \int_{\Omega_1^\varepsilon} \nabla^\varepsilon \cdot \mathbf{u}_1^\varepsilon d\mathbf{x} + \int_{V_a} \nabla^\varepsilon \cdot \mathbf{u}_{\text{II}}^\varepsilon d\mathbf{x} = -q^\varepsilon(t, 0) + \int_0^{w^\varepsilon(a)} u_{\text{II},1}^\varepsilon|_{x_1=a} dx_2,$$

that is, the total flux $q(t, a) := \int_0^{w^\varepsilon(a)} u_{\text{II},1}^\varepsilon|_{x_1=a} dx_2 = q^\varepsilon(t, 0)$ for all $a > \max_{s \in [0,1]} \gamma_1^\varepsilon(t, s)$. Within the interval $[\min_{s \in [0,1]} \gamma_1^\varepsilon(t, s), \max_{s \in [0,1]} \gamma_1^\varepsilon(t, s)]$, the same calculation shows that the sum of the two fluxes over the respective parts of the domain equals the total flux $q^\varepsilon(t, 0)$. This means that the total flux is independent of x_1 , so we will simply use $q^\varepsilon(t)$ in this result for the subsequent analysis.

3 | ASYMPTOTIC EXPANSIONS

In this section, we derive the formal solution for the two-phase flow system Equations (15–26) in the asymptotic limit as $\varepsilon \rightarrow 0$, that is, the behavior in the limit when the thin strip becomes infinitely thin. We start with the solution in the bulk domains $\Omega_m^\varepsilon(t)$, $m \in \{\text{I}, \text{II}\}$, away from the interface $\Gamma^\varepsilon(t)$, where either fluid I or II is present, respectively. In the subsequent section, we show that these bulk solutions are connected via a boundary layer solution in the vicinity of $\Gamma^\varepsilon(t)$. Altogether, the solution is of Hagen–Poiseuille type in the bulk coupled by a dynamic Young–Laplace law at the interface, such that the interface position and the total flux are given by differential algebraic equations. Furthermore, we show that the solution for vanishing viscosity ratio $M \rightarrow 0$ matches the asymptotic limit for unsaturated one-phase flow. Finally, a reformulation for hysteretic contact angle models is discussed.

For the following analysis, we use an asymptotic expansion technique with respect to ε to derive effective models. All variables are assumed to be smooth and to depend regularly on ε starting with the leading order $\mathcal{O}(\varepsilon^0)$. We apply the homogenization ansatz

$$\mathbf{u}_m^\varepsilon(t, \mathbf{x}) = \mathbf{u}_m^0(t, \mathbf{x}) + \varepsilon \mathbf{u}_m^1(t, \mathbf{x}) + \mathcal{O}(\varepsilon^2),$$

$$p_m^\varepsilon(t, \mathbf{x}) = p_m^0(t, \mathbf{x}) + \varepsilon p_m^1(t, \mathbf{x}) + \mathcal{O}(\varepsilon^2),$$

$$\gamma^\varepsilon(t, s) = \gamma^0(t, s) + \varepsilon \gamma^1(t, s) + \mathcal{O}(\varepsilon^2)$$

for $m \in \{\text{I}, \text{II}\}$. Inserting the asymptotic expansions into the two-phase flow equations Equations (15–26) and equating terms of the same order in ε , we will obtain the asymptotic equations and solutions in the limit as $\varepsilon \rightarrow 0$. To this end, we need some assumptions on the parameters of the model.

- (A1) The Reynolds number Re and its product with the density ratio R are uniformly bounded for all $0 < \varepsilon \ll 1$, that is, there exists $C \in (0, \infty)$ such that $\text{Re} \leq C$ and $R\text{Re} \leq C$ independent of ε . In other words, $\text{Re} = \mathcal{O}(\varepsilon^0)$ or $\text{Re} = o(\varepsilon^0)$, and $R\text{Re} = \mathcal{O}(\varepsilon^0)$ or $R\text{Re} = o(\varepsilon^0)$.
- (A2) The viscosity ratio M of the fluids is of order 1, $M = \mathcal{O}(\varepsilon^0)$.
- (A3) According to Remark 1, the slip length λ^ε has the form

$$\lambda^\varepsilon(t, x_1) = \lambda^0 + \lambda_e \exp\left(-\frac{|x_1 - x_1^*(t)|}{\varepsilon}\right)$$

for given constants $\lambda^0, \lambda_e \geq 0$ that are independent of ε . Moreover, there holds either $\lambda_e = 0$, or $\lambda^0 = 0$. Note that the latter represents the case of rapidly decaying slip away from the interface, so that λ^ε has the expansion $\lambda^\varepsilon(t, x_1) = \mathcal{O}(\varepsilon^N)$ for arbitrary $N \in \mathbb{N}$ as long as $x_1 - x_1^*(t) \gg \varepsilon$.

- (A4) The wall function w^ε has a uniform expansion

$$w^\varepsilon(x_1) = w^0(x_1) + \varepsilon w^1(x_1) + \mathcal{O}(\varepsilon^2),$$

where $w^\varepsilon, w^0 : [0, 1] \rightarrow (0, \infty)$ are continuously differentiable (and thus bounded away from zero). Moreover, there holds $w^0(0) = 1$ and $\partial_{x_1} w^0(0) = \partial_{x_1} w^0(1) = 0$.

- (A5) The contact angle relation θ^ε has a uniform expansion

$$\theta^\varepsilon(u) = \theta^0(u) + \varepsilon \theta^1(u) + \mathcal{O}(\varepsilon^2),$$

where $\theta^0 : \mathbb{R} \rightarrow (0, \pi)$ is Lipschitz-continuous.

- (A6) If the velocity boundary condition $\mathbf{u}_1^\varepsilon = \mathbf{u}_{\text{in}}^\varepsilon$ is used at the inlet $\Gamma_{\text{in}}^\varepsilon$, the velocity is given by

$$\mathbf{u}_{\text{in}}^\varepsilon(t, \mathbf{x}) = \left(3q(t) \frac{(1+2\lambda^0)-x_2^2}{6\lambda^0+2} + \mathcal{O}(\varepsilon) \right),$$

where $q : [0, \infty) \rightarrow \mathbb{R}$ is a continuous function independent of ε .

As will be seen below, (A1) ensures that the flow remains laminar. Furthermore, (A2) restricts the discussion to moderately viscous liquids. While $M \gg 1$ would result in a highly viscous second fluid which gets immobile as $\varepsilon \rightarrow 0$, we will discuss the case $M \ll 1$ of a extremely mobile fluid such as air (compared to water or oil) separately in Subsection 3.3. The asymptotic expansions stated in (A4) and (A5) are crucial for the derivation. As discussed in Section 2, slip is necessary to allow the movement of the contact point. Hence, (A3) requires a simple expression of the slip at

the pore walls close to the interface to avoid technical complexity, while allowing for the typical no-slip condition at the pore walls away from the interface ($\lambda^0 = 0$). The case of global slip conditions ($\lambda^0 > 0$) generalizes this to applications where the slip length is of the same order as the diameter, for example, in nanofluidic devices or for fluids with low viscosity. The assumption of a horizontal wall at the inlet and at the outlet ($\partial_{x_1} w^0(0) = \partial_{x_1} w^0(1) = 0$) in (A4) is used to exclude possible boundary-layer effects caused by nonmatching boundary conditions. The inlet velocity in (A6) is then the Hagen–Poiseuille profile incorporating the Navier-slip condition. Assumptions (A4) and (A6) can be relaxed if the boundary conditions at $\Gamma_{\text{in}}^\varepsilon$ and $\Gamma_{\text{out}}^\varepsilon$, Equations (20–21), are replaced appropriately, or if the resulting boundary layer matches the asymptotic solution of the following analysis. We observe that (A4) rules out the possibility that the pore has walls with rapidly oscillatory characteristics (so-called “rough walls”). Such walls can be characterized by a function $w^\varepsilon(x_1) = w^0(x_1) + \varepsilon w^1(x_1/\varepsilon) + \mathcal{O}(\varepsilon)$. Clearly, this would strongly affect the shape and position of the interface. A naive extension of the following results would yield unphysical oscillations of the interface, so that we restrict the discussion to slowly varying walls.

Note that the normal and tangential vectors $\mathbf{n}_\Gamma^\varepsilon$, $\mathbf{t}_\Gamma^\varepsilon$, \mathbf{n}_w^ε , and \mathbf{t}_w^ε depend on γ^ε and w^ε , respectively, such that these can be expanded, for example,

$$\mathbf{n}_w^\varepsilon = \begin{pmatrix} 0 \\ 1 \end{pmatrix} - \varepsilon \begin{pmatrix} \partial_{x_1} w^0 \\ 0 \end{pmatrix} + \mathcal{O}(\varepsilon^2), \quad (27)$$

$$\mathbf{n}_\Gamma^\varepsilon = \begin{cases} \begin{pmatrix} 0 \\ -\text{sign}(\partial_s \gamma_1^0) \end{pmatrix} + \varepsilon \frac{1}{|\partial_s \gamma_1^0|} \begin{pmatrix} \partial_s \gamma_2^0 \\ -\partial_s \gamma_1^0 \end{pmatrix} + \mathcal{O}(\varepsilon^2) & \text{for } \partial_s \gamma_1^0 \neq 0, \\ \frac{1}{\sqrt{(\partial_s \gamma_1^1)^2 + (\partial_s \gamma_2^0)^2}} \begin{pmatrix} \partial_s \gamma_2^0 \\ -\partial_s \gamma_1^1 \end{pmatrix} + \varepsilon \frac{1}{\sqrt{(\partial_s \gamma_1^1)^2 + (\partial_s \gamma_2^0)^2}} \begin{pmatrix} \partial_s \gamma_2^1 \\ -\partial_s \gamma_1^2 \end{pmatrix} \\ + \varepsilon \frac{\partial_s \gamma_1^1 \partial_s \gamma_1^2 + \partial_s \gamma_2^0 \partial_s \gamma_2^1}{((\partial_s \gamma_1^1)^2 + (\partial_s \gamma_2^0)^2)^{3/2}} \begin{pmatrix} -\partial_s \gamma_2^0 \\ \partial_s \gamma_1^1 \end{pmatrix} + \mathcal{O}(\varepsilon^2) & \text{otherwise.} \end{cases} \quad (28)$$

In particular, the direction of the normal vector $\mathbf{n}_\Gamma^\varepsilon$ depends on $\partial_s \gamma_1^0$. If $\partial_s \gamma_1^0 \neq 0$ for some $s \in [0, 1]$, the interface $\Gamma^\varepsilon(t)$ is largely deformed over a region that has a width $\mathcal{O}(\varepsilon^0)$, namely, $I = [\min_{s \in [0, 1]} \gamma_1^\varepsilon, \max_{s \in [0, 1]} \gamma_1^\varepsilon]$ with $|I| = \mathcal{O}(\varepsilon^0)$. Therefore, there are both fluids present along a transversal segment at any $x_1 \in I$, and complicated interface dynamics occur in the limit $\varepsilon \rightarrow 0$. On the other hand, if $\partial_s \gamma_1^0 \equiv 0$, only small deformations with $|I| = \mathcal{O}(\varepsilon)$ are possible, and we obtain asymptotically a sharp transition from fluid I to fluid II at γ_1^0 .

3.1 | Flow in the bulk domains

First, we consider the flow in the bulk domains Ω_m^ε , $m \in \{\text{I}, \text{II}\}$, and solve the resulting equations away from the interface. Inserting the homogenization ansatz into Equations (15–22) using (A1)–(A6) and a Taylor expansion around $x_2 = w^0(x_1)$ for Equation (22), one obtains

$$\mathcal{O}(\varepsilon) = \partial_{x_1} p_{\text{I}}^0 - \partial_{x_2}^2 u_{\text{I},1}^0 \quad \text{in } \Omega_{\text{I}}^\varepsilon(t), \quad (29)$$

$$\mathcal{O}(\varepsilon^0) = \varepsilon^{-1} \partial_{x_2} p_I^0 \quad \text{in } \Omega_I^\varepsilon(t), \quad (30)$$

$$\mathcal{O}(\varepsilon) = \partial_{x_1} p_{\text{II}}^0 - M \partial_{x_2}^2 u_{\text{II},1}^0 \quad \text{in } \Omega_{\text{II}}^\varepsilon(t), \quad (31)$$

$$\mathcal{O}(\varepsilon^0) = \varepsilon^{-1} \partial_{x_2} p_{\text{II}}^0 \quad \text{in } \Omega_{\text{II}}^\varepsilon(t), \quad (32)$$

$$\mathcal{O}(\varepsilon) = \varepsilon^{-1} \partial_{x_2} u_{m,2}^0 + \left(\partial_{x_1} u_{m,1}^0 + \partial_{x_2} u_{m,2}^1 \right) \quad \text{in } \Omega_m^\varepsilon(t), \quad (33)$$

$$\mathcal{O}(\varepsilon^2) = u_{m,2}^0 + \varepsilon u_{m,2}^1, \quad \mathcal{O}(\varepsilon) = \partial_{x_2} u_{m,1}^0 \quad \text{at } x_2 = 0, \quad (34)$$

$$\mathcal{O}(\varepsilon) = \partial_{x_2} p_m^0 \quad \text{at } x_2 = 0, \quad (35)$$

$$\mathcal{O}(\varepsilon) = p_I^0 - p_{\text{in}}^0, \quad \mathcal{O}(\varepsilon^2) = u_{I,2}^0 + \varepsilon u_{I,2}^1 \quad \text{or} \quad (36)$$

$$\mathcal{O}(\varepsilon^2) = \mathbf{u}_I^0 - \mathbf{u}_{\text{in}}^0 + \varepsilon (\mathbf{u}_I^1 - \mathbf{u}_{\text{in}}^1) \quad \text{at } x_1 = 0, \quad (37)$$

$$\mathcal{O}(\varepsilon) = p_{\text{II}}^0, \quad \mathcal{O}(\varepsilon^2) = u_{\text{II},2}^0 + \varepsilon u_{\text{II},2}^1 \quad \text{at } x_1 = 1, \quad (38)$$

$$\mathcal{O}(\varepsilon) = u_{m,1}^0 + \lambda^0 \partial_{x_2} u_{m,1}^0 \quad \text{at } x_2 = w^0(x_1), \quad (39)$$

$$\mathcal{O}(\varepsilon^2) = u_{m,2}^0 + \varepsilon \left(u_{m,2}^1 + w^1 \partial_{x_2} u_{m,2}^0 - u_{m,1}^0 \partial_{x_1} w^0 \right) \quad \text{at } x_2 = w^0(x_1). \quad (40)$$

Note that either Equation (36) or Equation (37) holds, depending on the choice of the boundary condition at the inlet $\Gamma_{\text{in}}^\varepsilon$.

Since we are interested in the flow behavior away from the interface $\Gamma^\varepsilon(t)$, we define

$$G_I(t) := \min_{s \in [0,1]} \gamma_1^0(s, t), \quad G_{\text{II}}(t) := \max_{s \in [0,1]} \gamma_1^0(s, t),$$

and investigate the problem for $x_1 < G_I(t)$ in fluid I and for $x_1 > G_{\text{II}}(t)$ in fluid II, respectively. In leading order, one obtains $\partial_{x_2} u_{m,2}^0 = 0$ in $\Omega_m^\varepsilon(t)$ for both $m \in \{\text{I}, \text{II}\}$ by the mass conservation Equation (33). The symmetry and wall boundary conditions, Equations (34,40), lead to

$$u_{m,2}^0 = 0 \text{ for } m = \text{I}, x_1 < G_I(t), \quad \text{and for } m = \text{II}, x_1 > G_{\text{II}}(t),$$

which agrees with Equations (36-38), the in- and outflow boundary conditions. The second component of the momentum equation (30) of fluid I yields in leading order $\partial_{x_2} p_I^0 = 0$ in $\Omega_I^\varepsilon(t)$, which is in agreement with the symmetry condition, Equation (35). We conclude

$$p_I^0 = p_I^0(t, x_1) \quad \text{for } x_1 < G_I(t).$$

Analogously, the second component of the momentum equation (32) of fluid II leads to $\partial_{x_2} p_{\text{II}}^0 = 0$ in $\Omega_{\text{II}}^\varepsilon(t)$ (in agreement with the symmetry condition, Equation (35)), and thus

$$p_{\text{II}}^0 = p_{\text{II}}^0(t, x_1) \quad \text{for } x_1 > G_{\text{II}}(t).$$

From the first component of the momentum equation (29) of fluid I one obtains

$$\partial_{x_1} p_I^0 = \partial_{x_2}^2 u_{I,1}^0 \quad \text{in } \Omega_I^\varepsilon(t).$$

Integrating twice over x_2 using the symmetry and wall boundary conditions, Equations (34,39), this leads to

$$u_{I,1}^0(t, \mathbf{x}) = \frac{x_2^2 - w^0(x_1)(2\lambda^0 + w^0(x_1))}{2} \partial_{x_1} p_I^0(t, x_1) \quad \text{for } x_1 < G_I(t). \quad (41)$$

In a similar fashion, one obtains for fluid II by Equations (31,34,39)

$$u_{II,1}^0(t, \mathbf{x}) = \frac{x_2^2 - w^0(x_1)(2\lambda^0 + w^0(x_1))}{2M} \partial_{x_1} p_{II}^0(t, x_1) \quad \text{for } x_1 > G_{II}(t). \quad (42)$$

Integrating Equations (41–42) over $x_2 \in [0, w^0(x_1)]$ for any $x_1 < G_I$ and $x_1 > G_{II}$, respectively, and using Remark 2 yields

$$q(t) = \int_0^{w^0(a)} u_{I,1}^0(t, \mathbf{x})|_{x_1=a} dx_2 = -\frac{(w^0(x_1))^2(3\lambda^0 + w^0(x_1))}{3} \partial_{x_1} p_I^0(t, x_1), \quad (43)$$

$$q(t) = \int_0^{w^0(a)} u_{II,1}^0(t, \mathbf{x})|_{x_1=a} dx_2 = -\frac{(w^0(x_1))^2(3\lambda^0 + w^0(x_1))}{3M} \partial_{x_1} p_{II}^0(t, x_1), \quad (44)$$

where $q(t) := \int_0^1 u_{I,1}^0(t, \mathbf{x}) dx_2$. Note that q is independent of x_1 , and it is equivalent to the one in (A6) if Equation (37) is given. Otherwise, q is unknown and must be found in the further solution process. Solving the above equations for p_m^0 , with the outflow boundary condition, Equation (38), we obtain

$$p_I^0(t, \mathbf{x}) = p_{in}^0(t) - q(t) \int_0^{x_1} \frac{3}{(w^0(\xi))^2(3\lambda^0 + w^0(\xi))} d\xi \quad \text{for } x_1 < G_I(t), \quad (45)$$

$$p_{II}^0(t, \mathbf{x}) = q(t) \int_{x_1}^1 \frac{3M}{(w^0(\xi))^2(3\lambda^0 + w^0(\xi))} d\xi \quad \text{for } x_1 > G_{II}(t). \quad (46)$$

Here, the inlet pressure $p_{in}^0(t)$ is either given by the inlet boundary condition, Equation (36), or has to be found in the further solution process. Note that since the inlet boundary condition is either Equation (36) or Equation (37), this means that either q or p_{in}^0 is given, while the other still must be determined. Inserting Equations (45–46) into Equations (41–42) yields

$$u_{I,1}^0(t, \mathbf{x}) = 3q(t) \frac{w^0(x_1)(2\lambda^0 + w^0(x_1)) - x_2^2}{2(w^0(x_1))^2(3\lambda^0 + w^0(x_1))} \quad \text{for } x_1 < G_I(t), \quad (47)$$

$$u_{\text{II},1}^0(t, \mathbf{x}) = 3q(t) \frac{w^0(x_1)(2\lambda^0 + w^0(x_1)) - x_2^2}{2(w^0(x_1))^2(3\lambda^0 + w^0(x_1))} \quad \text{for } x_1 > G_{\text{II}}(t). \quad (48)$$

Using Equations (47–48) in the mass conservation Equation (33), the first-order equations become

$$\partial_{x_2} u_{m,2}^1 = q(t) \left(\frac{1}{2(3\lambda^0 + w^0(x_1))^2} + \frac{1}{(w^0(x_1))^2} - \frac{9(2\lambda^0 + w^0(x_1))x_2^2}{2(w^0(x_1))^3(3\lambda^0 + w^0(x_1))^2} \right) \partial_{x_1} w^0(x_1),$$

for $m \in \{\text{I}, \text{II}\}$. Integration over x_2 using the symmetry condition, Equation (34), yields

$$u_{\text{I},2}^1(t, \mathbf{x}) = q(t) \left(\frac{x_2}{2(3\lambda^0 + w^0(x_1))^2} + \frac{x_2}{(w^0(x_1))^2} - \frac{3(2\lambda^0 + w^0(x_1))x_2^3}{2(w^0(x_1))^3(3\lambda^0 + w^0(x_1))^2} \right) \partial_{x_1} w^0(x_1) \quad \text{for } x_1 < G_{\text{I}}(t),$$

$$u_{\text{II},2}^1(t, \mathbf{x}) = q(t) \left(\frac{x_2}{2(3\lambda^0 + w^0(x_1))^2} + \frac{x_2}{(w^0(x_1))^2} - \frac{3(2\lambda^0 + w^0(x_1))x_2^3}{2(w^0(x_1))^3(3\lambda^0 + w^0(x_1))^2} \right) \partial_{x_1} w^0(x_1) \quad \text{for } x_1 > G_{\text{II}}(t),$$

which is in agreement with the boundary conditions, Equations (36–38,40).

Summarizing, we obtain the following solution in the bulk domains. There holds

$$\mathbf{u}_{\text{I}}^\varepsilon(t, \mathbf{x}) = q(t) \left(\begin{array}{c} 3 \frac{w^0(x_1)(2\lambda^0 + w^0(x_1)) - x_2^2}{2(w^0(x_1))^2(3\lambda^0 + w^0(x_1))} + \mathcal{O}(\varepsilon) \\ \varepsilon \left(\frac{x_2}{2(3\lambda^0 + w^0(x_1))^2} + \frac{x_2}{(w^0(x_1))^2} - \frac{3(2\lambda^0 + w^0(x_1))x_2^3}{2(w^0(x_1))^3(3\lambda^0 + w^0(x_1))^2} \right) \partial_{x_1} w^0(x_1) + \mathcal{O}(\varepsilon^2) \end{array} \right), \quad (49)$$

$$p_{\text{I}}^\varepsilon(t, \mathbf{x}) = p_{\text{in}}^0(t) - q(t) \int_0^{x_1} \frac{3}{(w^0(\xi))^2(3\lambda^0 + w^0(\xi))} d\xi + \mathcal{O}(\varepsilon) \quad (50)$$

for $x_1 < G_{\text{I}}(t)$, while for $x_1 > G_{\text{II}}(t)$ one gets

$$\mathbf{u}_{\text{II}}^\varepsilon(t, \mathbf{x}) = q(t) \left(\begin{array}{c} 3 \frac{w^0(x_1)(2\lambda^0 + w^0(x_1)) - x_2^2}{2(w^0(x_1))^2(3\lambda^0 + w^0(x_1))} + \mathcal{O}(\varepsilon) \\ \varepsilon \left(\frac{x_2}{2(3\lambda^0 + w^0(x_1))^2} + \frac{x_2}{(w^0(x_1))^2} - \frac{3(2\lambda^0 + w^0(x_1))x_2^3}{2(w^0(x_1))^3(3\lambda^0 + w^0(x_1))^2} \right) \partial_{x_1} w^0(x_1) + \mathcal{O}(\varepsilon^2) \end{array} \right), \quad (51)$$

$$p_{\text{II}}^\varepsilon(t, \mathbf{x}) = q(t) \int_{x_1}^1 \frac{3M}{(w^0(\xi))^2(3\lambda^0 + w^0(\xi))} d\xi + \mathcal{O}(\varepsilon). \quad (52)$$

This means that the solution in the bulk domains is of Hagen–Poiseuille type. Depending on the chosen inlet boundary condition, Equation (36) or Equation (37), either the inlet pressure p_{in}^0 or the total flux q is given. The other coefficient will be determined in the following subsection via

the coupling at the interface $\Gamma^\varepsilon(t)$. For upscaled models, we emphasize that the total flux q is independent of the position x_1 and that the pressures p_m^0 , $m \in \{I, II\}$, depend linearly on q with a coefficient that only depends on the geometry (w^0), the viscosity ratio M , and the slip length λ^0 .

3.2 | Interface with small deformations

We continue the analysis for the interface region around $\Gamma^\varepsilon(t)$. We first show that the bulk solutions are not compatible with the interface conditions Equations (23–26). However, introduction of a suitable scaling allows to find the asymptotic solution in the boundary layer around the interface $\Gamma^\varepsilon(t)$, which connects the bulk domain solutions. In addition to (A1)–(A6), we make the following assumptions:

(A7) The leading order interface position in x_1 is constant, that is, $\partial_s \gamma_1^0 \equiv 0$.

(A8) The capillary number is given by $\text{Ca} = \varepsilon^\alpha \overline{\text{Ca}}$ for some $\alpha \in \mathbb{N}_0$. Here, $\overline{\text{Ca}}$ denotes the effective capillary number and is independent of ε .

Note that (A7) means that the fluid–fluid interface Γ^ε has only small deformations, such that $G_I(t) = \gamma_1^0(t) = G_{II}(t)$. Furthermore, (A8) is used to distinguish whether interfacial tension is relevant or even dominating the interface movement (see also Remark 3). In the alternative case of a largely deformed interface ($\partial_s \gamma_1^0 \neq 0$), both fluids are present along a transversal segment since the interface is partly horizontal (cf. Equation (28)). This leads to complicated interface dynamics and requires a detailed analysis of further boundary layers due to the symmetry and boundary conditions Equations (25–26), which yield $\partial_s \gamma_1^0(t, s) = 0$ for $s \in \{0, 1\}$. However, this lies outside the scope of this paper.

Inserting the homogenization ansatz into the kinematic interface condition, Equation (23), gives

$$(\partial_t \gamma_1^0 - u_{I,1}^0) \partial_s \gamma_2^0 + u_{I,2}^0 \partial_s \gamma_1^1 = \mathcal{O}(\varepsilon).$$

Since γ_1^0 is constant in the parameter s , a nonsingular parameterization requires $\partial_s \gamma_2^0 > 0$. Inserting the bulk solution Equation (49), where $u_{I,2}^0 = 0$, yields in leading order

$$\partial_t \gamma_1^0 = 3q \frac{w^0(\gamma_1^0)(2\lambda^0 + w^0(\gamma_1^0)) - (\gamma_2^0)^2}{2(w^0(\gamma_1^0))^2(3\lambda^0 + w^0(\gamma_1^0))},$$

which contradicts the assumption that γ_1^0 does not depend on s , except for the trivial case $q(t) = 0$. Therefore, we expect the existence of a boundary layer around the interface $\Gamma^\varepsilon(t)$. Here, the idea of the matched asymptotic expansion method is to find an asymptotic solution of the problem in rescaled, so-called inner coordinates close to the interface (the boundary layer). This solution must satisfy the interface conditions and match the previously derived, so-called outer solution in the bulk regions given by Equations (49–52). The combination of inner and outer solutions then solves the problem in the whole domain. For a detailed introduction to matched asymptotic expansion method, we refer to Ref. 75.

To resolve the boundary layer, we apply the inner scaling

$$X_1(t, x_1) := (x_1 - \gamma_1^0(t))/\varepsilon, \quad X_2 := x_2$$

and use the rescaled variables and domains (see also Table 1)

$$\begin{aligned} \mathbf{Y}^\varepsilon &:= \begin{pmatrix} (\gamma_1^\varepsilon - \gamma_1^0)/\varepsilon \\ \gamma_2^\varepsilon \end{pmatrix}, \quad U_m^\varepsilon(t, \mathbf{X}) := \mathbf{u}_m^\varepsilon(t, \mathbf{x}), \quad P_m^\varepsilon(t, \mathbf{X}) := p_m^\varepsilon(t, \mathbf{x}), \\ \Omega_X^\varepsilon(t) &:= \{\mathbf{X} \in \mathbb{R}^2 \mid 0 < X_2 < w^\varepsilon(\gamma_1^0(t) + \varepsilon X_1)\}, \quad \Gamma_X^\varepsilon(t) := \{\mathbf{Y}^\varepsilon(t, s) \mid s \in [0, 1]\}, \\ \Omega_{X,1}^\varepsilon(t) &:= \{\mathbf{X}(t, \mathbf{x}) \mid \mathbf{x} \in \Omega_1^\varepsilon\}, \quad \Omega_{X,\mathbb{I}}^\varepsilon(t) := \{\mathbf{X}(t, \mathbf{x}) \mid \mathbf{x} \in \Omega_{\mathbb{I}}^\varepsilon\}, \\ \Gamma_{X,w,m}^\varepsilon(t) &:= \{\mathbf{X} \in \partial\Omega_{X,m}^\varepsilon(t) \mid X_2 = w^\varepsilon(\gamma_1^0(t) + \varepsilon X_1)\}. \end{aligned}$$

The matching conditions between inner expansion in terms of \mathbf{X} and outer expansion in terms of \mathbf{x} require the equivalence in the limit, that is, for any outer quantity $a_m^\varepsilon(t, \mathbf{x})$ with inner expansion $A_m^\varepsilon(t, \mathbf{X})$ there must hold $\lim_{x_1 \rightarrow \gamma_1^0} a_m^\varepsilon(t, \mathbf{x}) = \lim_{X_1 \rightarrow (-1)^m \infty} A_m^\varepsilon(t, \mathbf{X})|_{X_2=x_2}$. With the rescaled coordinates, Equations (15-19) and Equations (22-26) become

$$\varepsilon^2 \text{Re} \left(\varepsilon \partial_t U_I^\varepsilon - \partial_{X_1} U_I^\varepsilon \partial_t \gamma_1^0 + (U_I^\varepsilon \cdot \nabla_X) U_I^\varepsilon \right) + \nabla_X P_I^\varepsilon = \varepsilon \Delta_X U_I^\varepsilon \quad \text{in } \Omega_{X,\mathbb{I}}^\varepsilon(t), \quad (53)$$

$$\varepsilon^2 \text{RRe} \left(\varepsilon \partial_t U_{\mathbb{I}}^\varepsilon - \partial_{X_1} U_{\mathbb{I}}^\varepsilon \partial_t \gamma_1^0 + (U_{\mathbb{I}}^\varepsilon \cdot \nabla_X) U_{\mathbb{I}}^\varepsilon \right) + \nabla_X P_{\mathbb{I}}^\varepsilon = M \varepsilon \Delta_X U_{\mathbb{I}}^\varepsilon \quad \text{in } \Omega_{X,\mathbb{I}}^\varepsilon(t), \quad (54)$$

$$\nabla_X \cdot U_m^\varepsilon = 0 \quad \text{in } \Omega_{X,m}^\varepsilon(t), \quad (55)$$

$$U_m^\varepsilon \cdot \mathbf{n}_{\text{sym}} = 0, \quad \mathbf{t}_{\text{sym}} \cdot \nabla_X U_m^\varepsilon \mathbf{n}_{\text{sym}} = 0 \quad \text{at } X_2 = 0, \quad (56)$$

$$\nabla_X P_m^\varepsilon \cdot \mathbf{n}_{\text{sym}} = 0, \quad \text{at } X_2 = 0, \quad (57)$$

$$\mathbf{T}_w^\varepsilon \cdot (U_m^\varepsilon + 2\lambda^\varepsilon \mathbf{D}_X(U_m^\varepsilon) \mathbf{N}_w^\varepsilon) = 0, \quad U_m^\varepsilon \cdot \mathbf{N}_w^\varepsilon = 0 \quad \text{on } \Gamma_{X,w,m}^\varepsilon(t), \quad (58)$$

$$\partial_t \gamma_1^0 N_{\Gamma,1}^\varepsilon + \varepsilon \partial_t \mathbf{Y}^\varepsilon \cdot \mathbf{N}_\Gamma^\varepsilon = U_I^\varepsilon \cdot \mathbf{N}_\Gamma^\varepsilon, \quad U_I^\varepsilon = U_{\mathbb{I}}^\varepsilon \quad \text{on } \Gamma_X^\varepsilon(t), \quad (59)$$

$$-(P_I^\varepsilon - P_{\mathbb{I}}^\varepsilon) \mathbf{N}_\Gamma^\varepsilon + 2\varepsilon (\mathbf{D}_X(U_I^\varepsilon) - M \mathbf{D}_X(U_{\mathbb{I}}^\varepsilon)) \mathbf{N}_\Gamma^\varepsilon = \frac{\varepsilon^2}{\text{Ca}} K^\varepsilon \mathbf{N}_\Gamma^\varepsilon \quad \text{on } \Gamma_X^\varepsilon(t), \quad (60)$$

$$\mathbf{N}_\Gamma^\varepsilon \cdot \mathbf{n}_{\text{sym}} = 0 \quad \text{at } s = 0, \quad (61)$$

$$\cos \left(\theta^\varepsilon \left(-\partial_t (\gamma_1^0 T_{w,1}^\varepsilon + \varepsilon \mathbf{Y}^\varepsilon \cdot \mathbf{T}_w^\varepsilon)|_{X_1=Y_1^\varepsilon} \right) \right) = \mathbf{T}_\Gamma^\varepsilon \cdot \mathbf{T}_w^\varepsilon|_{X_1=Y_1^\varepsilon} \quad \text{at } s = 1. \quad (62)$$

The transformed normal and tangential vectors are given by

$$\mathbf{T}_w^\varepsilon = \mathbf{t}_w^\varepsilon|_{x_1=\gamma_1^0+\varepsilon X_1}, \quad \mathbf{N}_w^\varepsilon = \mathbf{n}_w^\varepsilon|_{x_1=\gamma_1^0+\varepsilon X_1},$$

$$\mathbf{T}_\Gamma^\varepsilon = \frac{1}{\sqrt{(\partial_s Y_1^\varepsilon)^2 + (\partial_s Y_2^\varepsilon)^2}} \partial_s \mathbf{Y}^\varepsilon, \mathbf{N}_\Gamma^\varepsilon = \frac{1}{\sqrt{(\partial_s Y_1^\varepsilon)^2 + (\partial_s Y_2^\varepsilon)^2}} \begin{pmatrix} \partial_s Y_2^\varepsilon \\ -\partial_s Y_1^\varepsilon \end{pmatrix},$$

and the rescaled curvature K^ε is

$$K^\varepsilon = \frac{\partial_s Y_1^\varepsilon \partial_s^2 Y_2^\varepsilon - \partial_s Y_2^\varepsilon \partial_s^2 Y_1^\varepsilon}{\varepsilon ((\partial_s Y_1^\varepsilon)^2 + (\partial_s Y_2^\varepsilon)^2)^{3/2}}.$$

Inserting the homogenization ansatz into Equations (53–62) using (A1)–(A5), (A7), (A8), and a Taylor expansion around $X_2 = w^0(\gamma_1^0(t))$ for Equation (58), one obtains

$$\mathcal{O}(\varepsilon^2) = \nabla_X P_I^0 + \varepsilon (\nabla_X P_I^1 - \Delta_X U_I^0) \quad \text{in } \Omega_{X,I}^\varepsilon(t), \quad (63)$$

$$\mathcal{O}(\varepsilon^2) = \nabla_X P_{II}^0 + \varepsilon (\nabla_X P_{II}^1 - M \Delta_X U_{II}^0) \quad \text{in } \Omega_{X,II}^\varepsilon(t), \quad (64)$$

$$\mathcal{O}(\varepsilon) = \nabla_X \cdot \mathbf{U}_m^0 \quad \text{in } \Omega_{X,m}^\varepsilon(t), \quad (65)$$

$$\mathcal{O}(\varepsilon) = U_{m,2}^0, \quad \mathcal{O}(\varepsilon) = \partial_{X_2} U_{m,1}^0 \quad \text{at } X_2 = 0, \quad (66)$$

$$\mathcal{O}(\varepsilon^2) = \partial_{X_2} P_m^0 + \varepsilon \partial_{X_2} P_m^1 \quad \text{at } X_2 = 0, \quad (67)$$

$$\mathcal{O}(\varepsilon) = U_{m,1}^0 + (\lambda^0 + \lambda_e \exp(-|X_1|)) (\partial_{X_2} U_{m,1}^0 + \partial_{X_1} U_{m,2}^0) \quad \text{at } X_2 = w^0(\gamma_1^0(t)), \quad (68)$$

$$\mathcal{O}(\varepsilon) = U_{m,2}^0 \quad \text{at } X_2 = w^0(\gamma_1^0(t)), \quad (69)$$

$$\mathcal{O}(\varepsilon) = (\partial_t \gamma_1^0 - U_{I,1}^0) \partial_s Y_2^0 + U_{I,2}^0 \partial_s Y_1^0 \quad \text{on } \Gamma_X^\varepsilon(t), \quad (70)$$

$$\mathcal{O}(\varepsilon) = \mathbf{U}_I^0 - \mathbf{U}_{II}^0 \quad \text{on } \Gamma_X^\varepsilon(t), \quad (71)$$

$$\mathcal{O}(\varepsilon^{\min(1,2-\alpha)}) = (P_I^0 - P_{II}^0) + \frac{\varepsilon^{1-\alpha}}{\text{Ca}} \frac{\partial_s Y_1^0 \partial_s^2 Y_2^0 - \partial_s Y_2^0 \partial_s^2 Y_1^0}{((\partial_s Y_1^0)^2 + (\partial_s Y_2^0)^2)^{3/2}} \quad \text{on } \Gamma_X^\varepsilon(t), \quad (72)$$

$$\mathcal{O}(\varepsilon) = \partial_s Y^0 \cdot (\mathbf{D}_X(\mathbf{U}_I^0) - M \mathbf{D}_X(\mathbf{U}_{II}^0)) \begin{pmatrix} \partial_s Y_2^0 \\ -\partial_s Y_1^0 \end{pmatrix} \quad \text{on } \Gamma_X^\varepsilon(t), \quad (73)$$

$$\mathcal{O}(\varepsilon) = \partial_s Y_1^0 \quad \text{at } s = 0, \quad (74)$$

$$\mathcal{O}(\varepsilon) = \frac{\partial_s Y_1^0}{\sqrt{(\partial_s Y_1^0)^2 + (\partial_s Y_2^0)^2}} + \cos(\theta^0(\partial_t \gamma_1^0)) \quad \text{at } s = 1. \quad (75)$$

The leading order terms in the momentum equations (63–64) yield $\nabla_X P_m^0 = \mathbf{0}$ in $\Omega_{X,m}^\varepsilon(t)$ for $m \in \{I, II\}$. This is in agreement with the symmetry condition, Equation (67). By matching with

the outer solution we obtain

$$P_m^0(t, \mathbf{X}) = p_m^0(t, \gamma_1^0(t)) \quad \text{for all } \mathbf{X} \in \Omega_{\mathbf{X}, m}^\varepsilon(t). \quad (76)$$

Remark 3. Recall that we assume $\text{Ca} = \varepsilon^\alpha \overline{\text{Ca}}$ for some $\alpha \in \mathbb{N}_0$. Considering Equation (72), one must distinguish the cases $\alpha < 1$, $\alpha = 1$, and $\alpha > 1$. For $\alpha < 1$, the interface tension force is negligible in leading order, such that the pressures P_I^0 and P_{II}^0 are equal. Formally, this allows to determine the leading order solution of the outer bulk-flow problem. However, this also means that the interface $\Gamma_{\mathbf{X}}^\varepsilon(t)$ is not stabilized by surface tension, but part of the first-order solution, such that we cannot guarantee solvability. Furthermore, one might expect the occurrence of topological changes due to, for example, formation of bubbles, thin films, and so forth, which are not part of this model. In the case $\alpha > 1$, the interfacial tension force is dominating Equation (72), so that the leading order curvature K^0 of the interface is zero. Due to the boundary conditions, Equations (74–75), this can only happen if the leading order contact angle $\theta^0(\partial_t \gamma_1^0)$ is $\pi/2$ for any $\gamma_1^0(t)$, that is, for a constant contact angle model for perfectly mixed-wet materials. Even worse, due to Equation (76), the leading order solution of the outer bulk-flow problem then depends on the first-order solution, such that we cannot assure the solvability in this case either. We therefore consider in what follows only the case $\alpha = 1$. Then the pressure difference is balanced by the surface tension force in Equation (72). This leads to a solution for the outer bulk-flow problem as well as for the interface shape.

In the regime $\alpha = 1$, plugging the constant pressures from Equation (76) into the interfacial force balance equation (72) yields a constant leading-order curvature K^0 given by

$$K^0 = \frac{\partial_s Y_2^0 \partial_s^2 Y_1^0 - \partial_s Y_1^0 \partial_s^2 Y_2^0}{((\partial_s Y_1^0)^2 + (\partial_s Y_2^0)^2)^{3/2}} = \overline{\text{Ca}}(p_{II}^0 - p_I^0)|_{x_1=\gamma_1^0}. \quad (77)$$

Therefore, the interface is a circular arc. By the contact-angle equation (75), one obtains

$$K^0 = -\frac{\cos(\theta^0(\partial_t \gamma_1^0))}{w^0(\gamma_1^0)}. \quad (78)$$

Combining Equations (77) and (78) and plugging the result into the bulk pressure solutions given in Equations (50, 52) leads to

$$p_{\text{in}}^0 - q \left(\int_0^{\gamma_1^0} \frac{3}{(w^0(x_1))^2 (3\lambda^0 + w^0(x_1))} dx_1 + \int_{\gamma_1^0}^1 \frac{3M}{(w^0(x_1))^2 (3\lambda^0 + w^0(x_1))} dx_1 \right) = \frac{\cos(\theta^0(\partial_t \gamma_1^0))}{\overline{\text{Ca}} w^0(\gamma_1^0)}. \quad (79)$$

Due to the constant curvature in Equation (78) and the symmetry condition, Equation (74), the leading order interface $\Gamma_X^0(t) := \{\mathbf{Y}^0(t, s) \mid s \in [0, 1]\}$ is given (up to a reparameterization) by

$$\mathbf{Y}^0(t, s) = \begin{cases} \frac{w^0(\gamma_1^0)}{\cos(\theta^0(\partial_t \gamma_1^0))} \begin{pmatrix} \cos\left(\left(\frac{\pi}{2} - \theta^0(\partial_t \gamma_1^0)\right)s\right) - \sin\left(\theta^0(\partial_t \gamma_1^0)\right) \\ \sin\left(\left(\frac{\pi}{2} - \theta^0(\partial_t \gamma_1^0)\right)s\right) \end{pmatrix} & \text{for } \theta^0 \neq \pi/2, \\ w^0(\gamma_1^0(t)) \begin{pmatrix} 0 \\ s \end{pmatrix} & \text{for } \theta^0 = \pi/2. \end{cases}$$

Analogously to Remark 2, by the mass conservation Equation (17), the interface velocity Equation (59), and the outer velocity solution given in Equation (49), we obtain

$$\begin{aligned} 0 &= \int_{\Omega_1^\varepsilon} \nabla^\varepsilon \cdot \mathbf{u}_1^\varepsilon d\mathbf{x} = \int_{\Gamma^\varepsilon} \mathbf{u}_1^\varepsilon \cdot \mathbf{n}_1^\varepsilon dl - \int_0^1 u_{1,1}^\varepsilon|_{x_1=0} dx_1 \\ &= \int_{\Gamma^\varepsilon} \partial_t \gamma_1^0 N_{\Gamma,1}^\varepsilon + \varepsilon \partial_t \mathbf{Y}^\varepsilon \cdot \mathbf{N}_\Gamma^\varepsilon dl - q + \mathcal{O}(\varepsilon) = \int_0^1 \partial_t \gamma_1^0 \partial_s Y_{w_2}^\varepsilon ds - q + \mathcal{O}(\varepsilon) \\ &= \partial_t \gamma_1^0 w^0(\gamma_1^0) - q + \mathcal{O}(\varepsilon). \end{aligned}$$

Therefore, the leading order position γ_1^0 of the interface fulfils

$$\partial_t \gamma_1^0(t) = \frac{q(t)}{w^0(\gamma_1^0(t))}. \quad (80)$$

To find the solution for \mathbf{u}_m^0, p_m^0 ($m \in \{\text{I}, \text{II}\}$), which is given by Equations (49–52), one has to determine γ_1^0, q , and p_{in}^0 . The derivation depends on the chosen inlet boundary condition. For a given inlet velocity $\mathbf{u}_1^\varepsilon = \mathbf{u}_{\text{in}}^\varepsilon$ at $\Gamma_{\text{in}}^\varepsilon$, the value of q is known. Plugging q into Equation (80) and solving for γ_1^0 yields

$$\gamma_1^0(t) = \mathcal{W}^{-1} \left(\mathcal{W}(\gamma_1^0|_{t=0}) + \int_0^t q(\tau) d\tau \right),$$

where $\mathcal{W}(\xi) := \int_0^\xi w^0(x_1) dx_1$. Note that $\mathcal{W}' = w^0 > 0$ by (A4), such that the inverse function \mathcal{W}^{-1} is well-defined. Finally, p_{in}^0 can be found by Equation (79).

For a given inlet pressure $p_1^\varepsilon = p_{\text{in}}^\varepsilon$ at $\Gamma_{\text{in}}^\varepsilon$, the value of p_{in}^0 is known. Then, the differential algebraic system of Equations (79–80) has index 1 and can be solved for q and γ_1^0 . Inserting Equation (80) into Equation (79) and applying the implicit function theorem to find q depending on γ_1^0 , a sufficient condition for solvability is

$$\sin \left(\theta^0 \left(\frac{q}{w^0(\gamma_1^0)} \right) \right) (\theta^0)' \left(\frac{q}{w^0(\gamma_1^0)} \right) \neq \overline{\text{Ca}}(w^0(\gamma_1^0))^2 \left(\int_0^{\gamma_1^0} \frac{3}{(w^0(x_1))^2 (3\lambda^0 + w^0(x_1))} dx_1 + \int_{\gamma_1^0}^1 \frac{3M}{(w^0(x_1))^2 (3\lambda^0 + w^0(x_1))} dx_1 \right),$$

where $(\theta^0)'$ denotes the derivative of θ^0 . Note that the right-hand side is always positive, so that any contact angle model which fulfils $(\theta^0)' \leq 0$ yields solvable differential algebraic equations.

Furthermore, from Equations (63-71,73), the velocity close to the interface is given by two coupled Stokes problems. More precisely, these problems are defined in the domains

$$\Omega_{\mathbf{X},\text{I}}^0(t) = \{\mathbf{X} \in \mathbb{R} \times (0, w^0(\gamma_1^0(t))) \mid \exists s \in [0, 1] : X_1 < Y_1^0(t, s) \wedge X_2 = Y_2^0(t, s)\},$$

$$\Omega_{\mathbf{X},\text{II}}^0(t) = \{\mathbf{X} \in \mathbb{R} \times (0, w^0(\gamma_1^0(t))) \mid \exists s \in [0, 1] : X_1 > Y_1^0(t, s) \wedge X_2 = Y_2^0(t, s)\}.$$

With this, the two problems are ($m \in \{\text{I}, \text{II}\}$)

$$0 = \nabla_{\mathbf{X}} P_{\text{I}}^1 - \Delta_{\mathbf{X}} \mathbf{U}_{\text{I}}^0 \quad \text{in } \Omega_{\mathbf{X},\text{I}}^0(t), \quad (81)$$

$$0 = \nabla_{\mathbf{X}} P_{\text{II}}^1 - M \Delta_{\mathbf{X}} \mathbf{U}_{\text{II}}^0 \quad \text{in } \Omega_{\mathbf{X},\text{II}}^0(t), \quad (82)$$

$$0 = \nabla_{\mathbf{X}} \cdot \mathbf{U}_m^0 \quad \text{in } \Omega_{\mathbf{X},m}^0(t), \quad (83)$$

$$0 = U_{m,2}^0, \quad 0 = \partial_{X_2} U_{m,1}^0, \quad 0 = \partial_{X_2} P_m^1 \quad \text{at } X_2 = 0, \quad (84)$$

$$0 = U_{m,1}^0 + (\lambda^0 + \lambda_e \exp(-|X_1|)) \partial_{X_2} U_{m,1}^0, \quad 0 = U_{m,2}^0 \quad \text{at } X_2 = w^0(\gamma_1^0(t)), \quad (85)$$

$$0 = \left(\partial_t \gamma_1^0 - U_{1,1}^0 \right) \partial_s Y_2^0 + U_{1,2}^0 \partial_s Y_1^0 \quad \text{on } \Gamma_{\mathbf{X}}^0(t), \quad (86)$$

$$0 = \mathbf{U}_{\text{I}}^0 - \mathbf{U}_{\text{II}}^0 \quad \text{on } \Gamma_{\mathbf{X}}^0(t), \quad (87)$$

$$0 = \partial_s \mathbf{Y}^0 \cdot \left(\mathbf{D}_{\mathbf{X}}(\mathbf{U}_{\text{I}}^0) - M \mathbf{D}_{\mathbf{X}}(\mathbf{U}_{\text{II}}^0) \right) \begin{pmatrix} \partial_s Y_2^0 \\ -\partial_s Y_1^0 \end{pmatrix} \quad \text{on } \Gamma_{\mathbf{X}}^0(t), \quad (88)$$

$$\mathbf{0} = \lim_{X_1 \rightarrow -\infty} \mathbf{U}_{\text{I}}^0 - \mathbf{u}_{\text{I}}^0|_{x_1=\gamma_1^0, x_2=X_2}, \quad (89)$$

$$\mathbf{0} = \lim_{X_1 \rightarrow \infty} \mathbf{U}_{\text{II}}^0 - \mathbf{u}_{\text{II}}^0|_{x_1=\gamma_1^0, x_2=X_2}. \quad (90)$$

3.3 | Unsaturated flow limit

In (A2), we assumed the viscosity ratio $M = \mathcal{O}(\varepsilon^0)$. Here, we investigate the case when the viscosity of fluid II is much smaller than that of fluid I, like in a system consisting of water and air. Hence, we replace (A2) by:

(A9) The viscosity ratio satisfies $M = \mathcal{O}(\varepsilon^\beta)$ for some $\beta \geq 1$.

Following the same steps as in the previous subsections, we obtain a model which only includes the flow of fluid I, while the flow of fluid II can be omitted. In other words, the upscaled model is an unsaturated flow in the thin strip. Furthermore, the effective solution for fluid I will coincide with the one obtained when letting $M \rightarrow 0$ in Equations (49, 50, 79, 80) derived previously.

To this end, we use the same asymptotic expansions and (A1), (A3)–(A8), and (A9) instead of (A2). For fluid I, we obtain again Equations (29,30,33-35,39,40) and work with either Equation

(36) or Equation (37) as inlet condition. Therefore, the solution for fluid I is again given by Equations (49, 50), where p_{in}^0 and q are given by the interface region and the inlet condition.

For fluid II, the leading order mass balance equations become

$$\mathcal{O}(\varepsilon) = \partial_{x_1} p_{\text{II}}^0 \quad \text{in } \Omega_{\text{II}}^\varepsilon(t), \quad (91)$$

$$\mathcal{O}(\varepsilon^0) = \varepsilon^{-1} \partial_{x_2} p_{\text{II}}^0 \quad \text{in } \Omega_{\text{II}}^\varepsilon(t). \quad (92)$$

Together with the leading order outflow condition $\mathcal{O}(\varepsilon) = p_{\text{II}}^0$ at $x_1 = 1$, we conclude that $p_{\text{II}}^0(t, \mathbf{x}) = 0$ in $\Omega_{\text{II}}^\varepsilon(t)$. Rescaling the interface region as in Subsection 3.2 and taking (A7) and (A8) into account, the leading order equations for fluid I are again Equations (63,65-69). Since $p_{\text{II}}^0 \equiv 0$, the interface conditions are Equations (68-70,74), as well as

$$\mathcal{O}(\varepsilon^{\min(1,2-\alpha)}) = P_{\text{I}}^0 + \frac{\varepsilon^{1-\alpha}}{\overline{\text{Ca}}} \frac{\partial_s Y_1^0 \partial_s^2 Y_2^0 - \partial_s Y_2^0 \partial_s^2 Y_1^0}{((\partial_s Y_1^0)^2 + (\partial_s Y_2^0)^2)^{3/2}} \quad \text{on } \Gamma_{\text{X}}^\varepsilon(t), \quad (93)$$

$$\mathcal{O}(\varepsilon) = \partial_s \mathbf{Y}^0 \cdot \mathbf{D}_{\text{X}}(\mathbf{U}_{\text{I}}^0) \begin{pmatrix} \partial_s Y_2^0 \\ -\partial_s Y_1^0 \end{pmatrix} \quad \text{on } \Gamma_{\text{X}}^\varepsilon(t). \quad (94)$$

In the regime $\alpha = 1$, this yields a constant leading-order curvature, implying

$$p_{\text{in}}^0 - q \int_0^{\gamma_1^0} \frac{3}{(w^0(x_1))^2 (3\lambda^0 + w^0(x_1))} dx_1 = \frac{\cos(\theta^0(\partial_t \gamma_1^0))}{\overline{\text{Ca}} w^0(\gamma_1^0)}, \quad (95)$$

$$\partial_t \gamma_1^0(t) = \frac{q(t)}{w^0(\gamma_1^0(t))}. \quad (96)$$

3.4 | Hysteretic contact angle model

The previous analysis requires that the dynamic contact angle relation is continuous, as expressed in (A5). However, experiments suggest the occurrence of contact angle hysteresis. For example, the reviews^{68,70} discuss this as a result of surface wettability and roughness. This means that static contact angles are not unique, but can vary due to pinning. Here, we allow that the contact angle relation θ^ε involves a multivalued graph if the velocity of the contact line is zero. To still obtain a well-defined contact angle law, we reformulate the respective condition under the following assumption, which replaces (A5).

(A10) Restricted to $\mathbb{R} \setminus \{0\}$, θ^ε is a Lipschitz-continuous and strictly monotonic function into $(0, \pi)$. For a zero velocity, it can take any values as follow:

$$\theta^\varepsilon(0) \in \begin{cases} [\lim_{u \nearrow 0} \theta^\varepsilon(u), \lim_{u \searrow 0} \theta^\varepsilon(u)] & \text{if } \theta^\varepsilon \text{ is increasing,} \\ [\lim_{u \searrow 0} \theta^\varepsilon(u), \lim_{u \nearrow 0} \theta^\varepsilon(u)] & \text{otherwise.} \end{cases}$$

Using the monotonicity of θ^ε , one can invert the relation with respect to the velocity. For this, let $\zeta^\varepsilon := (\cos(\theta^\varepsilon))^{-1}$ be the inverse of $\cos \theta^\varepsilon$. By (A10), ζ^ε is well-defined and Lipschitz-continuous. As before, we assume that ζ^ε depends regularly on ε .

(A11) ζ^ε has a uniform expansion

$$\zeta^\varepsilon(a) = \zeta^0(a) + \varepsilon \zeta^1(a) + \mathcal{O}(\varepsilon^2),$$

where $\zeta^0 : (-1, 1) \rightarrow \mathbb{R}$ is Lipschitz-continuous.

With this, we study the Navier–Stokes system for two-phase flow Equations (15–25), but replace Equation (26) by the following, inverted contact angle condition:

$$\zeta^\varepsilon \left(\mathbf{t}_\Gamma^\varepsilon|_{s=1} \cdot \mathbf{t}_w^\varepsilon|_{x_1=\gamma_1^\varepsilon} \right) = \partial_t \gamma_1^\varepsilon. \quad (97)$$

Since the analysis in Subsection 3.1 is independent of the interface region, and in particular does not use (A5) or the nonhysteretic contact angle equation (26), the derived bulk solutions given by Equations (49–52) remain unchanged.

Using (A1)–(A4), (A6)–(A8), and (A11) instead of (A5), we repeat the analysis close to the interface $\Gamma^\varepsilon(t)$ from Subsection 3.2. Following the same steps, we obtain a circular interface with constant curvature K^0 , which is then implicitly given by

$$\partial_t \gamma_1^0 = \zeta^0(w^0(\gamma_1^0)K^0).$$

Combining this, the pressure Equation (77), and the outer pressure solution Equations (50, 52), one obtains

$$\partial_t \gamma_1^0 = \zeta^0 \left(w^0(\gamma_1^0) \overline{\text{Ca}} (p_{\text{in}}^0 - qJ(\gamma_1^0)) \right), \quad (98)$$

where

$$J(\gamma_1^0) := \int_0^{\gamma_1^0} \frac{3}{(w^0(x_1))^2(3\lambda^0 + w^0(x_1))} dx_1 + \int_{\gamma_1^0}^1 \frac{3M}{(w^0(x_1))^2(3\lambda^0 + w^0(x_1))} dx_1.$$

Together with Equation (80), this forms a differential algebraic system of two equations for the two unknowns γ_1^0 and either p_{in}^0 or q . Furthermore, the Stokes problem for finding the velocity close to the interface remains unchanged as well.

The solution process depends again on the chosen inlet boundary condition, analogously to the discussion in Subsection 3.2. As before, it is sufficient to obtain γ_1^0 , p_{in}^0 , and q , since these are the unknown coefficients for the bulk solutions \mathbf{u}_m^0 and p_m^0 ($m \in \{\text{I}, \text{II}\}$) given by Equations (49–52). For an inlet velocity boundary condition $\mathbf{u}_1^\varepsilon = \mathbf{u}_{\text{in}}^\varepsilon$ (at $\Gamma_{\text{in}}^\varepsilon$), the value of q is given. Hence, plugging this into Equation (80) yields γ_1^0 , and thus one can solve Equation (98) for p_{in}^0 . However, the solution of the inlet pressure p_{in}^0 is not unique if the contact angle relation θ^ε is multivalued at velocity $u = 0$. On the other hand, for an inlet pressure condition $p_1^\varepsilon = p_{\text{in}}^\varepsilon$, the value of p_{in}^0 is known. Then, the differential algebraic system of Equations (80,98) has index 1 and can be solved for q and γ_1^0 . Inserting Equation (80) into Equation (98) and applying the implicit function

theorem to find q depending on γ_1^0 , a sufficient condition for solvability is

$$(\zeta^0)' \left(w^0(\gamma_1^0) \overline{\text{Ca}} (p_0^{\text{in}} - qJ(\gamma_1^0)) \right) \neq \frac{1}{\overline{\text{Ca}}(w^0(\gamma_1^0))^2 J(\gamma_1^0)}.$$

4 | AVERAGED MODELS AND EFFECTIVE QUANTITIES

Based on the asymptotic solution for pressures and velocities, we continue with the study of averaged models and effective quantities. First, we show that a local, one-dimensional version of Darcy's law holds for the transversally averaged pressures and velocities. In the second part, we derive effective quantities based on volume averages. The main result is a capillary pressure-saturation relationship involving dynamic effects.

In the following, we are only interested in the leading order relations. To simplify the notation, we therefore drop the indices $(\cdot)^\varepsilon$ and $(\cdot)^0$, and neglect higher-order terms. Hence, all following equations should be understood as up to terms of order ε .

4.1 | Transversal average: Darcy's law

In the following, we derive the transversal average of the quantities to demonstrate that the one-dimensional description of the thin strip yields a local version of Darcy's law. To this end, recall that the total flux (in the half strip) $q(t)$ is independent of x_1 as discussed in Remark 2. The transversally averaged velocity in x_1 -direction is therefore given by

$$\begin{aligned} \bar{u}(t, x_1) &:= \begin{cases} (w(x_1))^{-1} \int_0^{w(x_1)} u_{1,\text{I}}(t, \mathbf{x}) dx_2 & \text{for } x_1 < \gamma_1(t), \\ (w(x_1))^{-1} \int_0^{w(x_1)} u_{1,\text{II}}(t, \mathbf{x}) dx_2 & \text{for } x_1 > \gamma_1(t), \end{cases} \\ &= \frac{q(t)}{w(x_1)}. \end{aligned}$$

Since the pressures p_{I} and p_{II} are independent of x_2 , we obtain for the transversally averaged pressures

$$\begin{aligned} \bar{p}_{\text{I}}(t, x_1) &:= (w(x_1))^{-1} \int_0^{w(x_1)} p_{\text{I}}(t, \mathbf{x}) dx_2 \\ &= p_{\text{in}}(t) - q(t) \int_0^{x_1} \frac{3}{(w(\xi))^2 (3\lambda + w(\xi))} d\xi \quad \text{for } x_1 < \gamma_1(t), \\ \bar{p}_{\text{II}}(t, x_1) &:= (w(x_1))^{-1} \int_0^{w(x_1)} p_{\text{II}}(t, \mathbf{x}) dx_2 \\ &= q(t) \int_{x_1}^1 \frac{3M}{(w(\xi))^2 (3\lambda + w(\xi))} d\xi \quad \text{for } x_1 > \gamma_1(t). \end{aligned}$$

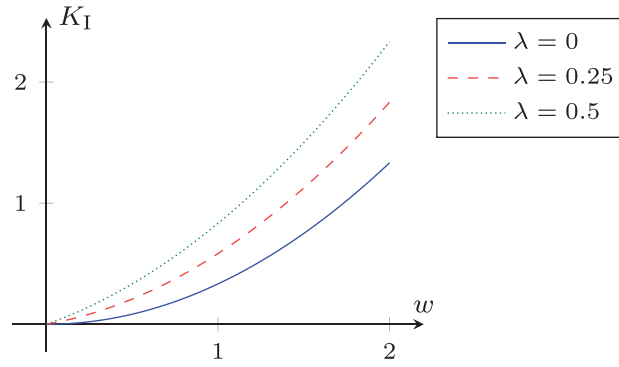


FIGURE 2 The local permeability K_I has a quadratic dependence on the width w and increases for increasing slip length λ

This means that the transversally averaged pressures satisfy a Darcy-type law

$$\bar{u}(t, x_1) = -K_m(x_1) \partial_{x_1} \bar{p}_m(t, x_1)$$

for $m \in \{I, II\}$, where the local permeabilities are given by

$$K_I(x_1) := \frac{1}{3} w(x_1) (3\lambda + w(x_1)),$$

$$K_{II}(x_1) := \frac{1}{3M} w(x_1) (3\lambda + w(x_1)).$$

These permeabilities depend only on the local width w of the thin strip, on the slip length λ , and on the viscosity ratio M of the fluids (Figure 2). Note that this resembles the typical relation $\bar{u} = \frac{d^2}{12} \partial_{x_1} p$ for single-phase flow in a thin strip of diameter $d = 2w$. Also note that the permeabilities are nondimensional due to the chosen scaling of the x_2 coordinate by $\hat{w}(0)$ and the reference viscosity μ_I .

4.2 | Effective quantities: Dynamic capillary pressure

To obtain effective quantities such as the saturation and the intrinsically averaged pressures, we use volume averages. With these, we obtain a capillary pressure–saturation relationship involving dynamic effects. In line with classical volume averaging theory,^{30,31} we define the volume average $\langle a_m \rangle$ of a quantity a_m defined in Ω_m , $m \in \{I, II\}$, to be

$$\langle a_m \rangle := \frac{\int_{\Omega_m} a_m d\mathbf{x}}{\int_{\Omega} d\mathbf{x}},$$

while the intrinsic average is

$$\langle a_m \rangle_m := \frac{\int_{\Omega_m} a_m d\mathbf{x}}{\int_{\Omega_m} d\mathbf{x}}.$$

The volume of the domain Ω_I is given by

$$\int_{\Omega_I} d\mathbf{x} = \int_0^{\gamma_1} w(x_1) dx_1 = \mathcal{W}(\gamma_1).$$

Analogously, we have $\int_{\Omega} d\mathbf{x} = \mathcal{W}(1)$ and $\int_{\Omega_{II}} d\mathbf{x} = \mathcal{W}(1) - \mathcal{W}(\gamma_1)$. Therefore, the saturation of fluid I is in leading order given by

$$S(t) := \langle 1_{\Omega_I(t)} \rangle = \frac{\int_{\Omega_I(t)} d\mathbf{x}}{\int_{\Omega} d\mathbf{x}} = \frac{\mathcal{W}(\gamma_1(t))}{\mathcal{W}(1)}. \quad (99)$$

Note that we only consider the case when both phases are present, so that $\gamma_1(t) \in (0, 1)$ and $S \in (0, 1)$. For simplicity, we define the function

$$\Psi(S) := \frac{1}{w(\mathcal{W}^{-1}(\mathcal{W}(1)S))}, \quad (100)$$

which represents the reciprocal of the local width depending on the saturation S and on the geometry of the thin strip. Note that the system of Equations (79–80) can be rewritten in terms of the saturation as

$$\begin{aligned} p_{\text{in}} - q\mathcal{W}(1) & \left(\int_0^S \frac{3(\Psi(\xi))^3}{3\lambda + (\Psi(\xi))^{-1}} d\xi + \int_S^1 \frac{3M(\Psi(\xi))^3}{3\lambda + (\Psi(\xi))^{-1}} d\xi \right) \\ & = \frac{\cos(\theta(\mathcal{W}(1)\Psi(S)\partial_t S))}{\overline{\text{Ca}}} \Psi(S), \\ \partial_t S & = \frac{q}{\mathcal{W}(1)}. \end{aligned}$$

However, this reformulation is less practical, since the function Ψ typically is not a closed-form expression.

Using Equation (50), the intrinsically averaged pressure of fluid I is

$$\langle p_I \rangle_I = \frac{1}{\mathcal{W}(\gamma_1)} \int_0^{\gamma_1} w(x_1) \left(p_{\text{in}} - q \int_0^{x_1} \frac{3}{(w(\xi))^2(3\lambda + w(\xi))} d\xi \right) dx_1,$$

which can be rewritten after integration by parts as

$$\langle p_I \rangle_I = p_I|_{x_1=\gamma_1} + \frac{3q}{\mathcal{W}(\gamma_1)} \int_0^{\gamma_1} \frac{\mathcal{W}(x_1)}{(w(x_1))^2(3\lambda + w(x_1))} dx_1. \quad (101)$$

Analogously, Equation (52) yields the intrinsically averaged pressure of fluid II to be

$$\langle p_{II} \rangle_{II} = p_{II}|_{x_1=\gamma_1} - \frac{3Mq}{\mathcal{W}(1) - \mathcal{W}(\gamma_1)} \int_{\gamma_1}^1 \frac{\mathcal{W}(1) - \mathcal{W}(x_1)}{(w(x_1))^2(3\lambda + w(x_1))} dx_1. \quad (102)$$

Using Equation (79), the difference of the intrinsically averaged pressures, in the following called phase-pressure difference, is given by

$$\langle p_I \rangle_I - \langle p_{II} \rangle_{II} = \frac{\cos(\theta(\partial_t \gamma_1))}{\overline{Ca} w(\gamma_1)} + 3q \left(\frac{1}{\mathcal{W}(\gamma_1)} \int_0^{\gamma_1} \frac{\mathcal{W}(x_1)}{(w(x_1))^2 (3\lambda + w(x_1))} dx_1 + \frac{M}{\mathcal{W}(1) - \mathcal{W}(\gamma_1)} \int_{\gamma_1}^1 \frac{\mathcal{W}(1) - \mathcal{W}(x_1)}{(w(x_1))^2 (3\lambda + w(x_1))} dx_1 \right). \quad (103)$$

Using Equations (80,99,100), this difference can be expressed in the form

$$\langle p_I \rangle_I - \langle p_{II} \rangle_{II} = p_{c,\text{loc}}(S, \partial_t S) + \tau(S) \partial_t S. \quad (104)$$

The first term on the right denotes the local capillary pressure $p_{c,\text{loc}} := (p_I - p_{II})|_{x_1=\gamma_1}$ given by

$$p_{c,\text{loc}}(S, \partial_t S) = \frac{\cos(\theta(\mathcal{W}(1)\Psi(S)\partial_t S))}{\overline{Ca}} \Psi(S). \quad (105)$$

The second term in Equation (104) can be interpreted as a dynamic capillarity due to the viscous drag. In particular, its coefficient is

$$\tau(S) = \frac{3(\mathcal{W}(1))^2}{S} \int_0^S \frac{\xi(\Psi(\xi))^3}{3\lambda + (\Psi(\xi))^{-1}} d\xi + \frac{3(\mathcal{W}(1))^2 M}{1-S} \int_S^1 \frac{(1-\xi)(\Psi(\xi))^3}{3\lambda + (\Psi(\xi))^{-1}} d\xi, \quad (106)$$

which depends on the slip length λ , the viscosity ratio M , and the wall function w . Note that under static conditions, when $q \ll 1$, we have $p_{\text{in}} \approx \langle p_I \rangle_I - \langle p_{II} \rangle_{II} = p_{c,\text{loc}}$, such that the measurement of the inlet pressure yields (static) capillary pressure–saturation relation, but under the dynamic conditions studied here, these quantities can considerably differ. This one must be aware of when performing experiments.

The local capillary pressure $p_{c,\text{loc}}$ depends reciprocally on the effective capillary number \overline{Ca} and on the local width $w(\mathcal{W}^{-1}(\mathcal{W}(1)S)) = 1/\Psi(S)$ of the thin strip. In case of a dynamic contact angle model of the form $\cos(\theta(u)) = \cos(\theta_s) + \eta \overline{Ca} u$, the molecular kinetic theory in Refs. 68, 69, Equation (105) yields

$$p_{c,\text{loc}}^{\text{MKT}}(S, \partial_t S) = \frac{\cos(\theta_s)}{\overline{Ca}} \Psi(S) + \eta \mathcal{W}(1) (\Psi(S))^2 \partial_t S. \quad (107)$$

The static and dynamic effects are decoupled in this case. The first term models the static (local) capillary pressure, while the second term is a dynamic contribution.

In case of a constant contact angle $\theta \equiv \theta_s \in (0, \pi)$, Equation (105) yields the local capillary pressure

$$p_{c,\text{loc}}^{\text{const}}(S) = \frac{\cos(\theta_s)}{\overline{Ca}} \Psi(S).$$

With $l(t) := \int_{\Gamma_X(t)} ds$ being the length of the circular interface $\Gamma_X(t)$ at time t , the local capillary pressure becomes

$$p_{c,\text{loc}}^{\text{const}}(l) = \frac{\frac{\pi}{2} - \theta_s}{\overline{Ca} l}.$$

TABLE 2 Standard parameters for the thin strip of constant width

Parameter	Symbol	Value
Capillary number	$\overline{\text{Ca}}$	1/2
Contact angle	θ	$\pi/3$
Slip length	λ	1/6
Viscosity ratio	M	1
Initial interface position	$\gamma_1 _{t=0}$	0
Inlet pressure	p_{in}	3

Observe that $l(t)$ can be assimilated to the interfacial area concept considered in Refs. 14, 15. Note that for a dynamic contact angle, there is no simple closed-form expression of the local capillary pressure as a function of the interface length (nor of its derivatives).

5 | NUMERICAL EXPERIMENTS

To illustrate the theoretical findings, we depict some numerical examples in this section. We start with a thin strip of constant width, and afterward consider a constricted “pore throat” with varying width. After a short discussion of the boundary conditions, we consider the resulting effective quantities. In particular, we study the effect of the slip length and the viscosity ratio and discuss the effect of a dynamic and a hysteretic contact angle model for both geometries.

We have implemented the numerical solutions using MATLAB[®] R2020a.⁷⁶ The source code is openly available under the CC-BY license in GitHub at <https://github.com/s-lunowa/AsymptoticThinStripMCLSolver>.⁷⁷

5.1 | Thin strip of constant width

First we consider a simple case, which is a thin strip of constant width $w^\varepsilon \equiv 1$, and study the velocity and pressure distribution of the two phases as well as the movement of the interface. After a short discussion of the effect of different inlet boundary conditions, we will consider the effect of different parameter choices in the following subsections—the slip length in Subsection 5.1.1, the viscosity ratio in Subsection 5.1.2, and dynamic and hysteretic contact angle models in Subsections 5.1.3 and 5.1.4, respectively. Except for the varying parameter mentioned in each subsection, all the other ones are fixed, as given in Table 2. In particular, the contact angle model considered when discussing the other parameters is constant, that is, the contact angle is static and fluid I is nonwetting.

For this geometry, the solution given in Equations (49–52) for the bulk domains becomes

$$\mathbf{u}_I(t, \mathbf{x}) = \begin{pmatrix} 3q(t) \frac{2\lambda+1-x_2^2}{6\lambda+2} \\ 0 \end{pmatrix}, \quad p_I(t, \mathbf{x}) = p_{\text{in}}(t) - q(t) \frac{3x_1}{3\lambda+1}, \quad \text{for } x_1 < \gamma_1(t), \quad (108)$$

$$\mathbf{u}_{II}(t, \mathbf{x}) = \begin{pmatrix} 3q(t) \frac{2\lambda+1-x_2^2}{6\lambda+2} \\ 0 \end{pmatrix}, \quad p_{II}(t, \mathbf{x}) = q(t) \frac{3M(1-x_1)}{3\lambda+1}, \quad \text{for } x_1 > \gamma_1(t). \quad (109)$$

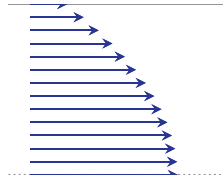
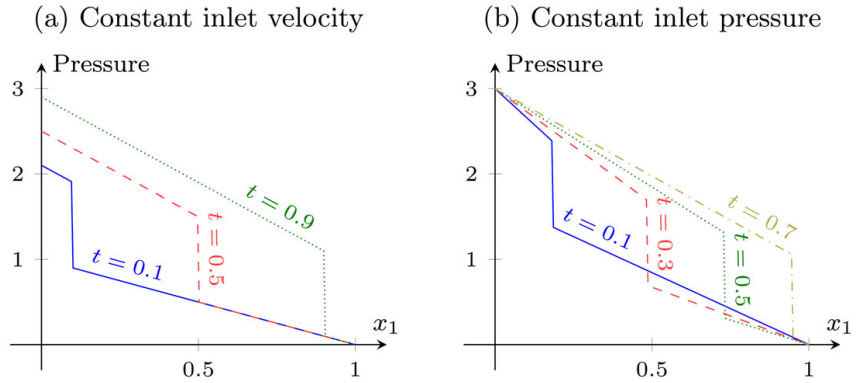


FIGURE 3 Velocity profile in the thin strip with constant width ($\lambda = 1/6$)

FIGURE 4 Pressure distribution over length x_1 at various times in the thin strip of constant width for viscosity ratio $M = 0.5$. The solution depends on the inlet boundary condition and shows a more dynamic behavior in case (b) than in case (a)



This means that the velocity profiles are of Hagen–Poiseuille type (Figure 3). The pressures decrease linearly inside the bulk phases due to the viscous forces. Furthermore, the interface system of Equations (79,80) simplifies into

$$p_{\text{in}}(t) - q(t) \frac{3\gamma_1(t) + 3M(1 - \gamma_1(t))}{3\lambda + 1} = \frac{\cos(\theta(q(t)))}{\text{Ca}}, \quad \partial_t \gamma_1(t) = q(t). \quad (110)$$

The actual size of the quantities and the movement of the interface depend on the inlet boundary conditions, on the effective capillary number, on the slip length, on the viscosity ratio, and on the contact angle model. Here, we shortly discuss the qualitatively different cases with respect to the inlet boundary conditions and the viscosity ratio, when all other parameters are given by Table 2 for simplicity.

(a) When the inlet velocity is fixed, for example, $u_{\text{in},1} = 4/3 - x_2^2$, one obtains $q(t) = 1$ and thus the constant (in time) velocities $u_{m,1} = 4/3 - x_2^2$ for $m \in \{\text{I}, \text{II}\}$, so that the interface moves linearly, $\gamma_1(t) = t$. The pressures are then given by

$$p_{\text{I}}(t, \mathbf{x}) = 1 + 2M + 2(1 - M)t - 2x_1, \quad p_{\text{II}}(t, \mathbf{x}) = 2M(1 - x_1).$$

For $M \neq 1$, the pressure of fluid I is time-dependent, as depicted in Figure 4, while both pressures are constant in time for $M = 1$.

(b) When the inlet pressure is fixed, for example, $p_{\text{in}} = 3$, the flow of both fluids is time-dependent. For a viscosity ratio $M < 1$, one obtains the solution

$$p_{\text{I}}(t, \mathbf{x}) = 3 - \frac{2(1 - M)x_1}{\sqrt{M^2 + 2(1 - M)t}}, \quad p_{\text{II}}(t, \mathbf{x}) = \frac{2M(1 - M)(1 - x_1)}{\sqrt{M^2 + 2(1 - M)t}},$$

$$u_{m,1}(t, \mathbf{x}) = \frac{(1 - M)\left(\frac{4}{3} - x_2^2\right)}{\sqrt{M^2 + 2(1 - M)t}}, \quad \gamma_1(t) = \frac{\sqrt{M^2 + 2(1 - M)t} - M}{1 - M},$$

for $m \in \{I, II\}$, shown in Figure 4. Analogous behavior can be observed when $M > 1$. Only for $M = 1$, both pressures are constant in time, like in (a).

From these examples, we observe a more dynamic behavior when the inlet pressure is given, which corresponds also to the typical setting for capillary pressure experiments. Thus, we restrict the following discussion to the case of given pressure boundary condition at the inlet.

Due to the constant width, the effective quantities have rather simple algebraic expressions. The saturation S coincides with the interface position, that is, $S = \gamma_1$. The local permeabilities are constant and given by

$$K_I \equiv \frac{1 + 3\lambda}{3}, \quad K_{II} \equiv \frac{1 + 3\lambda}{3M}. \quad (111)$$

The local capillary pressure, the dynamic coefficient and the phase-pressure difference are

$$p_{c,loc}(S, \partial_t S) = \frac{\cos \theta(\partial_t S)}{\text{Ca}}, \quad (112)$$

$$\tau(S) = 3 \frac{S + M(1 - S)}{6\lambda + 2}, \quad (113)$$

$$\langle p_I \rangle_I - \langle p_{II} \rangle_{II} = \frac{p_{in} + p_{c,loc}(S, \partial_t S)}{2}. \quad (114)$$

As direct consequence of the constant contact angle in Table 2, we obtain a constant local capillary pressure $p_{c,loc} \equiv 1$ by Equation (112) and a constant phase-pressure difference $\langle p_I \rangle_I - \langle p_{II} \rangle_{II} \equiv 2$ by Equation (114). Changing the static contact angle $\theta \equiv \theta_s \in (0, \pi)$ or the capillary number Ca influences the size of the local capillary pressure and the size of the phase-pressure difference in a straightforward way, while the behavior of the other quantities remains qualitatively the same. For simplicity, we do not discuss their detailed effects. Note that $p_{c,loc}$ and $\langle p_I \rangle_I - \langle p_{II} \rangle_{II}$ do not depend on the slip length nor on the viscosity ratio. Hence, we only consider their behavior for dynamic and hysteretic contact angle models. Meanwhile, the dynamic coefficient depends on the slip length and the viscosity ratio, which is relevant in case of a inlet velocity condition.

5.1.1 | Effect of the slip length

First, we consider the effect of the slip length λ while using all other parameters as above. The velocity at the wall is given by

$$u_{m,1}|_{x_2=1} = q \frac{3\lambda}{3\lambda + 1} \quad \text{for } m \in \{I, II\}.$$

It is zero for $\lambda = 0$, increases for an increasing slip length, and approaches q for $\lambda \rightarrow \infty$, which corresponds to a total slip (Figure 5). This is a result of the decreased friction of the fluid at the wall for an increased slip length. In addition, this leads to a smaller dynamic coefficient τ , compare Equation (113) and Figure 5. For constant inlet pressure, the decrease of the pressure gradients in Equations (108,109) for an increased slip length λ are compensated by a larger total flux q , and thus a faster movement of the interface position γ_1 (Figure 5). The local permeabilities K_I ,

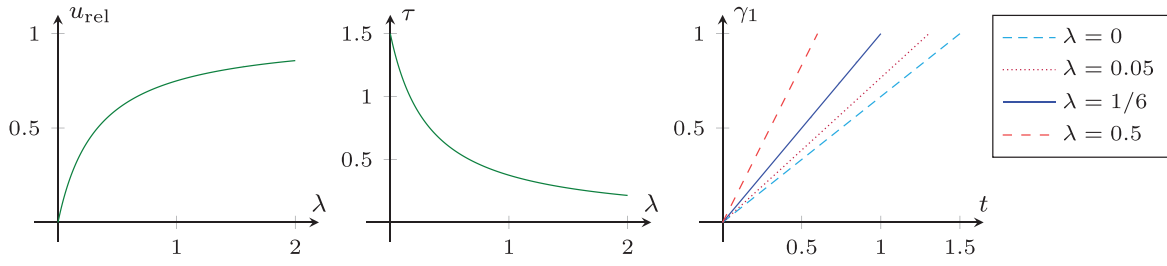


FIGURE 5 For an increasing slip length λ , the velocity ratio $u_{\text{rel}} = u_{m,1}|_{x_2=1}/q$ at the wall increases (left), while the dynamic parameter τ decreases (center). The interface position γ_1 moves faster for an increasing slip length λ (right)

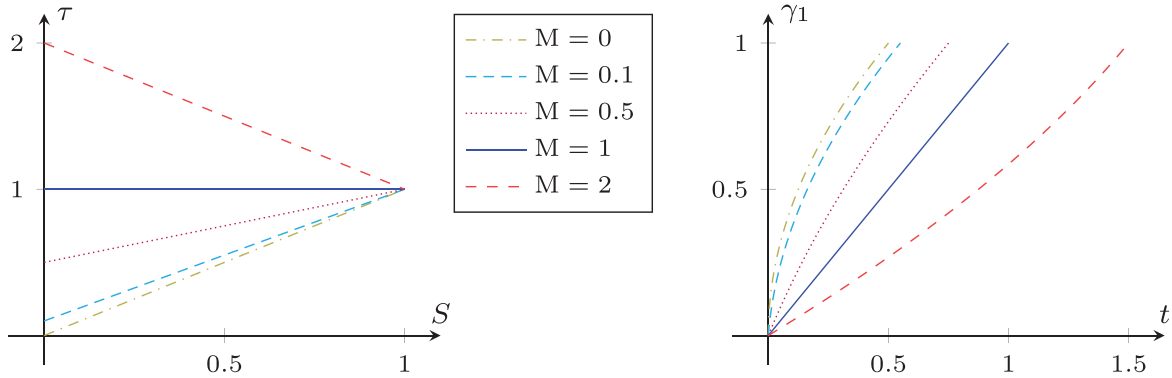


FIGURE 6 For increasing viscosity ratio M , the dynamic parameter τ increases (left), while the interface position γ_1 moves slower (right)

K_{II} show a similar behavior. Observe that since $w \equiv 1$, these only depend on the slip length. As follows from Equation (111) (cf. Figure 2), they increase linearly with λ .

5.1.2 | Effect of the viscosity ratio

Next, we continue the investigation for various viscosity ratios M . Since the viscous force in fluid II is proportional to the viscosity ratio M , the total flux q decreases when the viscosity ratio M increases (cf. Equation (110)). In particular, the interface position γ_1 moves faster when the thin strip is mainly filled by the less viscous fluid (Figure 6). Furthermore, we observe that the solutions converge for $M \rightarrow 0$ toward solution of the simplified, unsaturated flow model as discussed in Subsection 3.3. Note that we use $\gamma_1|_{t=0} = 10^{-3}$ when $M = 0$ to avoid the degeneration of the interface system in Equation (110).

The dynamic coefficient τ becomes larger for small saturations S , if the viscosity ratio is large ($M > 1$), and vice versa for $M < 1$ due to Equation (113), and shown in Figure 6. Note that one can observe even in this extremely simplified setting that the dynamic coefficient is saturation-dependent, except for fluids with the same viscosity ($M = 1$). In addition, the dynamic coefficient is monotonic in the saturation S for any viscosity ratio.

5.1.3 | Effect of a dynamic contact angle

Now, we consider the effect of a dynamic contact angle model. As we expect the similar qualitative behavior for different dynamic contact angle models, we restrict the discussion to the model

$$\theta(u) = \arccos(\max(\min(\cos(\theta_s) + \eta \overline{Cau}, 1), -1)), \quad (115)$$

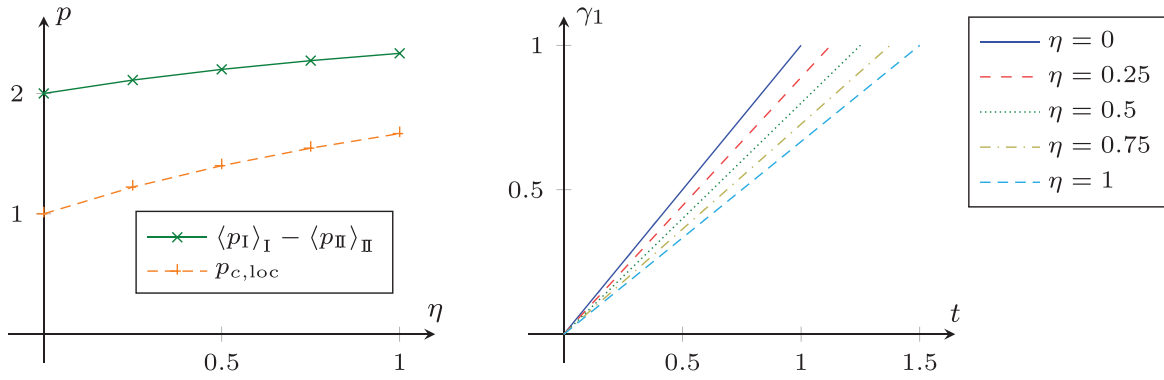


FIGURE 7 The local capillary pressure $p_{c,\text{loc}}$ increases for increasing dynamic contact angle coefficient η (left). Hence, the movement of the interface position γ_1 slows down (right)

which is the linearized molecular kinetic theory model (for small velocities) from Refs. 47,55 68,69,73,74 restricted to the possible range $[0, \pi]$. Here, the parameter $\eta \geq 0$ models the effective friction at the contact point leading to a dynamic contact angle. For comparability, we fix the static contact angle $\theta_s = \pi/3$ and all the other parameters as in Table 2. Note that for any $\eta \geq 0$, the differential algebraic system in Equation (110) has a unique solution, since cosine is monotonic decreasing on $[0, \pi]$.

In contrast to the previous examples, the dynamic contact angle model does not affect the dynamic coefficient τ , but has an impact on the local capillary pressure $p_{c,\text{loc}}$ and the phase-pressure difference $\langle p_I \rangle_I - \langle p_{II} \rangle_{II}$. Recall that the local capillary pressure is given in this case by Equation (107). In particular, its dynamic part is proportional to the parameter η . Hence, the interface position γ_1 moves slower when the parameter η increases (Figure 7). Note that the total flux q is constant, so that γ_1 is linear in time. Since $M = 1$, the local capillary pressure and the phase-pressure difference are constant over S , so that we only show the dependence on η in Figure 7.

5.1.4 | Effect of a hysteretic contact angle

Finally, we consider the effect of a hysteretic contact angle model and compare it to the static and dynamic ones. As before we use the dynamic contact angle model in Equation (115) with static contact angle $\theta_s = \pi/3$. For the hysteretic contact angle model, the advancing and receding contact angles (with respect to fluid I) are chosen $\theta_a = \pi/4$ and $\theta_r = 5\pi/12$, respectively. Together with the same dynamic contact angle model away from $u = 0$, this yields

$$\zeta(a) = \begin{cases} \frac{a - \cos(\theta_r)}{\eta \text{Ca}} & \text{if } a < \cos(\theta_r), \\ \frac{a - \cos(\theta_a)}{\eta \text{Ca}} & \text{if } a > \cos(\theta_a), \\ 0 & \text{otherwise.} \end{cases} \quad (116)$$

Recall that ζ is the inverse of $\cos \theta$. We consider a drainage and imbibition cycle by choosing the time-dependent inlet pressure $p_{\text{in}}(t) = 3 - t$, and stop the simulations when the interface position returns to the inlet. The other parameters are taken from Table 2.

As in the dynamic case, we observe that the movement of the interface position γ_1 is slower when the parameter η is increased (Figure 8 (top)). While the total flux q is linear for the static

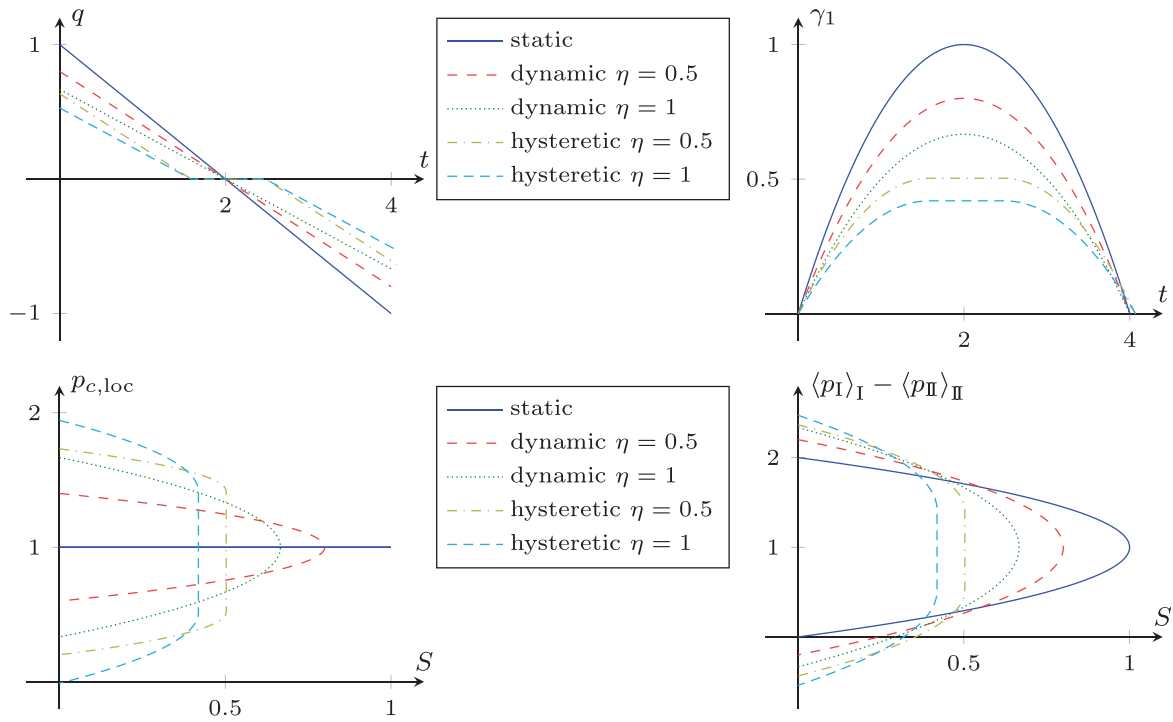


FIGURE 8 The total flux q (top-left) is linear for the static and dynamic contact angle model, while being zero for some time for the hysteretic model. The interface position γ_1 moves accordingly (top-right). In case of the hysteretic model, it is at rest, when the local capillary pressure $p_{c,loc}$ (bottom-left) lies in between the (static) capillary pressures for drainage and imbibition, that is, $p_{c,loc}$ is multivalued at the maximal reached saturation. For the dynamic models, $p_{c,loc}$ at the maximal saturation is exactly the static capillary pressure. The phase-pressure difference $\langle p_I \rangle_I - \langle p_{II} \rangle_{II}$ (bottom-right) shows the same qualitative behavior

and dynamic contact angle model, so that γ_1 is quadratic in time, the hysteretic model leads to a constant interface position when $\theta_a \leq \theta \leq \theta_r$. Therefore, the local capillary pressure $p_{c,loc}$ and the phase-pressure difference $\langle p_I \rangle_I - \langle p_{II} \rangle_{II}$ at the maximal reached saturation is multivalued taking all values between the (static) drainage and imbibition capillary pressures (Figure 8 (bottom)). On the other hand, for the dynamic contact angle model, $p_{c,loc}$ and $\langle p_I \rangle_I - \langle p_{II} \rangle_{II}$ at the maximal saturation are given by the static capillary pressure, since $\partial_t S = 0$. Furthermore, the hysteresis leads to higher deviations from the static capillary pressure and thus a smaller maximal saturation. Finally, note that p_{in} is linear and reaches $p_{c,loc}^{const}$ at $t = 2$ such that all curves with the dynamic contact angle model are symmetric. Since θ_a and θ_r have the same distance from θ_s , the same holds in the hysteretic cases.

5.2 | Constricted “pore throat”

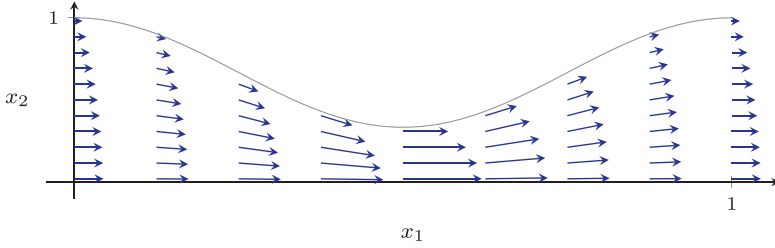
Next, we consider a strip with varying width

$$w(x_1) = 2/3 + \cos(2\pi x_1)/3,$$

which represents a constricted “pore throat.” As before, we shortly discuss the velocity and pressure distribution of the two phases as well as the movement of the interface, before proceeding with the detailed discussion of the effect of the slip length, of the viscosity ratio, and of a dynamic

TABLE 3 Standard parameters for the case of varying width

Parameter	Symbol	Value
Capillary number	$\overline{\text{Ca}}$	1/2
Contact angle	θ	$\pi/3$
Slip length	λ	1/6
Viscosity ratio	M	1
Initial interface position	$\gamma_1 _{t=0}$	0
Inlet pressure	p_{in}	12

FIGURE 9 Velocity profile in the thin strip of varying width ($\lambda = 1/6$)

and a hysteretic contact angle model, varying each individually, while fixing all other parameters as given in Table 3. Note that we choose a static contact angle such that fluid I is nonwetting.

While the overall trend is similar to the previous case with constant width, we additionally observe here a strong impact of the geometry on the flow behavior and thus on the effective quantities. In contrast to the constant-width case, the local capillary pressure $p_{c,\text{loc}}$ now depends on the saturation due to the constriction (Figure 11). Analogously, the phase-pressure difference $\langle p_I \rangle_I - \langle p_{II} \rangle_{II}$ varies in the saturation.

The solution in the bulk domains given by Equations (49–52) for this geometry then reads

$$u_{m,1}(t, \mathbf{x}) = 9q(t) \frac{(c(x_1))^2 + 5c(x_1) + 6 - x_2^2}{(c(x_1) + 2)^2(2c(x_1) + 7)},$$

$$u_{m,2}(t, \mathbf{x}) = \varepsilon 18\pi q(t) \sin(2\pi x_1) \left(\frac{18(c(x_1) + 3)x_2^3}{(c(x_1) + 2)^3(2c(x_1) + 7)^2} - \frac{(2(c(x_1))^2 + 12c(x_1) + 19)x_2}{(c(x_1) + 2)^2(2c(x_1) + 7)^2} \right)$$

for $m \in \{I, II\}$, where $c(x_1) := \cos(2\pi x_1)$, shown in Figure 9, while

$$p_I(t, \mathbf{x}) = \frac{3}{2 + c(\gamma_1(t))} + \frac{9q(t) \sin(2\pi x_1)}{\pi(c(x_1) + 2)} + \frac{24q(t) \left(\pi H(0.5 - x_1) - \arctan \left(\frac{\sqrt{5}}{3} \tan(\pi x_1) \right) \right)}{\pi \sqrt{5}},$$

for $x_1 < \gamma_1(t)$, and

$$p_{II}(t, \mathbf{x}) = \frac{9q(t) \sin(2\pi x_1)}{\pi(c(x_1) + 2)} + \frac{24q(t) \left(\pi H(0.5 - x_1) - \arctan \left(\frac{\sqrt{5}}{3} \tan(\pi x_1) \right) \right)}{\pi \sqrt{5}}$$

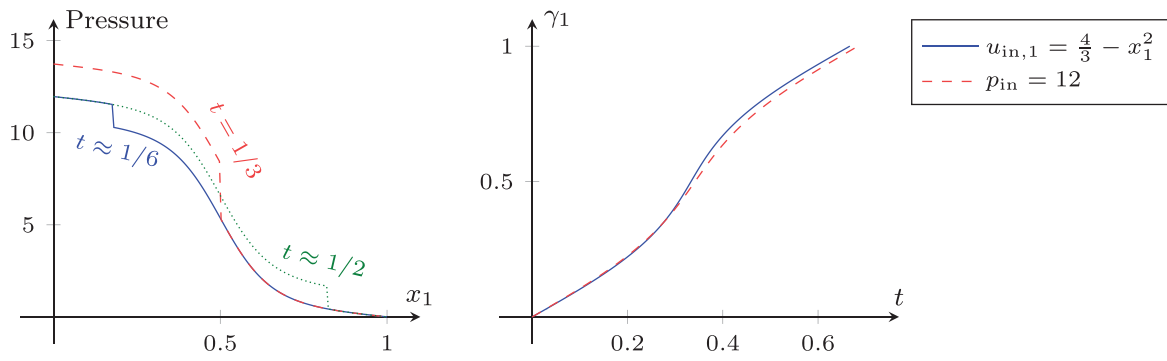


FIGURE 10 Pressure distribution over length x_1 at various times (left) for fixed inlet velocity $u_{\text{in},1} = 4/3 - x_1^2$ and interface position γ_1 over time t (right) for fixed inlet velocity $u_{\text{in},1} = 4/3 - x_1^2$ and fixed pressure condition $p_{\text{in}} = 12$ in the thin strip of varying width

for $x_1 > \gamma_1(t)$, where H denotes the Heaviside graph (Figure 10). The first velocity component is higher where the width is reduced, while the second component adjusts to the changes in width to maintain the incompressibility (Figure 9). Note that the second velocity component is of order ε due to the different scaling. Accordingly, the pressure gradients depend on the local width and are steeper around the constriction in the middle. This leads to the s-shaped pressure profiles instead of the linear ones in the constant-width case.

For fixed inlet velocity $u_{\text{in},1} = 4/3 - x_1^2$, that is, for $q \equiv 1$, the pressure solutions at several times are depicted in Figure 10 together with the evolution of the interface position $\gamma_1(t)$, which is given implicitly by $t = 2\gamma_1(t)/3 + \sin(2\pi\gamma_1(t))/(6\pi)$. Note that the interface position γ_1 moves faster in the vicinity of the constriction, since the average velocity $\bar{u} = q/w$ is higher around the constriction (cf. Figure 9). Furthermore, the movement is very similar to the one obtained with constant inlet pressure $p_{\text{in}} \equiv 12$. Hence, we restrict the following discussion to this inlet pressure condition. Note that this larger inlet pressure is necessary to obtain a similar total flux as in the constant-width case, since the width is reduced.

For this geometry, we still can derive relations for the effective quantities obtained in Subsection 4.2. We obtain for the saturation

$$S = \gamma_1 + \frac{1}{4\pi} \sin(2\pi\gamma_1), \quad \partial_t S = \frac{3}{2}q.$$

Since this function $S(\gamma_1)$ has no analytical inverse, there is no closed-form expression for the local capillary pressure $p_{c,\text{loc}}$ Equation (105) nor for the dynamic coefficient τ Equation (106). Their numeric approximations are depicted in Figure 11. Both have a peak at $S = 0.5$, where the interface passes the position $x_1 = 0.5$ with the smallest width. For the local capillary pressure, this results from the reciprocal dependence on the local width, while the dynamic coefficient is symmetric due to the symmetric wall and the viscosity ratio $M = 1$. Note that the dynamic effects are much stronger than in the constant-width setting due to the reduced width, which requires larger pressure gradients to maintain the flow. Hence, we conclude that the wall shape has a significant impact, especially on the dynamic effects.

5.2.1 | Effect of the slip length

We begin the investigation for various slip lengths λ . As in the previous, constant-width case, the movement of the interface position γ_1 is faster when the slip length is increased. However, the

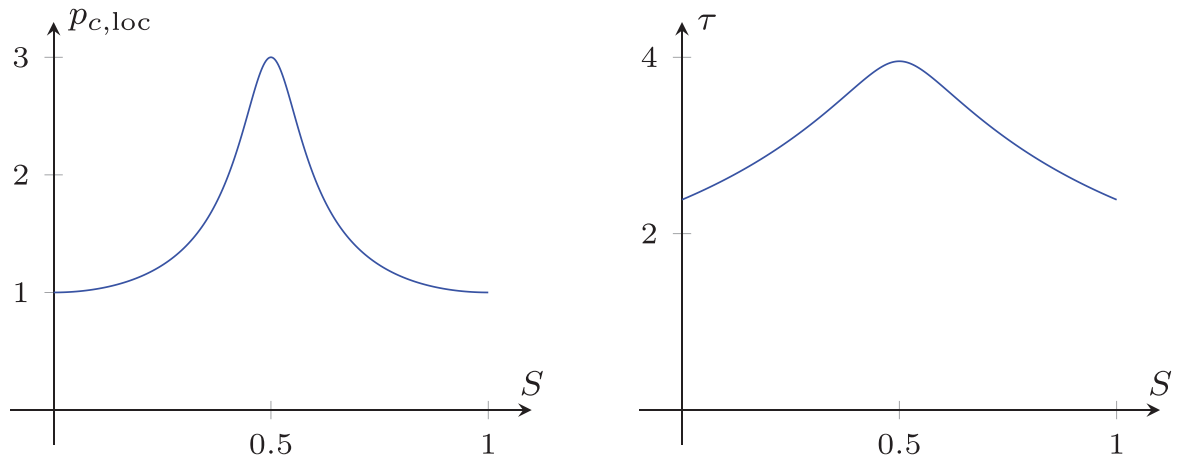


FIGURE 11 The local capillarity pressure $p_{c,loc}$ increases for saturations below $S = 0.5$, and decreases thereafter (left). The dynamic coefficient τ shows an analogous behavior (right). This is a result of the symmetric constriction of the thin strip

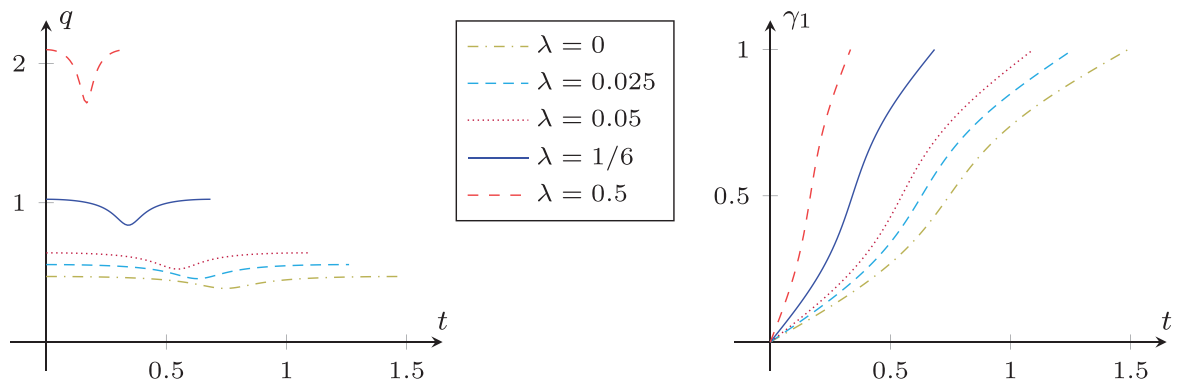


FIGURE 12 The total flux q is drastically reduced while the interface passes through the constriction due to the larger capillary pressure (left). It increases when the slip length λ is increased, so that the movement of the interface position γ_1 is faster (right)

total flux q is drastically reduced while the interface passes through the constriction due to the higher capillary pressure (Figure 12).

The dynamic coefficient τ is lower when the slip length increases as shown in Figure 13. In contrast to the constant-width case, it is nonmonotonic in the saturation, and maximal around $S = 0.5$, that is, when the interface passes through the constriction around $x_1 = 0.5$. Note that the combination of higher velocity with lower dynamic coefficient leads to almost no changes in the phase-pressure difference $\langle p_I \rangle_I - \langle p_{II} \rangle_{II}$ for all slip lengths (Figure 13).

5.2.2 | Effect of the viscosity ratio

Next, we consider the effect of the viscosity ratio M . As in the previous, constant-wall case, the total flux q is smaller when the viscosity ratio M increases (Figure 14). Especially at early times t , one can observe large total fluxes q , when the viscosity ratio is very small ($M \leq 0.1$), since the strip is filled with the extremely mobile fluid II. On the other hand, the total flux is reduced while the interface passes through the constriction, but this effect is very small compared to the effect of viscosity for $M < 1$. As before, the solutions converge for $M \rightarrow 0$ toward the simplified, unsat-

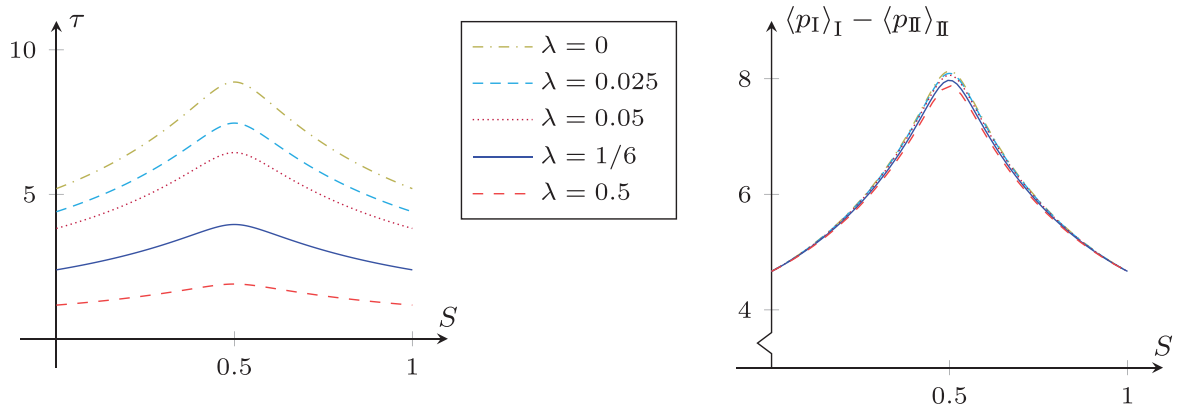


FIGURE 13 The dynamic coefficient τ decreases for increasing slip length λ (left). It is nonmonotonic in the saturation. The resulting phase-pressure difference $\langle p_I \rangle_I - \langle p_{II} \rangle_{II}$ is also nonmonotonic, but almost the same for all slip lengths (right)

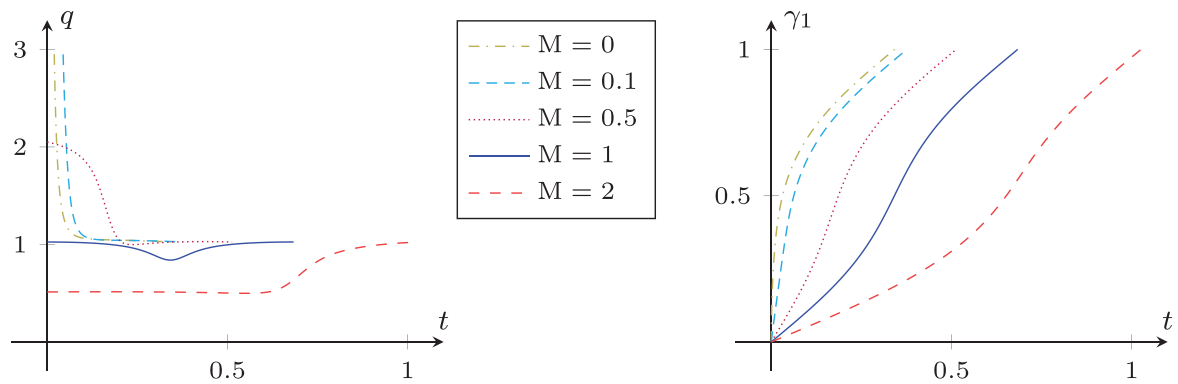


FIGURE 14 The total flux q is high when the thin strip is mainly filled with the less viscous fluid (left). It is smaller while the interface passes through the constriction. When the viscosity ratio M is increased, the interface position γ_1 moves generally slower (right)

urated flow model as discussed in Subsection 3.3 (cf. Figure 14). Note that we use $\gamma_1|_{t=0} = 10^{-3}$ when $M = 0$ to avoid the degeneration of the interface system of Equations (79,80).

The dynamic coefficient τ becomes larger for small saturations S , if the viscosity ratio is larger ($M > 1$), and vice versa for $M < 1$, as shown in Figure 15. The rapid change close to $S = 0.5$ is due to the strong influence of the region around $x_1 = 0.5$, where the thin strip has its minimal width. Note that for small viscosity ratio $M \leq 0.1$ and saturation below 0.4, the dynamic coefficient is almost zero. Furthermore, we observe here nonmonotonic behavior of the dynamic coefficient τ for every viscosity ratio, while it is monotonic in the constant-width case. This is due to the interplay between the constricted geometry and the nonlinear dynamic effect given by Equation (106). Finally, note that the combination of higher velocity with lower dynamic coefficient leads to almost no changes in the phase-pressure difference $\langle p_I \rangle_I - \langle p_{II} \rangle_{II}$ for all moderate viscosity ratios (Figure 15). Only for a very small viscosity ratio $M \leq 0.1$, the phase-pressure difference is slightly lower for saturations between 0 and 0.5.

5.2.3 | Effect of a dynamic contact angle

We consider the effect of a dynamic contact angle model. As for the constant-width case, we use Equation (115) with $\theta_s = \pi/3$. The total flux q is smaller when η is increased (Figure 16). This effect is amplified while the interface passes through the constriction.

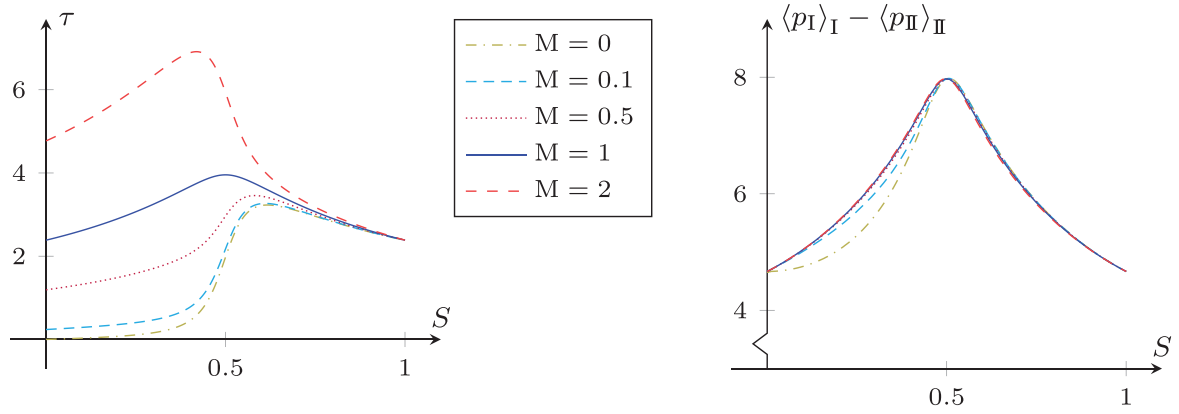


FIGURE 15 The dynamic parameter τ increases for increasing viscosity ratio M (left). It is nonmonotonic in the saturation. The resulting phase-pressure difference $\langle p_I \rangle_I - \langle p_{II} \rangle_{II}$ is also nonmonotonic, but almost the same for all moderate viscosity ratios (right)

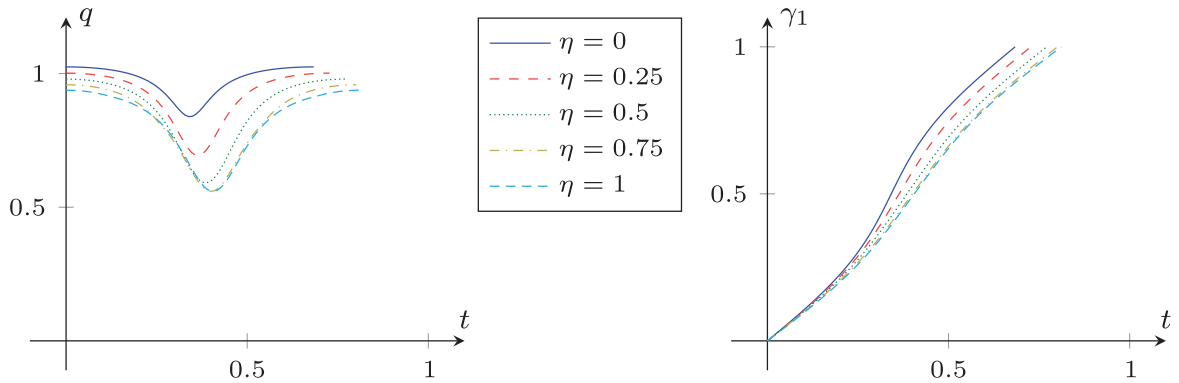


FIGURE 16 The total flux q decreases for higher values of η , since the (dynamic) local capillary pressure increases (left). Accordingly, the interface position γ_1 moves slower (right). Due to the constriction, the effect is maximal for $\gamma_1 = 0.5$

Although the total flux is smaller, the local capillary pressure $p_{c,loc}$ and the phase-pressure difference $\langle p_I \rangle_I - \langle p_{II} \rangle_{II}$ increase for increasing η (Figure 17). The maximum is attained at $S = 0.5$, when the interface passes the minimal width. There, the dynamic effect is also the highest. Note that the curves for $\eta = 0.75$ and $\eta = 1$ partly coincide because the dynamic contact angle reaches π in both cases. In a laboratory experiment, this could lead to instabilities and the formation of bubbles or a thin residual film. However, that such behavior is beyond the scope of the model presented here.

5.2.4 | Effect of a hysteretic contact angle

Finally, we consider the effect of a hysteretic contact angle model and compare it to the static and dynamic ones. As in the constant-width case, we use the dynamic contact angle model in Equation (115) with $\theta_s = \pi/3$ and the hysteretic contact angle model in Equation (116) with $\theta_a = \pi/4$ and $\theta_r = 5\pi/12$. We consider a drainage and imbibition cycle by choosing the time-dependent inlet pressure $p_{in}(t) = 9 - 4t$, and stop the simulations when the interface position returns to the inlet. The other parameters are taken from Table 3.

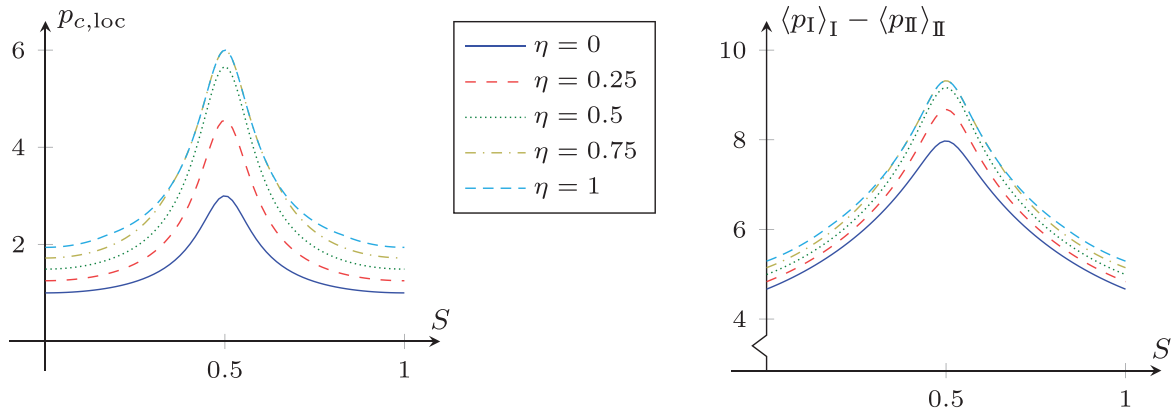


FIGURE 17 The local capillary pressure $p_{c,loc}$ increases for increasing dynamic contact angle coefficient η (left). It attains its maximum at $S = 0.5$, when the interface passes the minimal width. The resulting phase-pressure difference $\langle p_I \rangle_I - \langle p_{II} \rangle_{II}$ shows the same behavior (right)

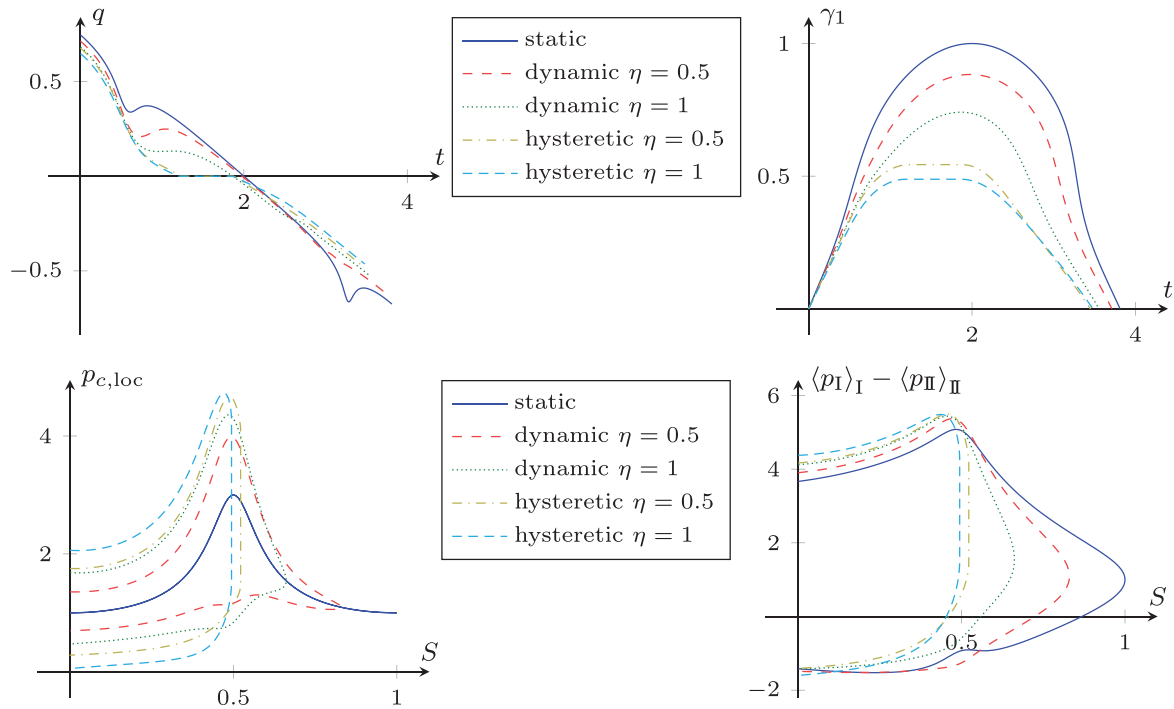


FIGURE 18 The total flux q (top-left) decreases faster when the interface passes through the constriction. In case of the hysteretic contact angle model, the interface position γ_1 (top-right) stops in the constriction when the local capillary pressure $p_{c,loc}$ (bottom-left) lies in between the (static) capillary pressures for drainage and imbibition, whereas $p_{c,loc}$ at the maximal saturation is exactly the static capillary pressure for the dynamic models. The phase-pressure difference $\langle p_I \rangle_I - \langle p_{II} \rangle_{II}$ (bottom-right) shows the same qualitative behavior

As before, the total flux q decreases faster, when the interface passes through the constriction (Figure 18 (top)). Note that the higher capillary pressure when passing the constriction counteracts the drainage, while it increases the imbibition speed. This results in a more negative velocity. In case of the hysteretic contact angle model, the interface position γ_1 stops in the constriction, while the pressure lies in between the (static) capillary pressures for drainage and imbibition, so that the local capillary pressure $p_{c,loc}$ and the phase-pressure difference $\langle p_I \rangle_I - \langle p_{II} \rangle_{II}$ are multivalued at the maximal saturation. In contrast, the dynamic model yields a direct switching between drainage and imbibition, when $p_{c,loc}$ is exactly the static capillary pressure (at the maximal

saturation) (Figure 18 (bottom)). Hence, hysteresis also leads to higher deviations from the static capillary pressure and thus a smaller maximal saturation.

6 | CONCLUSION

We have formally derived the asymptotic solution for the flow of two immiscible fluids in a two-dimensional thin strip of varying width, where the fluid–fluid interface is treated as a free boundary. The obtained effective models form a system of differential algebraic equations for the interface position and the total flux, and are applicable to a wide range of viscosity ratios M , of slip lengths λ , as well as contact angle models. The resulting effective relations are a Darcy-type equation for the local flow, and a capillary pressure–saturation relationship involving dynamic effects.

We have discussed the effects of a varying pore width, of the viscosity ratio, of the slip length as well as of having a dynamic and a hysteretic contact angle law through numerical experiments. In particular, the results for a varying pore width show that the geometry has a large influence on the effective quantities and their behavior. While dynamic effects occur even for a static contact angle model, hysteresis in the capillary pressure is only present when a hysteretic contact model is used.

The presented models and effective relations can be generalized to asymmetric as well as tube-like three-dimensional domains with heterogeneities in the contact angle. Furthermore, rough walls of type $w^\varepsilon(x_1) = w(x_1) + \varepsilon w^1(x_1/\varepsilon) + \mathcal{O}(\varepsilon)$ would strongly affect the shape and position of the interface. This needs to be investigated in the future. In addition, it remains to validate the effective models by a direct comparison with numerical simulations of the full model or with experiments in single pores. Our future work will focus on the radial-symmetric case in three dimensions including the effect of outer forces such as gravity. Such three-dimensional models can be further used in pore-network models or for upscaling in a bundle-of-tubes model.

ACKNOWLEDGMENTS

We thank Arjen Mascini, Tom Bultreys, and Veerle Cnudde for the helpful comments and discussions. This work was funded by the Hasselt University (project BOF17NI01) and the Research Foundation Flanders (FWO, projects G051418N and G0G1316M). We thank the Deutsche Forschungsgemeinschaft (DFG, German Research Foundation) for supporting this work by funding SFB 1313, Project Number 327154368.

ORCID

Stephan B. Lunowa  <https://orcid.org/0000-0002-5214-7245>

Carina Bringedal  <https://orcid.org/0000-0003-0495-2634>

Iuliu Sorin Pop  <https://orcid.org/0000-0001-9647-4347>

REFERENCES

1. Darcy HPG., *Les Fontaines publiques de la ville de Dijon. Exposition et application des principes à suivre et des formules à employer dans les questions de distribution d'eau, etc.* Paris: V. Dalmont; 1856.
2. Richards LA. Capillary conduction of liquids through porous mediums. *Physics*. 1931;1:318-333.
3. Morrow NR, Harris CC. Capillary equilibrium in porous materials. *Soc Pet Eng J*. 1965;5:15-24. <https://doi.org/10.2118/1011-PA>
4. Glass RJ, Steenhuis TS, Parlange J-Y. Mechanism for finger persistence in homogeneous, unsaturated, porous media: theory and verification. *Soil Sci*. 1989;148:60-70.

5. Shiozawa S, Fujimaki H. Unexpected water content profiles under flux-limited one-dimensional downward infiltration in initially dry granular media. *Water Resour Res.* 2004;40:W07404. <https://doi.org/10.1029/2003WR002197>
6. DiCarlo DA. Experimental measurements of saturation overshoot on infiltration. *Water Resour Res.* 2004;40:W04215.
7. Bottero S, Hassanizadeh SM, Kleingeld PJ, Heimovaara TJ. Nonequilibrium capillarity effects in two-phase flow through porous media at different scales. *Water Resour Res.* 2011;47:W10505.
8. Zhuang L, Hassanizadeh SM, Qin C-Z, de Waal A. Experimental investigation of hysteretic dynamic capillarity effect in unsaturated flow. *Water Resour Res.* 2017;53:9078-9088. <https://doi.org/10.1002/2017WR020895>
9. Parker JC, Lenhard RJ. A model for hysteretic constitutive relations governing multiphase flow: 1. Saturation-pressure relations. *Water Resour Res.* 1987;23:2187-2196. <https://doi.org/10.1029/WR023i012p02187>
10. Beliaev AY, Hassanizadeh SM. A theoretical model of hysteresis and dynamic effects in the capillary relation for two-phase flow in porous media. *Transp Porous Med.* 2001;43:487-510.
11. Beliaev AY, Schotting RJ. Analysis of a new model for unsaturated flow in porous media including hysteresis and dynamic effects. *Comput Geosci.* 2001;5:345-368.
12. Beljadid A, Cueto-Felgueroso L, Juanes R. A continuum model of unstable infiltration in porous media endowed with an entropy function. *Adv Water Resour.* 2020;144:103684. <https://doi.org/10.1016/j.advwatres.2020.103684>
13. Schweizer B. Hysteresis in porous media: modelling and analysis. *Interfaces Free Bound.* 2017;19:417-447.
14. Hassanizadeh SM, Gray WG. Thermodynamic basis of capillary pressure in porous media. *Water Resour Res.* 1993;29:3389-3405. <https://doi.org/10.1029/93WR01495>
15. Hassanizadeh SM, Gray WG. Toward an improved description of the physics of two-phase flow. *Adv Water Resour.* 1993;16:53-67.
16. Hilfer R. Capillary pressure, hysteresis and residual saturation in porous media. *Physica A.* 2006;359:119-128. <https://doi.org/10.1016/j.physa.2005.05.086>
17. Hilfer R. Macroscopic capillarity and hysteresis for flow in porous media. *Phys Rev E.* 2006;73:016307.
18. Hilfer R. Macroscopic capillarity without a constitutive capillary pressure function. *Physica A.* 2006;371:209-225. <https://doi.org/10.1016/j.physa.2006.04.051>
19. van Duijn CJ, Fan Y, Peletier LA, Pop IS. Travelling wave solutions for degenerate pseudo-parabolic equations modelling two-phase flow in porous media. *Nonlinear Anal Real World Appl.* 2013;14:1361-1383. <https://doi.org/10.1016/j.nonrwa.2012.10.002>
20. van Duijn CJ, Mitra K. Hysteresis and horizontal redistribution in porous media. *Transp Porous Media.* 2018;122:375-399. <https://doi.org/10.1007/s11242-018-1009-2>
21. Mitra K, van Duijn CJ. Wetting fronts in unsaturated porous media: the combined case of hysteresis and dynamic capillary pressure. *Nonlinear Anal Real World Appl.* 2019;50:316-341. <https://doi.org/10.1016/j.nonrwa.2019.05.005>
22. Doster F, Zegeling PA, Hilfer R. Numerical solutions of a generalized theory for macroscopic capillarity. *Phys Rev E.* 2010;81:036307.
23. Lamacz A, Rätz A, Schweizer B. A well-posed hysteresis model for flows in porous media and applications to fingering effects. *Adv Math Sci Appl.* 2011;21:33-64.
24. Hilfer R, Doster F, Zegeling PA. Nonmonotone saturation profiles for hydrostatic equilibrium in homogeneous porous media. *Vadose Zone J.* 2012;11:1-6. <https://doi.org/10.2136/vzj2012.0021>
25. Koch J, Rätz A, Schweizer B. Two-phase flow equations with a dynamic capillary pressure. *Eur J Appl Math.* 2013;24:49-75. <https://doi.org/10.1017/S0956792512000307>
26. Rätz A, Schweizer B. Hysteresis models and gravity fingering in porous media. *Z Angew Math Mech.* 2014;94:645-654. <https://doi.org/10.1002/zamm.201200052>
27. Zhuang L, Hassanizadeh SM, van Duijn C, Zimmermann S, Zizina I, Helmig R. Experimental and numerical studies of saturation overshoot during infiltration into a dry soil. *Vadose Zone J.* 2019;18:1-13. <https://doi.org/10.2136/vzj2018.09.0167>
28. Cushman JH, Bennethum LS, Hu BX. A primer on upscaling tools for porous media. *Adv Water Resour.* 2002;25:1043-1067. [https://doi.org/10.1016/S0309-1708\(02\)00047-7](https://doi.org/10.1016/S0309-1708(02)00047-7)
29. Hassanizadeh SM, Gray WG. General conservation equations for multi-phase systems: 1. Averaging procedure. *Adv Water Resour.* 1979;2:131-144.

30. Whitaker S. Flow in porous media II: the governing equations for immiscible, two-phase flow. *Transp Porous Media*. 1986;1:105-125.
31. Quintard M, Whitaker S. Two-phase flow in heterogeneous porous media: the method of large-scale averaging. *Transp Porous Media*. 1988;3:357-413. <https://doi.org/10.1007/BF00233177>
32. Hornung U., *Homogenization and Porous Media*. New York: Springer; 1997.
33. Auriault J. Nonsaturated deformable porous media: quasistatics. *Transp Porous Media*. 1987;2:45-64. <https://doi.org/10.1007/BF00208536>
34. Allaire G. Homogenization of the stokes flow in a connected porous medium. *Asymptotic Anal*. 1989;2:203-222. <https://doi.org/10.3233/ASY-1989-2302>
35. Allaire G. Homogenization of the Navier-Stokes equations with a slip boundary condition. *Commun Pure Appl Math*. 1991;44:605-641. <https://doi.org/10.1002/cpa.3160440602>
36. Mikelić A. Homogenization of nonstationary Navier-Stokes equations in a domain with a grained boundary. *Ann Mat Pura Appl*. 1991;158:167-179.
37. Mikelić A, Paoli L. On the derivation of the Buckley-Leverett model from the two fluid Navier–Stokes equations in a thin domain. *Comput Geosci*. 1997;1:59-83. <https://doi.org/10.1023/A:1011509010432>
38. Mikelić A. On an averaged model for the 2-fluid immiscible flow with surface tension in a thin cylindrical tube. *Comput Geosci*. 2003;7:183-196. <https://doi.org/10.1023/A:1025527716078>
39. Sharmin S, Bringedal C, Pop IS. On upscaling pore-scale models for two-phase flow with evolving interfaces. *Adv Water Resour*. 2020;142:103646. <https://doi.org/10.1016/j.advwatres.2020.103646>
40. Picchi D, Battiato I. The impact of pore-scale flow regimes on upscaling of immiscible two-phase flow in porous media. *Water Resour Res*. 2018;54:6683-6707. <https://doi.org/10.1029/2018WR023172>
41. van Noorden TL. Crystal precipitation and dissolution in a thin strip. *Eur J Appl Math*. 2009;20:69-91. <https://doi.org/10.1017/S0956792508007651>
42. Kumar K, van Noorden TL, Pop IS. Effective dispersion equations for reactive flows involving free boundaries at the microscale. *Multiscale Model Simul*. 2011;9:29-58. <https://doi.org/10.1137/100804553>
43. Bringedal C, Berre I, Pop IS, Radu FA. A model for non-isothermal flow and mineral precipitation and dissolution in a thin strip. *J Comput Appl Math*. 2015;289:346-355. <https://doi.org/10.1016/j.cam.2014.12.009>
44. Huh C, Scriven LE. Hydrodynamic model of steady movement of a solid/liquid/fluid contact line. *J Colloid Interface Sci*. 1971;35:85-101.
45. Dussan V EB, Davis SH. On the motion of a fluid-fluid interface along a solid surface. *J Fluid Mech*. 1974;65:71-95. <https://doi.org/10.1017/S0022112074001261>
46. Dussan V EB. On the spreading of liquids on solid surfaces: static and dynamic contact lines. *Annu Rev Fluid Mech*. 1979;11:371-400. <https://doi.org/10.1146/annurev.fl.11.010179.002103>
47. Ren W, Weinan E. Boundary conditions for the moving contact line problem. *Phys Fluids*. 2007;19:022101. <https://doi.org/10.1063/1.2646754>
48. Bonn D, Eggers J, Indekeu J, Meunier J, Rolley E. Wetting and spreading. *Rev Mod Phys*. 2009;81:739-805. <https://doi.org/10.1103/RevModPhys.81.739>
49. Sui Y, Ding H, Spelt PD. Numerical simulations of flows with moving contact lines. *Annu Rev Fluid Mech*. 2014;46:97-119. <https://doi.org/10.1146/annurev-fluid-010313-141338>
50. Hocking LM. A moving fluid interface on a rough surface. *J Fluid Mech*. 1976;76:801-817.
51. Huh C, Mason SG. The steady movement of a liquid meniscus in a capillary tube. *J Fluid Mech*. 1977;81:401-419. <https://doi.org/10.1017/S0022112077002134>
52. de Gennes PG. Wetting: statics and dynamics. *Rev Mod Phys*. 1985;57:827-863. <https://doi.org/10.1103/RevModPhys.57.827>
53. Haley PJ, Miksis MJ. The effect of the contact line on droplet spreading. *J Fluid Mech*. 1991;223:57-81. <https://doi.org/10.1017/S0022112091001337>
54. Sheng P, Zhou M. Immiscible-fluid displacement: contact-line dynamics and the velocity-dependent capillary pressure. *Phys Rev A*. 1992;45:5694-5708. <https://doi.org/10.1103/PhysRevA.45.5694>
55. Ren W, Hu D, Weinan E. Continuum models for the contact line problem. *Phys Fluids*. 2010;22:102103. <https://doi.org/10.1063/1.3501317>
56. Greenspan HP. On the motion of a small viscous droplet that wets a surface. *J Fluid Mech*. 1978;84:125-143. <https://doi.org/10.1017/S0022112078000075>

57. Cox RG. The dynamics of the spreading of liquids on a solid surface. Part 1. Viscous flow. *J Fluid Mech.* 1986;168:169-194. <https://doi.org/10.1017/S0022112086000332>
58. Baer TA, Cairncross RA, Schunk R, Rao RR, Sackinger PA. A finite element method for free surface flows of incompressible fluids in three dimensions. Part II. Dynamic wetting lines. *Int J Numer Meth Fluids.* 2000;33:405-427. [https://doi.org/10.1002/1097-0363\(20000615\)33:3<405::AID-FLD14>3.0.CO;2-4](https://doi.org/10.1002/1097-0363(20000615)33:3<405::AID-FLD14>3.0.CO;2-4)
59. Koplik J, Banavar JR, Willemsen JF. Molecular dynamics of Poiseuille flow and moving contact lines. *Phys Rev Lett.* 1988;60:1282-1285. <https://doi.org/10.1103/PhysRevLett.60.1282>
60. Koplik J, Banavar JR, Willemsen JF. Molecular dynamics of fluid flow at solid surfaces. *Phys. Fluids A Fluid Dyn.* 1989;1:781-794. <https://doi.org/10.1063/1.857376>
61. Thompson PA, Robbins MO. Simulations of contact-line motion: slip and the dynamic contact angle. *Phys Rev Lett.* 1989;63:766-769. <https://doi.org/10.1103/PhysRevLett.63.766>
62. Thompson PA, Brinckerhoff WB, Robbins MO. Microscopic studies of static and dynamic contact angles. *J Adhes Sci Technol.* 1993;7:535-554. <https://doi.org/10.1163/156856193X00844>
63. Koplik J, Banavar JR. Continuum deductions from molecular hydrodynamics. *Annu Rev Fluid Mech.* 1995;27:257-292. <https://doi.org/10.1146/annurev.fl.27.010195.001353>.
64. Jäger W, Mikelić A. On the roughness-induced effective boundary conditions for an incompressible viscous flow. *J Differ Equ.* 2001;170:96-122. <https://doi.org/10.1006/jdeq.2000.3814>
65. Maručić-Paloka E. Average of the Navier's law on the rapidly oscillating boundary. *J Math Anal Appl.* 2001;259:685-701. <https://doi.org/10.1006/jmaa.2001.7505>
66. Basson A, Gérard-Varet D. Wall laws for fluid flows at a boundary with random roughness. *Commun Pure Appl Math.* 2008;61:941-987. <https://doi.org/10.1002/cpa.20237>
67. Gérard-Varet D, Masmoudi N. Relevance of the slip condition for fluid flows near an irregular boundary. *Commun Math Phys.* 2010;295:99-137. <https://doi.org/10.1007/s00220-009-0976-0>
68. Blake TD. The physics of moving wetting lines. *J Colloid Interface Sci.* 2006;299:1-13. <https://doi.org/10.1016/j.jcis.2006.03.051>
69. Blake TD. Dynamic contact angles and wetting kinetics. In: Berg JC, ed. *Wettability*. New York: Marcel Dekker; 1993:251-309.
70. Ralston J, Popescu M, Sedev R. Dynamics of wetting from an experimental point of view. *Annu Rev Mater Res.* 2008;38:23-43. <https://doi.org/10.1146/annurev.matsci.38.060407.130231>
71. Voinov OV. Hydrodynamics of wetting. *Fluid Dyn.* 1976;11:714-721. <https://doi.org/10.1007/BF01012963>
72. Huh C, Mason SG. Effects of surface roughness on wetting (theoretical). *J Colloid Interface Sci.* 1977;60:11-38. [https://doi.org/10.1016/0021-9797\(77\)90251-X](https://doi.org/10.1016/0021-9797(77)90251-X)
73. Blake TD, Haynes JM. Kinetics of liquid/liquid displacement. *J Colloid Interface Sci.* 1969;30:421-423. [https://doi.org/10.1016/0021-9797\(69\)90411-1](https://doi.org/10.1016/0021-9797(69)90411-1)
74. Cherry BW, Holmes CM. Kinetics of wetting of surfaces by polymers. *J Colloid Interface Sci.* 1969;29:174-176. [https://doi.org/10.1016/0021-9797\(69\)90367-1](https://doi.org/10.1016/0021-9797(69)90367-1)
75. Van Dyke M., *Perturbation Methods in Fluid Mechanics*. Annotated edition. Stanford, CA: Parabolic Press; 1975.
76. The MathWorks Inc. *MATLAB® Version 9.8.0.1417392 (R2020a)*. 2020. <http://www.mathworks.com/products/matlab.html>
77. Lunowa SB. AsymptoticThinStripMCLSolver – Solver for the asymptotic model of immiscible two-phase flow with moving contact line in a thin strip. 2020. <https://github.com/s-lunowa/AsymptoticThinStripMCLSolver>

How to cite this article: Lunowa SB, Bringedal C, Pop IS. On an averaged model for immiscible two-phase flow with surface tension and dynamic contact angle in a thin strip. *Stud Appl Math.* 2021;1–43. <https://doi.org/10.1111/sapm.12376>

7 Two-phase flow in a periodic porous medium





The content of this chapter is based on the following original article:

S. Sharmin, M. Bastidas, C. Bringedal, and I. S. Pop. *Upscaling a Navier-Stokes-Cahn-Hilliard model for two-phase porous-media flow with solute-dependent surface tension effects*. *Applicable Analysis* (2022), doi: 10.1080/00036811.2022.2052858.

This is an accepted manuscript of an article published by Taylor & Francis Group in *Applicable Analysis* on 24.03.2022, available online: <https://www.tandfonline.com/10.1080/00036811.2022.2052858>.



Upscaling a Navier-Stokes-Cahn-Hilliard model for two-phase porous-media flow with solute-dependent surface tension effects

S. Sharmin ^a, M. Bastidas ^{a,b,c}, C. Bringedal ^d and I. S. Pop ^a

^aFaculty of Sciences, Hasselt University, Diepenbeek, Belgium; ^bInria, Paris, France; ^cCERMICS, Ecole des Ponts, Marne-la-Vallée, France; ^dStuttgart Center for Simulation Science, Institute for Modelling Hydraulic and Environmental Systems, University of Stuttgart, Stuttgart, Germany

ABSTRACT

We consider a model for the flow of two immiscible and incompressible fluid phases in a porous medium. A surfactant is dissolved in one of the fluid phases, and its concentration at the interface separating the two fluids can change the surface tension. At the scale of pores, we assume that the flow is governed by the Navier-Stokes equations, while for the phase separation, a Cahn-Hilliard phase-field model is adopted. Using formal homogenization, we derive a two-scale model describing the averaged behaviour of the system at the larger Darcy scale, where effective quantities are found through local (cell) problems at the smaller pore scale. For this two-scale model, we formulate a numerical scheme and present numerical results highlighting the influence of the solute-dependent surface tension.

ARTICLE HISTORY

Received 14 October 2021
Accepted 1 March 2022

COMMUNICATED BY

G. Allaire

KEYWORDS

Two-phase flow in porous media; variable surface tension; phase-field model; upscaling; homogenization

2020 MATHEMATICS

SUBJECT

CLASSIFICATIONS

35B27; 76S05; 35C20; 35L65; 76D05

1. Introduction

Many real-life applications of societal and technological relevance involve two-phase flow in porous media. Examples in this sense are groundwater remediation or oil recovery from reservoirs. In such situations, the flow and transport processes take place at the scale of pores, which is here considered the micro-scale. Moreover, in enhanced oil recovery [1,2], or applications involving, e.g. microfluidics [3,4], or thin-film flows [5,6], the surface tension between the two fluid phases is influenced by a solute present in one or both fluids.

Since the porous medium consists of many pores and its geometry is highly complex, numerical simulations using mathematical models defined at the pore scale would not be feasible for practical purposes. Moreover, in most cases, the primary interest is in the averaged behaviour of the system at a much larger scale, namely, the scale of the application. This scale will be named from now on the Darcy scale and can be viewed as a macro scale in contrast to the pore scale. From this prospect, it would be sufficient to use Darcy-scale models in the numerical simulation. However, when doing so, it becomes difficult to account properly for the processes at the pore scale. The main challenges are finding the appropriate equations, parameters at the Darcy scale and incorporating the pore-scale effects.

The starting point here is a pore-scale model, where two fluids occupy two disjoint subdomains of the pore space. The fluids are assumed incompressible and immiscible and are separated by an interface that moves with the fluids, thus in an *a priori* unknown manner. Furthermore, a (soluble)

surfactant species is present in one of the fluid phases. Its concentration affects the surface tension and, consequently, it influences the evolution of the fluid–fluid interface. As follows from the above, the pore-scale model involves a free boundary and is defined in a complex domain, namely, the pore space of a porous medium. It includes two major components: the flow of the two separate phases, and the diffusion and transport of the soluble surfactant.

When dealing with free-boundary problems, one can consider several mathematical modelling strategies. The simplest situation is when the domain is either one dimensional, or has a simple, rectangular or cylindrical structure, and the free boundary is along the symmetry axis. In this case, one can identify the free boundary through the distance to the domain boundary parts that are along the symmetry axis. Such a strategy is adopted, e.g. in [7,8]. In a similar context, but with a free boundary that is transversal to the symmetry axis, parametric curves or surfaces have been used to model two-phase flow in a pore [9,10].

More realistic situations can be considered when assuming periodically distributed grains. In this case, the simplest approach is to assume a radial symmetry for the grain, as well as for the free boundary. Then, the free boundary can be identified through the radius of the curve/surface, as done, e.g. in [11,12], where a model for water diffusion into absorbent particles is proposed. If the radial symmetry cannot be assumed, level sets can be used to identify the free boundary (see, e.g. [13–16]).

In the approaches mentioned above, the main difficulty in the analysis and numerical simulation of such mathematical models is related to the free boundary. To avoid using free boundaries and, consequently, working with time-dependent domains, the phase-field approach offers a good alternative. In this case, the free boundary is approximated by a diffuse interface region, and the model is hence defined in a fixed domain [17,18]. The phase-field indicator is a smooth approximation of, say, the characteristic function of the domain occupied by one of the fluid phases. Then, a critical aspect is to guarantee that, whenever the diffuse interface parameter approaches 0, the model reduces to the original one, involving free boundaries. Phase-field models can capture topological changes such as merging and splitting and have thus been used successfully for direct numerical simulation of multiphase flows [19,20]. For different applications, we refer to [21,22], where a (pore-scale) phase-field model is developed for a precipitation-dissolution model involving one fluid phase, to [23,24] for two fluid phases, to [25] for two-phase flow including temperature-dependent surface tension, and to [26,27] for fracture propagation in poroelastic media.

In this paper, we derive a two-scale model for the two-phase flow in a porous medium, in which surfactant-dependent surface-tension effects are taken into account. More specifically, at the pore scale, the surface tension depends on the concentration of the surfactant, which is soluble in one of the fluid phases. The starting point is a Cahn-Hilliard [28] approximation of the phase separation together with the Navier-Stokes equations for the flow of the two fluids. Such models have been considered in [29–31]. Alternatively, in [32–34], the pore-scale flow is described by the Stokes model. We prefer to use the Navier-stokes equation for capturing fully the physics of the two-phase fluid flow at the pore scale. We highlight that a thermodynamically consistent phase-field model for two-phase flow was first derived in [29], and later, two-phase flow models with surfactants were considered in [30]. Our model builds upon the model B derived in [30], where two-phase flow with variable surface tension is considered and the phase-field approach within a free energy framework is used to model the phase separation. We consider the instantaneous adsorption regime in [30] and simplify the model by assuming that the surfactant is only present in one of the fluid phases. Concerning numerical methods for similar types of models as discussed here, we refer to [35], where energy-stable schemes are proposed for a Cahn-Hilliard model for two-phase flow and surfactant transport, and to [36,37], where energy-stable methods based on discontinuous Galerkin discretization are analysed.

Referring strictly to two-phase flow in porous media, various upscaling techniques can be considered to derive Darcy-scale models. In this sense, we mention simple transversal averaging, volume averaging, and homogenization techniques. The former can be applied when a simple geometry is assumed, as done, e.g. in [7–10,38]. For volume averaging, we refer to [39,40]. For rigorous homogenization, we refer to [41–43], where the convergence of the upscaling process is proved.

Here we employ homogenization techniques for the formal derivation of the two-scale two-phase flow model, accounting for the surface-tension effects, as depending on the surfactant dissolved in one fluid phase. More precisely, we use formal asymptotic expansion methods and assume local periodicity at the pore scale. For similar results, we refer to [33,34,44,45] where no surfactant is present in the model, and to [32], where a solute transport component is included in the model, but without affecting the surface tension.

This paper is organized as follows. In Section 2, we present the Cahn-Hilliard-Navier-Stokes two-phase flow model with solute-dependent surface tension and give the sharp-interface limit of the phase-field model. In Section 3, we derive the upscaled model from the non-dimensional pore-scale phase-field model using the asymptotic expansion method. In Section 4, we present the numerical scheme for solving the two-scale model and then solve this model for some test cases in Section 5. Finally, in Section 6, we draw our conclusions and give some remarks for future research.

2. The pore-scale model

Here we discuss the pore-scale model for the two-phase flow in a porous medium. The fluids are assumed incompressible and immiscible. For each fluid phase, the flow is governed by the Navier-Stokes model, defined in the corresponding sub-domain, and with fluid-specific parameters. The model accounts for a concentration-dependent surface tension. The surfactant is assumed soluble in one of the two fluid phases, and its concentration solves a convection-diffusion equation defined in the sub-domain of the solvent.

The fluid–fluid interface appears as free boundaries at the pore scale. To describe its movement, one considers the force balance of stress connected to the surface tension and the tangential stress force. The surface tension varies with the surfactant concentration at the separating interface.

As mentioned before, to overcome the difficulties related to the free boundaries, we use the phase-field approximation developed in [30], in which one works with a mixture of both fluids. However, by excepting a thin, diffuse interface region, one can identify sub-domains in which one or another fluid is predominant. The evolution of the phase field is given by the Cahn-Hilliard equation.

In what follows, we let $\Omega_{\mathcal{P}}$ be the domain that can be occupied by the two fluids and denote its boundary by $\partial\Omega_{\mathcal{P}}$.

2.1. The sharp-interface model

In the sharp-interface model, one has two different fluid phases, indexed by i ($i = 1, 2$). We let $\rho^{(i)}, \mu^{(i)}, v^{(i)}, p^{(i)}$ ($i = 1, 2$) stand for the (constant) mass density, (constant) viscosity, velocity and pressure of fluid i . Moreover, these quantities are defined in the time-dependent subdomains $\Omega_{\mathcal{P}}^{(i)}(t)$, which correspond to the parts of $\Omega_{\mathcal{P}}$ occupied by fluid i . More precisely, the flow equations for fluid i read

$$\partial_t \left(\rho^{(i)} v^{(i)} \right) + \nabla \cdot \left(\rho^{(i)} v^{(i)} \otimes v^{(i)} \right) - \nabla \cdot \left(-p^{(i)} \mathbf{I} + 2\mu^{(i)} \mathcal{E}(v^{(i)}) \right) = 0, \quad (1a)$$

$$\nabla \cdot v^{(i)} = 0, \quad (1b)$$

for $t > 0$ and $x \in \Omega_{\mathcal{P}}^{(i)}(t)$. Here $\mathcal{E}(v^{(i)}) := \frac{1}{2}((\nabla v^{(i)}) + (\nabla v^{(i)})^T)$ is the symmetric stress tensor and \mathbf{I} is the identity matrix.

For the surfactant concentration c , soluble only in fluid 1, we have

$$\partial_t c + \nabla \cdot \left(v^{(1)} c \right) = \nabla \cdot (D \nabla c), \quad \text{in } \Omega_{\mathcal{P}}^{(1)}(t), \quad \text{for } t > 0, \quad (1c)$$

where $D > 0$ denotes the diffusion coefficient.

The fluid–fluid interface $\Gamma(t)$ is a free boundary, whose evolution is determined by the fluid velocities and the solute-dependent surface tension $\gamma(c)$. Several adsorption isotherms are proposed in [30],

stating the relationship between surface tension and the surface concentration of the solute. To relate the volume and surface concentrations, we follow the ideas in [30] and define the isotherm in terms of the product βc , where β is a length and c a volume concentration. In this way, βc is to be understood as the surface concentration. We assume that $\gamma(c)$ is linearly decreasing, namely, the Henry isotherm (see [30])

$$\gamma(c) = \gamma_0 - B\beta c. \quad (1d)$$

Here γ_0 is the surface tension of a clean interface and B is the sensitivity of the surface tension to the surfactant. For any $t > 0$, at $\Gamma(t)$, one has

$$\left[v^{(i)} \right] = 0, \quad (1e)$$

$$v^{(i)} \cdot n = v_n, \quad (1f)$$

$$\left[-p^{(i)} \mathbf{I} + 2\mu^{(i)} \mathcal{E}(v^{(i)}) \right] n = \gamma(c)\kappa n - \nabla_t \gamma(c), \quad (1g)$$

$$\left(-D\nabla c + v^{(1)} c \right) \cdot n = v_n c. \quad (1h)$$

Here $[\cdot]$ stands for the jump of the quantities from $\Omega_{\mathcal{P}}^{(1)}(t)$ to $\Omega_{\mathcal{P}}^{(2)}(t)$, κ is the mean curvature of $\Gamma(t)$ and v_n its normal velocity. Moreover, $\nabla_t \gamma(c) := \nabla \gamma(c) - n(n \cdot \nabla \gamma(c))$ is the tangential stress gradient, where n is the unit normal vector on $\Gamma(t)$ pointing into $\Omega_{\mathcal{P}}^{(1)}(t)$ from $\Omega_{\mathcal{P}}^{(2)}(t)$.

Note that the jump condition in (1g) has two components. In the direction normal to $\Gamma(t)$, the jump in the normal stress equal to $\gamma(c)\kappa$. In the tangential direction, the normal stress is given by the tangential component of $\nabla \gamma(c)$, multiplied by (-1) . In the case of constant surface tension, the tangential component vanishes. Finally, since no solute is present in fluid 2, (1h) expresses the conservation of solute across $\Gamma(t)$.

2.2. The phase-field model

In the phase-field model, the interface separating the two immiscible fluids is approximated by a diffuse interface. We consider the time interval $[0, \infty)$, and let $Q = (0, \infty) \times \Omega_{\mathcal{P}}$. A phase indicator $\phi : Q \rightarrow \mathbb{R}$ accounts for the presence of the two fluids, taking values either close to 1 in points occupied mainly by fluid 1 or close to -1 in points occupied mainly by fluid 2. Following [29,30], the energy of the fluid–fluid interface is approximated by the Ginzburg-Landau energy functional

$$e_{\text{free}}(\phi, \nabla \phi) = C \left(\frac{1}{\lambda} P(\phi) + \frac{\lambda}{2} |\nabla \phi|^2 \right), \quad (2)$$

where $\lambda > 0$ is the thickness of the diffuse interfacial region, $C = \frac{3}{2\sqrt{2}}$ is a calibration constant, while $P : \mathbb{R} \rightarrow \mathbb{R}$ is the double-well potential defined as

$$P(\phi) = \frac{1}{4} (1 - \phi^2)^2. \quad (3)$$

2.2.1. The Cahn-Hilliard equations

To describe the evolution of the phase field, we use the Cahn-Hilliard equation, written in mixed form as two coupled second-order equations. First,

$$\partial_t \phi + \nabla \cdot (v\phi) = m\lambda \Delta \psi, \quad \text{in } Q, \quad (4a)$$

where v is the velocity of the mixture and ψ is the potential. The Cahn-Hilliard mobility $m > 0$ is assumed here constant. Alternative choices for m are discussed in [29], leading to various sharp-interface models in the limit $\lambda \rightarrow 0$. Second, following Model B in [30], which corresponds to

instantaneous adsorption, and using (1d), one obtains

$$\psi = -\nabla \cdot (\mathcal{C}\lambda\gamma(c)\nabla\phi) + \frac{\mathcal{C}}{\lambda}\gamma(c)P'(\phi) + \frac{1}{\beta}\gamma(c)I'(\phi), \quad \text{in } Q, \quad (4b)$$

where $I : \mathbb{R} \rightarrow \mathbb{R}$ is defined as

$$I(\phi) = \frac{1}{2}(1 + \phi). \quad (4c)$$

As shown in [30], when $\lambda \rightarrow 0$, the phase field ϕ approaches the sign graph and, therefore, $I(\phi)$ approaches the characteristic function of fluid 1. Note the last term in (4b), which is added to include the effect of the varying surface tension.

For simplicity, we assume homogeneous Neumann boundary conditions for the phase field ϕ , as well as for the chemical potential ψ

$$\nabla\phi \cdot n = 0, \quad \text{and} \quad \nabla\psi \cdot n = 0, \quad \text{on } \partial\Omega_{\mathcal{P}}, \quad \text{for } t > 0, \quad (4d)$$

where n is the unit normal to $\partial\Omega_{\mathcal{P}}$ pointing out of $\Omega_{\mathcal{P}}$. The first boundary condition corresponds to a 90° contact angle, and the second is needed for conserving the mass of the phase field.

The Cahn-Hilliard Equations (4a) and (4b) are completed by the initial condition

$$\phi(0, \cdot) = \phi_{\text{init}}, \quad \text{in } \Omega_{\mathcal{P}}, \quad (4e)$$

where $\phi_{\text{init}} : \Omega_{\mathcal{P}} \rightarrow \mathbb{R}$ is a given function approximating the initial distribution of the two fluids in $\Omega_{\mathcal{P}}$.

2.2.2. The flow equations

Since the mixture velocity is volume averaged, and since we assume there is no excess volume after mixing, v is divergence free (see [29]),

$$\nabla \cdot v = 0, \quad \text{in } Q. \quad (4f)$$

Here, the density and viscosity of the mixture are defined as $\rho(\phi) = \frac{\rho^{(1)} \cdot (1+\phi)}{2} + \frac{\rho^{(2)} \cdot (1-\phi)}{2}$, $\mu(\phi) = \frac{\mu^{(1)} \cdot (1+\phi)}{2} + \frac{\mu^{(2)} \cdot (1-\phi)}{2}$.

The momentum conservation law is a modified Navier-Stokes equation

$$\begin{aligned} & \partial_t (\rho(\phi)v) + \nabla \cdot (\rho(\phi)v \otimes v) - \nabla \cdot (-p\mathbf{I} + 2\mu(\phi)\mathcal{E}(v) + v \otimes \rho'(\phi)\lambda m \nabla\psi) \\ & = \nabla \cdot (\gamma(c) (e_{\text{free}}(\phi, \nabla\phi)\mathbf{I} - \mathcal{C}\lambda\nabla\phi \otimes \nabla\phi)), \quad \text{in } Q, \end{aligned} \quad (4g)$$

where p is a rescaled pressure. Here the flux term $(v \otimes \rho'(\phi)\lambda m \nabla\psi)$ ensures thermodynamic consistency (see [29] and [30] for details) and the last two terms in (4g) account for the surface tension between the fluids. While such effects can be included in various ways (see [46]), here we adopt the approach in [30], based on the energy term $e_{\text{free}}(\phi, \nabla\phi)\mathbf{I}$ appearing in (4g). For convenience, from now on, we use the following equivalent formulation of the momentum equation (4g)

$$\begin{aligned} & \partial_t (\rho(\phi)v) + \nabla \cdot (\rho(\phi)v \otimes v) - \nabla \cdot (-p\mathbf{I} + 2\mu(\phi)\mathcal{E}(v) + v \otimes \rho'(\phi)\lambda m \nabla\psi) \\ & = \left(\frac{\mathcal{C}}{\lambda}\gamma(c)P'(\phi) - \nabla \cdot (\mathcal{C}\lambda\gamma(c)\nabla\phi) \right) \nabla\phi + \left(\frac{\mathcal{C}\lambda}{2}|\nabla\phi|^2 + \frac{\mathcal{C}}{\lambda}P(\phi) \right) \nabla\gamma(c), \quad \text{in } Q. \end{aligned} \quad (4h)$$

The solute transport model reads

$$\partial_t(I(\phi)c) + \nabla \cdot (I(\phi)vc) = \nabla \cdot (D I(\phi)\nabla c), \quad \text{in } Q. \quad (4i)$$

Note that as ϕ approaches -1 , $I(\phi)$ vanishes, which is in line with the assumption that the solute is only present in fluid 1.

We assume that the velocity and solute flux are zero on the boundary

$$v = \mathbf{0} \quad \text{and} \quad I(\phi) \nabla c \cdot n = 0 \quad \text{on } \partial\Omega_{\mathcal{P}}, \quad \text{for } t > 0. \quad (4j)$$

Furthermore, the initial velocity and concentration are assumed to be known, $v|_{t=0} = v_{\text{init}}$ and $in.in$.

Remark 2.1: Employing matched asymptotic expansions, in [30], it is shown that in the limit $\lambda \rightarrow 0$, the phase-field model discussed above reduces to the sharp-interface model in Section 2.1.

3. Upscaling the pore-scale model to the Darcy scale

As stated in the introduction, we assume that, at the pore scale, the porous medium Ω consists of small but many periodically distributed impermeable grains, surrounded by a void space (the pore space). We are interested in the averaged behaviour of the system, observed at the larger (Darcy) scale. At the same time, smaller (pore) scale information should not be disregarded. The pore scale and the Darcy scale are assumed well separated. With ℓ and L being the characteristic lengths of the pore scale and of the Darcy scale, we use $\epsilon = \frac{\ell}{L} \ll 1$ as the scale separation parameter.

To define the pore-scale domain, we write $Y = [0, \ell]^d$, ($d = 2, 3$) as the union of the grain \mathcal{G} , its boundary $\partial\mathcal{G}$ and the surrounding pore space \mathcal{P} ,

$$Y = \mathcal{P} \cup \mathcal{G} \cup \partial\mathcal{G}.$$

The entire porous medium occupies the domain

$$\Omega = \cup_{w \in W_{\Omega}} \{\ell w + Y\},$$

where $W_{\Omega} \subset \mathbb{Z}^d$ is a set of multi-indices. We assume that W_{Ω} is such that Ω is a connected set.

The phase-field model is defined in the entire pore space,

$$\Omega_{\mathcal{P}}^{\epsilon} = \cup_{w \in W_{\Omega}} \{\ell w + \mathcal{P}\},$$

which is also assumed to be connected.

The boundary of $\Omega_{\mathcal{P}}^{\epsilon}$ consists of the outer part, $\partial\Omega$, and the inner part, which is the union of the grain boundaries,

$$\Gamma_{\mathcal{G}}^{\epsilon} = \cup_{w \in W_{\Omega}} \{\ell w + \partial\mathcal{G}\}.$$

Note that the grains are not part of $\Omega_{\mathcal{P}}^{\epsilon}$. We refer to Figure 1 for a sketch of the domain.

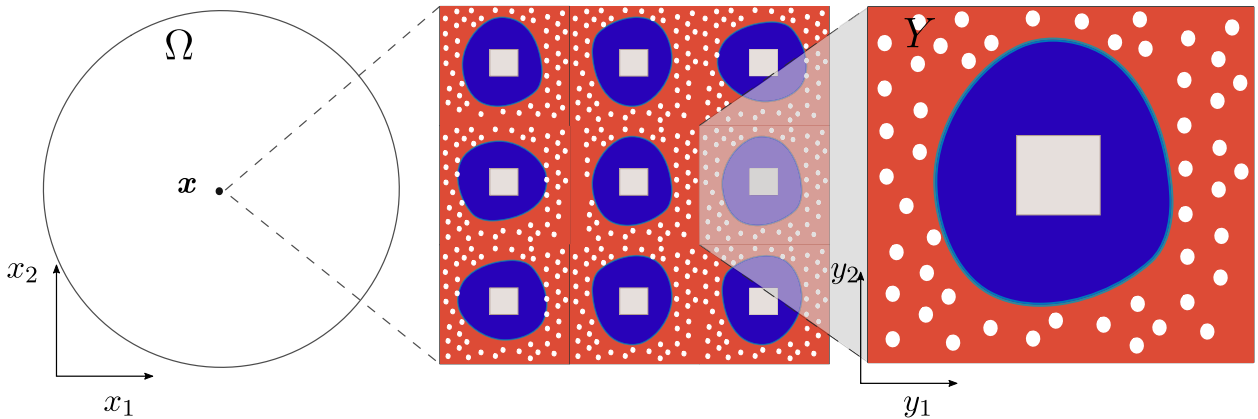


Figure 1. Schematic representation of the porous medium Ω . The figure in the middle presents periodically repeating grains (coloured gray) surrounded by void space (the pores) occupied by two immiscible fluids (blue, closer to the grains, and red, the outermost region). A surfactant soluble in fluid 1 is present (white particles). The right figure is a typical representation of a pore.

Table 1. Reference values and non-dimensional quantities.

Variables and parameters	Reference values	Units	Non-dimensional quantities
Time	t_{ref}	[s]	$\hat{t} = t/t_{\text{ref}}$
Space (Darcy scale)	$x_{\text{ref}} = L$	[m]	$\hat{x} = x/x_{\text{ref}}$
Space (pore scale)	$y_{\text{ref}} = \ell$	[m]	$\hat{y} = y/y_{\text{ref}}$
Velocity	$v_{\text{ref}} = x_{\text{ref}}/t_{\text{ref}}$	$[\frac{\text{m}}{\text{s}}]$	$\hat{v} = v/v_{\text{ref}}$
Pressure	p_{ref}	$[\frac{\text{kg}}{\text{m s}^2}]$	$\hat{p} = p/p_{\text{ref}}$
Molar concentration	c_{ref}	$[\frac{\text{mol}}{\text{m}^3}]$	$\hat{c} = c/c_{\text{ref}}$
Density	ρ_{ref}	$[\frac{\text{kg}}{\text{m}^3}]$	$\hat{\rho} = \rho/\rho_{\text{ref}}$
Viscosity	μ_{ref}	$[\frac{\text{kg}}{\text{m s}}]$	$\hat{\mu} = \mu/\mu_{\text{ref}}$
Surface tension	γ_{ref}	$[\frac{\text{kg}}{\text{s}^2}]$	$\hat{\gamma}(\hat{c}) = \gamma(c_{\text{ref}} \hat{c})/\gamma_{\text{ref}}$
Diffuse interface thickness	$\lambda_{\text{ref}} = y_{\text{ref}} = \ell$	[m]	$\hat{\lambda} = \lambda/y_{\text{ref}}$
	$\beta_{\text{ref}} = y_{\text{ref}} = \ell$	[m]	$\hat{\beta} = \beta/y_{\text{ref}}$
Free energy	$e_{\text{free,ref}} = \frac{1}{x_{\text{ref}}}$	$[\frac{1}{\text{m}}]$	$\hat{e}_{\text{free}} = e_{\text{free}} x_{\text{ref}}$
Cahn-Hilliard chemical potential	ψ_{ref}	$[\frac{\text{kg}}{\text{m s}^2}]$	$\hat{\psi} = \psi/\psi_{\text{ref}}$
Diffusion coefficient	D	$[\frac{\text{m}^2}{\text{s}}]$	
Cahn-Hilliard mobility	m	$[\frac{\text{m}^2 \text{s}}{\text{kg}}]$	

3.1. Non-dimensional model equations

For deriving the Darcy-scale model, we first bring the pore-scale model to a dimensionless form. To do so, we use the reference values and the non-dimensional quantities in Table 1, and the non-dimensional numbers

$$\begin{aligned}
 \text{Eu} &= \frac{p_{\text{ref}}}{\rho_{\text{ref}} v_{\text{ref}}^2}, & \text{Re} &= \frac{\rho_{\text{ref}} v_{\text{ref}} x_{\text{ref}}}{\mu_{\text{ref}}}, & \text{Ca} &= \frac{\mu_{\text{ref}} v_{\text{ref}}}{\gamma_{\text{ref}}}, \\
 \text{Pe}_c &= \frac{v_{\text{ref}} x_{\text{ref}}}{D}, & A_\phi &= \frac{m \psi_{\text{ref}}}{v_{\text{ref}}}, & A_\psi &= \frac{\gamma_{\text{ref}}}{x_{\text{ref}} \psi_{\text{ref}}}.
 \end{aligned} \tag{5}$$

Observe that the diffuse interface parameters λ and β are assumed to have the order of the pore-scale length ℓ . This corresponds to λ, β being of order $\mathcal{O}(\epsilon)$, as defined in Table 1. Here $\hat{\lambda}, \hat{\beta} \leq 1$, but these factors are independent of ϵ . Using the reference values and non-dimensional quantities from Table 1, and the non-dimensional numbers in (5), we obtain the dimensionless model

$$\begin{aligned}
 \partial_{\hat{t}}(\hat{\rho}(\phi)\hat{v}) + \hat{\nabla} \cdot (\hat{\rho}(\phi)\hat{v} \otimes \hat{v}) &= \hat{\nabla} \cdot \left(-\text{Eu} \hat{p} \mathbf{I} + \frac{1}{\text{Re}} 2\hat{\mu}(\phi) \mathcal{E}(\hat{v}) \right) \\
 &+ \hat{\nabla} \cdot \left(\epsilon A_\phi \hat{\lambda} \hat{\rho}'(\phi) \hat{v} \otimes \hat{\nabla} \hat{\psi} \right) + \frac{1}{\text{Re Ca}} \left(\frac{\mathcal{C}}{\epsilon \hat{\lambda}} \hat{\gamma}(\hat{c}) P'(\phi) - \hat{\nabla} \cdot (\epsilon \mathcal{C} \hat{\lambda} \hat{\gamma}(\hat{c}) \hat{\nabla} \phi) \right) \hat{\nabla} \phi \\
 &+ \frac{1}{\text{Re Ca}} \left(\frac{\epsilon \mathcal{C} \hat{\lambda}}{2} |\hat{\nabla} \phi|^2 + \frac{\mathcal{C}}{\epsilon \hat{\lambda}} P(\phi) \right) \hat{\nabla} \hat{\gamma}(\hat{c}),
 \end{aligned} \tag{6a}$$

$$\hat{\nabla} \cdot \hat{v} = 0, \tag{6b}$$

$$\partial_{\hat{t}}(I(\phi)\hat{c}) + \hat{\nabla} \cdot (I(\phi)\hat{v}\hat{c}) = \frac{1}{\text{Pe}_c} \hat{\nabla} \cdot (I(\phi)\hat{\nabla}\hat{c}), \tag{6c}$$

$$\partial_{\hat{t}}\phi + \hat{\nabla} \cdot (\hat{v}\phi) = \epsilon A_\phi \hat{\lambda} \hat{\Delta} \hat{\psi}, \tag{6d}$$

$$\hat{\psi} = A_\psi \left(\frac{\mathcal{C}}{\epsilon \hat{\lambda}} \hat{\gamma}(\hat{c}) P'(\phi) + \frac{1}{\epsilon \hat{\beta}} \hat{\gamma}(\hat{c}) I'(\phi) - \hat{\nabla} \cdot (\epsilon \mathcal{C} \hat{\lambda} \hat{\gamma}(\hat{c}) \hat{\nabla} \phi) \right), \tag{6e}$$

for all $x \in \hat{\Omega}_{\mathcal{P}}^{\epsilon}$ and $t > 0$. At the inner boundary $\hat{\Gamma}_{\mathcal{G}}^{\epsilon}$ and for $t > 0$, one has

$$\hat{v} = 0, \quad (6f)$$

$$I(\phi) \hat{\nabla} \hat{c} \cdot n = 0, \quad (6g)$$

$$\hat{\nabla} \phi \cdot n = 0, \quad (6h)$$

$$\hat{\nabla} \hat{\psi} \cdot n = 0. \quad (6i)$$

For the ease of presentation, since from now on, only the non-dimensional quantities are considered, the hat is omitted in all notations.

3.2. Derivation of the two-scale model

We derive the upscaled counterpart of the phase-field model in Section 2.2. To do so, we employ formal asymptotic expansions w.r.t. ϵ . More precisely, we assume that all variables can be expanded regularly in terms of ϵ . For example, for ϕ , one has

$$\phi(t, x) = \phi_0\left(t, x, \frac{x}{\epsilon}\right) + \epsilon \phi_1\left(t, x, \frac{x}{\epsilon}\right) + \mathcal{O}(\epsilon^2), \quad (7)$$

where the functions ϕ_i are Y -periodic w.r.t. the last argument. In other words, for $j = 1, \dots, d$ and with \mathbf{e}_j being the unit vector in the j -th direction, one has $\phi_i(t, x, y + \mathbf{e}_j) = \phi_i(t, x, y)$. Similar expansions are used for p, v, c . Note that the spatial variable x is doubled into the slow one, x , accounting for the changes at the Darcy scale, and the fast variable $y = \frac{x}{\epsilon}$, where the rapid oscillations occur. With this the j -th spatial derivative ∂_{x_j} becomes $\partial_{x_j} + \frac{1}{\epsilon} \partial_{y_j}$ and

$$\nabla = \frac{1}{\epsilon} \nabla_y + \nabla_x. \quad (8)$$

Observe that, unlike [45], we do not consider an additional fast time scale and do not disregard the $O(\epsilon)$ terms in the expansion of the phase field and of the velocity. At this point, we assume the following scaling of the dimensionless numbers (5),

$$\begin{aligned} \text{Eu} &= \epsilon^{-2} \overline{\text{Eu}}, & \text{Re} &= \overline{\text{Re}}, & \text{Ca} &= \overline{\text{Ca}}, \\ \text{Pe}_c &= \overline{\text{Pe}_c}, & A_\phi &= \overline{A_\phi}, & A_\psi &= \epsilon \overline{A_\psi}, \end{aligned} \quad (9)$$

where $\overline{\text{Eu}}, \overline{\text{Re}}, \overline{\text{Ca}}, \overline{\text{Pe}_c}, \overline{A_\phi}$ and $\overline{A_\psi}$ do not depend on ϵ . By choosing this scaling of the Euler number Eu and of the Reynolds number Re , we make sure that we are in the regime where Darcy's law is applicable, which corresponds to a laminar flow driven by the pressure gradient. The scaling of the capillary number Ca is chosen moderate w.r.t. ϵ . This choice results in equal pressures in both phases. Further, the Péclet number Pe_c is of order 1, which corresponds to the time scales of solute transport by advection and diffusion being of the same order. For simplicity, here $\overline{\text{Ca}} = \overline{\text{Pe}_c} = 1$. The scaling of A_ϕ and A_ψ is needed for the phase-field interface dynamics to be active at the pore scale.

For the ease of presentation, the dependency of t, x and y will in the following only be written whenever needed. Also, recall that all model variables are Y -periodic.

3.2.1. The flow equations

Inserting the asymptotic expansions in the reformulated momentum and mass conservation Equations (6a) and (6b), and in the no-slip boundary condition (6f), and applying (8), one obtains for all $t > 0$

$$-\frac{1}{\epsilon^3} \overline{\text{Eu}} \nabla_y p_0 - \frac{1}{\epsilon^2} \overline{\text{Eu}} (\nabla_x p_0 + \nabla_y p_1) + \frac{1}{\epsilon^2} \frac{1}{\overline{\text{Re}}} \nabla_y \cdot (2\mu(\phi_0) \mathcal{E}_y(v_0))$$

$$\begin{aligned}
 & + \frac{1}{\text{Re Ca}} \frac{1}{\epsilon^2} \left\{ \left(\frac{C}{\lambda} \gamma(c_0) P'(\phi_0) - C \lambda \nabla_y \cdot (\gamma(c_0) \nabla_y \phi_0) \right) \nabla_y \phi_0 \right. \\
 & \left. + C \left(\frac{\lambda}{2} |\nabla_y \phi_0|^2 + \frac{1}{\lambda} P(\phi_0) \right) \nabla_y \gamma(c_0) \right\} + \mathcal{O}(\epsilon^{-1}) = 0, \quad \text{in } \Omega \times \mathcal{P}, \quad (10a)
 \end{aligned}$$

$$\frac{1}{\epsilon} \nabla_y \cdot v_0 + \nabla_x \cdot v_0 + \nabla_y \cdot v_1 + \mathcal{O}(\epsilon) = 0, \quad \text{in } \Omega \times \mathcal{P}, \quad (10b)$$

$$v_0 + \epsilon v_1 + \mathcal{O}(\epsilon^2) = 0, \quad \text{on } \Omega \times \partial \mathcal{G}. \quad (10c)$$

Here \mathcal{E}_y is the counterpart of \mathcal{E} , but involving derivatives in the fast variable y . Since $|Y| = 1$, for all $t > 0$ and $x \in \Omega$ we define the averaged velocity as

$$\bar{v}(t, x) := \int_{\mathcal{P}} v_0(t, x, y) dy. \quad (11)$$

The lowest order term in (10b) provides

$$\nabla_y \cdot v_0 = 0, \quad (12)$$

for all $y \in \mathcal{P}$. Next, the ϵ^0 -order terms give

$$\nabla_x \cdot v_0 + \nabla_y \cdot v_1 = 0, \quad (13)$$

for all $y \in \mathcal{P}$. Integrating the above w.r.t y , applying the Gauss theorem, and using the periodicity of v_1 and the boundary condition $v_1 = 0$ on $\partial \mathcal{G}$, one gets

$$\nabla_x \cdot \bar{v} = 0, \quad (14)$$

for all $t > 0$ and $x \in \Omega$. Equating the dominating $\mathcal{O}(\epsilon^{-3})$ term in (10a) gives

$$\nabla_y p_0 = 0,$$

for all $y \in \mathcal{P}$, so $p_0 = p_0(t, x)$. Further, in Section 3.2.3 we also show that $c_0 = c_0(t, x)$ is independent of y , and, therefore, the last $\mathcal{O}(\epsilon^{-2})$ terms in (10a) are vanishing. Hence, the $\mathcal{O}(\epsilon^{-2})$ terms in (10a) yield

$$\begin{aligned}
 \overline{\text{Eu}} \nabla_y p_1 - \frac{1}{\text{Re}} \nabla_y \cdot (2\mu(\phi_0) \mathcal{E}_y(v_0)) &= -\overline{\text{Eu}} \nabla_x p_0 \\
 + \frac{1}{\text{ReCa}} \gamma(c_0) \left(\frac{C}{\lambda} P'(\phi_0) - C \lambda \Delta_y \phi_0 \right) \nabla_y \phi_0, & \quad (15)
 \end{aligned}$$

for all $t > 0$, $x \in \Omega$ and $y \in \mathcal{P}$. Observe that (15) and (12) form a Stokes system in terms of the unknowns p_1 and v_0 , depending on p_0 , ϕ_0 and c_0 . This dependence can be made more precise through the cell problems, defined for all $x \in \Omega$ and $t > 0$,

$$\begin{cases} \overline{\text{Eu}} (\mathbf{e}_j + \nabla_y \Pi_j) = -\frac{1}{\text{Re}} \nabla_y \cdot (2\mu(\phi_0) \mathcal{E}_y(\mathbf{w}_j)), & \text{in } \mathcal{P}, \\ \nabla_y \cdot \mathbf{w}_j = 0, & \text{in } \mathcal{P}, \\ \mathbf{w}_j = \mathbf{0}, & \text{on } \partial \mathcal{G}, \\ \Pi_j, \mathbf{w}_j \text{ are } Y\text{-periodic} \quad \text{and} \quad \int_{\mathcal{P}} \Pi_j dy = 0, & \end{cases} \quad (16)$$

for $j = 1, \dots, \bar{d}$, and

$$\begin{cases} \overline{\text{Eu}} \nabla_y \Pi_0 = -\frac{1}{\text{Re}} \nabla_y \cdot (2\mu(\phi_0) \mathcal{E}_y(\mathbf{w}_0)) \\ \quad + \frac{1}{\text{Re Ca}} \left(\frac{C}{\lambda} P'(\phi_0) - C\lambda \Delta_y \phi_0 \right) \nabla_y \phi_0, & \text{in } \mathcal{P}, \\ \nabla_y \cdot \mathbf{w}_0 = 0, & \text{in } \mathcal{P}, \\ \mathbf{w}_0 = \mathbf{0}, & \text{on } \partial \mathcal{G}, \\ \Pi_0, \mathbf{w}_0 \text{ are } Y\text{-periodic} \quad \text{and} \quad \int_{\mathcal{P}} \Pi_0 \, dy = 0. \end{cases} \quad (17)$$

By linearity, having solved the cell problems above, one immediately gets v_0 and p_1 as functions of p_0 , c_0 and, implicitly, of ϕ_0

$$v_0(t, x, y) = - \sum_{j=1}^d \mathbf{w}_j(t, x, y) \partial_{x_j} p_0(t, x) - \mathbf{w}_0(t, x, y) \gamma(c_0(t, x)), \quad (18)$$

$$p_1(t, x, y) = \tilde{p}_1(t, x) + \sum_{j=1}^d \Pi_j(t, x, y) \partial_{x_j} p_0(t, x) + \Pi_0(t, x, y) \gamma(c_0(t, x)). \quad (19)$$

Here $\tilde{p}_1 = \tilde{p}_1(t, x)$ is an arbitrary function not depending on y . Integrating (19) w.r.t. y over \mathcal{P} and using (11) yields

$$\bar{v} = -\mathcal{K} \nabla_x p_0 - M \gamma(c_0), \quad (20)$$

for all $x \in \Omega$ and $t > 0$. The elements of the effective matrix $\mathcal{K}(t, x)$ and the components of the effective vector $M(t, x)$ are obtained using the solutions of the cell problems (16) and (17),

$$\mathcal{K}_{i,j} = \int_{\mathcal{P}} \mathbf{w}_{i,j} \, dy \quad \text{and} \quad M_i = \int_{\mathcal{P}} \mathbf{w}_{i,0} \, dy, \quad \text{with } i, j = 1, \dots, \bar{d}, \quad (21)$$

where $\mathbf{w}_{i,\alpha}$ is the i -th component of \mathbf{w}_α ($\alpha \in \{0, \dots, \bar{d}\}$).

3.2.2. The Cahn-Hilliard equations

By Taylor expansions about ϕ_0 and c_0 , we can write

$$P(\phi) = P(\phi_0) + \epsilon \phi_1 P'(\phi_0) + \mathcal{O}(\epsilon^2), \quad \gamma(c) = \gamma(c_0) + \epsilon c_1 \gamma'(c_0) + \mathcal{O}(\epsilon^2). \quad (22)$$

Using this and the homogenization ansatz (7) in Equation (6d), (6e), (6h) and (6i), one gets for all $t > 0$

$$\begin{aligned} \mathcal{O}(\epsilon) = & \frac{1}{\epsilon} \nabla_y \cdot (v_0 \phi_0) - \frac{1}{\epsilon} \overline{A_\phi} \lambda \Delta_y \psi_0 + \partial_t \phi_0 + \nabla_x \cdot (v_0 \phi_0) \\ & - \overline{A_\phi} \lambda (\nabla_x \cdot (\nabla_y \psi_0) + \nabla_y \cdot (\nabla_x \psi_0) + \Delta_y \psi_1), \quad \text{in } \Omega \times \mathcal{P}, \end{aligned} \quad (23a)$$

$$\mathcal{O}(\epsilon) = \psi_0 - \gamma(c_0) \overline{A_\psi} \left(\frac{C P'(\phi_0)}{\lambda} + \frac{I'(\phi_0)}{\beta} - C\lambda \Delta_y \phi_0 \right), \quad \text{in } \Omega \times \mathcal{P}, \quad (23b)$$

$$\mathcal{O}(\epsilon) = \frac{1}{\epsilon} \nabla_y \phi_0 \cdot n + \nabla_x \phi_0 \cdot n + \nabla_y \phi_1 \cdot n, \quad \text{on } \Omega \times \partial \mathcal{G}, \quad (23c)$$

$$\mathcal{O}(\epsilon) = \frac{1}{\epsilon} \nabla_y \psi_0 \cdot n + \nabla_x \psi_0 \cdot n + \nabla_y \psi_1 \cdot n, \quad \text{on } \Omega \times \partial \mathcal{G}. \quad (23d)$$

Since $|Y| = 1$, the porosity of the medium is defined as

$$\Phi := |\mathcal{P}|. \quad (24)$$

We also define

$$\bar{\phi}(t, x) := \frac{1}{\Phi} \int_{\mathcal{P}} \phi_0(t, x, y) \, dy. \quad (25)$$

Since ϕ_0 approaches 1 inside fluid 1, we use (4c) to define the fluid 1 saturation as

$$S := \frac{1}{\Phi} \int_{\mathcal{P}} I(\phi_0) \, dy = \frac{1}{2} (1 + \bar{\phi}), \quad (26)$$

for all $t > 0$ and $x \in \Omega$. Equating the lowest order terms in (23a)–(23d), and using (26), one gets the local cell problem for the phase field and the potential,

$$\begin{cases} \nabla_y \cdot (v_0 \phi_0) = \overline{A_\phi} \lambda \Delta_y \psi_0, & \text{in } \mathcal{P}, \\ \psi_0 = \gamma(c_0) \overline{A_\psi} \left(\frac{CP'(\phi_0)}{\lambda} + \frac{I'(\phi_0)}{\beta} - C\lambda \Delta_y \phi_0 \right), & \text{in } \mathcal{P}, \\ \nabla_y \phi_0 \cdot n = 0, & \text{on } \partial \mathcal{G}, \\ \nabla_y \psi_0 \cdot n = 0, & \text{on } \partial \mathcal{G}, \\ \phi_0, \psi_0 \text{ are } Y\text{-periodic, and } \frac{1}{\Phi} \int_{\mathcal{P}} \phi_0 \, dy = 2S - 1, \end{cases} \quad (27)$$

for all $t > 0$ and $x \in \Omega$, where v_0 is defined in (19). Observe that in the above equations only spatial derivatives w.r.t. y are present. The constraint $\frac{1}{\Phi} \int_{\mathcal{P}} \phi_0 \, dy = 2S - 1$ follows from (26) and ensures the uniqueness of a solution.

The ϵ^0 -order terms in (23a) equate to

$$\partial_t \phi_0 + \nabla_x \cdot (v_0 \phi_0) = \overline{A_\phi} \lambda \{ \nabla_x \cdot (\nabla_y \psi_0) + \nabla_y \cdot (\nabla_x \psi_0) + \Delta_y \psi_1 \}, \quad (28)$$

for all $t > 0$, $x \in \Omega$ and $y \in \mathcal{P}$. Integrating the above equation over \mathcal{P} w.r.t y and using the periodicity of ψ_0 and ψ_1 yields

$$\partial_t \int_{\mathcal{P}} \phi_0 \, dy + \nabla_x \cdot \int_{\mathcal{P}} (v_0 \phi_0) \, dy = 0, \quad (29)$$

for all $t > 0$ and $x \in \Omega$. Using (26), this becomes

$$\Phi \partial_t S + \frac{1}{2} \nabla_x \cdot \bar{v}^\phi = 0, \quad (30)$$

for all $t > 0$ and $x \in \Omega$, where \bar{v}^ϕ is the ϕ -dependent velocity given by

$$\bar{v}^\phi(t, x) := \int_{\mathcal{P}} v_0(t, x, y) \phi_0(t, x, y) \, dy. \quad (31)$$

Using (19) in the above equation, one finds

$$\bar{v}^\phi = -\mathcal{K}^\phi \nabla_x p_0 - M^\phi \gamma(c_0), \quad (32)$$

for all $t > 0$ and $x \in \Omega$, where the elements of the effective matrix $\mathcal{K}^\phi(t, x)$ and the components of the effective vector $M^\phi(t, x)$ are defined by

$$\mathcal{K}_{i,j}^\phi := \int_{\mathcal{P}} \mathbf{w}_{i,j} \phi_0 \, dy \quad \text{and} \quad M_i^\phi := \int_{\mathcal{P}} \mathbf{w}_{i,0} \phi_0 \, dy, \quad \text{for } i, j = 1, \dots, d. \quad (33)$$

Again, \mathbf{w}_j and \mathbf{w}_0 are the solutions of the cell problems (16) and (17).

3.2.3. Solute conservation equation

Using the homogenization ansatz in (6c) and (6g) provides

$$\begin{aligned}
& -\frac{1}{\epsilon^2} \frac{1}{\text{Pe}_c} \nabla_y \cdot (I(\phi_0) \nabla_y c_0) + \frac{1}{\epsilon} \nabla_y \cdot (I(\phi_0) v_0 c_0) - \frac{1}{\epsilon} \frac{1}{\text{Pe}_c} \nabla_x \cdot (I(\phi_0) \nabla_y c_0) \\
& - \frac{1}{\epsilon} \frac{1}{\text{Pe}_c} \nabla_y \cdot \left(I(\phi_0) (\nabla_x c_0 + \nabla_y c_1) + \phi_1 \frac{1}{2} \nabla_y c_0 \right) + \partial_t (I(\phi_0) c_0) + \nabla_x \cdot (I(\phi_0) v_0 c_0) \\
& + \nabla_y \cdot \left(I(\phi_0) (v_0 c_1 + v_1 c_0) + \phi_1 \frac{1}{2} v_0 c_0 \right) \\
& - \frac{1}{\text{Pe}_c} \nabla_y \cdot \left(I(\phi_0) (\nabla_x c_1 + \nabla_y c_2) + \phi_1 \frac{1}{2} (\nabla_x c_0 + \nabla_y c_1) \right) \\
& - \frac{1}{\text{Pe}_c} \nabla_x \cdot \left(I(\phi_0) (\nabla_x c_0 + \nabla_y c_1) + \phi_1 \frac{1}{2} \nabla_y c_0 \right) + \mathcal{O}(\epsilon) = 0, \quad \text{in } \Omega \times \mathcal{P}, \tag{34a}
\end{aligned}$$

$$\begin{aligned}
& \frac{1}{\epsilon} I(\phi_0) \nabla_y c_0 \cdot n + I(\phi_0) (\nabla_x c_0 + \nabla_y c_1) \cdot n + \epsilon I(\phi_0) (\nabla_x c_1 + \nabla_y c_2) \cdot n \\
& + \epsilon \phi_1 \frac{1}{2} \nabla_y c_0 \cdot n + \mathcal{O}(\epsilon^2) = 0, \quad \text{on } \Omega \times \partial \mathcal{G}. \tag{34b}
\end{aligned}$$

The lowest order term from the above equations gives, for all $t > 0$ and $x \in \Omega$,

$$\begin{aligned}
& \nabla_y \cdot (I(\phi_0) \nabla_y c_0) = 0, \quad \text{in } \mathcal{P}, \quad \text{and} \\
& I(\phi_0) \nabla_y c_0 \cdot n = 0, \quad \text{on } \partial \mathcal{G}.
\end{aligned}$$

Using the Y -periodicity of c_0 , one immediately gets that $c_0 = c_0(t, x)$ is independent of y . Further, the ϵ^{-1} -order terms in (34a) equate to

$$\frac{1}{\text{Pe}_c} \nabla_y \cdot (I(\phi_0) \nabla_y c_1) = -\frac{1}{\text{Pe}_c} \nabla_y \cdot (I(\phi_0) \nabla_x c_0) + c_0 (\nabla_y \cdot (I(\phi_0) v_0)), \tag{35}$$

for all $t > 0$, $x \in \Omega$ and $y \in \mathcal{P}$. This, together with the boundary condition (34a), allows obtaining c_1 in terms of ϕ_0 , c_0 and v_0 , by solving the cell problems

$$\begin{cases} \nabla_y \cdot [I(\phi_0) (\nabla_y \chi_j + \mathbf{e}_j)] = 0, & \text{in } \mathcal{P}, \\ I(\phi_0) (\nabla_y \chi_j + \mathbf{e}_j) \cdot n = 0, & \text{on } \partial \mathcal{G}, \\ \chi_j \text{ is } Y\text{-periodic and } \int_{\mathcal{P}} \chi_j \, dy = 0, \end{cases} \tag{36}$$

for $j = 1, \dots, d$, and

$$\begin{cases} \nabla_y \cdot [I(\phi_0) \nabla_y \chi_0] = \nabla_y \cdot (I(\phi_0) v_0), & \text{in } \mathcal{P}, \\ I(\phi_0) \nabla_y \chi_0 \cdot n = 0, & \text{on } \partial \mathcal{G}, \\ \chi_0 \text{ is } Y\text{-periodic and } \int_{\mathcal{P}} \chi_0 \, dy = 0. \end{cases} \tag{37}$$

With (36) and (37), one has for all $t > 0$, $x \in \Omega$ and $y \in \mathcal{P}$

$$c_1(t, x, y) = \tilde{c}_1(t, x) + \sum_{j=1}^d \chi_j(t, x, y) \partial_{x_j} c_0(t, x) + \chi_0(t, x, y) c_0(t, x), \tag{38}$$

where $\tilde{c}_1 = \tilde{c}_1(t, x)$ is arbitrary. Finally, the ϵ^0 -order terms in (34a) equate to

$$\partial_t (I(\phi_0) c_0) + \nabla_x \cdot (I(\phi_0) v_0 c_0) - \frac{1}{\text{Pe}_c} \nabla_x \cdot (I(\phi_0) (\nabla_x c_0 + \nabla_y c_1))$$

$$\begin{aligned}
 &= -\nabla_y \cdot \left(I(\phi_0) (v_0 c_1 + v_1 c_0) + \phi_1 \frac{1}{2} v_0 c_0 \right) + \frac{1}{\text{Pe}_c} \nabla_y \cdot (I(\phi_0) (\nabla_x c_1 + \nabla_y c_2)) \\
 &\quad + \frac{1}{\text{Pe}_c} \nabla_y \cdot \left(\phi_1 \frac{1}{2} (\nabla_x c_0 + \nabla_y c_1) \right), \tag{39}
 \end{aligned}$$

for all $t > 0$, $x \in \Omega$ and $y \in \mathcal{P}$. Integrating the above w.r.t y over \mathcal{P} , using the definitions of the averaged velocity and ϕ -dependent velocity in (11) and (31), together with the periodicity, one gets the macroscopic law for the solute conservation

$$\Phi \partial_t (S c_0) + \frac{1}{2} \nabla_x \cdot (c_0 (\bar{v} + \bar{v}^\phi)) = \frac{1}{\text{Pe}_c} \nabla_x \cdot (\mathcal{B} \nabla_x c_0 + H c_0), \tag{40}$$

for all $t > 0$ and $x \in \Omega$. Here the elements of the effective matrix $\mathcal{B}(t, x)$ and the components of the effective vector $H(t, x)$ are determined by

$$\mathcal{B}_{i,j} = \int_{\mathcal{P}} I(\phi_0) (\delta_{ij} + \partial_{y_i} \chi_j) dy, \quad H_i = \int_{\mathcal{P}} I(\phi_0) \partial_{y_i} \chi_0 dy, \tag{41}$$

for $i, j = 1, \dots, d$, and where χ_j and χ_0 solve the cell problems (36) and (37).

3.3. Summary of upscaled model

To simplify the notation, from here we give up the indices 0 in v_0, ϕ_0, ψ_0, p_0 , and c_0 . With this, the Darcy-type laws in (20) and (32) for the velocities, and the mass conservation laws for the two fluids and for the solute in (14), (30), and (40) can be written as follows:

$$\bar{v} = -\mathcal{K} \nabla p - M \gamma(c), \tag{42a}$$

$$\nabla \cdot \bar{v} = 0, \tag{42b}$$

$$\Phi \partial_t S + \frac{1}{2} \nabla \cdot \bar{v}^\phi = 0, \tag{42c}$$

$$\bar{v}^\phi = -\mathcal{K}^\phi \nabla p - M^\phi \gamma(c), \tag{42d}$$

$$\Phi \partial_t (S c) + \frac{1}{2} \nabla \cdot (c (\bar{v} + \bar{v}^\phi)) = \frac{1}{\text{Pe}_c} \nabla \cdot (\mathcal{B} \nabla c + H c), \tag{42e}$$

defined for all $t > 0$ and $x \in \Omega$. The Darcy-scale unknowns are $\bar{v}(t, x)$, $S(t, x)$, $\bar{v}^\phi(t, x)$, $p(t, x)$, and $c(t, x)$. This system is completed with boundary conditions on $\partial\Omega$, and the initial solute concentration c_{init} . Moreover, an initial (pore-scale) phase field ϕ_{init} is prescribed at each Darcy-scale point, yielding an initial saturation S_{init} satisfying (26). The effective parameters $\mathcal{K}, \mathcal{K}^\phi, M, M^\phi, \mathcal{B}$ and H are obtained by solving cell problems, as given in Table 2.

To calculate the effective quantities, one needs the phase field $\phi(t, x, y)$. This is obtained by solving for all $t > 0$ and $x \in \Omega$ the problem

$$\begin{cases}
 \nabla_y \cdot (v\phi) = \overline{A_\phi} \lambda \Delta_y \psi, & \text{in } \mathcal{P}, \\
 \psi = \overline{A_\psi} \gamma(c) \left(\frac{CP'(\phi)}{\lambda} + \frac{I'(\phi)}{\beta} - C\lambda \Delta_y \phi \right), & \text{in } \mathcal{P}, \\
 \nabla_y \phi \cdot n = 0, \nabla_y \psi \cdot n = 0 & \text{on } \partial\mathcal{G}, \\
 \phi \text{ and } \psi \text{ are } Y\text{-periodic and } \frac{1}{\Phi} \int_{\mathcal{P}} \phi dy = 2S - 1. &
 \end{cases} \tag{43}$$

Here v is nothing but the pore-scale velocity v_0 in (19), namely,

$$v(t, x, y) = - \sum_{j=1}^d \mathbf{w}_j(t, x, y) \partial_{x_j} p(t, x) - \mathbf{w}_0(t, x, y) \gamma(c(t, x)). \tag{44}$$

Table 2. Parameters for the upscaled model (42a).

Effective parameters	Cell problems
$\mathcal{K}_{i,j} = \int_{\mathcal{P}} \mathbf{w}_{i,j} \, dy,$	$\overline{\mathbf{E}u}(\mathbf{e}_j + \nabla_y \Pi_j) = -\frac{1}{\text{Re}} \nabla_y \cdot (2\mu(\phi) \mathcal{E}_y(\mathbf{w}_j)),$ in $\mathcal{P},$
$\mathcal{K}_{i,j}^\phi = \int_{\mathcal{P}} \mathbf{w}_{i,j} \phi \, dy.$	$\nabla_y \cdot \mathbf{w}_j = 0,$ in $\mathcal{P},$
	$\mathbf{w}_j = \mathbf{0},$ on $\partial\mathcal{G},$
	Π_j, \mathbf{w}_j are Y -periodic and $\int_{\mathcal{P}} \Pi_j \, dy = 0,$ for $j = 1, \dots, d.$
$M_i = \int_{\mathcal{P}} \mathbf{w}_{i,0} \, dy,$	$\overline{\mathbf{E}u} \nabla_y \Pi_0 = -\frac{1}{\text{Re}} \nabla_y \cdot (2\mu(\phi) \mathcal{E}_y(\mathbf{w}_0)) + \frac{1}{\text{Re Ca}} \left(\frac{C}{\lambda} P'(\phi) - C\lambda \Delta_y \phi \right) \nabla_y \phi,$ in $\mathcal{P},$
$M_i^\phi = \int_{\mathcal{P}} \mathbf{w}_{i,0} \phi \, dy.$	$\nabla_y \cdot \mathbf{w}_0 = 0,$ in $\mathcal{P},$
	$\mathbf{w}_0 = \mathbf{0},$ on $\partial\mathcal{G},$
	Π_0, \mathbf{w}_0 are Y -periodic and $\int_{\mathcal{P}} \Pi_0 \, dy = 0.$
$\mathcal{B}_{i,j} = \int_{\mathcal{P}} l(\phi)(\delta_{ij} + \partial_{y_i} \chi_j) \, dy.$	$\nabla_y \cdot [l(\phi)(\nabla_y \chi_j + \mathbf{e}_j)] = 0,$ in $\mathcal{P},$
	$l(\phi)(\nabla_y \chi_j + \mathbf{e}_j) \cdot \mathbf{n} = 0,$ on $\partial\mathcal{G},$
	χ_j is Y -periodic and $\int_{\mathcal{P}} \chi_j \, dy = 0,$ for $j = 1, \dots, d.$
$H_i = \int_{\mathcal{P}} l(\phi) \partial_{y_i} \chi_0 \, dy.$	$\nabla_y \cdot [l(\phi) \nabla_y \chi_0] = \nabla_y \cdot (l(\phi_0) \mathbf{v}),$ in $\mathcal{P},$
	$l(\phi) \nabla_y \chi_0 \cdot \mathbf{n} = 0,$ on $\partial\mathcal{G},$
	χ_0 is Y -periodic and $\int_{\mathcal{P}} \chi_0 \, dy = 0.$

Remark 3.1: Inspired by the definition of the fluid 1 saturation S in (26), and since $\frac{1}{2}(\bar{v} + \bar{v}^\phi) = \frac{1}{2} \int_{\mathcal{P}} v_0(1 + \phi) \, dy$ and $\frac{1}{2}(\bar{v} - \bar{v}^\phi) = \frac{1}{2} \int_{\mathcal{P}} v_0(1 - \phi) \, dy$, one can identify the quantities corresponding to fluid i and reformulate the Darcy-scale equations accordingly. More precisely, we consider the (Darcy-scale) fluid-specific quantities

$$S^{(1)} = S, \quad \bar{v}^{(1)} = \frac{1}{2}(\bar{v} + \bar{v}^\phi), \quad \mathcal{K}^{(1)} = \frac{\mathcal{K} + \mathcal{K}^\phi}{2}, \quad M^{(1)} = \frac{M + M^\phi}{2},$$

$$S^{(2)} = 1 - S, \quad \bar{v}^{(2)} = \frac{1}{2}(\bar{v} - \bar{v}^\phi), \quad \mathcal{K}^{(2)} = \frac{\mathcal{K} - \mathcal{K}^\phi}{2}, \quad M^{(2)} = \frac{M - M^\phi}{2}.$$

Then, for all $t > 0$ and $x \in \Omega$, the Darcy-scale Equations (42a)–(42d) become

$$\bar{v}^{(i)} = -\mathcal{K}^{(i)} \nabla p - M^{(i)} \gamma(c), \quad (45a)$$

$$\Phi \partial_t S^{(i)} + \nabla \cdot \bar{v}^{(i)} = 0, \quad (45b)$$

Note that (45a) is an enriched Darcy law, where the last term accounts for the surfactant effects, leading to a variable surface-tension. Additionally, $\mathcal{K}^{(i)}$ is the relative permeability of fluid i multiplied by the absolute permeability of the medium, and $M^{(i)}$ is connected to the effective variable surface-tension effect of the fluid phases. Finally, since $\bar{v}^{(1)} + \bar{v}^{(2)} = \bar{v}$, (42b) implies that the total flow is divergence-free. Moreover, even if the surface tension is constant, (45a) is still an enriched Darcy law because $\mathcal{K}^{(i)}$ and $M^{(i)}$ both depend on ϕ , which is determined from (43).

Observe that (45a) and (45b) are similar to the standard effective model for two-phase flow when assuming a zero capillary pressure, respectively, that the phase pressures are equal. In simplified geometries, such models are derived by transversal averaging, but assuming that the capillary number is moderate compared to ϵ , namely, $O(1)$ (see [8,10]). Additionally, a nonlinear fourth-order parabolic equation is obtained in [9] for constant surface tension with capillary pressure, whereas in [7], the Buckley–Leverett equations are derived in the absence of surface tension.

Models disregarding the capillary pressure effects are quite popular in the numerical simulation of two-phase porous-media flows. Compared to these, even if the presence of a soluble surfactant is disregarded, one aspect is much different in the Darcy-scale model derived here. Commonly used models build on a relationship between the relative permeability of a fluid phase and its saturation. Here, no such relationship is assumed, as the permeability is obtained from the pore scale, by solving the corresponding cell problems.

4. An explicit numerical scheme

For solving the two-scale model summarized in Section 3.3, we consider a simple, explicit numerical scheme. Given $N \in \mathbb{N}$, we define the time step $\Delta t := T/N$ and let $t^n = n\Delta t$. The time-discrete functions are denoted by

$$\phi^n := \phi(t^n, \cdot, \cdot), \quad v^n := v(t^n, \cdot) \quad \text{and} \quad \eta_j^n := \eta_j(t^n, \cdot),$$

where $v \in \{\mathcal{K}^\phi, \mathcal{K}, M^\phi, M, \mathcal{B}, H, p, \bar{v}, \bar{v}^\phi, S, c\}$, and $\eta_j \in \{\Pi_j, \mathbf{w}_j, \chi_j\}$ with $j = 0, 1, \dots, \bar{d}$. We denote the given initial data c^0, ϕ^0 and S^0 , where S^0 satisfies (26). At each time step $n \geq 0$, the following steps are carried out.

Step 1. For each $x \in \Omega$, compute the solution of the time-discrete counterpart of (16) and (17), i.e. obtain $(\Pi_j^n, \mathbf{w}_j^n)$ with $j = 0, 1, \dots, \bar{d}$.

Step 2. Compute the time-discrete effective parameters $\mathcal{K}^{\phi,n}, \mathcal{K}^n, M^{\phi,n}$ and M^n .

Step 3. Compute the solution of the time-discrete counterpart of (42a) and (42b). Specifically, obtain p^n and \bar{v}^n by solving

$$\begin{aligned} \bar{v}^n &= -\mathcal{K}^n \nabla p^n - M^n \gamma(c^n), \\ \nabla \cdot \bar{v}^n &= 0. \end{aligned} \quad (46)$$

Step 4. Use the explicit, time-discrete counterpart of (42c) and (42d) to compute

$$\begin{aligned} \bar{v}^{\phi,n} &= -\mathcal{K}^{\phi,n} \nabla p^n - M^{\phi,n} \gamma(c^n), \\ S^{n+1} &= S^n - \frac{\Delta t}{2\Phi} \nabla \cdot \bar{v}^{\phi,n}. \end{aligned} \quad (47)$$

Step 5. For each $x \in \Omega$, compute the pore-scale velocity v^n as in (19). Solve the time-discrete counterpart of (36) and (37), i.e. obtain $\chi^{j,n}$ with $j = 0, 1, \dots, \bar{d}$.

Step 6. Compute the second set of time-discrete effective parameters \mathcal{B}^n and H^n .

Step 7. Compute the solution of the time-discrete counterpart of (42e). Specifically, obtain c^{n+1} by solving the following time-discrete problem

$$S^{n+1} c^{n+1} = S^n c^n + \frac{\Delta t}{\text{Pe}_c \Phi} \nabla \cdot (\mathcal{B}^n \nabla c^{n+1}) - \frac{\Delta t}{2\Phi} \nabla \cdot \left[\left(\bar{v}^n + \bar{v}^{\phi,n} - \frac{1}{\text{Pe}_c} \vec{H}^n \right) c^n \right]. \quad (48)$$

Step 8. For each $x \in \Omega$, compute ϕ^{n+1} , the solution of (43) at $t = t^{n+1}$.

Remark 4.1: Observe that the problem (43) is nonlinear. For solving it, we have adopted a linear iterative approach. More precisely, at each Darcy-scale mesh point $x \in \Omega$ and time t^n , with $L > 0$ large enough and letting $i \in \mathbb{N}$ be the iteration index, assuming $\phi^{n+1,i-1}$ known and Y -periodic, one solves the system

$$\begin{cases} \nabla_y \cdot (v^n \phi^{n+1,i}) = \overline{A_\phi} \lambda \Delta_y \psi^{n+1,i}, & \text{in } \mathcal{P}, \\ \psi^{n+1,i} = \overline{A_\psi} \gamma(c^{n+1}) \left(\frac{\mathcal{C}P'(\phi^{n+1,i-1})}{\lambda} + \frac{I'(\phi^{n+1,i-1})}{\beta} \right. \\ \quad \left. + L(\phi^{n+1,i} - \phi^{n+1,i-1}) - \mathcal{C}\lambda \Delta_y \phi^{n+1,i} \right), & \text{in } \mathcal{P}, \\ \nabla_y \phi^{n+1,i} \cdot n = 0, \quad \nabla_y \psi^{n+1,i} \cdot n = 0, & \text{on } \partial \mathcal{G}, \\ \phi^{n+1,i} \quad \text{and} \quad \psi^{n+1,i} \text{ are } Y\text{-periodic} \quad \text{and} \quad \frac{1}{\Phi} \int_{\mathcal{P}} \phi^{n+1,i} dy = 2S^{n+1} - 1. \end{cases} \quad (49)$$

The velocity v^n is given in (44), computed for $t = t^n$. As a starting guess, we choose the phase field at the previous time, $\phi^{n+1,0} = \phi^n$. However, the numerical experiments showed that the iterations are convergent regardless of the initial guess.

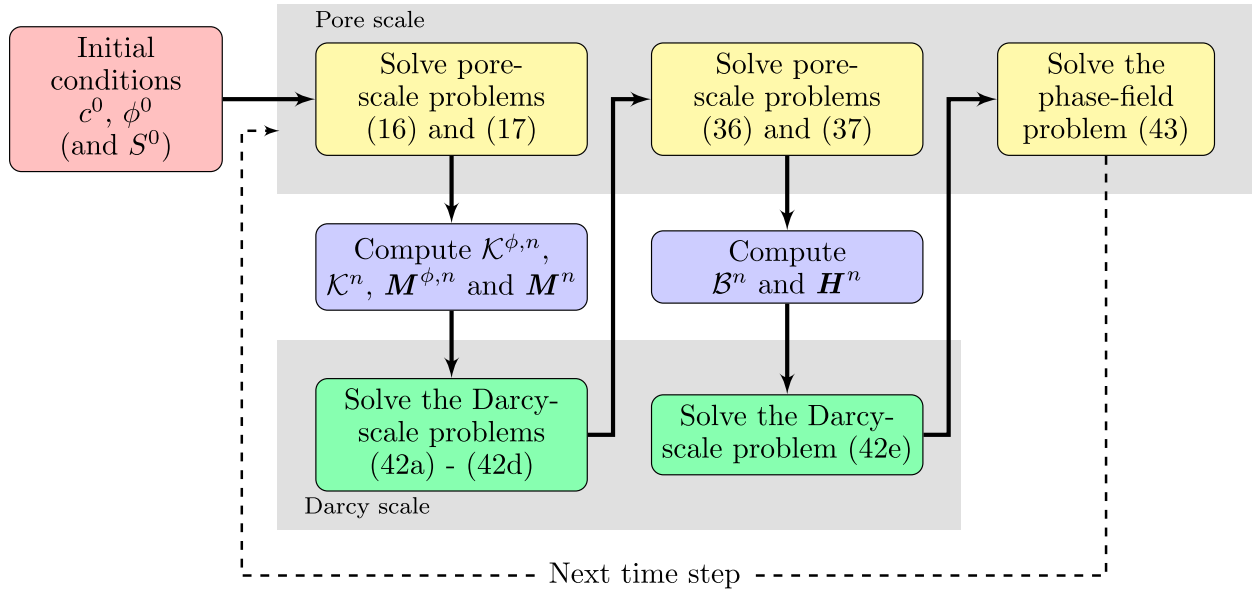


Figure 2. The two-scale scheme.

The two-scale scheme is presented in Figure 2. Observe that the time stepping in (47) is explicit. For the spatial discretization, we consider \mathfrak{T}_H , a Darcy-scale triangular partition of the domain Ω . An element $T \in \mathfrak{T}_H$ has diameter H_T . For each Darcy-scale element T , the effective quantities are computed by solving the cell problems defined in a pore-scale domain \mathcal{P} . The triangular partition \mathfrak{T}_h of \mathcal{P} consists of elements T_μ of diameter h_{T_μ} . We let $H := \max_{T \in \mathfrak{T}_H} H_T$ and $h := \max_{T_\mu \in \mathfrak{T}_h} h_{T_\mu}$. The numerical solutions of the pore- and Darcy-scale problems (17), (37), (43), (46) and (48) are computed using the lowest order Raviart-Thomas elements (see [47]). For the pore-scale problems (16) and (36) we use the Crouzeix-Raviart elements (see [48, Section 8.6.2]).

To compute the evolution of the phase field accurately and, implicitly, of the effective parameters, one needs a fine pore-scale mesh for each cell problem. This mesh needs to be fine enough to resolve the diffuse interface zone of the phase-field. More details on the mesh construction can be found in [49–51].

5. Numerical results

In this section, we present two numerical experiments, carried out in the 2D case. We consider the (Darcy-scale) domain $\Omega = (0, 1) \times (0, \frac{1}{2})$ and take $T = 1$ as final time. In both tests, a zero initial concentration is considered, $c^0 \equiv 0$, while the initial phase field ϕ^0 does not change with the vertical Darcy-scale variable x_2 (see below). Therefore, the saturation S^0 , obtained from (26), depends only on the horizontal variable, $S^0(x) = f(x_1)$. The function f is within the range $[0.66, 0.86]$ (see Figure 3).

Every pore-scale domain Y has a centred inner grain $\mathcal{G} = (0.4, 0.6) \times (0.4, 0.6)$. This gives a constant porosity, $\Phi = 0.96$. For each $x \in \Omega$, the initial phase field $\phi^0(x, \cdot)$ is radially symmetric up to not being defined on \mathcal{G} . Its value changes from -1 (fluid 2, around \mathcal{G}) to 1 (fluid 1, the outer part of \mathcal{P}) in a thin, diffuse region around a circle. The radius of it changes in the x_1 -direction but not in the x_2 -direction.

Homogeneous Neumann boundary conditions are imposed for c and p at the upper and lower boundaries of Ω . The same applies for c at the right boundary. The pressure and concentration are prescribed at the left boundary, $p = p_{in} = 2$ and $c = c_{in}$. In the two tests, the only varying data is c_{in} . At the right boundary, a lower pressure is imposed, $p = p_{out} = 0$, causing a horizontal flow to the right. Therefore, the left and right boundaries are called in- and outflow boundaries. This is sketched in Figure 3.

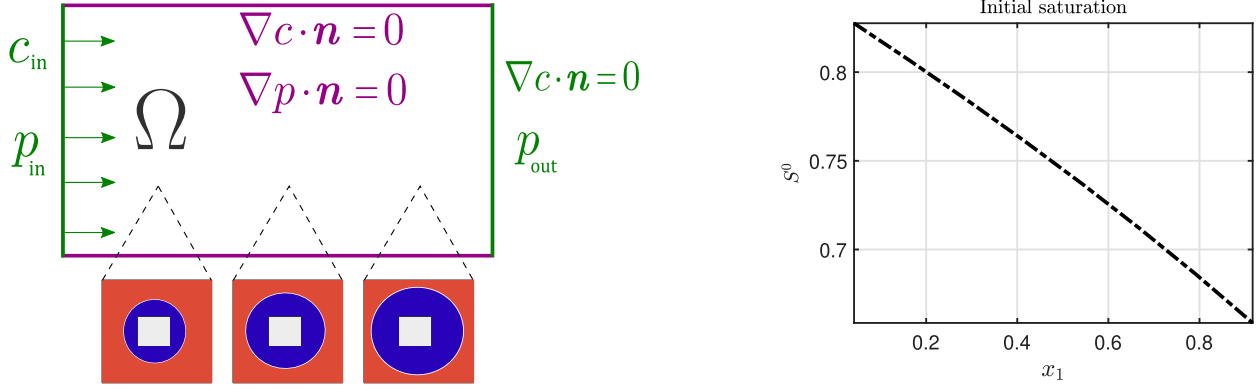


Figure 3. A sketch of the Darcy-scale boundary conditions and of the initial phase field at various locations (left), and the corresponding initial saturation (right).

We use the following non-dimensional parameters

$$\lambda = 0.02, \quad \mu_1 = 1, \quad \mu_2 = 0.9, \quad \beta = \overline{Ca} = \overline{Eu} = \overline{Re} = \overline{Pe_c} = \overline{A_\phi} = \overline{A_\psi} = 1,$$

and the given constant $\mathcal{C} = \frac{3}{2\sqrt{2}}$. To illustrate the effect of the solute-dependent surface tension, we let $\gamma(c) = -(100c + 1)$ and consider the following situations.

- Test case 1. First we let $c = c_{in} = 0$. Then, the concentration remains 0 during the whole simulation.
 Test case 2. With $c = c_{in} = 1$, the concentration is increasing in time for every x but remains decreasing in the x_1 -direction for any t .

For the numerical simulation, we use $\Delta t = 0.04$, thus carry out 25 time steps. For the spatial discretization, we construct a uniform Darcy-scale (coarse) mesh with mesh diameter $H = 0.1767$. At the pore scale, we consider a uniform (fine) mesh with mesh diameter $h = 0.0283$.

In both test cases, the Darcy-scale solution components do not change with the vertical variable x_2 . Therefore, these solutions are presented as a 1D projection/cut in the x_1 -direction. Also, to illustrate the evolution in time of various Darcy-scale quantities, we choose $x_{ref} = (0.9167, 0.2917)$ as a reference Darcy-scale point. The behaviour in other points is similar. Also, to compare the results obtained in the two test cases, we present the evolution in time of the difference in the variables, calculated at x_{ref} . E.g. for the saturation S , we compute

$$\delta S(t, x_{ref}) := S(t, x_{ref})|_{(TestCase2)} - S(t, x_{ref})|_{(TestCase1)},$$

for $t \in [0, 1]$, and similarly for other Darcy-scale variables or effective matrix components and vector elements.

The left plots in Figure 4 present the numerical approximation of the concentration c for the two test cases. Observe that, as expected, c remains 0 everywhere in the first test case. The right plot in Figure 4 shows the evolution of the concentration at the Darcy-scale reference point x_{ref} for the second test case.

The left plot in Figure 5 shows the numerical approximation of the saturation S for the test case 1. The saturation increases with time but remains decreasing in the x_1 -direction. The evolution in time of $S(\cdot, x_{ref})$ is presented in the upper right plot. The lower right plot shows the difference in the saturation between the two test cases. Note that the saturation S is lower in the second test case as it increases less with time compared to the first test case. This is indirectly caused by the difference in the surface tension, leading to, as we will see below, a difference in the ϕ -weighted Darcy-scale velocity \bar{v}^ϕ .

Due to the setup, the horizontal component of the Darcy-scale velocity \bar{v} will remain constant over the domain. However, the velocity \bar{v}^ϕ can still vary, and, as follows from (42c), this causes changes

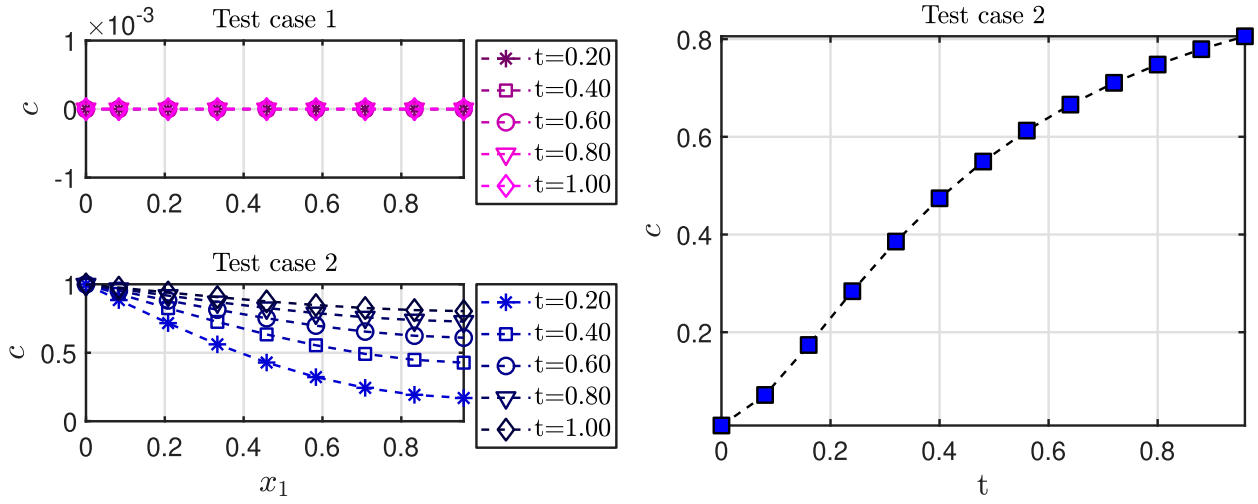


Figure 4. The concentration $c(t, \cdot)$ at five time steps for test case 1 (left-top) and test case 2 (left-bottom). The evolution of $c(\cdot, x_{\text{ref}})$ for test case 2 (right).

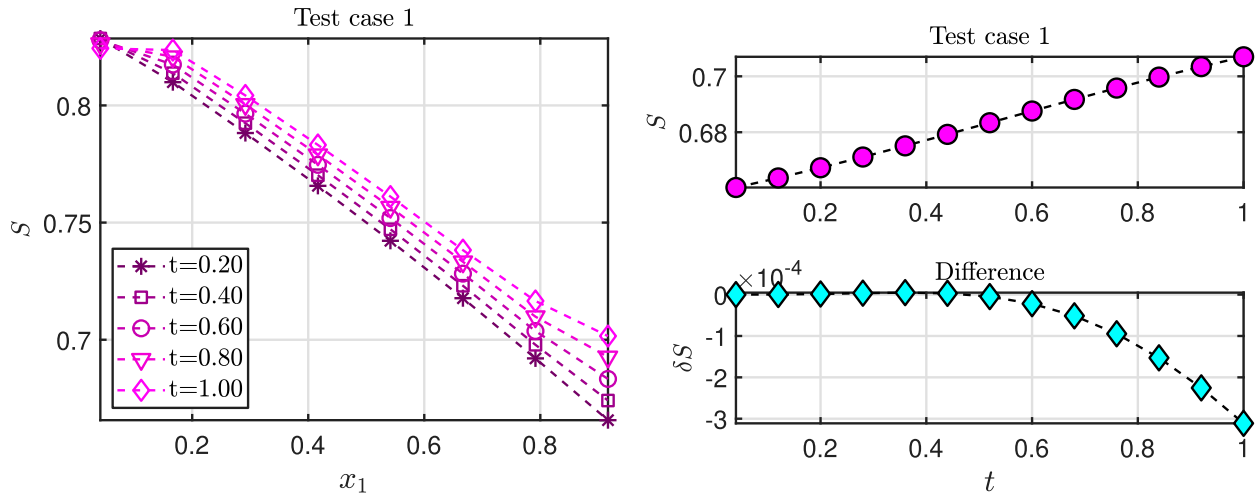


Figure 5. The saturation $S(t, \cdot)$ at five time steps, for the test case 1 (left). The evolution of $S(\cdot, x_{\text{ref}})$ for the test case 1 (right-top) and of the difference $\delta S(\cdot, x_{\text{ref}})$ between the two test cases (right-bottom).

in the saturation. Moreover, this change becomes more natural when considering (45a), in which the phase velocity depends on the (here, constant) \bar{v} and the variable \bar{v}^ϕ . We note that the vertical component of \bar{v}^ϕ is zero, hence only the horizontal component is shown in Figure 6. As we see from the left plot in Figure 6, the horizontal component has a negative derivative with respect to x_1 throughout the domain, yielding an increasing saturation. However, from the difference shown in the lower right plot of Figure 6, the horizontal component of \bar{v}^ϕ is higher in the test case 2 than in the test case 1. Hence, its derivative, though negative, is closer to 0, yielding a smaller increase in the saturation. Note that the reference point x_{ref} is at the right part of the domain and that saturation and velocity changes in points further left are less than in x_{ref} .

Figures 7 and 8 are displaying the evolution of the effective parameters from (42d), which are influencing \bar{v}_1^ϕ . The left plot in Figure 7 displays $\mathcal{K}_{1,1}^\phi$, while the time evolution of M_1^ϕ is shown in Figure 8. Comparing the sizes, and accounting for the fact that the horizontal pressure drop is around -2 , and $\gamma(c)$ is in the range $[-101, -1]$, it becomes clear that the horizontal pressure drop and the evolution of $\mathcal{K}_{1,1}^\phi$ dominate the changes in \bar{v}_1^ϕ in both test cases considered here. Observe that, similarly to \bar{v}_1^ϕ , $\mathcal{K}_{1,1}^\phi$ increases with time in the right part of the domain, and stronger for the test case 2, causing a decreased divergence of \bar{v}^ϕ .

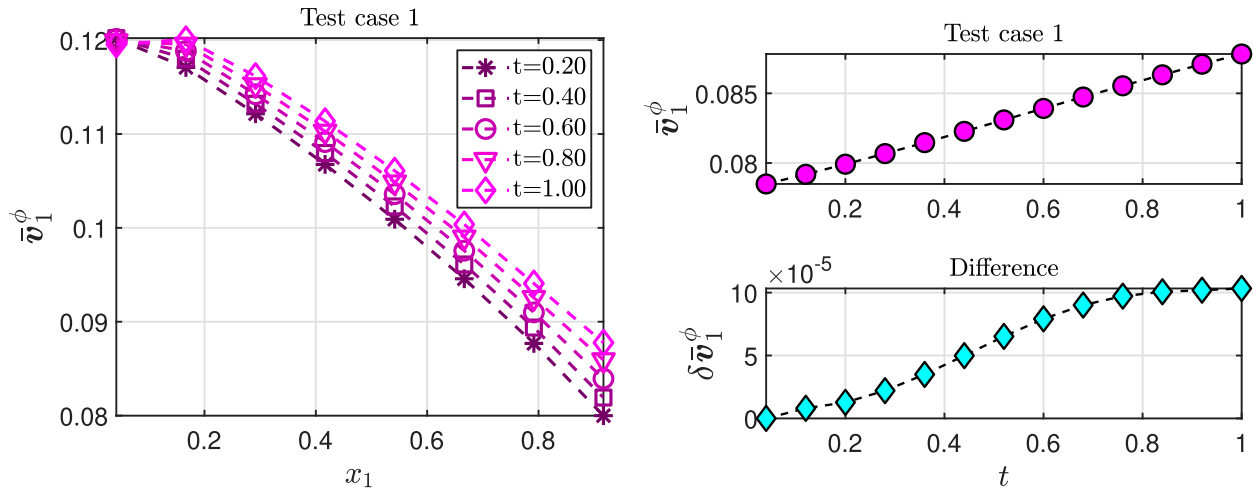


Figure 6. The horizontal component of the (Darcy-scale) velocity $\bar{v}^\phi(t, \cdot)$, computed at five time steps, for the test case 1 (left). The evolution of $\bar{v}_1^\phi(\cdot, x_{\text{ref}})$ for the test case 1 (right-top) and of the difference $\delta \bar{v}_1^\phi(\cdot, x_{\text{ref}})$ between the two test cases (right-bottom).

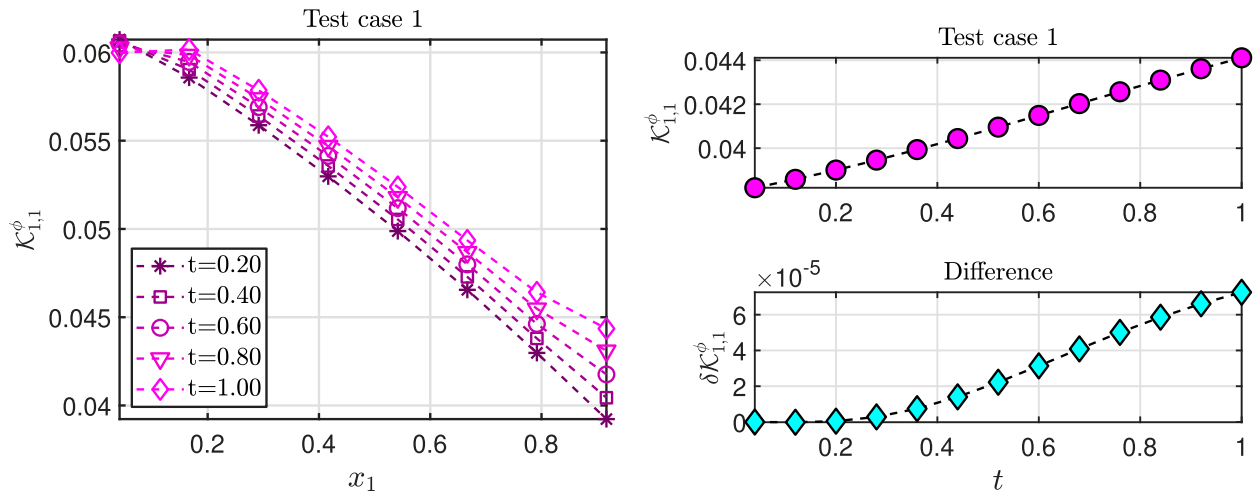


Figure 7. The first component of $\mathcal{K}^\phi(t, \cdot)$, computed at five time steps, for test case 1 (left). The evolution of $\mathcal{K}_{1,1}^\phi(\cdot, x_{\text{ref}})$ for the test case 1 (right-top) and of the difference $\delta \mathcal{K}_{1,1}^\phi(\cdot, x_{\text{ref}})$ between the two test cases, at x_{ref} (right-bottom).

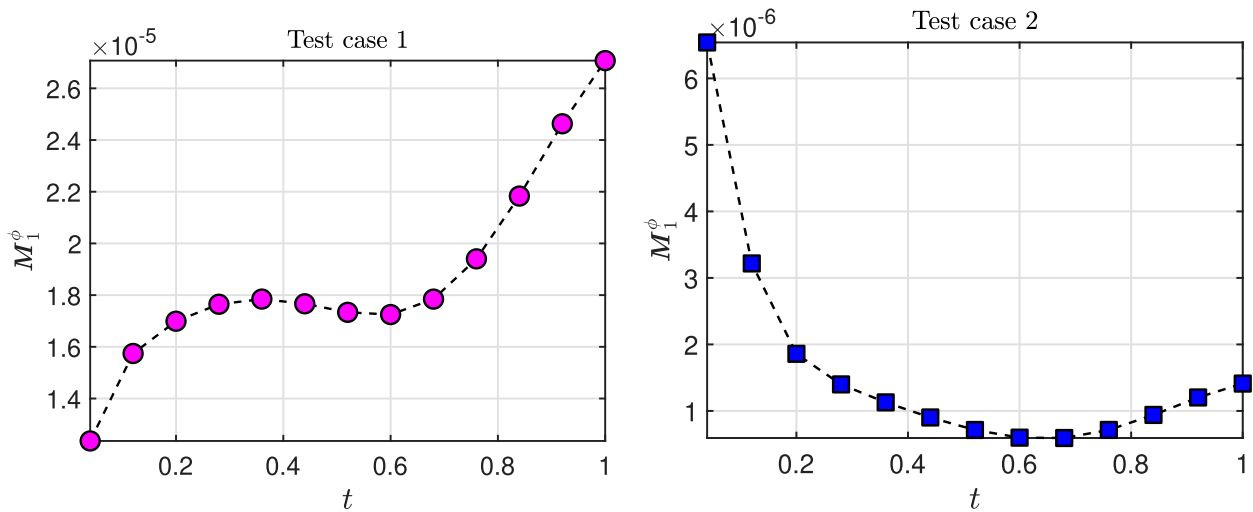


Figure 8. The evolution of the first element of $M^\phi(\cdot, x_{\text{ref}})$ for the two test cases.

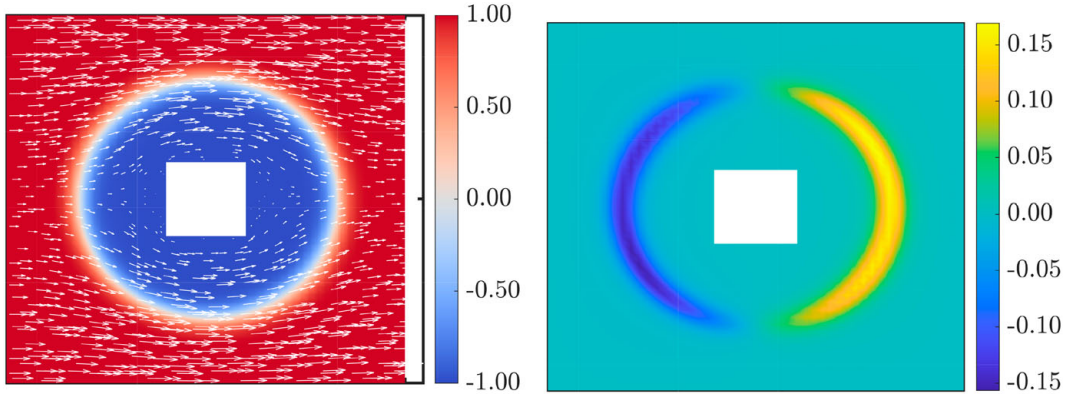


Figure 9. The evolution of the pore-scale phase field in the test case 1 (left) and the difference of the phase field $\delta\phi$ between the two test cases (right) corresponding to the Darcy-scale location x_{ref} at time $t = 1$.

The changes of \mathcal{K}^ϕ is depending on how the pore-scale phase-field evolves, which again depends on the surface tension. In Figure 9, we display the pore-scale phase-field obtained at the final time $t = 1$, at the reference point x_{ref} . The left plot in Figure 9 shows the numerical approximation of the phase field $\phi(1, x_{\text{ref}}, y)$ and the pore-scale velocity $v(1, x_{\text{ref}}, y)$ (with $y \in \mathcal{P}$), obtained in the first test case. Note that the pore-scale flow field is oriented mainly towards right. This immediately implies that the Darcy-scale velocity \bar{v} has the same orientation. The difference in the phase fields between the two test cases is displayed in the right plot. This difference is calculated for $t = 1$ and at x_{ref} , using

$$\delta\phi(1, x_{\text{ref}}, y) = \phi(1, x_{\text{ref}}, y)|_{(\text{TestCase2})} - \phi(1, x_{\text{ref}}, y)|_{(\text{TestCase1})}.$$

As follows from the right plot, the phase-field profile in the second case corresponds to fluid 2 being shifted slightly to the left compared to the test case 1.

6. Conclusion

We have derived a two-scale model for the two-phase flow in a porous medium. The model takes into account the variations in the surface tension caused by a surfactant soluble in one fluid phase. The starting point is the pore-scale model proposed in [30]. This is a Navier-Stokes-Cahn-Hilliard model for the flow, coupled with an advection-diffusion equation for solute concentration. In this way, the free boundaries separating the two fluid phases at the pore scale are approximated by thin diffuse interface regions, which allows formulating the problem in a fixed domain.

Using formal homogenization methods, we have derived a two-scale model consisting of mass conservation laws for the two phases and for the solute concentration, and of Darcy-type laws for the effective velocities. The latter include terms accounting for the concentration-dependent surface tension. These Darcy-scale laws involve effective parameters, which are obtained by solving local cell problems. These cell problems depend on the evolution of the phase field at the pore scale.

We have proposed a numerical algorithm building on the Euler explicit time discretization and on the lowest order Raviart-Thomas approximation in space. The explicit scheme requires solving seven pore-scale cell problems, defined for each Darcy-scale point. These cell problems depend on Darcy-scale variables concentration, pressure and saturation. At the same time, for solving the Darcy-scale equations, one requires accurate calculations of the effective parameters, based on pore-scale quantities. These cell problems are generally small and parallelizable, allowing for efficient numerical strategies. In particular, for the phase-field cell problem, which is nonlinear and elliptic, we propose a simple, linear iterative scheme having a robust convergence, regardless of the initial guess.

Two test cases are presented, where the surface tension either remains constant, or where the changes in the concentration induce a varying surface tension. The fluids have different viscosities, but the viscosity ratio is small. The profiles of the Darcy-scale quantities display a similar behaviour

in time and space in both test cases. Though small, differences in the results can be observed. In particular, the surfactant leads to decreased values of the saturation, as it affects the effective quantities, which depend on the pore-scale phase-field distribution.

Open issues are related to mesh refinement strategies at both the pore scale and the Darcy scale, as mentioned in [51]. Furthermore, adaptive strategies allowing to identify Darcy-scale points where the effective parameters need to be recalculated, and those where these values can be copied from points with a similar behaviour, could also improve the efficiency of the algorithm. Finally, implicit or semi-implicit higher-order numerical schemes for the two-scale model derived here need to be developed, as well as the rigorous analysis of the model and of the numerical approximation.

Disclosure statement

No potential conflict of interest was reported by the authors.

Funding

This research is supported by the Research Foundation - Flanders (FWO) through the Odysseus programme (Project G0G1316N) and by the German Research Foundation (DFG) through the SFB 1313, Project Number 327154368 and under Germany's Excellence Strategy- EXC 2075 - 390740016. The authors acknowledge the support by the Stuttgart Center for Simulation Science (SimTech).

ORCID

S. Sharmin  <http://orcid.org/0000-0002-1984-3185>

M. Bastidas  <http://orcid.org/0000-0002-3006-2363>

C. Bringedal  <http://orcid.org/0000-0003-0495-2634>

I. S. Pop  <http://orcid.org/0000-0001-9647-4347>

References

- [1] Landa-Marban D, Radu FA, Nordbotten JM. Modeling and simulation of microbial enhanced oil recovery including interfacial area. *Transp Porous Media*. 2017;120(2):395–413.
- [2] Wu Z, Yue X, Cheng T, et al. Effect of viscosity and interfacial tension of surfactant-polymer flooding on oil recovery in high-temperature and high-salinity reservoirs. *J Petrol Explor Prod Technol*. 2014;4(1):9–16.
- [3] Mulligan MK, Rothstein JP. The effect of confinement-induced shear on drop deformation and breakup in microfluidic extensional flows. *Phys Fluids*. 2011;23(2):022004.
- [4] Kovalchuk NM, Simmons MJ. Effect of surfactant dynamics on flow patterns inside drops moving in rectangular microfluidic channels. *J Colloid Interface Sci*. 2021;5(3):40.
- [5] Craster RV, Matar OK. Dynamics and stability of thin liquid films. *Rev Modern Phys*. 2009;81(3):1131–1198.
- [6] Hartnett C, Seric I, Mahady K, et al. Exploiting the Marangoni effect to initiate instabilities and direct the assembly of liquid metal filaments. *Langmuir*. 2017;33(33):8123–8128.
- [7] Mikelić A, Paoli L. On the derivation of the Buckley-Leverett model from the two fluid Navier-Stokes equations in a thin domain. *Comput Geosci*. 1997;1(1):59–83.
- [8] Sharmin S, Bringedal C, Pop IS. On upscaling pore-scale models for two-phase flow with evolving interfaces. *Adv Water Res*. 2020;142:103646.
- [9] Mikelić A. On an averaged model for the 2-fluid immiscible flow with surface tension in a thin cylindrical tube. *Comput Geosci*. 2003;7(3):183–196.
- [10] Lunowa SB, Bringedal C, Pop IS. On an averaged model for immiscible two-phase flow with surface tension and dynamic contact angle in a thin strip. *Stud Appl Math*. 2021;1:43.
- [11] Fasano A, Mikelić A. The 3D flow of a liquid through a porous medium with absorbing and swelling granules. *Interfaces Free Bound*. 2002;4(3):239–261.
- [12] Sweijen T, van Duijn CJ, Hassanizadeh SM. A model for diffusion of water into a swelling particle with a free boundary: application to a super absorbent polymer. *Chem Eng Sci*. 2017;172:407–413.
- [13] van Noorden TL. Crystal precipitation and dissolution in a porous medium: effective equations and numerical experiments. *Multiscale Model Simul*. 2008;7(3):1220–1236.
- [14] Bringedal C, Berre I, Pop IS, et al. Upscaling of non-isothermal reactive porous media flow with changing porosity. *Transp Porous Media*. 2016;114(2):371–393.
- [15] Bringedal C, Kumar K. Effective behavior near clogging in upscaled equations for non-isothermal reactive porous media flow. *Transp Porous Media*. 2017;120(3):553–577.

- [16] Gaerttner S, Frolkovic P, Knabner P, et al. Efficiency and accuracy of micro-macro models for mineral dissolution. *Water Resour Res.* 2020 Aug;56(8):e2020WR027585.
- [17] Caginalp G, Fife PC. Dynamics of layered interfaces arising from phase boundaries. *SIAM J Appl Math.* 1988;48(3):506–518.
- [18] Li X, Lowengrub J, Rätz A, et al. Solving PDEs in complex geometries: a diffuse domain approach. *Commun Math Sci.* 2009;7(1):81–107.
- [19] Boyer F, Lapuerta C, Minjeaud S, et al. Cahn-Hilliard/Navier-Stokes model for the simulation of three-phase flows. *Transp Porous Media.* 2010;82(3):463–483.
- [20] Kim J. Phase-field models for multi-component fluid flows. *Commun Comput Phys.* 2012;12(3):613–661.
- [21] van Noorden TL, Eck C. Phase field approximation of a kinetic moving-boundary problem modelling dissolution and precipitation. *Interfaces Free Bound.* 2011;13(1):29–55.
- [22] Bringedal C, Von Wolff L, Pop IS. Phase field modeling of precipitation and dissolution processes in porous media: upscaling and numerical experiments. *Multiscale Model Simul.* 2020;18(2):1076–1112.
- [23] Redeker M, Rohde C, Pop IS. Upscaling of a tri-phase phase-field model for precipitation in porous media. *IMA J Appl Math.* 2016;81(5):898–939.
- [24] Rohde C, von Wolff L. Homogenization of nonlocal Navier–Stokes–Korteweg equations for compressible liquid–Vapor flow in porous media. *SIAM J Math Anal.* 2020;52(6):6155–6179.
- [25] Guo Z, Lin P. A thermodynamically consistent phase–field model for two-phase flows with thermocapillary effects. *Journal of Fluid Mechanics.* 2015;766:226–271.
- [26] Mikelić A, Wheeler MF, Wick T. Phase-field modeling of a fluid-driven fracture in a poroelastic medium. *Comput Geosci.* 2015;19(6):1171–1195.
- [27] Lee S, Mikelić A, Wheeler MF, et al. Phase-field modeling of two phase fluid filled fractures in a poroelastic medium. *Multiscale Model Simul.* 2018;16(4):1542–1580.
- [28] Cahn JW, Hilliard JE. Free energy of a nonuniform system. i. interfacial free energy. *J Chem Phys.* 1958;28(2):258–267.
- [29] Abels H, Garcke H, Grün G. Thermodynamically consistent, frame indifferent diffuse interface models for incompressible two-phase flows with different densities. *Math Models Methods App Sci.* 2012;22(03):1150013. 40.
- [30] Garcke H, Lam KF, Stinner B. Diffuse interface modelling of soluble surfactants in two-phase flow. *Commun Math Sci.* 2014;12(8):1475–1522.
- [31] Chen J, Sun S, Wang X. Homogenization of two-phase fluid flow in porous media via volume averaging. *J Comput Appl Math.* 2019;353:265–282.
- [32] Schmuck M, Pradas M, Pavliotis GA, et al. Derivation of effective macroscopic Stokes-Cahn-Hilliard equations for periodic immiscible flows in porous media. *Nonlinearity.* 2013;26(12):3259–3277.
- [33] Daly KR, Roose T. Homogenization of two fluid flow in porous media. *Proc A.* 2015;471(2176):20140564. 20.
- [34] Bañas V, Mahato HS. Homogenization of evolutionary Stokes-Cahn-Hilliard equations for two-phase porous media flow. *Asymptot Anal.* 2017;105(1–2):77–95.
- [35] Zhu G, Li A. Interfacial dynamics with soluble surfactants: A phase-field two-phase flow model with variable densities. *Adv Geo-Energy Res.* 2020;4(1):86–98.
- [36] Frank F, Liu C, Alpak FO, et al. A finite volume / discontinuous Galerkin method for the advective Cahn-Hilliard equation with degenerate mobility on porous domains stemming from micro-CT imaging. *Comput Geosci.* 2018;22(2):543–563.
- [37] Ray D, Liu C, Riviere B. A discontinuous Galerkin method for a diffuse-interface model of immiscible two-phase flows with soluble surfactant. *Comput Geosci.* 2021;25(5):1775–1792.
- [38] Picchi D, Battiato I. The impact of pore-scale flow regimes on upscaling of immiscible two-phase flow in porous media. *Water Resour Res.* 2018;54(9):6683–6707.
- [39] Quintard M, Whitaker S. Transport in ordered and disordered porous media: volume-averaged equations, closure problems, and comparison with experiment. *Chem Eng Sci.* 1993;48(14):2537–2564.
- [40] Lasseux D, Ahmadi A, Arani AAA. Two-phase inertial flow in homogeneous porous media: A theoretical derivation of a macroscopic model. *Transp Porous Media.* 2008;75(3):371–400.
- [41] Mikelić A. A convergence theorem for homogenization of two-phase miscible flow through fractured reservoirs with uniform fracture distributions. *Appl Anal.* 1989;33(3–4):203–214.
- [42] Bourgeat A, Luckhaus S, Mikelić A. Convergence of the homogenization process for a double-porosity model of immiscible two-phase flow. *SIAM J Math Anal.* 1996;27(6):1520–1543.
- [43] Amaziane B, Jurak M, Vrbaški A. Homogenization results for a coupled system modelling immiscible compressible two-phase flow in porous media by the concept of global pressure. *Appl Anal.* 2013;92(7):1417–1433.
- [44] Bunoïu R, Cardone G, Kengne R, et al. Homogenization of 2D Cahn-Hilliard-Navier-Stokes system. *J Elliptic Parabol Equ.* 2020;6(1):377–408.
- [45] Metzger S, Knabner P. Homogenization of two-phase flow in porous media from pore to Darcy scale: a phase-field approach. *Multiscale Model Simul.* 2021;19(1):320–343.

- [46] Kim J. A continuous surface tension force formulation for diffuse-interface models. *J Comput Phys.* [2005](#);204(2):784–804.
- [47] Bahriawati C, Carstensen C. Three MATLAB implementations of the lowest-order Raviart-Thomas MFEM with a posteriori error control. *Comput Methods Appl Math.* [2005](#);5(4):333–361.
- [48] Boffi D, Brezzi F, Fortin M. *Mixed finite element methods and applications.* Vol. 44. Berlin: Springer; [2013](#).
- [49] Bastidas M, Bringedal C, Pop IS. A two-scale iterative scheme for a phase-field model for precipitation and dissolution in porous media. *Appl Math Comput.* [2021](#);396:125933.
- [50] Bastidas M, Bringedal C, Pop IS, et al. Numerical homogenization of non-linear parabolic problems on adaptive meshes. *J Comput Phys.* [2020](#);425:109903.
- [51] Bastidas M, Sharmin S, Bringedal C. A numerical scheme for two-scale phase-field models in porous media. *Conference Proceedings of the 6th ECCOMAS Young Investigators Conference YIC2021*; Spain: Universitat Politècnica de València; 2021. (accepted).

Part C

Reactive transport with heterogeneous reactions

The third part of this thesis consists of three chapters that are based on three journal publications. Each publication concerns modeling and simulation of reactive transport in porous media, where mineral precipitation and dissolution alter the pore-scale geometry. All three publications rely on or use homogenization, but focus on different aspects of the arising challenges for understanding the interplay between pore-scale geometry changes and Darcy-scale effective behavior.

Chapter 8: Pore-scale and two-scale model for mineral precipitation and dissolution

In this chapter, a new phase-field model for coupled fluid flow and solute transport, where the solute participates in a mineral dissolution/precipitation reaction, is developed. Unlike earlier phase-field models, the flow of the fluid and interactions between the flow and the solid mineral are incorporated. The sharp-interface limit of the phase-field model is found using matched asymptotic expansions. The phase-field model is shown to reduce to the expected sharp-interface model, but with an additional curvature-driven motion of the fluid-solid interface. This curvature-driven motion causes a circular mineral to dissolve too quickly, which is shown by comparing to available benchmarks numerically. By formulating the phase-field model in a periodic pore-scale geometry, homogenization is applied to derive an effective Darcy-scale model. The Darcy-scale equations depend on local pore-scale cell problems for the evolution of the pore-scale geometry through solving the phase-field equation, and for effective permeability and effective diffusion coefficient. By comparing the effective parameters found by the derived cell problems to effective parameters found by sharp-interface cell problems for effective permeability and effective diffusivity, the diffuse interface is found to influence the value of the effective parameters, but less when the diffuse-interface width is smaller.

Chapter 9: Two-scale simulation of mineral precipitation and dissolution In this chapter, the resulting two-scale model from Chapter 8 is implemented using heterogeneous multiscale methods. The focus is especially on measures to ensure that a robust, efficient and accurate scheme is obtained. Since the Darcy-scale model equations and pore-scale cell problems depend on each other through the reaction rate and effective parameters, an iterative approach is taken to solve the two scales. By introducing a regularization, convergence for a simplified case of the two-scale scheme is proven by showing that the iterations form contracting fixed-point iterations. The proof relies on relatively mild restrictions on the time-step size and on the phase-field parameters. Adaptivity is applied to ensure efficiency of the scheme without losing accuracy. A strategy inspired by [85] is applied to only update a smaller portion of the cell problems for effective parameters. By comparing to simulations where all cell problems are solved, we show that this causes a large gain through less computational effort, with only a small loss in accuracy.

Chapter 10: Comparison of level-set and phase-field models for three-phase systems

In the last chapter of Part C, a system with one fluid phase and two solid minerals is investigated. Three solutes are transported through advection and diffusion in the fluid,

and participate in mineral precipitation/dissolution reactions of the two minerals. This is hence a three-phase system, which requires modification of the common approaches for modeling evolving interfaces. Adapted level-set and phase-field models are formulated and implemented, and the goal of this chapter is to compare their behavior. For the phase-field model this means that a ternary phase-field approach is needed. Except from that, the phase-field model shows similarities to the model in Chapter 8. The sharp-interface limit of the phase-field model is found by matched asymptotic expansions, and reduces to the expected sharp-interface equations but with additional curvature-driven motion. Numerically, the phase-field model implementation is conservative (in contrast to the level-set model implementation), and needs less unknowns and Newton-iterations on the same grid compared to the level-set model implementation. However, the curvature-driven motion of the phase-field model is found to have a negative influence on the behavior, especially near the fluid-solid-solid triple points. By homogenization, cell problems for effective solute diffusivity and permeability can be found. Here, the level-set model and the phase-field model are found to provide comparable results as the minerals dissolve and precipitate.

8 Pore-scale and two-scale model for mineral precipitation and dissolution

The content of this chapter is based on the following original article:

C. Bringedal, L. von Wolff, and I. S. Pop. *Phase Field Modeling of Precipitation and Dissolution Processes in Porous Media: Upscaling and Numerical Experiments*. *Multiscale Modeling & Simulation* 18.2 (2020), pp. 1076–1112. doi: 10.1137/19M1239003.

With courtesy of SIAM.

PHASE FIELD MODELING OF PRECIPITATION AND DISSOLUTION PROCESSES IN POROUS MEDIA: UPSCALING AND NUMERICAL EXPERIMENTS*

CARINA BRINGEDAL[†], LARS VON WOLFF[‡], AND IULIU SORIN POP[§]

Abstract. We consider a model for precipitation and dissolution in a porous medium, where ions transported by a fluid through the pores can precipitate at the pore walls and form mineral. Also, the mineral can dissolve and become part of the fluid as ions. These processes lead to changes in the flow domain, which are not known a priori but depend on the concentration of the ions dissolved in the fluid. Such a system can be formulated through conservation equations for mass, momentum, and solute in a domain that evolves in time. In this case the fluid and mineral phases are separated by a sharp interface, which also evolves. We consider an alternative approach by introducing a phase field variable, which has a smooth, diffuse transition of nonzero width between the fluid and mineral phases. The evolution of the phase field variable is determined through the Allen–Cahn equation. We show that as the width of the diffuse transition zone approaches zero, the sharp-interface formulation is recovered. When we consider a periodically perforated domain mimicking a porous medium, the phase field formulation is upscaled to Darcy scale by homogenization. Then, the average of the phase field variable represents the porosity. Through cell problems, the effective diffusion and permeability matrices are dependent on the phase field variable. We consider numerical examples to show the behavior of the phase field formulation. We show the effect of flow on the mineral dissolution, and we address the effect of the width of the diffuse interface in the cell problems for both a perforated porous medium and a thin strip.

Key words. porous media, phase field model, reactive transport, homogenization

AMS subject classifications. 35C20, 35L65, 65M08, 76D05, 76M50, 76R50, 76S05, 76V05, 80A22, 80A32

DOI. 10.1137/19M1239003

1. Introduction. Understanding mineral dissolution and precipitation processes in porous media is important, as these processes appear in many applications of highest societal relevance. Examples in this sense are soil salinization, geological CO₂ sequestration, copper leaching, and harnessing geothermal energy. In many of these situations, experiments are unfeasible or even impossible, and hence creating simulations based on reliable and accurate mathematical modeling is a key strategy. The most challenging aspect of mathematical modeling appears when the flow domain is

*Received by the editors January 15, 2019; accepted for publication (in revised form) March 5, 2020; published electronically June 11, 2020.

<https://doi.org/10.1137/19M1239003>

Funding: The authors were supported by the Research Foundation – Flanders (FWO) through the project G0G1316N DynScale through the Odysseus programme, and by the Deutsche Forschungsgemeinschaft (DFG, German Research Foundation) through project 327154368 – SFB 1313. The second author was supported by Hasselt University through the project BOF19BL12. The computational resources and services used in this work were provided by the VSC (Flemish Supercomputer Center), funded by the Research Foundation – Flanders (FWO) and the Flemish Government – department EWI.

[†]Faculty of Sciences, Hasselt University, Diepenbeek, BE3590, Belgium, and Institute for Modelling Hydraulic and Environmental Systems, University of Stuttgart, 70569 Stuttgart, Germany (carina.bringedal@iws.uni-stuttgart.de).

[‡]Institute of Applied Analysis and Numerical Simulation, University of Stuttgart, 70569 Stuttgart, Germany, and Faculty of Sciences, Hasselt University, Diepenbeek, BE3590, Belgium (lars.von-wolff@mathematik.uni-stuttgart.de).

[§]Faculty of Sciences, Hasselt University, Diepenbeek, BE3590, Belgium, and Department of Mathematics, University of Bergen, N-5020 Bergen, Norway (sorin.pop@uhasselt.be).

altered due to dissolution and precipitation. More precisely, the dissolved ions can form a mineral, and hence they can leave the fluid domain and become part of the stationary mineral domain. Due to this, the space available for flow (the fluid domain) is reduced, whereas the mineral domain is increasing. In contrast, the mineral domain shrinks as minerals dissolve into ions and become part of the fluid. To mathematically model such processes one needs conservation laws for mass, momentum, and solute in two time-dependent domains, where the evolution of the interface separating these domains is not known a priori. Hence, we have a free boundary problem, where the development of the boundary—and hence also the domains—must be accounted for.

When encountered in a porous medium, mineral precipitation and dissolution can significantly alter the pore structure and hence affect the porosity and the large-scale flow through the medium as the permeability evolves. For porous media flow, we distinguish between two spatial scales. The detailed behavior is found at the pore scale (the microscale), and the average behavior of the system is considered to be at the Darcy scale (the macroscale). Mineral precipitation and dissolution at the Darcy scale have been considered from a theoretical point of view by [25], where consistent reaction rates are formulated for the dissolution and precipitation processes, and traveling wave solutions are found. The existence and uniqueness of such solutions are further analyzed in [44]. At the pore scale, the existence of weak solutions is proved in [46], while uniqueness is obtained in [51]. Paper [46] also analyzes the occurrence of dissolution fronts in a thin strip, introducing a free boundary separating regions where mineral is present from those which are mineral-free. In [26], homogenization techniques are employed to prove rigorously that the Darcy-scale model in [25, 44] is the upscaled counterpart of the pore-scale model in [46].

In all of the cases mentioned above, the mineral layer is assumed to have a negligible thickness even when compared to the microscale (the pores), and therefore the presence of a mineral is accounted for in the form of a concentration. A different approach is adopted in [50], where the mineral layer is assumed to have a nonnegligible thickness, and therefore precipitation and dissolution can alter the flow domain at the microscale. The existence and uniqueness of a weak solution for this free boundary model is proved, however, in the simplified case of a one-dimensional domain. This situation has extended to the higher dimensional case. In [48] the pore-scale model is defined in a two-dimensional thin strip, where a free boundary model for precipitation and dissolution is included. The Darcy-scale model is derived by transversal averaging. Paper [47] extends this by considering a general porous medium with periodic grains, and a level-set formulation is used to account for the presence of the free boundary at the pore scale. These models were later extended to include temperature dependence for a thin strip [10] and for a periodic porous medium [11], and the effective properties of the latter model were considered further in [13]. Also, the upscaling in advection-dominated regimes, leading to models that are similar to Taylor dispersion, is performed in [12, 28]. A similar model is considered in [43] but restricted to pore-scale diffusion processes in evolving domains. There a Darcy-scale model is derived, for which the existence of strong solutions is proved up to clogging.

Different approaches are possible when considering free boundary models. One can formulate an explicit equation for the location of the free boundary through, e.g., the width of the mineral phase in a thin strip as in [12, 10, 28, 48, 50]. For more general geometries, a level-set formulation has been widely used, as in [11, 43, 47]. Upscaling using asymptotic expansions of level-set formulations can be tedious due to the strong coupling between the level-set equation and the other model equations, as the asymptotic expansion has to be applied also for the level set and hence for the

location of the interface, as done in [11, 43, 47]. However, the upscaled model still relies on solving the pore-scale level-set equation, which is quite challenging for the numerical implementation.

To obtain mathematical models valid at the Darcy scale, asymptotic expansion and homogenization techniques (see, e.g., [23]) are employed in the above-mentioned papers. This is the strategy adopted in the current paper as well. Alternatively, one can consider volume averaging techniques [36, 37, 52, 53, 54]. We refer the reader to [19] for a comparison between the two methods. We mention that the results are obtained under the assumption that diffusion is the result of a standard random walk process at the molecular scale. Alternatively, one can start with a continuous time random walk (CTRW) approach [29] and end up with other diffuse regimes, expressed, e.g., through fractional time derivatives. Considering such models, including the upscaling from the pore to the Darcy scale (see [20]) is certainly interesting but is beyond the scope of the current work.

Darcy-scale models are derived through assuming a certain relation between the time scales of the different processes (diffusion, advection, reaction) at the pore scale, where different relations lead to different upscaled models. These time scales are assumed either to be in balance or to differ in a certain way. This can be expressed through the order of magnitude of dimensionless numbers, such as Péclet and Damköhler numbers, in terms of the ratio of the typical length scales of the pores, respectively, of the porous medium (the Darcy scale). In this work we will assume these time scales to be in balance. The resulting Darcy-scale model reflects nonequilibrium chemical kinetics. Certainly, equilibrium kinetics may appear at the scale of pores, in which case one needs to adapt the mathematical models at the pore scale, with impact on the upscaled ones (see, e.g., [7]). Homogenization techniques can still be employed in other regimes, including high Péclet and Damköhler numbers, but, in particular, the former needs to remain within a regime that avoids turbulent flows and allows diffusion to dominate at the scale of pores. We mention [4, 6, 12, 17, 28, 32, 36, 45, 53, 54] for the derivation of Darcy-scale models by either homogenization or volume averaging, and under dominating advection or for fast reaction kinetics. A comprehensive discussion can be found in [7], addressing models with mixing-controlled heterogeneous reactions at different scales and under various regimes for the Péclet and Damköhler numbers.

To model the evolving fluid-mineral interface, an alternative approach to the level-set method is through phase fields. A phase field is an approximation of the characteristic function and hence attains the value 1 in one domain, and 0 in the other, but has a smooth, diffuse transition zone of nonzero width across the interface [14, 30]. The evolution of the phase field is through a phase field equation, which can be derived from a minimization of the free energy. Most commonly used are the Allen–Cahn [5] and Cahn–Hilliard [15] equations for evolution of the phase field. While the Cahn–Hilliard equation has the advantage of conserving the phase field parameter, it introduces fourth-order spatial derivatives which can lead to numerical difficulties. For the Allen–Cahn formulation, one can prove that the phase field remains bounded by 0 and 1 and thus in the physical regime, as it involves only second-order derivatives. On the other hand, it is generally not conservative, although conservative reformulations for two-phase flow [24] and multicomponent systems [35] exist. However, these formulations are globally rather than locally conservative. The Allen–Cahn equation allows the interface to evolve due to curvature effects (the Gibbs–Thomson effect), which may or may not be desirable from a chemical point of view [40]. We will use an Allen–Cahn equation for our phase field formulation, although curvature effects are

not our primary point of interest. We mention that [55] formulated an Allen–Cahn equation for a solid–liquid interface evolving due to solute precipitation and dissolution, where surface curvature effects were removed. However, the model does not include fluid flow.

To introduce a diffuse transition zone, the model equations (i.e., the conservation of mass, momentum, and solute) need to be reformulated in the combined domain of fluid and mineral in a consistent manner. The combined domain is then stationary. This reformulated model has to incorporate the boundary conditions of the original model at the evolving interface as part of the model equations. An essential property of a phase field formulation is that the corresponding sharp-interface formulation (i.e., the original model equations and boundary conditions at the evolving interface) is recovered when the width of the diffuse interface approaches zero [21, 30]. This limit can be investigated using matched asymptotic expansions [14].

Considering mineral precipitation and dissolution, [49] proposed a phase field formulation based on the Allen–Cahn equation for the movement of the solid–liquid interface but without flow in the fluid phase. Later [38] extended an equivalent formulation of [49] to include two fluid phases—with curvature effects between them—but still without flow. There, the interfaces are moving due to curvature effects. An Allen–Cahn formulation for two-phase Stokes flow with curvature effects on the evolving fluid–fluid interface, but without chemical reactions, was formulated in [1]. A Cahn–Hilliard model for two fluid phases and a solid phase, including mineral precipitation, is proposed in [39]. Using matched asymptotic expansion techniques, in each of these four papers it is shown that the phase field models reduce to the corresponding sharp-interface models. The aim in this paper is to formulate a phase field model for mineral precipitation and dissolution, in which the flow of a fluid phase transporting the precipitating solute is also taken into account. The model builds on the ones in [38, 49]. Compared to [1], where the moving interface separates two mobile fluid phases, the current moving interface separates a mobile phase (the fluid) and an immobile (mineral) phase. Therefore, the formulation in [1] cannot be applied here. In this respect, the present situation is more similar to the melt convection model considered in [8], where the interface between stationary solid and flowing fluid is evolving due to melting. However, [8] did not consider the sharp-interface limit for their phase field formulation.

This paper is organized as follows. In section 2 the phase field formulation is introduced, based on the sharp interface formulation. Next, in section 3 we show that the phase field formulation reduces to the sharp-interface formulation when the width of the diffuse interface approaches zero. Two numerical examples showing the behavior of the phase field formulation are included in section 4. In particular, we show how the flow affects the dissolution process. Then homogenization techniques are applied in section 5 to derive a Darcy-scale counterpart for a specific setting of the phase field model. Finally, section 6 provides some further numerical examples: First, we study the behavior of the upscaled model parameters in terms of the diffuse interface parameter, and then the convergence of the homogenization process for a simplified situation, where the model is defined in a thin strip.

2. Formulation of the reactive transport problem. Before introducing the phase field formulation, first we formulate the corresponding sharp-interface model including a free boundary. Both models are restricted to the case where only one fluid phase is present, which, in the case of a porous medium, can be seen as a single-phase, fully saturated flow. Moreover, the density and viscosity of the fluid are

assumed constant. Furthermore, we only consider a simplified electrochemical system, where the precipitate is formed at the boundaries of the flow domain (the pore walls) and is the product of the reaction between two ions diffusing into and transported by the flowing fluid. If the diffusion coefficients of the two ions are the same, and if the system is electroneutral, one can simplify the chemistry by only considering one equation for the solute concentration, as knowing the concentration of one solute and using the electroneutrality of the system enables us to obtain the other concentration straightforwardly (see [25, 46, 50]).

The models below are given in a dimensional framework. The nondimensionalization is discussed later in subsection 5.2.

2.1. Sharp-interface formulation. We start with the sharp-interface formulation, which later motivates the phase field model. In this case, we let Ω denote the entire domain (the porous medium), which is divided into two disjoint subdomains: one occupied by the fluid, and the other occupied by the mineral. The mineral layer is the result of precipitation and dissolution and therefore has a variable thickness that is not known a priori. Hence, the domains occupied by the fluid and the mineral are both time dependent. Letting $t \geq 0$ stand for the time variable and denoting by $\Omega_f(t)$ the (time-dependent) fluid domain, the conservation laws for the fluid and its momentum and for the solute are

$$(2.1a) \quad \nabla \cdot \mathbf{q} = 0 \quad \text{in } \Omega_f(t),$$

$$(2.1b) \quad \rho_f \partial_t \mathbf{q} + \rho_f \nabla \cdot (\mathbf{q} \otimes \mathbf{q}) + \nabla p = \mu_f \nabla^2 \mathbf{q} \quad \text{in } \Omega_f(t),$$

$$(2.1c) \quad \partial_t u + \nabla \cdot (\mathbf{q}u) = D \nabla^2 u \quad \text{in } \Omega_f(t).$$

Here \mathbf{q} is velocity and p is pressure in the fluid, and ρ_f and μ_f are the constant density and viscosity of the fluid. Finally, u is solute concentration and D its diffusivity.

In the mineral domain $\Omega_m(t)$, the mineral is immobile and has a constant concentration u^* , which reduces (2.1a)–(2.1c) to

$$\mathbf{q} = \mathbf{0} \quad \text{in } \Omega_m(t).$$

In what follows, we assume that the concentration in the mineral is always larger than the one in the fluid, namely $u^* > u(x, t)$ for all $t \geq 0$ and $x \in \Omega_f(t)$.

We let $\Gamma(t)$ stand for the free boundary separating $\Omega_f(t)$ and $\Omega_m(t)$. Observe that for any time t , one has

$$\Omega = \Omega_f(t) \cup \Omega_m(t) \cup \Gamma(t) \quad \text{and} \quad \Omega_f(t) \cap \Omega_m(t) = \emptyset.$$

At $\Gamma(t)$, to guarantee the mass balance we adopt the Rankine–Hugoniot boundary conditions for the fluid and the solute. We assume that the chemistry does not lead to any volume change, which means that one mineral mole takes exactly the same volume as the one occupied in the fluid by the ion moles forming the mineral (see [11, 47]). With this, the conditions at the moving interface are

$$(2.2a) \quad v_n + \gamma \kappa = -\frac{1}{u^*} f(u) \quad \text{on } \Gamma(t),$$

$$(2.2b) \quad \mathbf{q} = \mathbf{0} \quad \text{on } \Gamma(t),$$

$$(2.2c) \quad v_n(u^* - u) = \mathbf{n} \cdot D \nabla u \quad \text{on } \Gamma(t),$$

where v_n is the speed of the moving interface in the normal direction \mathbf{n} pointing into the mineral, γ is the diffusivity of the interface, and κ is the curvature of the moving interface.

Observe that (2.2a) is describing the movement of the free boundary due to precipitation and dissolution. More precisely, the function f is the difference between the precipitation rate and the dissolution rate. Without being restricted to this choice, we use a simple reaction rate inspired by the mass action kinetics, namely,

$$(2.3) \quad f(u) = f_p(u) - f_d = k \left(\frac{u^2}{u_{\text{eq}}^2} - 1 \right),$$

where u_{eq} is the (known) equilibrium concentration for which $u^* > u_{\text{eq}}$, and k is a reaction constant of dimension $\frac{\text{mol}}{\text{m}^2 \text{ s}}$. This choice of reaction rate corresponds to a precipitation rate increasing with ion concentration and a constant dissolution rate. Note that to avoid dissolution whenever no mineral is present, in [25, 46] the dissolution rate is given as a multivalued rate involving the Heaviside graph.

As follows from (2.2a), next to the precipitation and dissolution, the free boundary is also moving due to surface curvature. The latter effect is more common for two-phase flow but can also occur for interfaces separating a fluid from a solid phase. This assumption is natural when minimizing the free energy of the surface [2, 40]. In our case, γ will be very small.

The last two conditions at $\Gamma(t)$ ensure the mass balance for the fluid and the solute. Since we assume no volume change in connection with the chemistry, the normal component of the fluid velocity is zero at the moving boundary. Combined with the no-slip condition, it follows that the fluid velocity \mathbf{q} is zero at the moving boundary. Finally, (2.2c) is the Rankine–Hugoniot condition for the ions. The flux on the right-hand side is due to diffusion as the convective flux is zero, following from (2.2b). Also, the mineral is immobile, so the flux in the mineral subdomain is 0, whereas the concentration u^* is fixed.

For completeness we mention that the location of the moving interface $\Gamma(t)$ can be determined as the 0 level set of a function $S : \Omega \times [0, \infty) \rightarrow \mathbb{R}$ satisfying

$$S(x, t) = \begin{cases} < 0 & \text{if } x \in \Omega_f(t), \\ 0 & \text{if } x \in \Gamma(t), \\ > 0 & \text{if } x \in \Omega_m(t). \end{cases}$$

Then, S satisfies the equation

$$\partial_t S + v_n |\nabla S| = 0 \quad \text{for } x \in \Omega.$$

The level-set approach is adopted in [11, 13, 43, 47].

2.2. Phase field formulation. An alternative to the sharp-interface formulation given above is to consider a phase field formulation. In this case, one uses a phase field, which is an approximation of the characteristic function. The nondimensional phase field ϕ is close to and approaches 1 in the fluid phase, is close to and approaches 0 in the mineral, and has a smooth transition of (dimensional) width $O(\lambda) > 0$ separating the phases. In other words, $\lambda > 0$ is a phase field parameter related to the thickness of the diffusive transition region. It is to be expected that when passing λ to 0, one obtains in the limit the original sharp-interface model. In consequence, the phase field approach replaces the interface between the two phases by a smooth transition region where diffusive effects are included. The advantage is that the model equations can now be defined on a stationary domain (here Ω) instead of on time-evolving domains. This approach, however, requires the flow and transport equations

to also be defined in the mineral phase. Here we extend the phase field models in [38, 49] as follows to include flow:

$$(2.4a) \quad \lambda^2 \partial_t \phi + \gamma P'(\phi) = \gamma \lambda^2 \nabla^2 \phi - 4\lambda \phi(1 - \phi) \frac{1}{u^*} f(u),$$

$$(2.4b) \quad \nabla \cdot (\phi \mathbf{q}) = 0,$$

$$(2.4c) \quad \rho_f \partial_t (\phi \mathbf{q}) + \rho_f \nabla \cdot (\phi \mathbf{q} \otimes \mathbf{q}) = -\phi \nabla p + \mu_f \phi \nabla^2 (\phi \mathbf{q}) - g(\phi, \lambda) \mathbf{q} + \frac{1}{2} \rho_f \mathbf{q} \partial_t \phi,$$

$$(2.4d) \quad \partial_t (\phi(u - u^*)) + \nabla \cdot (\phi \mathbf{q} u) = D \nabla \cdot (\phi \nabla u).$$

The model is explained in detail below.

2.2.1. Comments on the phase field equation (2.4a). The parameter $\lambda > 0$ appearing in the phase field equation is assumed small and is related to the width of the diffuse interface. Further, $P(\phi) = 8\phi^2(1 - \phi)^2$ is the double-well potential, which ensures that the phase field mainly attains values (close to) 0 and 1 for small values of λ . Formally, this follows from the observation that if λ is small, the term $P'(\phi)$ dominates in (2.4a), implying that ϕ approaches one of the three equilibrium values 0, 1/2, 1. Later we show that 1/2 is an unstable equilibrium, from which the conclusion follows.

The reaction rate $f(u)$ and diffusion parameter γ are the same as those in the sharp-interface formulation. Note that due to the $4\phi(1 - \phi)$ factor, the reaction term is nonzero only in the diffuse transition zone between the two phases, and this factor ensures that ϕ stays between 0 and 1. Note that in sharp-interface models, further dissolution after all mineral is dissolved is usually avoided by using a multivalued dissolution rate based on a Heaviside graph (see [25, 46]), which complicates the analysis and the development of numerical schemes (see [3, 27]). This is superfluous for the phase field formulation proposed here because in the absence of mineral, only the water phase is present, implying $\phi \equiv 1$, and therefore no dissolution can take place.

2.2.2. Comments on the flow equations (2.4b) and (2.4c). The flow equations are now also defined in the mineral phase. To ensure that flow only occurs in the fluid and not in the mineral, some modifications have been made. First, the flow velocity \mathbf{q} and pressure gradient ∇p have become $\phi \mathbf{q}$ and $\phi \nabla p$. This leaves the flow equations unchanged in the fluid phase when $\phi = 1$, whereas these quantities are vanishing in the mineral phase where $\phi = 0$.

Second, the term $g(\phi, \lambda) \mathbf{q}$ is added. Here, $g(\phi, \lambda)$ is decreasing in the first argument, surjective, and twice differentiable and fulfills $g(1, \lambda) = 0$ and $g(0, \lambda) > 0$. This way, $\mathbf{q} = \mathbf{0}$ is the only possible solution when $\phi = 0$ (also see assumption A.4 in [22]). Moreover, this term must also ensure that the velocities in the diffuse transition zone between $\phi = 0$ and $\phi = 1$ are low, and therefore it works as an interpolation function for velocities in this zone. In [8], dealing with a similar model for melting and solidification, an artificial friction term is introduced to ensure the desired behavior for $\phi \mathbf{q}$ inside the diffuse interface. Using the current notation, their friction term would correspond to $g(\phi, \lambda) = \frac{K(1-\phi)^2 \phi}{\lambda^2}$ for some constant K [8]. However, as will be explained in Remark 3.1, a term of $O(\lambda^{-2})$ would restrict the phase field model from approaching the sharp-interface model when $\lambda \searrow 0$, and therefore it is not adopted here.

A similar idea is adopted in [22], focusing on shape optimization, where the term $g(\phi, \lambda) = \frac{K}{\sqrt{\lambda}} \frac{(1-\phi)^n}{\phi+n}$ is applied. The constant $n > 0$ determines the shape of the

function g . More precisely, a larger value of n leads to a function that is close to an affine one, behaving as $(1 - \phi)$. In [22], $n = 10$ was found to work better regarding numerical results. Inspired by [22], here we let $g(\phi, \lambda) = \frac{K}{\lambda} \frac{(1-\phi)^n}{\phi+n}$ with $n = 10$. Later we will see that this gives good numerical results for the present model too. However, any function g fulfilling the requirements listed previously can be adopted, the specific choice being based on the impact on the numerical behavior.

Finally, the term $\frac{1}{2}\rho_f \mathbf{q} \partial_t \phi$ added to (2.4c) accounts for the combined flow with accumulation of the phase field variable to ensure conservation of kinetic energy when there is precipitation. Note that the two time derivatives can be combined and rewritten as $\rho_f \sqrt{\phi} \partial_t (\sqrt{\phi} \mathbf{q})$, a formulation used in, e.g., [9].

2.2.3. Comments on the ion transport equation (2.4d). Compared to [38], the only difference appearing in the ion transport equation (2.4d) is in the presence of the convective term. Note that the time derivative can be rewritten as $\partial_t(\phi u + (1 - \phi)u^*)$. This is nothing but the derivative of the phase field weighted convex combination of ion concentrations u (in the fluid phase) and the mineral concentration u^* (in the mineral phase). Recalling that in the mineral phase there is no diffusive or convective transport, we see that (2.4d) represents the total mass balance of the species.

2.2.4. Decreasing energy of the phase field formulation. The energy associated with the model (2.4) is given by

$$E = \frac{1}{2}\rho_f \phi \mathbf{q}^2 + \gamma \lambda^{-1} P(\phi) + \frac{1}{2} \gamma \lambda |\nabla \phi|^2 + \phi F(u)$$

and is the sum of the kinetic energy, the free energy of the phase field, and the energy of the ions. The function $F(u)$ is defined implicitly as a solution to the equation

$$\frac{1}{u^*} f(u) = F(u) - F'(u)u + F'(u)u^*.$$

As $f(u)$ is increasing with u , $F(u)$ is convex for $u < u^*$. Differentiating the above, we get that

$$\partial_t(\phi F(u)) = F'(u) \partial_t(\phi(u - u^*)) + \frac{1}{u^*} f(u) \partial_t \phi.$$

When considering (2.4) on a bounded domain Ω with no-slip boundary conditions for \mathbf{q} and zero Neumann boundary conditions for ϕ and u at the boundary $\partial\Omega$, one gets

$$\begin{aligned} \frac{d}{dt} \int_{\Omega} E dx = \int_{\Omega} & \left[-\mu_f \nabla(\phi \mathbf{q}) : \nabla(\phi \mathbf{q}) - g(\phi, \lambda) \mathbf{q}^2 - D\phi F''(u) |\nabla u|^2 \right. \\ & \left. - \lambda^{-1} \left(\nu - \frac{1}{u^*} f(u) \right) \left(\nu - 4\phi(1 - \phi) \frac{1}{u^*} f(u) \right) \right] dx, \end{aligned}$$

where $\nu = \gamma \lambda \nabla^2 \phi - \gamma \lambda^{-1} P'(\phi)$. The first three terms on the right-hand side describe energy dissipation due to viscosity, friction close to the mineral, and diffusion of ions. The fourth term might be positive and thus lead to an increasing energy. This will be the case if curvature effects (see (2.2a)) counteract the ion reaction. However, for fixed λ , we get a bounded energy growth as in [38]. Note that the increasing energy is possible due to the factor $4\phi(1 - \phi)$ in the reactive term in (2.4a). Using a multivalued Heaviside graph for the dissolution rate instead of the $4\phi(1 - \phi)$ factor, as commented on in subsection 2.2.1, would result in a model with decreasing energy,

while a regularized Heaviside graph would not. To limit the values of ϕ between 0 and 1 and to ease the following analysis and numerical implementation, we choose to keep the $4\phi(1 - \phi)$ factor and not use a Heaviside graph.

2.3. Regularized phase field formulation. The model (2.4) is formulated in the full domain Ω . In doing so, we include the term $g(\phi, \lambda)\mathbf{q}$ to ensure that $\mathbf{q} = \mathbf{0}$ in the mineral phase. Observe that the ion concentration u and the fluid pressure p are also defined in the region occupied by the mineral in the sharp-interface formulation. For u , a possible extension in the mineral domain is u^* , but this may lead to difficulties related to the regularity of u in the transition from the phase field model to the sharp-interface one, when $\lambda \rightarrow 0$. Moreover, there is no indication about how to extend p in the mineral domain. At the same time, the model in (2.4) does not provide any information about what values u and p should attain in the mineral domain. Although the structure of the phase field equation (2.4a) ensures that ϕ will never reach 0 (or 1), unless initialized or if appearing on the boundary $\partial\Omega$, ϕ can become arbitrarily close to 0 (and 1). From a numerical point of view, this can lead to a badly conditioned discretization, as the last two equations in (2.4) are close to degenerate whenever $\phi \searrow 0$ and cannot be used to determine u and p in the mineral. To avoid this, we regularize the model by adding a small, nondimensional $\delta > 0$ to the phase field ϕ in the mass, momentum, and solute conservation equations. The regularized model becomes

$$(2.5a) \quad \lambda^2 \partial_t \phi + \gamma P'(\phi) = \gamma \lambda^2 \nabla^2 \phi - 4\lambda \phi(1 - \phi) \frac{1}{u^*} f(u),$$

$$(2.5b) \quad \nabla \cdot ((\phi + \delta)\mathbf{q}) = 0,$$

$$(2.5c) \quad \rho_f \partial_t((\phi + \delta)\mathbf{q}) + \rho_f \nabla \cdot ((\phi + \delta)\mathbf{q} \otimes \mathbf{q}) = -(\phi + \delta)\nabla p + \mu_f(\phi + \delta)\nabla^2((\phi + \delta)\mathbf{q}) - g(\phi, \lambda)\mathbf{q} + \frac{1}{2}\rho_f \mathbf{q} \partial_t \phi,$$

$$(2.5d) \quad \partial_t((\phi + \delta)(u - u^*)) + \nabla \cdot ((\phi + \delta)\mathbf{q}u) = D\nabla \cdot ((\phi + \delta)\nabla u).$$

Note that this regularization is only needed to facilitate the numerical discretization. For completeness, we use it also in the analysis given below.

Remark 2.1. The results for decreasing and limited growth of the free energy discussed in subsection 2.2.4 are also valid for the regularized formulation. To see this, one only needs to replace ϕ by $\phi + \delta$ in the terms associated with the kinetic energy and the energy of the ions.

3. The sharp-interface limit of the phase field formulation. As stated before, the phase field model can be seen as an approximation of the sharp-interface model, defined in the entire domain and where the free boundary is replaced by a diffuse interface region. To justify this, we investigate the limit of the phase field model in (2.5) as λ , the width of the diffuse transition zone, approaches zero and show that this limit is exactly the model in subsection 2.1. We follow the ideas of [14] and distinguish between the behaviors of the solution close to the interface and far away from it. To this aim we first let L be a typical length in the model and introduce the new, dimensionless parameter $\xi = \lambda/L$ related to thickness of the diffuse interface region. We investigate the behavior of the solution as $\xi \searrow 0$ by expanding the unknowns in terms of ξ and equating terms of similar order. This is done in two different ways, close to the diffuse interface (the inner expansions) and away from it (the outer expansions), which are connected by applying matching conditions in the transition region where both expansions are valid.

Before proceeding we mention that for the phase field equation, the steps are the same as in [38] and therefore are only shown briefly. Throughout this matched asymptotic analysis we take the regularization parameter as $\delta = \xi$. This choice is made for convenience as δ is not needed in the sharp-interface model. In subsequent sections, δ and ξ (or λ) can be chosen independently.

3.1. The two expansions and matching conditions. Away from the interface, we consider the *outer expansion* of ϕ , u , p , and \mathbf{q} . For ϕ this reads as

$$(3.1) \quad \phi^{\text{out}}(t, \mathbf{x}) = \phi_0^{\text{out}}(t, \mathbf{x}) + \xi \phi_1^{\text{out}}(t, \mathbf{x}) + \xi^2 \phi_2^{\text{out}}(t, \mathbf{x}) + \dots$$

and similarly for the other unknowns.

For the *inner expansion*, valid near the diffuse interface, we switch to local coordinates. More precisely, we let $\Gamma(t)$ denote the set of points $\mathbf{y}_\xi \in \Omega$ along which $\phi(\mathbf{y}_\xi, t) = 1/2$. Observe that these points depend on t , and on ξ as the model depends on $\lambda = L\xi$. With \mathbf{s} being the parameterization along $\Gamma_\xi(t)$ (\mathbf{s} being a scalar in the two-dimensional case) and \mathbf{n}_ξ the normal vector at $\Gamma_\xi(t)$ pointing into the mineral, one can define r , the signed distance from a point \mathbf{x} near $\Gamma_\xi(t)$ to this interface. Clearly, r depends on \mathbf{x} and t and is positive in the mineral region. One gets

$$(3.2) \quad \mathbf{x} = \mathbf{y}_\xi(t, \mathbf{s}) + r\mathbf{n}_\xi(t, \mathbf{s}),$$

as presented in Figure 1. It can be shown (see [14]) that

$$|\nabla r| = 1, \quad \nabla r \cdot \nabla s_i = 0, \quad \partial_t r = -v_n, \quad \nabla^2 r = \frac{\kappa + 2\Pi r}{1 + \kappa r + \Pi r^2},$$

where κ and Π are the mean and Gaussian curvatures of the interface. Further, the point \mathbf{y}_ξ has the expansion $\mathbf{y}_\xi = \mathbf{y}_0 + \xi\mathbf{y}_1 + \dots$, where \mathbf{y}_0 is a point on the interface $\Gamma_0^{\text{out}}(t)$ defined through $\phi_0^{\text{out}} = 1/2$, and similarly $\mathbf{n}_\xi = \mathbf{n}_0 + \xi\gamma_1\mathbf{n}_1 + O(\xi^2)$, where \mathbf{n}_0 is the normal vector of $\Gamma_0^{\text{out}}(t)$.

With $z = r/\xi$ and in terms of z and \mathbf{s} , we consider the *inner expansions*

$$(3.3) \quad \phi^{\text{in}}(t, \mathbf{x}) = \phi_0^{\text{in}}(t, z, \mathbf{s}) + \xi \phi_1^{\text{in}}(t, z, \mathbf{s}) + \xi^2 \phi_2^{\text{in}}(t, z, \mathbf{s}) + \dots$$

and similarly for the other unknowns. In the curvilinear coordinates (3.2), by the scaling of the z variable, the derivatives are rewritten as follows. For a generic variable v or \mathbf{v} , we obtain [14]

$$\begin{aligned} \partial_t v &= -\xi^{-1}v_{n,0}\partial_z v^{\text{in}} + (\partial_t + \partial_t s \cdot \nabla_{\mathbf{s}})v^{\text{in}} + O(\xi), \\ \nabla_x v &= \xi^{-1}\partial_z v^{\text{in}}\mathbf{n}_0 + \nabla_\Gamma v^{\text{in}} + O(\xi), \\ \nabla_x \cdot \mathbf{v} &= \xi^{-1}\partial_z \mathbf{v}^{\text{in}} \cdot \mathbf{n}_0 + \nabla_\Gamma \cdot \mathbf{v}^{\text{in}} + O(\xi), \\ \nabla_x^2 v &= \xi^{-2}\partial_{zz} v + \xi^{-1}\kappa_0\partial_z v + O(1), \end{aligned}$$

where we have used $\nabla_x^2 r = \kappa_0 + O(\xi)$ as the lowest order mean curvature and $v_n = v_{n,0} + O(\xi)$. Here, κ_0 and $v_{n,0}$ are the curvature and normal velocity of the interface $\Gamma_0^{\text{out}}(t)$. Further, in the last equality the properties $|\nabla r| = 1$ and $\nabla r \cdot \nabla s_i = 0$ have been used.

For the outer expansion and a fixed t and \mathbf{s} , we let $\mathbf{y}_{1/2\pm}$ denote the limit $r \searrow 0$ (i.e., from the mineral side), respectively $r \nearrow 0$ (from the fluid side), of \mathbf{x} rewritten in terms of the local coordinates in (3.2). We associate the corresponding limit values of the outer expansion with the ones for the inner expansion, obtained when $z \rightarrow \pm\infty$.

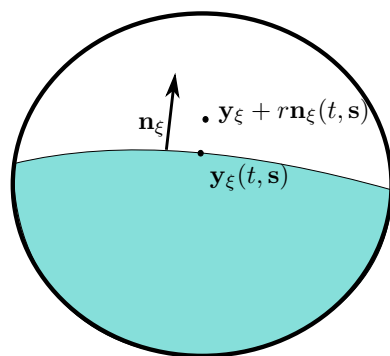


FIG. 1. Local coordinates near the interface.

More precisely, we assume that the two expansions of the phase field ϕ fulfill the following matching conditions [14]:

$$(3.4a) \quad \lim_{z \rightarrow \pm\infty} \phi_0^{\text{in}}(t, z, \mathbf{s}) = \phi_0^{\text{out}}(t, \mathbf{y}_{1/2\pm}),$$

$$(3.4b) \quad \lim_{z \rightarrow \pm\infty} \partial_z \phi_0^{\text{in}}(t, z, \mathbf{s}) = 0,$$

$$(3.4c) \quad \lim_{z \rightarrow \pm\infty} (\phi_1^{\text{in}}(t, z, \mathbf{s}) - (z + y_1) \nabla \phi_0^{\text{out}}(t, \mathbf{y}_{1/2\pm}) \cdot \mathbf{n}_0) = \phi_1^{\text{out}}(t, \mathbf{y}_{1/2\pm}),$$

$$(3.4d) \quad \lim_{z \rightarrow \pm\infty} \partial_z \phi_1^{\text{in}}(t, z, \mathbf{s}) = \nabla \phi_0^{\text{out}}(t, \mathbf{y}_{1/2\pm}) \cdot \mathbf{n}_0,$$

and similarly for the other unknowns.

3.2. Outer expansions. Following the steps in [38], we substitute the outer expansion (3.1) for ϕ into the phase field equation (2.5a). For the $O(1)$ term, which is the leading order, one obtains

$$P'(\phi_0^{\text{out}}) = 0.$$

This equation has three solutions: $\phi_0^{\text{out}} = 0$, $1/2$, and 1 . Using the formal argument in [49], the first and last solutions are stable since $P''(0)$ and $P''(1)$ are positive, whereas $\phi_0^{\text{out}} = 1/2$ is unstable since $P''(1/2) < 0$. In view of this, we see that in the limit $\xi \rightarrow 0$, one obtains the solutions $\phi_0^{\text{out}} = 0$ and $\phi_0^{\text{out}} = 1$, and we let $\Omega_0^f(t)$ and $\Omega_0^m(t)$ be the (time-dependent) subdomains of Ω where ϕ_0^{out} is 1 and 0 , respectively.

Using the outer expansions in the flow equations (2.5b) and (2.5c) and the ion conservation (2.5d), it is straightforward to show that the original sharp-interface model equations (2.1) are recovered for the points in $\Omega_0^f(t)$. Moreover, for the flow equations, one also obtains $\mathbf{q}_0^{\text{out}} = \mathbf{0}$ in $\Omega_0^m(t)$.

3.3. Inner expansions. We now apply the inner expansions and the matching conditions to the phase field model to recover the boundary conditions at the evolving interface.

3.3.1. Phase field equation. For the phase field equation (2.5a) we follow the steps in [38] and obtain that the dominating $O(1)$ terms satisfy

$$(3.5) \quad P'(\phi_0^{\text{in}}) = L^2 \partial_z^2 \phi_0^{\text{in}}.$$

Due to (3.4), one has $\lim_{z \rightarrow -\infty} \phi_0^{\text{in}}(t, z, \mathbf{s}) = 1$ and $\lim_{z \rightarrow \infty} \phi_0^{\text{in}}(t, z, \mathbf{s}) = 0$. Further, $\phi_0^{\text{in}}(t, 0, \mathbf{s}) = 0.5$, as this should define the moving interface when $\xi \rightarrow 0$. Hence, multiplying (3.5) by $\partial_z^2 \phi_0^{\text{in}}$, integrating the result in z , and using the matching conditions fulfilled by ϕ_0^{in} and the specific form of $P(\phi)$, one gets

$$(3.6) \quad \partial_z \phi_0^{\text{in}} = -\frac{4}{L} \phi_0^{\text{in}}(1 - \phi_0^{\text{in}}).$$

Since $\phi_0^{\text{in}}(t, 0, \mathbf{s}) = 1/2$, the solution is

$$(3.7) \quad \phi_0^{\text{in}}(t, z, \mathbf{s}) = \phi_0^{\text{in}}(z) = \frac{1}{1 + e^{4z/L}} = \frac{1}{2} \left(1 + \tanh \left(\frac{2z}{L} \right) \right).$$

For the $O(\xi)$ terms, one obtains

$$(P''(\phi_0^{\text{in}}) - L^2 \partial_z^2) \phi_1^{\text{in}} = (L^2 v_{n,0} + L^2 \gamma \kappa_0) \partial_z \phi_0^{\text{in}} - 4L \phi_0^{\text{in}}(1 - \phi_0^{\text{in}}) \frac{1}{u^*} f(u_0^{\text{in}}).$$

We view the left-hand side as an operator \mathcal{L} depending on ϕ_0^{in} and applied to ϕ_1^{in} . As \mathcal{L} is a Fredholm operator of index zero, the above equation has a solution if and only if the right-hand side, denoted by $A(\phi_0^{\text{in}})$, is orthogonal to the kernel of \mathcal{L} . As follows from (3.5), $\partial_z \phi_0^{\text{in}}$ lies in the kernel of \mathcal{L} . Since $v_{n,0}$, κ_0 , and u_0^{in} are independent of z (the latter will be shown in the following section), the solvability condition implies

$$\begin{aligned} 0 &= \int_{-\infty}^{\infty} A(\phi_0^{\text{in}}) \partial_z \phi_0^{\text{in}} dz \\ &= L^2 (v_{n,0} + \gamma \kappa_0) \int_{-\infty}^{\infty} (\partial_z \phi_0^{\text{in}})^2 dz - 4L \frac{1}{u^*} f(u_0^{\text{in}}) \int_{-\infty}^{\infty} \phi_0^{\text{in}}(1 - \phi_0^{\text{in}}) \partial_z \phi_0^{\text{in}} dz \\ &= \frac{2}{3} L \left(v_{n,0} + \gamma \kappa_0 + \frac{1}{u^*} f(u_0^{\text{in}}) \right). \end{aligned}$$

From this, by applying matching conditions for u at the moving interface, we obtain the condition

$$v_{n,0} = -\gamma \kappa_0 - \frac{1}{u^*} f(u_0^{\text{out}}(t, \mathbf{y}_{1/2-})),$$

which is the first boundary condition (2.2a) at the moving interface.

3.3.2. Mass conservation equation. The dominating $O(\xi^{-1})$ term arising from inserting the inner expansions into (2.5b) is

$$(3.8) \quad \partial_z (\phi_0^{\text{in}} \mathbf{q}_0^{\text{in}}) \cdot \mathbf{n}_0 = 0.$$

By integrating with respect to z and using matching conditions, we obtain

$$\mathbf{q}_0^{\text{out}}(t, \mathbf{y}_{1/2-}) \cdot \mathbf{n}_0 = 0.$$

In other words, the normal component of the velocity is zero at the moving interface. To conclude the same for the tangential component, we consider the momentum conservation equation.

3.3.3. Momentum conservation equation. The dominating $O(\xi^{-2})$ term in the momentum equation (2.5c) is

$$\mu_f \phi_0^{\text{in}} \partial_z^2 (\phi_0^{\text{in}} \mathbf{q}_0^{\text{in}}) = \mathbf{0}.$$

Integrating with respect to z and using matching conditions results in

$$\mathbf{q}_0^{\text{out}}(t, \mathbf{y}_{1/2-}) = \mathbf{0},$$

which is the second boundary condition (2.2b) at the moving interface.

Remark 3.1. Note that choosing $g(\phi, \lambda) = \frac{K\phi(1-\phi)^2}{\lambda^2}$ as in [8] would lead to the dominating $O(\xi^{-2})$ terms being

$$\mu_f \phi_0^{\text{in}} \partial_z^2 (\phi_0^{\text{in}} \mathbf{q}_0^{\text{in}}) = K \phi_0^{\text{in}} (1 - \phi_0^{\text{in}})^2 \mathbf{q}_0^{\text{in}}.$$

Although μ_f and K are constants, and ϕ_0^{in} is known through (3.7), solving this equation for \mathbf{q}_0^{in} is not straightforward, and therefore it is unclear whether $\mathbf{q}_0^{\text{out}}(t, \mathbf{y}_{1/2-}) = \mathbf{0}$ is recovered in this case.

3.3.4. Ion conservation equation. The dominating $O(\xi^{-2})$ term obtained by inserting the inner expansions into (2.5d) is

$$\partial_z (\phi_0^{\text{in}} \partial_z u_0^{\text{in}}) = 0.$$

Integrating with respect to z and using matching conditions and the fact that $\phi_0^{\text{in}} > 0$, we obtain

$$\partial_z u_0^{\text{in}} = 0,$$

and hence $u_0^{\text{in}} = u_0^{\text{in}}(t, \mathbf{s})$ as mentioned in the previous section.

Taking advantage of $\partial_z u_0^{\text{in}} = 0$ and (3.8), the $O(\xi^{-1})$ terms satisfy

$$-v_{n,0}(u_0^{\text{in}} - u^*) \partial_z \phi_0^{\text{in}} = D \partial_z (\phi_0^{\text{in}} \partial_z u_1^{\text{in}}).$$

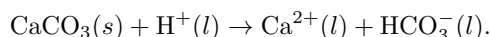
Integrating with respect to z from $-\infty$ to $+\infty$ and applying matching conditions lead to

$$v_{n,0}(u_0^{\text{out}}(t, \mathbf{y}_{1/2-}) - u^*) = -D \nabla u_0^{\text{out}}(t, \mathbf{y}_{1/2-}) \cdot \mathbf{n}_0,$$

which is the third boundary condition (2.2c) at the moving interface.

4. Numerical behavior of the phase field model. We consider two numerical examples showing the applicability and the potential of the model (2.5) by studying the dissolution of a mineral crystal located in a channel and subject to a flow field. The first example is from the benchmark study [33], and we assess how the phase field model (2.5) behaves for a specific case compared to the results in the benchmark study. In the second example, we make a qualitative assessment of how the mineral dissolution process is affected by the strength of the flow field, inspired by the sharp-interface simulations in [34].

4.1. Dissolution of a calcite crystal. We consider the benchmark problem II from [33]. Here, calcite dissolves through the chemical reaction



Since H^+ is needed for calcite to dissolve, we model this as a one-way reaction, where (2.5d) is replaced by

$$(4.1) \quad \partial_t((\phi + \delta)(u_{H^+} + u^*)) + \nabla \cdot ((\phi + \delta)\mathbf{q}u_{H^+}) = D \nabla \cdot ((\phi + \delta)\nabla u_{H^+}),$$

and use the simple, linear reaction rate

$$(4.2) \quad f(u_{H^+}) = -ku_{H^+}$$

in (2.5a). This means there is no precipitation, and the dissolution rate increases with larger access to H^+ . Note the change in sign in the time derivative in (4.1) compared to (2.5d). This occurs because H^+ is consumed, not produced, for calcite to dissolve. Writing the time derivative as $\partial_t(\phi u_{H^+} - (1 - \phi)u^*)$ as in subsection 2.2.3 shows that we are conserving the difference between H^+ and the mineral, reflecting that as one calcite molecule dissolves, one H^+ atom is consumed. We do not model the concentrations of the solutes Ca^{2+} and HCO_3^- as they do not affect the reaction rate.

We follow the same setup as in [33] by considering a two-dimensional channel of length 1 mm and width 0.5 mm, where a circular calcite crystal of initial radius 0.1 mm is centered in (0.5, 0.25) mm. A uniform flow field of given velocity $q_{in} = 0.0012$ m/s is applied at $x = 0$ mm. Initially and at the inlet a concentration of $u_{H^+} = 10$ mol/m³ is applied. The top and bottom of the channel are no-slip boundaries, while fluid can leave through the outlet at $x = 1$ mm. We refer the reader to Table 1 for all specified parameters for model (2.5a)–(2.5c) and (4.1). All parameters not related to the phase field are taken from [33].

TABLE 1
Parameters corresponding to benchmark II in [33] and phase field parameters.

Parameter	Symbol	Value	Units
Fluid density	ρ_f	10^3	kg m ⁻³
Fluid viscosity	μ_f	10^{-3}	kg m ⁻¹ s ⁻¹
Diffusion coefficient	D	10^{-9}	m ² s ⁻¹
Inlet velocity	q_{in}	0.0012	m s ⁻¹
Reaction rate constant in (4.2)	k	8.9×10^{-3}	mol m ⁻² s ⁻¹
Inlet and initial concentration	u_{H^+}	10	mol m ⁻³
Calcite molar density	u^*	27100	mol m ⁻³
Phase field diffuse interface width	λ	2.5×10^{-5}	m
Phase field interface diffusivity	γ	2.8×10^{-14}	m ² s ⁻¹
Phase field regularization	δ	10^{-6}	-
Phase field flow interpolation; $g(\phi, \lambda) = \frac{10K(1-\phi)}{\lambda(\phi+10)}$	K	25	kg m ⁻² s ⁻¹

The model equations are discretized using a control volume method on a uniform, rectangular staggered grid of 200×200 grid cells. The phase field, pressure, and solute are defined in the centers of the control volumes, while the velocity is defined at the center of the edges. Convective fluxes are approximated by an upstream approximation, and diffusive fluxes are discretized using a two-point approximation. The model is discretized in time using the backward Euler scheme with a constant time-step size $\Delta t = 1.35$ s until the end time $t = 2700$ s = 45 min. The resulting nonlinear systems of equations are solved using Newton iterations in each time step, with the previous time step as an initial guess.

Figure 2 shows the shape of the calcite crystal initially and after 15, 30, and 45 minutes. The shapes are shown by plotting the $\phi = 0.5$ isolines of the phase field. The initially circular calcite crystal dissolves unevenly due to the accessibility of H^+ varying with the flow around the crystal. Since the flow takes place from left to right, the dissolution is strongest at the left part of the calcite crystal and reduces while moving to the right part of the crystal. Comparing this to the corresponding Figure 8 in [33], we see the same qualitative change in shape. The crystal dissolves slightly faster in our approach compared to [33], which could be due to the nonconservative property of the Allen–Cahn equation.

4.2. Effect of flow field strength on dissolution. We consider a qualitative comparison with respect to how mineral dissolves when located in flow fields of

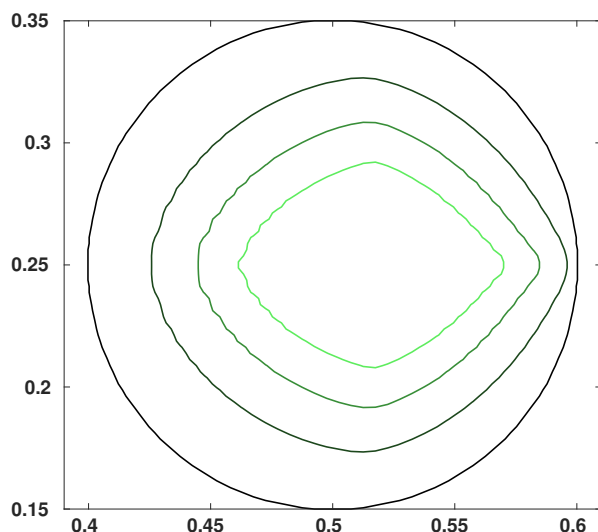


FIG. 2. The mineral shape while dissolving (zoomed-in view of the channel where the calcite is present initially). The evolution of the calcite boundary at $t = 0, 15 \text{ min}, 30 \text{ min},$ and 45 min (from the outermost curve to the innermost one). The axis scales are in mm.

different strengths, inspired by the setup in [34, sect. 3.1]. As in the previous test, we consider a channel of length 1 mm and width 0.5 mm, with an initially circular mineral located in $(0.5, 0.25)$ mm having radius 0.1 mm. At $x = 0$, a uniform flow field of a given velocity is applied and the fluid can flow out at $x = 1$, while the top and bottom are no-slip boundaries. We now use the original model (2.5) and reaction rate (2.3). To trigger dissolution of the mineral, we apply an equilibrium concentration $u_{\text{eq}} = 0.5 \text{ mol/m}^3$, and for the solute we use an initial concentration of u_{eq} and a Dirichlet boundary condition at the inlet of $u_{\text{eq}}/2$. The Péclet and Damköhler numbers are defined as

$$\text{Pe} = \frac{Lq_{\text{in}}}{D}, \quad \text{Da} = \frac{k}{u_{\text{eq}}q_{\text{in}}},$$

where $D = 5 \times 10^{-9}$ is the diffusivity of the solute, $k = 1.9 \times 10^{-5}$ is the reaction constant, and L is the length of the channel. By varying q_{in} among (a) 1.2×10^{-5} m/s, (b) 1.2×10^{-4} m/s, (c) 1.2×10^{-3} m/s, and (d) 0.012 m/s, we consider the four Péclet and Damköhler numbers given in Table 2, which are the same cases applied in [34]. We use a mineral concentration of $u^* = 1 \text{ mol/m}^3$. This is an artificially low value of a mineral density but causes the mineral to change shape faster as it dissolves. For the phase field, we use the same parameters as in Table 1.

TABLE 2
Nondimensional numbers in the four simulations.

Simulation	(a)	(b)	(c)	(d)
Péclet number	2.4	24	240	2400
Damköhler number	3.173	0.317	0.032	0.003

The model (2.5) is discretized using the same control volume method as before using a uniform, rectangular staggered grid of 200×200 grid cells. The model is time stepped using backward Euler with a constant time-step size $\Delta t = \Delta y/q_{in}$, and the nonlinear systems of equations are solved using Newton iterations in each time step, with the previous time step as an initial guess.

The four simulations are carried out until the mineral is dissolved completely. Figure 3 shows the isolines $\phi = 0.5$ at different time steps to indicate the shape of the mineral as it dissolves. Although we consider a different chemical system from that in [34], we see how the later isolines go from being circular for low velocities to more elongated at larger velocities as in [34, Figure 2]. For low velocities, the reaction rate is quite similar for the entire mineral surface, although with an increase at the front where lower solute concentrations are first met. At larger velocity, dissolution is faster on the sides as dissolved solute is more efficiently transported away, triggering further dissolution. The mineral generally dissolves faster when the Péclet number increases, although the same reaction rate has been used. This is caused by the dissolving mineral creating a local increase in the solute concentration, which is transported away more quickly when the flow velocity is large. We see how the interplay between velocity and diffusion gives the different shapes of the mineral as it dissolves, and also different effective reaction rates [20].

5. Upscaling using periodic homogenization. We now consider the phase field model (2.5) to be defined in a periodic porous medium. The pore scale, where grain, mineral, and fluid-filled void space are explicitly separated, will be the microscale, and in the following we will derive a macroscale model describing the effective behavior of the system. More precisely, we consider a domain \mathcal{D} containing small, periodically distributed grains, as sketched in Figure 4. In a porous medium, \mathcal{D} represents the union of the void space, mineral space, and grain space, where the grains will be considered as perforations. We will refer to the union of the void space and mineral space as the pore space. The grains are impermeable to fluid, and no reactions take place there. Hence, the phase field model (2.5) is not defined in the grain space but only in the pore space of \mathcal{D} . The grains do not change with time, while the moving boundary between mineral and fluid, located in the pore space of \mathcal{D} , is still handled by the phase field equation as a diffuse interface. We assume that the mineral precipitates on the boundary of the perforations or at already existing minerals and not inside the void space. Two important assumptions are that the void space in \mathcal{D} is connected and that the mineral never grows in such a way that the pore space is clogged.

The porous medium \mathcal{D} contains many periodically repeating grains. This means that the phase field model (2.5) is defined on a domain of high complexity. In such cases, the averaged behavior of the system is of primary interest. In consequence we apply periodic homogenization techniques to find effective equations valid at a larger scale, where the microscale oscillations are no longer visible, but their effect is still taken into account. This is done by identifying a scale separation and applying asymptotic expansions on nondimensional versions of the model equations.

When nondimensionalizing the model (2.5), one must address the size of the appearing nondimensional numbers (e.g., Reynolds, Péclet, Cahn, and Damköhler), in particular, their internal ordering. The size of these nondimensional numbers describes which regime we consider, and in the following we will consider a regime in the range of Darcy's law [23] and where time scales for macroscale solute diffusion, advection, and reaction are approximately the same size [6]. As we will see in the following, this leads to diffusion dominating at the pore scale. Finally, we want the

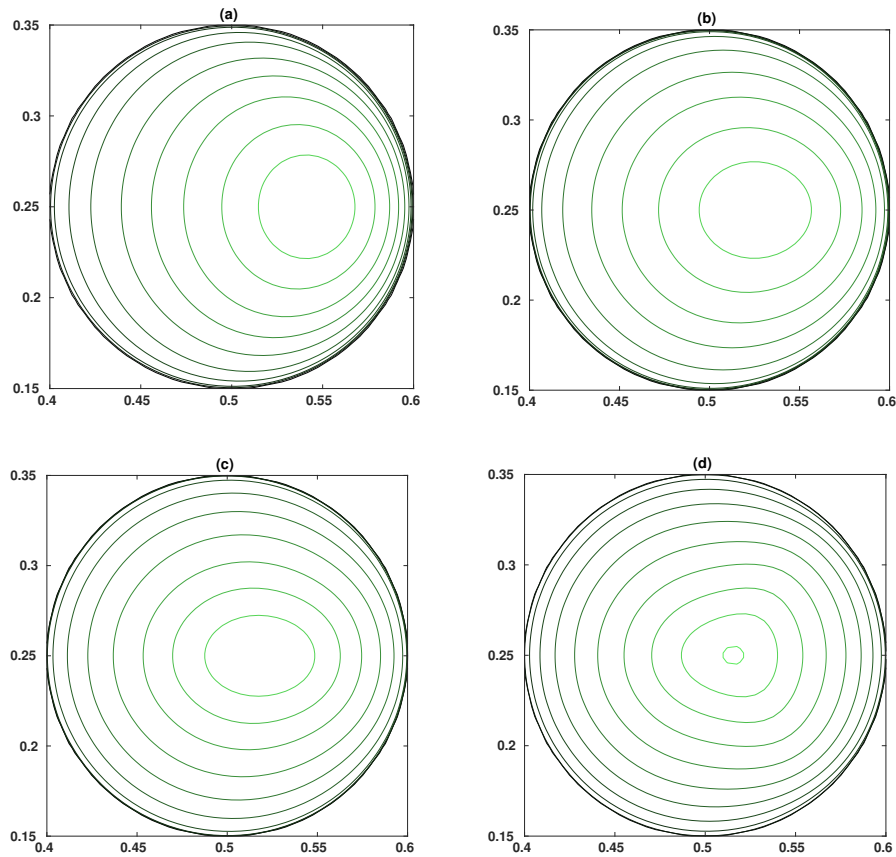


FIG. 3. The mineral shapes while dissolving (zoomed-in view of the channel where the calcite is present initially). Black line shows initial shape, while increasingly brighter green shows the shape at later time steps. Cases (a)–(d) correspond to the cases in Table 2. The last isolines are at times (a) $t = 3.4$ s, (b) $t = 1.6$ s, (c) $t = 1.1$ s, (d) $t = 0.79$ s. The axis scales are in mm. (See online version for color.)

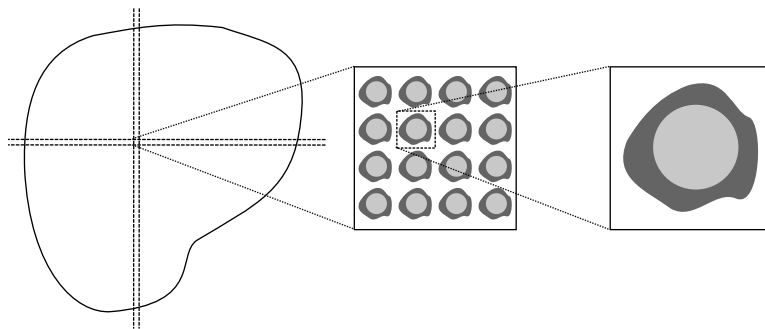


FIG. 4. Structure of porous medium. Fluid-filled void space is marked with white, mineral is dark grey, and nonreactive grain is light grey. The pore space is the union of the void space and mineral space.

phase field to appear as a local, microscale variable, and we will address the choices necessary to achieve this. Note that other choices for the nondimensional numbers are possible but will result in different upscaled models.

5.1. The scale separation. In the dimensional setting, we let ℓ be a typical length scale at the microscale (that is, the pore scale), e.g., the width of the rightmost box in Figure 4, and let L be a typical length scale at the macroscale, e.g., the width of the domain \mathcal{D} or of the Darcy scale, as commonly made for homogenization [19, 23]. With this we define $\varepsilon = \ell/L$, reflecting the ratio between the micro- and macroscales and hence giving us the scale separation. We assume that ℓ is much smaller than L , and hence ε is a small number. We mention that [46, Remark 1.2] discusses a different definition of the scale separation and shows how this leads to the same nondimensional model.

In what follows we rewrite the model in nondimensional form. In doing so we introduce a local unit cell $Y = [0, 1]^{\dim}$, as seen in Figure 5, where \dim is 2 or 3, depending on spatial dimension, and we let the local variable $\mathbf{y} \in (0, 1)^{\dim}$ describe points within Y . The local cell consists of the fluid part F and mineral part M , and the grain part G is as sketched in Figure 5. Hence, locally the phase field model is defined in the pore space $P = F \cup M$, while G defines the perforation. The boundary Γ_P defines the (stationary) internal boundary between the perforation and the domain for the phase field model. The boundary ∂Y denotes the outer boundary of the unit cell Y . At this boundary we will later apply periodic boundary conditions, allowing us to decouple the unit cells from one another. However, when referring to internal boundaries, the boundary Γ_P is meant.

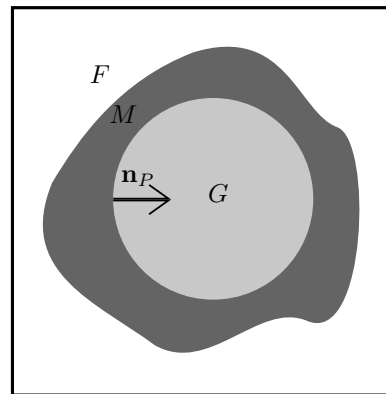


FIG. 5. Local pore $Y = [0, 1]^d$. The fluid part (white) is F , mineral part (dark grey) is M , and grain part (light grey) is G , along with a normal vector \mathbf{n}_P at the internal boundary Γ_P . The outer boundary of the local pore, ∂Y , is marked with black.

To distinguish between the two scales in the model, we use \mathbf{x} as the variable at the macroscale, which is then connected to the local, microscale variable \mathbf{y} through $\mathbf{y} = \varepsilon^{-1}\mathbf{x}$. This can be interpreted as \mathbf{x} only seeing the macroscale behavior, while the zoomed-in \mathbf{y} sees the microscale rapid changes in a single cell. Hence for each macroscale point \mathbf{x} , we can identify a unit cell, with its own local variable \mathbf{y} .

With this we have that the perforated domain of the phase field model is the union of all local pores P , scaled by ε . This means that the domain depends on ε and

can be written as

$$\Omega^\varepsilon = \cup_{w \in W_{\mathcal{D}}} \{\varepsilon(w + P)\},$$

where $W_{\mathcal{D}}$ is a subset of \mathbb{Z}^{dim} satisfying $\mathcal{D} = \cup_{w \in W_{\mathcal{D}}} \{\varepsilon(w + Y)\}$, which is the complete (nonperforated) medium domain seen to the left in Figure 4. We use ε as a superscript to indicate dependence on ε . The union of all internal boundaries Γ_P is denoted by

$$\Gamma^\varepsilon = \cup_{w \in W_{\mathcal{D}}} \{\varepsilon(w + \Gamma_P)\}.$$

5.2. Nondimensional model equations. To identify which terms are dominating in the model and hence are important for the upscaling, we first nondimensionalize the model equations (2.5). The assumptions made below on the typical flow rate, viscosity, and pressure difference ensure that we are in the range of Darcy's law, which means that at the macroscale the conservation of momentum equation (2.5c) becomes a Darcy-like law. Also, we ensure that the diffuse interface (that is, the transition between mineral and fluid) stays within a local pore. Nondimensional variables and quantities are denoted with a hat and are defined as

$$\begin{aligned} \hat{t} &= t/t_{\text{ref}}, & \hat{\mathbf{x}} &= \mathbf{x}/L, & \hat{\mathbf{y}} &= \mathbf{y}/\ell, & \hat{\lambda} &= \lambda/\lambda_{\text{ref}}, \\ \hat{\mathbf{q}}^\varepsilon &= \mathbf{q}/q_{\text{ref}}, & \hat{u}^\varepsilon &= u/u_{\text{ref}}, & \hat{p}^\varepsilon &= p/p_{\text{ref}}, & \hat{u}^* &= u^*/u_{\text{ref}}, \\ \hat{D} &= D/D_{\text{ref}}, & \hat{\mu}_f &= \mu_f/\mu_{\text{ref}}, & \hat{\rho}_f &= \rho_f/\rho_{\text{ref}}, & \hat{k} &= k/k_{\text{ref}}, \\ & & \hat{\gamma} &= \gamma/\gamma_{\text{ref}}, & \hat{K} &= K/K_{\text{ref}}. \end{aligned}$$

Note the superscript ε for the variables having a highly oscillatory behavior. The relations between the reference quantities are given through several nondimensional numbers. The size of these nondimensional numbers describes which regime we consider. As already mentioned, here we are interested in the regime where Darcy's law is valid and where solute advection, diffusion, and reaction time scales are about the same order of magnitude. Darcy's law is valid when fluid flow is laminar and when the pressure drop dominates the flow behavior. This corresponds to the Reynolds and Euler numbers being

$$\text{Re} = \rho_{\text{ref}} q_{\text{ref}} L / \mu_{\text{ref}} = O(\varepsilon^0), \quad \text{Eu} = p_{\text{ref}} / q_{\text{ref}}^2 \rho_{\text{ref}} = O(\varepsilon^{-2}),$$

respectively. Different choices can, e.g., lead to the Forchheimer law [16]. Solute advection, diffusion, and reaction time scales are identified as $t_{\text{adv}} = L/q_{\text{ref}}$, $t_{\text{diff}} = L^2/D_{\text{ref}}$, and $t_{\text{react}} = u_{\text{ref}}\ell/k_{\text{ref}}$, respectively. These time scales are assumed to be about the same, that is, that advection, diffusion, and reaction are equally important, which corresponds to the Péclet and Damköhler numbers being

$$\text{Pe} = t_{\text{diff}}/t_{\text{adv}} = O(\varepsilon^0), \quad \text{Da} = t_{\text{adv}}/t_{\text{react}} = O(\varepsilon^0),$$

respectively. Upscaled models have also been derived for other regimes with respect to the Péclet and Damköhler numbers by employing either homogenization [4, 12, 17, 28, 32, 45] or volume averaging techniques [53, 54]. The observation time scale t_{ref} is set to be equal to t_{adv} .

For reference quantities and parameters affecting the phase field variable, we assume that the diffuse interface width is proportional to, but still smaller than, the pore size ℓ . This corresponds to the Cahn number being

$$\text{Ca} = \lambda_{\text{ref}}/L = O(\varepsilon).$$

Hence, $\hat{\lambda}$ is a small number but independent of ε . This way, the interface width is small relative to the pore size but remains a microscale quantity without approaching its sharp-interface limit as ε approaches zero. Similar choices are made in the upscaling of the phase field models found in [18, 31, 38], while an interface width that is large compared to the pore size is upscaled in [41, 42]. In the latter two papers, the phase field appears as a macroscale variable in the upscaled model. The microscale diffusive time scale of the phase field, that is, $t_{\text{diff},\gamma} = \ell^2/\gamma_{\text{ref}}$, is chosen to be comparable to the reactive time scale, but where $\hat{\gamma}$ is still allowed to be small but independent of ε (that is, $O(\varepsilon^0)$). Hence, the diffusive Damköhler number of the phase field is

$$\text{Da}_\phi = t_{\text{diff},\gamma}/t_{\text{react}} = O(\varepsilon^0).$$

This choice supports the phase field variable as a microscale variable, without affecting the sharp-interface limit as ε approaches zero. Finally, the reference value K_{ref} is chosen in relation to the other flow-related reference values to ensure low velocities in the diffuse transition zone as ε approaches zero. Interpreting K_{ref} as viscosity divided by a slip length, this corresponds to the Navier number being

$$\text{Na} = \ell_s/L = O(\varepsilon),$$

where $\ell_s = \mu_{\text{ref}}/K_{\text{ref}}$ is the associated slip length.

For readability, in the following we let the nondimensional numbers that are equal to $O(\varepsilon^k)$ be exactly equal to ε^k , but other choices for the proportionality constants are straightforward. Hence, we now have that $\text{Re} = 1$, $\text{Eu} = \varepsilon^{-2}$, etc. This corresponds to letting $\mu_{\text{ref}} = \rho_{\text{ref}}Lq_{\text{ref}}$ and $p_{\text{ref}} = q_{\text{ref}}^2\rho_{\text{ref}}L^2/\ell^2$. From the Péclet and Damköhler numbers, we get $k_{\text{ref}} = u_{\text{ref}}\ell/t_{\text{ref}}$ and $D_{\text{ref}} = L^2/t_{\text{ref}}$. With this choice of k_{ref} , the nondimensional reaction rate can be defined as $\hat{f}(\hat{u}) = \hat{k}(\hat{u}^2/\hat{u}_{\text{eq}}^2 - 1)$. $\text{Ca} = \varepsilon$ corresponds to letting $\lambda_{\text{ref}} = \ell$, and $\text{Da}_\phi = 1$ corresponds to $\gamma_{\text{ref}} = \ell^2/t_{\text{ref}}$. Finally, $\text{Na} = \varepsilon$ means that $K_{\text{ref}} = \rho_{\text{ref}}q_{\text{ref}}L/\ell$.

Table 3 summarizes the choices made in the nondimensionalization.

TABLE 3
Nondimensional quantities and their relation to the upscaling parameter ε .

Dimensionless number	Definition	Size w.r.t. ε
Scale separation	$\varepsilon = \ell/L$	ε
Reynolds number	$\text{Re} = \rho_{\text{ref}}q_{\text{ref}}L/\mu_{\text{ref}}$	ε^0
Euler number	$\text{Eu} = p_{\text{ref}}/q_{\text{ref}}^2\rho_{\text{ref}}$	ε^{-2}
Péclet number	$\text{Pe} = Lq_{\text{ref}}/D_{\text{ref}}$	ε^0
Damköhler number	$\text{Da} = k_{\text{ref}}L/u_{\text{ref}}q_{\text{ref}}\ell$	ε^0
Cahn number	$\text{Ca} = \lambda_{\text{ref}}/L$	ε
Phase field Damköhler number	$\text{Da}_\phi = k_{\text{ref}}\ell/\gamma_{\text{ref}}u_{\text{ref}}$	ε^0
Navier number	$\text{Na} = \mu_{\text{ref}}/K_{\text{ref}}L$	ε

Remark 5.1. The (nondimensional) diffuse interface width $\hat{\lambda}$, phase field diffusivity $\hat{\gamma}$, and regularization parameter δ are all small, positive numbers that are independent of ε . That means they remain fixed as $\varepsilon \rightarrow 0$ in the following section. These three numbers affect the behavior of the phase field model. In particular, $\hat{\lambda}$ is the microscale diffuse interface width, and $\hat{\gamma}$ dictates the equilibration speed of the diffuse interface, while δ assures the model is not degenerate. These numbers will be set to small numbers in the numerical examples, but they neither rely on any internal ordering nor depend on one another.

Since from now on we will only use nondimensional variables, we omit the hat on all variables. With this, the dimensionless model reads as

$$(5.1a) \quad \lambda^2 \partial_t \phi^\varepsilon + \gamma P'(\phi^\varepsilon) = \varepsilon^2 \gamma \lambda^2 \nabla^2 \phi^\varepsilon - 4\lambda \phi^\varepsilon (1 - \phi^\varepsilon) \frac{1}{u^*} f(u^\varepsilon) \quad \text{in } \Omega^\varepsilon,$$

$$(5.1b) \quad \nabla \cdot ((\phi^\varepsilon + \delta) \mathbf{q}^\varepsilon) = 0 \quad \text{in } \Omega^\varepsilon,$$

$$(5.1c) \quad \varepsilon^2 \rho_f \left(\partial_t ((\phi^\varepsilon + \delta) \mathbf{q}^\varepsilon) - \frac{1}{2} \mathbf{q}^\varepsilon \partial_t \phi^\varepsilon + \nabla \cdot ((\phi^\varepsilon + \delta) \mathbf{q}^\varepsilon \otimes \mathbf{q}^\varepsilon) \right) + (\phi^\varepsilon + \delta) \nabla p^\varepsilon \\ = \varepsilon^2 \mu_f (\phi^\varepsilon + \delta) \nabla^2 ((\phi^\varepsilon + \delta) \mathbf{q}^\varepsilon) - \frac{K(1 - \phi^\varepsilon)n}{\lambda \phi^\varepsilon + n} \mathbf{q}^\varepsilon \quad \text{in } \Omega^\varepsilon,$$

$$(5.1d) \quad \partial_t ((\phi^\varepsilon + \delta)(u^\varepsilon - u^*)) + \nabla \cdot ((\phi^\varepsilon + \delta) \mathbf{q}^\varepsilon u^\varepsilon) = D \nabla \cdot ((\phi^\varepsilon + \delta) \nabla u^\varepsilon) \quad \text{in } \Omega^\varepsilon,$$

$$(5.1e) \quad \nabla \phi^\varepsilon \cdot \mathbf{n}^\varepsilon = 0 \quad \text{on } \Gamma^\varepsilon,$$

$$(5.1f) \quad (\phi^\varepsilon + \delta) \nabla u^\varepsilon \cdot \mathbf{n}^\varepsilon = 0 \quad \text{on } \Gamma^\varepsilon,$$

$$(5.1g) \quad \mathbf{q}^\varepsilon = \mathbf{0} \quad \text{on } \Gamma^\varepsilon.$$

Remark 5.2. Note that the analysis below remains unchanged if $\delta = 0$, when clogging is not considered. In other words, including an ε -independent regularization parameter δ does not affect the upscaling. The presence of $\delta > 0$ ensures that the resulting model is not degenerate, which is important for the numerical examples.

5.3. The formal asymptotic expansions. We apply the homogenization ansatz, namely we assume that the unknowns can be written as a series expansion in terms of ε with explicit dependence on the micro- and macroscale variables. For the phase field ϕ^ε this reads as

$$(5.2) \quad \phi^\varepsilon(t, \mathbf{x}) = \phi_0(t, \mathbf{x}, \mathbf{y}) + \varepsilon \phi_1(t, \mathbf{x}, \mathbf{y}) + \varepsilon^2 \phi_2(t, \mathbf{x}, \mathbf{y}) + \dots,$$

where the functions $\phi_i(t, \mathbf{x}, \mathbf{y})$ are Y -periodic in \mathbf{y} . Similar expansions are assumed for all dependent variables. The introduction of the microscale variable \mathbf{y} is an important aspect: While the ϕ^ε needs to resolve both the microscale and macroscale behaviors, we assume that the functions in the series expansion can distinguish between slow variability through \mathbf{x} and fast variability through \mathbf{y} . Further, the series expansion allows us to capture the dominating behavior in ϕ_0 , while lower order behavior is captured through the subsequent terms. Also note that macroscale \mathbf{x} is defined in the entire (nonperforated) domain \mathcal{D} , while \mathbf{y} is defined locally in a pore P .

As \mathbf{y} is a local variable behaving like $\mathbf{y} = \varepsilon^{-1} \mathbf{x}$, the spatial derivatives need to be rewritten accordingly. Hence, for a generic variable v , one has

$$(5.3) \quad \nabla v(\mathbf{x}, \mathbf{y}) = \nabla_{\mathbf{x}} v(\mathbf{x}, \mathbf{y}) + \frac{1}{\varepsilon} \nabla_{\mathbf{y}} v(\mathbf{x}, \mathbf{y}),$$

where $\nabla_{\mathbf{x}}$ and $\nabla_{\mathbf{y}}$ are the gradients with respect to \mathbf{x} , respectively, \mathbf{y} . We insert the asymptotic expansions (5.2) and the rescaled derivatives (5.3) into the model equations (5.1), and equate terms of the same order with respect to ε to isolate the behavior of the system on different scales. In the regularized equations, the term $\phi_0 + \delta$ will appear frequently, and we will use the notation $\phi_0^\delta = \phi_0 + \delta$ in this case. Note that $\phi_0^\delta > 0$.

5.3.1. Phase field equation. Equating the dominating $O(1)$ terms in the phase field equation (5.1a) gives

$$\lambda^2 \partial_t \phi_0 + \gamma P'(\phi_0) = \gamma \lambda^2 \nabla_{\mathbf{y}}^2 \phi_0 - 4\lambda \phi_0 (1 - \phi_0) \frac{1}{u^*} f(u_0).$$

The dominating term of the corresponding boundary condition (5.1e) gives $\nabla_{\mathbf{y}}\phi_0 \cdot \mathbf{n}_P = 0$. Observe that the above equation is similar to the original (5.1a) but involves only spatial derivatives with respect to \mathbf{y} . Although ϕ_0 still depends on \mathbf{x} , \mathbf{x} only appears as a parameter, as no derivatives with respect to \mathbf{x} are involved. Recalling the Y -periodicity in \mathbf{y} , ϕ_0 solves the following *cell problem* for the phase field:

$$(5.4) \quad \begin{aligned} \lambda^2 \partial_t \phi_0 + \gamma P'(\phi_0) &= \gamma \lambda^2 \nabla_{\mathbf{y}}^2 \phi_0 - 4\lambda \phi_0 (1 - \phi_0) \frac{1}{u^*} f(u_0) && \text{in } P, \\ \nabla_{\mathbf{y}} \phi_0 \cdot \mathbf{n}_P &= 0 && \text{on } \Gamma_P, \\ \text{periodicity in } \mathbf{y} &&& \text{across } \partial Y. \end{aligned}$$

These cell problems are defined for each macroscale \mathbf{x} , which corresponds to each pore as in Figure 5. However, the cell problems are decoupled locally due to the periodicity requirement.

5.3.2. Mass conservation equation. The dominating $O(\varepsilon^{-1})$ term in (5.1b) gives

$$(5.5) \quad \nabla_{\mathbf{y}} \cdot (\phi_0^\delta \mathbf{q}_0) = 0 \text{ in } P,$$

which will be needed in the derivation for the momentum and ion conservation equations. Next, the $O(1)$ terms provide

$$\nabla_{\mathbf{x}} \cdot (\phi_0^\delta \mathbf{q}_0) + \nabla_{\mathbf{y}} \cdot (\phi_0^\delta \mathbf{q}_1 + \phi_1 \mathbf{q}_0) = 0.$$

Integrating with respect to \mathbf{y} over P and applying the Gauss theorem and the boundary conditions $\mathbf{q}_0 = \mathbf{q}_1 = \mathbf{0}$ on Γ_P , together with periodicity, one gets

$$(5.6) \quad \nabla_{\mathbf{x}} \cdot (\overline{\phi_0^\delta \mathbf{q}_0}) = 0 \text{ in } \mathcal{D}.$$

The overline notation indicates a quantity averaged over the microscale. Formally, one can extend the quantities defined in the pore space P by 0 inside the perforations G , allowing for an average over the entire cell Y . For a scalar variable $v(t, \mathbf{x}, \mathbf{y})$, we define $\bar{v}(t, \mathbf{x}) = \frac{1}{|Y|} \int_Y v(t, \mathbf{x}, \mathbf{y}) d\mathbf{y} = \int_P v(t, \mathbf{x}, \mathbf{y}) d\mathbf{y}$. Note that $|Y|$, the volume of Y , is 1. In this way, the average of the highest order term of the phase field, $\overline{\phi_0}(t, \mathbf{x})$, will correspond to the porosity at time t at the macroscale location \mathbf{x} .

5.3.3. Momentum conservation equation. The dominating $O(\varepsilon^{-1})$ term in (5.1c) yields

$$\phi_0^\delta \nabla_{\mathbf{y}} p_0 = \mathbf{0},$$

meaning that $p_0 = p_0(t, \mathbf{x})$ is independent of \mathbf{y} . The $O(1)$ terms give

$$(5.7) \quad \phi_0^\delta (\nabla_{\mathbf{x}} p_0 + \nabla_{\mathbf{y}} p_1) = \mu_f \phi_0^\delta \nabla_{\mathbf{y}}^2 (\phi_0^\delta \mathbf{q}_0) - \frac{K(1 - \phi_0)n}{\lambda \phi_0 + n} \mathbf{q}_0.$$

We use the linearity of the equation and determine p_1 and \mathbf{q}_0 in terms of (the gradient of) p_0 . With $\Pi^j(t, \mathbf{x}, \mathbf{y})$ and $\mathbf{w}^j(t, \mathbf{x}, \mathbf{y})$ solving the cell problems

$$(5.8) \quad \begin{aligned} \phi_0^\delta (\mathbf{e}_j + \nabla_{\mathbf{y}} \Pi^j) + \mu_f \phi_0^\delta \nabla_{\mathbf{y}}^2 (\phi_0^\delta \mathbf{w}^j) &= \frac{K(1 - \phi_0)n}{\lambda \phi_0 + n} \mathbf{w}^j && \text{in } P, \\ \nabla_{\mathbf{y}} \cdot (\phi_0^\delta \mathbf{w}^j) &= 0 && \text{in } P, \\ \mathbf{w}^j &= \mathbf{0} && \text{on } \Gamma_P, \\ \text{periodicity in } \mathbf{y} \text{ across } \partial Y, &&& j \in \{1, \dots, \dim\}, \end{aligned}$$

we observe that

$$p_1(t, \mathbf{x}, \mathbf{y}) = \sum_{j=1}^{\dim} \Pi^j(t, \mathbf{x}, \mathbf{y}) \partial_{x_j} p_0(t, \mathbf{x}),$$

$$\mathbf{q}_0(t, \mathbf{x}, \mathbf{y}) = - \sum_{j=1}^{\dim} \mathbf{w}^j(t, \mathbf{x}, \mathbf{y}) \partial_{x_j} p_0(t, \mathbf{x})$$

now fulfill (5.5) and (5.7). The boundary condition for \mathbf{w}^j on Γ_P follows from $\mathbf{q}_0 = \mathbf{0}$ on Γ_P . Note that the cell problems are solved in \mathbf{y} for a fixed \mathbf{x} . Hence, as with the phase field cell problem, one can solve for single pores independently.

Multiplying by ϕ_0^δ in the last equality and averaging over Y gives

$$(5.9) \quad \overline{\phi_0^\delta \mathbf{q}_0} = -\mathcal{K} \nabla_{\mathbf{x}} p_0 \quad \text{in } \mathcal{D},$$

where the components of the *permeability tensor* $\mathcal{K}(t, \mathbf{x})$ are given by

$$k_{ij}(t, \mathbf{x}) = \int_P \phi_0^\delta w_i^j d\mathbf{y} \quad \text{with } i, j \in \{1, \dots, \dim\}.$$

Here, w_i^j are the components of \mathbf{w}^j , which are the solutions of the cell problems (5.8) with the continuous extension $\mathbf{w}^j = \mathbf{0}$ inside the grain.

5.3.4. Ion conservation equation. The dominating $O(\varepsilon^{-2})$ term from the ion conservation equation (5.1d) and dominating $O(\varepsilon^{-1})$ term from the corresponding boundary condition (5.1f) give

$$\begin{aligned} \nabla_{\mathbf{y}} \cdot (\phi_0^\delta \nabla_{\mathbf{y}} u_0) &= 0 && \text{in } P, \\ \phi_0^\delta \nabla_{\mathbf{y}} u_0 \cdot \mathbf{n}_P &= 0 && \text{on } \Gamma_P, \end{aligned}$$

along with periodicity in \mathbf{y} . This implies that $u_0 = u_0(t, \mathbf{x})$ is independent of \mathbf{y} .

Further, the $O(\varepsilon^{-1})$ terms from (5.1d) and $O(1)$ terms from (5.1f) give

$$\begin{aligned} \nabla_{\mathbf{y}} \cdot (\phi_0^\delta (\nabla_{\mathbf{x}} u_0 + \nabla_{\mathbf{y}} u_1)) &= 0 && \text{in } P, \\ \phi_0^\delta (\nabla_{\mathbf{x}} u_0 + \nabla_{\mathbf{y}} u_1) \cdot \mathbf{n}_P &= 0 && \text{on } \Gamma_P, \end{aligned}$$

where we used (5.5) for the convective term. We exploit again the linearity of the problem and formulate $u_1(t, \mathbf{x}, \mathbf{y})$ in terms of (the derivatives of) $u_0(t, \mathbf{x})$. We let the weight functions $\omega^j(t, \mathbf{x}, \mathbf{y})$ solve the cell problems

$$(5.10) \quad \begin{aligned} \nabla_{\mathbf{y}} \cdot (\phi_0^\delta (\nabla_{\mathbf{y}} \omega^j + \mathbf{e}_j)) &= 0 && \text{in } P, \\ \phi_0^\delta (\nabla_{\mathbf{y}} \omega^j + \mathbf{e}_j) \cdot \mathbf{n}_P &= 0 && \text{on } \Gamma_P, \\ \text{periodicity in } \mathbf{y} \text{ across } \partial Y, &&& j \in \{1, \dots, \dim\}, \end{aligned}$$

As earlier, the cell problems are solved in \mathbf{y} for a fixed \mathbf{x} . Then, for an arbitrary $\tilde{u}_1 = \tilde{u}_1(t, \mathbf{x})$, we obtain that

$$u_1(t, \mathbf{x}, \mathbf{y}) = \tilde{u}_1(t, \mathbf{x}) + \sum_{j=1}^{\dim} \omega^j(t, \mathbf{x}, \mathbf{y}) \partial_{x_j} u_0(t, \mathbf{x}).$$

As will follow from below, only $\nabla_{\mathbf{y}}u_1$ will be needed for obtaining the upscaled model; therefore the function \tilde{u}_1 plays no role in the upscaling, and it is not necessary to specify it.

The $O(1)$ terms from (5.1d) and $O(\varepsilon)$ terms from (5.1f) give

$$\begin{aligned} \partial_t(\phi_0^\delta(u_0 - u^*)) + \nabla_{\mathbf{x}} \cdot (\phi_0^\delta \mathbf{q}_0 u_0) + \nabla_{\mathbf{y}} \cdot \mathbf{A} \\ = D(\nabla_{\mathbf{y}} \cdot \mathbf{B} + \nabla_{\mathbf{x}} \cdot (\phi_0^\delta(\nabla_{\mathbf{x}}u_0 + \nabla_{\mathbf{y}}u_1)) \quad \text{in } \mathcal{D} \times P, \\ \mathbf{B} \cdot \mathbf{n}_P = 0 \quad \text{on } \Gamma_P. \end{aligned}$$

where $\mathbf{A} = \phi_1 \mathbf{q}_0 u_0 + \phi_0^\delta \mathbf{q}_1 u_0 + \phi_0^\delta \mathbf{q}_0 u_1$ and $\mathbf{B} = \phi_0^\delta \nabla_{\mathbf{x}}u_1 + \phi_0^\delta \nabla_{\mathbf{y}}u_2 + \phi_1 \nabla_{\mathbf{x}}u_0 + \phi_1 \nabla_{\mathbf{y}}u_1$. The above equation contains derivatives in both \mathbf{x} and \mathbf{y} . To find the upscaled model, we integrate in \mathbf{y} over the domain P , apply Gauss's theorem in \mathbf{y} , and use the boundary condition on Γ_P and the periodicity requirement to remove the $\nabla_{\mathbf{y}} \cdot \mathbf{A}$ and $\nabla_{\mathbf{y}} \cdot \mathbf{B}$ terms. For the velocity terms in \mathbf{A} , we also apply the boundary condition (5.1g), which gives $\mathbf{q}_0 = \mathbf{q}_1 = \mathbf{0}$ on Γ_P . This leads to the upscaled reaction-advection-diffusion equation

$$(5.11) \quad \partial_t(\overline{\phi_0^\delta(u_0 - u^*)}) + \nabla_{\mathbf{x}} \cdot (\overline{\phi_0^\delta \mathbf{q}_0 u_0}) = D \nabla_{\mathbf{x}} \cdot (\mathcal{A} \nabla_{\mathbf{x}} u_0) \text{ in } \mathcal{D}.$$

The components of the matrix $\mathcal{A}(t, \mathbf{x})$ are

$$a_{ij}(t, \mathbf{x}) = \int_P \phi_0^\delta (\delta_{ij} + \partial_{y_i} \omega^j) d\mathbf{y} \quad \text{with } i, j \in \{1, \dots, \dim\},$$

where ω^j is the solution of the cell problem (5.10). Hence, the upscaled ion conservation equation (5.11) is to be solved for $\mathbf{x} \in \mathcal{D}$ only but receives information from the microscale \mathbf{y} through the effective diffusion matrix and the effective velocity.

5.4. Summary of upscaled equations. To summarize, the upscaled system of equations consists of the three equations (5.6), (5.9), and (5.11) on the macroscale for the unknowns $\overline{\phi_{\mathbf{q}_0}}(t, \mathbf{x})$, $p_0(t, \mathbf{x})$ and $u_0(t, \mathbf{x})$. The upscaled system is completed by three supplementary cell problems (5.4), (5.8), and (5.10) to be solved locally in each single pore, providing effective properties for the upscaled system.

The regularization δ was kept throughout the upscaling procedure for consistency. We introduced this regularization for avoiding a degeneracy in the system, which would create difficulties in the numerical implementations. For the upscaled model, these difficulties are encountered in the cell problems. Hence, we only consider ϕ_0^δ in the effective properties and set $\delta = 0$ in (5.6), (5.9), and (5.11). Then, for macroscale $\mathbf{x} \in \mathcal{D}$ and for $t > 0$,

$$\begin{aligned} \nabla_{\mathbf{x}} \cdot (\overline{\phi_0 \mathbf{q}_0}) &= 0 && \text{in } \mathcal{D}, \\ \overline{\phi_0 \mathbf{q}_0} &= -\mathcal{K} \nabla_{\mathbf{x}} p_0 && \text{in } \mathcal{D}, \\ \partial_t(\overline{\phi_0(u_0 - u^*)}) + \nabla_{\mathbf{x}} \cdot (\overline{\phi_0 \mathbf{q}_0 u_0}) &= D \nabla_{\mathbf{x}} \cdot (\mathcal{A} \nabla_{\mathbf{x}} u_0) && \text{in } \mathcal{D}, \end{aligned}$$

where the phase field $\phi_0(t, \mathbf{x}, \mathbf{y})$ is updated locally in each pore by solving

$$\begin{aligned} \lambda^2 \partial_t \phi_0 + \gamma P'(\phi_0) &= \gamma \lambda^2 \nabla_{\mathbf{y}}^2 \phi_0 - 4\lambda \phi_0 (1 - \phi_0) \frac{1}{u^*} f(u_0) && \text{in } P, \\ \nabla_{\mathbf{y}} \phi_0 \cdot \mathbf{n}_P &= 0 && \text{on } \Gamma_P \end{aligned}$$

for all $\mathbf{x} \in \mathcal{D}$ and $t > 0$. The effective matrices $\mathcal{K}(t, \mathbf{x})$ and $\mathcal{A}(t, \mathbf{x})$ are found through

$$\begin{aligned}
 k_{ij}(t, \mathbf{x}) &= \int_P \phi_0^\delta w_i^j d\mathbf{y}, \text{ where} \\
 \phi_0^\delta (\mathbf{e}_j + \nabla_{\mathbf{y}} \Pi^j) + \mu_f \phi_0^\delta \nabla_{\mathbf{y}}^2 (\phi_0^\delta \mathbf{w}^j) &= \frac{K}{\lambda} \frac{(1 - \phi_0)n}{\phi_0 + n} \mathbf{w}^j && \text{in } P, \\
 \nabla_{\mathbf{y}} \cdot (\phi_0^\delta \mathbf{w}^j) &= 0 && \text{in } P, \\
 \mathbf{w}^j &= \mathbf{0} && \text{on } \Gamma_P,
 \end{aligned}$$

and

$$\begin{aligned}
 a_{ij}(t, \mathbf{x}) &= \int_P \phi_0^\delta (\delta_{ij} + \partial_{y_i} \omega^j) d\mathbf{y}, \text{ where} \\
 \nabla_{\mathbf{y}} \cdot (\phi_0^\delta (\nabla_{\mathbf{y}} \omega^j + \mathbf{e}_j)) &= 0 && \text{in } P, \\
 \phi_0^\delta (\nabla_{\mathbf{y}} \omega^j + \mathbf{e}_j) \cdot \mathbf{n}_P &= 0 && \text{on } \Gamma_P
 \end{aligned}$$

for $i, j \in \{1, \dots, \dim\}$. The unknowns $\mathbf{w}^j(t, \mathbf{x}, \mathbf{y})$, $\Pi^j(t, \mathbf{x}, \mathbf{y})$, and $\omega^j(t, \mathbf{x}, \mathbf{y})$ fulfill periodicity requirements in \mathbf{y} across ∂Y .

6. Numerical experiments for the upscaled model. To illustrate the behavior of the phase field model and its dependence on the diffuse interface width and on the upscaling parameter, we consider two examples. First, we will solve the cell problems for various choices of λ and compare our solution to the corresponding sharp-interface solution, showing how the effective ion diffusivity and the flow permeability depend on the width of the diffuse interface. Second, to illustrate the behavior of the full system of equations, while at the same time addressing the effect of the upscaling, we consider a thin strip. The thin strip allows for an upscaled model where the effective quantities are known explicitly, allowing us to easily address the influence of ε . Note that in all examples, we solve using the corresponding nondimensional model and that all specified parameters are also nondimensional.

6.1. Solutions to cell problems. For sharp-interface models, cell problems for flow and diffusion for moving-boundary problems using a level-set formulation have been derived in [11, 47]. Note that in both formulations, the local reaction rate is uniform inside each pore as the local ion concentration is constant (cf. subsection 5.3.4). Hence, if the minerals are initially shaped as circles (or cylinders), the mineral layer will evolve in a radially symmetric manner, and the mineral remains a circle (or cylinder); see [47]. Hence, the level-set formulation can be rewritten into an equation for the radius $R(t, \mathbf{x})$ of the solid (grain and mineral), where the cell problems depend on $R(t, \mathbf{x})$ [13, 47]. In the radially symmetric case, the effective ion diffusivity and the permeability will be scalar quantities.

We adopt a similar approach here by solving the cell problems (5.8) and (5.10) to determine the effective permeability and ion diffusivity by assuming that the phase field has a smooth transition (of $O(\lambda)$) at some distance R from the center of the cell. We do not attempt to determine permeability and diffusivity curves as functions of R as in [13, 47] (see, e.g., Figure 3 in [47]), but instead we choose some values of R and investigate the behavior as we let the diffuse interface width λ vary.

The cell problems (5.8) and (5.10) are discretized using a control volume method on a staggered cartesian grid as in section 4, where the cell problem unknowns ω^j

and Π^j are defined in the centers of the control volumes, and the vectors \mathbf{w}^j are at the edges. The grid is uniform and quadratical with 800 grid cells in each direction, so that we have at least eight grid cells through the diffuse transition zone for the smallest λ . Note that the size of the nonreactive part G does not affect the resulting values of the effective variables as long G is well within the mineral phase. For all cell problems, we use a regularization of $\delta = 10^{-8}$.

Remark 6.1. Specifying a phase field corresponding to a circular mineral with radius R is not straightforward as no analytical expression exists. An approximate phase field can be found by assuming radial symmetry and considering the reaction-free version of (5.4) in polar coordinates. That is, we seek $\phi(t, r)$ solving

$$(6.1) \quad \lambda^2 \partial_t \phi + \gamma P'(\phi) = \gamma \lambda^2 \frac{1}{r} \partial_r (r \partial_r \phi).$$

Because of the nonconservative property of the Allen–Cahn equation, a radially symmetric phase field drop will always shrink towards the center due to curvature effects. Using this, we consider the initial condition

$$(6.2) \quad \phi(t = 0, r) = \frac{1}{1 + \exp(-4(r - R_0)/\lambda)},$$

where R_0 is larger than the radius R , which is the mineral radius for which we seek a phase field. Following from the curvature-driven movement, the mineral will shrink according to the radial Allen–Cahn equation (6.1). The simulation is stopped when the radius of the transition region reaches R , that is, when $\phi = 0.5$ at $r = R$. Hence, this resulting phase field is used when solving the cell problems. As boundary conditions, we apply $\phi = 0$ at $r = 0$ and $\phi = 1$ at $r = 1$. It could be tempting to directly specify (6.2) with $R_0 = R$ as the phase field, but this would not fulfill the steady-state version of (6.1). Although (6.2) has a structure similar to (3.7), which is the solution of the one-dimensional steady-state version of the Allen–Cahn equation, this finding cannot be extended to the radially symmetric case due to the structure of the Laplace operator in polar coordinates. This also means that the initial condition (6.2) is only an approximate initial condition.

6.1.1. Permeability. For the cell problem (5.8) providing the permeability, we consider mineral radii of $R = 0.2, 0.3, 0.4$. The corresponding permeability values for these mineral radii are $\mathcal{K} = 3.3 \times 10^{-2}, 1.1 \times 10^{-2}, 1.8 \times 10^{-3}$, respectively [13]. The applied values of λ in (6.2) will be $\lambda = 0.05, 0.04, 0.03, 0.02, 0.01, 0.0075, 0.005$. In Figure 6, the phase field permeability values are compared to the permeability values resulting from the corresponding sharp-interface models. It becomes clear that the phase field permeability values are approaching those for the sharp-interface models as the values of λ are decreasing. However, the relative errors are large and for $\lambda = 0.01$ are equal to 5%, 7%, and 15% for $R = 0.2, 0.3, 0.4$, respectively. These deviations can be explained by the fact that flow takes place in the diffuse transition zone, which enhances the flow through the entire cell and hence overestimates the permeability. This effect is diminished when the parameter K in the phase field cell problem (5.8) is increased, but larger values of K could also lead to an underestimation of the permeability if λ is large. For the results in Figure 6, $K = 25$ was used. Hence, finding a good choice for the interpolation function $g(\phi, \lambda)$ in (2.5c) is essential in the numerical implementation.

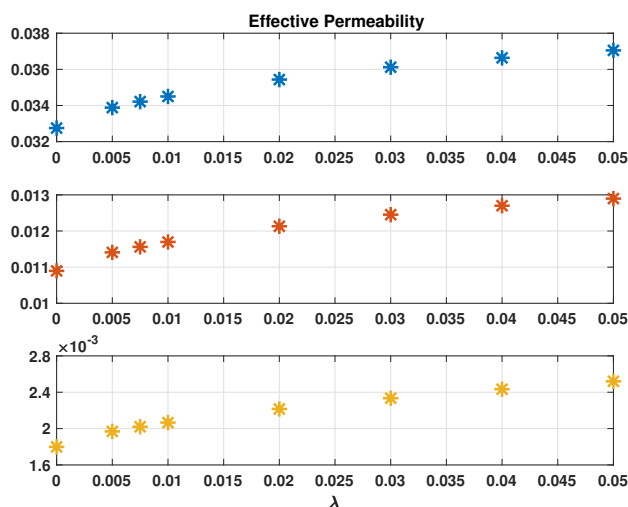


FIG. 6. Permeability values for $R = 0.2$ (top), $R = 0.3$ (middle), and $R = 0.4$ (bottom) for various values of λ . The sharp-interface values are plotted at $\lambda = 0$.

6.1.2. Effective ion diffusivity. For the effective diffusivity cell problem (5.10), we consider the same values for R and λ . The effective diffusivities for the sharp-interface model are, for these three values of R , $\mathcal{A} = 0.78, 0.56, 0.32$, respectively. These values have been found by solving the corresponding sharp-interface cell problems for the diffusion tensor, whose formulation can be found, e.g., in [47], using the PDE toolbox in MATLAB on recursively finer grids until four digits of accuracy are obtained. The phase field effective diffusion values are compared to the corresponding sharp-interface effective diffusion values in Figure 7. Although the phase field values seemingly converge towards a slightly different value than the value provided by the sharp-interface model, it is worth noting that the relative errors are rather small ($< 0.3\%$ in all cases), and hence the effective diffusion tensors are well approximated even for large values of λ . Note that when defining the transition zone as being where $\phi = 0.5$ leads to a slightly overestimated size of the grain as the transition zone spreads out radially, which can explain why the diffusion values approaches a value that is slightly too low. For example, for $R = 0.3$ the relative difference between the true porosity and that found through Remark 6.1 using $\lambda = 0.01$ is 0.03% . Other potential sources of error would be the difference in numerical solvers between the diffuse and sharp-interface discretizations.

6.2. Flow through a thin strip. A simple but instructive test case is when the general model (5.1) is formulated in a two-dimensional thin strip, mimicking the flow through a long pore. In this case, the scale separation is defined through the ratio $\varepsilon = \ell/L$ between the width ℓ and the length L of the strip. In the nondimensional case, the domain of the thin strip is $(x, y) \in (0, 1)^2$ due to different scaling of the transversal coordinate y . Note that y now plays the role of the transversal variable, rather than a local one, but is still scaled as $y = \varepsilon^{-1}x$ and represents the direction where rapid changes are occurring.

The model equations for the original two-dimensional strip are (5.1). The resulting effective model for the thin strip is one-dimensional and is found through

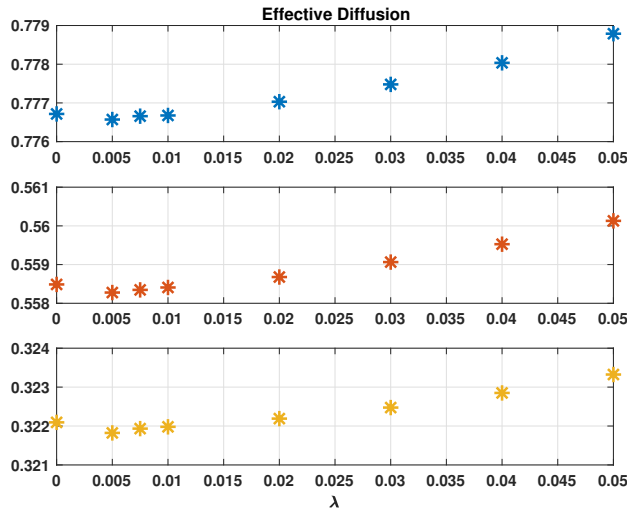


FIG. 7. Effective diffusion values for $R = 0.2$ (top), $R = 0.3$ (middle), and $R = 0.4$ (bottom) for various values of λ . The sharp-interface values are plotted at $\lambda = 0$.

asymptotic expansions and transversal averaging of the model equations. Sharp interface formulations for models in a thin strip and that consider reactive transport leading to changes in the pore geometry have been formulated and upscaled in [10, 12, 28, 48].

When transversally averaging the model equations, we use a slight reformulation for the phase field equation. Assuming that the mineral is only present as a layer on the upper and lower walls of the strip, and using symmetry across the middle of the strip, we approximate the phase field for the lower half of the strip by

$$(6.3) \quad \phi(t, x, y) = \frac{1}{1 + e^{-4(y-d)/\lambda}},$$

where $d(t, x)$ is the mineral layer width. This form of the phase field is similar to that used in the matched asymptotic expansions (3.7); however, it remains an approximation because zero Neumann conditions at the bottom wall $y = 0$ and symmetry at $y = 1/2$ are not fulfilled. With the unknowns $d(t, x)$, $\bar{\phi}(t, x)$, $u_0(t, x)$, and $\bar{\phi}q_0^x(t, x)$, the upscaled equations obtained by transversal averaging are

$$(6.4a) \quad \partial_t d = f(u_0),$$

$$(6.4b) \quad \bar{\phi} = 1 + \frac{\lambda}{2} \log(1 + e^{-4(0.5-d)/\lambda}) - \frac{\lambda}{2} \log(1 + e^{4d/\lambda}),$$

$$(6.4c) \quad \bar{\phi}q_0^x = 1,$$

$$(6.4d) \quad \partial_t(\bar{\phi}(u_0 - u^*)) = -\partial_x(\bar{\phi}q_0^x(u_0 - u^*)) + D\partial_x(\bar{\phi}\partial_x(u_0 - u^*))$$

for $x \in (0, 1)$ and $t > 0$. The derivation of these equations can be found in Appendix A. Note the absence of a momentum conservation equation; hence the pressure is not obtained here. Further, we assume that clogging of the pore due to mineral precipitation does not occur, which means that no degeneracy occurs. This allows taking $\delta = 0$, but performing the upscaling for $\delta > 0$ is straightforward.

The original equations (5.1) are formulated on the scaled strip $(x, y) \in [0, 1]^2$ but using symmetry at $y = 0.5$. Therefore, only half of the strip needs to be considered.

For both the original system (5.1) and the transversally averaged system (6.4), we design an example including dissolution. We let $u_0(t=0) = u^\varepsilon(t=0) = 0.5$ in the entire domain initially and inject an ion concentration of $u_0 = u^\varepsilon = 0.25$ at $x = 0$. At the outlet $x = 1$ we assume zero Neumann condition for the ion concentration. The reaction rate is chosen to be $f(u) = u^2/0.5^2 - 1$, corresponding to an equilibrium concentration of $u_{\text{eq}} = 0.5$. Hence, net dissolution will occur when injecting a lower ion concentration. Initially, the strip is assumed to be halfway filled with a mineral layer at the top and the bottom, that is, $d(t=0) = 0.25$. The phase field in the original equations is initialized with (6.3) using $d = 0.25$. Also, we apply a zero Neumann condition for the phase field at both the inlet and the outlet. The original model (5.1) is initiated with constant pressure and zero velocity. In the upscaled system (6.4), the inlet condition $\overline{\phi}q_0^x = 1$ also gives the flow through the strip. For the original equations (5.1), the inlet condition for the horizontal component of the flow rate \mathbf{q}^ε , $q^{\varepsilon,x}$, is formulated using a time-dependent parabolic profile such that $q_x^\varepsilon = 0$ at $y = d(t,0)$, $\partial_y q^{\varepsilon,x} = 0$ at the symmetry line $y = 0.5$, and $\overline{\phi^\varepsilon q^{\varepsilon,x}} = 1$ is fulfilled. The outlet condition for pressure is a zero Neumann condition.

The following (nondimensional) constants have been used in the simulations:

$$D = 1, \quad u^* = 1, \quad \gamma = 0.0075, \quad K = 25, \quad \rho_f = 1, \quad \mu_f = 1.$$

The value of γ is chosen small to ensure low surface curvature effects, while the value of K is chosen large to avoid too much flow in the diffuse transition zone. Also note that the mineral concentration is chosen artificially low so that large changes in the mineral width occur [48]. We let $\delta = 10^{-6}$ in the original model (5.1) for all simulations.

Similarly as in subsection 6.1 and section 4, both the original equations (5.1) and the averaged system (6.4) are discretized using a control volume method on a staggered cartesian grid where ion concentration, pressure, and phase field are defined in the centers of the control volumes, and the velocities are defined in the centers of the edges. For the original equations, rectangular grids are used, where the resolution in the transversal direction is fine enough to resolve the diffuse transition zone properly.

6.2.1. Comparison to sharp-interface formulation. For the upscaled system of equations (6.4), we can compare the obtained solution to similar upscaled models based on a sharp-interface formulation, such as those found in [10, 48]. Discretizing the sharp-interface model with the same method, and choosing the same initial and boundary conditions, we can investigate the effect of the diffuse interface λ on the model variables.

There are some minor differences in ion concentration u_0 and, accordingly, in the value of mineral width d as the reaction rate depends on u_0 . Figure 8 shows the ion concentrations in the sharp-interface model and in the phase field model for various values of λ at $t = 0.5$. For smaller values of λ , the ion concentration approaches the values found through the sharp-interface model. The differences in values for the mineral width are small (the largest absolute difference for $\lambda = 0.05$ is 0.003).

6.2.2. Comparison to original two-dimensional formulation. We can also check the quality of the upscaling procedure, namely whether the transversal averages of the output from the original equations (5.1) approach the model output found by the upscaled model (6.4) as ε approaches zero. For this comparison we fix a value of λ and let ε vary. For simplicity we consider $\lambda = 0.05, 0.01$, and $\varepsilon = 0.1, 0.05, 0.025, 0.01, 0.005$, where $\varepsilon = 0.005$ corresponds to a strip that is 200

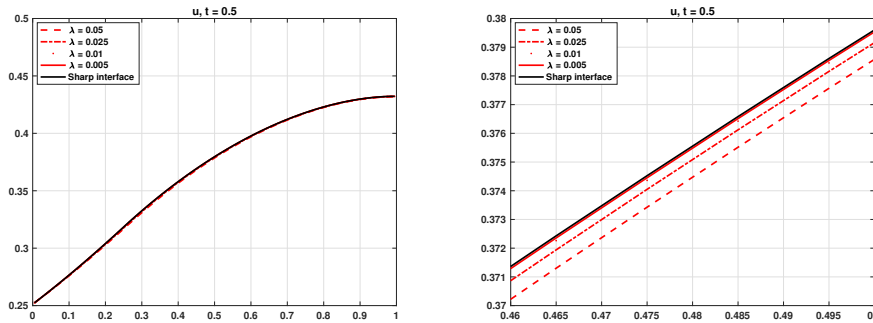


FIG. 8. Ion concentration inside thin strip at $t = 0.5$. Right figure shows zoomed-in view near the middle of the strip, where the largest differences between the model runs are found.

times longer than its width. A typical snapshot from a simulation, with $\lambda = 0.05$ and $\varepsilon = 0.1$, is shown in Figure 9. Even for such a “large” value of ε , the derivatives with respect to y of, e.g., ion concentration, is practically zero. The flow field is found through solving Navier–Stokes equations, and the along-strip component shows a parabola-like profile as expected for this regime. Some flow inside the diffuse interface can be seen.

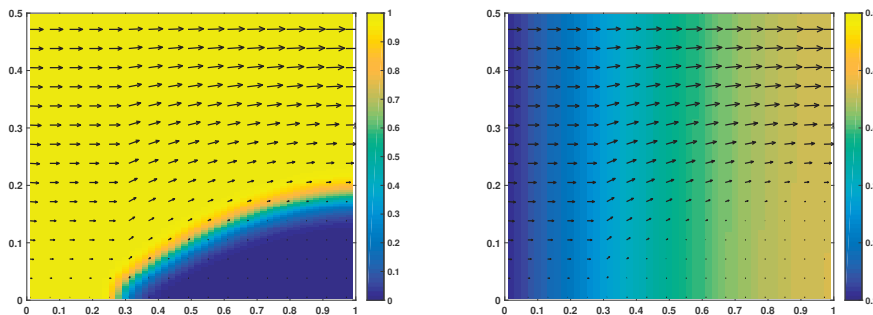


FIG. 9. Phase field (left) and ion concentration (right) in a thin strip at $t = 0.5$. Note that the y -axis is scaled to fit between 0 and 0.5 but should be between 0 and 0.5ε . Velocity field is given as vector overlay and is mainly along the strip. The transversal component of the velocity field has been scaled with $1/\varepsilon$. For this simulation, $\varepsilon = 0.1$ and $\lambda = 0.05$. The domain was discretized with 50 control volumes in the x -direction and 150 control volumes in the y -direction.

By vertically averaging the results from the original equations (5.1) and comparing them to the results from the already upscaled model (6.4), we find in general good correspondence. There is little variability in the transversal direction for ion concentration already for relatively large values of ε , as illustrated in Figure 9 for $\varepsilon = 0.1$. Hence, the averaged ion concentration does not deviate much when decreasing ε . However, some differences are found in the dissolution of the mineral between the two-dimensional model (5.1) and the upscaled model (6.4). These differences do not change with smaller ε . The upscaled system of equations uses directly $\partial_t d = f(u)/u^*$, which is equivalent to the reaction rate found in a sharp-interface model, while the original phase field equation still experiences an effect from the interface width λ in

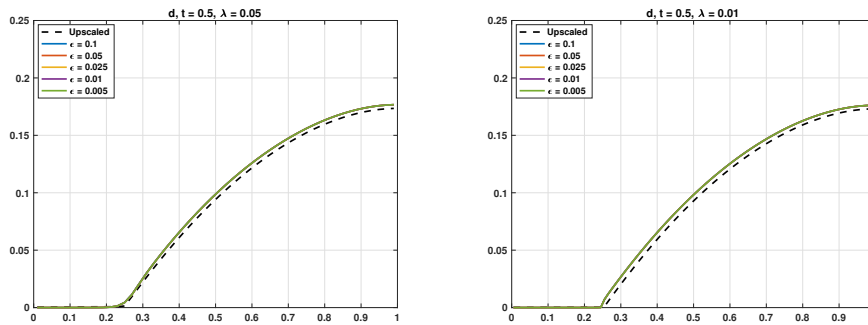


FIG. 10. Width of mineral layer $d(t, x)$ inside (the lower half of) the thin strip at $t = 0.5$ for $\lambda = 0.05$ (left) and $\lambda = 0.01$ (right). Note that the colored lines, corresponding to averaged results from the original equations (5.1), are (almost) on top of each other. The mineral width is found through the phase field by $(0.5 - 0.5\bar{\phi}^E)$. (See online version for color.)

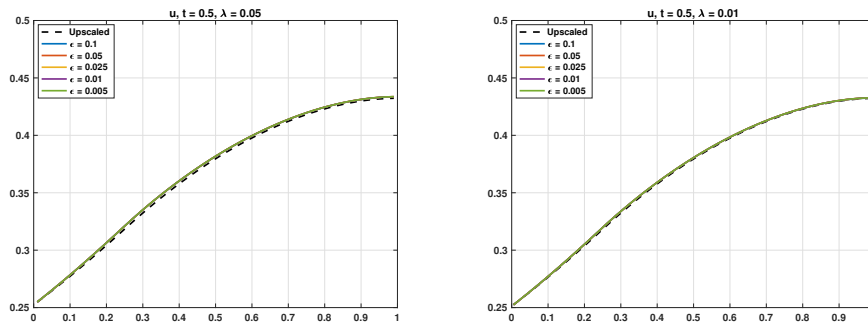


FIG. 11. Transversally averaged ion concentration inside a thin strip at $t = 0.5$ for $\lambda = 0.05$ (left) and $\lambda = 0.01$ (right). Note that the colored lines, corresponding to averaged results from the original equations (5.1), are (almost) on top of each other. (See online version for color.)

the reaction rate. Also, the upscaled model uses an approximated phase field which does not fulfill the boundary conditions at the top and bottom boundaries. However, as seen from Figures 10 and 11, the differences in d and u are very small already for $\lambda = 0.05$.

7. Conclusions. We have derived a phase field model for reactive transport with mineral precipitation and dissolution. Compared to other modeling approaches involving free boundaries moving due to precipitation and dissolution, the phase field model has the advantage of being formulated in a fixed domain. The free boundary is then replaced by a diffuse interface region.

The model proposed here extends the one in [38] by incorporating fluid flow. The extension provides mass and momentum conservation by modifying the Navier–Stokes equations, where the phase field variable is incorporated. The momentum conservation equation is further modified by adding a source term to ensure no flow in the pure mineral phase. Using matched asymptotic expansions, we have shown that the phase field model reduces to the expected sharp-interface model when the width of the diffuse interface approaches zero. Hence, the phase field model captures fluid

flow and solute transport in the fluid phase and, as anticipated, no-slip and Rankine–Hugoniot jump conditions at the evolving fluid–mineral interface. The behavior of the phase field model has been illustrated by considering two numerical experiments where a mineral dissolves when located in flow fields of various strengths. Comparing to a benchmark [33], we find the phase field model to behave qualitatively and quantitatively as expected, although with a slight overestimation of the dissolution rate.

When considering a porous medium, the model proposed here can be seen as a pore scale model. By considering the medium as periodically perforated, an upscaled counterpart of the phase field model is obtained by means of homogenization techniques. The resulting effective equations are valid at the Darcy scale. We obtain the cell problems that provide the effective ion diffusion as in [38]. Here we also obtain cell problems for obtaining the effective permeability and porosity. In particular, since the porosity in a cell is the average of the phase field over that cell, the model also provides an equation describing the evolution of the porosity in time, depending on the macroscale location. Numerical experiments show the behavior of the cell problems with respect to the width of the diffuse interface, where the diffusive cell problems provide accurate results for relatively large values of the width of the diffuse interface, while the permeability is prone to being overestimated.

The use of a phase field model instead of a sharp-interface formulation avoids some potential numerical pitfalls, as there is no need to, e.g., solve the level-set equation. Using a diffuse interface as a replacement for a sharp-interface simplifies the development of numerical simulation tools but also introduces a relaxation which can lead to inaccurate numerical results. As seen from the numerical experiments, the mineral dissolved a bit faster than expected due to the nonconservative property of the Allen–Cahn equation, and the permeability could easily be overestimated or underestimated due to artificial flow in the diffuse transition zone. Hence, using small values for the interface diffusivity and of diffuse interface width are important for obtaining a good representation of the flow at the pore scale or in the cell problems, which in turn puts constraints on how fine the grid has to be near the diffuse interface.

Appendix A. Thin strip model. Here we derive the averaged thin strip model using a phase field formulation, as given in (6.4). The starting point is the original phase field model for a porous medium (5.1), but formulated in a thin strip having width ℓ and length L , such that $\varepsilon = \ell/L$ defines the scale separation. Hence, in the nondimensional setting, the strip has width and length 1 but where derivatives in the y -direction (across the strip) are scaled with $1/\varepsilon$. Hence, for a dummy variable $v(x, y)$ one gets

$$\nabla v(x, y) = \partial_x v \mathbf{i} + \frac{1}{\varepsilon} \partial_y v \mathbf{j},$$

where \mathbf{i} and \mathbf{j} are unit vectors in the along-strip and transversal direction. Due to symmetry we consider only the lower half of the strip. As explained earlier, the phase field approaching value 1 in the fluid part and 0 in the mineral part is given by

$$(A.1) \quad \phi(t, x, y) = \frac{1}{1 + e^{-4(y-d)/\lambda}},$$

where $y = d(t, x)$ defines the transition between fluid and mineral where $\phi = 0.5$. This formulation uses $d(t, x)$ as an unknown as in sharp-interface models but still incorporates a phase field variable that affects the model formulation. However, as ϕ in (A.1) does not fulfill the zero Neumann and symmetry boundary conditions, we are

making a small error by using this phase field. Here we derive the upscaled (transversally averaged) model for the current formulation. As there will be no problems with degeneracy in the equations for the resulting thin strip model, we let $\delta = 0$. It is, of course, possible to do the transversal averaging also with $\delta > 0$, and would only require the phase field ϕ being replaced with $\phi + \delta$ in the ion and mass conservation equations.

A.1. Equation for $d(t, x)$. The equation for $d(t, x)$ is obtained by inserting (A.1) into the phase field equation (5.1a) and collecting the lowest order terms in ε , $O(\varepsilon^0)$. This gives

$$\lambda^2 \partial_t \phi_0 + \gamma P'(\phi_0) = \gamma \lambda^2 \partial_y^2 \phi_0 - 4\lambda \phi_0 (1 - \phi_0) \frac{1}{u^*} f(u_0).$$

Inserting (A.1) for ϕ , using the equalities

$$\begin{aligned} \partial_t \phi &= -\frac{4}{\lambda} \phi (1 - \phi) \partial_t d, \\ \partial_y^2 \phi &= \frac{4^2}{\lambda^2} \phi (1 - \phi) (1 - 2\phi), \end{aligned}$$

and cancelling equal terms and common factors results in

$$(A.2) \quad \partial_t d = \frac{1}{u^*} f(u).$$

Hence, the phase field $\phi(t, x, y)$ is given by (A.1), where the mineral width $d(t, x)$ follows from (A.2).

Note that the resulting equation for $d(t, x)$ is the same model equation as used in the sharp-interface thin strip formulations of [10, 48]. However, the phase field $\phi(t, x, y)$ will still appear in the upscaled solute transport and flow equations. This allows us to illustrate the behavior of the phase field model with respect to λ and ε in a simple setting.

A.2. Equation for the averaged phase field. The transversally averaged phase field will be needed in the upscaled thin strip model. In view of the symmetry, the transversal average of (A.1) is

$$\bar{\phi} = 2 \int_0^{1/2} \frac{1}{1 + e^{-4(y-d)/\lambda}} dy = 1 + \frac{\lambda}{2} \log(1 + e^{-\frac{4}{\lambda}(0.5-d)}) - \frac{\lambda}{2} \log(1 + e^{\frac{4}{\lambda}d}).$$

A.3. Equation for mass conservation. The lowest order term arising from the mass conservation equation (5.1b) yields

$$\partial_y(\phi q_0^y) = 0,$$

which, together with the boundary condition (5.1g), gives that the lowest order transversal velocity component q_0^y is independent of y . The next order provides

$$\partial_x(\phi q_0^x) + \partial_y(\phi q_1^y) = 0,$$

where q_0^x is the lowest order along-strip velocity component, and q_1^y is the first-order transversal velocity component. This equation is integrated in y from 0 to 1/2, which, together with boundary condition (5.1g) at $y = 0$ and symmetry at $y = 1/2$, gives

$$\partial_x(\bar{\phi} q_0^x) = 0.$$

A.4. Equation for average flow rate. Inserting asymptotic expansions into (5.1c), from the lowest order term, one gets

$$\phi \partial_y p_0 = 0,$$

implying that $p_0 = p_0(t, x)$ is independent of y . The horizontal (along the strip) component of the $O(1)$ terms provides

$$0 = -\phi \partial_x p_0 + \mu_f \phi \partial_y^2 (\phi q_0^x) - \frac{K(1-\phi)n}{\lambda} \frac{1}{\phi+n} q_0^x.$$

We let $v = \phi q_0^x$ represent the unknown and insert the expression for ϕ , (A.1), when necessary. Then,

$$(A.3) \quad \mu_f v'' - \frac{K n e^{-4(y-d)/\lambda} (1 + e^{-4(y-d)/\lambda})^2}{\lambda (1 + n(1 + e^{-4(y-d)/\lambda}))} v = \partial_x p_0,$$

where ' indicates derivative with respect to y . The variables t and x appearing in d and p are considered parameters. Hence, we have an inhomogeneous, second-order, linear ODE with nonconstant coefficients. Finding simple analytical expressions for the solution of v is not straightforward. Instead, the boundary condition $\overline{\phi q_0^x} = 1$ can be used to resolve the flow through the strip together with mass conservation. This means that we will not be able to solve the pressure inside the thin strip.

A.5. Equation for ion concentration. Inserting (A.1) for ϕ and asymptotic expansion for u^ε into (5.1d) and equating the lowest order terms yields

$$\partial_y (\phi \partial_y u_0) = 0.$$

Together with the lowest order boundary condition $\phi \partial_y u_0 = 0$ at $y = 0, 1$ and the fact that $\phi > 0$, it follows that

$$u_0 = u_0(t, x).$$

Hence, u_0 is independent of the transversal variable y . Integrating (5.1d) in y from 0 to 1/2, and applying boundary conditions (5.1f) and (5.1g) on the lower boundary and symmetry conditions on $y = 1/2$, results in

$$\int_0^{1/2} \partial_t (\phi (u^\varepsilon - u^*)) dy + \int_0^{1/2} \partial_x (\phi q^{\varepsilon, x} (u^\varepsilon - u^*)) dy = D \int_0^{1/2} \partial_x (\phi \partial_x (u^\varepsilon - u^*)) dy,$$

where $q^{\varepsilon, x}$ is the along-strip component of the \mathbf{q}^ε . Using the asymptotic expansions and the fact that u_0 is independent of y leads to

$$\partial_t (\overline{\phi} (u_0 - u^*)) + \partial_x (\overline{\phi q_0^x} (u_0 - u^*)) = D \partial_x (\overline{\phi} \partial_x (u_0 - u^*)).$$

Acknowledgments. We would like to thank Profs. Christian Rohde (Stuttgart) and Harald Garcke (Regensburg) for useful discussions on the phase field formulation.

REFERENCES

- [1] H. ABELS AND Y. LIU, *Sharp interface limit for a Stokes/Allen-Cahn system*, Arch. Ration. Mech. Anal., 229 (2018), pp. 417–502, <https://doi.org/10.1007/s00205-018-1220-x>.
- [2] A. W. ADAMSON AND A. P. GAST, *Physical Chemistry of Surfaces*, Interscience Publishers, New York, 1967.

- [3] A. AGOSTI, B. GIOVANARDI, L. FORMAGGIA, AND A. SCOTTI, *A numerical procedure for geochemical compaction in the presence of discontinuous reactions*, Adv. Water Resour., 94 (2016), pp. 332–344, <https://doi.org/10.1016/j.advwatres.2016.06.001>.
- [4] G. ALLAIRE AND H. HUTRIDURGA, *Homogenization of reactive flows in porous media and competition between bulk and surface diffusion*, IMA J. Appl. Math., 77 (2012), pp. 788–815.
- [5] S. M. ALLEN AND J. W. CAHN, *A microscopic theory for antiphase boundary motion and its application to antiphase domain coarsening*, Acta Metallurgica, 27 (1979), pp. 1085–1095, [https://doi.org/10.1016/0001-6160\(79\)90196-2](https://doi.org/10.1016/0001-6160(79)90196-2).
- [6] I. BATTIATO AND D. TARTAKOVSKY, *Applicability regimes for macroscopic models of reactive transport in porous media*, J. Contaminant Hydrology, 120–121 (2011), pp. 18–26, <https://doi.org/10.1016/j.jconhyd.2010.05.005>.
- [7] I. BATTIATO, D. TARTAKOVSKY, A. TARTAKOVSKY, AND T. SCHEIBE, *On breakdown of macroscopic models of mixing-controlled heterogeneous reactions in porous media*, Adv. Water Resour., 32 (2009), pp. 1664–1673, <https://doi.org/10.1016/j.advwatres.2009.08.008>.
- [8] C. BECKERMANN, H.-J. DIEPERS, I. STEINBACH, A. KARMA, AND X. TONG, *Modeling melt convection in phase-field simulations of solidification*, J. Comput. Phys., 154 (1999), pp. 468–496, <https://doi.org/10.1006/jcph.1999.6323>.
- [9] F. BOYER, C. LAPUERTA, S. MINJEAUD, B. PIAR, AND M. QUINTARD, *Cahn–Hilliard/Navier–Stokes model for the simulation of three-phase flows*, Transp. Porous Media, 82 (2010), pp. 463–483, <https://doi.org/10.1007/s11242-009-9408-z>.
- [10] C. BRINGEDAL, I. BERRE, I. S. POP, AND F. A. RADU, *A model for non-isothermal flow and mineral precipitation and dissolution in a thin strip*, J. Comput. Appl. Math., 289 (2015), pp. 346–355, <https://doi.org/10.1016/j.cam.2014.12.009>.
- [11] C. BRINGEDAL, I. BERRE, I. S. POP, AND F. A. RADU, *Upscaling of non-isothermal reactive porous media flow with changing porosity*, Transp. Porous Media, 114 (2016), pp. 371–393, <https://doi.org/10.1007/s11242-015-0530-9>.
- [12] C. BRINGEDAL, I. BERRE, I. S. POP, AND F. A. RADU, *Upscaling of nonisothermal reactive porous media flow under dominant Péclet number: The effect of changing porosity*, Multiscale Model. Simul., 14 (2016), pp. 502–533, <https://doi.org/10.1137/15M1022781>.
- [13] C. BRINGEDAL AND K. KUMAR, *Effective behavior near clogging in upscaled equations for non-isothermal reactive porous media flow*, Transp. Porous Media, 120 (2017), pp. 553–577, <https://doi.org/10.1007/s11242-017-0940-y>.
- [14] G. CAGINALP AND P. C. FIFE, *Dynamics of layered interfaces arising from phase boundaries*, SIAM J. Appl. Math., 48 (1988), pp. 506–518, <https://doi.org/10.1137/0148029>.
- [15] J. W. CAHN AND J. E. HILLIARD, *Free energy of a nonuniform system I: Interfacial free energy*, J. Chem. Phys., 28 (1958), pp. 258–267, <https://doi.org/10.1063/1.1744102>.
- [16] Z. CHEN, S. L. LYONS, AND G. QIN, *Derivation of the Forchheimer law via homogenization*, Transp. Porous Media, 44 (2001), pp. 325–335, <https://doi.org/10.1023/A:1010749114251>.
- [17] C. CHOQUET AND A. MIKELIĆ, *Rigorous upscaling of the reactive flow with finite kinetics and under dominant Péclet number*, Contin. Mech. Thermodyn., 21 (2009), pp. 125–140, <https://doi.org/10.1007/s00161-009-0099-z>.
- [18] K. R. DALY AND T. ROOSE, *Homogenization of two fluid flow in porous media*, Proc. Roy. Soc. A Math. Phys. Engrg. Sci., 471 (2015), 20140564, <https://doi.org/10.1098/rspa.2014.0564>.
- [19] Y. DAVIT, C. G. BELL, H. M. BYRNE, L. A. CHAPMAN, L. S. KIMPTON, G. E. LANG, K. H. L. LEONARD, J. M. OLIVER, N. C. PEARSON, R. J. SHIPLEY, S. L. WATERS, J. P. WHITELEY, B. D. WOOD, AND M. QUINTARD, *Homogenization via formal multiscale asymptotics and volume averaging: How do the two techniques compare?*, Adv. Water Resour., 62, part B (2013), pp. 178–206, <https://doi.org/10.1016/j.advwatres.2013.09.006>.
- [20] M. DENTZ, T. L. BORGNE, A. ENGLERT, AND B. BIJELJIC, *Mixing, spreading and reaction in heterogeneous media: A brief review*, J. Contaminant Hydrology, 120–121 (2011), pp. 1–17, <https://doi.org/10.1016/j.jconhyd.2010.05.002>.
- [21] K. R. ELDER, M. GRANT, N. PROVATAS, AND J. M. KOSTERLITZ, *Sharp interface limits of phase-field models*, Phys. Rev. E, 64 (2001), 021604, <https://doi.org/10.1103/PhysRevE.64.021604>.
- [22] H. GARCKE, C. HECHT, M. HINZE, AND C. KAHLE, *Numerical approximation of phase field based shape and topology optimization for fluids*, SIAM J. Sci. Comput., 37 (2015), pp. A1846–A1871, <https://doi.org/10.1137/140969269>.
- [23] U. HORNUNG, ED., *Homogenization and Porous Media*, Interdiscip. Appl. Math. 6, Springer-Verlag, New York, 1996, <https://doi.org/10.1007/978-1-4612-1920-0>.
- [24] D. JEONG AND J. KIM, *Conservative Allen–Cahn–Navier–Stokes system for incompressible two-phase fluid flows*, Comput. & Fluids, 156 (2017), pp. 239–246, <https://doi.org/10.1016/j.compfluid.2017.07.009>.

- [25] P. KNABNER, C. J. VAN DUJIN, AND S. HENGST, *An analysis of crystal dissolution fronts in flows through porous media part 1: Compatible boundary conditions*, Adv. Water Resour., 18 (1995), pp. 171–185, [https://doi.org/10.1016/0309-1708\(95\)00005-4](https://doi.org/10.1016/0309-1708(95)00005-4).
- [26] K. KUMAR, M. NEUSS-RADU, AND I. S. POP, *Homogenization of a pore scale model for precipitation and dissolution in porous media*, IMA J. Appl. Math., 81 (2016), pp. 877–897, <https://doi.org/10.1093/imamat/hxw039>.
- [27] K. KUMAR, I. S. POP, AND F. A. RADU, *Convergence analysis of mixed numerical schemes for reactive flow in a porous medium*, SIAM J. Numer. Anal., 51 (2013), pp. 2283–2308, <https://doi.org/10.1137/120880938>.
- [28] K. KUMAR, T. L. VAN NOORDEN, AND I. S. POP, *Effective dispersion equations for reactive flows involving free boundaries at the microscale*, Multiscale Model. Simul., 9 (2011), pp. 29–58, <https://doi.org/10.1137/100804553>.
- [29] T. LE BORGNE, D. BOLSTER, M. DENTZ, P. DE ANNA, AND A. TARTAKOVSKY, *Effective pore-scale dispersion upscaling with a correlated continuous time random walk approach*, Water Resour. Res., 47 (2011), W12538, <https://doi.org/10.1029/2011WR010457>.
- [30] X. LI, J. LOWENGRUB, A. RÄTZ, AND A. VOIGT, *Solving PDEs in complex geometries: A diffuse domain approach*, Commun. Math. Sci., 7 (2009), pp. 81–107, <https://doi.org/10.4310/cms.2009.v7.n1.a4>.
- [31] S. METZGER AND P. KNABNER, *Homogenization of Two-Phase Flow in Porous Media from Pore to Darcy Scale: A Phase-Field Approach*, preprint, <https://arxiv.org/abs/2002.02531>, 2020.
- [32] A. MIKELIĆ, V. DEVIGNE, AND C. J. VAN DUJIN, *Rigorous upscaling of the reactive flow through a pore, under dominant Peclet and Damkohler numbers*, SIAM J. Math. Anal., 38 (2006), pp. 1262–1287, <https://doi.org/10.1137/050633573>.
- [33] S. MOLINS, C. SOULAINÉ, N. I. PRASIANAKIS, A. ABBASI, P. PONCET, A. J. C. LADD, V. STARCHENKO, S. ROMAN, D. TREBOTICH, H. A. TCHELEPI, AND C. L. STEEFEL, *Simulation of mineral dissolution at the pore scale with evolving fluid-solid interfaces: Review of approaches and benchmark problem set*, Comput. Geosci., to appear (published online January 23, 2020), <https://doi.org/10.1007/s10596-019-09903-x>.
- [34] S. MOLINS, D. TREBOTICH, G. H. MILLER, AND C. I. STEEFEL, *Mineralogical and transport controls on the evolution of porous media texture using direct numerical simulation*, Water Resour. Res., 53 (2017), pp. 3645–3661, <https://doi.org/10.1002/2016WR020323>.
- [35] X. MU, F. FRANK, B. RIVIERE, F. O. ALPAK, AND W. G. CHAPMAN, *Mass-conserved density gradient theory model for nucleation process*, Ind. Eng. Chem. Res., 57 (2018), pp. 16476–16485, <https://doi.org/10.1021/acs.iecr.8b03389>.
- [36] M. QUINTARD AND S. WHITAKER, *Convection, dispersion, and interfacial transport of contaminants: Homogeneous porous media*, Adv. Water Resour., 17 (1994), pp. 221–239, [https://doi.org/10.1016/0309-1708\(94\)90002-7](https://doi.org/10.1016/0309-1708(94)90002-7).
- [37] M. QUINTARD AND S. WHITAKER, *Dissolution of an immobile phase during flow in porous media*, Ind. Eng. Chem. Res., 38 (1999), pp. 833–844, <https://doi.org/10.1021/ie980212t>.
- [38] M. REDEKER, C. ROHDE, AND I. S. POP, *Upscaling of a tri-phase phase-field model for precipitation in porous media*, IMA J. Appl. Math., 81 (2016), pp. 898–939, <https://doi.org/10.1093/imamat/hxw023>.
- [39] C. ROHDE AND L. VON WOLFF, *A Ternary Cahn-Hilliard Navier-Stokes Model for Two Phase Flow with Precipitation and Dissolution*, preprint, <https://arxiv.org/1912.09181>, 2019.
- [40] F. SCHLÖGL, *Chemical reaction models for non-equilibrium phase transitions*, Z. Phys., 253 (1972), pp. 147–161, <https://doi.org/10.1007/BF01379769>.
- [41] M. SCHMUCK, M. PRADAS, G. A. PAVLIOTIS, AND S. KALLIADASIS, *Upscaled phase-field models for interfacial dynamics in strongly heterogeneous domains*, Proc. Roy. Soc. A Math. Phys. Eng. Sci., 468 (2012), pp. 3705–3724, <https://doi.org/10.1098/rspa.2012.0020>.
- [42] M. SCHMUCK, M. PRADAS, G. A. PAVLIOTIS, AND S. KALLIADASIS, *Derivation of effective macroscopic Stokes–Cahn–Hilliard equations for periodic immiscible flows in porous media*, Nonlinearity, 26 (2013), pp. 3259–3277, <https://doi.org/10.1088/0951-7715/26/12/3259>.
- [43] R. SCHULZ, N. RAY, F. FRANK, H. S. MAHATO, AND P. KNABNER, *Strong solvability up to clogging of an effective diffusion-precipitation model in an evolving porous medium*, Eur. J. Appl. Math., 28 (2017), pp. 179–207, <https://doi.org/10.1017/S0956792516000164>.
- [44] C. VAN DUJIN AND P. KNABNER, *Travelling wave behaviour of crystal dissolution in porous media flow*, Eur. J. Appl. Math., 8 (1997), pp. 49–72.
- [45] C. J. VAN DUJIN, A. MIKELIĆ, I. S. POP, AND C. ROSIER, *Effective dispersion equations for reactive flows with dominant Péclet and Damkohler numbers*, in Advances in Chemical Engineering, G. B. Marin, D. West, and G. S. Yablonsky, eds., Adv. Chem. Eng. 34, Academic

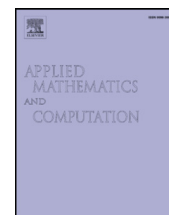
- Press, New York, 2008, pp. 1–45, [https://doi.org/10.1016/S0065-2377\(08\)00001-X](https://doi.org/10.1016/S0065-2377(08)00001-X).
- [46] C. J. VAN DUIN AND I. S. POP, *Crystal dissolution and precipitation in porous media: Pore scale analysis*, *J. Reine Angew. Math.*, 577 (2004), pp. 171–211, <https://doi.org/10.1515/crll.2004.2004.577.171>.
- [47] T. L. VAN NOORDEN, *Crystal precipitation and dissolution in a porous medium: Effective equations and numerical experiments*, *Multiscale Model. Simul.*, 7 (2009), pp. 1220–1236, <https://doi.org/10.1137/080722096>.
- [48] T. L. VAN NOORDEN, *Crystal precipitation and dissolution in a thin strip*, *Eur. J. Appl. Math.*, 20 (2009), pp. 69–91, <https://doi.org/10.1017/S0956792508007651>.
- [49] T. L. VAN NOORDEN AND C. ECK, *Phase field approximation of a kinetic moving-boundary problem modelling dissolution and precipitation*, *Interfaces Free Boundaries*, 13 (2011), pp. 29–55, <https://doi.org/10.4171/IFB/247>.
- [50] T. L. VAN NOORDEN AND I. S. POP, *A Stefan problem modelling crystal dissolution and precipitation*, *IMA J. Appl. Math.*, 73 (2008), pp. 393–411, <https://doi.org/10.1093/imamat/hxm060>.
- [51] T. L. VAN NOORDEN, I. S. POP, AND M. RÖGER, *Crystal dissolution and precipitation in porous media: L^1 -contraction and uniqueness*, in *Discrete Contin. Dyn. Syst., Dynamical Systems and Differential Equations*, Proceedings of the 6th AIMS International Conference, suppl., 2007, pp. 1013–1020, <https://doi.org/10.3934/proc.2007.2007.1013>.
- [52] S. WHITAKER, *The Method of Volume Averaging*, *Theory Appl. Transp. Porous Media* 13, Springer Netherlands, 1999, <https://doi.org/10.1007/978-94-017-3389-2>.
- [53] B. D. WOOD, *Inertial effects in dispersion in porous media*, *Water Resour. Res.*, 43 (2007), W12S16, <https://doi.org/10.1029/2006WR005790>.
- [54] B. D. WOOD, F. GOLPIER, AND M. QUINTARD, *Dispersive transport in porous media with biofilms: Local mass equilibrium in simple unit cells*, *Internat. J. Environ. Waste Manag.*, 7 (2011), pp. 24–48, <https://doi.org/10.1504/IJEW.2011.037364>.
- [55] Z. XU AND P. MEAKIN, *Phase-field modeling of solute precipitation and dissolution*, *J. Chem. Phys.*, 129 (2008), 014705, <https://doi.org/10.1063/1.2948949>.

9 Two-scale simulation of mineral precipitation and dissolution

The content of this chapter is based on the following original article:

M. Bastidas Olivares, C. Bringedal, and I. S. Pop. *A two-scale iterative scheme for a phase-field model for precipitation and dissolution in porous media*. Applied Mathematics and Computation 396 (2021), p. 125933. doi: 10.1016/j.amc.2020.125933.

With courtesy of Elsevier.



A two-scale iterative scheme for a phase-field model for precipitation and dissolution in porous media



Manuela Bastidas Olivares^{a,*}, Carina Bringedal^b, Iuliu Sorin Pop^a

^a Faculty of Sciences, UHasselt - Hasselt University, Diepenbeek, Belgium

^b Institute for Modelling Hydraulic and Environmental Systems, University of Stuttgart, Stuttgart, Germany

ARTICLE INFO

Article history:

Received 14 July 2020

Revised 20 October 2020

Accepted 19 December 2020

Available online 7 January 2021

2020 MSC:

65M12

65M50

65M55

65M60

Keywords:

Phase-field model

Homogenization

Multi-scale methods

Iterative schemes

Adaptive strategy

ABSTRACT

Mineral precipitation and dissolution processes in a porous medium can alter the structure of the medium at the scale of pores. Such changes make numerical simulations a challenging task as the geometry of the pores changes in time in an a priori unknown manner. To deal with such aspects, we here adopt a two-scale phase-field model, and propose a robust scheme for the numerical approximation of the solution. The scheme takes into account both the scale separation in the model, as well as the non-linear character of the model. After proving the convergence of the scheme, an adaptive two-scale strategy is incorporated, which improves the efficiency of the simulations. Numerical tests are presented, showing the efficiency and accuracy of the scheme in the presence of anisotropies and heterogeneities.

© 2021 Elsevier Inc. All rights reserved.

1. Introduction

Processes involving precipitation and dissolution in porous media are encountered in many real-life applications. Notable examples in this sense appear in environmental engineering (the management of freshwater in the subsurface), geothermal energy, and agriculture (soil salinization). Particularly challenging for the mathematical modeling and numerical simulations are the situations when the chemistry is affecting the microstructure of the medium, in the sense that the pore geometry and even morphology is altered by dissolution or precipitation. At the scale of pores (from now on the micro scale), the geometry changes due to chemistry, which also impacts the averaged model behavior at the Darcy-scale (from now on the macro scale).

Mathematical models for dissolution and precipitation in porous media have been extensively discussed in the past decades. In this sense, we mention the model proposed in Knabner et al. [1], in which the possibility of having an under- or oversaturated regime is expressed in rigorous mathematical terms. Various mathematical aspects for such models, like the existence and uniqueness of a (weak) solution, the rigorous derivation of the macro-scale model from a micro-scale one, the

* Corresponding author.

E-mail addresses: manuela.bastidas@uhasselt.be (M. Bastidas Olivares), carina.bringedal@iws.uni-stuttgart.de (C. Bringedal), sorin.pop@uhasselt.be (I.S. Pop).

numerical approximation, or qualitative properties like traveling waves are studied in Knabner et al. [1], Moszkowicz et al. [2], Bouillard et al. [3], Kumar et al. [4], Agosti et al. [5], Kumar et al. [6], Hoffmann et al. [7]. The models discussed there do not take explicitly into account any evolution of the micro-scale geometry. In those cases one can work with the mineral as a surface concentration and the micro-scale volumetric changes in the mineral phase are neglected (see [8,9]). At the macro scale, this implies that the porosity does not depend on the solute concentration. An exception is the macro-scale model proposed in Agosti et al. [5], including an equation relating the changes in the porosity to the (macro-scale) concentration of the mineral.

Whenever the changes in the mineral layer thickness are large compared to the typical micro-scale length (the size of pores), the micro-scale changes in porosity and morphology cannot be neglected. This impacts the flow at the micro scale, and implicitly the averaged macro-scale quantities of primary interest for real-life applications. In this context, upscaling is a natural way to derive macro-scale models incorporating the micro-scale processes accurately. We recall that, due to the chemical processes mentioned above, the structure of the pores (the micro structure) changes in time, depending on the concentration of the dissolved components, which is a model unknown. In other words, one deals with free boundaries appearing at the micro scale. The challenges related to such models are two-fold; on the one hand, related to the free boundaries, and on the other hand, to the fact that these appear at the micro scale.

The evolution of the pore-scale geometry can be described in various ways; in one spatial dimension, a free boundary model for dissolution and precipitation in porous media is proposed in van Noorden and Pop [10]. There, the existence and uniqueness of a solution are proved. For closely related results, we mention [11,12], where the existence of solutions for similar, one-dimensional free-boundary problems is proved. For the multi-dimensional case, we mention [13–15] where mathematical models for reactive transport models in moving domains are proposed. Similarly, in Mabuza et al. [16] the existence of a solution for a model describing reactive solute transport in deformable two-dimensional channels with adsorption-desorption at the walls is proved, relying on the techniques in Muha and Čanić [17].

Though more complicated than the one-dimensional case, there are various ways to deal with the (freely) moving boundaries in multiple spatial dimensions. For instance, when dealing with a strip or a radially symmetric channel, a layer thickness function can be defined to locate the free boundary. This approach is adopted in van Noorden [8], Kumar et al. [9], Bringedal et al. [18]. A level set approach can be considered in more general porous domains, as done in van Noorden [19], Schulz et al. [20, 21], Bringedal et al. [22]. Under certain conditions on the evolution of the free boundary and on the geometry, e.g., assuming local periodicity and that the scales are well separated, upscaled models can be derived using transversal averaging or homogenization techniques. In the first case, one arrives at upscaled models where the layer thickness is related to the changes in porosity and permeability. In the other case, the homogenization leads to upscaled models where the effective parameters are determined by solving local cell problems involving level sets.

A third option, which inspired the present work, is the phase-field approach. In this case, a thin, diffuse interface layer approximates the freely moving interfaces separating the fluid from the mineral (the precipitate). Building on the idea of minimizing the free energy (see, e.g., [23]) the phase-field indicator ϕ is an approximation of the characteristic function that approaches 1 in the fluid phase and 0 in the mineral phase. In between, a smooth transition zone of width $\lambda > 0$ is encountered (see e.g. [24]). This approach was considered in van Noorden and Eck [25] for describing the dissolution and precipitation processes as encountered at the micro scale. There, two phases are encountered (the mineral and the solvent), both being immobile; the solute concentration changes due to chemistry (precipitation and dissolution) and diffusion. An extension to two fluid phases and the mineral is proposed in Redeker et al. [26]. There, the Darcy-scale counterpart is derived by homogenization techniques but still for the case without fluid motion. The model in van Noorden and Eck [25] is further extended in Bringedal et al. [27] to incorporate fluid flow at the micro scale, and where a Darcy-scale counterpart is derived. In this context, we also mention [28] where model order reduction techniques are employed to build an efficient multi-scale algorithm applicable to the phase-field model proposed in Redeker et al. [26].

Here we focus on the two-scale model in Bringedal et al. [27], in which the so-called cell problems defined at the micro scale are solved for determining the effective parameters appearing in the macro-scale equations modeling the flow and the chemical processes. In other words, we compute effective parameters such as the effective diffusion and the effective permeability tensors to resolve the homogenized problem. These macro-scale quantities are found through local micro-scale problems that depend on the evolution of the phase field at the micro scale. This paper is proposing a two-scale iterative scheme for approximating the solution of the two-scale model in Bringedal et al. [27]. The scheme deals with the non-linearities in the model and at the same time with the scale separation. Though being motivated by the mathematical model mentioned above, the approach proposed here can be applied to other two-scale models obtained by homogenization. Unlike classical multi-scale schemes, e.g., [29], where one has the same type of equations at both the macro and micro scales, the scheme proposed here allows for different equations at the micro and the macro scale. This approach is hence in line with the heterogeneous multi-scale methods in Engquist et al. [30]. In the present context, we mention the similarities with [31,32], where a multi-scale scheme is developed for reactive flow and transport in porous media where a level-set is employed to track the evolution of the solid-fluid interface at the micro scale.

The scheme proposed here is a two-scale iterative one and relies on the backward Euler method for the time discretization. Here, we extend the general ideas of the multi-scale iterative method presented in Bastidas et al. [33]. Inspired by Brun et al. [34], an artificial term is included in the (micro-scale) phase-field equation. This parameter stabilizes the coupling with the (macro-scale) flow and reactive transport equations. We mention that, compared to [34], this coupling is bridging here

two different scales. In a simplified setting, we give the rigorous convergence proof of the scheme. This result is obtained without specifying any particular spatial discretization.

To guarantee mass conservation, the mixed finite element method (MFEM) is employed for the spatial discretization at both scales. Since effective quantities are needed for each macro-scale element, the finer the macro-scale mesh is, the more micro-scale problems have to be solved numerically. This increases the computational effort significantly. To deal with this aspect, a macro-scale adaptive strategy is included, inspired by Redeker and Eck [35]. The main idea is to select at each time step a representative fraction of the macro-scale points (so-called active nodes), for which the cell problems are solved and the effective quantities updated. The results are then transferred to the remaining (inactive) nodes, which are assigned to an active node based on a similarity criterion. A similar approach was also applied in Redeker et al. [26], Gärtner et al. [31].

Adaptivity is further applied at the micro scale, where it is crucial to have an accurate description of the diffuse transition zone. In such regions, a fine mesh is necessary to capture the phase-field changes at every time step. On the other hand, away from such transition zones, the phase field is barely varying in both the mineral and the fluid phases. There a coarser mesh is sufficient to obtain an accurate numerical solution. Therefore we use an adaptive mesh that follows the movement of the phase-field transition zone. We start with a coarse micro-scale mesh and apply a prediction-correction strategy as described in Heister et al. [36] for a phase-field model for fracture propagation. Finally, since the cell problems for the phase field are non-linear, we use a fixed-point iterative scheme called L-scheme, as described in Pop et al. [37], List and Radu [38]. Incorporating this linearization scheme in the two-scale iterative one mentioned above can be made with no effort, as they both involve similar stabilization terms. Moreover, this scheme has the advantage of being convergent regardless of the starting point and the spatial discretization (the method itself, and the mesh size). Finally, as much as the spatial discretization allows it, the iterative scheme guarantees the lower and upper bounds for the phase field.

The remainder of this paper is structured as follows. In Section 2, the geometry and the details of the model are presented. In Section 3, we formulate the iterative scheme and in Section 4, we introduce the non-linear solver used on the micro-scale problems. In Section 5, we prove the convergence of the two-scale iterative scheme. The micro- and macro-scale adaptive strategies are described in Section 6. Finally, in Section 7, two numerical test cases are applied in which we study in detail the effect of different choices of parameters.

1.1. Notations

In this paper we use common notations from the functional analysis. For a general domain $\mathcal{D} \subset \mathbb{R}^d$ with $d = 2, 3$, we denote by $L^p(\mathcal{D})$ the space of the p -integrable real-valued functions equipped with the usual norm and by $H^1(\mathcal{D})$ the Sobolev space of $L^2(\mathcal{D})$ functions having weak derivatives in the same space.

We let $\langle \cdot, \cdot \rangle_{\mathcal{D}}$ represent the inner product on $L^2(\mathcal{D})$ and norm $\|v\|_{L^2(\mathcal{D})}^2 = \|v\|_{\mathcal{D}}^2 := \langle v, v \rangle_{\mathcal{D}}$. Take $Y = (-0.5, 0.5)^d$, for defining a solution in a weak sense we use the space $H^1_{\#}(Y) = \{p \in H^1(Y) \mid p \text{ is } Y\text{-periodic}\}$ with $H^{-1}_{\#}(Y)$ being its dual space. With $\mathcal{D}_1, \mathcal{D}_2 \subset \mathbb{R}^d$ being two domains, we use the Bochner spaces $L^p(\mathcal{D}_1; L^q(\mathcal{D}_2))$ for $p, q \in [1, \infty)$, equipped with the usual norm. In the case $p = q = 2$ we denote the corresponding norm $\|v\|_{\mathcal{D}_1 \times \mathcal{D}_2} := \|v\|_{L^2(\mathcal{D}_1; L^2(\mathcal{D}_2))}^2$.

We use the positive and negative cut of a real number v , defined as $[v]_+ := \max(v, 0)$ and $[v]_- := \min(v, 0)$.

2. The two-scale model

The two-scale model considered here describes the single-phase flow and reactive transport through a porous medium, where the solid interface evolves due to mineral precipitation and dissolution. Here $\Omega \subset \mathbb{R}^d$ is a bounded macro-scale domain with Lipschitz continuous boundary $\partial\Omega$ and $T \in (0, \infty)$ is the final time. The macro-scale domain should be interpreted as a homogenized porous medium in which the micro-scale complexities (e.g., the alternating solid and void parts) are averaged out. Following the homogenization procedure, to each macro-scale point $\mathbf{x} \in \Omega$, a micro-scale domain $Y \subset \mathbb{R}^d$ is assigned, representing an idealization of the complex structure at the micro scale. These micro-scale domains are used to define the cell problems, yielding the effective parameters and functions required at the macro scale.

Following [27], the model considered here has been derived by homogenization techniques. At the micro scale the geometry consists of solid grains surrounded by void space (pores). The precipitation and dissolution processes are encountered on the boundary of already existing mineral (grains) and not in the interior of the void space. We assume that the mineral never dissolves entirely and that the void space is always connected; thus the porosity is never vanishing.

We write the model in non-dimensional form by following the non-dimensionalization in Bringedal et al. [27]. In doing so, we use a local unit cell Y defined before and to identify the variations at the micro scale we define a fast variable \mathbf{y} . We associate one micro-scale cell Y to every macro-scale location $\mathbf{x} \in \Omega$ (see Fig. 1).

The macro-scale parameters $\bar{\phi}$, \mathbb{A} and \mathbb{K} appearing below are obtained from the micro scale by following the homogenization procedure. At the macro scale, the unknowns \mathbf{q} , p denote the (macro-scale) velocity and pressure in the fluid and

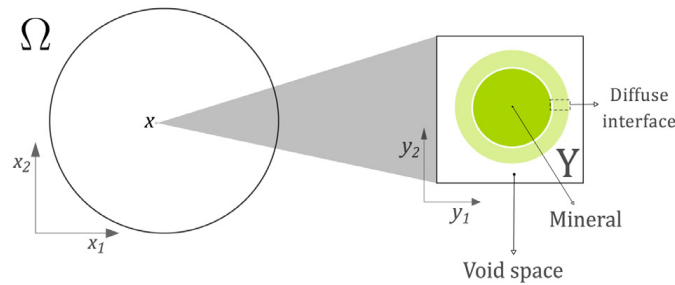


Fig. 1. The two-scale domain: the macro scale, homogenized porous medium Ω (left) and the micro-scale domain Y (right) corresponding to a point $\mathbf{x} \in \Omega$.

u is the upscaled solute concentration. All of them are functions of $\mathbf{x} \in \Omega$ and $t > 0$. The macro-scale flow is given by

$$\begin{cases} \nabla \cdot \mathbf{q} &= 0, & \text{in } \Omega, \\ \mathbf{q} &= -\mathbb{K} \nabla p, & \text{in } \Omega, \\ \nabla p \cdot \mathbf{n} &= 0, & \text{on } \partial\Omega, \\ \int_{\Omega} p \, d\mathbf{x} &= 0. \end{cases} \quad \mathbf{P}_p^M$$

Observe that the time t entry in (\mathbf{P}_p^M) implicitly, through \mathbb{K} . The solute concentration is given by

$$\begin{cases} \partial_t(\bar{\phi}(u - u^*)) + \nabla \cdot (\mathbf{q}u) &= D \nabla \cdot (\mathbb{A} \nabla u), & \text{in } \Omega \times (0, T], \\ \nabla u \cdot \mathbf{n} &= 0, & \text{on } \partial\Omega \times (0, T], \\ u &= u_I, & \text{in } \Omega \text{ and } t = 0, \end{cases} \quad \mathbf{P}_u^M$$

where all the spatial derivatives are taken with respect to the macro-scale variable \mathbf{x} . Here D denotes the pore-scale diffusivity of the solute and \mathbf{n} denotes the outward unit normal to the boundary $\partial\Omega$. The mineral has a constant concentration u^* . To derive the macro-scale parameters $\bar{\phi}$, \mathbb{A} and \mathbb{K} , the phase field $\phi(\mathbf{x}, \cdot, \cdot)$ is determined for all $\mathbf{x} \in \Omega$ by solving the following micro-scale problem

$$\begin{cases} \lambda^2 \partial_t \phi + \gamma P'(\phi) &= \gamma \lambda^2 \Delta \phi - \lambda M(\phi) \frac{1}{u^*} f(u), & \text{in } Y \times (0, T], \\ \phi &\text{is } Y\text{-periodic,} \\ \phi &= \phi_I, & \text{in } Y \text{ for } t = 0, \end{cases} \quad \mathbf{P}^{\mu_\phi}$$

where all the spatial derivatives are taken with respect to the micro-scale variable \mathbf{y} . The function $f(u)$ is the reaction rate, $\lambda > 0$ is related to the width of the fluid-mineral transition zone, and γ is the diffusion coefficient controlling the diffusive time scale of the transition zone. Additionally, P is the double-well potential and its local minima are the values corresponding to the two phases (fluid or mineral) and M is a function that ensures that the reactions only take place in the transition zone between the fluid and the mineral. The particular form of P and M used here will be specified below. More details about the model parameters can be found in Bringedal et al. [27], Bastidas et al. [33]. For improving the local conservation of the phase field ϕ , one may follow [39,40] and include an additional Y -averaged term in the phase-field equation.

While ϕ enters in the micro-scale problems through the effective parameters defined below, the reverse coupling with the micro scale is given through the reaction rate $f(u)$, with u being constant w.r.t the variable $\mathbf{y} \in Y$. The macro-scale porosity in (\mathbf{P}_u^M) is defined for each $\mathbf{x} \in \Omega$ and $t > 0$ by averaging the phase field

$$\bar{\phi}(\mathbf{x}, t) = \int_Y \phi(\mathbf{x}, \mathbf{y}, t) \, d\mathbf{y}.$$

To determine the effective matrices \mathbb{A} and \mathbb{K} one has to solve two types of cell problems. We use a regularized phase field $\phi_\delta := \phi + \delta$ with $\delta > 0$, ensuring that the cell problems are well defined. Notice that the regularization only plays a role in the calculation of the effective parameters and does not appear explicitly in $(\mathbf{P}^{\mu_\phi}), (\mathbf{P}_p^M)$ and (\mathbf{P}_u^M) . For each $\mathbf{x} \in \Omega$ and $t > 0$, the functions ω^s, Π^s and $\mathbf{z}^s = [\mathbf{z}_1^s, \dots, \mathbf{z}_d^s]^t$ with $s \in \{1, \dots, a\}$ are the solutions of the following cell problems

$$\begin{cases} \nabla \cdot (\phi_\delta (\nabla \omega^s + \mathbf{e}_s)) &= 0, & \text{in } Y, \\ \omega^s \text{ is } Y\text{-periodic and } \int_Y \omega^s \, d\mathbf{y} &= 0, \end{cases} \quad \mathbf{P}_A^\mu$$

$$\begin{cases} \nabla \Pi^s + \mathbf{e}_s + \mu_f \Delta (\phi_\delta \mathbf{z}^s) &= \frac{g(\phi, \lambda)}{\phi_\delta} \mathbf{z}^s, & \text{in } Y, \\ \nabla \cdot (\phi_\delta \mathbf{z}^s) &= 0, & \text{in } Y, \\ \Pi^s \text{ is } Y\text{-periodic and } \int_Y \Pi^s \, d\mathbf{y} &= 0. \end{cases} \quad \mathbf{P}_K^\mu$$

Here \mathbf{e}_s is the s -th canonical vector and μ_f is the constant fluid viscosity. The role of the function $g(\phi, \lambda)$ is to guarantee that there is no flow in the mineral phase. As motivated by [41] we take $g(\phi, \lambda) := \frac{250(1-\phi)}{\lambda(\phi+10)}$.

The elements of the effective matrices \mathbb{A} and \mathbb{K} are defined for each $\mathbf{x} \in \Omega$ and $t > 0$ by

$$\begin{aligned} \mathbb{A}_{rs}(\mathbf{x}, t) &= \int_Y \phi_\delta(\mathbf{x}, \mathbf{y}, t) (\delta_{rs} + \partial_r \omega^s(\mathbf{x}, \mathbf{y}, t)) d\mathbf{y}, \\ \mathbb{K}_{rs}(\mathbf{x}, t) &= \int_Y \phi_\delta(\mathbf{x}, \mathbf{y}, t) \mathbf{z}_r^s(\mathbf{x}, \mathbf{y}, t) d\mathbf{y}, \end{aligned} \tag{1}$$

for $r, s \in \{1, \dots, d\}$ and where δ_{rs} denotes the Kronecker delta. We highlight that even though we denote the micro-scale problems (\mathbf{P}^μ_ϕ) , $(\mathbf{P}^\mu_{\mathbb{A}})$ and $(\mathbf{P}^\mu_{\mathbb{K}})$, each of these problems depend on the macro scale and on time.

Finally, the initial conditions in (\mathbf{P}^μ_u) and (\mathbf{P}^μ_ϕ) satisfy the following assumptions

- (A1) The function $u_l \in L^\infty(\Omega)$ and it is such that $0 \leq u_l \leq u^*$ a.e. in Ω .
- (A2) The function $\phi_l \in L^\infty(\Omega \times Y)$ and it is such that $0 \leq \phi_l \leq 1$ a.e. in $\Omega \times Y$.

2.1. Preliminaries

For a fixed micro-scale domain Y corresponding to one macro-scale point $\mathbf{x} \in \Omega$, we write the non-linear part of (\mathbf{P}^μ_ϕ) , namely $F : \mathbb{R} \times \mathbb{R} \rightarrow \mathbb{R}$, as follows

$$F(\phi, u) := -\gamma P'(\phi) - \lambda M(\phi) \frac{1}{u^*} f(u). \tag{2}$$

Further, we choose the reaction rate $f(u)$, the double-well potential $P(\phi)$ and the function $M(\phi)$ to be

$$\begin{aligned} f(u) &:= \begin{cases} k \left(\frac{u^2_+}{u^2_{eq}} - 1 \right), & \text{for } u \leq u^*, \\ k \left(\frac{u^*}{u^2_{eq}} - 1 \right), & \text{for } u > u^*, \end{cases} \\ P(\phi) &:= \begin{cases} 8\phi^2(1-\phi)^2, & \text{for } \phi \in [0, 1], \\ 0, & \text{otherwise,} \end{cases} \quad \text{and} \quad M(\phi) := \begin{cases} 4\phi(1-\phi), & \text{for } \phi \in [0, 1], \\ 0, & \text{otherwise,} \end{cases} \end{aligned}$$

where u_{eq} is the equilibrium concentration and k is a reaction constant.

With this choice the function F is Lipschitz continuous with respect to both arguments and we denote by $\partial_\ell F$ the partial derivative of F with respect to the ℓ -th argument. Specifically, there exist two constants $\mathfrak{M}_{F_1}, \mathfrak{M}_{F_2} \geq 0$ such that $|\partial_\ell F| \leq \mathfrak{M}_{F_\ell}$ a.e. in \mathbb{R}^2 with $\ell = 1, 2$.

For each $u \in \mathbb{R}$, the function $F(\cdot, u)$ is continuous and can be decomposed as $F(\cdot, u) := F_+(\cdot, u) + E(\cdot, u)$ with $E_\ell(\cdot, u)$ denoting the increasing part of $F(\cdot, u)$ and $E(\cdot, u)$ the decreasing part of $F(\cdot, u)$, namely

$$E_+(\alpha, u) = \int_0^\alpha [\partial_1 F(z, u)]_+ dz, \quad \text{and} \quad E(\alpha, u) = \int_0^\alpha [\partial_1 F(z, u)]_- dz.$$

In Section (4) we propose a micro-scale non-linear solver and there the splitting of the non-linear term $F(\cdot, u)$ guarantees the convergence. In the following sections we treat E implicitly and E_+ explicitly. A similar strategy splitting of the nonlinearities into their convex and concave components can be found in Frank et al. [42].

3. The two-scale iterative scheme

We propose an iterative scheme to simulate the two-scale behavior of the phase-field model presented in Section 2. Here we use an artificial coupling parameter between the two scales, namely \mathcal{L}_{coup} . In [34,43] similar approaches about handling the coupling between scales and non-linear systems of equations can be found.

We first discretize the equations in time. With $N \in \mathbb{N}$ we let $\Delta t = T/N$ be the time step size and define $t^n = n\Delta t$. We use a backward Euler scheme for the time discretization and denote the time-discrete solutions by $\phi^n := \phi(\cdot, \cdot, t^n)$ and $v^n := v(\cdot, t^n)$ for $v \in \{\mathbb{A}, \mathbb{K}, p, \mathbf{q}, u\}$. Accordingly, at each time t^n one has to determine a six-tuple $\{\phi^n, \mathbb{A}^n, \mathbb{K}^n, p^n, \mathbf{q}^n, u^n\}$ depending on the solution of the previous time step. The time stepping starts with $\phi^0 = \phi_l$ and $u^0 = u_l$.

In order to approximate the discrete solutions $\{\phi^n, \mathbb{A}^n, \mathbb{K}^n, p^n, \mathbf{q}^n, u^n\}$ we consider an iterative algorithm. With $i > 0$ being the iteration index, the two-scale iterative scheme defines a sequence $\{\phi_i^n, \mathbb{A}_i^n, \mathbb{K}_i^n, p_i^n, \mathbf{q}_i^n, u_i^n\}$. The initial guess for the iterations ϕ^n_0 and u^n_0 are the solution at the previous time step, i.e. $\phi^n_0 = \phi^{n-1}$ and $u^n_0 = u^{n-1}$.

The iterative scheme is defined as follows. First, for $n > 0, i > 0$ and $\mathcal{L}_{coup} > 0$ with given $u^{n-1}, u_{i-1}^n, \bar{\phi}^{n-1}$ and ϕ_{i-1}^n , for each $\mathbf{x} \in \Omega$ one solves the micro-scale phase-field problem

$$\begin{cases} \phi_i^n - \Delta t \gamma \Delta \phi_i^n - \frac{\Delta t}{\lambda^2} E(\phi_i^n, u_{i-1}^n) + \mathcal{L}_{coup} (\phi_i^n - \phi_{i-1}^n) \\ \quad = \phi^{n-1} + \frac{\Delta t}{\lambda^2} E(\phi^{n-1}, u_{i-1}^n), & \text{in } Y, \\ \phi_i^n & \text{is } Y\text{-periodic.} \end{cases} \tag{P}^{\mu,i}_\phi$$

By using the solution ϕ_i^n in (1), $(\mathbf{P}^\mu_{\mathbb{A}})$ and $(\mathbf{P}^\mu_{\mathbb{K}})$ we calculate the iterative effective parameters \mathbb{A}_i^n and \mathbb{K}_i^n . Then, one continues with the macro-scale problems

$$\begin{cases} \nabla \cdot \mathbf{q}_i^n & = 0, & \text{in } \Omega, \\ \mathbf{q}_i^n & = -\mathbb{K}_i^n \nabla p_i^n, & \text{in } \Omega, \\ \nabla p_i^n \cdot \mathbf{n} & = 0, & \text{on } \partial\Omega, \\ \int_\Omega p_i^n d\mathbf{x} & = 0. \end{cases} \tag{P}^{\mathbf{M},i}_p$$

$$\begin{cases} \bar{\phi}_i^n (u_i^n - u^*) + \Delta t \nabla \cdot (\mathbf{q}_i^n u_i^n) \\ \qquad \qquad \qquad = \Delta t D \nabla \cdot (\mathbb{A}_i^n \nabla u_i^n) + \bar{\phi}^{n-1} (u^{n-1} - u^*), & \text{in } \Omega, \\ \nabla u_i^n \cdot \mathbf{n} = 0, & \text{on } \partial \Omega, \end{cases} \quad \mathbf{P}_u^{M,i}$$

The two-scale iteration steps For $n > 0$ and $i > 0$ with given u^{n-1} , u_{i-1}^n , $\bar{\phi}^{n-1}$ and ϕ_{i-1}^n , to compute the next iteration one performs the following steps

- (S1) For each $\mathbf{x} \in \Omega$, find ϕ_i^n by solving the phase-field problem $\mathbf{P}_\phi^{\mu,i}$.
- (S2) Given ϕ_i^n , find the effective matrices \mathbb{A}_i^n and \mathbb{K}_i^n in (1) by solving the cell problems (\mathbf{P}_Δ^μ) and $(\mathbf{P}_\mathbb{K}^\mu)$.
- (S3) Given $\bar{\phi}_i^n$, \mathbb{K}_i^n and \mathbb{A}_i^n , find p_i^n , \mathbf{q}_i^n and u_i^n by solving the macro-scale problems $(\mathbf{P}_p^{M,i})$ and $(\mathbf{P}_u^{M,i})$.

The two-scale iteration steps (S1) - (S3) take place until the L^2 -norm of the difference of two iterations drops below a prescribed threshold $tol_M > 0$, i.e.

$$\epsilon_M^{n,i} := \|\bar{\phi}_i^n - \bar{\phi}_{i-1}^n\|_\Omega \leq tol_M.$$

We highlight that this stopping criterion is chosen according to the results in Theorem 2 in Section 5. There we show that the convergence of the porosity $\bar{\phi}_i^n$ guarantees the convergence of the macro-scale concentration u_i^n , so the stopping criterion above is sufficient. However, different stopping criteria can also be used, including, e.g., the residuals of the macro-scale concentration and velocity.

Proving the existence and uniqueness of a solution to the coupled system (\mathbf{P}_p^M) , (\mathbf{P}_u^M) , $(\mathbf{P}^{\mu\phi})$, (\mathbf{P}_Δ^μ) and $(\mathbf{P}_\mathbb{K}^\mu)$ is beyond the scope of this paper. Such results are known if each model component is considered apart. For example, when taken individually the problems (\mathbf{P}_p^M) , (\mathbf{P}_u^M) , (\mathbf{P}_Δ^μ) and $(\mathbf{P}_\mathbb{K}^\mu)$ are linear and elliptic, while the non-linearity in $(\mathbf{P}^{\mu\phi})$ is monotone and Lipschitz continuous. For such problems the existence and uniqueness of a weak solution are guaranteed by standard arguments. The same holds for $(\mathbf{P}_p^{M,i})$ and $(\mathbf{P}_u^{M,i})$. For the parabolic counterparts, before applying the time discretization, we refer to [26,44–46]. There the existence and uniqueness of solutions to similar problems related to phase-field modeling or the interaction between scales are addressed.

4. The micro-scale non-linear solver

At each time step and for each $\mathbf{x} \in \Omega$, the step (S1) of the two-scale iterative scheme involve a non-linear problem $(\mathbf{P}_\phi^{\mu,i})$ at the micro-scale. For this we construct an iterative non-linear solver based on the L-scheme [37,38], which is a contraction-based approach. The main advantages of the L-scheme are that, unlike the Newton method, it does not involve the calculation of derivatives and its convergence is guaranteed regardless of the initial approximation, the spatial discretization and the mesh size.

To be specific, let $n > 0$ and $\mathbf{x} \in \Omega$ be fixed and $\phi^{n-1}(\mathbf{x}, \cdot) \in L^2(Y)$, $u^n(\mathbf{x}) \in \mathbb{R}$ be given. The weak solution of the time discrete counterpart of $\mathbf{P}^{\mu\phi}$ is defined as follows

Definition 1. A weak solution to the time discrete counterpart of $(\mathbf{P}^{\mu\phi})$ is a function $\phi^n(\mathbf{x}, \cdot) \in H_\#^1(Y)$ satisfying

$$\begin{aligned} \langle \phi^n, \psi \rangle_Y + \Delta t \gamma \langle \nabla \phi^n, \nabla \psi \rangle_Y - \frac{\Delta t}{\lambda^2} \langle F(\phi^n, u^n), \psi \rangle_Y \\ = \langle \phi^{n-1} + \frac{\Delta t}{\lambda^2} F_+(\phi^{n-1}, u^n), \psi \rangle_Y, \end{aligned} \quad (3)$$

for all $\psi \in H_\#^1(Y)$.

Further, let $i > 0$ be the two-scale iteration index and $\phi_{i-1}^n(\mathbf{x}, \cdot) \in L^2(Y)$, $u_{i-1}^n(\mathbf{x}) \in \mathbb{R}$ be given. The weak solution of $(\mathbf{P}_\phi^{\mu,i})$ is defined as follows

Definition 2. A weak solution to $(\mathbf{P}_\phi^{\mu,i})$ is a function $\phi_i^n(\mathbf{x}, \cdot) \in H_\#^1(Y)$ satisfying

$$\begin{aligned} \langle \phi_i^n, \psi \rangle_Y + \Delta t \gamma \langle \nabla \phi_i^n, \nabla \psi \rangle_Y - \frac{\Delta t}{\lambda^2} \langle F(\phi_i^n, u_{i-1}^n), \psi \rangle_Y + \langle \mathcal{L}_{\text{coup}}(\phi_i^n - \phi_{i-1}^n), \psi \rangle_Y \\ = \langle \phi^{n-1} + \frac{\Delta t}{\lambda^2} F_+(\phi^{n-1}, u_{i-1}^n), \psi \rangle_Y, \end{aligned} \quad (4)$$

for all $\psi \in H_\#^1(Y)$.

Observe that $(\mathbf{P}_\phi^{\mu,i})$ is a non-linear problem and to approximate its solution a linearization scheme is needed. To this aim we take $\mathcal{L}_{\text{lin}} \in \mathbb{R}^+$ such that $\mathcal{L}_{\text{lin}} \geq \mathfrak{M}_{F_+}$. Let $j \in \mathbb{N}$, $j \geq 1$ be the micro-scale iteration index and $\phi_{i,j-1}^n(\mathbf{x}, \cdot) \in L^2(Y)$ be given. The weak solution of the linear problem associated to $(\mathbf{P}_\phi^{\mu,i})$ is defined as follows

Definition 3 (Micro-scale linear iteration). A weak solution to the linearized version of $(\mathbf{P}_\phi^{\mu,i})$ is a function $\phi_{i,j}^n(\mathbf{x}, \cdot) \in H_\#^1(Y)$ satisfying

$$\begin{aligned} \langle (1 + \mathcal{L}_{\text{coup}}) \phi_{i,j}^n, \psi \rangle_Y + \Delta t \gamma \langle \nabla \phi_{i,j}^n, \nabla \psi \rangle_Y - \frac{\Delta t}{\lambda^2} \langle F(\phi_{i,j-1}^n, u_{i-1}^n), \psi \rangle_Y \\ + \frac{\Delta t}{\lambda^2} \langle \mathcal{L}_{\text{lin}}(\phi_{i,j}^n - \phi_{i,j-1}^n), \psi \rangle_Y = \langle \phi^{n-1} + \frac{\Delta t}{\lambda^2} F_+(\phi^{n-1}, u_{i-1}^n) + \mathcal{L}_{\text{coup}} \phi_{i-1}^n, \psi \rangle_Y, \end{aligned} \quad (5)$$

for all $\psi \in H_{\#}^1(Y)$.

The natural choice for the initial micro-scale iteration $\phi_{i,0}^n$ is ϕ_{i-1}^n , that is the phase field from the previous two-scale iteration. Nevertheless, this choice is not compulsory for the convergence of the micro-scale linear solver as the convergence is independent of the initial guess. The iterations (5) are performed until one reaches a prescribed threshold $tol_{\mu} \ll tol_M$ for the L^2 -norm of the difference of two successive iterations, e.i.

$$\epsilon_{\mu}^{n,i,j} := \|\phi_{i,j}^n(\mathbf{x}, \cdot) - \phi_{i,j-1}^n(\mathbf{x}, \cdot)\|_Y \leq tol_{\mu}, \tag{6}$$

where $i > 0$ is the two-scale iteration index of the two-scale scheme and $j > 0$ indicates the micro-scale iterations index of the non-linear solver.

We highlight that in this specific case and due to the strong coupling between the flow, chemistry and the phase field over two scales, an accurate solution of the micro-scale problems is crucial to achieve convergence of the iterations. For this reason we solve the micro-scale non-linear problem at every iteration and take $tol_{\mu} \ll tol_M$.

We show that the solution of the phase-field problem $\mathbf{P}_{\phi}^{\mu,i}$ at every $\mathbf{x} \in \Omega$ remains bounded.

Lemma 1 (Maximum principle for the phase-field). *For a fixed $\mathbf{x} \in \Omega$ and for each $n > 0$ and $i > 0$, with $\phi^{n-1}(\mathbf{x}, \cdot)$, $\phi_{i-1}^n(\mathbf{x}, \cdot)$ and $\phi_{i,j-1}^n(\mathbf{x}, \cdot) \in L^{\infty}(Y)$ given and essentially bounded by 0 and 1. Then $\phi_{i,j}^n(\mathbf{x}, \cdot) \in H_{\#}^1(Y)$ in Definition 3 satisfies the same essential bounds.*

Proof. First, we test in (5) with $\psi := [\phi_{i,j}^n(\mathbf{x}, \cdot)]_{-}$, then

$$\begin{aligned} & (1 + \mathcal{L}_{\text{coup}} + \frac{\Delta t}{\lambda^2} \mathcal{L}_{\text{lin}}) \|[\phi_{i,j}^n]_{-}\|_Y^2 + \Delta t \gamma \|\nabla[\phi_{i,j}^n]_{-}\|_Y^2 \\ & = \langle \phi^{n-1} + \frac{\Delta t}{\lambda^2} F_{+}(\phi^{n-1}, \mathbf{u}_{i-1}^n) + \mathcal{L}_{\text{coup}} \phi_{j-1}^n, [\phi_{i,j}^n]_{-} \rangle_Y \\ & \quad + \frac{\Delta t}{\lambda^2} \langle F(\phi_{i,j-1}^n, \mathbf{u}_{i-1}^n) + \mathcal{L}_{\text{lin}} \phi_{i,j-1}^n, [\phi_{i,j}^n]_{-} \rangle_Y. \end{aligned} \tag{7}$$

Using the mean value theorem on the right hand side of (7) one obtains

$$\begin{aligned} & \langle \phi^{n-1} + \frac{\Delta t}{\lambda^2} F_{+}(\phi^{n-1}, \mathbf{u}_{i-1}^n) + \mathcal{L}_{\text{coup}} \phi_{j-1}^n, [\phi_{i,j}^n]_{-} \rangle_Y \\ & = \langle (1 + \frac{\Delta t}{\lambda^2} \partial_1 F_{+}(\xi, \mathbf{u}_{i-1}^n)) \phi^{n-1} + \mathcal{L}_{\text{coup}} \phi_{j-1}^n, [\phi_{i,j}^n]_{-} \rangle_Y, \end{aligned} \tag{8}$$

and

$$\begin{aligned} & \frac{\Delta t}{\lambda^2} \langle F(\phi_{i,j-1}^n, \mathbf{u}_{i-1}^n) + \mathcal{L}_{\text{lin}} \phi_{i,j-1}^n, [\phi_{i,j}^n]_{-} \rangle_Y \\ & = \frac{\Delta t}{\lambda^2} \langle (\partial_1 F(\eta, \mathbf{u}_{i-1}^n) + \mathcal{L}_{\text{lin}}) \phi_{i,j-1}^n, [\phi_{i,j}^n]_{-} \rangle_Y, \end{aligned} \tag{9}$$

where $\xi : Y \rightarrow \mathbb{R}$ and $\eta : Y \rightarrow \mathbb{R}$ are two functions such that $\xi(\mathbf{y}) \in (0, \phi^{n-1}(\mathbf{x}, \mathbf{y}))$ and $\eta(\mathbf{y}) \in (0, \phi_{i,j-1}^n(\mathbf{x}, \mathbf{y}))$ for all $\mathbf{y} \in Y$. Knowing that $\mathcal{L}_{\text{coup}}, \partial_1 F_{+} \geq 0$ and $\mathcal{L}_{\text{lin}} \geq \mathfrak{M}_{F_1}$, we get that the right-hand sides of (8) and (9) are negative. Consequently,

$$\left(1 + \mathcal{L}_{\text{coup}} + \frac{\Delta t}{\lambda^2} \mathcal{L}_{\text{lin}}\right) \|[\phi_{i,j}^n]_{-}\|_Y^2 + \Delta t \gamma \|\nabla[\phi_{i,j}^n]_{-}\|_Y^2 \leq 0,$$

which implies $(1 + \mathcal{L}_{\text{coup}} + \frac{\Delta t}{\lambda^2} \mathcal{L}_{\text{lin}}) \|[\phi_{i,j}^n]_{-}\|_Y^2 = 0$. In conclusion $[\phi_{i,j}^n(\mathbf{x}, \cdot)]_{-} = 0$ a.e. in Y , and with this we obtain the lower bound of $\phi_{i,j}^n(\mathbf{x}, \cdot)$.

The upper bound follows by testing (5) with $[\phi_{i,j}^n(\mathbf{x}, \cdot) - 1]_{+}$ and following the same steps. We obtain $\phi_{i,j}^n(\mathbf{x}, \cdot) \leq 1$ a.e. in Y . \square

Solving the non-linear problem accurately is crucial to guarantee the convergence of the two-scale iterative scheme. The following theorem ensures the convergence of the micro-scale non-linear iterations under mild restrictions on Δt , \mathcal{L}_{lin} and $\mathcal{L}_{\text{coup}}$.

Theorem 1 (Convergence of the non-linear solver). *For a fixed $\mathbf{x} \in \Omega$ and for each $n > 0$ and $i > 0$; with \mathfrak{M}_{F_1} as above and $\mathcal{L}_{\text{coup}} \geq 0$. If $\mathcal{L}_{\text{lin}} \geq \mathfrak{M}_{F_1}$ and $\Delta t \leq \frac{\lambda^2(1+\mathcal{L}_{\text{coup}})}{\mathfrak{M}_{F_1}}$, the micro-scale linear iteration introduced in Definition 3 is convergent in $H_{\#}^1(Y)$.*

The proof of Theorem 1 follows the same steps as the proof in [4, Lemma 4.1]. We omit the details here.

Remark. For a fixed $\mathbf{x} \in \Omega$ and given the initial condition $\phi^0(\mathbf{x}, \cdot) \in L^{\infty}(Y)$ as explained before, the choice of the initial two-scale iterations is $\phi_0^1 = \phi^0$ and the choice of the initial micro-scale iterations is $\phi_{1,0}^1 = \phi_0^1$. Therefore, Lemma 1 implies that for all $j \geq 1$ the solution $\phi_{1,j}^1(\mathbf{x}, \cdot)$ in Definition 3 is essentially bounded by 0 and 1. Moreover, the convergence of the non-linear solver (see Theorem 1) implies the same boundedness of $\phi_1^1(\mathbf{x}, \cdot)$. Additionally, the convergence of the two-scale iterative scheme (proved in Section 5) implies the boundedness of $\phi^1(\mathbf{x}, \cdot)$. Likewise, by induction, we conclude that for all $n \geq 1, i \geq 0, j \geq 0$ the solutions $\phi^n(\mathbf{x}, \cdot), \phi_i^n(\mathbf{x}, \cdot)$ and $\phi_{i,j}^n(\mathbf{x}, \cdot)$ are all essentially bounded by 0 and 1.

5. Analysis of the two-scale iterative scheme

In this section we show the convergence of the two-scale iterative scheme in steps (S1) - (S3). We verify a relation between the effective diffusivity and the porosity and prove the convergence of the scheme. The main difficulty in the convergence proof is due to the two-scale characteristics of the scheme and the presence of the non-linear terms.

Assumptions Next to (A1) and (A2), to prove the convergence of the two-scale iterative scheme we consider a simplified setting. Specifically,

(A3) The flow component is disregarded.

(A4) For $n > 0$, the porosity $\bar{\phi}^n$ is bounded away from 0 and 1. That is, there exists two constants $\bar{\phi}_m$ and $\bar{\phi}_M$ such that $0 < \bar{\phi}_m \leq \bar{\phi}^n \leq \bar{\phi}_M < 1$ a.e. in Ω .

(A5) For $n > 0$, the concentration is such that $\|\nabla u^n\|_{L^\infty(\Omega)} \leq C_u$ for some constant $C_u > 0$.

(A6) For every time step $n > 0$, iteration $i > 0$ and macro-scale location $\mathbf{x} \in \Omega$, the solution of the cell problems (\mathbf{P}_Δ^μ) is such that $\|\nabla \omega^s(\mathbf{x}, \cdot, t^n)\|_{L^\infty(Y)} \leq C_w$ for some constant $C_w > 0$ and for all $s \in \{1, \dots, d\}$.

We remark that (A3) and (A4) are assumptions related to the physical context of the numerical analysis below. Specifically, in (A4) we assume the porosity to be bounded away from zero to avoid clogging, which would lead to no solute diffusion. Further, we assume the porosity to be bound away from one to ensure that we still have a solid part in the porous medium. We refer to [47,48] for the analysis of models including a vanishing porosity and to [49] for a comparison of different approaches used in the context near clogging. Assuming (A5) and (A6), the essential boundedness of the gradients of u^n and ω^s , is justified under certain conditions. For example, since u_{i-1}^n is constant in Y , the solutions to the micro-scale elliptic problems are bounded uniformly w.r.t. i in $H^1(Y)$, and have a better regularity than H^1 . Assuming that $\nabla \phi^{n-1}$ is essentially bounded, one obtains bounds for $\nabla \phi_i^n$ by deriving the problem $\mathbf{P}_{\phi_i^n}^{\mu, i}$ in space. Furthermore, with a fixed $\delta > 0$ and recalling the essential bounds proved in Lemma 1, the problem \mathbf{P}_Δ^μ solved by ω^s is linear, elliptic, and the coercivity constant is uniformly bounded. In view of the regularity and boundedness of ϕ_i^n , one obtains that $\nabla \omega^s$ is essentially bounded as well. Finally, for the macro-scale problem $\mathbf{P}_u^{M, i}$, assuming the domain Ω and the initial data are sufficiently smooth, the essential boundedness of the gradient of u^n can be obtained e.g. as in [50, Chapter 3.15]. Nevertheless, the rigorous proofs of (A5) and (A6) are beyond the scope of this manuscript.

For $n > 0$, let $u^{n-1} \in L^2(\Omega)$ and $\bar{\phi}^n, \bar{\phi}^{n-1} \in L^\infty(\Omega)$ be given. In the absence of flow, the weak solution of the time discrete counterpart of (\mathbf{P}_u^M) is defined as follows

Definition 4. A weak solution to the time discrete counterpart of (\mathbf{P}_u^M) is a function $u^n \in H^1(\Omega)$ satisfying

$$\left\langle \bar{\phi}^n (u^n - u^*), v \right\rangle_{\Omega} + \Delta t D \langle \mathbb{A}^n \nabla u^n, \nabla v \rangle_{\Omega} = \left\langle \bar{\phi}^{n-1} (u^{n-1} - u^*), v \right\rangle_{\Omega}, \tag{10}$$

for all $v \in H^1(\Omega)$.

We let $i \in \mathbb{N}$ denote the two-scale iteration index. The iterated porosity $\bar{\phi}_i^n(\mathbf{x}) := \int_Y \phi_i^n(\mathbf{x}, \mathbf{y}) d\mathbf{y}$ is given for all $\mathbf{x} \in \Omega$ and the diffusivity tensor \mathbb{A}_i^n depends on ϕ_i^n as explained in (1). In the absence of flow, the weak solution of $(\mathbf{P}_u^{M, i})$ is defined as follows

Definition 5. A weak solution to $(\mathbf{P}_u^{M, i})$ is a function $u_i^n \in H^1(\Omega)$ satisfying

$$\left\langle \bar{\phi}_i^n (u_i^n - u^*), v \right\rangle_{\Omega} + \Delta t D \langle \mathbb{A}_i^n \nabla u_i^n, \nabla v \rangle_{\Omega} = \left\langle \bar{\phi}^{n-1} (u^{n-1} - u^*), v \right\rangle_{\Omega}, \tag{11}$$

for all $v \in H^1(\Omega)$.

For proving the convergence of the two-scale iterative scheme we start by showing that the changes in the phase field are bounding the variations in the diffusion tensor. We refer to [21,49,51] for numerical studies revealing the relation between diffusivity (and permeability) and porosity.

Proposition 1. For each $n > 0$ and $i > 0$, the effective diffusion tensors \mathbb{A}^n and \mathbb{A}_i^n are symmetric, continuous and positive definite. In other words, the constants $a_m, a_M > 0$ exist such that for all $\psi \in \mathbb{R}^d$ and $\mathbf{x} \in \Omega$

$$a_m \|\psi\|^2 \leq \psi^T \mathbb{A}^n(\mathbf{x}) \psi \leq a_M \|\psi\|^2, \quad \text{and} \quad a_m \|\psi\|^2 \leq \psi^T \mathbb{A}_i^n(\mathbf{x}) \psi \leq a_M \|\psi\|^2.$$

We refer to [52, Proposition 6.12] for the proof of the symmetry and positive definiteness of the effective diffusion tensor.

Lemma 2. For each $n > 0$ and $i > 0$, there exists a constant $C_A > 0$ such that

$$\|\mathbb{A}_i^n - \mathbb{A}^n\|_{\Omega} \leq C_A \|\phi_i^n - \phi^n\|_{\Omega \times Y}. \tag{12}$$

Proof. For each $\mathbf{x} \in \Omega$ we denote $\omega_{i,n}^s$ and ω_n^s the s -component of the solution of the cell problems (\mathbf{P}_Δ^μ) that correspond to ϕ_i^n and ϕ^n . By subtracting those two cell problems we get formally that

$$\nabla \cdot ((\phi_i^n + \delta)(\nabla(\omega_{i,n}^s - \omega_n^s))) = -\nabla \cdot ((\phi_i^n - \phi^n)(\mathbf{e}_s + \nabla \omega_n^s)).$$

From this one immediately obtains that

$$| \langle (\phi_i^n + \delta) \nabla(\omega_{i,n}^s - \omega_n^s), \nabla \psi \rangle_Y | = | \langle (\phi_i^n - \phi_i^n)(\mathbf{e}_s + \nabla \omega_n^s), \nabla \psi \rangle_Y | \tag{13}$$

for all $\psi \in H^1_{\#}(Y)$. Since $|Y| = 1$ and $0 \leq \phi_i^n$, by taking $\psi = \omega_{i,n}^s - \omega_n^s$ in (13), applying Cauchy–Schwartz and due to Assumption (A6) we obtain

$$\| \nabla(\omega_{i,n}^s - \omega_n^s) \|_{L^1(Y)} \leq \| \nabla(\omega_{i,n}^s - \omega_n^s) \|_{L^2(Y)} \leq \frac{1 + C_w}{\delta} \| \phi_i^n - \phi^n \|_Y. \tag{14}$$

On the other hand, for each component r_s of $\mathbb{A}_i^n(\mathbf{x}) - \mathbb{A}^n(\mathbf{x})$ it is easy to show that

$$\begin{aligned} | [\mathbb{A}_i^n(\mathbf{x})]_{rs} - [\mathbb{A}^n(\mathbf{x})]_{rs} | &\leq \int_Y | \phi_i^n - \phi^n | d\mathbf{y} + \int_Y | (\phi_i^n + \delta) \partial_r \omega_{i,n}^s - (\phi_i^n + \delta) \partial_r \omega_n^s | d\mathbf{y} \\ &\leq \int_Y | \phi_i^n - \phi^n | d\mathbf{y} \\ &\quad + \int_Y | (\phi_i^n + \delta) (\partial_r \omega_{i,n}^s - \partial_r \omega_n^s) | + | (\phi_i^n - \phi^n) \partial_r \omega_n^s | d\mathbf{y} \\ &\leq (1 + C_w) \| \phi_i^n - \phi^n \|_Y + \int_Y | (\phi_i^n + \delta) (\partial_r \omega_{i,n}^s - \partial_r \omega_n^s) | d\mathbf{y}. \end{aligned}$$

By using (14) and the equivalence of norms in $\mathbb{R}^{d \times d}$ one gets

$$C_f \| [\mathbb{A}_i^n(\mathbf{x})] - [\mathbb{A}^n(\mathbf{x})] \|_{2, \mathbb{R}^{d \times d}} \leq \| [\mathbb{A}_i^n(\mathbf{x})] - [\mathbb{A}^n(\mathbf{x})] \|_{1, \mathbb{R}^{d \times d}} \leq \frac{d(1 + C_w)(1 + \delta)}{\delta} \| \phi_i^n - \phi^n \|_Y,$$

where $\| \cdot \|_{p, \mathbb{R}^{d \times d}}$ denotes the matrix p -norm induced by the p -norm for vectors with either $p = 1$ or $p = 2$. The constant $C_f > 0$ is coming from the equivalence between the induced norms. By integrating over Ω , we conclude that

$$\| \mathbb{A}_i^n - \mathbb{A}^n \|_{\Omega} \leq \frac{d(1 + C_w)(1 + \delta)}{C_f \delta} \| \phi_i^n - \phi^n \|_{\Omega \times Y}.$$

□

Now we show the maximum principle for the concentration under mild restrictions on the phase-field parameters.

Lemma 3 (Maximum principle for the concentration). *For each $n > 0$, given $u^{n-1} \in H^1(\Omega)$ essentially bounded by 0 and u^* . If $4\gamma \leq \frac{\lambda k}{u^*}$ then $u^n \in H^1(\Omega)$ solving (10) satisfies the same essential bounds.*

Proof. We test (10) with the cut function $[u^n - u^*]_+$ to obtain

$$\left\langle \bar{\phi}^n (u^n - u^*), [u^n - u^*]_+ \right\rangle_{\Omega} + \Delta t D \langle \mathbb{A}^n \nabla u^n, \nabla [u^n - u^*]_+ \rangle_{\Omega} = \left\langle \bar{\phi}^{n-1} (u^{n-1} - u^*), [u^n - u^*]_+ \right\rangle_{\Omega}.$$

Since the diffusion tensor \mathbb{A}^n is positive definite and by using Assumption (A4), it follows that $\| [u^n - u^*]_+ \|_{\Omega}^2 \leq 0$, implying $[u^n - u^*]_+ = 0$ a.e in Ω . For proving the lower bound of the concentration u^n we test (10) with the cut function $[u^n]_-$ to obtain

$$\left\langle \bar{\phi}^n u^n, [u^n]_- \right\rangle_{\Omega} + \Delta t D \langle \mathbb{A}^n \nabla u^n, \nabla [u^n]_- \rangle_{\Omega} = \left\langle \bar{\phi}^{n-1} u^{n-1}, [u^n]_- \right\rangle_{\Omega} + \left\langle (\bar{\phi}^n - \bar{\phi}^{n-1}) u^*, [u^n]_- \right\rangle_{\Omega}.$$

Since $\bar{\phi}^{n-1}$, u^{n-1} and $\bar{\phi}^n$ are all positive and \mathbb{A}^n is positive definite, there exists a constant $C > 0$ such that

$$C \| [u^n]_- \|_{\Omega}^2 \leq \left\langle (\bar{\phi}^n - \bar{\phi}^{n-1}) u^*, [u^n]_- \right\rangle_{\Omega}. \tag{15}$$

It is sufficient to show that $\bar{\phi}^n - \bar{\phi}^{n-1} \geq 0$ a.e. in Ω in the case of $u^n \leq 0$. From the definition of the non linear term (2) we have that $F(\cdot, u^n) = F(\cdot, 0)$ for all $u^n \leq 0$ and if $4\gamma \leq \frac{\lambda k}{u^*}$ one can show that $\partial_1 F(\cdot, 0) = 0$ only at $z^* = \frac{1}{2} + \frac{1}{24\gamma} (\sqrt{48\gamma^2 + \zeta^2} - \zeta)$ with $\zeta = \frac{\lambda k}{u^*}$. Clearly $z^* \in (0, 1)$ and knowing this we rewrite F_+ and F_- as follows

$$\begin{aligned} F(\phi^n, 0) &= \begin{cases} 0, & \text{for } \phi^n \in [0, z^*], \\ F(\phi^n, 0) - F(z^*, 0), & \phi^n \in (z^*, 1], \end{cases} \\ F_-(\phi^{n-1}, 0) &= \begin{cases} F(\phi^{n-1}, 0), & \text{for } \phi^{n-1} \in [0, z^*], \\ F(z^*, 0), & \phi^{n-1} \in (z^*, 1]. \end{cases} \end{aligned}$$

Consider the partition of $Y = \cup_{i=0}^3 Y_i$, where the subsets Y_i are defined as

$$\begin{aligned} Y_0 &:= \{ \mathbf{y} \in Y \mid 0 \leq \phi^{n-1}(\mathbf{y}) \leq \phi^n(\mathbf{y}) \leq 1 \}, \\ Y_1 &:= \{ \mathbf{y} \in Y \mid 0 \leq \phi^n(\mathbf{y}) \leq \phi^{n-1}(\mathbf{y}) \leq z^* \}, \\ Y_2 &:= \{ \mathbf{y} \in Y \mid 0 \leq \phi^n(\mathbf{y}) \leq z^* \leq \phi^{n-1}(\mathbf{y}) \leq 1 \}, \\ Y_3 &:= \{ \mathbf{y} \in Y \mid z^* \leq \phi^n(\mathbf{y}) \leq \phi^{n-1}(\mathbf{y}) \leq 1 \}. \end{aligned}$$

We test (3) with $\psi = 1$ to obtain

$$\bar{\phi}^n - \bar{\phi}^{n-1} = \left(\sum_{i=0}^3 \int_{Y_i} \phi^n - \phi^{n-1} d\mathbf{y}\right) = \frac{\Delta t}{\lambda^2} \int_Y E(\phi^n, 0) + E_+(\phi^{n-1}, 0) d\mathbf{y}.$$

In Y_1 we get that $E(\phi^n, 0) + E_+(\phi^{n-1}, 0) = F(\phi^{n-1}, 0)$. Analogously, in Y_2 and Y_3 one obtains $E(\phi^n, 0) + E_+(\phi^{n-1}, 0) = F(z^*, 0)$ and $E(\phi^n, 0) + E_+(\phi^{n-1}, 0) = F(\phi^n, 0)$ respectively. Therefore,

$$\begin{aligned} \bar{\phi}^n - \bar{\phi}^{n-1} &= \int_{Y_0} \phi^n - \phi^{n-1} d\mathbf{y} + \frac{\Delta t}{\lambda^2} \left(\sum_{i=1}^3 \int_{Y_i} E(\phi^n, 0) + E_+(\phi^{n-1}, 0) d\mathbf{y}\right) \\ &\geq \frac{\Delta t}{\lambda^2} \left(\int_{Y_1} F(\phi^{n-1}, 0) d\mathbf{y} + \int_{Y_2} F(z^*, 0) d\mathbf{y} + \int_{Y_3} F(\phi^n, 0) d\mathbf{y}\right). \end{aligned} \tag{16}$$

Finally, we observe that $F(\phi^n, 0)$ is positive if and only if

$$\min_{\phi^n \in [0,1]} M(\phi^n) \left(4\gamma(2\phi^n - 1) + \frac{\lambda k}{u^n}\right) \geq 0.$$

For $\phi^n \in [0, 1]$, this is achieved if

$$\min_{\phi^n \in [0,1]} \left(4\gamma(2\phi^n - 1) + \frac{\lambda k}{u^n}\right) \geq 0.$$

Consequently, $F(\phi^n, 0) \geq 0$ in the case of $4\gamma \leq \frac{\lambda k}{u^n}$. Following the same argument one has that $F(\phi^{n-1}, 0) \geq 0$ and $F(z^*, 0) \geq 0$. Using this in (16) we conclude that $\bar{\phi}^n - \bar{\phi}^{n-1} \geq 0$ when $u^n \leq 0$. Hence (15) implies that $\| [u^n]_- \|_{\Omega}^2 \leq 0$ and the lower bound for the concentration is proven. \square

Remark. Note that, given the choice of $u^0 \in L^\infty(\Omega)$ as explained before, Lemma 3 implies by induction that for each $n > 0$, the weak solution u^n in Definition 4 is such that $0 \leq u^n \leq u^*$ a.e. in Ω .

To prove the convergence of the two-scale iterative scheme we introduce some notation: for a fixed $n > 0$ and the two-scale iteration index $i > 0$, we define $e_i^\phi := \phi_i^n - \phi^n$, $e_i^u := u_i^n - u^n$ and $e_i^{\bar{\phi}} := \bar{\phi}_i^n - \bar{\phi}^n$. Subtracting (4) from (3) and (11) from (10) the following equations are satisfied by the errors e_i^ϕ , e_i^u and $e_i^{\bar{\phi}}$

$$\begin{aligned} \langle e_i^\phi, \psi \rangle_Y + \Delta t \gamma \langle \nabla e_i^\phi, \nabla \psi \rangle_Y + \mathcal{L}_{\text{coup}} \langle (e_i^\phi - e_{i-1}^\phi), \psi \rangle_Y \\ = \frac{\Delta t}{\lambda^2} \langle E(\phi_i^n, u_{i-1}^n) - E(\phi^n, u^n), \psi \rangle_Y \\ + \frac{\Delta t}{\lambda^2} \langle E_+(\phi^{n-1}, u_{i-1}^n) - E_+(\phi^{n-1}, u^n), \psi \rangle_Y, \end{aligned} \tag{17}$$

$$\langle \bar{\phi}_i^n e_i^u, v \rangle_{\Omega} + \Delta t D \langle (\mathbb{A}_i^n \nabla u_i^n, \nabla v)_{\Omega} - \langle \mathbb{A}^n \nabla u^n, \nabla v \rangle_{\Omega} \rangle = \langle (u^* - u^n) e_i^{\bar{\phi}}, v \rangle_{\Omega}, \tag{18}$$

for all $\psi \in H^1_{\#}(Y)$ and $v \in H^1(\Omega)$. Note that (17) is defined for every $\mathbf{x} \in \Omega$.

Theorem 2 (Convergence of the two-scale iterative scheme). *For each $n > 0$, under the Assumptions (A1)–(A6), with $\mathfrak{M} := \max(\mathfrak{M}_{F_1}, \mathfrak{M}_{F_2})$, $4\gamma \leq \frac{\lambda k}{u^n}$ and $\mathcal{L}_{\text{coup}} > 12\mathfrak{M}$. If the time step is small enough (i.e. satisfying (22) below), the two-scale iterative scheme in steps (S1)–(S3) is convergent.*

Proof. For a fixed macro-scale point $\mathbf{x} \in \Omega$ and the two-scale iteration index $i > 0$, we consider the error Eq. (17) and take the test function $\psi = e_i^\phi$. By the mean value theorem, one gets

$$\begin{aligned} \|e_i^\phi\|_Y^2 + \Delta t \gamma \| \nabla e_i^\phi \|_Y^2 + \mathcal{L}_{\text{coup}} \|e_i^\phi\|_Y^2 \leq \mathcal{L}_{\text{coup}} \langle e_{i-1}^\phi, e_i^\phi \rangle_Y \\ + \frac{\Delta t}{\lambda^2} \langle 2\mathfrak{M} e_{i-1}^u, e_i^\phi \rangle_Y + \frac{\Delta t}{\lambda^2} \langle \mathfrak{M} e_i^{\bar{\phi}}, e_i^\phi \rangle_Y. \end{aligned}$$

Using Young's inequality on the first two terms on the right hand side, with $\delta_1, \delta_2 > 0$ one obtains

$$\begin{aligned} \left(1 + \mathcal{L}_{\text{coup}} - \frac{\Delta t}{\lambda^2} \mathfrak{M}\right) \|e_i^\phi\|_Y^2 + \Delta t \gamma \| \nabla e_i^\phi \|_Y^2 \\ \leq \mathcal{L}_{\text{coup}} \frac{\delta_1}{2} \|e_{i-1}^\phi\|_Y^2 + \mathcal{L}_{\text{coup}} \frac{1}{2\delta_1} \|e_i^\phi\|_Y^2 + \mathfrak{M} \frac{\Delta t \delta_2}{\lambda^2} \|e_{i-1}^u\|_Y^2 + \mathfrak{M} \frac{\Delta t}{\lambda^2} \frac{1}{\delta_2} \|e_i^{\bar{\phi}}\|_Y^2. \end{aligned}$$

By taking $\delta_1 = 1$ and $\delta_2 = \frac{1}{2}$, we get

$$\left(1 + \frac{\mathcal{L}_{\text{coup}}}{2} - \frac{3\Delta t}{\lambda^2} \mathfrak{M}\right) \|e_i^\phi\|_Y^2 \leq \frac{\mathcal{L}_{\text{coup}}}{2} \|e_{i-1}^\phi\|_Y^2 + \mathfrak{M} \frac{\Delta t}{2\lambda^2} \|e_{i-1}^u\|_Y^2.$$

Integrating over the macro-scale domain Ω and since e_{i-1}^u is constant w.r.t \mathbf{y} , we obtain

$$\left(1 + \frac{\mathcal{L}_{\text{coup}}}{2} - \frac{3\Delta t}{\lambda^2} \mathfrak{M}\right) \|e_i^\phi\|_{\Omega \times Y}^2 \leq \frac{\mathcal{L}_{\text{coup}}}{2} \|e_{i-1}^\phi\|_{\Omega \times Y}^2 + \mathfrak{M} \frac{\Delta t}{2\lambda^2} \|e_{i-1}^u\|_{\Omega}^2. \tag{19}$$

On the other hand, taking the test function $v = e_i^u$ on the macro-scale error Eq. (18) and using the Assumption (A4) and the Proposition 1, we have

$$\bar{\phi}_m \|e_i^u\|_{\Omega}^2 + \Delta t D a_m \| \nabla e_i^u \|_{\Omega}^2 \leq \Delta t D \langle (\mathbb{A}_i^n - \mathbb{A}^n) \nabla u^n, \nabla e_i^u \rangle_{\Omega} + \langle (u^* - u^n) e_i^{\bar{\phi}}, e_i^u \rangle_{\Omega}.$$

When using Young’s inequality twice with $\delta_3, \delta_4 > 0$, we obtain

$$\begin{aligned} \bar{\phi}_m \|e_i^u\|_\Omega^2 + \Delta t D a_m \|\nabla e_i^u\|_\Omega^2 &\leq \Delta t D \left(\frac{\delta_3}{2} \|(\mathbb{A}_i^n - \mathbb{A}^n) \nabla u^n\|_\Omega^2 + \frac{1}{2\delta_3} \|\nabla e_i^u\|_\Omega^2 \right) \\ &\quad + \frac{\delta_4}{2} \|(u^* - u^n) e_i^\phi\|_\Omega^2 + \frac{1}{2\delta_4} \|e_i^u\|_\Omega^2. \end{aligned}$$

We take $\delta_3 = \frac{1}{a_m}$ and $\delta_4 = \frac{1}{\phi_m}$ and due to Lemmas 2 and 3 we obtain

$$\frac{\bar{\phi}_m}{2} \|e_i^u\|_\Omega^2 + \frac{\Delta t D a_m}{2} \|\nabla e_i^u\|_\Omega^2 \leq \frac{\Delta t D}{2 a_m} C_u^2 C_A^2 \|e_i^\phi\|_{\Omega \times Y}^2 + \frac{1}{2 \phi_m} u^{*2} \|e_i^\phi\|_\Omega^2.$$

Moreover, one can easily show that $\|e_i^\phi\|_\Omega \leq \|e_i^\phi\|_{\Omega \times Y}$, implying

$$\|e_i^u\|_\Omega^2 \leq \left(\frac{\Delta t D}{a_m \bar{\phi}_m} C_u^2 C_A^2 + \frac{u^{*2}}{\phi_m} \right) \|e_i^\phi\|_{\Omega \times Y}^2. \tag{20}$$

Observe that the constants in (20) do not depend on the two-scale iteration index, i.e. (20) can be written for the index $i - 1$ as well. Using this in (19) we obtain

$$\begin{aligned} &\left(1 + \frac{\mathcal{L}_{\text{coup}}}{2} - \frac{3 \Delta t}{\lambda^2} \mathfrak{M} \right) \|e_i^\phi\|_{\Omega \times Y}^2 \\ &\leq \left(\frac{\mathcal{L}_{\text{coup}}}{2} + \mathfrak{M} \frac{\Delta t}{2 \lambda^2} \left(\frac{\Delta t D}{a_m \bar{\phi}_m} C_u^2 C_A^2 + \frac{u^{*2}}{\phi_m} \right) \right) \|e_{i-1}^\phi\|_{\Omega \times Y}^2. \end{aligned} \tag{21}$$

Clearly, (21) can be rewritten to $\|e_i^\phi\|_{\Omega \times Y}^2 \leq C \|e_{i-1}^\phi\|_{\Omega \times Y}^2$. By taking the time step Δt sufficiently small, one obtains $C < 1$, so the error is contractive. Specifically, if $\Delta t > 0$ satisfies the inequality

$$\left(\frac{\mathfrak{M} D C_u^2 C_A^2}{2 \lambda^2 a_m \bar{\phi}_m} \right) \Delta t^2 + \frac{\mathfrak{M}}{\lambda^2} \left(\frac{u^{*2}}{2 \phi_m} + 3 \right) \Delta t < 1, \tag{22}$$

then (21) is a contraction. By the Banach theorem we conclude that $\|e_i^\phi\|_{\Omega \times Y} \rightarrow 0$ as $i \rightarrow \infty$. This, together with (20) implies that $\|e_i^u\|_\Omega \rightarrow 0$ as $i \rightarrow \infty$, which proves the convergence of the two-scale iterative scheme. \square

Remark. To summarize, we highlight that the convergence of the two-scale iterative scheme is guaranteed under (A1)–(A6) and the following conditions

- The motion of the diffuse interface and the width of the transition zone are related such that $4\gamma \leq \frac{\lambda k}{u^*}$.
- The coupling parameter $\mathcal{L}_{\text{coup}}$ is such that $\mathcal{L}_{\text{coup}} > 12 \max(\mathfrak{M}_{F_1}, \mathfrak{M}_{F_2})$.
- The time step Δt is such that (22) is fulfilled. Note that (22) can clearly be fulfilled for some real $\Delta t > 0$. This restriction does not depend on the spatial discretization. Also note that the convergence is achieved for any starting point. Nevertheless, finding specific bounds for Δt from (22) is not obvious because it depends on unknown constants. In Section 7 we choose Δt based on numerical experiments inspired by Storvik et al. [53], where a coarse spatial discretization is used to estimate a suitable time step size.

6. The adaptive strategy

We design an adaptive strategy to localize and reduce the error and to optimize the computational cost of the simulations.

Let \mathfrak{T}_H be a triangular partition of the macro-scale domain Ω with elements T of diameter H_T and $H := \max_{T \in \mathfrak{T}_H} H_T$. We assign one micro-scale domain Y to the barycentre (or integration point) of each macro-scale element T . At each micro-scale domain Y we define another triangular partition \mathfrak{T}_h with elements T_μ of diameter h_{T_μ} and $h := \max_{T_\mu \in \mathfrak{T}_h} h_{T_\mu}$. In Fig. 2, the structure and the notation of the meshes are shown. We first present the mesh refinement strategy used in the micro scale and thereafter we turn to the macro-scale adaptive strategy used to optimize the computations.

6.1. The micro-scale mesh adaptivity

The accuracy in the solution of the phase field is influenced by the mesh size of the micro-scale discretization. It is necessary to create a fine mesh such that $h \ll \lambda$ to capture the diffuse transition zone. Nevertheless, such a fine uniform mesh would make the computation of the phase field and the effective parameters very expensive. Here we propose an adaptive micro-scale mesh with fine elements only in the diffuse transition zone of the phase field.

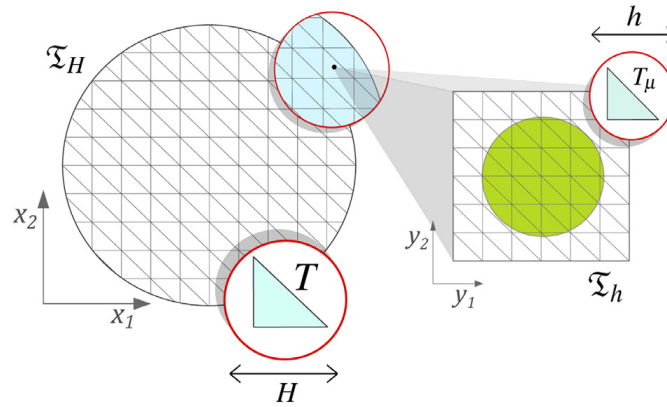


Fig. 2. Sketch of the macro-scale and micro-scale meshes. For each $T \in \mathfrak{T}_H$ there is one corresponding micro-scale domain Y with a micro-scale mesh \mathfrak{T}_h .

The mesh refinement strategy relies on an estimation of the evolution of the phase field. Here we use the fact that ϕ is essentially bounded by 0 and 1 a.e. in Y and that the large changes in the gradient of ϕ are encountered in the transition zone. Nevertheless, other methods or refinement criteria can be used without modifying the whole strategy.

Here the local mesh adaptivity is divided into three main steps: prediction - projection - correction. This strategy is an extension of the predictor-corrector algorithm proposed in Heister et al. [36] and by construction, our strategy avoids nonconforming meshes.

For a fixed time $n > 0$, consider a micro-scale domain Y and let ϕ^{n-1} be given over a mesh \mathfrak{T}_h^{n-1} . The mesh \mathfrak{T}_h^{n-1} is "optimal" in the sense that it is fine only in the diffuse transition zone of ϕ^{n-1} . Take also an auxiliary coarse mesh \mathfrak{T}_c , which is uniform with mesh size $h_{\max} \gg \lambda$.

Prediction. Given the mesh \mathfrak{T}_h^{n-1} compute a first approximation to the solution of problem $(P_\phi^{\mu,1})$. We call this approximation the auxiliary solution ϕ_1^{n*} . Project the solution ϕ_1^{n*} on the coarse mesh \mathfrak{T}_c . The elements marked to be refined are $T_\mu \in \mathfrak{T}_c$ such that

$$\theta_r \lambda \leq \phi_1^{n*}|_{T_\mu} \leq 1 - \theta_r \lambda$$

for some constant $0 < \theta_r < \frac{1}{2\lambda}$. After marking the triangles, we refine the mesh in the selected zone. The refinement process is repeated until the smallest element is such that $h_{T_\mu} \leq h_{\min} \ll \lambda$. The result is a refined mesh \mathfrak{T}_h^{n*} that is fine enough at the predicted transition zone of the phase field ϕ_1^{n*} .

Projection Create a projection mesh \mathfrak{T}_r that is the union of the previous mesh and the predicted mesh. The mesh $\mathfrak{T}_r = \mathfrak{T}_h^{n-1} \cup \mathfrak{T}_h^{n*}$ is fine enough at the transition zone of ϕ^{n-1} and ϕ_1^{n*} . To properly describe the interface of both ϕ^{n-1} and ϕ_1^{n*} we project the previous solution ϕ^{n-1} over \mathfrak{T}_r .

Correction Given the mesh \mathfrak{T}_r and the projection of ϕ^{n-1} compute once more the solution of problem $(P_\phi^{\mu,1})$. The projection of this result over the mesh \mathfrak{T}_h^n corresponds to the solution ϕ_1^n .

This process is necessary at every time step and every micro-scale domain but we perform the mesh refinement only in the first iteration of the coupled scheme. However, this procedure could be extended for further iterations. Notice that higher values of the parameter θ_r lead to coarser meshes and less error control. We will illustrate the role of θ_r in Section 7.

In Fig. 3 we sketch the prediction-projection-correction strategy by zooming in on the transition zone of a phase field. There the mineral is shrinking from the time $n-1$ to n . In Fig. 3(a) and (d) we mark the center of the transition zone of the auxiliary solution ϕ_1^{n*} and the corrected solution ϕ_1^n , and we see how the mesh follows the transition zone of the phase field.

6.2. The macro-scale adaptivity

The computations on the micro scale can be optimized by the mesh adaptivity discussed before and the cell problems can be computed in parallel. Nevertheless, it is demanding to compute the micro-scale quantities at every element (or integration point) of the macro-scale mesh. Here, the scale separation allows us to solve the model adaptively in the sense of the strategy introduced in Redeker and Eck [35] and further studied in Redeker et al. [26]. There the macro-scale adaptivity uses only the solute concentration to locate where the micro-scale features need to be recalculated. Here we implement a modified adaptive strategy on the micro scale that depends on the solute concentration and the phase-field evolution. With this, we extend the method in Redeker and Eck [35] to more general settings, including heterogeneous macro-scale domains.

To be more precise, we define the metric d_E such that it measures the distance of two macro-scale points $\mathbf{x}_1, \mathbf{x}_2 \in \Omega$ in terms of the solute concentration and the phase-field evolution, i.e.

$$d_E(\mathbf{x}_1, \mathbf{x}_2; t; \Lambda) := \int_0^t e^{-\Lambda(t-s)} \left(d_u(\mathbf{x}_1, \mathbf{x}_2; s) + \int_Y d_\phi(\mathbf{x}_1, \mathbf{x}_2, \mathbf{y}; s) d\mathbf{y} \right) ds.$$

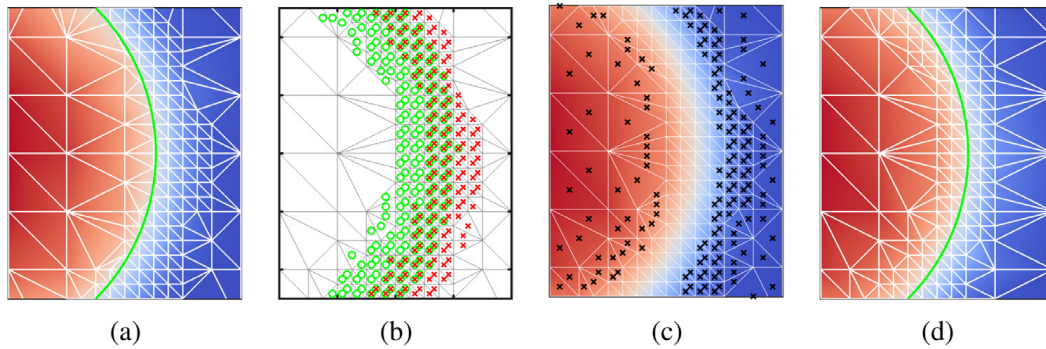


Fig. 3. Prediction- projection - correction strategy. (a) The auxiliary solution ϕ_1^{n*} over the mesh \mathfrak{T}^{n-1} and the (green) line marks where $\phi_1^{n*} = 0.5$ indicating the center location of the predicted transition zone. (b) The auxiliary mesh \mathfrak{T}_r and the triangles that belong to the transition zone of $\phi^{n-1}(\mathbf{x})$ and $\phi_1^{n*}(\circ)$. (c) The solution of problem $(P_\phi^{\mu,1})$ over \mathfrak{T}_r and the elements outside of the transition zone (\times). (d) The solution ϕ_1^n over the optimal mesh \mathfrak{T}_h^n and the (green) line marks where $\phi_1^n = 0.5$ indicating the center location of the transition zone. (For interpretation of the references to color in this figure legend, the reader is referred to the web version of this article.)

Here d_u and d_ϕ are defined as follows

$$d_u(\mathbf{x}_1, \mathbf{x}_2; s) := |u(\mathbf{x}_1, s) - u(\mathbf{x}_2, s)| \text{ and } d_\phi(\mathbf{x}_1, \mathbf{x}_2, \mathbf{y}; s) := |\phi(\mathbf{x}_1, \mathbf{y}, s) - \phi(\mathbf{x}_2, \mathbf{y}, s)|,$$

and $\Lambda \geq 0$ is a history parameter. In the discrete setting we calculate the distance d_E recursively, i.e.

$$d_E(\mathbf{x}_1, \mathbf{x}_2; n\Delta t; \Lambda) \approx e^{-\Lambda\Delta t} d_E(\mathbf{x}_1, \mathbf{x}_2; (n-1)\Delta t; \Lambda) + \Delta t \left(d_u(\mathbf{x}_1, \mathbf{x}_2; n\Delta t) + \int_Y d_\phi(\mathbf{x}_1, \mathbf{x}_2, \mathbf{y}; n\Delta t) d\mathbf{y} \right).$$

The spatial integrals are also calculated numerically depending on the spatial discretization.

At each time $n \geq 0$ we divide the set of macro-scale points (elements) into a set of *active* points ($N_A(n)$) and a set of *inactive* points ($N_I(n)$). Specifically, $N_{\text{Total}} = N_A(n) \cup N_I(n)$ and $N_A(n) \cap N_I(n) = \emptyset$ for all $n \geq 0$.

The cell problems will only be solved for points that are active. In this way, the effective parameters and the porosity are updated only in such points. For the inactive point, the effective parameters and the porosity are updated by using the *Copy method* described in Redeker et al. [26] and explained below.

Let $0 \leq C_r, C_c < 1$ be given and define the refinement and coarsening tolerances as follows

$$tol_r(t) := C_r \cdot \max_{\mathbf{x}_1, \mathbf{x}_2 \in \Omega} \{d_E(\mathbf{x}_1, \mathbf{x}_2; t; \Lambda)\} \text{ and } tol_c(t) := C_c \cdot tol_r(t).$$

For $n > 0$ and on the first iteration, i.e. before the iterative process, the solutions $u^{n-1}(\mathbf{x})$ and $\phi^{n-1}(\mathbf{x}, \mathbf{y})$ for all $\mathbf{x} \in \Omega$ and $\mathbf{y} \in Y$ are given. The adaptive process consists of the following steps

- Initially, for $n = 0$ all the points are inactive, i.e. $N_A(0) = \emptyset$ and $N_I(0) = N_{\text{Total}}$.
- Update the set of active points $N_A(n)$ and $N_I(n)$.
 - Set $N_A(n) = N_A(n-1)$ and $N_I(n) = N_I(n-1)$. For each active point $\mathbf{x}_A \in N_A(n)$ repeat the following: if there exists another active node $\mathbf{x}_B \in N_A(n)$ such that $d_E(\mathbf{x}_A, \mathbf{x}_B; (n-1)\Delta t; \Lambda) < tol_c$, then \mathbf{x}_A is deactivated, i.e. $\mathbf{x}_A \in N_I(n)$. Otherwise, $\mathbf{x}_A \in N_A(n)$.
 - For each inactive point $\mathbf{x}_I \in N_I(n)$ repeat the following: if $N_A(n) = \emptyset$ the point \mathbf{x}_I is activated. Otherwise, calculate the distance to all the active nodes. If $\min_{\mathbf{x}_A \in N_A(n)} \{d_E(\mathbf{x}_I, \mathbf{x}_A; (n-1)\Delta t; \Lambda)\} > tol_r$ then the point \mathbf{x}_I is activated, i.e., $\mathbf{x}_I \in N_A(n)$.
- Associate all the inactive points to the most similar active point. In other words, an inactive point $\mathbf{x}_I \in N_I(n)$ is associated with $\mathbf{x}_A \in N_A(n)$ if $\mathbf{x}_A = \operatorname{argmin}_{\mathbf{x} \in N_A(n)} \{d_E(\mathbf{x}_I, \mathbf{x}; (n-1)\Delta t; \Lambda)\}$.

After updating the sets of active and inactive points we use the two-scale iterations to solve the micro- and macro-scale problems. At each iteration ($i > 0$) we solve $(P_\phi^{\mu,i}), (P_A^\mu)$ (and (P_K^μ)) and transfer the solutions ϕ_i^n, Δ_i^n (and \mathbb{K}_i^n) from the active points to their associated inactive ones. We then solve $(P_u^{M,i})$ (and $(P_p^{M,i})$) and continue the iterations until convergence.

The two tolerances tol_r and tol_c are controlled through the values of C_r and C_c . For a fixed value of C_r the role of C_c is to control the upper bound for the distance between active points. In other words, higher values of C_c imply that more active points in $N_A(n-1)$ remain active in $N_A(n)$. On the other hand, for a fixed value of C_c the role of C_r is to control the upper bound for the distance between active and inactive points. Namely, higher values of C_r imply that less inactive points in $N_I(n)$ become active. In accordance with [35] and to avoid a complete update of the set of active nodes, it is wise to use smaller values for tol_c than for tol_r . Therefore, in Section 7.1 we analyze the role of C_r in the macro-scale error control when C_c is fixed and is chosen to be small.

Result: Concentration u , porosity $\bar{\phi}$ (and pressure p).
 Given the initial conditions u_I and ϕ_I
for time t^n **do**
 Adjust the set $N_A(n)$ of the active macro-scale points
 Take $i = 1$ and $u_0^n = u^{n-1}$
 while $\varepsilon_M^{n,i} \geq tol_M$ **do**
 for $\mathbf{x} \in N_A(n)$ **do**
 if $i=I$ **then**
 | Adaptivity on the micro-scale meshes
 end
 Solve $(\mathbf{P}_\phi^{\mu,i})$ using the L-scheme until $\varepsilon_\mu^{n,i,j} \leq tol_\mu$
 Compute the effective matrix A_i^n (and \mathbb{K}_i^n)
 end
 For $\mathbf{x} \in N_I(n)$ copy the solution from the nearest $\mathbf{x} \in N_A(n)$
 Solve $(\mathbf{P}_u^{M,i})$ (and $(\mathbf{P}_p^{M,i})$)
 Next iteration $i = i + 1$
 end
 Next time $n = n + 1$
end

Algorithm 1. The two-scale iterative scheme using adaptive strategies on both scales.

6.3. The adaptive algorithm

We combine the two-scale iterative scheme and the adaptive strategies in a simple algorithm, see [Algorithm 1](#). Even though we showed the convergence of the two-scale iterative scheme in a simplified setting disregarding the flow, we mention the solution of the effective permeability \mathbb{K}_i^n and the flow problem $\mathbf{P}_p^{M,i}$ in [Algorithm 1](#). The reason for this is that in the numerical tests, specifically in [Section 7.2](#), we evidence that the iterative scheme also converges in the complete scenario.

7. The numerical results

In this section, we present two numerical tests for the two-scale iterative scheme. We restrict our implementations to the 2D case and all parameters specified in the following examples are non-dimensional according to the non-dimensionalization in [Bringedal et al. \[27\]](#).

For the first test, in [Section 7.1](#) we use a simple setting where the performance of the adaptive techniques are investigated. In [Section 7.2](#) we analyze an anisotropic and heterogeneous case where different shapes of the initial phase field are used. The numerical solutions of macro- and micro-scale problems (\mathbf{P}_p^M) , (\mathbf{P}_u^M) , $(\mathbf{P}^{\mu,\phi})$ and $(\mathbf{P}_\Delta^{\mu,\phi})$ are computed using the lowest order Raviart-Thomas elements (see [\[54\]](#)). For the micro-scale problems $(\mathbf{P}_\mathbb{K}^{\mu,\phi})$ we use the Crouzeix-Raviart elements (see [\[55, Section 8.6.2\]](#)). The following (non-dimensional) constants have been used in all the simulations

$$\begin{aligned}
 D = 1; \quad \mu_f = 1; \quad u^* = 1; \quad u_{eq} = 0.5; \\
 \gamma = 0.01; \quad \lambda = 0.08; \quad \delta = 1E-4; \quad k = 1.
 \end{aligned}
 \tag{23}$$

Note that for these choices of u^* , k , λ and γ , the restriction $4\gamma \leq \frac{\lambda k}{u^*}$ in [Lemma 3](#) is fulfilled.

7.1. Test case 1. Circular shaped phase field

Consider the macro-scale domain $\Omega = (0, 1) \times (0, \frac{1}{2})$ and take $T = 0.25$. The system is initially in equilibrium, i.e. the initial concentration is $u(\mathbf{x}, 0) = u_{eq}$ and $p(\mathbf{x}, 0) = 0$ for all $\mathbf{x} \in \Omega$. We impose a Dirichlet boundary condition $u = 0$ in a portion of the lower-left corner of the domain Ω , i.e., from $(0,0)$ to $(0, H)$ and $(H, 0)$. Further, we take homogeneous Neumann boundary conditions everywhere else for both the solute concentration and pressure problems. This choice of the boundary conditions initiates a dissolution process. At every micro-scale domain Y the initial phase field ϕ_I has a circular shape with initial porosity $\bar{\phi}_0 = 0.5$. This configuration is displayed in [Fig. 4](#). We allow the mineral to dissolve until a maximum porosity $\bar{\phi}_M = 0.9686$ is reached.

For the time discretization, even though [Theorem 2](#) gives a theoretical restriction on Δt , the estimation of an accurate bound is not evident. Here we choose Δt experimentally by choosing an initial value of Δt which is sufficiently small to ensure convergence of the micro-scale non-linear solver (see [Theorem 1](#)). If the multi-scale iterations converge in the first

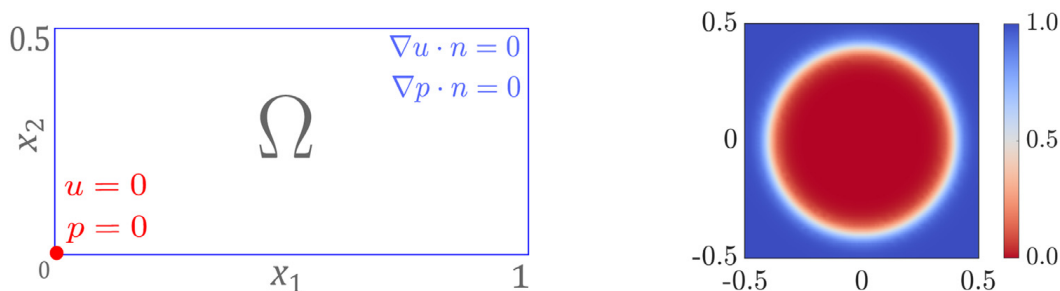


Fig. 4. The configuration of the macro scale (left) and phase-field initial condition (right) - Test case 1.

Table 1

The micro-scale adaptive results for a varying refining parameter θ_r . The column %Elements corresponds to the percentage of the original number of elements used in each mesh and %E ϕ is the relative error compared to the reference solution .

θ_r	#Elements	%Elements	E_ϕ	%E ϕ
0.5	1200	16.72%	9.69E-3	2.27%
1	1040	14.51%	1.01E-2	2.37%
2	864	12.00%	1.19E-2	2.79%
5	560	7.77%	1.99E-2	4.68%

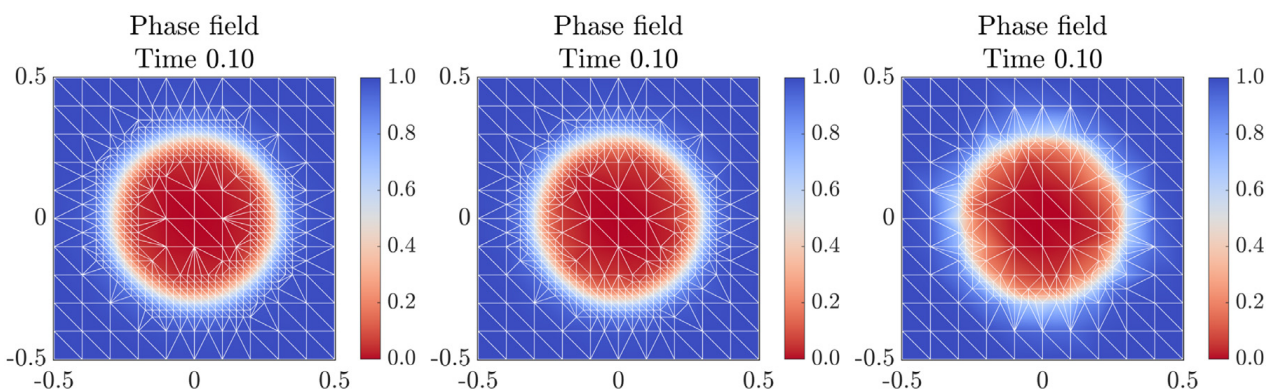


Fig. 5. The phase field $\phi^n(\mathbf{x})$ corresponding to the macro-scale location $\mathbf{x} = (0, 0)$ at the time $t^n = 0.10$. Refinement parameters $\theta_r = 1, 2,$ and 5 (left to right).

time step, this value of Δt is used in the whole simulation. Otherwise, smaller values of Δt are tested. Here the time step is chosen to be $\Delta t = 0.01$, and was found to always ensure convergence in these tests.

7.1.1. The micro-scale non-linear solver and adaptivity

To study the features of the micro-scale non-linear solver and the micro-scale refinement strategy, we look closer at the micro-scale domain Y corresponding to the macro-scale location $\mathbf{x} = (0, 0)$ with an initial phase field as shown in Fig. 4 and a constant concentration $u = 0$.

Concerning the behavior of the micro-scale non-linear solver, we take dynamically the value of the linearization parameter $\mathcal{L}_{lin} = \max(|2\lambda f(u) + 8\gamma|, |2\lambda f(u) - 8\gamma|)$, which changes at every two-scale iteration if the solute concentration u changes. This choice of \mathcal{L}_{lin} gives convergence of the micro-scale iterations, as shown in Pop et al. [37]. We use this choice of \mathcal{L}_{lin} in all the simulations below as well as the micro-scale stopping criterion $tol_\mu = 1E-8$. We choose tol_μ so small to ensure sufficient accuracy of the micro-scale problems and to not influence the convergence. For all the micro-scale meshes used in Table 1 the average number of micro-scale iterations is 13 in the prediction stage and 6 in the correction stage. Here we do not iterate between scales and we choose $\mathcal{L}_{coup} = 0$ having no effect on the convergence of the non-linear solver.

In Fig. 5 we show the phase field at time $t^n = 0.10$. On each micro-scale domain Y we use an initial uniform mesh with 200 elements and apply three different values for the mesh refinement parameter, namely $\theta_r = 1, 2,$ and 5 .

It is clear that the micro-scale refinement parameter slightly changes the representation of the phase-field transition zone. This result is also evident in Table 1. There we show a comparison between the micro-scale solutions when using different values of θ_r and the reference solution ϕ_{ref} . We use a fixed uniform mesh with 7200 elements and mesh size $h_{ref} = 2.36E-2 \ll \lambda$ to compute the reference solution ϕ_{ref} . In Table 1 we report the average number of elements for each micro-scale mesh (#Elements) and there the accuracy of the numerical solution is provided through the L^2 -error, namely $E_\phi := \|\phi_{ref} - P_h(\phi)\|_{L^2([0,T],L^2(Y))}$ with $P_h(\phi)$ being the projection of the solution ϕ over the reference mesh.

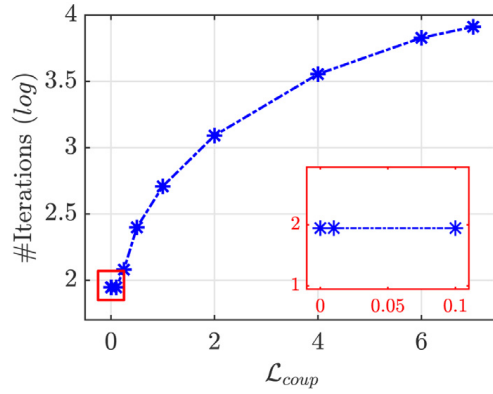


Fig. 6. The number of two-scale iterations (log) at time $t = 0.01$ for different values of $\mathcal{L}_{\text{coup}}$. Zoom in of the plot for small values of $\mathcal{L}_{\text{coup}}$.

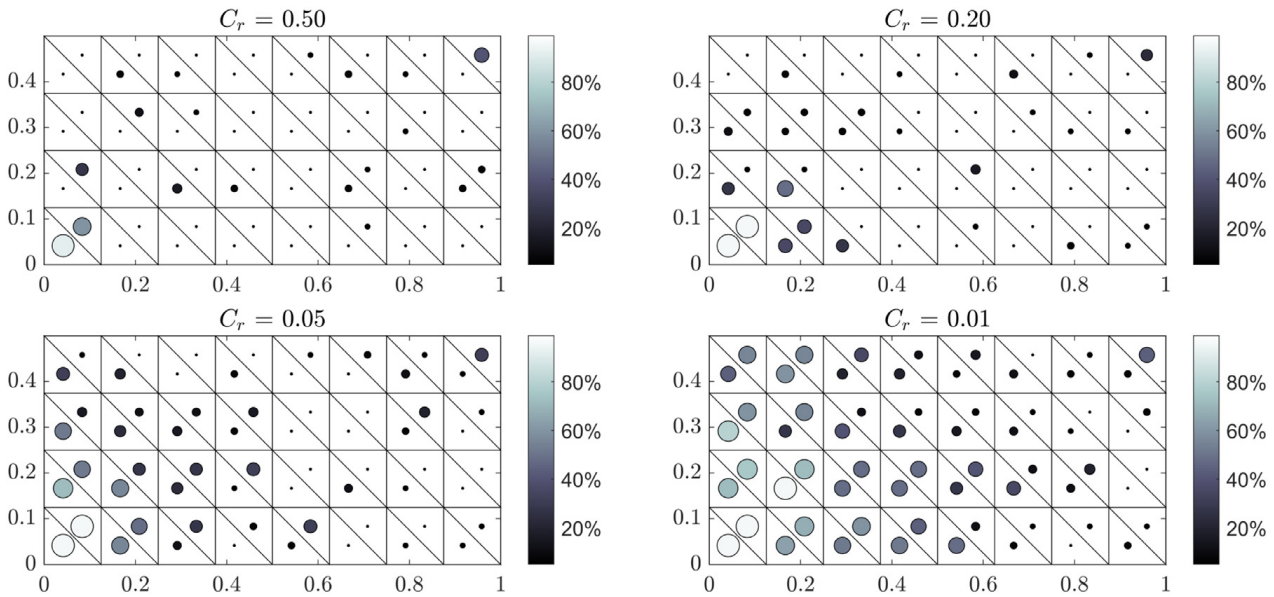


Fig. 7. The results of the macro-scale adaptive strategy for different values of the refinement parameter $C_r = 0.5, 0.2, 0.05,$ and 0.01 . Different intensities and sizes indicate the percentage of times that each macro-scale element was active.

All the meshes in Fig. 5 and Table 1 are constructed such that the minimum diameter in the mesh is $h_{T_\mu} \leq h_{\min} = \frac{\lambda}{3}$. In Fig. 5, the length of the smallest edge in the meshes is $\min_{T_\mu \in \mathfrak{T}_h} h_{T_\mu} = 2.50\text{E-}2$ and the length of the largest edge (located far from the transition zone) is $h_{\max} = 1.41\text{E-}1$. We remark that the uniform reference mesh size h_{ref} is only slightly smaller than h_{\min} . In Fig. 5 and Table 1 we have used the same h_{\min} for all θ_r , while $h_{\text{ref}} \approx h_{\min}$ to ensure a fair comparison between and to address the effect of θ_r .

Smaller values of θ_r lead to better error control, but those values also imply more degrees of freedom and therefore increase the computational effort. In the following numerical experiments, we choose $\theta_r = 2$ to control the error on the micro scale and, at the same time, limit the number of elements at each micro-scale domain.

7.1.2. The two-scale coupling and the macro-scale adaptivity

We study the convergence of the two-scale iterative scheme for different values of the parameter $\mathcal{L}_{\text{coup}}$. In Theorem 2 the value of $\mathcal{L}_{\text{coup}}$ is restricted to be $\mathcal{L}_{\text{coup}} > 12\mathfrak{M}$. Using the parameters in (23) we obtain that $\mathfrak{M} \geq 1.12$. In Fig. 6 we compare the convergence of the two-scale iterative scheme when using different values of $\mathcal{L}_{\text{coup}}$. Specifically, in Fig. 6 we show the number of iterations used at the first time step for eleven different values of $\mathcal{L}_{\text{coup}}$. It is evident that the conditions in Theorem 2 are rather restrictive and in practice, one can achieve convergence using smaller values of $\mathcal{L}_{\text{coup}} \geq 0$. For very small values of $\mathcal{L}_{\text{coup}}$, the iterations needed in the two-scale iterative scheme remain constant, which we highlight in Fig. 6. Here we choose $\text{tol}_M = 1\text{E-}6$ for the stopping criterion and we do not use the macro-scale adaptive strategy, i.e., we solve all the micro-scale problems. After this study, we choose $\mathcal{L}_{\text{coup}} = 1\text{E-}4$ in all the simulations below.

In Fig. 7 and Table 2 the results of the macro-scale adaptivity are shown. We choose the history parameter $\Lambda = 0.1$ and the coarsening parameter $C_c = 0.2$ based on the sensitivity analysis presented in Redeker and Eck [35] and used in Redeker et al. [26]. Fig. 7 illustrates the effect of the refinement parameter C_r on the proportion of active nodes. There, the different

Table 2

The adaptive results for $\Lambda = 0.1$, $C_c = 0.2$ and a varying refining parameter C_r . The columns %Active, $\%E_u$ and $\%E_{\bar{\phi}}$ correspond to the average percentage of the original number of active elements used in each case and the relative errors with respect to the reference solution.

C_r	#Active	%Active	E_u	$\%E_u$	$E_{\bar{\phi}}$	$\%E_{\bar{\phi}}$
0.50	82	5.13%	8.26E-3	5.23%	2.00E-2	10.16%
0.20	134	8.38%	7.11E-3	4.50%	1.26E-2	6.41%
0.05	257	16.06%	2.05E-3	1.30%	4.92E-3	2.51%
0.01	512	32.00%	7.14E-4	0.45%	1.81E-3	0.92%

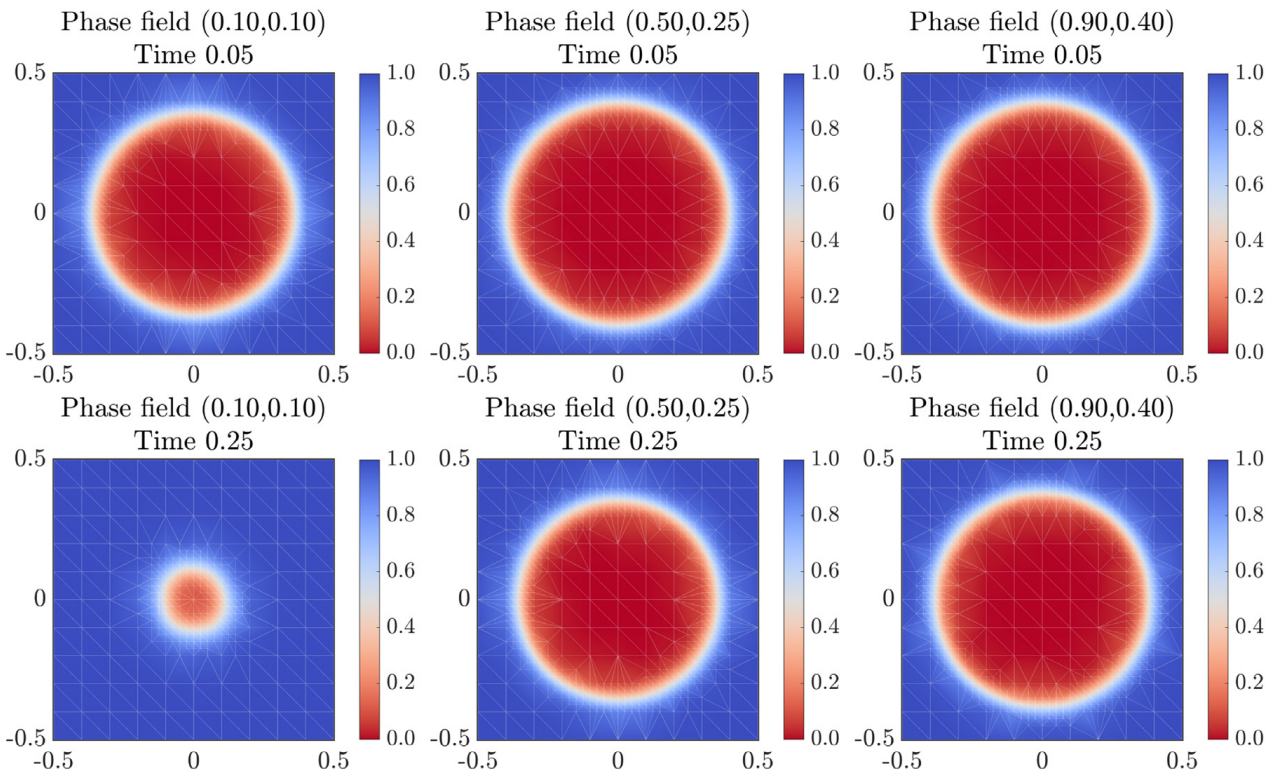


Fig. 8. The evolution of the phase fields corresponding the macro-scale locations $\mathbf{x} = (0.1, 0.1)$, $\mathbf{x} = (0.5, 0.25)$, $\mathbf{x} = (0.9, 0.4)$ (left to right) at two times $t^n = 0.05$ (top) and $t^n = 0.25$ (bottom).

intensities and sizes represent the percentage of the total number of times that each element was active during the whole simulation.

In Table 2 we analyze the effect of the macro-scale adaptive strategy on the L^2 -error of the concentration and porosity. We call u_{ref} and $\bar{\phi}_{\text{ref}}$ the solutions that corresponds to $C_r = 0$, i.e., the solutions of the test case without using the macro-scale adaptive strategy. The number of active nodes in the reference case is 1600. Table 2 compares the following L^2 -errors with the number of macro-scale active elements during the whole simulation

$$E_u := \|u_{\text{ref}} - u\|_{L^2([0,T];L^2(\Omega))} \quad \text{and} \quad E_{\bar{\phi}} := \|\bar{\phi}_{\text{ref}} - \bar{\phi}\|_{L^2([0,T];L^2(\Omega))}.$$

As expected and coinciding with [35], larger values of C_r imply less error control. Nevertheless, when C_r increases the computational cost of the simulations decreases and the convergence of the two-scale iterative scheme is not affected.

Finally, we show the results of the complete algorithm when using $\mathcal{L}_{\text{coup}} = 1\text{E-}4$ and $C_r = 0.05$. Fig. 8 shows the evolution of the phase field corresponding to three different macro-scale locations. There we also show the corresponding micro-scale mesh that captures the movement of the phase-field transition zone.

The macro-scale solute concentration and porosity are displayed in Fig. 9. The effective parameters are shown in Fig. 10. The boundary conditions trigger the decrease of the solute concentration and its effect is the dissolution of the mineral. This translates into higher porosity and effective diffusivity. Moreover in Fig. 10 we show that the effective permeability can be calculated although we do not consider flow in this test case.

Due to the symmetry of the phase field at the micro scale, the expected results are isotropic effective tensors. The non-diagonal components of \mathbb{A} and \mathbb{K} are close to zero and can be neglected. Moreover, due to the similarity between $\mathbb{K}_{1,1}$ and $\mathbb{K}_{2,2}$ and between $\mathbb{A}_{1,1}$ and $\mathbb{A}_{2,2}$ we only show one of the components of the effective parameters in Fig. 10.

In this test case the average number of degrees of freedom in both scales is 52,216 per time step. At the macro scale we have 64 elements and for each active element we solve the phase-field problem and update the porosity and the effective parameters at each iteration. All the micro-scale problems have been solved in parallel.

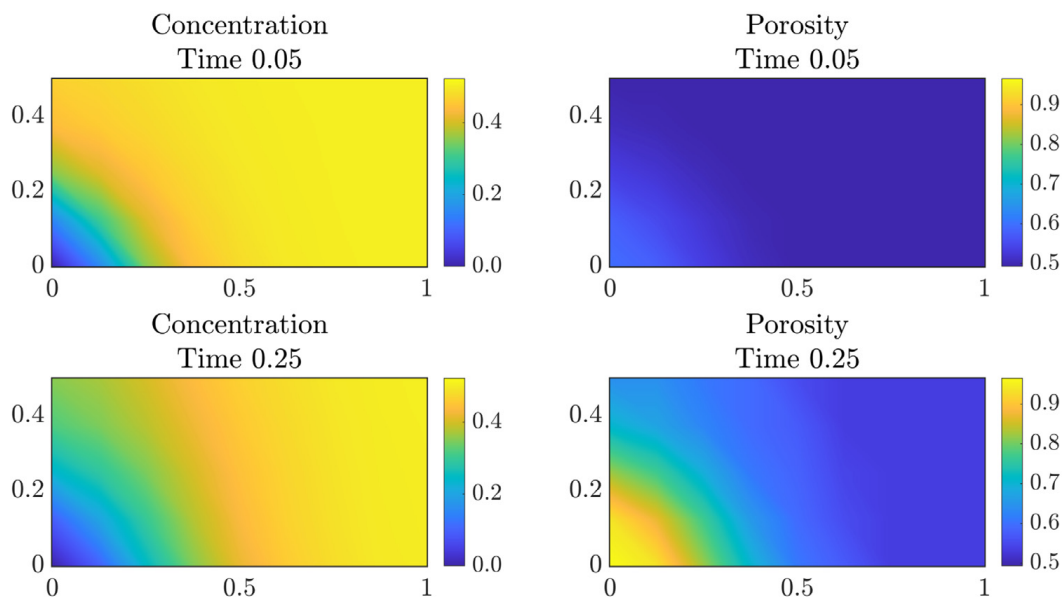


Fig. 9. The numerical solution of the concentration u^n (left) and porosity $\bar{\phi}$ (right) at two times $t^n = 0.05$ (top) and 0.25 (bottom).

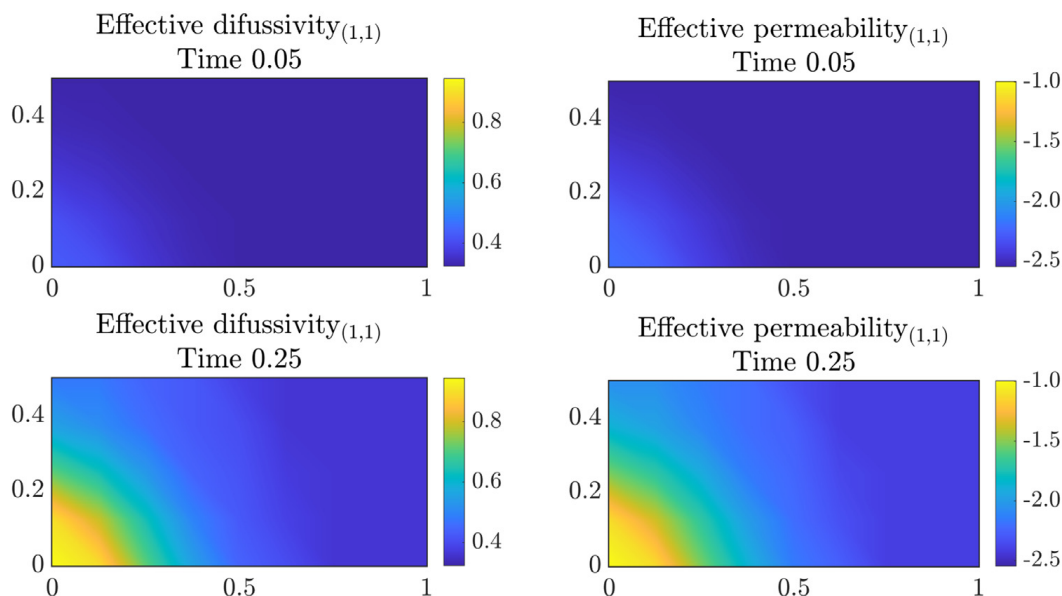


Fig. 10. The first components of the effective difussivity tensor (left) and the effective permeability tensor (Log_{10}) (right) at two times $t^n = 0.05$ (top) and 0.25 (bottom).

Finally, in Fig. 11 we show the convergence of $\epsilon_M^{n,i}$ at different times. The linear convergence of the two-scale iterative scheme is evident in Fig. 11. We highlight that the total number of iterations in the two-scale iterative scheme does not increase in time. By comparing Fig. 11 and Fig. 6 we evidence that the convergence of the two-scale iterative scheme is not being affected by the macro-scale adaptivity.

7.2. Test case 2. Anisotropic case

Consider the macro-scale domain $\Omega = (0, 1) \times (0, \frac{1}{2})$ where the system is initially in equilibrium, i.e. the initial concentration is $u(\mathbf{x}, 0) = u_{\text{eq}}$ and $p(\mathbf{x}, 0) = 0$ for all $\mathbf{x} \in \Omega$. We take $u = 0$ and $p = 0$ on the right boundary of Ω ; $p = 0.25$ on the left boundary of Ω and homogeneous Neumann boundary conditions everywhere else for both the solute concentration and pressure problems. On the micro scale, we consider an initially inhomogeneous distribution of the mineral. We define two sub-domains of Ω ; the left half is $\Omega_l := (0, 0.5) \times (0, 0.5)$ and the right half $\Omega_r := (0.5, 1) \times (0, 0.5)$. The initial phase field is chosen to be

$$\phi_l(\mathbf{x}, \mathbf{y}) = \begin{cases} \phi_l^0(\mathbf{y}), & \text{if } \mathbf{x} \in \Omega_l, \\ \phi_r^0(\mathbf{y}), & \text{otherwise,} \end{cases}$$

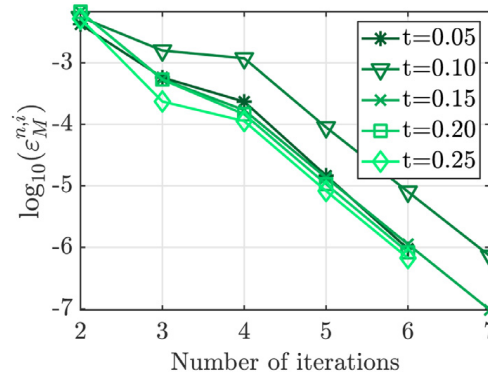


Fig. 11. The convergence of the two-scale iterative scheme for five different times.

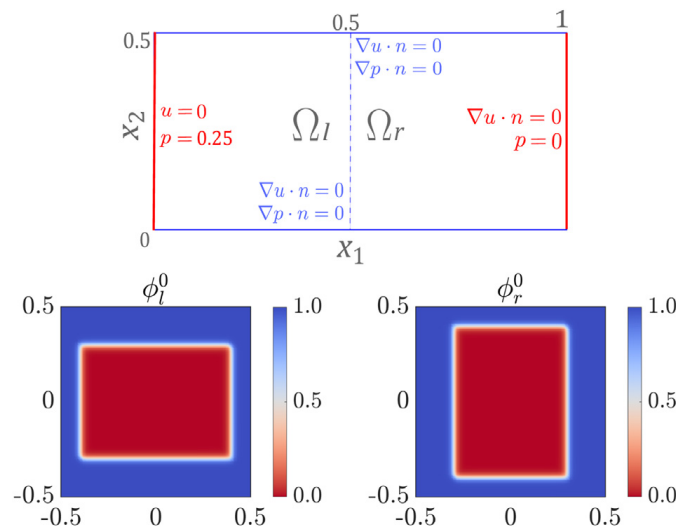


Fig. 12. The configuration of the macro scale (top) and the phase-field initial conditions (bottom) - Test case 2.

where the micro-scale functions ϕ_l^0 and ϕ_r^0 are taken as follows

$$\phi_l^0(\mathbf{y}) = \begin{cases} 0, & \text{if } \mathbf{y} \in [-0.4, 0.4] \times [-0.3, 0.3], \\ 1, & \text{otherwise,} \end{cases}$$

$$\phi_r^0(\mathbf{y}) = \begin{cases} 0, & \text{if } \mathbf{y} \in [-0.3, 0.3] \times [-0.4, 0.4], \\ 1, & \text{otherwise.} \end{cases}$$

The configuration of the test case 2 is displayed in Fig. 12. With this example we show the potential of the model and the numerical strategy in a heterogeneous scenario. Here we add the flow that was dismissed during the proofs in Section 5. The following parameters have been used in the simulation

$$\mathcal{L}_{\text{coup}} = 1\text{E-}4; \quad \theta_r = 2; \quad C_r = 0; \quad \bar{\phi}_M = 0.9686.$$

For the simulation time we take $T = 0.25$ and the time step is chosen to be $\Delta t = 0.01$ as explained before.

Due to the structure of this example and the chosen boundary and initial conditions, the macro-scale solution does not depend on the vertical component. Therefore the 1D projection of the macro-scale solutions in the horizontal direction is sufficient to understand the behavior of the whole system. The macro-scale adaptive strategy is unnecessary as the natural choice is to fix the nodes located at the lowest part of the macro-scale domain to be active.

In Figs. 13 and 14 we show the evolution of the phase field corresponding to different macro-scale locations. On each micro-scale domain Y we use an initial uniform mesh with 800 elements and the minimum diameter h_{T_μ} in the refined mesh is $h_{T_\mu} = 0.025$. Moreover, for the micro-scale non-linear solver we choose $\mathcal{L}_{\text{lin}} = \max(|2\lambda f(u) + 8\gamma|, |2\lambda f(u) - 8\gamma|)$ and $\text{tol}_\mu = 1\text{E-}8$.

The 1D projection of the macro-scale solute concentration, pressure and porosity is displayed in Fig. 15. As expected, where the concentration decreases, the dissolution of the mineral is induced, which then increases the porosity. This effect is also evident in Fig. 16, where the 1D projection of the effective parameters is displayed.

In this test case, the phase fields ϕ_l^0 and ϕ_r^0 are both asymmetric and for this reason, the expected results are anisotropic effective tensors. The non-diagonal components of \mathbb{A} and \mathbb{K} are however close to zero and can be neglected. In Fig. 16 we

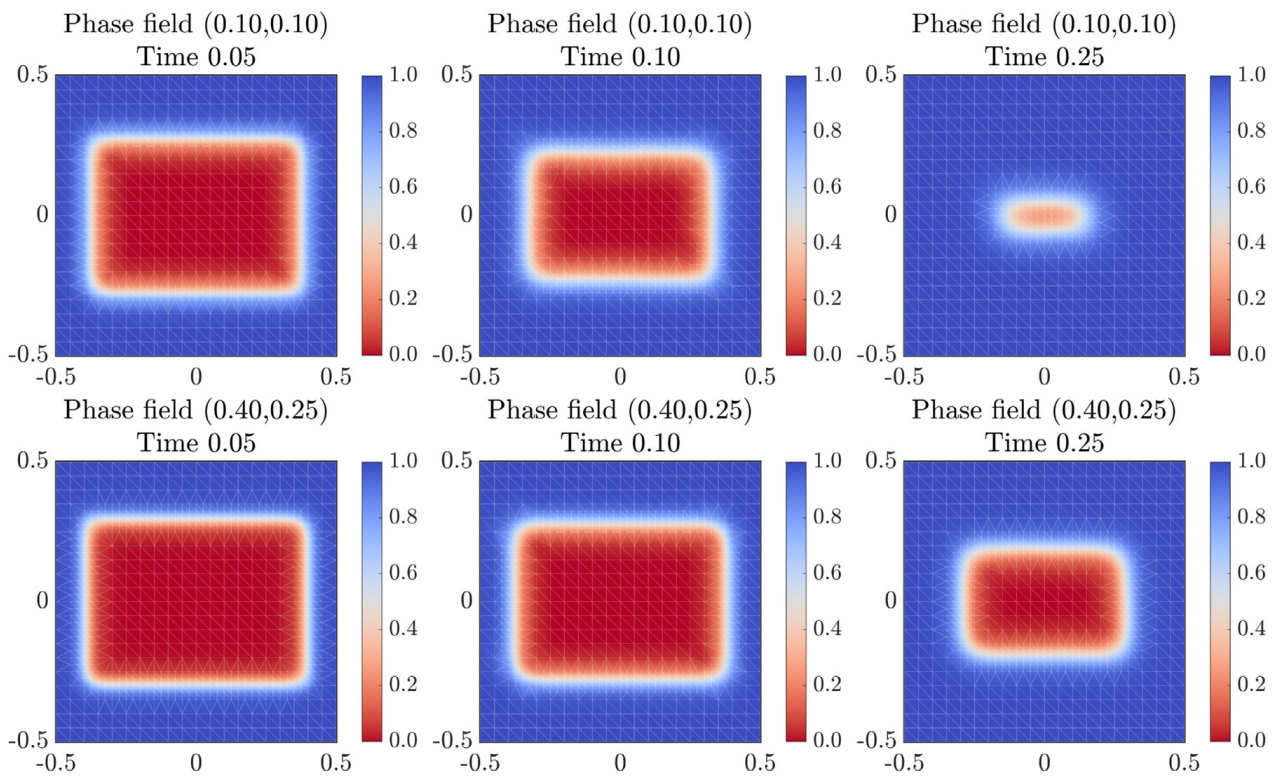


Fig. 13. The evolution of the phase fields ϕ_i corresponding to the macro-scale locations $\mathbf{x} = (0.1, 0.1)$ (top) and $\mathbf{x} = (0.4, 0.25)$ (bottom) at three times $t^n = 0.05, 0.10$ and 0.25 (left to right).

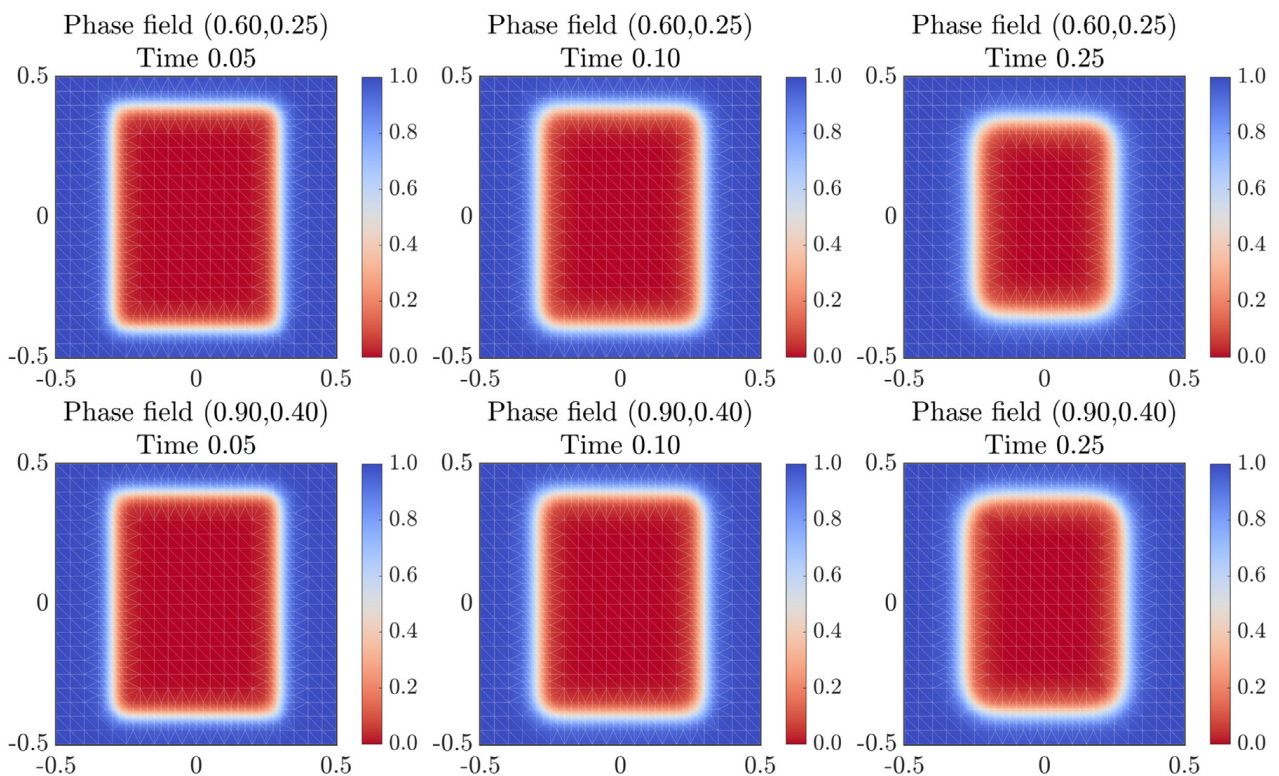


Fig. 14. The evolution of the phase fields ϕ_i corresponding to the macro-scale locations $\mathbf{x} = (0.6, 0.25)$ (top) and $\mathbf{x} = (0.9, 0.4)$ (bottom) at three times $t^n = 0.05, 0.10$ and 0.25 (left to right).

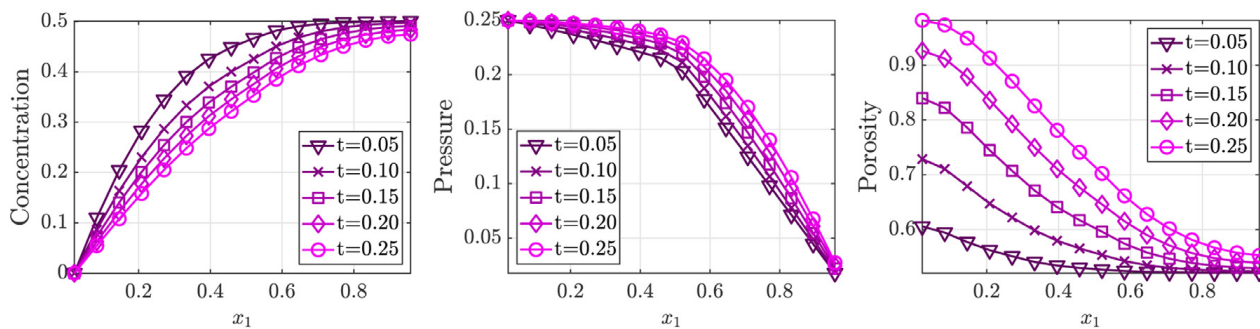


Fig. 15. The 1D projection of the concentration $u^n(\mathbf{x})$, pressure $p(\mathbf{x})$ and porosity $\bar{\phi}(\mathbf{x})$ for five different times.

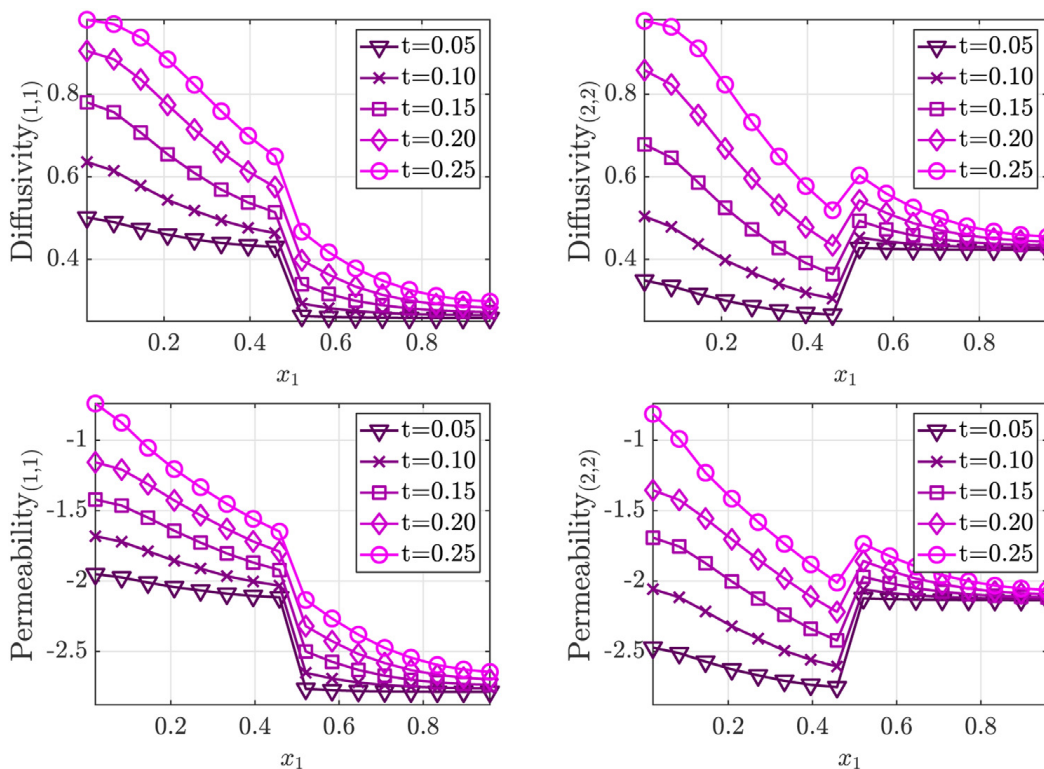


Fig. 16. The 1D projection of the diagonal components of effective diffusion tensor (top) and the effective permeability tensor (Log_{10}) (bottom) for five different times.

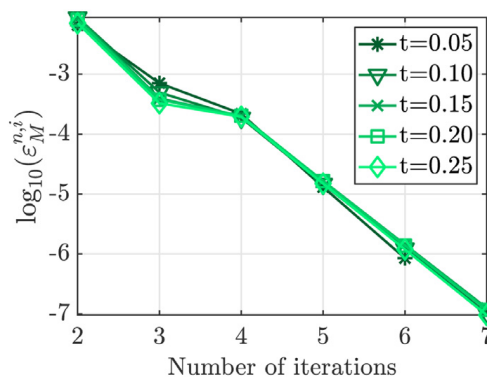


Fig. 17. The convergence of the two-scale iterative scheme for five different times.

display the diagonal components of both effective tensors. Notice the discontinuous behavior of the effective parameters as a result of the macro-scale heterogeneous distribution.

In the 2D macro-scale domain we have 256 elements. The porosity and the effective parameters must be updated only on the 32 elements located at the lowest part of the domain (1D projection) and copied (transferred in a sense explained in Section 6) over the whole 2D macro-scale domain. Following this, we obtain that the average number of degrees of freedom in both scales is 213 031 per time step.

Finally, in Fig. 17, we show the convergence of $\epsilon_M^{n,i}$ at different times when the stopping criterion is $tol_M = 1E-6$. Notice that in this test case the total number of iterations remains constant in time and the convergence is shown to be linear.

8. Conclusions

We have presented a two-scale iterative strategy that can be applied to models involving coupling of scales. In particular, we used this two-scale iterative scheme to solve the two-scale phase-field model proposed in Bringedal et al. [27]. In the numerical examples we show how the changes within the micro-scale geometry are influencing the macro-scale parameters and the macro-scale solution.

We calculate macro-scale quantities that are valid at the Darcy scale. Besides the macro-scale concentration and pressure, we calculate effective permeability, diffusivity, and porosity, which depend on the evolution of the phase field at the micro scale. We have proven the convergence of the two-scale iterative scheme and combined it with a robust micro-scale linearization strategy and adaptive strategies on both scales. We use mesh refinement to reduce the numerical error in the solution of the phase-field evolution on the micro scale. For the macro scale, our adaptive strategy aims to localize where the effective parameters need to be recalculated. The two-scale iterative scheme is shown to be convergent under a certain choice on the coupling parameter $\mathcal{L}_{\text{coup}}$ and for sufficiently small time steps. However, the numerical examples show that the scheme converges under even milder restrictions on the coupling parameter $\mathcal{L}_{\text{coup}}$ and the linearization parameter \mathcal{L}_{lin} .

Moreover, our numerical scheme can be parallelized. The local cell problems related to the micro scale are decoupled and can straightforwardly be solved in parallel.

It is relevant to mention that besides the theory considered in this paper, the applicability of this strategy is vast. Extensions of our adaptive algorithm, including more complex micro-scale models, are possible. Also, in a further step the convergence proof of the two-scale numerical scheme including the flow will be considered. Moreover, we pursue the rigorous proofs of the essential boundedness of the gradients of the macro-scale solution and the solution of the cell problems.

Acknowledgments

We thank Kundan Kumar, Markus Gahn, Thomas Wick and Florin Adrian Radu who contributed to the ideas behind this manuscript. This research is supported by the Research Foundation - Flanders (FWO) through the Odysseus programme (Project G0G1316N) and by the German Research Foundation (DFG) through the SFB 1313, Project Number 327154368. The resources and services used in this work were provided by the VSC (Flemish Supercomputer Center), funded by the Research Foundation - Flanders (FWO) and the Flemish Government.

References

- [1] P. Knabner, C. van Duijn, S. Hengst, An analysis of crystal dissolution fronts in flows through porous media. Part 1: compatible boundary conditions, *Adv. Water Resour.* 18 (3) (1995) 171–185, doi:10.1016/0309-1708(95)00005-4.
- [2] P. Moszkowicz, J. Pousin, F. Sanchez, Diffusion and dissolution in a reactive porous medium: mathematical modelling and numerical simulations, *J. Comput. Appl. Math.* 66 (1–2) (1996) 377–389, doi:10.1016/0377-0427(95)00192-1.
- [3] N. Bouillard, R. Eymard, R. Herbin, P. Montarnal, Diffusion with dissolution and precipitation in a porous medium: mathematical analysis and numerical approximation of a simplified model, *ESAIM Math. Model. Numer. Anal.* 41 (6) (2007) 975–1000, doi:10.1051/m2an:2007047.
- [4] K. Kumar, I.S. Pop, F.A. Radu, Convergence analysis for a conformal discretization of a model for precipitation and dissolution in porous media, *Numer. Math.* 127 (4) (2014) 715–749, doi:10.1007/s00211-013-0601-1.
- [5] A. Agosti, L. Formaggia, A. Scotti, Analysis of a model for precipitation and dissolution coupled with a Darcy flux, *J. Math. Anal. Appl.* 431 (2) (2015) 752–781, doi:10.1016/j.jmaa.2015.06.003.
- [6] K. Kumar, M. Neuss-Radu, I.S. Pop, Homogenization of a pore scale model for precipitation and dissolution in porous media, *IMA J. Appl. Math.* 81 (5) (2016) 877–897, doi:10.1093/imamat/hxw039.
- [7] J. Hoffmann, S. Kräutle, P. Knabner, Existence and uniqueness of a global solution for reactive transport with mineral precipitation-dissolution and aquatic reactions in porous media, *SIAM J. Math. Anal.* 49 (6) (2017) 4812–4837, doi:10.1137/16m1109266.
- [8] T. van Noorden, Crystal precipitation and dissolution in a thin strip, *Eur. J. Appl. Math.* 20 (1) (2009) 69–91, doi:10.1017/s0956792508007651.
- [9] K. Kumar, T. van Noorden, I.S. Pop, Effective dispersion equations for reactive flows involving free boundaries at the microscale, *Multiscale Model. Simul.* 9 (1) (2011) 29–58, doi:10.1137/100804553.
- [10] T. van Noorden, I.S. Pop, A Stefan problem modelling crystal dissolution and precipitation, *IMA J. Appl. Math.* 73 (2) (2008) 393–411, doi:10.1093/imamat/hxm060.
- [11] A. Muntean, M. Böhm, A moving-boundary problem for concrete carbonation: global existence and uniqueness of weak solutions, *J. Math. Anal. Appl.* 350 (1) (2009) 234–251, doi:10.1016/j.jmaa.2008.09.044.
- [12] K. Kumazaki, A. Muntean, Global weak solvability, continuous dependence on data, and large time growth of swelling moving interfaces., *Interface Free Bound.* 22 (1) (2020) 27–50, doi:10.4171/ifb/431.
- [13] K. Kumar, M.F. Wheeler, T. Wick, Reactive flow and reaction-induced boundary movement in a thin channel, *SIAM J. Sci. Comput.* 35 (6) (2013), doi:10.1137/130913134. B1235-B1266
- [14] S. Mabuza, D. Kuzmin, S. Čanić, M. Bukač, A conservative, positivity preserving scheme for reactive solute transport problems in moving domains, *J. Comput. Phys.* 276 (2014) 563–595, doi:10.1016/j.jcp.2014.07.049.

- [15] S. Mabuza, D. Kuzmin, A nonlinear ALE-FCT scheme for non-equilibrium reactive solute transport in moving domains, *Int. J. Numer. Methods Fluids* 76 (11) (2014) 875–908, doi:[10.1002/fld.3961](https://doi.org/10.1002/fld.3961).
- [16] S. Mabuza, S. Čanić, B. Muha, Modeling and analysis of reactive solute transport in deformable channels with wall adsorption-desorption, *Math. Methods Appl. Sci.* 39 (7) (2016) 1780–1802, doi:[10.1002/mma.3601](https://doi.org/10.1002/mma.3601).
- [17] B. Muha, S. Čanić, Existence of a weak solution to a nonlinear fluid-structure interaction problem modeling the flow of an incompressible, viscous fluid in a cylinder with deformable walls, *Arch. Rational Mech. Anal.* 207 (2013) 919–968, doi:[10.1007/s00205-012-0585-5](https://doi.org/10.1007/s00205-012-0585-5).
- [18] C. Bringedal, I. Berre, I.S. Pop, F.A. Radu, A model for non-isothermal flow and mineral precipitation and dissolution in a thin strip, *J. Comput. Appl. Math.* 289 (2015) 346–355, doi:[10.1016/j.cam.2014.12.009](https://doi.org/10.1016/j.cam.2014.12.009).
- [19] T. van Noorden, Crystal precipitation and dissolution in a porous medium: effective equations and numerical experiments, *Multiscale Model. Simul.* 7 (3) (2009) 1220–1236, doi:[10.1137/080722096](https://doi.org/10.1137/080722096).
- [20] R. Schulz, N. Ray, F. Frank, H. Mahato, P. Knabner, Strong solvability up to clogging of an effective diffusion-precipitation model in an evolving porous medium, *Eur. J. Appl. Math.* 28 (2) (2017) 179–207, doi:[10.1017/S0956792516000164](https://doi.org/10.1017/S0956792516000164).
- [21] R. Schulz, N. Ray, S. Zech, A. Rupp, P. Knabner, Beyond Kozeny–Carman: predicting the permeability in porous media, *Transp. Porous Med.* 130 (2) (2019) 487–512, doi:[10.1007/s11242-019-01321-y](https://doi.org/10.1007/s11242-019-01321-y).
- [22] C. Bringedal, I. Berre, I.S. Pop, F.A. Radu, Upscaling of non-isothermal reactive porous media flow with changing porosity, *Transp. Porous Med.* 114 (2) (2016) 371–393, doi:[10.1007/s11242-015-0530-9](https://doi.org/10.1007/s11242-015-0530-9).
- [23] G. Caginalp, P.C. Fife, Dynamics of layered interfaces arising from phase boundaries, *SIAM J. Appl. Math.* 48 (3) (1988) 506–518, doi:[10.1137/0148029](https://doi.org/10.1137/0148029).
- [24] A. Rätz, Diffuse-interface approximations of osmosis free boundary problems, *SIAM J. Appl. Math.* 76 (3) (2016) 910–929, doi:[10.1137/15m1025001](https://doi.org/10.1137/15m1025001).
- [25] T. van Noorden, C. Eck, Phase field approximation of a kinetic moving-boundary problem modelling dissolution and precipitation, *Interface Free Bound.* 13 (1) (2011) 29–55, doi:[10.4171/ifb/247](https://doi.org/10.4171/ifb/247).
- [26] M. Redeker, C. Rohde, I.S. Pop, Upscaling of a tri-phase phase-field model for precipitation in porous media, *IMA J. Appl. Math.* 81 (5) (2016) 898–939, doi:[10.1093/imamat/hxw023](https://doi.org/10.1093/imamat/hxw023).
- [27] C. Bringedal, L. von Wolff, I.S. Pop, Phase field modeling of precipitation and dissolution processes in porous media: upscaling and numerical experiments, *Multiscale Model. Simul.* 18 (2) (2020) 1076–1112, doi:[10.1137/19m1239003](https://doi.org/10.1137/19m1239003).
- [28] M. Redeker, B. Haasdonk, A POD-EIM reduced two-scale model for precipitation in porous media, *Math. Comput. Model. Dyn. Syst.* 22 (4) (2016) 323–344, doi:[10.1080/13873954.2016.1198384](https://doi.org/10.1080/13873954.2016.1198384).
- [29] Y. Efendiev, T.Y. Hou, *Multiscale Finite Element Methods: Theory and Applications*, 4, Springer Science and Business Media, 2009.
- [30] B. Engquist, X. Li, W. Ren, E. Vanden-Eijnden, Heterogeneous multiscale methods: a review, *Commun. Comput. Phys.* 2 (3) (2007) 367–450.
- [31] S. Gärtner, P. Frolkovič, P. Knabner, N. Ray, Efficiency and accuracy of micro-macro models for mineral dissolution, *Water Resour. Res.* 56 (8) (2020), doi:[10.1029/2020wr027585](https://doi.org/10.1029/2020wr027585).
- [32] N. Ray, J. Oberlander, P. Frolkovic, Numerical investigation of a fully coupled micro-macro model for mineral dissolution and precipitation, *Comput. Geosci.* 23 (5) (2019) 1173–1192, doi:[10.1007/s10596-019-09876-x](https://doi.org/10.1007/s10596-019-09876-x).
- [33] M. Bastidas, C. Bringedal, I.S. Pop, Numerical simulation of a phase-field model for reactive transport in porous media, *Numerical Mathematics and Advanced Applications ENUMATH 2019, Lecture Notes in Computational Science and Engineering*, 139, Springer International, 2020.
- [34] M.K. Brun, T. Wick, I. Berre, J.M. Nordbotten, F.A. Radu, An iterative staggered scheme for phase field brittle fracture propagation with stabilizing parameters, *Comput. Methods Appl. Mech. Eng.* 361 (2020) 112752, doi:[10.1016/j.cma.2019.112752](https://doi.org/10.1016/j.cma.2019.112752).
- [35] M. Redeker, C. Eck, A fast and accurate adaptive solution strategy for two-scale models with continuous inter-scale dependencies, *J. Comput. Phys.* 240 (2013) 268–283, doi:[10.1016/j.jcp.2012.12.025](https://doi.org/10.1016/j.jcp.2012.12.025).
- [36] T. Heister, M.F. Wheeler, T. Wick, A primal-dual active set method and predictor-corrector mesh adaptivity for computing fracture propagation using a phase-field approach, *Comput. Methods Appl. Mech. Eng.* 290 (2015) 466–495, doi:[10.1016/j.cma.2015.03.009](https://doi.org/10.1016/j.cma.2015.03.009).
- [37] I.S. Pop, F.A. Radu, P. Knabner, Mixed finite elements for the Richards' equation: linearization procedure, *J. Comput. Appl. Math.* 168 (1–2) (2004) 365–373, doi:[10.1016/j.cam.2003.04.008](https://doi.org/10.1016/j.cam.2003.04.008).
- [38] F. List, F.A. Radu, A study on iterative methods for solving Richards' equation, *Comput. Geosci.* 20 (2) (2016) 341–353, doi:[10.1007/s10596-016-9566-3](https://doi.org/10.1007/s10596-016-9566-3).
- [39] X. Chen, D. Hilhorst, E. Logak, Mass conserving Allen–Cahn equation and volume preserving mean curvature flow, *Interface Free Bound.* 12 (4) (2011) 527–549, doi:[10.4171/ifb/244](https://doi.org/10.4171/ifb/244).
- [40] C. Bringedal, A conservative phase-field model for reactive transport, in: R. Klöforn, E. Keilegavlen, A.F. Radu, J. Fuhrmann (Eds.), *Finite Volumes for Complex Applications IX - Methods, Theoretical Aspects, Examples*, Springer Proceedings in Mathematics and Statistics, 323, Springer International Publishing, 2020, pp. 537–545, doi:[10.1007/978-3-030-43651-3_50](https://doi.org/10.1007/978-3-030-43651-3_50).
- [41] H. Garcke, C. Hecht, M. Hinze, C. Kahle, Numerical approximation of phase field based shape and topology optimization for fluids, *SIAM J. Sci. Comput.* 37 (4) (2015) A1846–A1871, doi:[10.1137/140969269](https://doi.org/10.1137/140969269).
- [42] F. Frank, C. Liu, F.O. Alpak, B. Riviere, A finite volume/discontinuous galerkin method for the advective Cahn–Hilliard equation with degenerate mobility on porous domains stemming from micro-ct imaging, *Comput. Geosci.* 22 (2) (2018) 543–563, doi:[10.1007/s10596-017-9709-1](https://doi.org/10.1007/s10596-017-9709-1).
- [43] A. Mikić, M.F. Wheeler, Convergence of iterative coupling for coupled flow and geomechanics, *Comput. Geosci.* 17 (3) (2013) 455–461, doi:[10.1007/s10596-012-9318-y](https://doi.org/10.1007/s10596-012-9318-y).
- [44] A. Friedman, A.E. Tzavaras, Combustion in a porous medium, *SIAM J. Math. Anal.* 19 (3) (1988) 509–519, doi:[10.1137/0519036](https://doi.org/10.1137/0519036).
- [45] A. Friedman, P. Knabner, A transport model with micro and macro-structure, *J. Differ. Equ.* 98 (2) (1992) 328–354, doi:[10.1016/0022-0396\(92\)90096-6](https://doi.org/10.1016/0022-0396(92)90096-6).
- [46] A. Muntean, M. Neuss-Radu, A multiscale Galerkin approach for a class of nonlinear coupled reaction-diffusion systems in complex media, *J. Math. Anal. Appl.* 371 (2) (2010) 705–718, doi:[10.1016/j.jmaa.2010.05.056](https://doi.org/10.1016/j.jmaa.2010.05.056).
- [47] R. Schulz, Degenerate equations in a diffusion-precipitation model for clogging porous media, *Eur. J. Appl. Math.* (2019) 1–20, doi:[10.1017/s0956792519000391](https://doi.org/10.1017/s0956792519000391).
- [48] R. Schulz, Degenerate equations for flow and transport in clogging porous media, *J. Math. Anal. Appl.* 483 (2) (2020) 123613, doi:[10.1016/j.jmaa.2019.123613](https://doi.org/10.1016/j.jmaa.2019.123613).
- [49] C. Bringedal, K. Kumar, Effective behavior near clogging in upscaled equations for non-isothermal reactive porous media flow, *Transp. Porous Med.* 120 (3) (2017) 553–577, doi:[10.1007/s11242-017-0940-y](https://doi.org/10.1007/s11242-017-0940-y).
- [50] O.A. Ladyzhenskaya, N.N. Ural'tseva, *Linear and Quasilinear Elliptic Equations, Mathematics In Science And Engineering*, 46, Academic Press New York And London, 1968.
- [51] N. Ray, A. Rupp, R. Schulz, P. Knabner, Old and new approaches predicting the diffusion in porous media, *Transp. Porous Med.* 124 (3) (2018) 803–824, doi:[10.1007/s11242-018-1099-x](https://doi.org/10.1007/s11242-018-1099-x).
- [52] D. Cioranescu, P. Donato, *An Introduction to Homogenization*, 17, Oxford University Press Oxford, 1999.
- [53] E. Storvik, J.W. Both, K. Kumar, J.M. Nordbotten, F.A. Radu, On the optimization of the fixed-stress splitting for Biot's equations, *Int. J. Numer. Methods Eng.* 120 (2) (2019) 179–194, doi:[10.1002/nme.6130](https://doi.org/10.1002/nme.6130).
- [54] C. Bahriawati, C. Carstensen, Three matlab implementations of the lowest-order Raviart–Thomas MFEM with a posteriori error control, *Comput. Methods Appl. Math.* 5 (4) (2005) 333–361, doi:[10.2478/cmam-2005-0016](https://doi.org/10.2478/cmam-2005-0016).
- [55] D. Boffi, F. Brezzi, M. Fortin, *Mixed Finite Element Methods and Applications*, 44, Springer, 2013.

10 Comparison of level-set and phase-field models for three-phase systems

The content of this chapter is based on the following original article:

M. Kelm, S. Gärttner, C. Bringedal, B. Flemisch, P. Knabner, N. Ray. *Comparison study of phase-field and level-set method for three-phase systems including two minerals*. Computational Geosciences (2022). doi: 10.1007/s10596-022-10142-w

This publication is an open access article and distributed under the Creative Commons CC BY license.



Comparison study of phase-field and level-set method for three-phase systems including two minerals

Mathis Kelm¹ · Stephan Gärttner² · Carina Bringedal¹ · Bernd Flemisch¹ · Peter Knabner^{2,3} · Nadja Ray²

Received: 22 July 2021 / Accepted: 11 March 2022
© The Author(s) 2022

Abstract

We investigate reactive flow and transport in evolving porous media. Solute species that are transported within the fluid phase are taking part in mineral precipitation and dissolution reactions for two competing mineral phases. The evolution of the three phases is not known a-priori but depends on the concentration of the dissolved solute species. To model the coupled behavior, phase-field and level-set models are formulated. These formulations are compared in three increasingly challenging setups including significant mineral overgrowth. Simulation outcomes are examined with respect to mineral volumes and surface areas as well as derived effective quantities such as diffusion and permeability tensors. In doing so, we extend the results of current benchmarks for mineral dissolution/precipitation at the pore-scale to the multiphase solid case. Both approaches are found to be able to simulate the evolution of the three-phase system, but the phase-field model is influenced by curvature-driven motion.

Keywords Pore-scale · Moving boundary · Reactive transport · Phase-field method · Level-set method · Multiphase solid

1 Introduction

Porous media research is conducted from different spatial perspectives such as the pore-scale or the macro-scale. At the pore-scale different fluid and solid phases can be distinguished and their respective interfaces are directly accessible. Macro-scale models, on the contrary, contain parameters such as permeability, effective diffusivity, and reactive surface area. These are obtained by fitting experimental data, applying heuristic laws, or conducting supplementary pore-scale simulations. In the latter case, an accurate knowledge and correct representation of the spatial distribution of the fluid and solid phases and their interfaces are again essential, in particular if they evolve with time. This can

typically be caused by minerals dissolving or precipitating, in case the alteration of the mineral layer is non-negligible. When the evolution of the fluid-solid interface depends on a solute concentration transported in the fluid, the evolution is not known a-priori and we have a free-boundary problem. To capture such evolving pore-scale geometries, most commonly level-set or phase-field methods are applied. The level-set method captures interfaces separating different phases as lower dimensional submanifolds within the computational domain, while the phase-field approach utilizes smoothed indicator functions for phase separation.

A comparison of level-set and phase-field methods in the context of precipitation/dissolution of a solute is found in [34]. Likewise, various approaches including level-set and phase-field methods were recently investigated in benchmark scenarios for mineral dissolution in [20]. Furthermore, both geometry evolution methods were compared regarding their respective strengths and weaknesses for the simulation of multi-phase flow problems on fixed domains in [2]. In contrast to these considerations, we apply the two approaches and compare them in the situation of a three-phase system. Extending a phase-field model to the ternary case is feasible through generalizing the usual double-well potential to a triple-well. Applications to three-phase flow [4, 5] and two-phase flow together with one evolving solid phase [25, 26] have earlier been derived and analyzed,

✉ Mathis Kelm
mathis.kelm@iws.uni-stuttgart.de

¹ Institute for Modelling Hydraulic and Environmental Systems, University of Stuttgart, Pfaffenwaldring 61, 70569, Stuttgart, Germany

² Department of Mathematics, Friedrich-Alexander Universität Erlangen-Nürnberg, Cauerstr. 11, 91058, Erlangen, Germany

³ Stuttgart Center for Simulation Science (SC SimTech), University of Stuttgart, Pfaffenwaldring 5a, 70569, Stuttgart, Germany

and we here extend these approaches to the case of one fluid phase and two competing minerals. In this setting, we compare the level-set and phase-field approaches by means of simulation scenarios, but also in terms of sharp-interface limits. For modeling issues related to the case of one fluid phase and two mineral phases we refer to [13] in the context of level-set and to [15] in the context of phase-field approaches.

Contrary to the two-phase system, in which only one fluid phase and one mineral phase are present, interfaces are likely to develop high local curvature in three-phase systems even for regular initial conditions. Thus, their numerical treatment poses additional challenges in particular in the proximity of possible triple points. For the level-set approach, we apply the Voronoi Implicit Interface Method (VIIM) as presented in [10, 13, 29]. This method has been successfully applied to several physical problems such as curvature flow, multi-phase fluid flow and foam dynamics [29]. The phase-field equations do not need any particular tracking of interfaces and triple points, but the Allen-Cahn phase fields, which are considered here, include implicitly curvature-driven motion of the diffuse interfaces [3], which can lead to unwanted effects [30].

Inspired by [9, 20], three scenarios with increasing complexity are studied. First, the ordinary differential equations (ODEs) related to a dissolution-precipitation reaction system are examined together with the corresponding evolving pore-scale geometry. Thereafter, the model is extended to additionally cover diffusive transport processes. Finally, single-phase fluid flow and advective transport are included into the model.

For all three scenarios, characteristic quantities such as the volume occupied by the individual mineral phases, the mass of the mobile species and the mineral's surface area are investigated and compared. Moreover, the time-dependence of the corresponding effective diffusion and permeability tensors is additionally evaluated.

The paper is outlined as follows: In Section 2, we introduce the chemical reaction system under investigation as well as the transport and flow model in their level-set and phase-field formulation. Additionally, the sharp-interface limits are discussed briefly. This is followed by a description of the numerical methods used for both approaches in Section 3. In Section 4, we compare and discuss the simulation results of all three scenarios including characteristic quantities and the evaluation of the effective diffusion and permeability tensors. Finally, in Section 5, we point out directions for further research.

2 Mathematical modeling

For an overview of quantities used in this paper, see Table 1. We consider a three-phase system in the two-dimensional,

Table 1 Overview of quantities used. Units are abbreviated as follows: L - length, M - mass, N - number (of particles), T - time

Symbol	Quantity	Unit
A,B,C	solute species	–
χ	indicator function	–
c	concentration	NL^{-3}
D,P	mineral species	–
D_m	(molecular) diffusion coefficient	L^2T^{-1}
ϵ	level-set parameter	–
f_D, f_P	reaction rates	LT^{-1}
g	velocity interpolation	$ML^{-3}T^{-1}$
γ_{ij}	interface indicator	L
$\Gamma_{\text{int,D}}, \Gamma_{\text{int,P}}$	fluid-mineral interfaces	–
$\Gamma_{\text{int,M}}$	mineral-mineral interface	–
k_D, k_P	reaction constants	LT^{-1}
K_D, K_P	equilibrium constants	–, L^6N^{-2}
κ	interface curvature	L^{-1}
μ	fluid viscosity	$ML^{-1}T^{-1}$
Ω	total domain	–
Ω_f	fluid domain	–
Ω_s	solid domain	–
ω	phase-field diffusivity	L^2T^{-1}
p	Stokes pressure	$ML^{-1}T^{-2}$
ϕ_i	phase-field function	–
Φ	level-set function	–
\mathbf{q}	advective velocity	LT^{-1}
ρ_D, ρ_P	mineral densities	NL^{-3}
σ	specific surface area	L^{-1}
V	volume	L^3
v_n	normal interface velocity	LT^{-1}
W	well potential	–
ξ	diffuse-interface width	L

rectangular domain $\Omega = (0, 1) \times (0, 1)$ with exterior boundary $\partial\Omega$. More precisely, the domain Ω is time-dependently decomposed into the fluid domain $\Omega_f(t)$ and the solid part $\Omega_s(t)$ for all times t in the time interval $(0, T)$. At initial time $t = 0$, the solid $\Omega_s(0)$ comprises two different mineral phases denoted D and P, cf. Figure 1. The fluid-solid interface (interior boundary of $\Omega_f(t)$) is disjointed into $\Gamma_{\text{int,D}}(t)$ and $\Gamma_{\text{int,P}}(t)$ accordingly. Furthermore, we denote the interface separating the two minerals by $\Gamma_{\text{int,M}}(t)$.

The fluid-solid interfaces and mineral phases individually evolve with time according to heterogeneous reactions which are specific to the two minerals, cf. Section 2.1 below. The mobile reaction partners may potentially be transported within the fluid domain $\Omega_f(t)$ by molecular diffusion and advection.

In this paper, we investigate the following three situations of increasing complexity:

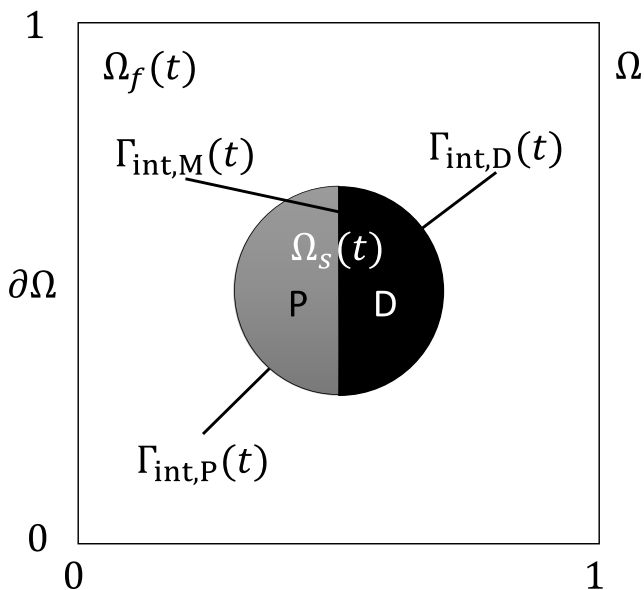


Fig. 1 Geometrical set up: The unit square Ω is time-dependently decomposed into the fluid domain $\Omega_f(t)$ and the solid part $\Omega_s(t)$ consisting of two different minerals P (gray) and D (black). Different parts of the phase-separating interior interfaces are denoted as $\Gamma_{\text{int},\dots}$. The figure reflects the geometrical initial conditions used in our simulations, see Section 4

First, the reaction system for precipitation and dissolution of the mineral phases is investigated. Disregarding diffusive and advective transport, the temporal evolution of the mobile species' concentrations within the fluid domain is described using ordinary differential equations (ODEs). Accordingly, the interface parts $\Gamma_{\text{int},D}$ and $\Gamma_{\text{int},P}$ each move with spatially uniform but time-dependent velocity. Since this approach does not resolve the potential spatial distribution of the concentration fields, it is only a valid approximation for regimes featuring strong diffusion and slow reactions. In the single-mineral case, such a simple setting with uniform interface velocity would not require a level-set nor a phase-field formulation, as an ODE for the mineral radius would be sufficient to describe the evolving geometry. Such a simplified approach was for instance first investigated in [21]. However, due to the interactions between the two competing minerals, level sets or phase fields are needed to resolve the geometry in the more complex two-mineral setting.

Secondly, we additionally resolve the spatial distribution of the concentrations. To this end, we consider a transport equation for the mobile chemical species including molecular diffusion and describe the chemical reactions as surface reactions on the two distinct fluid-solid interfaces (level-set approach) or highly localized volume reactions neighboring phase boundaries (phase-field approach). As the resulting chemical reactions are no longer uniform with respect to space, the geometry evolution becomes more challenging

and results in the formation of complex mineral shapes. This again requires the usage of sophisticated methods in terms of modeling and numerics, also for the single-mineral case, as provided by means of a level-set or phase-field approach [21, 22].

In our final simulation scenario, we additionally include the transport of the mobile species by advection. The related division of the interfaces into upwind and downwind parts with respect to the flow direction further increases the complexity of the solid-solute interaction and the evolution of the mineral shapes. Along these lines, we underline the capability of the level-set and phase-field methods.

Finally, the time dependence of the effective diffusion and permeability tensors is evaluated for all three scenarios. Based on upscaling theory, auxiliary cell problems are solved and their (flux) solutions are averaged as described in Section 4.2.2 for the level-set and phase-field approach.

In all settings, the chemical reactions drive the evolution of the pore-space geometry into an equilibrium state. In order to capture this evolution, level-set and phase-field methods are applied and compared. For a detailed description of the modeling and implementation details see Sections 2.2 and 3.1 for the level-set approach and Sections 2.3 and 3.2 for the phase-field approach, respectively.

2.1 Chemical reactions

In this section, we present the chemical setup of concern. We consider a reaction system describing dissolution/precipitation, e.g. the carbonation of silicates, as introduced in [9]. This involves the dissolving mineral D and the precipitating mineral P as well as mobile species A, B, C with reaction paths



The reaction kinetics are chosen according to the classical law of mass action for a one-sided chemical reaction by including the back reaction via an equilibrium condition, cf. (2), [9]. Since the chemical system in our simulations will be deflected in such a manner that both reaction paths in (1) effectively proceed in one direction from left to right, it is meaningful to refer to D as the dissolving mineral which will either dissolve or reach an equilibrium state when the net reaction rate is zero, while P denotes the precipitating mineral which will either precipitate or encounter zero net reaction rate. As this paper is mainly focused on the geometry evolution, we refrain from incorporating textbook data for a specific chemical system and formulate the equations without units. Nevertheless, dimensions are provided in order to clarify the physical meaning of the presented quantities, such as length L , mass M , number of particles N and time T . We use the following volumetric

reaction rates $[\text{LT}^{-1}]$ for the concentrations of the mobile species $\mathbf{c} = (c_A, c_B, c_C)^T$, $[\text{NL}^{-3}]$ as introduced in [9]

$$f_D(\mathbf{c}) = k_D \left(1 - K_D \frac{c_B}{c_A} \right), \quad (2a)$$

$$f_P(\mathbf{c}) = k_P (1 - K_P c_B c_C), \quad (2b)$$

with reaction constants k_D, k_P $[\text{LT}^{-1}]$ and equilibrium constants K_D [-], K_P $[\text{L}^6\text{N}^{-2}]$. Throughout this paper, precipitation of a mineral is assumed to occur on the surface of that mineral only. Hence, we do not consider nucleation.

Within the following sections, we introduce the three different modelling scenarios of increasing complexity each presented using a level-set and phase-field formulation.

2.2 Level-set formulation

In the level-set framework, we represent the geometry contained within the domain Ω using a real-valued function $\Phi : \mathbb{R}^2 \mapsto \mathbb{R}$, the level-set function [23, 29, 32]. For further details we refer to Section 3.

Accordingly, the time evolution induced by a space and time dependent normal velocity v_n is implemented by solving the following advection equation for the level-set function Φ

$$\frac{\partial \Phi}{\partial t} + v_n |\nabla \Phi| = 0, \quad \text{in } \Omega \times (0, T), \quad (3)$$

where the parameter $v_n : \mathbb{R}^2 \mapsto \mathbb{R}$, $[\text{LT}^{-1}]$ prescribes the normal velocity with which level sets are transported. For our application, we define:

$$v_n(t, x) = \begin{cases} v_{n,D}(t, x) = -f_D(\mathbf{c}(t, x)), & x \in \Gamma_{\text{int},D}(t), \\ v_{n,P}(t, x) = -f_P(\mathbf{c}(t, x)), & x \in \Gamma_{\text{int},P}(t). \end{cases} \quad (4)$$

Note that the normal velocities are defined only at the interfaces themselves and require to be suitably extended to the whole domain Ω , see Section 3.1 for details. Level-set models as derived here are well suited for formal upscaling into a two-scale model using periodic homogenization [13, 21].

2.2.1 ODE model

In the ODE case, the chemical reactions presented in Section 2.1 are modeled by a system of three coupled ODEs, one for each solute concentration. This approximation is suitable if negligible spatial variation in the concentrations is expected.

In order to obtain molar reaction rates from the volumetric quantities f_D, f_P $[\text{L}^3(\text{L}^2\text{T})^{-1}]$, we multiply by the molar density ρ_D, ρ_P $[\text{NL}^{-3}]$ of the reacting minerals. Assuming a closed system, concentrations additionally evolve driven by displacement as a secondary effect. That

is, precipitation leads to a shrinking fluid domain Ω_f and therefore an increasing concentration of all solute species while dissolution decreases concentrations. Summarizing, the total change of the species' concentrations is then given by the two volumetric reaction rates on the different mineral interfaces multiplied by the difference in particle density between solid and fluid, each scaled by the respective specific reactive surface area

$$\sigma_i(t) = |\Gamma_{\text{int},i}(t)| / |\Omega_f(t)| \quad [\text{L}^{-1}]$$

for $i \in \{D, P\}$. Note that this quantity is 'specific' with respect to the time-dependent fluid volume. These considerations lead to the following ODE system for the concentrations of the mobile species A,B,C:

$$\begin{aligned} \frac{\partial \mathbf{c}}{\partial t}(t) = & \sigma_D(t) f_D(\mathbf{c}(t)) \begin{pmatrix} -\rho_D - c_A(t) \\ \rho_D - c_B(t) \\ -c_C(t) \end{pmatrix} \\ & + \sigma_P(t) f_P(\mathbf{c}(t)) \begin{pmatrix} -c_A(t) \\ \rho_P - c_B(t) \\ \rho_P - c_C(t) \end{pmatrix}. \end{aligned} \quad (5)$$

The prescription of normal velocities according to (4) ensures the conservation of mass within our model. Furthermore, the level-set framework allows to conveniently obtain a piecewise-linear approximation of the phase-separating interfaces. As such, characteristic geometrical quantities such as phase volumes or interface lengths $\sigma_i(t)$ are simple to derive from the level-set function Φ at any time t , cf. Section 3.1.

2.2.2 Diffusion model

In contrast to the ODE case, we now include diffusive transport into our model, i.e. the vector of concentrations \mathbf{c} comprising the three mobile species A, B, C solves the following diffusion equation within the fluid domain $\Omega_f(t)$:

$$\frac{\partial \mathbf{c}}{\partial t} = \nabla \cdot (D_m \nabla \mathbf{c}), \quad (6)$$

using a scalar and uniform molecular diffusion $D_m > 0$, $[\text{L}^2\text{T}^{-1}]$. For convenience only, we suppose that the same diffusion coefficient applies for all mobile species.

In order to model the insertion or extraction of solute particles to or from the fluid domain due to the heterogeneous chemical reactions described in Section 2.1, we impose the following flux conditions at the two distinct parts $\Gamma_{\text{int},D}(t), \Gamma_{\text{int},P}(t)$ of the interior boundary:

$$D_m \frac{\partial \mathbf{c}}{\partial \nu}(t, x) = -v_{n,D}(t, x) \begin{pmatrix} -\rho_D - c_A(t, x) \\ \rho_D - c_B(t, x) \\ -c_C(t, x) \end{pmatrix}, \quad (7)$$

$$x \in \Gamma_{\text{int},D}(t),$$

$$D_m \frac{\partial \mathbf{c}}{\partial \nu}(t, x) = -v_{n,P}(t, x) \begin{pmatrix} -c_A(t, x) \\ \rho_P - c_B(t, x) \\ \rho_P - c_C(t, x) \end{pmatrix}, \quad (8)$$

$$x \in \Gamma_{\text{int},P}(t),$$

using the normal interface velocities $v_{n,i}$, $i \in \{D,P\}$ from (4). As such, the solute species concentrations are coupled to the geometry via time-dependent interior boundaries. The back coupling from the concentrations to the geometry is again realized by equations (4).

2.2.3 Flow model

In order to additionally account for an advective flux, we consider

$$\frac{\partial \mathbf{c}}{\partial t} = \nabla \cdot (D_m \nabla \mathbf{c}) - \nabla \cdot (\mathbf{q} \otimes \mathbf{c}) \quad (9)$$

in $\Omega_f(t)$ with advective velocity field \mathbf{q} [LT^{-1}] in our final example. For a matrix in column representation $A = (a^{(1)}, \dots, a^{(n)})$ we define $\nabla \cdot A = (\nabla \cdot a^{(i)})_i$ as the column-wise divergence. The boundary conditions supplementing (9) are again (7)–(8) as no advective flux is considered traversing the interior boundary, cf. (11). The velocity field is given by the solution of the stationary, incompressible Stokes problem

$$\begin{aligned} -\mu \Delta \mathbf{q} + \nabla p &= 0 \text{ in } \Omega_f(t), \\ \nabla \cdot \mathbf{q} &= 0 \text{ in } \Omega_f(t), \end{aligned} \quad (10)$$

with viscosity $\mu > 0$, [$\text{ML}^{-1}\text{T}^{-1}$] and the related pressure field p , [$\text{ML}^{-1}\text{T}^{-2}$]. In this example, boundary conditions are chosen as follows:

$$\mathbf{q}(t, x) = 0, \quad x \in \Gamma_{\text{int}}(t) \quad (11)$$

using $\Gamma_{\text{int}}(t) = \Gamma_{\text{int},D}(t) \cup \Gamma_{\text{int},P}(t)$. Note that using the above no-slip condition at the solid-fluid interface, potential non-zero fluid velocity in the normal direction at the boundary is disregarded. Depending on the density differences between solute and minerals, some small non-zero velocity could appear in the normal direction [21]. Neglecting this non-zero normal component is justified in most applications since the solid-fluid interface velocity is small compared to the fluid flow as discussed in [18].

2.3 Phase-field formulation

The phase-field formulation does not consider sharp interfaces between the different physical phases but instead models them using regularised characteristic functions. These so-called phase-field variables ϕ_i [-] (for $i = 1, 2, 3$) are evolved such that they always sum to 1. With these phase

fields, we aim to approximate the equations of the level-set formulation in order to describe the same physical system as presented in Section 2.2. In our setup, ϕ_1 corresponds to the fluid phase, ϕ_2 to the mineral phase D, and ϕ_3 to the mineral phase P. Within each bulk phase the corresponding phase field is equal to (or close to) 1, with all other phase-field functions being equal to (or close to) 0.

Near the interface of two phases the respective phase fields transition smoothly between 0 and 1. The width of this diffuse-interface regions is regulated by the phase-field parameter $\xi > 0$ [L] and a limit process for $\xi \rightarrow 0$ in Section 2.3.4 is able to recover a sharp-interface formulation corresponding to the one used in the level-set model above but with an additional term corresponding to curvature-driven interface evolution. The position of the interface can be approximated by the contour line of $\phi_i = 0.5$ or be recovered using a Voronoi method as for the level-set formulation. However, the simulation itself does not require such a reconstruction. Instead, the diffuse-interface region is captured by indicator functions γ_{ij} and in these regions the chemical reactions impact the evolution of the phase-field variables. The variables for the dissolved concentrations are defined on the entire domain Ω and the boundary flux conditions (7), (8) are integrated into the conservation equations.

Thus the interfaces need not be tracked and no special consideration is necessary for the description of contact lines and triple points. The phase-field model is well suited for upscaling into a two-scale model using periodic homogenization [6, 25].

We here use a phase-field model that is an extended version of the two models presented in [6, 25]. In [25] a ternary phase-field model (two fluids and one mineral) is considered, and our phase-field evolution equations resemble the model there. The model in [6] considers only two phases (one fluid and one mineral), but also allows flow in the fluid phase. Hence, our extension to flow in Section 2.3.3 builds on this model.

The phase-field variables are evolved using the Allen-Cahn formulation [3]. In addition to a diffusive term this includes derivatives of a fourth order polynomial called the triple-well potential:

$$W(\phi) = 2 \sum_{i=1}^3 \phi_i^2 (1 - \phi_i)^2. \quad (12)$$

Derivatives of this potential enforce the phase fields towards the values 0 and 1, while the diffusive term ensures a smooth, but steep transition between these values. The interface locations are captured using the indicator functions

$$\gamma_{ij}(t, x) = 4\xi \phi_i(t, x) \phi_j(t, x), \quad (13)$$

which attain their maximum for $\phi_i = \phi_j = 0.5$. These introduce a dependence of the phase fields on the chemical reactions by adding source terms

$$\begin{aligned}\hat{f}_1(t, x) &= -\hat{f}_2 - \hat{f}_3, \\ \hat{f}_2(t, x) &= \gamma_{12}(t, x) f_D(\mathbf{c}(t, x)), \\ \hat{f}_3(t, x) &= \gamma_{13}(t, x) f_P(\mathbf{c}(t, x)).\end{aligned}\quad (14)$$

Here, f_D and f_P are the respective reaction rates (2). With diffuse interface width ξ and diffusivity parameter ω [L^2T^{-1}] the evolution equations are ($i = 1, 2, 3$)

$$\xi^2 \frac{\partial \phi_i}{\partial t} - \omega \xi^2 \nabla^2 \phi_i = -\frac{8}{3} \omega \sum_{j \neq i} (\partial_{\phi_i} - \partial_{\phi_j}) W(\phi) + \hat{f}_i. \quad (15)$$

2.3.1 ODE model

As for the sharp-interface description with the level-set framework, the dissolved concentrations and thus the volumetric reaction rates and their contributions to the evolution of the geometry are first assumed to be independent of the spatial variable x . These concentrations could be evolved using the same system of ODEs (5), altering only the method of determining the specific surface area. In the phase-field model the interfaces are not tracked directly so the interfacial areas and the fluid volume would be computed as

$$\begin{aligned}V_f &= \int_{\Omega} \phi_1 \, dx, \\ V_D &= \int_{\Omega} \phi_2 \, dx, & V_P &= \int_{\Omega} \phi_3 \, dx, \\ S_D &= \int_{\Omega} 4\xi \phi_1 \phi_2 \, dx, & S_P &= \int_{\Omega} 4\xi \phi_1 \phi_3 \, dx, \\ \sigma_D &= S_D/V_f, & \sigma_P &= S_P/V_f.\end{aligned}\quad (16)$$

However, in the phase-field model the shift of the interfaces is not solely driven by the chemical reaction, but also by curvature of the interface. This would only impact the above system of ODEs by changing the fluid volume, altering the change to dissolved concentrations slightly. The loss of mineral volume and the corresponding change in dissolved species would not be directly captured in this case.

Instead of additionally approximating the geometric changes due to this curvature effect, we prescribe conservation of species in the entire domain rather than only within the fluid volume. Hence, our system of ODEs for the evolution of the solute concentrations is

$$\frac{\partial}{\partial t} (V_f \mathbf{c} + V_D \mathbf{b}_D + V_P \mathbf{b}_P) = 0, \quad (17)$$

where

$$\mathbf{b}_D = \rho_D(-1, 1, 0)^T, \quad \mathbf{b}_P = \rho_P(0, 1, 1)^T \quad (18)$$

capture the stoichiometric coefficients of the chemical reactions and molar densities ρ_D, ρ_P of the respective minerals.

When $\frac{\partial}{\partial t} V_D = \sigma_D V_f f_D$ and $\frac{\partial}{\partial t} V_P = \sigma_P V_f f_P$, this setup is equivalent to the system of ODEs used in the level-set formulation.

2.3.2 Diffusion model

With spatially resolved concentrations transported by diffusion, we adapt (6) to account for the phase distribution. Since the phase-field model is defined in the entire domain, we add terms accounting for the species bound in the minerals instead of using a boundary flux condition for the fluid-solid interfaces. The equations are given as

$$\frac{\partial(\phi_1 \mathbf{c})}{\partial t} + \frac{\partial \phi_2}{\partial t} \mathbf{b}_D + \frac{\partial \phi_3}{\partial t} \mathbf{b}_P = \nabla \cdot (\phi_1 D_m \nabla \mathbf{c}). \quad (19)$$

2.3.3 Flow model

To include fluid flow and advection of dissolved species in the phase-field model the (Navier-)Stokes (10) are modified to account for the distribution of phases, similar as done in [6]. The existing terms receive factors of the phase-field ϕ_1 while two new terms are added to account for moving interfaces and ensure vanishing velocity \mathbf{q} inside the mineral phases:

$$-\mu \phi_1 \Delta(\phi_1 \mathbf{q}) + \phi_1 \nabla p = \frac{1}{2} \frac{\partial \phi_1}{\partial t} - g(\phi_1, \xi) \mathbf{q}, \quad (20)$$

$$\nabla \cdot (\phi_1 \mathbf{q}) = 0. \quad (21)$$

The function $g(\phi_1, \xi)$ enforces $\mathbf{q} = 0$ in the sharp-interface limit and is chosen as

$$g(\phi_1, \xi) = \frac{K(1 - \phi_1)n}{\xi \phi_1 + n}. \quad (22)$$

The main properties of this function are $g(1, \xi) = 0$ and $g(0, \xi) = K\xi^{-1} > 0$, such that for $\phi_1 = 1$ the stationary Stokes (10) is obtained, while for $\phi_1 = 0$ only $\mathbf{q} = 0$ remains. As the term $g(\phi_1, \xi) \mathbf{q}$ serves to enforce a disappearing velocity inside the solid phases, the parameter K controls how strongly this is enforced in the phase-field simulation, since ϕ_1 can be slightly positive inside the minerals.

In addition to diffusive transport the dissolved species $\mathbf{c}(t, x)$ are now advected by the velocity \mathbf{q} :

$$\frac{\partial(\phi_1 \mathbf{c})}{\partial t} + \frac{\partial \phi_2}{\partial t} \mathbf{b}_D + \frac{\partial \phi_3}{\partial t} \mathbf{b}_P = \nabla \cdot [\phi_1 D_m \nabla \mathbf{c} - \mathbf{q} \otimes \mathbf{c}]. \quad (23)$$

2.3.4 Sharp-interface limit

For the limit of $\xi \rightarrow 0$ a sharp-interface model can be recovered from the phase-field formulation. The steps recovering the sharp-interface limit build upon the ideas in [8] and are analogous to the limits derived for the corresponding models in [6, 25], and are therefore only shown briefly.

The Allen-Cahn model used in this comparison introduces an additional curvature effect to the interface velocities, but aside from that the corresponding sharp-interface model is obtained. To show this, the main idea is using matched asymptotic expansions; outer expansions are used to recover the bulk phases, and inner expansions for behavior near the diffuse interface. These are then matched through matching conditions [8].

Assuming outer asymptotic expansions

$$\phi_i^{\text{out}} = \sum_{k=0}^{\infty} \xi^k \phi_{i,k}^{\text{out}}, \tag{24}$$

inserting them into the phase-field evolution (15) and gathering coefficients of powers of ξ , one obtains the leading order equation

$$\sum_{j \neq i} (\partial_{\phi_i} - \partial_{\phi_j}) W(\phi^{\text{out}}) = 0. \tag{25}$$

The stable minimizers of the potential $W(\phi)$ are the unit vectors $e_1, e_2, e_3 \in \mathbb{R}^3$, corresponding to the three bulk phases.

Inside the fluid domain the constant value $\phi_1 = 1$ is obtained. Considering this value for the phase field and inserting expansions for $\phi^{\text{out}}, \mathbf{c}^{\text{out}}$ and \mathbf{q}^{out} into the flow and transport equations (20), (19) and (23), the limit process of letting $\xi \rightarrow 0$ recovers the sharp-interface versions (10), (6) and (9), respectively. Inside the solid phases $\phi_1 = 0$ and the equations simplify to $0 = g(0, \xi)\mathbf{q}$, recovering the desired no-flow condition.

The boundary conditions are recovered from the same equations using so-called inner expansions. Between the bulk phases designated by the stable solutions $\phi \in \{\mathbf{e}_1, \mathbf{e}_2, \mathbf{e}_3\}$ there are transition zones where two or all three phase-field functions are positive. At such transitions between two phases we can define an interface Γ^d as the 1/2-level-set of the involved phase fields. Along this interface we define our unknowns in curvilinear coordinates (r, s) , where s describes the position along the interface, and r indicates the signed distance from the interface in the direction of the outer normal v_ξ , $x = y_\xi(t, s) + r v_\xi(t, s)$. Introducing the scaled variable $z = r/\xi$, we consider the asymptotic expansions in ξ :

$$\phi_i^{\text{in}}(t, z, s) = \sum_{k=0}^{\infty} \xi^k \phi_{i,k}^{\text{in}}(t, z, s), \tag{26}$$

with corresponding expansions for \mathbf{c} and \mathbf{q} . These are combined with rewritten derivatives and matching conditions. For outer expansions such as ϕ_0^{out} and fixed t, s, z the limit for $\xi \rightarrow 0$ for $z > 0$ respectively $z < 0$ are written as $\phi_0^{\text{out}}(t, y_{1/2\pm})$. The matching conditions relate limits of

inner expansions for $z \rightarrow \pm\infty$ to the outer expansions at the interface, e.g.

$$\lim_{z \rightarrow \pm\infty} \phi_0^{\text{in}}(t, z, s) = \phi_0^{\text{out}}(t, y_{1/2\pm}). \tag{27}$$

Together this allows recovery of the interface conditions [8].

The leading order terms of the phase-field equations at the transition zone between ϕ_1 and ϕ_2 , which corresponds to the interface $\Gamma_{\text{int,D}}(t)$, are

$$\frac{\partial^2}{\partial z^2} \phi_{1,0}^{\text{in}} = 8P'(\phi_{1,0}^{\text{in}}), \tag{28}$$

$$\begin{aligned} v_{n,0} \frac{\partial}{\partial z} \phi_{1,0}^{\text{in}} + \omega \phi_{1,1}^{\text{in}} 8P''(\phi_{1,0}^{\text{in}}) + 4\sqrt{P(\phi_{1,0}^{\text{in}})} f_D(\mathbf{c}_0^{\text{in}}) \\ = \omega \frac{\partial^2}{\partial z^2} \phi_{1,1}^{\text{in}} + \omega \kappa_0 \frac{\partial}{\partial z} \phi_{1,0}^{\text{in}}, \end{aligned} \tag{29}$$

where $v_{n,0}$ is the local normal velocity of the interface, κ_0 the curvature of the interface, and

$$P(\phi_1^{\text{in}}) = (\phi_1^{\text{in}})^2 (1 - \phi_1^{\text{in}})^2. \tag{30}$$

From (28) one arrives at an equation describing the shape of $\phi_{1,0}^{\text{in}}$, while (29) yields the boundary condition

$$v_{n,0} = -\omega \kappa_0 - f_D(\mathbf{c}_0^{\text{out}}), \quad x \in \Gamma_{\text{int,D}}(t). \tag{31}$$

Analogously, one obtains the boundary conditions for the other two interior interfaces

$$\begin{aligned} v_{n,0} &= -\omega \kappa_0 - f_P(\mathbf{c}_0^{\text{out}}), & x \in \Gamma_{\text{int,P}}(t), \\ v_{n,0} &= -\omega \kappa_0, & x \in \Gamma_{\text{int,M}}(t), \end{aligned}$$

where $\Gamma_{\text{int,M}}(t)$ denotes the interface separating both mineral phases, cf. Figure 1. These boundary conditions differ from the sharp-interface velocities given in (4) and introduce a curvature-driven movement. The strength of this effect is limited by the diffusivity parameter ω but it cannot be chosen arbitrarily small. This parameter controls how quickly a reasonably sharp interface is enforced, hence a small value of ω allows the reactions to cause an overly diffusive transition zone.

Remark 1 Note that in the recent publication [1], a different scaling of the Allen-Cahn equation is suggested to avoid curvature-driven motion in the sharp-interface limit. Instead of (15), a form corresponding to

$$\xi^2 \frac{\partial \phi_i}{\partial t} - \omega \xi^3 \nabla^2 \phi_i = -\frac{8}{3} \omega \xi \sum_{j \neq i} (\partial_{\phi_i} - \partial_{\phi_j}) W(\phi) + \hat{f}_i$$

is analyzed. As shown in [1], the curvature-driven motion of the interface disappears at the dominating order of ξ . However, the analysis in [1] is performed for a case without chemical reactions. When the reaction rates \hat{f}_i are included, the outer expansions can no longer recover stable solutions corresponding to the three phases. Hence, such an approach

would either require no chemical reactions, or a further reformulation of the reaction rates such that the sharp-interface limit can be recovered.

Remark 2 For a system with two phases, [35] presents a modified Allen-Cahn equation, where an extra term is added so that the curvature contribution in the limit $\xi \rightarrow 0$ is cancelled. A naive application to this three-phase problem has the desired effect at the interfaces between two phases, but also affects the evolution of the triple point. Without an analytical consideration such as done for the unmodified equations in [7], the precise effect on the limit behavior is unclear. However, for the phase-field equations with $\xi > 0$, the introduced term violates the conservation of $\phi_1 + \phi_2 + \phi_3 = 1$ near triple points.

Inserting the inner expansions into the remaining model equations yields the desired boundary conditions (11) for flow as well as (7) and (8) for transport. The leading order term of the continuity equation,

$$0 = \frac{\partial}{\partial z}(\phi_{1,0}^{\text{in}} \mathbf{q}_0^{\text{in}}) \cdot \nu_0, \tag{32}$$

is integrated over \mathbb{R} with respect to z and applying the matching condition (27) yields, at the fluid-solid interfaces,

$$0 = \mathbf{q}_0^{\text{out}}(t, y_{1/2-}) \cdot \nu_0, \tag{33}$$

where $y_{1/2-}$ corresponds to a point x on the interface ($\phi_1(x) = 0.5$). Here ν_0 denotes the first order term of the interface normal. From the leading order term of the momentum equation,

$$0 = \mu \phi_{1,0}^{\text{in}} \frac{\partial^2}{\partial z^2}(\phi_{1,0}^{\text{in}} \mathbf{q}_0^{\text{in}}), \tag{34}$$

one can then obtain the desired boundary condition $\mathbf{q}_0^{\text{out}} = 0$. Evaluating the transport equations near the interface yields the following equations. The leading term is

$$0 = \frac{\partial}{\partial z} \left(\phi_{1,0}^{\text{in}} \frac{\partial}{\partial z} \mathbf{c}_0^{\text{in}} \right). \tag{35}$$

After integration with respect to z and using $\phi_{1,0}^{\text{in}} > 0$ as well as the matching condition (27) one arrives at

$$0 = \frac{\partial}{\partial z} \mathbf{c}_0^{\text{in}}, \tag{36}$$

namely that \mathbf{c}_0^{in} does not depend on z . Considering the next order terms $O(\xi^{-1})$, along the interface $\Gamma_{\text{int,P}}(t)$ where $\phi_2 = 0$ and applying (32) and (36) yields the equation

$$0 = -v_{n,0} \frac{\partial}{\partial z}(\phi_{1,0}^{\text{in}}(\mathbf{c}_0^{\text{in}} - \mathbf{b}_P)) - \frac{\partial}{\partial z} \left(\phi_{1,0}^{\text{in}} D_m \frac{\partial}{\partial z} \mathbf{c}_1^{\text{in}} \right). \tag{37}$$

Finally, integration with respect to z and application of the matching conditions yields the boundary condition on the interface $\Gamma_{\text{int,P}}(t)$

$$v_{n,0}(\mathbf{c}_0^{\text{out}} - \mathbf{b}_P) = D_m \nabla \mathbf{c}_0^{\text{out}} \cdot \nu_0. \tag{38}$$

Analogously, the corresponding condition with \mathbf{b}_D instead of \mathbf{b}_P is derived at the interface $\Gamma_{\text{int,D}}$. While this recovers the sharp-interface conditions (7) and (8), the interface velocity v_n differs between the two models in accordance to (31).

2.4 Discussion of level-set and phase-field formulation

In contrast to the phase-field model, in which the chemical reactions occur as right hand sides, cf. Section 2.3, the chemical reaction enter the level-set model as boundary conditions. This is due to the fact that the boundary region of phase fields has a positive volume while the level-set interfaces are of codimension one. As a remark, note that using the level-set method, the specific surface areas $\sigma_i(t)$ must be constructed from the level-set function at each time-step (for more details see Section 3.1), whereas in the phase-field model this quantity is given by a simple integral of phase-field functions, cf. (16). Furthermore, the level-set approach requires a complex numerical scheme (see Section 3) due to the need of reconstructing the actual interfaces at every time-step. The phase-field equations, however, can be solved using standard schemes, and the phase-field variables can be directly incorporated into the equations describing chemistry and transport.

We note that both modeling approaches require the choice of artificial parameters influencing the solution quality. For the level-set approach, only two adjustable parameters are present. $\epsilon > 0$ is used in order to control the size of the area where a Voronoi reconstruction of the interfaces is applied while the frequency of reinitialization poses the other degree of freedom. Details on the effect and practical choice of these parameters are given in Section 3.1. The phase-field model introduces several parameters to deal with the diffuse-interface behavior. As seen in Section 2.3.4, the expected sharp-interface model is captured as $\xi \rightarrow 0$, except for an additional curvature-driven motion. The role of the parameters ξ, ω and K , which the phase-field model relies on, and the used numerical values are discussed in Section 3.2. For the level-set as well as the phase-field approach, parameters will be chosen specifically to minimize approximation errors in interface position and the influence of curvature terms on a given mesh.

3 Numerical methods

In this section we provide detailed information on the numerical methods used for geometry evolution, fluid flow and

solute transport. A list of spatial discretizations and time-integration schemes used for the three different simulation cases is provided in Table 2 summarizing the different numerical approaches for level-set and phase-field models. In order to ensure comparability of the simulation results between both geometry-capturing methods, solution algorithms are chosen carefully in conjunction with robust and well-established low-order discretizations.

3.1 Level-set implementation

In order to capture the geometry using sharp interfaces, we make use of generalized level-set methods. More precisely, the Voronoi Implicit Interface Method [29] (VIIM) is applied as three interacting phases need to be treated. As such, the interfaces are encoded in the level sets of a real valued function Φ . In conjunction with an indicator function $\chi : \mathbb{R}^2 \mapsto \{0, 1, 2\}$ the total of three phases (0: fluid, 1: mineral D, 2: mineral P) are distinguished in our setting [29, 32]. While the indicators serve the purpose of identifying the bulk of the different phases, the interfaces separating them are captured within level sets of Φ .

The Voronoi Implicit Interface Method constitutes a generalization of classical level-set methods in the sense that it does not rely on the neighboring phases to be distinguishable by the sign of the level-set function. Clearly, this restriction would not allow for the formation of triple points.

Instead, VIIM uses an ϵ -shifted version of an unsigned distance function d^V with respect to the interfaces to encode their position. Accordingly, at the initial time we set $\Phi = \epsilon - d^V$ for a small positive parameter $\epsilon \ll 1$. As proposed in [29], we use the doubled mesh size $\epsilon = 2h$. This choice corresponds to the smallest possible ϵ to ensure finite-difference stencils at points neighboring the 0-level sets of Φ to completely stay within a single phase and not cross interfaces. Therefore, a stable evolution via the

level-set equation (3) including a correct assignment of each computational node to its phase is ensured. Also note that the 0-level set of Φ corresponds to the ϵ -level set of d^V . As Φ has the signed distance function property in a neighbourhood of its 0-level set, application of equation (3) transports the 0-level set in a numerically stable manner. In order to recover the position of the actual interfaces (corresponding to $\{d^V = 0\}$), a Voronoi reconstruction step is performed. By having chosen the minimal reasonable ϵ , approximation errors within the reconstruction procedure are minimized.

We note that VIIM, like many other level-set methods, is unable to precisely conserve the mass of each single phase as we will discuss in more detail in Section 4. In the recent literature, several approaches are available to counteract this phenomenon beyond application of higher-order discretizations or mesh-refinement. In [28], a volume-reinitialization scheme is introduced actively correcting the mass error introduced by the level-set evolution. Alternatively, adjusted level-set equations are available using normal interface velocity corrections to improve mass conservation, cf. [33]. However, such approaches are typically developed to simulate incompressible multi-phase fluid flow where additional regularizing curvature-terms are present. These terms are not only nonphysical in our specific application but also require at least second-order spatial discretizations to evaluate properly. Since errors in mass are found to be reasonable low throughout our simulations in Section 4, we use plain VIIM as presented in [29] as a robust first-order accurate scheme. Despite the large number of available discretization options such as finite element or finite volume approaches, we further adhere to finite differences schemes as employed in [29] due to their straight-forward implementation on regular grids.

In our application, a movement of the interfaces in normal direction is induced by dissolution and precipitation reactions at the two different mineral-fluid boundaries,

Table 2 Spatial discretizations and time-integration schemes used in the sub-problems of the three different cases ODE, diffusive PDE (diff) and diffusive-advective PDE (flow) for both level-set and phase-field approach, cf. Section 2. Note that in the phase-field simulation, flow equations are assembled together with the solute and geometry equations into a common non-linear system

Case	Problem	Level-set	Phase-field
ODE	geometry	explicit Euler, first-order finite differences (FD) + full upwinding	implicit Euler, finite volumes (FV) + two point flux approximation (tpfa)
	solute	implicit Euler	implicit Euler
Diff	geometry	explicit Euler, first-order FD + full upwinding	implicit Euler, FV + tpfa
	solute	implicit Euler, RT ₀ /P ₀	implicit Euler, FV + tpfa
Flow	geometry	explicit Euler, first-order FD + full upwinding	implicit Euler, FV + tpfa
	solute	implicit Euler, RT ₀ /P ₀ + exponential upwinding	implicit Euler, FV + tpfa
	Stokes	P ₂ /P ₁	implicit Euler, staggered FV + tpfa + full upwinding

cf. (4). For this research, the numerical algorithm presented in [10] is therefore supplemented with the derivation of normal velocity field from the chemical concentrations according to (4).

Denoting the connected components of the 0-level set of Φ by Γ_ϵ^i , $i = 1, 2, 3$ our geometry evolution algorithm consists of the following steps, cf. [10].

1. Initialize geometry via Φ , χ
2. Calculate signed distance functions $d^i = d^i(x)$ to the interfaces Γ_ϵ^i by solving the Eikonal equation using the Fast Marching Method [31].

$$|\nabla d^i(x)| = 1, \quad x \in \Omega, \quad d^i(\gamma) = 0, \quad \gamma \in \Gamma_\epsilon^i.$$

3. Voronoi reconstruction step: Retrieve approximation Γ^V of original interface Γ

$$\Gamma^V = \{x \in \Omega : 0 < d^p(x) = d^q(x) \leq d^r(x)\}$$

for $p, q, r \in \{1, 2, 3\}$ distinct and update the indicator χ accordingly.

4. Calculate signed distance function d^V wrt. Γ^V via

$$|\nabla d^V(x)| = 1, \quad x \in D, \quad d^V(\gamma) = 0, \quad \gamma \in \Gamma^V.$$

5. Initialize velocity values $v_n^V(\gamma)$ in a neighborhood of the interfaces, calculated from concentration fields according to (4).
6. Calculate velocity extension v_n by solving

$$\begin{aligned} \nabla d^V(x) \cdot \nabla v_n(x) &= 0, \quad x \in \Omega, \\ v_n(\gamma) &= v_n^V(\gamma), \quad \gamma \in \Gamma^V. \end{aligned}$$

7. Evolve Φ for a small time-increment using the level-set equation (3) applying a suitable upwind scheme, e.g. [31].

Steps 2 through 7 are iterated until the final simulation time is reached. In order to improve stability and accuracy of the algorithm, periodic reinitializations of the level-set function by setting $\Phi = \epsilon - d^V$ are applied [29]. In particular, the implementation of step 5 poses several difficulties. For the initialization of the normal velocity field, nodes on both sides of the interface must be labelled according to the local concentrations. Furthermore, a change in sign is needed when crossing the interface as gradients of d^V switch orientation. In order to meet these requirements the following strategy is applied:

First, information from the level-set function and the indicators is used to identify all nodes neighboring a node which belongs to a different phase. This constitutes the set of all nodes that require an initialization value. Each node is then given a label from $1, \dots, 6$ according to the following scheme: Initially, we assign each element to one of the three phase separating interfaces $\Gamma_{\text{int},M}$, $\Gamma_{\text{int},D}$, $\Gamma_{\text{int},P}$. Then, we further discriminate with respect to the side of interfaces the points are located.

Second, we identify all finite elements belonging to the fluid phase which at least feature one solid edge. We will further call them boundary elements. These contain the concentration values from which normal interface velocities are calculated. Matching initialization nodes and boundary elements by distance minimization, velocity data are prescribed according to the labels given before.

The implementation is performed within the MATLAB [19] compatible framework of RTSPHEM [11]. Besides finite differences Eikonal- and level-set solvers using the well-known first-order upwinding scheme by Rouy and Tourin [27], it includes mixed finite element solvers for transport equation (6) on irregular triangular meshes using a mass-conserving lowest-order Raviart-Thomas RT_0/P_0 discretization. An exponential upwinding scheme is implemented to stabilize advection dominated transport. Additionally, our code allows for adaptive alignment of boundary elements' edges to a piecewise linear approximation of the interior boundary. More precisely, we track intersections of the interfaces with the edges of a fixed underlying mesh. Adding the intersection points to the set of nodes, an aligned mesh is generated by applying a Delaunay triangulation algorithm. Rewriting the inhomogeneous flux conditions (7) equivalently as source terms on the boundary triangles, the nonlinearities are resolved using Newton's method, cf. [12]. As the arising source term is highly localized, we iterate until the residual is decreased by at least six orders of magnitude. Moreover, time-stepping for the reaction PDEs is adaptively coupled to the CFL condition of the level set evolution.

In the advective PDE case, Stokes equations (10) are solved on the well-established and stable lowest-order Taylor-Hood elements P_2/P_1 . In order to cope with the inherent saddle-point structure of the problem, we employ the iterative Uzawa algorithm [17]. Choosing a low relative tolerance of 10^{-7} as the stopping criterion, high solution accuracy is ensured. Within each time-step of the overall solution algorithm, the Stokes flow field \mathbf{q} is computed on the current geometry and subsequently passed to the transport equation (9) as a coefficient.

3.2 Phase-field implementation

The phase-field model is implemented in DuMu^x [16] using a cell-centered finite volume discretization with two-point flux approximation for both the phase-field equations as well as the transport equations for the dissolved chemical species. In the flow scenario also the continuity equation is discretized using these control volumes and the pressure degrees of freedom are placed at their centers. Without fluid flow, the model equations are not very complex, with simple storage, flux and source terms. The system is solved using an implicit Newton solver with adaptive time-stepping

according to the number of needed Newton iterations as indicator. The Jacobians are assembled using numerical differentiation.

To include tightly coupled fluid flow and advection, additional care should be taken. We solve for the velocity components on staggered grids with control volumes and degrees of freedom shifted by half a cell in the respective spatial coordinates. The degrees of freedom are placed at the centers of these new control volumes, which corresponds to the normal velocities at the centers of the faces of the original cells. In DuMu^x this is implemented using multiple domains which are linked via a coupling manager [16]. The coupling manager shares the data between the so-called momentum and mass sub-problems and approximates values where there is no adequate degree of freedom available. The two sub-problems are not solved individually but assembled into a single matrix. With the fluid flow depending on the phase-field variables and their derivatives, the existing manager is extended to expose and approximate values at the desired points of the mesh.

As mentioned in Section 2.4, the phase-field model relies on several parameters that affect its numerical behavior. The parameter K controls how strongly a zero-velocity is enforced inside the solid phases and how the velocity develops within the transition zone. Investigating the flow inside the minerals and the velocity profiles near $\phi_1 = 1/2$ for expected velocities can give a reasonable choice for this parameter. For the presented simulations in Section 4.5, K was chosen $K = 10000$, and $n = 10$. While a high value of K is required to prevent significant nonphysical velocities inside the solid phases, this term also suppresses flow in the diffuse interface, which can lead to an underestimation of permeability [6]. The choice of K should scale with the fluid velocities expected near the minerals. In Section 4.5 relatively high inlet velocities are used, which leads to quite high velocities along the mineral grain. When calculating the permeability in the cell problems in Section 4.2.2, much lower velocities are used and thus a value of $K = 200$ is applied here.

The phase-field parameters ξ and ω control the profile of the phase-field functions and the shape of the bulk phases. The diffuse-interface width ξ affects the steepness of ϕ_i in the transition zones. Meanwhile ω balances the diffusive and potential-driven effects on the phase-fields against reaction and storage terms in (15), and also controls the impact of the curvature effect. A small value of ξ enables a better approximation of the interfaces but the choice of ξ is limited by the spatial resolution. This means, ξ should be large enough for the transition zone to be spread over multiple degrees of freedom and we use a value of five times the mesh size to resolve the interface. As such, ξ plays a similar role as ϵ in VIIM, cf. Section 3.1, and its choice is

likewise constrained from below in terms of multiples of the discretization lengths.

A smaller value of ω allows for a temporarily diffuse transition zone and reduces the impact of interface curvature, which can lead to more overgrowth of solids by small mineral tendrils. This makes it a central parameter affecting the simulation quality. However, if the changes caused by the chemical reaction dominate the contribution of the triple-well potential in the phase-field evolution (15), the resulting variables ϕ are prone to attaining values in between 0 and 1 in a larger transition zone and no longer exhibit an interface character. These transition zones, however, stray significantly from a sharp-interface description and can cause additional challenges for the numerical simulation. In the presented simulations the diffusivity parameter ω is chosen as $2.5 \cdot 10^{-3}$. Varying this value allows for finding a sufficiently small choice, which reduces curvature effects without losing cohesion of the diffuse interface. A small value of ω furthermore requires a sufficiently small value of ξ and thus a fine spatial resolution and increased computational effort.

In the equations for the conservation of dissolved species (19) and (23) as well as the modified incompressible Stokes (20) ϕ_1 enters as a multiplicative factor. To avoid degeneration of these equations, we instead use $\phi_\delta = \phi_1 + \delta$, adding a small regularization parameter [25]. The exception being the function $g(\phi_1, \xi)$ which is unmodified. This regularization slightly disrupts the conservation equations and the momentum (20) no longer collapses fully to $0 = \mathbf{q}$. In the presented simulations this value was chosen as 10^{-10} for the ODE and PDE formulations and as 10^{-6} for the flow model.

4 Simulations

In this section, we specify all physical parameters, initial and boundary conditions used in the simulation scenarios. We moreover define characteristic quantities such as the volume of the individual mineral phases, the mass of the mobile species and the mineral's surface area and recall how they are specified using the level-set and phase-field approach, cf. Section 4.1. Based on the characteristic quantities, the three simulation scenarios as presented in Section 2 are investigated. Moreover, based on upscaling theory, time-dependent effective diffusion and permeability tensors are additionally evaluated. We emphasize the similarities, but also outline the differences resulting from the two problem formulations by means of level-set and phase-field description. Note that the following simulations are performed in two spatial dimensions. In order to stress the physical meaning of all appearing quantities, we still refer to a mineral volume and a surface area.

4.1 Simulation setup

All calculations are performed using a regular 200x200 mesh. This corresponds to the finest resolution used in similar studies [20, 34] and is therefore considered practically feasible in applications. Furthermore, grid convergence studies presented in the Appendix indicate a sufficient resolution and discretization order for our setup. Due to the different kinds of underlying discretizations used in this paper, the mesh resolution specified above only refers to the number of nodes which is the same in both our simulation approaches. The only exception is made in the discretization of the transport equation using the level-set approach and the framework provided by the RTSPHEM [11] toolbox, where nodes are adaptively added to the triangular mesh in order to align edges with the fluid-solid interface, cf. Section 3.1. To provide insights into the complexity of the different sub-problems arising in both level-set and phase-field approaches, we compare the number of degrees of freedom (DoFs) and computation steps in Table 3. Note that the solutions to all sub-problems obtained by iterative methods are computed to high accuracy (relative residuum smaller than 10^{-6} or two subsequent residua with difference smaller than 10^{-8}) not to compromise the simulation results by numerical artefacts.

As it is apparent from Table 3, the level-set approach requires less DoFs for geometry description than the phase-field method due to the ability of encoding the whole information within a single function. However, flow and transport equations involve a larger number of Dofs in the level-set framework. This is essentially due to underlying triangular mesh (instead of quadrilaterals) to simplify mesh adaptivity, cf. Section 3.1. Moreover, we note that in the diffusive and flow scenarios the number of time-steps is lower in the phase-field simulations due to a fully implicit scheme simultaneously solving all sub-problems, allowing for larger time-steps. However, since the solute concentrations in the discretization of the ODE scenario are updated after each time-step, sufficiently small time-steps are required for both approaches. Finally, we note that the number of Newton-steps is significantly larger in the level-set approach in exchange for higher solution tolerances of the linear solver (less Krylov steps). However, accuracy is solely determined by the non-linear residuum.

At initial time $t = 0$, a circular solid inclusion is placed in the unit square Ω with midpoint (0.5, 0.5) and radius $r = 0.2$ for all three scenarios, see Fig. 1 for a to-scale visualization. For simplicity, we assume the minerals D, P to be arranged in two hemicycles of the circle. For the phase-field model this corresponds to initializing ϕ such that without contributions from reactions or curvature effects the

Table 3 Simulation statistics: Comparison of number of degrees of freedom for the discretizations of the different sub-problems for level-set (LS) and phase-field approach (PF) on a 200×200 mesh

Case	Quantity	Level-set	Phase-field
	# DoFs geometry	40,000	80,000
	# DoFs Stokes	313,358	120,400
	# DoFs solute	522,276	120,000
ODE	# time-steps	190	201
	# Newton-steps	–	648
Diff	# time-steps	175	85
	# Newton-steps	1,278	351
Flow	# time-steps	81	38
	# Newton-steps	554	251

Numbers are itemized by geometry solver (level-set or phase-field equation), Stokes-flow solver and transport equation for solute species. Note that, since the computational domain changes in LS over time, the numbers are presented with respect to the first time-step and deviate by less than 3% from these values over simulation time. Furthermore, number of time-steps and Newton-iterations are displayed for the different scenarios ODE, diffusive PDE (diff) and diffusive-advective PDE (flow). The numerical results of the given scenarios are compared and discussed in Sections 4.3.2, 4.4 and 4.5 respectively

initial conditions are close to stationarity. This is achieved by using the base kernel of

$$\varphi(s) = \frac{1}{1 + \exp(-s/\xi)} \tag{39}$$

with

$$\begin{aligned} \phi_1(0, x) &= \varphi(10 \cdot (\|\mathbf{x} - (0.5, 0.5)^\top\|_2^2 - 0.2^2)), \\ \phi_2(0, x) &= (1 - \phi_1)\varphi(3.8 \cdot (x_1 - 0.5)), \\ \phi_3(0, x) &= 1 - \phi_1(0, x) - \phi_2(0, x). \end{aligned} \tag{40}$$

For our simulations, we use the molar densities $\rho_D = 20$ [NL⁻³], $\rho_P = 4$ [NL⁻³], cf. (5). Therefore, changes in mineral volume are expected to be larger for the precipitating phase facilitating mineral overgrowth. In addition, reaction constants $k_D = k_P = 1.0$ [LT⁻¹] and equilibrium constants $K_D = 1.0$ [-], $K_P = 1.0$ [L⁶N⁻²] are set, cf. (2). For both simulations involving diffusion driven transport, we set the molecular diffusivity to $D_m = 0.2$ [L²T⁻¹]. In the advection case, we consider the Stokes equation with unit viscosity $\mu = 1$ [ML⁻¹T⁻¹], cf. (10), (20). Finally, we choose the following initial conditions for the PDE cases

$$\begin{aligned} c_A(0, x) &= 2, & x \in \Omega_f(0) \\ c_B(0, x) &= 1, & x \in \Omega_f(0) \\ c_C(0, x) &= 1, & x \in \Omega_f(0) \end{aligned} \tag{41}$$

as well as for the ODE model Section 2.2.1 disregarding the spatial variable x . Note that for the phase-field model, these

initial conditions are chosen for the entire domain Ω , but correspond (in the sharp-interface limit) to (41) as $\phi_1 \mathbf{c}$ is the relevant quantity.

According to (41), solute species B and C are in chemical equilibrium at the initial time. Due to the oversaturation with respect to solute A, mineral D will immediately start to dissolve according to reaction (1) and release B. The resulting oversaturation with respect to species B will then trigger the precipitation of mineral P. The final simulation times T for each individual simulation are chosen in such a way that the steady state is approximated to a good extent, i.e. no further qualitative change of the system is expected to occur beyond that time.

Finally, we specify details on the boundary conditions on the exterior boundary $\partial\Omega$ for the different scenarios. For the diffusive PDE system, we choose homogeneous Neumann boundary conditions at the exterior boundary $\partial\Omega$ which correspond to no-flux conditions:

$$D_m \frac{\partial c_i}{\partial \nu}(t, x) = 0, \quad (t, x) \in (0, T) \times \partial\Omega, \quad (42)$$

$$i \in \{A, B, C\}$$

For the advective flow case, we implement the following conditions at the outer boundary $\partial\Omega = \Gamma_{\text{inlet}} \cup \Gamma_{\text{outlet}} \cup \Gamma_{\text{top}} \cup \Gamma_{\text{bottom}}$ with $\Gamma_{\text{inlet}} = \{0\} \times (0, 1)$, $\Gamma_{\text{outlet}} = \{1\} \times (0, 1)$, $\Gamma_{\text{top}} = (0, 1) \times \{1\}$ and $\Gamma_{\text{bottom}} = (0, 1) \times \{0\}$ in the Stokes equation (10)

$$\mathbf{q}(t, x) = 0, \quad x \in \Gamma_{\text{top}} \cup \Gamma_{\text{bottom}},$$

$$\mathbf{q}(t, x) = \left(1 - 4(x2 - 0.5)^2, 0\right)^T, \quad x \in \Gamma_{\text{inlet}},$$

$$p(t, x) = 0, \quad x \in \Gamma_{\text{outlet}}, \quad (43)$$

for $t \in (0, T)$ corresponding to an inflow boundary on the left, no-slip at top/bottom and an outflow boundary at the right hand side of the domain. Note that the flow at the left boundary shows a parabolic profile as expected for a Stokes flow within a long pipe. This results in a total volume flux of $\frac{2}{3} [\text{L}^3 \text{T}^{-1}]$ and a maximal fluid velocity of $q_{\text{max}} = 1 [\text{LT}^{-1}]$ at the inlet.

In order to attain an equilibrium state over time, we adapt the boundary conditions of the transport equations at the inlet (42) in the following way:

$$D_m \frac{\partial c_i}{\partial \nu}(t, x) - \mathbf{q}(t, x) c_i(t, x) = -\mathbf{q}(t, x) c_{i,eq}, \quad (44)$$

$$x \in \Gamma_{\text{inlet}}, \quad i \in \{A, B, C\}$$

using the equilibrium concentrations calculated in Section 4.3.1. Thus, the inflow will flush the over-saturated fluid domain and push the system towards the equilibrium state. We note that the resulting equilibrium volumes differ significantly from the characteristics of the previous cases as the flux boundary conditions dynamically change the total mass of solute species contained in Ω .

4.2 Measures

In the following, we define the five characteristic measures to quantitatively evaluate and compare the quality of the performed simulations for the different approaches.

4.2.1 Direct measures

The first measure is the mineral volumes and their evolution of over time as regarded in [20]. In the level-set approach, this quantity is easily inferred from a linear interpolation of the unsigned distance function d^V on the underlying grid, see Section 3.1. Using the phase-field method, the mineral volume is given as the integral of the respective phase-field function ϕ_i , see Section 2.3. Given the setup presented in Section 4.1, the initial volumes of both minerals amount to $0.2^2 \frac{\pi}{2} \approx 0.0628$.

As a second measure, we compare the surface area of both minerals, cf. [20]. That is, we compute the length [L] of the interior interfaces $\Gamma_{\text{int,D}}$, $\Gamma_{\text{int,P}}$, cf. Figure 1, separating the fluid domain and the respective mineral. In the given context, the resulting quantity therefore equals the reactive surface area. In the level-set framework, a linear reconstruction of the interface is used to approximate its length. Suitable interface indicators are used to obtain the related quantity using phase fields, cf. (16). Given the setup presented in Section 4.1, the initial surface areas of both minerals amount to $0.2\pi \approx 0.628$.

The third measure is the conservation of mass with respect to each chemical species. Although the formulation of the reactive problem presented in Section 2 is analytically mass conservative, the numerical schemes may not be capable of preserving this property precisely. Furthermore, as indicated in Section 4.3.1, orbits in the system's phase space regarding different total masses \mathbf{M} have a positive distance. Hence, the relative loss or gain in total mass is a useful indicator to assess the simulators' predictive power as already used in [13].

Taking the fluxes $\mathbf{j}_i = D_m \nabla c_i - \mathbf{q} c_i$ related to solute i , $i \in \{A, B, C\}$, at the inlet and outlet (Γ_{inlet} , Γ_{outlet}) for the advective example into account, the total mass $M_B(t)$, $M_C(t)$ of species B, C in the PDE cases is given by (cf. (51))

$$M_B(t) = \int_{\Omega_f(t)} c_B(t, x) dx + (V_D(t)\rho_D + V_P(t)\rho_P)$$

$$+ \int_0^t \int_{\Gamma_{\text{inlet}} \cup \Gamma_{\text{outlet}}} \mathbf{j}_B(t, x) \cdot \nu d\sigma ds, \quad (45)$$

$$M_C(t) = \int_{\Omega_f(t)} c_C(t, x) dx + V_P(t)\rho_P$$

$$+ \int_0^t \int_{\Gamma_{\text{inlet}} \cup \Gamma_{\text{outlet}}} \mathbf{j}_C(t, x) \cdot \nu d\sigma ds.$$

In this expression, the first term accounts for the amount of species i being dissolved in the fluid whereas the second

describes the amount ligated within the minerals. Last, the third term is related to mass exchange across the domain's boundaries. In the context of the phase-field model the first term is adjusted slightly, integrating instead over the entire domain and including a factor of ϕ_1 to account for the fluid phase.

$$\begin{aligned}
 M_B(t) &= \int_{\Omega} \phi_1(t, x) c_B(t, x) dx + V_D(t) \rho_D + V_P(t) \rho_P \\
 &\quad + \int_0^t \int_{\Gamma_{inlet} \cup \Gamma_{outlet}} \mathbf{j}_B(t, x) \cdot \nu d\sigma ds, \quad (46) \\
 M_C(t) &= \int_{\Omega} \phi_1(t, x) c_C(t, x) dx + V_P(t) \rho_P \\
 &\quad + \int_0^t \int_{\Gamma_{inlet} \cup \Gamma_{outlet}} \mathbf{j}_C(t, x) \cdot \nu d\sigma ds.
 \end{aligned}$$

Note that the related quantity $M_A(t)$ is not considered in this paper as the solid shares would need to be weighted with a negative sign compromising physical interpretability. As the fluxes are explicitly discretized in both numerical schemes (Section 3), total in- and outflow are simple to determine by integration in the level-set as well as phase-field framework. Volumes and integrated concentrations in (45) and (46) are derived similarly.

4.2.2 Effective measures

Finally, we consider two effective quantities derived from the geometrical setup. Assuming the domain of interest Ω to be a representative elementary volume of a larger scale porous medium, we can ask for the effective diffusion and permeability tensors of that respective medium. These quantities are of high importance concerning flow and transport properties on a macroscopic scale. Both tensors are derived solving different auxiliary PDEs (cell problems) using periodic boundary conditions on the exterior boundary. In the context of periodic homogenization, the following sharp-interface representation is derived, cf. [14] for the static case and [21] for time-evolving domains:

The diffusion tensor is given as

$$\mathbb{D}_{i,j}(t) = \int_{\Omega_f(t)} (\partial_{x_i} \zeta_j + \delta_{ij}) dx$$

for $i, j \in \{1, 2\}$ and Kronecker delta δ_{ij} , where ζ_j are the solutions of the elliptic problems

$$\begin{aligned}
 -\nabla \cdot (\nabla \zeta_j) &= 0 \quad \text{in } \Omega_f(t), \\
 \nabla \zeta_j \cdot \nu &= -e_j \cdot \nu \quad \text{on } \Gamma_{int}(t), \quad (47)
 \end{aligned}$$

$$\zeta_j \text{ periodic in } x, \quad \int_{\Omega_f(t)} \zeta_j dx = 0,$$

for $j \in \{1, 2\}$ and outer unit normal ν , denoting again the total interior boundary by $\Gamma_{int}(t) = \Gamma_{int,D}(t) \cup \Gamma_{int,P}(t)$.

The permeability tensor is given as

$$\mathbb{K}_{i,j}(t) = \int_{\Omega_f(t)} \omega_j^i dx$$

for $i, j \in \{1, 2\}$, where (ω_j, π_j) are the solutions to

$$\begin{aligned}
 -\Delta \omega_j + \nabla \pi_j &= e_j \quad \text{in } \Omega_f(t), \\
 \nabla \cdot \omega_j &= 0 \quad \text{in } \Omega_f(t), \quad (48) \\
 \omega_j &= 0 \quad \text{on } \Gamma_{int}(t)
 \end{aligned}$$

$$\omega_j, \pi_j \text{ periodic in } x, \quad \int_{\Omega_f(t)} \pi_j dx = 0.$$

In case of the phase-field framework, the above equations change their form. To calculate effective diffusion and permeability tensors we also solve auxiliary cell problems incorporating the phase-field parameter, with periodic boundary conditions on the exterior boundary. However, in the phase-field formulation the domain is not split along an interior interface, hence the cell problems are solved not only in the fluid domain Ω_f but in Ω . Boundary conditions on the interior solid boundary are hence not needed, as they are already incorporated in the phase-field formulation. The effective tensors are then calculated with the regularization factor ϕ_δ [6] and are defined as, for $i, j \in \{1, 2\}$

$$\mathbb{D}_{i,j}(t) = \int_{\Omega} \phi_\delta (\partial_{x_i} \zeta_j + \delta_{ij}) dx$$

and

$$\mathbb{K}_{i,j}(t) = \int_{\Omega} \phi_\delta \omega_j dx,$$

with ζ_j and (ω_j, π_j) solutions to [6]

$$\begin{aligned}
 -\nabla \cdot (\phi_\delta D(\nabla \zeta_j + e_j)) &= 0 \quad \text{in } \Omega, \quad (49) \\
 \zeta_j \text{ periodic in } x, \quad \int_{\Omega} \zeta_j dx &= 0,
 \end{aligned}$$

and

$$\begin{aligned}
 -\phi_\delta \Delta(\phi_\delta \omega_j) + \phi_\delta (\nabla \pi_j - e_j) &= -\frac{g(\phi_1, \xi)}{\mu} \omega_j \quad \text{in } \Omega, \\
 \nabla \cdot (\phi_\delta \omega_j) &= 0 \quad \text{in } \Omega, \quad (50) \\
 \omega_j, \pi_j \text{ periodic in } x, \quad \int_{\Omega} \pi_j dx &= 0,
 \end{aligned}$$

for $j \in \{1, 2\}$.

As the off-diagonal components of the effective tensors remained small and generally several orders of magnitude smaller than the diagonal components, we will restrict to reporting and discussing the evolution of the diagonal elements.

4.3 Comparison for ODE system

For the ODE case it is possible to theoretically deduce the system's long term behavior for several characteristic

quantities. As such, we start by providing important analytical properties of the ODE system.

4.3.1 Theoretical considerations

In this section, we briefly discuss existence of solution to the ODE problem (5) introduced in Section 2.2.1 as well as stability and positivity of equilibrium points.

Assuming continuous dependence of fluid volume and interface lengths on time, system (5) admits a unique solution local in time by the Picard-Lindelöf theorem. In case those quantities and the concentrations are bounded from above and away from zero, the solution can be extended globally.

Next, we are concerned with the stability of equilibria. In the following, we approach stability by investigating the equilibrium points as a function of the system's invariants. Let us denote the volume of minerals D and P being present at time t by $V_D(t)$ and $V_P(t)$, respectively. Due to the conservation of mass, the following quantities are conserved over time, cf. (45), (46) in Section 4.2.1:

$$\begin{aligned} M_A(t) &= c_A(t)|\Omega_f(t)| - V_D(t)\rho_D, \\ M_B(t) &= c_B(t)|\Omega_f(t)| + V_D(t)\rho_D + V_P(t)\rho_P, \\ M_C(t) &= c_C(t)|\Omega_f(t)| + V_P(t)\rho_P, \end{aligned} \quad (51)$$

using the apparent relation $|\Omega_f(t)| = 1 - V_D(t) - V_P(t)$. Accordingly, we have the following function mapping G from the system's state space to a set of invariants and characteristics for an equilibrium state with $\mathbf{M} = (M_A(0), M_B(0), M_C(0))$:

$$G(\mathbf{c}, V_D, V_P) = (\mathbf{M}, f_D, f_P). \quad (52)$$

More precisely, G maps the current solute concentrations and mineral volumes to the total masses and interface reaction rates. Clearly, all equilibrium points for a given \mathbf{M} are characterized by the preimage $G^{-1}(\mathbf{M}, 0, 0)$ assuming $\sigma_i(t)$ being bounded from below by a positive constant. As such, a possibly continuous G^{-1} would lead to a curve of equilibria points in the phase space, rendering linearized theory inconclusive due to a zero eigenvalue. Furthermore, all equilibria reachable from positive initial conditions are located within the positive octant as easily seen by application of the quasi-positivity theorem [24]. Evaluating the expression for the initial conditions given in (41) we find

$$\begin{aligned} c_{A,\text{eq}} &= c_{B,\text{eq}} = 1.4056, \\ c_{C,\text{eq}} &= 0.7114, \\ V_{P,\text{eq}} &= 0.1333, \\ V_{D,\text{eq}} &= 0.0339, \end{aligned} \quad (53)$$

as an equilibrium state. Investigating the Jacobian ∇G at that point shows local bijectivity of G . Accordingly, the system is not asymptotically stable. This is expected as

disturbances changing \mathbf{M} cannot be compensated by the system due to conservation of mass. As such, discretization errors with respect to the geometry evolution will add up. This inherent property underlines the necessity for well-designed numerical algorithms.

4.3.2 Comparison simulations

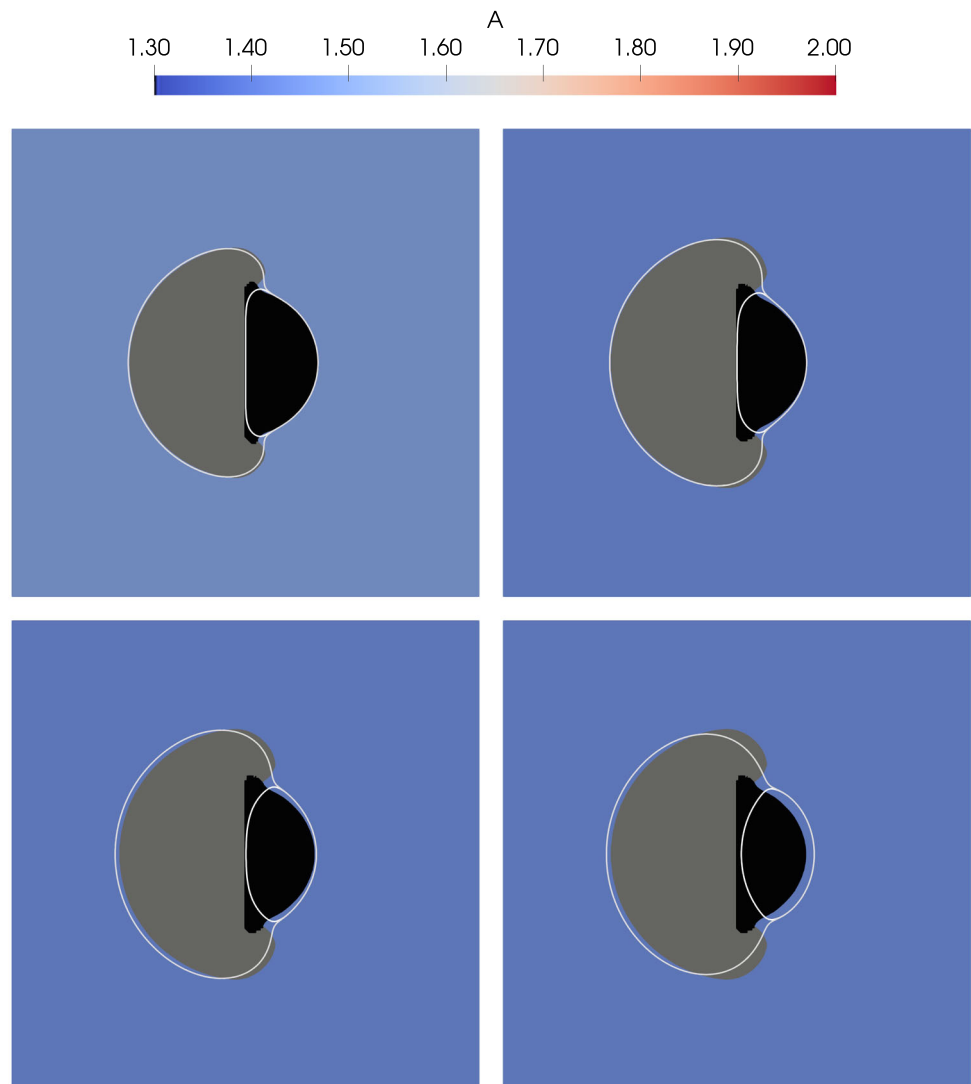
The simulation results for the ODE case as outlined in Sections 2.2.1, and 2.3.1 are depicted in Fig. 2 for different time-steps and in Fig. 3 the evolution of quantitative measures is shown until the final simulated time of $T = 2$. At final time of the level-set simulation, the concentrations of all solute species deviated by less than one per mille from their calculated equilibrium values (53). As such, the system reaches equilibrium to high precision. In the case of the phase-field model the solved system of equations corresponds to a modified sharp-interface formulation, with additional curvature-driven interface motion. The simulation approaches an equilibrium with constant curvature along each interface and dissolved concentrations slightly perturbed relative to the calculated equilibrium such that the curvature-driven motion and reactive effects cancel out. At final time of the phase-field simulation the concentration c_C matches up to three per mille but c_A is two percent lower and c_B two percent higher.

Figure 2 displays and compares the resulting geometrical configuration of the three-phase system for different simulation times and both approaches. More precisely, the minerals as obtained using the level-set method are shown in grey (P) and black (D). In the surrounding fluid domain, the (spatially independent, but time-dependent) concentration of solute species A is displayed. Finally, the phase-separating interfaces as obtained using the phase-field model are overlaid in white.

Overall, we observe a good match between level-set and phase-field simulation results. However, it is evident that the level-set shows overgrowth of the minerals, while the phase-field does not, see Fig. 2. Due to curvature effects, the phase-field model cannot resolve the corners of the dissolving mineral very well, and the initially straight interface between the two minerals becomes curved.

Although the shapes evolve slightly differently, a good match in characteristic measures as depicted for both level-set and phase-field solution in Fig. 3 is observed. In particular, the volumes of the two minerals almost perfectly coincide as seen in Fig. 3. Both predicted volumes of mineral P at final simulation time differ less than 0.3% from the analytical equilibrium volume, for mineral D the relative deviation is less than 2.5%. These disagreements are considered fairly small given that, starting from an initial volume of 0.0628, equilibrium volumes of 0.1333 and 0.0339, respectively, are targeted. As such, initial volumes

Fig. 2 ODE case: Geometry of both mineral phases surrounded by concentration field of species A at time $t = 0.25$, $t = 0.5$, $t = 1$ and $t = 2$. Black and gray shapes refer to the level-set simulation, white contours to the phase-field approach



are approximately doubled (mineral P) or halved (mineral D) in the course of the simulation. The evolution of the surface area is, except from the initial period, also comparable. Due to the large increase of mineral volume, the surface area of mineral P almost doubles within our simulation from 0.628 to 1.215 in the level-set simulation, see Fig. 3. Simultaneously, originating from the same initial value, the surface area corresponding to mineral D decreased by more than 35%. Approaching the equilibrium state, both modelling methods concur well with relative differences of 5% and 11% for minerals D and P, respectively.

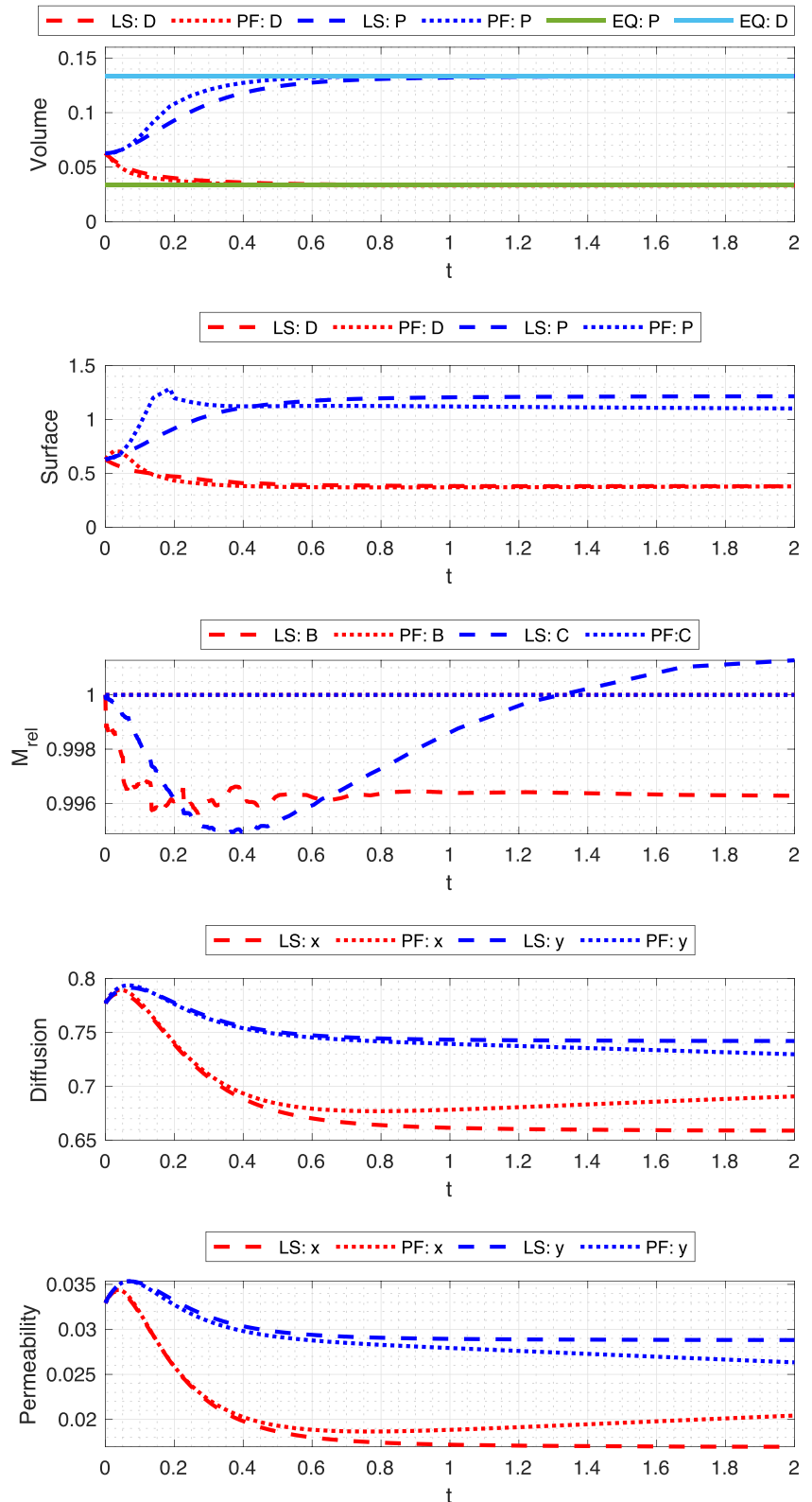
The initially peaking surface areas for the phase-field simulation seen in Fig. 3 are caused by how they are determined from the phase-field variables ϕ . Without reactive contributions the phase-field variables develop a specific profile and the surface area is calculated as the integral of $\frac{4}{\xi}\phi_i\phi_j$. During the early evolution in the ODE

case, the reaction rates are high and the shape of the phase-field variables fail to keep the expected shape. The transition zones get drawn out and the changed profile across the interfaces causes the above integral to overestimate the interface length. As the phase-field ODE formulation does not depend on this explicit evaluation of the surface area, this does not have a strong effect on the further evolution of geometry and concentrations.

We further note that the formulation used for the phase-field approach is perfectly mass conservative (up to 10 significant digits), while small deviations within 0.5% are seen for the level-set approach. As indicated by the grid convergence studies performed in Fig. 8, mass errors in the level-set framework decrease consistently with higher spatial resolution.

Finally, Fig. 3 shows an almost perfect match of the effective diffusion and permeability tensors for small times $t \leq 0.3$. Across both directions and tensors, relative

Fig. 3 ODE case: Evolution of mineral volume over time, reactive surface area and relative total mass calculated with level-set method (LS, dashed lines) and phase-field approach (PF, dotted lines). The precalculated exact values for the mineral volumes in equilibrium (EQ) are highlighted. The last two pictures illustrate the evolution of the diffusion and permeability tensors along the main axes over time



deviations are below 2% at $t = 0.3$. This agreement is remarkable since the permeability in x direction has already undergone a decrease of 33% (from 0.0329 to 0.0222) up

to that time according to the phase-field simulation. As the chemical reactions come to a standstill, the level-set data plateau whereas the phase field data further evolve

due to curvature effects. For both effective quantities, the phase-field simulation reduces the distance between the measurements in x and y direction. Apparently, curvature effects diminish anisotropy over time.

4.4 Comparison for diffusion model

The simulation results of the diffusive PDE case as outlined in Sections 2.2.2, and 2.3.2 are depicted in Figs. 4 and 5 for both approaches. The concentration of solute species A is displayed according to the level-set simulation. Intermediate and a close to equilibrium state of both mineral phases are illustrated for the level-set method including also the phase-field solution as an overlay, cf. Figure 4. As both simulation agree on generating mineral overgrowth (in contrast to the ODE case), the modeling approaches recover important qualitative physical behavior of the underlying problem. This is a direct consequence of the increased and contrast rich interface velocities at the triple points. These again result from focusing reactive activity to the neighborhood of the triple points made possible by taking the spatial distribution of the solute species into account. Therefore, the difference in interface velocity between both fluid-solid

interfaces is significantly higher, facilitating overgrowth behavior. As such, the system is naturally forced to develop and maintain higher interface curvatures than in the ODE case. However this increased curvature causes a stronger deviation between the two models.

As earlier, the phase-field formulation cannot properly resolve corners due to the curvature-driven movement of the interfaces. Therefore, mineral D is increasingly displaced by mineral P within the solid close to the interface. This behavior is also visible in Fig. 5, wherein the concentration fields of the mobile species as well as the area/volume of the mineral species are investigated with respect to time. Due to the no-flux exterior boundary conditions, the system approaches an equilibrium state for large times similar to the ODE case discussed in Section 4.3. In fact, both systems' equilibrium states are identical in terms of mineral volumes and solute concentrations due to the same total masses of species A, B and C. Yet, the rate of convergence is much slower due to the time consuming transport of solute species between the two different mineral interfaces, see Fig. 4. As the transport speed is governed by the concentration gradients, convergence to equilibrium is additionally decelerated. At the final time

Fig. 4 Diffusion case: Geometry of both mineral phases surrounded by concentration field of species A at time $t = 1$, $t = 2$, $t = 3$ and $t = 4$. Black and gray shapes refer to the level-set simulation, white contours to the phase-field approach

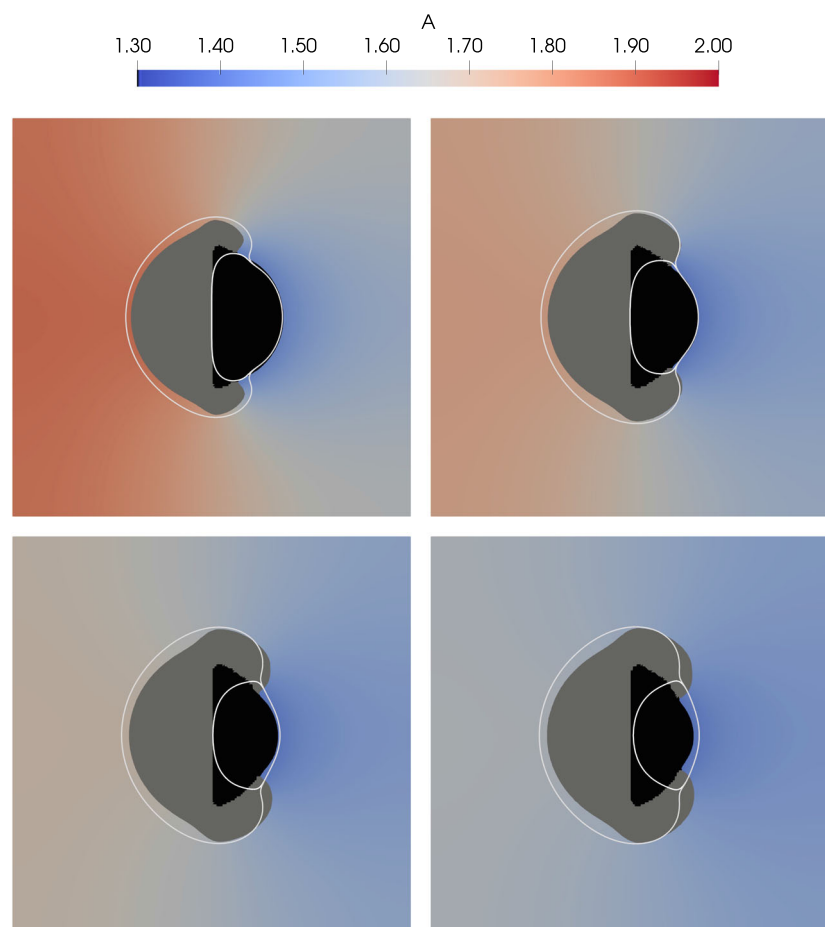
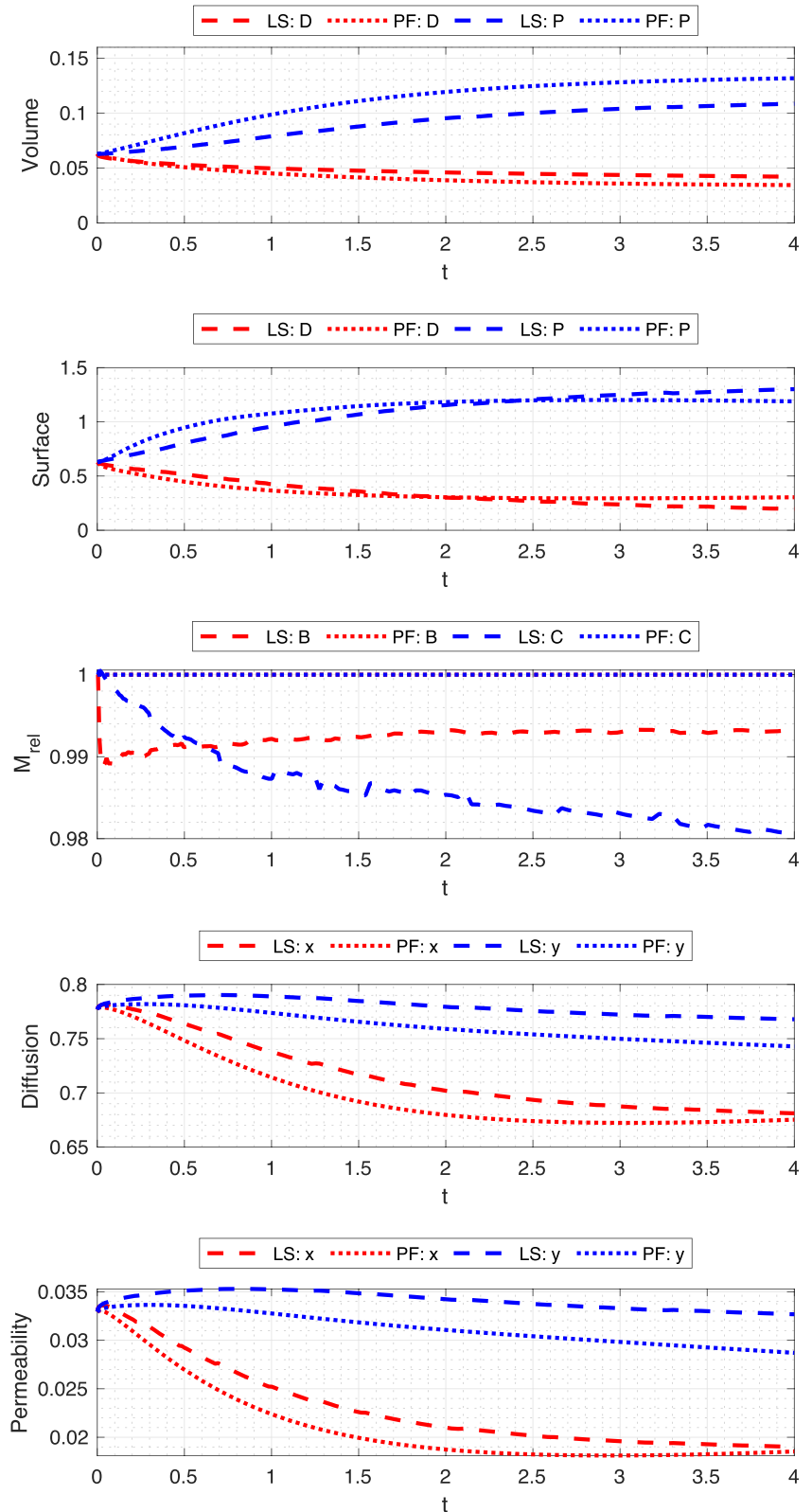


Fig. 5 Diffusion case: Evolution of mineral volume over time, reactive surface area and relative total mass calculated with level-set method (LS, dashed lines) and phase-field approach (PF, dotted lines). The last two pictures illustrate the evolution of diffusion and permeability tensors along the main axes over time



$T = 4$, the volume average concentration of solute A is 1.56. Accordingly, the transition from initial chemical disturbances to the equilibrium state is already completed

by 74%. Yet, within the final simulation time unit $3 \leq t \leq 4$ (cf. Figure 4) an insignificant amount of geometry evolution is identified.

The overall mineral volumes in the two models evolve qualitatively similarly, yet slightly differently. More precisely, the volume of mineral P is predicted progressively higher by the phase-field than by the level-set method (19% at final time) and vice versa for mineral D (22% at final time). Given a total volume growth of mineral P of 72% (from 0.0628 to 0.1081) as predicted by the level-set simulation, these deviations are not negligible yet reasonably small. A similar conclusion is drawn for mineral D, which shrinks by 32% from 0.0628 to 0.0424 over simulation time. This effect is assumed to essentially result from the artificial displacement at the mineral-separating interface in the phase-field simulation. In conclusion, we observe significantly higher deviations between the two simulation approaches compared to the ODE case presented in Section 4.3.2, due to the more pronounced mineral overgrowth and the resulting higher interface curvatures.

The surface area evolutions predicted by both approaches are also quite similar. At final time, we observe a relative deviation in mineral P's surface area of 9%. This is comparable to the deviation of 11% measured in the ODE case. According to the level-set prediction, the mineral underwent a growth of surface area by 111% from 0.628 to 1.325,

which is about 17 percent points more than in the ODE case. Due to the significantly decreased surface of mineral D by 69% (from 0.628 to 0.197), relative differences appear to be high. Yet, in absolute measure, they are comparable to the deviations measured for the precipitating mineral.

Again, the phase-field model conserves mass up to 10 significant digits, while the level-set model experiences an error of about 2%. As illustrated in Fig. 8, the error in mass conservation consistently reduces with increased resolution in the level-set simulations.

Since the precipitation of P is concentrated at the poles of the initially circular geometry, both modelling approaches agree that only a slight change of effective permeability and diffusivity in y-direction takes place over time, cf. Figures 5 and 4. The associate values at final time differ by 12% and 3% among both modeling approaches, respectively. Due to the resulting increase in vertical extend, both quantities decrease significantly with respect to the x direction by 44% (from 0.0329 to 0.0185) and 13% (from 0.778 to 0.677), respectively, according to the phase-field computations. At final time, the results obtained by level-set and phase field approach differ by less than 2% for both effective tensors in y-direction.

Fig. 6 Equilibrium flow case: Geometry of both mineral phases surrounded by concentration field of species A at time $t = 0.25$, $t = 0.5$, $t = 1$ and $t = 1.5$. Black and gray shapes refer to the level-set simulation, white contours to the phase-field approach

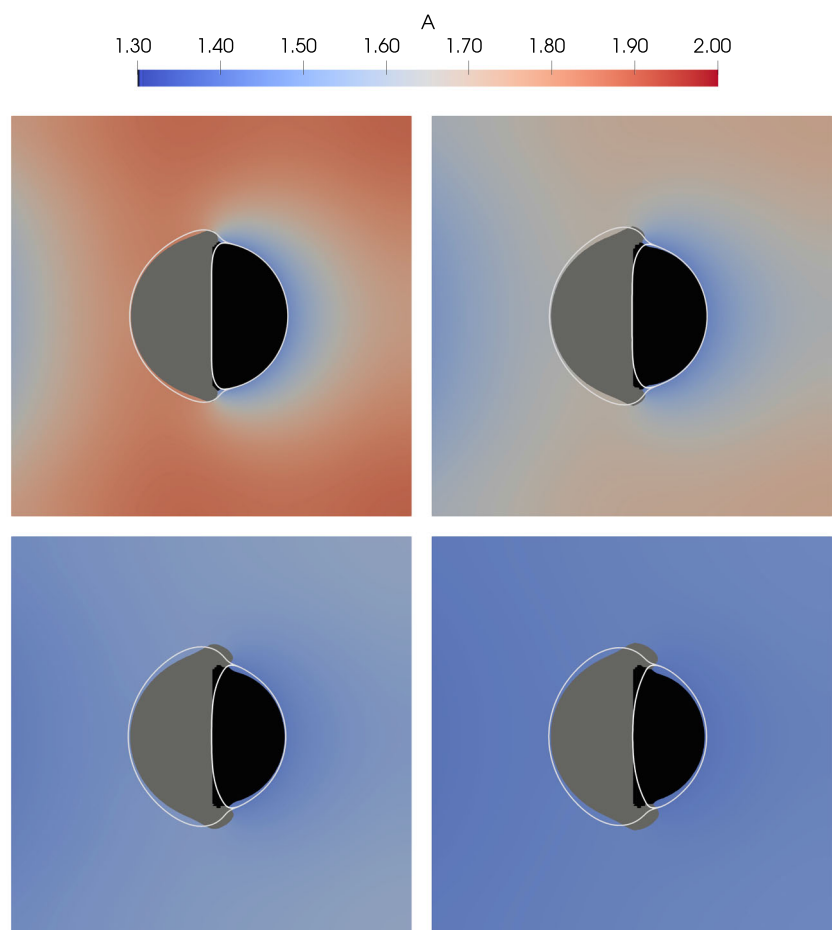
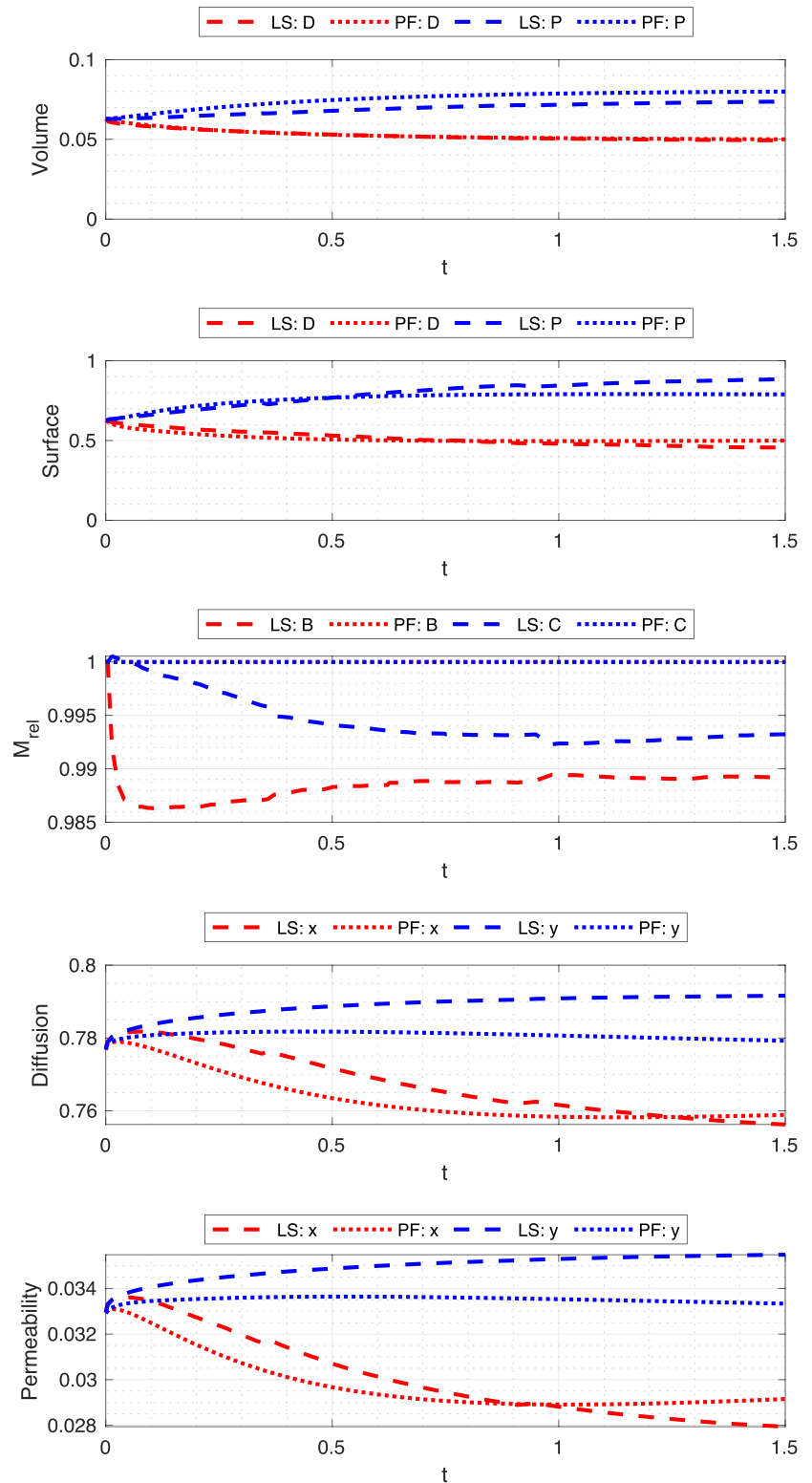


Fig. 7 Equilibrium flow case: Evolution of mineral volume over time, reactive surface area and relative total mass calculated with level-set method (LS, dashed lines) and phase-field approach (PF, dotted lines). The last two pictures illustrate the evolution of diffusion and permeability tensors along the main axes over time



4.5 Comparison for flow model

For this final example, transport of solute species is subjected to an additional advective flow field according to models introduced in Sections 2.2.3, and 2.3.3.

Figure 6 displays and compares the resulting geometrical configuration of the three-phase system for different simulation times and both approaches. As in the previous cases (Figs. 2 and 4), the minerals as obtained using the level-set method are shown in grey (P) and black (D).

In the surrounding fluid domain, the (spatially and time-dependent) concentration of solute species A is displayed. Interfaces as obtained using the phase-field model are overlaid in white. Apparently, both the level-set and phase-field approach nicely agree on geometry evolution. The system has reached an equilibrium state at the final time $T = 1.5$ to a reasonable extent. Throughout the domain $\Omega_f(1.5)$, a maximal deviation of 6.4% from the equilibrium values is measured across all solute species. Similar to our previous scenarios curvature effects are visible in the phase-field simulation close to the triple points. Due to the reduced amount of mineral overgrowth compared to Section 4.4, the implications are less severe. Figure 7 proves good agreement in mineral volume (relative deviations of 8% and 2% for minerals P and D) as well as surface area prediction (relative deviations of 11% and 10% for minerals P and D) among both simulation approaches. Still this variance is reasonably small compared to the loss of 22% and 27% in volume and surface area for mineral D and gain of 18% and 41% in volume and surface area for mineral P over simulation time according to the level-set approach. The phase-field method again achieved almost perfect mass conservation, while the level-set method's error is below 1.5%.

Due to the reduced difference between initial and final geometry in comparison to the diffusive PDE and ODE case, also the evolution of the effective tensors is less pronounced. As such, both permeability and diffusivity in y direction remain nearly constant over time. Here, relative deviations of 6% and 2% are observed at final time between both modeling approaches for diffusion and permeability, respectively. The evolution with respect to the x-direction appeared again to be more significant. A decrease of 11% (from 0.0329 to 0.0292) and 2% (from 0.778 to 0.759) are measured according to the phase-field simulation, respectively. At final time, both models agreed on the effective quantities with a deviation less than 5% with respect to the x direction.

5 Conclusion

As shown in Section 4, both the level-set model and phase-field model are able to simulate geometrical changes in a three-phase system involving two minerals and a fluid including the solutes taking part in heterogeneous reactions. Upscaled quantities like permeability and diffusivity predicted by the two approaches show a comparable evolution as the mineral shapes evolve. However, each of the two approaches inhibit strengths and weaknesses.

As it is apparent from the simulation results in Section 4, the phase-field model is capable of conserving mass up to 10 significant digits. Using a finite volume discretization the

presented phase-field model can conserve mass almost perfectly, with minor losses due to the regularization of the conservation equations. In contrast, the level-set method used does not generally guarantee conservation of mass. Yet, with a maximal deviation of 2% throughout our experimental lineup, the loss/gain in mass in the level-set simulations is relatively low. Furthermore, grid convergence tests conducted in the appendix (Fig. 8) show a diminishing effect on higher resolution. This is due to the fact that the changes in mineral volumes V_i are determined by

$$\dot{V}_i(t) = v_{n,i}(t)|\Gamma_{\text{int},i}(t)|$$

for $i \in \text{D,P}$ using an explicit first-order time discretization. In theory, the error in mass is controlled linearly by the time-step size. Assuming piece-wise smooth interfaces, the error could be reduced in higher-order by applying a higher-order discretization scheme or additionally taking local curvature into account.

On the other hand, the results of Section 4 certify the level-set method to properly handle high curvature within the interfaces. Although the reconstruction procedure applied within VIIM (see Section 3.1) loses accuracy in these situations, the errors remain highly localized and do not propagate along the whole interface over time. As such, high interface curvatures along the static interface separating both solid minerals are recovered very well. In contrast, the phase-field model performs increasingly unsatisfactory close to the equilibrium as interface velocity becomes curvature dominated. In general, the curvature-driven motion of the phase-field model affects the simulation results. As remarked in Section 2.3.4, existing approaches for diminishing curvature-driven motion are not applicable for the current setup. Although one can choose the relevant parameters controlling the curvature-driven motions small, they cannot be chosen zero and are limited by the choice of the grid. As a fine grid is needed to resolve the diffuse interfaces, a natural extension would be using adaptive grid refinement for the diffuse transition zones since one can generally accept a much coarser grid away from the interfaces. Furthermore, the phase-field model requires well chosen parameters, in particular the phase-field diffusivity ω . As described in Section 3.2 the phase-field parameters strongly influence the simulation quality, but for ω there is no simple way to predict a good choice.

Overall, the two presented modeling approaches and their implementations highlight the difficulty with capturing evolving interfaces attaining high curvatures. As the numerical experiments do not indicate any major difficulties for the level-set approach except from some mass loss/gain, the phase-field approach is influenced by the curvature-driven motion. Further work is required to find a suitable strategy to eliminate curvature-driven motion and determine suitable parameters in the phase-field approach.

Appendix

In order to justify the resolutions chosen in our simulations, we provide a grid convergence analysis for the cases where

no analytical results are available for comparison. Note that in both level-set and phase-field approach parameters ϵ and ξ are used respectively to adjust the spatial extent of the stripe in which the interfaces are treated. As

Fig. 8 Level-Set: Simulation results for different spatial resolution and choice of the level-set parameter ϵ in case of the diffusive case (top), equilibrium flow case (bottom). Volume and surface area of mineral P as well as mass conservation with respect to solute B are presented

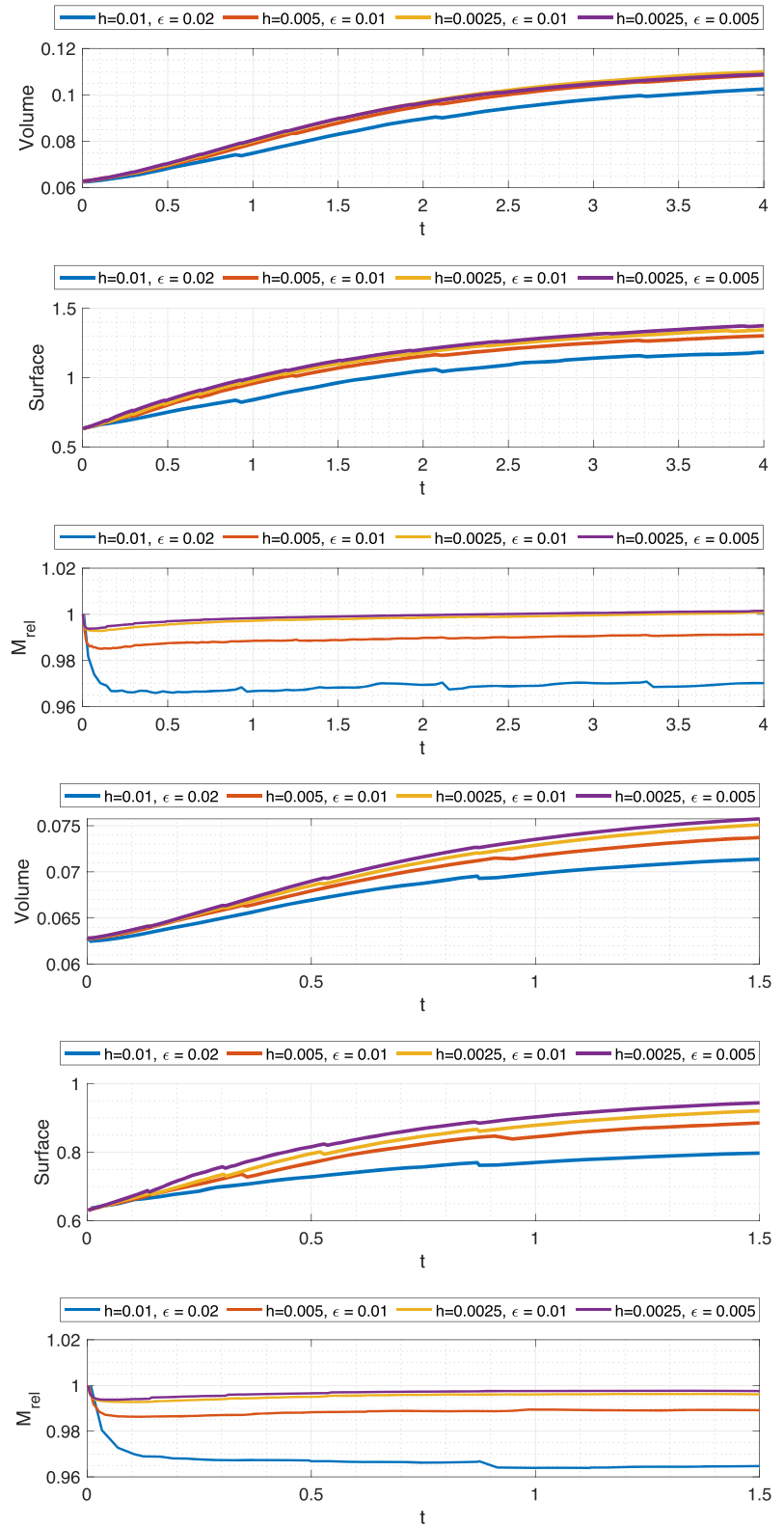
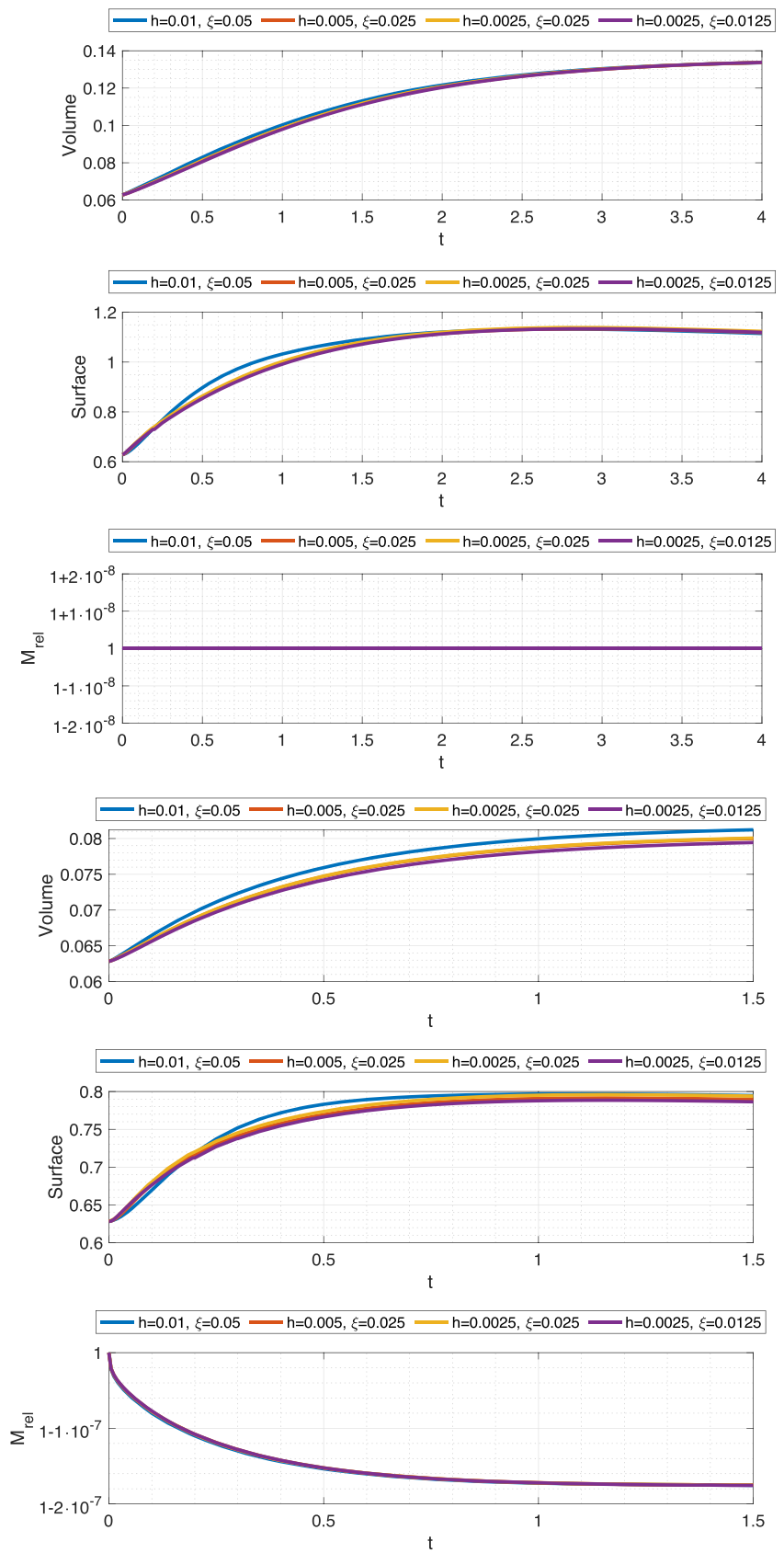


Fig. 9 Phase-field: Simulation results for different spatial resolution and choice of the phase-field parameter ξ in case of the diffusive case (top), equilibrium flow case (bottom). Volume and surface area of mineral P as well as mass conservation with respect to solute B are presented



already mentioned, a smaller choice of parameters increases precision of the geometry evolution. Yet, a lower bound is given by some multiple of the discretization length. As such, we investigate both the impact of mesh refinement as well as parameter reduction ϵ , ξ on constant meshes. The results of our convergence studies are presented in Fig. 8 for the level-set model and in Fig. 9 for the phase-field approach. For clarity, the data at final simulation time T are additionally listed in Tables 4 and 5.

Table 4 Level-Set: Comparison of values in Fig. 8 at final simulation time T

Diffusive case	Volume	M_{rel}	Surface
$h=0.01, \epsilon=0.02$	0.1026	0.9673	1.1825
$h=0.005, \epsilon=0.01$	0.1086	0.9933	1.3025
$h=0.0025, \epsilon=0.01$	0.1100	1.0008	1.3438
$h=0.0025, \epsilon=0.005$	0.1088	1.0015	1.3742
Advective case	Volume	M_{rel}	Surface
$h=0.01, \epsilon=0.02$	0.0714	0.9647	0.7975
$h=0.005, \epsilon=0.01$	0.0737	0.9891	0.8855
$h=0.0025, \epsilon=0.01$	0.0751	0.9961	0.9205
$h=0.0025, \epsilon=0.005$	0.0757	0.9976	0.9441

Table 5 Phase-Field: Comparison of values in Fig. 9 at final simulation time T

Diffusive case	Volume	M_{rel}	Surface
$h=0.01, \xi=0.05$	0.1336	1.0000	1.1150
$h=0.005, \xi=0.025$	0.1337	1.0000	1.1187
$h=0.0025, \xi=0.025$	0.1337	1.0000	1.1235
$h=0.0025, \xi=0.0125$	0.1337	1.0000	1.1195
Advective case	Volume	M_{rel}	Surface
$h=0.01, \xi=0.05$	0.0812	1.0000	0.7946
$h=0.005, \xi=0.025$	0.0800	1.0000	0.7895
$h=0.0025, \xi=0.025$	0.0801	1.0000	0.7940
$h=0.0025, \xi=0.0125$	0.0794	1.0000	0.7864

Acknowledgments Funded by Deutsche Forschungsgemeinschaft (DFG, German Research Foundation) under Germany's Excellence Strategy - EXC 2075 - 390740016. We acknowledge the support by the Stuttgart Center for Simulation Science (SimTech). This research was supported by the DFG Research Training Group 2339 Interfaces, Complex Structures, and Singular Limits and Research Unit 2179 MadSoil. The authors thank Sergi Molins, Berkeley Lab, for bringing [9] to our attention. We further acknowledge the insightful discussions with Florian Frank and Helmut Abels.

Funding Open Access funding enabled and organized by Projekt DEAL.

Data Availability The codes used in this paper will be made available within their respective frameworks of DuMu^x [16] and RTSPHEM [11] upon publication.

Open Access This article is licensed under a Creative Commons Attribution 4.0 International License, which permits use, sharing, adaptation, distribution and reproduction in any medium or format, as long as you give appropriate credit to the original author(s) and the source, provide a link to the Creative Commons licence, and indicate if changes were made. The images or other third party material in this article are included in the article's Creative Commons licence, unless indicated otherwise in a credit line to the material. If material is not included in the article's Creative Commons licence and your intended use is not permitted by statutory regulation or exceeds the permitted use, you will need to obtain permission directly from the copyright holder. To view a copy of this licence, visit <http://creativecommons.org/licenses/by/4.0/>.

References

- Abels, H.: (Non-)Convergence of solutions of the convective Allen-Cahn equation. *Partial Differ. Equ. Appl.* 3. <https://doi.org/10.1007/s42985-021-00140-5> (2022)
- Akhlaghi Amiri, H., Hamouda, A.: Evaluation of level set and phase field methods in modeling two phase flow with viscosity contrast through dual-permeability porous medium. *Int. J. Multiphase Flow* **52**, 22–34 (2013). <https://doi.org/10.1016/j.ijmultiphaseflow.2012.12.006>
- Allen, S.M., Cahn, J.W.: A microscopic theory for antiphase boundary motion and its application to antiphase domain coarsening. *Acta Metall.* **27**(6), 1085–1095 (1979). [https://doi.org/10.1016/0001-6160\(79\)90196-2](https://doi.org/10.1016/0001-6160(79)90196-2)
- Boyer, F., Lapuerta, C.: Study of a three component Cahn-Hilliard flow model. *Math Model Anal.* **40**, 653–687 (2006). <https://doi.org/10.1051/m2an:2006028>
- Boyer, F., Lapuerta, C., Minjead, S., Piar, B., Quintard, M.: Cahn-hilliard/navier-stokes model for the simulation of three-phase flows. *Transport in Porous Media* **82**, 463–483 (2010). <https://doi.org/10.1007/s11242-009-9408-z>
- Bringedal, C., von Wolff, L., Pop, I.S.: Phase field modeling of precipitation and dissolution processes in porous media: Upscaling and numerical experiments. *Multiscale Modeling & Simulation* **18**(2), 1076–1112 (2020). <https://doi.org/10.1137/19M1239003>
- Bronsard, L., Reitich, F.: On three-phase boundary motion and the singular limit of a vector-valued ginzburg-landau equation. *Arch Ration Mech An* **124**, 355–379 (1993). <https://doi.org/10.1007/BF00375607>
- Caginalp, G., Fife, P.: Dynamics of layered interfaces arising from phase boundaries. *SIAM J. Appl. Math.* **48**(3), 506–518 (1988). <https://doi.org/10.1137/0148029>
- Chen, L., Kang, Q., Carey, B., Tao, W.Q.: Pore-scale study of diffusion–reaction processes involving dissolution and precipitation using the lattice boltzmann method. *Int. J. Heat Mass Transfer* **75**, 483–496 (2014). <https://doi.org/10.1016/j.ijheatmasstransfer.2014.03.074>
- Frolov, P., Gajdošová, N., Gärtner, S., Ray, N.: Voronoi implicit interface method for geometry evolution of two minerals with applications in reactive porous media. In: *Proceedings of the conference algorithmy*, pp 121–130. <http://www.iam.fmph.uniba.sk/amuc/ojs/index.php/algorithmy/article/view/1566> (2020)
- Gärtner, S., Frank, F.: RTSPHEM – reactive transport solver in porous homogenized evolving media. <https://github.com/cupperfreeze/RTSPHEM/>. Department Mathematik, Friedrich-Alexander-Universität Erlangen-Nürnberg, Accessed: 07/10/2021 (2021)

12. Gärtner, S., Frolkovič, P., Knabner, P., Ray, N.: Efficiency and accuracy of micro-macro models for mineral dissolution. *Water Resour. Res.* **56**. <https://doi.org/10.1029/2020WR027585> (2020)
13. Gärtner, S., Frolkovič, P., Knabner, P., Ray, N.: Efficiency of micro-macro models for reactive two-mineral systems. *Multiscale Modeling & Simulation* **20**(1), 433–461 (2022). <https://doi.org/10.1137/20M1380648>
14. Hornung, U. (ed.): *Homogenization and Porous Media*. Springer, Berlin (1996)
15. Kelm, M.: *Phasenfeldansatz zum Skalenübergang für Fällungsprozesse in porösen Medien mit zwei konkurrierenden Mineralen*. Master's thesis, Friedrich-Alexander-Universität Erlangen-Nürnberg (FAU) (2020)
16. Koch, T., Gläser, D., Weishaupt, K., Ackermann, S., Beck, M., Becker, B., Burbulla, S., Class, H., Coltman, E., Emmert, S., Fetzer, T., Grüninger, C., Heck, K., Hommel, J., Kurz, T., Lipp, M., Mohammadi, F., Scherrer, S., Schneider, M., Seitz, G., Stadler, L., Utz, M., Weinhardt, F., Flemisch, B.: Dumux 3 – an open-source simulator for solving flow and transport problems in porous media with a focus on model coupling. *Computers & Mathematics with Applications* **81**, 423–443 (2021). <https://doi.org/10.1016/j.camwa.2020.02.012>. Development and Application of Open-source Software for Problems with Numerical PDEs
17. Koko, J.: Efficient MATLAB codes for the 2D/3D Stokes equation with the mini-element. *Informatica, Lith. Acad. Sci.* **30**, 243–268 (2019)
18. Li, X., Huang, H., Meakin, P.: Level set simulation of coupled advection-diffusion and pore structure evolution due to mineral precipitation in porous media. *Water Resour. Res.* **44**(12). <https://doi.org/10.1029/2007WR006742> (2008)
19. MATLAB: version 9.6.0.1072779 (R2019a). The MathWorks Inc., Natick, Massachusetts (2019)
20. Molins, S., Soulaire, C., Prasianakis, N., Abbasi, A., Poncet, P., Ladd, A., Starchenko, V., Roman, S., Trebotich, D., Tchelepi, H., Steefel, C.: Simulation of mineral dissolution at the pore scale with evolving fluid-solid interfaces: Review of approaches and benchmark problem set. *Computat Geosci.* <https://doi.org/10.1007/s10596-019-09903-x> (2020)
21. van Noorden, T.: Crystal precipitation and dissolution in a porous medium: Effective equations and numerical experiments. *Multiscale Modeling & Simulation* **7**(3), 1220–1236 (2009). <https://doi.org/10.1137/080722096>
22. van Noorden, T.L., Eck, C.: Phase field approximation of a kinetic moving-boundary problem modelling dissolution and precipitation. *Interface Free Bound* **13**(1), 29–55 (2011). <https://doi.org/10.4171/IFB/247>
23. Osher, S., Sethian, J.: Fronts propagating with curvature-dependent speed: Algorithms based on hamilton-Jacobi formulations. *J. Comput. Phys.* **79**, 12–49 (1988). [https://doi.org/10.1016/0021-9991\(88\)90002-2](https://doi.org/10.1016/0021-9991(88)90002-2)
24. Pierre, M.: Global existence in reaction-diffusion systems with control of mass: A survey. *Milan J. Math.* **78**, 417–455 (2010). <https://doi.org/10.1007/s00032-010-0133-4>
25. Redeker, M., Rohde, C., Sorin Pop, I.: Upscaling of a tri-phase phase-field model for precipitation in porous media. *IMA J. Appl. Math.* **81**(5), 898–939 (2016). <https://doi.org/10.1093/imamat/hxw023>
26. Rohde, C., von Wolff, L.: A ternary Cahn–Hilliard–Navier–Stokes model for two-phase flow with precipitation and dissolution. *Math. Models Method Appl. Sci.* **31**(01), 1–35 (2021). <https://doi.org/10.1142/S0218202521500019>
27. Rouy, E., Tourin, A.: A viscosity solutions approach to shape-from-shading. *SIAM J. Numer. Anal.* **29**(3), 867–884 (1992)
28. Salih, A., Ghosh Moulic, S.: A mass conservation scheme for level set method applied to multiphase incompressible flows. *Int. J. Comput. Methods Eng.* **14**, 271–289 (2013). <https://doi.org/10.1080/15502287.2012.711991>
29. Saye, R., Sethian, J.: Analysis and applications of the voronoi implicit interface method. *J. Comput. Phys.* **231**, 6051–6085 (2012). <https://doi.org/10.1016/j.jcp.2012.04.004>
30. Schlögl, F.: Chemical reaction models for non-equilibrium phase transitions. *Zeitschrift für Physik* **253**(2), 147–161 (1972). <https://doi.org/10.1007/BF01379769>
31. Sethian, J.A.: Fast marching methods. *SIAM Rev.* **41**, 199–235 (1998). <https://doi.org/10.1137/S0036144598347059>
32. Sethian, J.A.: *Level set methods and fast marching methods: evolving interfaces in computational geometry, fluid mechanics, computer vision, and materials science*. vol. 3, Cambridge University Press (1999)
33. Wen, H.L., Yu, C.H., Sheu, T.W.H.: A mass-preserving level set method for simulating 2d/3d fluid flows with evolving interface (2019)
34. Xu, Z., Huang, H., Li, X., Meakin, P.: Phase field and level set methods for modeling solute precipitation and/or dissolution. *Comput. Phys. Commun.* **183**(1), 15–19 (2012). <https://doi.org/10.1016/j.cpc.2011.08.005>
35. Xu, Z., Meakin, P.: Phase-field modeling of solute precipitation and dissolution. *J. Chem. Phys.* **129**(1), 014705 (2008). <https://doi.org/10.1063/1.2948949>

Publisher's note Springer Nature remains neutral with regard to jurisdictional claims in published maps and institutional affiliations.

Part D

Evaporation from porous media

The final part of this thesis consists of one chapter that is based on a journal publication, and is followed by the Conclusion and outlook of this thesis.

Chapter 11: Stability analysis of evaporation-induced density instabilities This chapter addresses evaporation from a porous medium. The analysis in this chapter is motivated by the occurrence of soil salinization, which can happen when there is evaporation from soils that are saturated with saline water. As the water evaporates, salts stay behind and gradually accumulate near the upper part of the porous medium. Then, salt will precipitate and create a salt crust if the solubility limit of the salt is reached. However, since this setting is also gravitationally unstable, density instabilities can develop. By applying a linear stability analysis, onset times for the onset of instabilities are found as a function of model parameters such as permeability, evaporation rate and diffusion coefficient. Numerical simulations are applied to also analyze the further fate of the instabilities. In particular, it is found that the instabilities develop rather slowly in terms of strength, and salts can therefore still precipitate after instabilities have occurred. This is because it takes time before the instabilities cause a net downwards transport of salt.

Chapter 12: Conclusion and outlook In this last chapter of this thesis, we summarize the main findings of this thesis and discuss some directions for further research within multiscale approaches for transport processes in porous media. In particular, we discuss how to improve the analysis in Chapter 11. This chapter does not apply any multiscale approach to analyze the density instabilities and salt precipitation, but would have benefited from such approaches.

11 Stability analysis of evaporation-induced density instabilities


The content of this chapter is based on the following original article:

C. Bringedal, T. Schollenberger, G.J.M. Pieters, C.J. van Duijn, R. Helmig. *Evaporation-Driven Density Instabilities in Saturated Porous Media*. Transport in Porous Media (2022). doi: 10.1007/s11242-022-01772-w

This publication is an open access article and distributed under the Creative Commons CC BY license.



Evaporation-Driven Density Instabilities in Saturated Porous Media

Carina Bringedal¹  · Theresa Schollenberger¹ · G. J. M. Pieters² · C. J. van Duijn³ · Rainer Helmig¹

Received: 27 August 2021 / Accepted: 7 March 2022
© The Author(s) 2022

Abstract

Soil salinization is a major cause of soil degradation and hampers plant growth. For soils saturated with saline water, the evaporation of water induces accumulation of salt near the top of the soil. The remaining liquid gets an increasingly larger density due to the accumulation of salt, giving a gravitationally unstable situation, where instabilities in the form of fingers can form. These fingers can, hence, lead to a net downward transport of salt. We here investigate the appearance of these fingers through a linear stability analysis and through numerical simulations. The linear stability analysis gives criteria for onset of instabilities for a large range of parameters. Simulations using a set of parameters give information also about the development of the fingers after onset. With this knowledge, we can predict whether and when the instabilities occur, and their effect on the salt concentration development near the top boundary.

Keywords Evaporation · Density instabilities · Linear stability analysis

Mathematics Subject Classification 76S05 · 76E20 · 35P15 · 65L60 · 65M08

1 Introduction

Evaporation of saline water from soils can cause accumulation of salts in the upper part of the soil, which has a large environmental impact as it hampers plant growth and affects biological activities (Daliakopoulos et al. 2016). As water evaporates, the salts accumulate near the top of the porous medium, which has a negative impact on root water uptake (Chaves et al. 2008). If the solubility limit of the salt is exceeded, the salts precipitate. In this case, a salt crust at the top of the soil is formed, disconnecting the soil from the

✉ Carina Bringedal
carina.bringedal@iws.uni-stuttgart.de

¹ Department of Hydromechanics and Modelling of Hydrosystems, University of Stuttgart, Stuttgart, Germany

² Department of Earth Sciences, Utrecht University, Utrecht, The Netherlands

³ Department of Mechanical Engineering, Eindhoven University of Technology, Eindhoven, The Netherlands

atmosphere (Chen 1992; Jambhekar et al. 2015; Mejri et al. 2017). The appearance of the salt crust strongly affects the growth conditions for many agricultural plants (Pitman and Läuchli 2002; Singh 2016). In arid regions, for example in Tunisia, soil salinization and soil crust formation are already interfering with and disabling agricultural activities (Mejri et al. 2020). This is not a new problem, but is gradually causing a greater impact as larger areas are affected (Vereecken et al. 2009).

Different observations in natural systems show that evaporation processes from soils cause an accumulation of salts in the upper part of the soil (Allison and Barnes 1985). This can again lead to salt precipitation, creating salt lakes and/or density-driven currents due to varying salt concentrations (Duffy and Al-Hassan 1988; Geng and Boufadel 2017). As salts accumulate at the top of the soil due to water evaporating, the density of the remaining liquid increases with increased salt concentrations (Geng and Boufadel 2015, 2017). This may lead to a gravitationally unstable setting since the liquid near the top of the soil is the heaviest, due to the accumulated salts (Gilman and Bear 1996; Nield and Bejan 2017; Wooding et al. 1997). When the soil is permeable, density instabilities in the form of fingers can be triggered (Wooding et al. 1997), which is also relevant in the context of CO₂ storage (Elenius et al. 2012; Riaz et al. 2006). The formation of density instabilities in the form of fingers induces a downward transport of the accumulated salts from the upper part of the soil toward the lower part, where the salt concentration is lower. Hence, when the density instabilities develop, they can hinder the salt concentrations near the top of the soil to exceed its solubility limit. However, for soils of low permeability, these instabilities will typically not develop, or they develop at a later time. Under these conditions, salts will continue to accumulate until salt precipitates, and a salt crust at the top of the soil is formed. This means that the occurrence of salt precipitation is tightly connected to the development of convective instabilities. Hence, understanding the process of soil salinization and the interplay with density instabilities is key questions to prevent degradation of soil quality and to ensure food production (Shokri et al. 2010; Shokri-Kuehni et al. 2020).

It is well-known that the question of whether the density instabilities occur, can be addressed by a linear stability analysis. Such an analysis has been applied to a wide range of porous-media problems where the density difference creates a gravitationally unstable setting (Nield and Bejan 2017). The onset of instabilities where an increased salt concentration at the top of the porous domain triggers the instabilities, is analyzed in Elenius et al. (2012); Riaz et al. (2006); van Duijn et al. (2019). Fingers are found to appear when the strength of the density difference overcomes the resistance of the porous medium. This is usually expressed and quantified through a critical threshold of the Rayleigh number, such that when the Rayleigh number is larger than this threshold, instabilities can occur. A density difference, and hence a change in salt concentration, is needed to induce instabilities. Hence, a strong diffusion would hinder the density difference to be strong enough, as the concentration profile is smoothed. A large resistance of the porous medium, which corresponds to a small permeability, makes it more difficult for the density difference to trigger instabilities.

The above-mentioned works on salt-induced instabilities consider a prescribed salt concentration or a prescribed density on the top boundary (Elenius et al. 2012; Riaz et al. 2006; van Duijn et al. 2019). When considering evaporation from a porous medium, the salt concentration at the top boundary develops with time as the water gradually evaporates and the dissolved salts remain. As we will see later, this can be modeled with a Robin-type boundary condition for the salt, which means that the value of the salt concentration is connected to its gradient at the top boundary. Such boundary conditions have been considered in other linear stability problems, see e.g., Barletta et al. (2009); Hattori et al. (2015).

In this work, we consider soils that remain fully saturated with water throughout the evaporation. This means that we consider a case where the modeled porous medium is connected to a deeper groundwater aquifer, which is also fully saturated. The deeper groundwater aquifer supplies the modeled soil with water during the evaporation. We also assume that the capillary pressure of the system remains below the entry pressure of the soil, such that the soil remains fully saturated. If conditions of partial saturation occur, it would be necessary to include also the flow of air through the unsaturated zone, or to use Richards equation. Evaporation would typically lead to an unsaturated zone in the upper part of the porous medium, which again has an impact on the evolution of the salt concentration (Shokri et al. 2010; Shokri-Kuehni et al. 2020).

Following the above assumptions, the evaporation of water induces a vertical, upward throughflow through the domain. The effect of upward throughflow with a given density difference between the top and bottom boundaries has been found to have a stabilizing effect on the onset of instabilities (Homsy and Sherwood 1976; van Duijn et al. 2002). That means, a stronger upward throughflow would increase the critical Rayleigh number, making it more difficult for the density difference to trigger the formation of downward-flowing fingers. It is, hence, not obvious whether an increased evaporation flux of water would have a stabilizing or destabilizing effect: an increased evaporation leads to an increased upward throughflow, which stabilizes the system, but at the same time the accumulation of salts near the top boundary is increased, which destabilizes.

The method of linear stability gives estimates for the onset of gravitational instabilities and for the time of their appearance, by considering a simplified system of equations. However, estimates for a large range of parameters can be found at low costs. After the instabilities have formed, one has to rely on numerical simulations of the governing model equations to address the further development of the salt concentration. Numerical simulations can give information on the strength and shape of the appearing convection pattern, as well as their effect on the salt transport and salt precipitation. However, these numerical simulations are expensive and need to be performed on bounded domains. Although we consider a simplified setup by assuming fully saturated conditions, this proposed analysis gives valuable insight for this idealized case and creates a starting point for further analysis when incorporating an unsaturated zone in the future.

This paper is organized as follows. In Sect. 2, we formulate the general model equations together with initial and boundary condition to address evaporation from a porous medium saturated with saline water. In Sect. 3, we consider a simplified model, for which we perform a linear stability analysis, giving criteria for when instabilities can occur. Section 4 explains the numerical framework used to simulate the general model. The results from the linear stability analysis and the numerical simulations are compared and discussed in Sect. 5, before final remarks are given in Sect. 6.

2 Mathematical Model

This section describes the physical assumptions, the domain, the partial differential equations and the boundary and initial conditions which form the mathematical model considered in this paper to describe evaporation from the top of a porous medium and the subsequent changes within the medium. Figure 1 sketches the domain together with the most important model choices. All variables and parameters are summarized in Table 1.

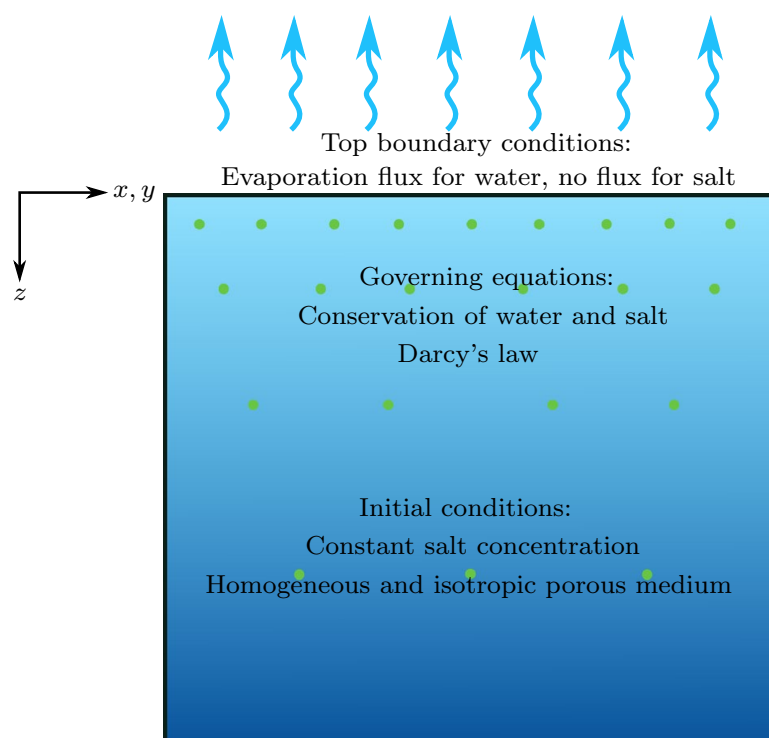
Table 1 Nomenclature

Variables	Explanation	Dimension
P	Pressure	$\text{kg m}^{-1}\text{s}^{-2}$
$\mathbf{Q} = (U, V, W)$	Darcy-velocity	m s^{-1}
X	Salt mass fraction	–
x	Mole fraction	–
t	Time	s
x, y, z	Spatial coordinates	m
p	Non-dimensional perturbed pressure	–
$\mathbf{q} = (u, v, w)$	Non-dimensional perturbed Darcy-velocity	–
χ	Perturbed salt mass fraction	–
r	Reaction rate	$\text{mol m}^{-3} \text{s}^{-1}$
$\rho(X)$	Liquid density	kg m^{-3}
$\rho_{\text{mol}}(X)$	Molar liquid density	mol m^{-3}
ζ, η, \mathcal{L}	Basis functions	–
Parameters	Explanation	Dimension
a	Wavenumber	m^{-1}
A	Amplitude of perturbation	–
d	Depth of the numerical domain	m
D	Diffusion coefficient	$\text{m}^2 \text{s}^{-1}$
\mathbf{e}	Vertical unit vector	–
E	Evaporation rate	m s^{-1}
E_{mol}	Molar evaporation rate	$\text{mol m}^{-2} \text{s}^{-1}$
γ	Salt expansion coefficient	–
ϕ	Porosity	–
g	Gravity	m s^{-2}
K	Permeability	m^2
λ	Wave length	m
μ	Dynamic viscosity	$\text{kg m}^{-1} \text{s}^{-1}$
$\mu_{x_{\text{NaCl}}}$	Mean value of NaCl mole fraction	–
m, n	Integers	–
M	Molar mass	kg mol^{-1}
\mathbf{n}	Horizontal unit vector	–
$\Omega, \Omega_{\mathcal{W}}$	Domains	–
σ	Exponential growth rate	–
$\sigma_{x_{\text{NaCl}}}$	Standard deviation of NaCl mole fraction	–
\mathcal{W}	Half width of domain or wavelength	m
Non-dimensional quantities	Explanation	Definition
$\hat{\beta}$	Relative half width or wavelength	$\mathcal{W}E/D$
k	Proportionality constant	$Q_{\text{ref}}\mathcal{W}/D\pi$
R	Evaporative Rayleigh number	$\gamma\rho_0gKX_0/E\mu$
Subscripts	Explanation	
0	Initial condition	

Table 1 (continued)

Subscripts	Explanation
max	Solubility limit
mol	Molar-based quantity
m, n	Expansion indices
p	Perturbation
ref	Reference value
solid	Solid salt phase
x, y, z	Corresponding directions
Superscripts	Explanation
0	Ground state solution
κ	Components
NaCl	Salt component
top	Top row of grid cells
w	Water component
Accents	Explanation
\wedge	Non-dimensional variable
\sim	Fourier amplitude

Dimensions are given for variables and parameters

**Fig. 1** Sketch of evaporation from porous medium and effect on salt concentration

2.1 Domain and Model Equations

The considered domain is unbounded in the vertical direction and either bounded or unbounded in the horizontal directions. Specifically, we consider either

$$\Omega = \{(x, y, z) \in \mathbb{R} : z > 0\}. \quad (1)$$

or

$$\Omega_{\mathcal{W}} = \{(x, y, z) \in \mathbb{R} : |x|, |y| < \mathcal{W}, z > 0\}, \quad (2)$$

where \mathcal{W} denotes the horizontal half width. Note that the positive vertical direction is pointing downward: hence, $z = 0$ indicates the top of the domain. Within our domain, we consider mass conservation of water and salt, along with Darcy's law representing the momentum conservation. The porous medium is assumed to be fully saturated with liquid, and the liquid consists of water and dissolved salt. Exemplary, the salt sodium chloride NaCl is used. We formulate the conservation of each of these two components independently. Both water and salt are advected with the liquid's velocity, and both are subject to diffusion:

$$\partial_t(\phi \rho_{\text{mol}} x^\kappa) = \nabla \cdot \left(-\rho_{\text{mol}} x^\kappa \mathbf{Q} + D \rho_{\text{mol}} M \nabla \left(\frac{x^\kappa}{M} \right) \right) + r^\kappa. \quad (3)$$

Here, $\kappa \in \{w, \text{NaCl}\}$ represents the two components of the liquid phase, and x^κ denotes the mole fraction of the component κ . Hence, the sum of these two mole fractions is by definition 1, which is also reflected in (3). Further, ϕ is porosity, ρ_{mol} is the molar density of the liquid phase, and M is the molar mass of the liquid mixture. Finally, D is the effective diffusivity of the components in the mixture. Note that D represents the diffusion of water mixed with salt, which is why we use the same diffusion coefficient for both components. A large diffusivity D would lead to disturbances and gradients in the concentration fields being quickly smoothed away. The reaction term r^κ accounts for chemical reactions inside the domain and is only non-zero when salt precipitation takes place within the porous medium. This means, $r^w = 0$ while

$$r^{\text{NaCl}} = \begin{cases} 0 & \text{when } x^{\text{NaCl}} \leq x_{\text{max}}^{\text{NaCl}}, \\ < 0 & \text{when } x^{\text{NaCl}} > x_{\text{max}}^{\text{NaCl}}, \end{cases} \quad (4)$$

where $x_{\text{max}}^{\text{NaCl}}$ is the solubility limit of NaCl. Hence, we have a sink term for NaCl in (3) when x^{NaCl} exceeds its solubility limit. The Darcy flux \mathbf{Q} is given by

$$\mathbf{Q} = -\frac{K}{\mu} (\nabla P - \rho g \mathbf{e}_z), \quad (5)$$

where the permeability K is assumed to be a scalar, as the porous medium is assumed to be isotropic. The liquid viscosity μ is assumed to be constant. Here we use the mass density ρ of the liquid phase. Finally, P is the pressure, and g is gravity. Note that the unit vector \mathbf{e}_z points downward. Also note that a larger density of the liquid supports a stronger downward flow.

We assume that the liquid density varies with the salt mass fraction X^{NaCl} through the linear dependence

$$\rho(X^{\text{NaCl}}) = \rho_0 (1 + \gamma (X^{\text{NaCl}} - X_0^{\text{NaCl}})), \quad (6)$$

where ρ_0 and X_0^{NaCl} are the initial liquid density and salt mass fraction, and γ is a volumetric constant. Note that the initial salt mass fraction is a constant and hence corresponds to a uniform salt distribution in space. The conversion between molar density and mass density is through

$$\rho = \rho_{\text{mol}} \cdot M, \quad (7)$$

where the molar mass M of the liquid mixture also depends on the salt content. Both molar and mass liquid density increase with the salt concentration. Note that if a different type of solute is considered, expression (6) still applies, although with a different value of γ .

If the salt exceeds its solubility limit, salt precipitates and becomes part of the solid. In this case, the porosity ϕ will change with time, and we apply a mole balance for the solid salt to describe this process:

$$\rho_{\text{mol,solid}} \partial_t \phi = -r_{\text{solid}}. \quad (8)$$

Here, $\rho_{\text{mol,solid}}$ is the molar density of the solid salt phase and r_{solid} the reaction term. We have that $r_{\text{solid}} = -r^{\text{NaCl}}$. When there is precipitation, the porosity of the porous medium and thus the permeability decreases. For the calculation of the permeability, a Kozeny-Carman-type relationship based on the initial values ϕ_0, K_0 , is used:

$$K = K_0 \left(\frac{1 - \phi_0}{1 - \phi} \right)^2 \left(\frac{\phi}{\phi_0} \right)^3. \quad (9)$$

Note that as long the salt remains below the solubility limit, there is no precipitation, and ϕ, K remain equal to their initial values ϕ_0, K_0 . These initial values are constants, and hence correspond to an initially homogeneous porous medium.

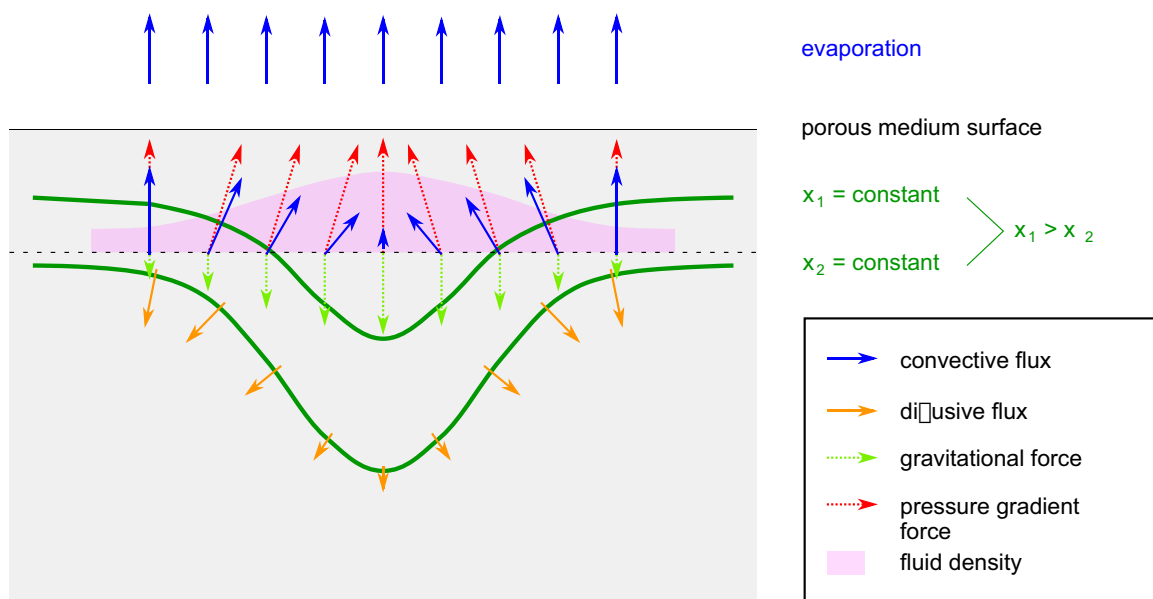


Fig. 2 Relevant forces and fluxes for the development of instabilities

2.2 Discussion of Physical Processes

In Fig. 2, the relevant fluxes described by Eq. (3) and (5) are illustrated in the context of the development of instabilities. Darcy's law describes the convective flux depending on a pressure gradient force and a gravitational force. In the considered setup, the pressure gradient generates an upward force due to evaporation at the top, while the gravitational force, however, points downward. Hence, the resulting convective flux depends on the balance of the two counter-effective forces.

Considering a perturbation with increased salt concentration and liquid density, the increased density induces stronger gravitational forces. In case of a still dominating pressure gradient force, the convective flux is in upward direction but slowed down at the location of the perturbation. This leads to a compensation of the flux by the fluxes from the surrounding, which accumulates salt and thus enhances the perturbation. This means that the salt accumulation increases the density and gravitational force even more, which can lead to a dominating gravitational force. In this case, a resulting convective downward flux is generated, which leads to a development of so-called fingers which transport the accumulated salt downward. In addition, diffusive fluxes are considered in Eq. (3). The development of instabilities is counteracted by the diffusive transport, which tries to balance out the concentration differences. Hence, the balance of the counteracting convective and diffusive fluxes determines if and how fast instabilities develop.

Parameters like the permeability for the porous medium, the diffusion coefficient for the fluid mixture or the evaporation rate as boundary condition have also an important influence on the development of the instabilities. In case of higher permeabilities, for example the convective flux is enhanced compared to the diffusive flux. This leads to a faster development of the instabilities.

2.3 Initial and Boundary Conditions

As initial conditions, we take, see (6) and (8),

$$\mathbf{x}^{\text{NaCl}}|_{t=0} = \mathbf{x}_0^{\text{NaCl}}, \quad (10)$$

$$\phi|_{t=0} = \phi_0. \quad (11)$$

At the top of the domain, we allow water to evaporate while salt remains behind. This corresponds to specifying a given molar flux E_{mol} for the water component, while a zero flux is considered for NaCl:

$$(\rho_{\text{mol}} \mathbf{x}^{\text{w}} \mathbf{Q} - D \rho_{\text{mol}} \nabla \mathbf{x}^{\text{w}}) \cdot \mathbf{e}_z|_{z=0} = -E_{\text{mol}}, \quad (12)$$

$$(\rho_{\text{mol}} \mathbf{x}^{\text{NaCl}} \mathbf{Q} - D \rho_{\text{mol}} \nabla \mathbf{x}^{\text{NaCl}}) \cdot \mathbf{e}_z|_{z=0} = 0. \quad (13)$$

Since the vertical unit vector \mathbf{e}_z points downward, the evaporation flux $E_{\text{mol}} > 0$ corresponds to an upward flux of water. In general, the Darcy flux \mathbf{Q} will be non-zero on the top boundary due to the presence of the evaporative flux. This also means that the no-flux boundary for salt (13) is a Robin boundary condition. Since water escapes through the top boundary while salt remains behind, we expect an accumulation of salt concentration near the top boundary. Increasing $E_{\text{mol}} > 0$ yields the concentration of NaCl increasing faster

near the top boundary. We will here assume a prescribed evaporation flux that is constant with respect to both time and space. This is a simplification, especially when time periods of more than a few hours are considered (Heck et al 2020) and should in this case be interpreted as an averaged evaporation flux.

Since the domain is semi-infinite in the vertical direction, boundary conditions at the bottom boundary are not needed. There the values are inherited from the initial conditions.

For the horizontal extent of the domain, we separate between the bounded and unbounded case. In the unbounded case, we do not need any boundary conditions in the horizontal direction. For the bounded case, we apply no-flux boundary conditions at the vertical walls. This corresponds to

$$\mathbf{Q} \cdot \mathbf{n}|_{x,y=\pm\mathcal{W}} = 0, \quad \nabla x^k \cdot \mathbf{n}|_{x,y=\pm\mathcal{W}} = 0, \quad (14)$$

where \mathbf{n} is the horizontal unit vector pointing out of the sidewalls of the bounded domain $\Omega_{\mathcal{W}}$.

The general equations formulated here form the starting point for our further investigation of evaporation from the porous medium and subsequent onset of density instabilities. For the linear stability analysis in Sect. 3, we use a slightly simplified system of equations and cast the equations in non-dimensional form to keep the analysis as general as possible. The numerical setup described in Sect. 4 uses the model as described above, but using bounded domains. The comparison between the two approaches in Sect. 5 considers the dimensional case in order to connect back to the physical problem.

3 Linear Stability Analysis

To address when instabilities can occur and give a criterion for the onset of instabilities depending on the model parameters, we perform a linear stability analysis following relatively standard steps, but giving a non-standard outcome due to the special setup following the evaporation from the top boundary.

To accommodate the linear stability analysis, we consider here slightly simplified model equations than the general presented in Sect. 2. These simplified equations are non-dimensionalized to find ratio of parameters that characterize the overall behavior. The equations are non-dimensionalized using identified reference values characterizing the setup. As we have somewhat untypical boundary conditions due to the evaporation at the top boundary, the chosen reference values are non-standard. From the non-dimensional formulation, we derive a time-dependent stable solution ("the ground state"). Due to the gradually growing salt concentration following the evaporation, the salt ground state is unbounded and does not exhibit a steady state. For finite times, the time-dependent ground state is perturbed using the frozen-profile approach, in order to address its stability. Since the perturbed quantities are small, we linearize the equations for the perturbed quantities. The linearized perturbation equations are then finally formulated as an eigenvalue problem, which is solved numerically. This will give information on the stability of the ground state as a function of time.

Note that the linear stability analysis is made general in the sense that it is also applicable for salt types other than NaCl by adjusting the value of corresponding parameters, in particular of the volumetric constant γ .

3.1 Simplified Model Equations

We apply the method of linear stability for a simplified version of the model presented in Sect. 2. We assume that the salt is completely dissolved and that its mass fraction is small compared to the mass fraction of water. We take advantage of the fact that $x^w \approx 1$ and hence simplify the mass conservation equation for water. Then we invoke the Boussinesq approximation, meaning that the liquid density ρ can be considered constant except in the gravity term of Darcy's law. Further, we disregard salt precipitation, which means that the simplified model is only valid up to the salt reaches its solubility limit. Porosity and permeability will, hence, remain constant. With these simplifications, Eq. (3) reduce to

$$\nabla \cdot \mathbf{Q} = 0, \quad (15)$$

$$\phi \partial_t X = \nabla \cdot (-\mathbf{Q}\mathbf{X} + D\nabla X), \quad (16)$$

where X is the mass fraction of salt. Since only salt mass fraction is used as a variable in the following, we skip the superscript. Darcy's law is kept as in (5), and the density of the liquid is still depending linearly on the salt concentration (6). Note that these model equations are simplified since varying water mass fraction is not accounted for, and since we apply the Boussinesq approximation. However, for relatively low variability in the salt content (i.e., below the solubility limit of salt), these assumptions are reasonable.

As initial condition for the salt, we use the corresponding version of (10), namely

$$X|_{t=0} = X_0, \quad (17)$$

where X_0 is the initial mass fraction, and the boundary conditions (14) at the sidewalls are, hence, correspondingly formulated for X .

Due to the difference in addressing the mass of water and salt, the boundary conditions (12) and (13) are replaced with

$$\mathbf{Q}|_{z=0} = -E\mathbf{e}_z \quad (18)$$

$$(\mathbf{X}\mathbf{Q} - D\nabla X)|_{z=0} \cdot \mathbf{e}_z = 0, \quad (19)$$

where E is the evaporation rate in terms of a volume flux of water. The two evaporation fluxes E_{mol} and E are related through

$$E_{\text{mol}} = E \cdot M \cdot \rho. \quad (20)$$

For convenience and to identify parameter dependencies, we will recast the equations in a dimensionless form.

3.2 Non-dimensional Model

The corresponding non-dimensional variables are denoted by a hat:

$$(\hat{x}, \hat{y}, \hat{z}) = \frac{(x, y, z)}{\ell_{\text{ref}}}, \quad \hat{t} = \frac{t}{t_{\text{ref}}}, \quad \hat{P} = \frac{P}{P_{\text{ref}}}, \quad (21)$$

$$\hat{\mathbf{Q}} = \frac{\mathbf{Q}}{Q_{\text{ref}}}, \quad \hat{\rho} = \frac{\rho}{\rho_{\text{ref}}}, \quad \hat{X} = \frac{X}{X_{\text{ref}}}. \quad (22)$$

We choose reference quantities that are meaningful to address the effect of evaporation, taking into account that the domain is vertically unbounded and that no prescribed density difference is given.

As length reference, we choose an intrinsic length, namely the ratio between diffusion and evaporation $\ell_{\text{ref}} = D/E$, which quantifies the length scale at which diffusion can smooth out concentration differences caused by the evaporation. As time reference, we use $t_{\text{ref}} = \phi \ell_{\text{ref}}^2 / E = \phi D / E^2$, which corresponds to the natural time scale for evaporative transport inside the porous medium. As reference concentration and density, we use the initial concentration and density; $X_{\text{ref}} = X_0$, $\rho_{\text{ref}} = \rho_0 \gamma X_0$. Note that the salt mass fraction is itself non-dimensional, hence the new variable \hat{X} is only a scaled version of X . For density-driven instability problems, there is usually a prescribed density difference, which is used as the reference density. However, this is not the case here due to the no-flux boundary condition used for salt. Since the salt concentration, and hence, the density could grow unbounded, this model problem does not exhibit a natural density difference. Hence, the initial density scaled with γ and X_0 is used as reference density. We have here chosen to include also γ and X_0 in the reference density for convenience. This choice is not essential for the non-dimensionalization and not including these two factors would essentially give the same results in the linear stability analysis, just accordingly scaled. The reference velocity is set as a gravitational velocity $Q_{\text{ref}} = \rho_{\text{ref}} g K / \mu$, and the reference pressure is chosen to balance the velocity in Darcy's law $P_{\text{ref}} = \mu \ell_{\text{ref}} Q_{\text{ref}} / K$. To summarize all choices, we list them below:

$$\ell_{\text{ref}} = \frac{D}{E}, \quad t_{\text{ref}} = \frac{\phi \ell_{\text{ref}}^2}{E}, \quad X_{\text{ref}} = X_0, \quad (23)$$

$$\rho_{\text{ref}} = \rho_0 \gamma X_0, \quad Q_{\text{ref}} = \frac{\rho_{\text{ref}} g K}{\mu}, \quad P_{\text{ref}} = \frac{\mu \ell_{\text{ref}} Q_{\text{ref}}}{K} \quad (24)$$

We finally introduce the evaporative Rayleigh number $R = Q_{\text{ref}} / E$. Hence, the Rayleigh number describes the ratio between the gravitational flow and the flow induced by the evaporative flux at the top boundary. Note that a larger evaporation rate corresponds to a smaller Rayleigh number. Summarizing, we have

$$R = \frac{Q_{\text{ref}}}{E} \text{ where } Q_{\text{ref}} = \frac{\gamma \rho_0 g X_0 K}{\mu}. \quad (25)$$

Remark 1 In many density-driven instability problems, a typical density difference is used in the reference velocity Q_{ref} and hence in the Rayleigh number R (see e.g., Riaz et al. 2006). However, in our model setup no typical density difference appears as we do not prescribe a fixed density at the top of the domain. Instead, we propose a reference velocity that only involves the initial density ρ_0 . The choice of reference velocity does not affect the linear stability analysis results.

Remark 2 Note that the definition of the Rayleigh number does not include the diffusion coefficient D . Here it appears in the reference length, and hence also in the reference time.

As we will see later, the critical Rayleigh number will be a function of non-dimensional time and a non-dimensional length parameter, which indirectly gives the dependence of the onset of instabilities on the diffusion.

The non-dimensional model equations are then

$$\hat{\mathbf{V}} \cdot \hat{\mathbf{Q}} = 0, \quad (26)$$

$$\hat{\mathbf{Q}} = -\hat{\mathbf{V}}\hat{P} + \hat{\rho}(\hat{X})\mathbf{e}_z, \quad (27)$$

$$\partial_{\hat{t}}\hat{X} = \hat{\mathbf{V}} \cdot (-R\hat{\mathbf{Q}}\hat{X} + \hat{\mathbf{V}}\hat{X}), \quad (28)$$

where the non-dimensional density is given as

$$\hat{\rho}(\hat{X}) = \frac{1}{\gamma X_0} + \hat{X} - 1. \quad (29)$$

For the non-dimensional variables, we have the initial condition

$$\hat{X}|_{\hat{t}=0} = 1, \quad (30)$$

and boundary conditions at the top boundary

$$\hat{\mathbf{Q}}|_{\hat{z}=0} = -\frac{1}{R}\mathbf{e}_z, \quad (31)$$

$$(\hat{X} + \hat{\mathbf{V}}\hat{X})|_{\hat{z}=0} \cdot \mathbf{e}_z = 0. \quad (32)$$

In the bounded case, the no-flux boundary conditions are imposed on $\hat{x}, \hat{y} = \pm\hat{\beta}$, where $\hat{\beta} = \mathcal{W}E/D$. Hence

$$\hat{\mathbf{Q}} \cdot \mathbf{n}|_{\hat{x}, \hat{y} = \pm\hat{\beta}} = 0, \quad \hat{\mathbf{V}}\hat{X} \cdot \mathbf{n}|_{\hat{x}, \hat{y} = \pm\hat{\beta}} = 0. \quad (33)$$

3.3 Ground State Solution

We will investigate the stability of a particular solution of the system of Eqs. (26)–(28) under the conditions (30)–(32). This solution depends on \hat{z} and \hat{t} . It is called the *ground state* and is denoted by $\{\hat{\mathbf{Q}}^0, \hat{X}^0, \hat{P}^0\}$.

For the ground state discharge $\hat{\mathbf{Q}}^0(\hat{t}, \hat{z})$, it is clear from (26) together with the boundary condition (31) that the only possible solution is

$$\hat{\mathbf{Q}}^0(\hat{t}, \hat{z}) = -\frac{1}{R}\mathbf{e}_z, \quad (34)$$

that is, a constant upward velocity according to the prescribed evaporation rate.

The ground state salt mass fraction $\hat{X}^0(\hat{t}, \hat{z})$ fulfills the following problem:

$$\partial_{\hat{t}}\hat{X}^0 = \partial_{\hat{z}}\hat{X}^0 + \partial_{\hat{z}}^2\hat{X}^0 \quad \hat{z} > 0, \hat{t} > 0, \quad (35)$$

$$\hat{X}^0 + \partial_{\hat{z}}\hat{X}^0 = 0 \quad \hat{z} = 0, \hat{t} > 0, \quad (36)$$

$$\hat{X}^0 = 1 \quad \hat{z} > 0, \hat{t} = 0. \quad (37)$$

In Appendix A, we show that this problem has the explicit solution

$$\hat{X}^0(\hat{t}, \hat{z}) = 1 + \int_0^{\hat{t}} \partial_{\hat{z}} f(\theta, \hat{z}) d\theta, \quad (38)$$

where

$$f(\theta, \hat{z}) = 1 - \frac{1}{2} e^{-\hat{z}} \operatorname{erfc}\left(\frac{\hat{z} - \theta}{2\sqrt{\theta}}\right) - \frac{1}{2} \operatorname{erfc}\left(\frac{\hat{z} + \theta}{2\sqrt{\theta}}\right). \quad (39)$$

Note in particular that

$$\partial_{\hat{z}} f(\theta, \hat{z}) = \frac{1}{2} e^{-\hat{z}} \operatorname{erfc}\left(\frac{\hat{z} - \theta}{2\sqrt{\theta}}\right) + \frac{1}{\sqrt{\pi\theta}} e^{-\left(\frac{\hat{z} + \theta}{2\sqrt{\theta}}\right)^2}, \quad (40)$$

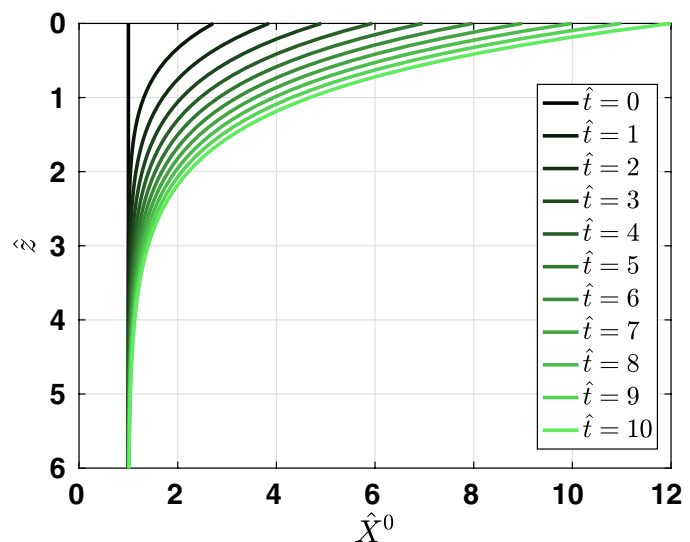
enabling a simple evaluation of the integral in (38). The solution is shown in Fig. 3. Clearly, the salt concentration at the top of the domain gradually increases with time and diffuses down through the domain.

Note that since (28) (and hence (35)) does not incorporate the precipitation rate in case the salt mass fraction exceeds the solubility limit, the solution (38) is only valid up to the point where the salt mass fraction at the top reaches the solubility limit. The (non-dimensional) solubility limit depends on the type of salt and the initial concentration. Note, however, that the ground state (38) does not depend on the type of salt. Our analysis can, hence, be straightforwardly applied to any salt type, but only up to times where the corresponding solubility limit is reached.

The ground state pressure $\hat{P}^0(\hat{t}, \hat{z})$ is such that

$$\partial_{\hat{z}} \hat{P}^0 = \frac{1}{R} + \hat{\rho}(\hat{X}^0). \quad (41)$$

Fig. 3 Ground state salt mass fractions \hat{X}^0 (horizontal axis) varying with depth \hat{z} (vertical axis) for various times \hat{t}



As we only have boundary conditions for the value of the velocity, the pressure is only known up to a constant. Hence,

$$\hat{P}^0(\hat{t}, \hat{z}) = C(\hat{t}) + \left(\frac{1}{R} + \frac{1}{\gamma X_0} - 1\right)\hat{z} + \int_0^{\hat{z}} \hat{X}^0(\hat{t}, \zeta) d\zeta, \quad (42)$$

where the integration constant $C(\hat{t})$ cannot be determined, but where a natural choice would be atmospheric pressure at the top boundary. This is, however, not necessary as the following analysis does not depend on the value of the pressure.

3.4 Linear Perturbation and Eigenvalue Problem

Our purpose is to investigate the linear stability of the ground state $\{\hat{Q}^0, \hat{X}^0, \hat{P}^0\}$. We present the main steps in this section, while details and intermediate steps are given in Appendix B. We write

$$\hat{Q}(\hat{t}, \hat{x}, \hat{y}, \hat{z}) = \hat{Q}^0(\hat{t}, \hat{z}) + \mathbf{q}(\hat{t}, \hat{x}, \hat{y}, \hat{z}), \quad (43)$$

$$\hat{X}(\hat{t}, \hat{x}, \hat{y}, \hat{z}) = \hat{X}^0(\hat{t}, \hat{z}) + \chi(\hat{t}, \hat{x}, \hat{y}, \hat{z}), \quad (44)$$

$$\hat{P}(\hat{t}, \hat{x}, \hat{y}, \hat{z}) = \hat{P}^0(\hat{t}, \hat{z}) + p(\hat{t}, \hat{x}, \hat{y}, \hat{z}), \quad (45)$$

where $\mathbf{q} = (u, v, w)$, χ and p are small, perturbed quantities, which we will now study further. Note that although these are all non-dimensional, we write them without the hat to simplify the notation. By inserting (43)–(45) into (26)–(28) and into (31)–(32) and linearizing the result, we obtain the linear perturbation equations with corresponding homogeneous boundary conditions for the perturbed quantities. These equations can be expressed using w , χ and p only.

Since the perturbed quantities fulfill a linear initial-boundary value system, in which none of the coefficients depend on the spatial coordinates \hat{x} and \hat{y} , we consider solutions of the form

$$\{w, \chi, p\}(\hat{t}, \hat{x}, \hat{y}, \hat{z}) = \{\tilde{w}, \tilde{\chi}, \tilde{p}\}(\hat{t}, \hat{z}) \cos(\hat{a}_x \hat{x}) \cos(\hat{a}_y \hat{y}). \quad (46)$$

Here \hat{a}_x and \hat{a}_y are horizontal wavenumbers. Let $\hat{a}^2 = \hat{a}_x^2 + \hat{a}_y^2$. When the domain is unbounded, i.e., the half space $\{\hat{z} > 0\}$, we allow any $\hat{a} > 0$. In case of the bounded domain $\{(\hat{x}, \hat{y}, \hat{z}) : |\hat{x}|, |\hat{y}| < \hat{\beta}, \hat{z} > 0\}$, we need to choose \hat{a}_x and \hat{a}_y so that the boundary conditions (33) are satisfied. This requires

$$\hat{a}_x = n_x \frac{\pi}{\hat{\beta}}, \quad \hat{a}_y = n_y \frac{\pi}{\hat{\beta}}, \quad n_x, n_y = 1, 2, \dots \quad (47)$$

Using (46) allows us to eliminate the amplitude \tilde{p} as a dependent variable, and only consider amplitudes \tilde{w} and $\tilde{\chi}$.

Assuming, in addition, that the coefficients of the initial-boundary value problem do not depend on time \hat{t} , we can further separate the variables according to

$$\{\tilde{w}, \tilde{\chi}\}(\hat{t}, \hat{z}) = \{\hat{w}, \hat{\chi}\}(\hat{z}) e^{\sigma \hat{t}}, \quad (48)$$

see e.g., Subrahmanyam (1961); Nield and Bejan (2017). Here, σ is the exponential growth rate in time, while \hat{w} and $\hat{\chi}$ describe the variability of the perturbation with \hat{z} . For $\sigma < 0$, small perturbations decay in time and the ground state is stable. For $\sigma > 0$, perturbations grow in time, and the ground state is unstable.

Since $\hat{X}^0 = \hat{X}^0(\hat{t}, \hat{z})$, the separation of variables as proposed in (48) does not directly apply. This is circumvented by assuming that the rate of change of $\hat{X}^0(\hat{t}, \hat{z})$ is small compared to any exponentially growing instability. This is known as the quasi steady state approach (QSSA) or the "frozen profile" approach (Riaz et al. 2006; van Duijn et al. 2002). Hence, \hat{X}^0 is considered to be evaluated at a fixed time.

Thus, we arrive at an eigenvalue problem in terms of $\{\hat{w}, \hat{\chi}\}$ and R , with independent parameters \hat{a} , \hat{t} and σ . The object is to determine the smallest positive eigenvalue $R = R_*(\hat{a}, \hat{t}, \sigma)$. We verified numerically, see Appendix C and van Duijn et al. (2019), that there is exchange of stability; i.e., the ground state loses its stability, corresponding to perturbations start growing and $\sigma > 0$, for $R > R_*(\hat{a}, \hat{t}, 0)$. Hence, it suffices to analyze the eigenvalue problem for the case of neutral stability; that is, $\sigma = 0$. Thus, we need to consider the problem (skipping the asterisk in R_*):

Given $\hat{a} > 0$, $\hat{t} > 0$, and $\hat{X}^0 = \hat{X}^0(\hat{t}, \hat{z})$ by (38), find the smallest $R = R(\hat{a}, \hat{t}) > 0$ such that

$$\left. \begin{aligned} \hat{w}'' + \hat{a}^2 \hat{\chi} - \hat{a}^2 \hat{w} &= 0 & \hat{z} > 0, \\ \hat{\chi}' - R\hat{w}\partial_z \hat{X}^0 + \hat{\chi}'' - \hat{a}^2 \hat{\chi} &= 0 & \hat{z} > 0, \\ \text{where } \hat{w} \text{ and } \hat{\chi} \text{ fulfill} & & \\ \hat{w} = 0, \hat{\chi} + \hat{\chi}' &= 0 & \hat{z} = 0, \\ \hat{w} \rightarrow 0, \hat{\chi} \rightarrow 0 & & \hat{z} \rightarrow \infty, \end{aligned} \right\} \quad (49)$$

has a non-trivial solution.

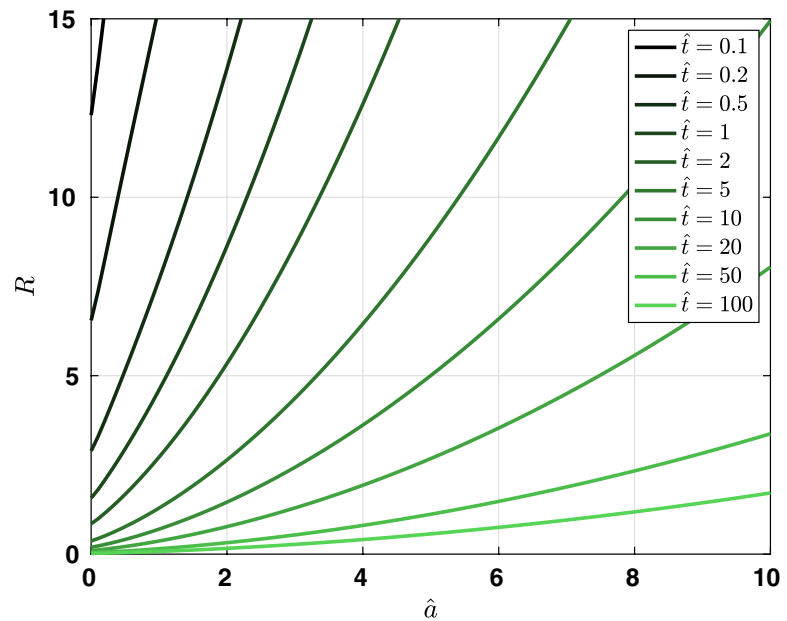
Note that $'$ denotes the derivative with respect to \hat{z} .

Remark 3 In the work of Riaz et al. (2006), the ground state results from a diffusion process and depends on $\hat{\xi} = \frac{\hat{z}}{\sqrt{\hat{t}}}$ only. This allows them to perform the coordinate transformation $(\hat{t}, \hat{z}) \rightarrow (\hat{t}, \hat{\xi})$ and then apply the QSSA to the transformed linear problem. This yields a sharp stability bound. In our case, the ground state results from diffusion and upward convection due to evaporation. Consequently, the ground state (38) does not have such a simple dependence. Therefore, we apply the QSSA directly to the original coordinates (\hat{t}, \hat{z}) .

3.5 Solution of the Eigenvalue Problem

The eigenvalue problem (49) is solved via a Laguerre-Galerkin method. Again, details are given in Appendix B. This results in a system of linear equations for the unknown weights, which can be expressed as a matrix multiplied with a vector containing the weights. Through the eigenvalues of the resulting matrix, we can find the corresponding minimal R as a function of \hat{a} for given \hat{t} , i.e., $R = R(\hat{a}, \hat{t})$. Results are shown in Fig. 4. From the figure, we observe that the system becomes gradually more unstable for increasing \hat{t} . With the Rayleigh number specified by model parameters $R_s = \frac{\gamma \rho_0 g k X_0}{E \mu}$, the system remains stable when $R_s < R$ in Fig. 4. As the curves for R move downward with increasing time, we can for given parameters find a corresponding onset time, which is when $R_s = R$. For a fixed time \hat{t} , the minimum R always appears for \hat{a} approaching 0. This corresponds to longer wavelengths being more unstable. The behavior of R for small wavenumbers \hat{a} is detailed

Fig. 4 Resulting minimal eigenvalue R (vertical axis) as a function of \hat{a} (horizontal axis) for various \hat{t}



in Appendix D. There we also derive an approximation (in fact a lower bound) for the value of R at $\hat{a} = 0$. We find

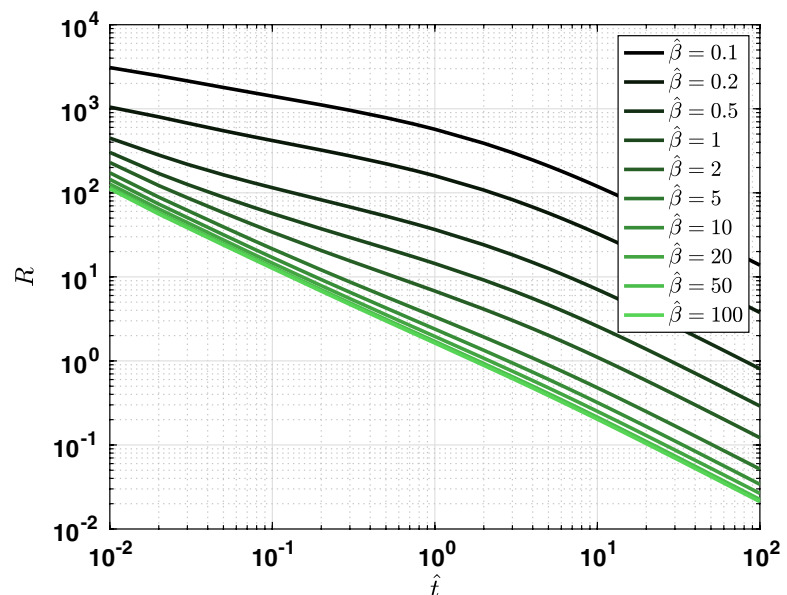
$$R(0, \hat{t}) \geq \frac{2}{\hat{X}^0(\hat{t}, 0) - 1} \text{ for all } \hat{t} > 0.$$

Hence, the evaporation problem is stable as long as

$$R_s < \frac{2}{\hat{X}^0(\hat{t}, 0) - 1}.$$

In Fig. 4, we treat \hat{a} as a continuous variable. This is allowed when the domain is unbounded. For bounded domains, with zero-flux boundary conditions on the sidewalls, only values of \hat{a} that are multiples of $\pi/\hat{\beta}$ are allowed (see (47)). We observe in Fig. 4 that

Fig. 5 Critical Rayleigh number R (vertical axis) as a function of \hat{t} (horizontal axis) for various $\hat{\beta}$



for fixed \hat{t} , the minimum R always occurs for the lowest possible \hat{a} . Hence in the bounded case, we would only need to solve the eigenvalue problem for $\hat{a} = \pi/\hat{\beta}$. For a fixed $\hat{\beta}$ (and hence a fixed \hat{a}), the system becomes generally more unstable for later times \hat{t} . In Fig. 5, we show the critical Rayleigh number for various choices of $\hat{\beta}$ as a function of \hat{t} , which hence are the R -values from Fig. 4 corresponding to $\hat{a} = \pi/\hat{\beta}$. Note that for larger values of $\hat{\beta}$, the critical Rayleigh numbers tend to those for $\hat{a} \rightarrow 0$, which corresponds to an infinitely wide domain or an infinitely long wavelength, where no effect of the imposed boundary conditions at the sidewalls are found. These results imply that we can find unique times for onset of instabilities for a given set of parameters, both in the bounded and unbounded case. For a given $\hat{\beta}$ and model parameters R_s , the corresponding unique onset time can be found in Fig. 5 by finding the corresponding time where $R = R_s$ for our choice of $\hat{\beta}$. Similarly, for a given \hat{a} and model parameters R_s , we can find the corresponding unique onset time in Fig. 4.

Note that although we show results for a large range of non-dimensional times in Figs. 4 and 5, the results are only physically meaningful when the stable salt concentration does not reach its non-dimensional solubility limit. However, the eigenvalue problem (49) can be used for any salt.

3.6 Effect of Varying the Evaporation Rate

Although the solutions of the eigenvalue problem (49) can be used to discuss the effect of all model parameters, we discuss here in particular the effect of the evaporation rate E . The expected influence of E on the stability is a-priori not obvious as it affects the system in two different ways: firstly, a larger evaporation rate corresponds to a stronger vertical, upward throughflow, and secondly, a larger evaporation rate means that the accumulation of salts at the top of the domain is faster. As shown by Homsy and Sherwood (1976); van Duijn et al. (2002), an increased throughflow corresponds to the system being more stable. However, an increased accumulation of salts at the top of the domain is expected to destabilize the system as the density difference is then larger.

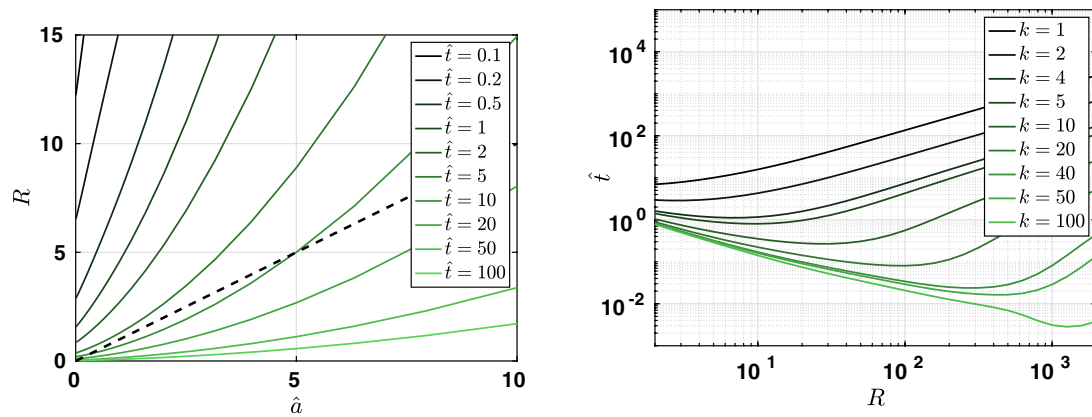
To investigate the overall effect of increasing evaporation rate, we recall the definitions

$$R = \frac{Q_{\text{ref}}}{E}, \quad \hat{\beta} = \frac{\mathcal{W}E}{D}, \quad \hat{a} = \frac{\pi}{\hat{\beta}} = \frac{\pi D}{\mathcal{W}E}, \quad (50)$$

where \hat{a} is the lowest possible wavenumber in the bounded domain case and hence the most unstable mode. Eliminating E from (50) yields

$$R = k\hat{a} \quad \text{with } k = \frac{Q_{\text{ref}}\mathcal{W}}{D\pi}. \quad (51)$$

Recall that \mathcal{W} is the half width of the domain, Q_{ref} is the reference velocity, and D is the diffusivity of the salt. For a given setup, these numbers would remain constant, but different setups result in different values of k . Returning to Fig. 4, this means that for a given k we look for the points where the curves for fixed times cross the curves $R = k\hat{a}$. As a given E corresponds to a given \hat{a} (and also R), we can find a corresponding onset time \hat{t} for each E . Due to the shape of the curves from Fig. 4, there will be an evaporation rate for which a minimum non-dimensional onset time is found. In Fig. 6, we re-plot Fig. 4 together with the line corresponding to $k = 1$, as well as the corresponding onset times as a function of R



(a) Repetition of Figure 4 including the line $R = k\hat{a}$ for $k = 1$ as dashed line. **(b)** Non-dimensional onset time \hat{t} (vertical axis) as a function of Rayleigh number R (horizontal axis) for various k .

Fig. 6 Relation between onset time and critical Rayleigh number for varying evaporation rate

for various choices of k . The minimum onset times seen in Fig. 6b correspond to the times where the line $R = k\hat{a}$ is tangential to a line corresponding to a fixed time in Fig. 6a.

When the evaporation rate increases, R decreases. Hence, as E increases, we follow a specific curve (corresponding to the chosen value of k) in Fig. 6b, from right to left. We see that as evaporation increases, the corresponding non-dimensional onset time decreases until it reaches a minimum, but then increases as E increases even further. Hence, it appears that for large evaporation rates, increasing E further has a stabilizing effect since the onset time increases. However, Fig. 6b shows *non-dimensional* onset times. To re-dimensionalize the onset times, we multiply with $t_{\text{ref}} = \phi D/E^2$. Hence, for increased evaporation rates, the time scaling is smaller. Therefore, when considering the dimensional onset times, these are found to always decrease as the evaporation rate increases. This is independent of the choice of k . Hence, an increased evaporation rate always has a destabilizing effect on the system, since instabilities can appear earlier in dimensional time.

4 Numerical Simulation of the Original Model

We apply a numerical, REV-scale model to simulate the model equations described in Sect. 2. In line with the formulation in Sect. 2, and due to the applied numerical model using dimensional variables, we now consider the dimensional model. Using dimensional variables also helps to connect back to the physical problem. The numerical model is able to give insights in the distribution and development of the salt concentration in the entire domain. This means that the onset as well as the development of instabilities can be observed in detail. However, it is computationally cost intensive as quite a fine spatial, and temporal discretization is necessary to reduce the influence of numerical diffusion and resolve the instabilities. The numerical model is implemented in the open-source simulator DuMur^x (Koch et al. 2020) for multi-phase, multi-component flow and transport in porous media. It is a research code written in C++ and based on Dune (Bastian et al. 2021), a scientific numerical software framework.

The model considers the precipitation of salt if the solubility limit is exceeded. In this section, we, therefore, first define the reaction term. Additional boundary and initial

conditions are specified as we here consider a vertically bounded domain and introduce initial perturbations for the salt mole fraction. Further the spatial and temporal discretizations are described. The domain is discretized by a cell-centered finite volume scheme, and an implicit Euler method is used for the time discretization. In the end, the evaluation method of the simulation results is described, the numerical onset time is defined, and the influence of different initial perturbations is shown.

4.1 Salt Precipitation Reaction in the Numerical Model

In the numerical model, the precipitation of solid salt is considered if the solubility limit is exceeded. Therefore, the reaction term in the mole balance of the solute and solid salt (Eq. (3) and (8)) has to be specified. For the reaction terms of NaCl $r_{\text{solid}} = -r^{\text{NaCl}}$, an equilibrium reaction is assumed. This is based on the assumption that the chemical reaction is so fast that every mol of NaCl above the solubility limit $x_{\text{max}}^{\text{NaCl}}$ can precipitate within one numerical time step Δt .

$$r_{\text{solid}} = -r^{\text{NaCl}} = \rho_{\text{mol}} \phi \frac{x^{\text{NaCl}} - x_{\text{max}}^{\text{NaCl}}}{\Delta t}. \quad (52)$$

4.2 Boundary and Initial Conditions

The numerical model uses additional boundary and initial conditions to the ones described in Sect. 2.3. As the domain is finite at the bottom for the numerical simulation, boundary conditions for the bottom are necessary. A Dirichlet boundary condition sets the pressure in the liquid phase corresponding to the hydro-static pressure at the domain depth, and the salt concentration is set equal to the initial mole fraction x_0^{NaCl} . The depth d of the domain is chosen so that at the time of onset no increase in concentration is observable at the bottom, and so, the influence of the bottom boundary is assumed to be negligible.

$$P|_{z=d} = P_{\text{atm}} + \rho(x_0^{\text{NaCl}})gd, \quad (53)$$

$$x^{\text{NaCl}}|_{z=d} = x_0^{\text{NaCl}}, \quad (54)$$

where P_{atm} corresponds to atmospheric pressure.

As initial condition additionally a hydro-static pressure profile is used which leads to better convergence at the beginning of the simulations:

$$P|_{t=0} = P_{\text{atm}} + \rho(x_0^{\text{NaCl}})gz. \quad (55)$$

The numerical model uses also an initial perturbation for x^{NaCl} , denoted $x_{0,p}^{\text{NaCl}}$, to correspond to the perturbations used in the analytical analysis. If no initial perturbations are applied, instabilities are triggered by tiny numerical errors in the order of machine precision. Instead, two different types of perturbations are used, a periodic and a random one, which can either be applied in the top row of cells or in the whole domain. The periodic perturbation is applied by using a cosine function along the x -coordinate:

$$x_{0,p}^{\text{NaCl}}(x) = x_0^{\text{NaCl}} + A \cdot \cos\left(\frac{2\pi}{\lambda} \cdot x\right), \quad (56)$$

with the wavelength λ and the amplitude A . The wavelength and amplitude need to be prescribed. Which amplitude to use will be discussed in Sect. 4.5, while the choice of wavelength is discussed in Sect. 5.1. Alternatively, a random perturbation for $x_{0,p}^{\text{NaCl}}$ is used. In this case, values for $x_{0,p}^{\text{NaCl}}$ are randomly picked for every discrete cell from a normal distribution \mathcal{N} using a mean value of $\mu_{x^{\text{NaCl}}} = x_0^{\text{NaCl}}$ and a standard deviation $\sigma_{x^{\text{NaCl}}}$:

$$x_{0,p}^{\text{NaCl}} \sim \mathcal{N}(\mu_{x^{\text{NaCl}}}, \sigma_{x^{\text{NaCl}}}^2). \quad (57)$$

The choice of standard deviation is discussed in Sect. 4.5.

4.3 Discretization

For the spatial discretization, a cell-centered finite volume scheme applying the two-point flux approach is used, with a first order upwind scheme for the convective flux and a second order scheme for the diffusive fluxes (Helmig 1997). A first order, implicit Euler method is used for time discretization (Helmig 1997). A convergence study for the spatial and temporal discretization is conducted (see Appendix E), ensuring that there is a negligible influence of numerical diffusion effects. For the spatial discretization, it is important to use finer grid cells than the expected wavelength in order to resolve the instabilities: $\Delta x \ll \lambda$. Through preliminary testing we found that the expected wavelength depends on the permeability and the vertical density difference and is smaller for higher permeabilities. At least 10 cells are used per wavelength of the highest investigated permeability, as the convergence study shows tolerable errors for this discretization. For longer wavelengths, the error should be even less. Studies on the discretization of CO₂-brine systems in the context of CO₂-storage were done by Elenius and Johannsen (2012). Elenius and Gasda (2021) state also that 10-20 cells per finger are sufficient to resolve the convective flow in the most cases.

As the instabilities are initiated at the top, a fine resolution in z -direction is important near the top boundary ($z = 0$). Due to the steep gradient of the salt mole fraction near the top boundary, a smaller Δz better represents these changes and gives also a lower influence of numerical diffusion. Based on the convergence study, a relatively fine Δz is used near the top with $\Delta z^{\text{top}} = 3.3 \cdot 10^{-4}$ m. To lower the computational costs in the lower parts of the domain, coarser cell sizes can be used. Hence, Δz increases continuously toward the bottom.

A time step of $\Delta t = 50$ s is used. This means that the grid velocity of the top cell in z -direction $\Delta z^{\text{top}}/\Delta t$ is higher than the evaporation rate E and thus is able to capture the evaporation process correctly.

4.4 Evaluation of Numerical Simulations

To estimate the numerical onset time, the mean value $\mu_{x^{\text{NaCl}}}^{\text{top}}$ and the standard deviation $\sigma_{x^{\text{NaCl}}}^{\text{top}}$ of the salt mole fraction x^{NaCl} of the grid cells in the top row are calculated. The standard deviation is a measure for the variation of the salt mole fraction, where a standard deviation of zero would correspond to homogeneous salt mole fraction in the top row. Since the development of fingers gradually lead to variations in the salt mole

fraction, we expect an increasing standard deviation as the fingers develop. As we start out with a perturbed initial salt mole fraction, the standard deviation will first decrease before it later increases as density instabilities develop. Hence, as a measure for the onset time for the numerical simulations we use the time when the standard deviation is at its minimum. Physically, this corresponds to the case where the convective flux starts to dominate the diffusive fluxes in horizontal direction, which leads to the enhancement of the perturbations. The development of $\mu_{x^{\text{NaCl}}}^{\text{top}}$ and $\sigma_{x^{\text{NaCl}}}^{\text{top}}$ and their physical interpretation will be discussed in detail in Sect. 5.4.

4.5 Influence of Initial Perturbation on Onset

Figure 7 shows the development of the standard deviation $\sigma_{x^{\text{NaCl}}}^{\text{top}}$ and onset time for different parameters for the periodic initial perturbation (Fig. 7a) and the random initial perturbation (Fig. 7b). Also the case without perturbations is shown, where the perturbations are triggered by tiny numerical errors. This figure shows that the amplitude and the standard deviation of the initial perturbation do not affect the onset time. If the initial perturbation is applied only to the top of the domain and not in the whole domain, the onset is later for both perturbation types. However, for the periodic perturbations the difference in onset is relatively small. For the periodic perturbations (56), it is of importance that the width of the domain is a multiple of the initial wavelength. Here, simulations with $\lambda = 0.03\text{m}$ are used, hence $\mathcal{W} = 0.30\text{m}$ is a multiple of it, while $\mathcal{W} = 0.25\text{m}$ is not. For the latter case, the onset time is earlier.

In the following investigations, we use a perturbation in the whole domain. This corresponds better to the manner perturbations are applied in the linear stability analysis and hence benefits the comparison of the onset times between the linear stability analysis and the numerical simulations. An amplitude of $A = 10^{-6}$ is used for the periodic perturbations and a standard deviation of $\sigma_{x^{\text{NaCl}}} = 10^{-6}$ for the random perturbations.

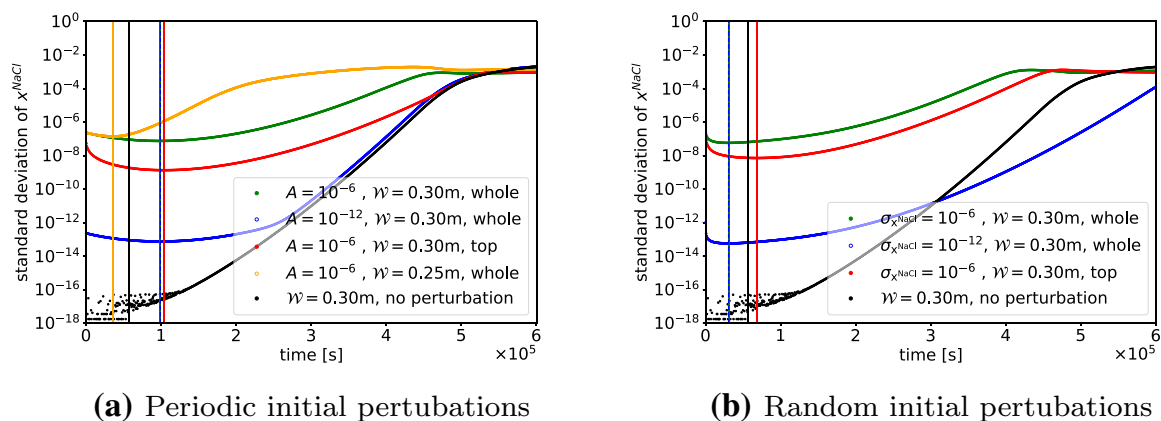


Fig. 7 Influence of different initial perturbations for the numeric simulation on the onset time for periodic initial perturbations **(a)** and random initial perturbations **(b)**. For the simulations, the parameters listed in Table 2 are used with a permeability of $K = 10^{-11} \text{ m}^2$. The parameters amplitude A , half domain width \mathcal{W} , standard deviation $\sigma_{x^{\text{NaCl}}}$ are as described in the legend as well as the application area (top or whole). The vertical lines indicate the time of onset for the respective cases. Note that the blue and green vertical lines are in both cases on top of each other

Table 2 Fixed parameter choices

Parameter	Value	Dimension
X_0 or x_0	0.035 or 0.011	–
ρ_0	1025	kg m ⁻³
μ	$1.1 \cdot 10^{-3}$	kg m ⁻¹ s ⁻¹
ϕ_0	0.4	–
γ	0.7	–
g	9.8	m s ⁻²
E or E_{mol}	$1.08 \cdot 10^{-8}$ or $6.165 \cdot 10^{-4}$	m s ⁻¹ or mol m ⁻² s ⁻¹
D	$4.42 \cdot 10^{-10}$	m ² s ⁻¹
Additional numerical parameters		
d	0.2	m
P_{atm}	$1.0 \cdot 10^5$	Pa
$x_{\text{max}}^{\text{NaCl}}$	0.0977	–

5 Onset and Development of Density Instabilities

Here we compare results from linear stability analysis and numerical simulations with respect to predicted onset times for instabilities and with respect to the behavior of the salt concentration before onset of instabilities. The comparison is kept dimensional, hence results from the linear stability analysis are re-dimensionalized. Most parameters are for simplicity kept fixed and are as specified in Table 2. These parameters are chosen to realistically represent saline water in a porous domain, with evaporation corresponding to 34.7 cm/year. The permeability K of the porous medium is varied. We consider the cases $K = 10^{-10} \text{ m}^2$, $K = 10^{-11} \text{ m}^2$, $K = 10^{-12} \text{ m}^2$ and $K = 10^{-13} \text{ m}^2$.

Note that the specified evaporation rate is used for the numerical simulations as an input parameter. For the linear stability analysis, the choice of evaporation rate translates into a Rayleigh number, which determines the onset time, as described in Sect. 3.5. We separate between the bounded case, where the domain has a fixed width, and the unbounded case, where we investigate the onset of a specific wavelength and use periodic boundary conditions. For both cases, we can compare the onset times from the linear stability analysis and from the numerical simulations.

Table 3 Onset times from the linear stability analysis for a domain of fixed width. A width of 60 cm has been used for all cases

Permeability	Analytic onset time	Numeric onset time
$K = 10^{-10} \text{ m}^2$	$6.57 \cdot 10^2 \text{ s}$	$4.80 \cdot 10^3 \text{ s}$
$K = 10^{-11} \text{ m}^2$	$1.16 \cdot 10^4 \text{ s}$	$3.06 \cdot 10^4 \text{ s}$
$K = 10^{-12} \text{ m}^2$	$1.34 \cdot 10^5 \text{ s}$	$9.12 \cdot 10^4 \text{ s}$
$K = 10^{-13} \text{ m}^2$	$2.11 \cdot 10^6 \text{ s}$	$1.04 \cdot 10^5 \text{ s}$

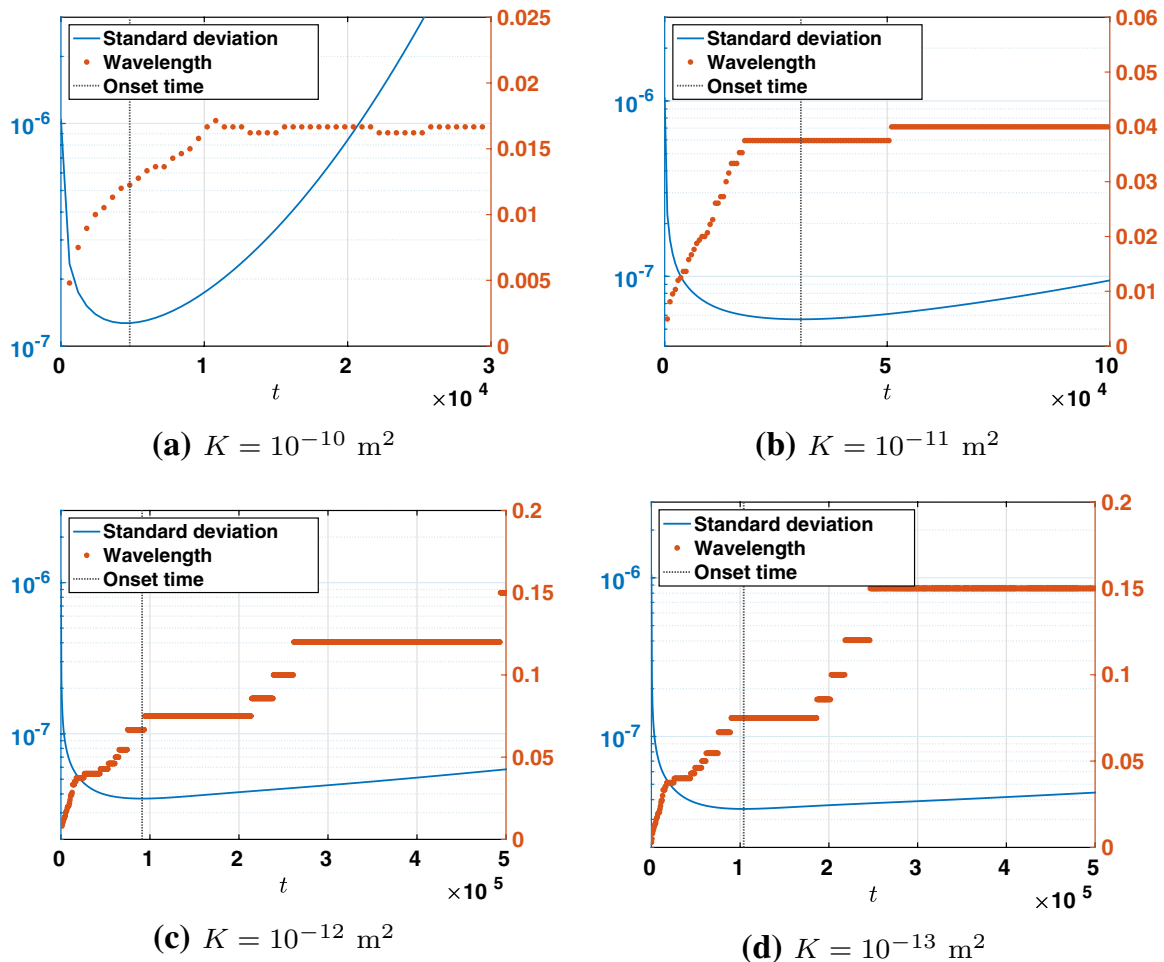


Fig. 8 Standard deviation and average wavelength (in m) over time for fixed width for $K = 10^{-10} \text{ m}^2$ (top left), $K = 10^{-11} \text{ m}^2$ (top right), $K = 10^{-12} \text{ m}^2$ (bottom left) and $K = 10^{-13} \text{ m}^2$ (bottom right). The dotted vertical line indicates time of minimum standard deviation, which is used as the onset time

5.1 Onset Times for a Domain of Fixed Width

We here investigate the onset of instabilities in the bounded case. We use a domain with a fixed width of 60 cm. In the linear stability analysis, we assume that the most unstable wavelength will be dominating, and we find the corresponding onset time for this wavelength, as described in Sect. 3.5. In the numerical simulations, we use an initial random perturbation, which is assumed to trigger the onset of the most unstable wavelength. The development of the standard deviation and the appearing (average) wavelength is shown in Fig. 8. The resulting onset times are in Table 3. Both the analytic and numerical approach show that lower permeabilities correspond to later onset times. Although the numbers are of the same order of magnitude, the deviation between onset times estimated by the linear analysis and numerical simulations is quite large.

This analysis reveals some fundamental differences in the underlying assumptions in the two approaches. The linear stability analysis indicates that the most unstable wavelength should be the longest one that will fit into the domain, as lower wavenumbers \hat{a} are more unstable, as seen in Fig. 4. For this case that would correspond to a wavelength of 60 cm. In the simulations, we can observe that different wavelengths are dominating before and after the estimated onset time. Since we use a random perturbation, several wavelengths

are represented, and they can also interact with each other. The appearing wavelengths after onset are generally found to be shorter for increasing permeability, as seen in Fig. 8. For the lower permeabilities $K = 10^{-13} \text{ m}^2$ and $K = 10^{-12} \text{ m}^2$, the early appearing dominating wavelengths are 15 cm and 12 cm, respectively, which is close to the ones assumed by the linear stability analysis. For the larger permeabilities $K = 10^{-11} \text{ m}^2$ and $K = 10^{-10} \text{ m}^2$, the appearing dominating wavelengths are 4 cm and 1.5 cm, respectively. Although the linear stability analysis indicates that the wavelength of 60 cm should be more unstable and hence preferred, the initial random perturbation have triggered modes that are much shorter in wavelength. The wavelengths that do appear in the numerical simulations depend on the permeability, following a similar trend as observed in Riaz et al. (2006). This is remarkable since the setup is different. Also, using a random perturbation in the numerical simulations can give nonlinear effects as the different wavelengths interact with each other, possibly affecting the resulting onset mode and time. However, the linear stability analysis assumes that the perturbation is a specific wavelength and hence does not account for any interaction between different wavelengths. This motivates to rather use a specific wavelength for the numerical perturbation and compare with the onset time of this wavelength from the linear stability analysis.

5.2 Onset Times of a Fixed Wavelength

We here investigate the onset of instabilities in the unbounded case. Although we use a domain of a width 60 cm for the numerical simulations, we apply periodic boundary conditions on the sidewalls to mimic the domain being unbounded. By using an initial perturbation with a fixed wavelength in the numerical simulations, we investigate the onset of this particular wavelength. This means that the same type of perturbation is used for both numerical simulation and for the linear stability analysis. We use wavelengths based on those that appeared after onset in the numerical simulations in Sect. 5.1, but adjusted such that they fit within the domain. For the linear stability analysis, we then investigate the onset of this particular wavelength, as explained in Sect. 3.5. For the numerical simulations, a small amplitude of the cos-perturbation is used, and the development of the standard deviation and average appearing wavelength is seen in Fig. 9. The used wavelengths and resulting onset times are found in Table 4. For two of the lower permeabilities, no onset time could be found from the numerical simulations. For one case ($K = 10^{-12}$

Table 4 Onset times from the linear stability analysis and the numerical simulations for specific wavelengths

Permeability	Fixed wavelength	Analytic onset time	Numeric onset time
$K = 10^{-10} \text{ m}^2$	0.01 m	$1.78 \cdot 10^4 \text{ s}$	$9.60 \cdot 10^3 \text{ s}$
$K = 10^{-10} \text{ m}^2$	0.015 m	$3.02 \cdot 10^3 \text{ s}$	$1.80 \cdot 10^3 \text{ s}$
$K = 10^{-11} \text{ m}^2$	0.03 m	$9.72 \cdot 10^4 \text{ s}$	$9.84 \cdot 10^4 \text{ s}$
$K = 10^{-11} \text{ m}^2$	0.04 m	$5.14 \cdot 10^4 \text{ s}$	$3.18 \cdot 10^4 \text{ s}$
$K = 10^{-12} \text{ m}^2$	0.06 m	$1.59 \cdot 10^6 \text{ s}$	$1.75 \cdot 10^6 \text{ s}$
$K = 10^{-12} \text{ m}^2$	0.12 m	$4.33 \cdot 10^5 \text{ s}$	0.0 s
$K = 10^{-13} \text{ m}^2$	0.15 m	$8.16 \cdot 10^6 \text{ s}$	–
$K = 10^{-13} \text{ m}^2$	0.3 m	$3.63 \cdot 10^6 \text{ s}$	$3.65 \cdot 10^6 \text{ s}$

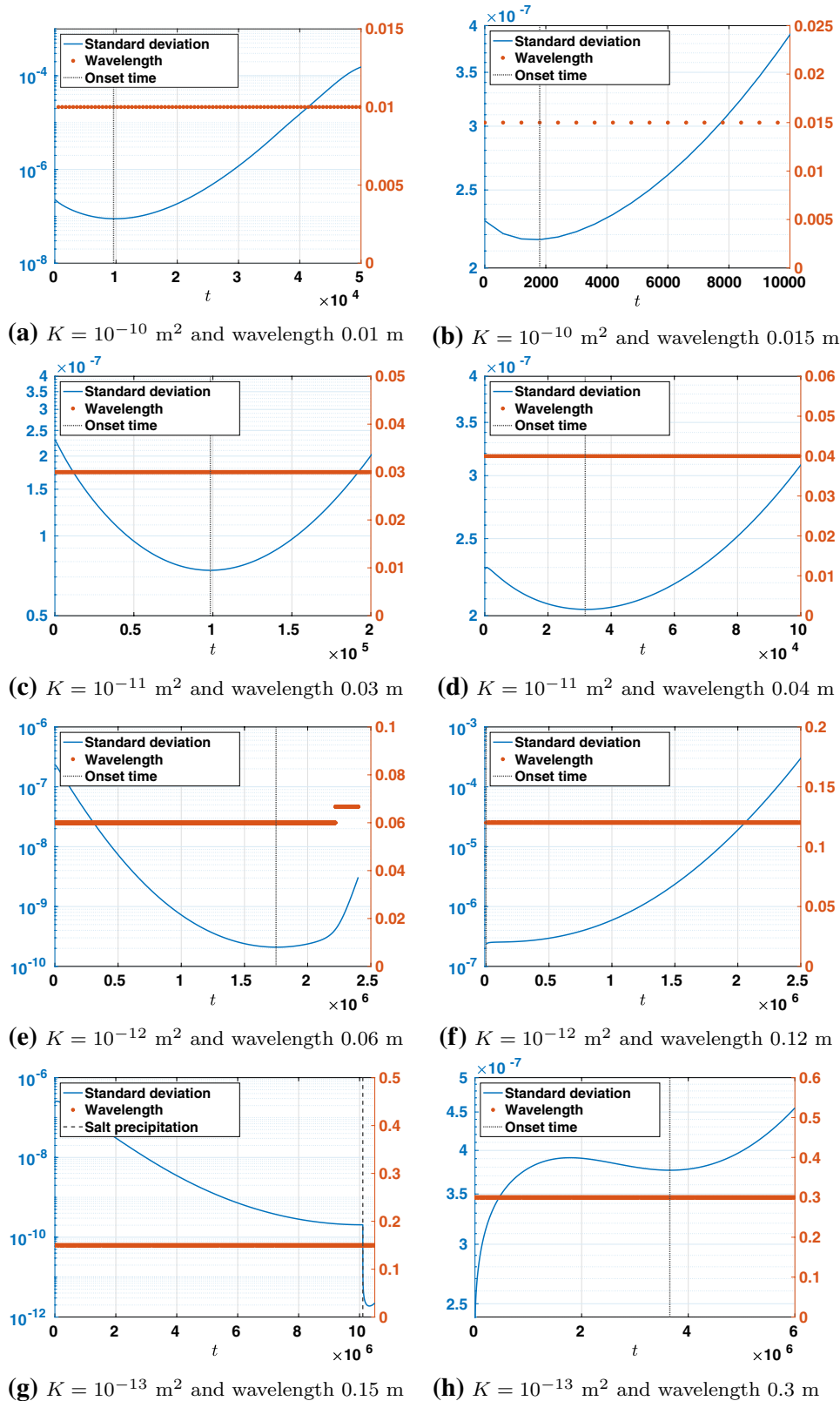


Fig. 9 Standard deviation and average wavelength (in m) over time for fixed wavelengths for $K = 10^{-10} \text{ m}^2$ (top row), $K = 10^{-11} \text{ m}^2$ (second row), $K = 10^{-12} \text{ m}^2$ (third row) and $K = 10^{-13} \text{ m}^2$ (bottom row) for two chosen wavelengths (left and right). The dotted vertical line indicates time of minimum standard deviation, which is used as the onset time. For the case of $K = 10^{-13} \text{ m}^2$ and wavelength 0.15 m (bottom right), time of initial salt precipitation is marked

m^2 and wavelength 0.12 m), the standard deviation increases throughout the simulation,

which means that no local minimum could be detected. For another case ($K = 10^{-13} \text{ m}^2$ and wavelength 0.15 m), salt precipitation occurred before onset of instabilities.

For the cases where numeric onset times could be determined, the onset times generally agree well with the ones predicted by the linear stability analysis. For high permeabilities, the numeric onset times deviate from the analytical ones with less than 40%, whereas for low permeabilities, the deviations are less than 10 %. For the $K = 10^{-10} \text{ m}^2$ simulations, we see that the onset of instabilities occurs shortly after the perturbation is applied, possibly because the size of the perturbation was too large, since only a small density increase is needed for fingers to develop (cf. Fig. 11), and hence, triggered the development of the instabilities at an earlier time than expected. In general, we see that lower permeabilities correspond to larger onset times, as also observed by Riaz et al. (2006).

In the numerical simulations, the appearing wavelength at onset is the one used in the initial perturbation. For the permeability $K = 10^{-12} \text{ m}^2$ and using a wavelength of 0.06 m, a slightly longer average wavelength appears shortly after onset as two waves merge. The merging of waves is a common development after onset of instabilities, although it usually appears some time after the instabilities are developed.

5.3 Behavior of Top Salt Concentration Before and Near Onset of Instabilities

Using the explicit solution (38) for the ground state salt concentration, we can address the expected development of the salt concentration over time before onset of instabilities. For convenience, the comparison is shown using salt mole fractions, but the numbers could also be converted to salt mass fractions. The largest salt concentration is always found at the top of the domain, hence we focus on this one in the following. Salt precipitates if exceeding $x_{\max}^{\text{NaCl}} = 0.0977$ (corresponding to $X_{\max} = 0.26$). That means, if the ground state salt concentration (38) at the top exceeds this x_{\max}^{NaCl} before onset of instabilities is expected, then salt will instead precipitate. In this case, instabilities will not develop, as the salt mole fraction cannot extend beyond x_{\max}^{NaCl} , hence the corresponding density difference is not large enough to trigger instabilities. This occurred for the numerical simulation of $K = 10^{-13} \text{ m}^2$ and using a wavelength of 0.015 m, as seen in Fig. 9g. Note however, as seen from the numerical simulations, the salt concentration at the top of the domain can still increase after the onset of instabilities, before the instabilities are too strong. Hence, one could have salt precipitating after instabilities develop. The linear stability analysis can, however, only determine whether salt precipitation would occur before onset of instabilities.

We compare the salt mole fraction found from the explicit solution (38) with the one from the numerical simulations. For the numerical simulations, we take the average over all the cells in the top row. Since DuMu^x uses a cell-centered scheme, this means that we are not looking at the salt mass fraction at the top, but $\frac{1}{2}\Delta z_{\text{top}}$ away from the top. Hence, the explicit solution is, therefore, also evaluated at the height corresponding to the center of the top grid cells.

The time evolution of the salt mole fractions are found in Fig. 10 for the bounded cases from Sect. 5.1, and in Fig. 11 for the unbounded cases from Sect. 5.2. Since the development of the salt mole fraction is not varying with the applied perturbation, we only show the cases corresponding to wavelengths 0.01 m, 0.03 m, 0.06 m and 0.3 m for the permeabilities $K = 10^{-10} \text{ m}^2$, $K = 10^{-11} \text{ m}^2$, $K = 10^{-12} \text{ m}^2$ and $K = 10^{-13} \text{ m}^2$, respectively. The salt mole fractions coming from numerical simulations and explicit solutions are expected to coincide until onset of instabilities. The explicit solutions are plotted beyond the corresponding onset time for comparison, but develop as if instabilities do not occur. Hence, the

numerical and explicit solutions should deviate after onset of instabilities. We see, however, that especially for low permeabilities, the explicit and numerical salt mole fractions deviate also slightly before onset of instabilities. For the low permeabilities, the salt mole fraction increases much more before onset of instabilities, compared to the high-permeability cases. This also causes a larger change in the density at the top of the domain, which disrupts the Boussinesq approximation used to derive the explicit solution. However, the overall fit between the explicit solution and the numerical solution is very good. The explicit solution deviate from the numeric one with less than 2% before the onset time, giving confidence that the simplifications used to derive the explicit ground state solution (i.e., neglecting the water mole fraction and applying the Boussinesq approximation) were applicable. We also see clearly that the simulated salt concentration at the top follows to a large extent the analytic solution also after onset of instabilities. This is due to the instabilities being so weak in the beginning, hence their capability to transport salt downward is not developed.

5.4 Development of the Salt Concentration After Onset of Instabilities

In this section, the development of instabilities before and after their onset is discussed, using the results of the numerical simulations. Here we also show the case of salt precipitation which occurs for some parameter sets. Different phases of the development are defined with help of the mean value $\mu_{x^{\text{NaCl}}}^{\text{top}}$ and the standard deviation $\sigma_{x^{\text{NaCl}}}^{\text{top}}$ of the salt mole fraction x^{NaCl} of the grid cells in the top row. These phases can be explained and distinguished by the different dominant physical processes.

In Fig. 12, the evaluation of the numeric simulations is shown for the different permeabilities and initial perturbations. We here present only one wavelength (0.01 m, 0.03 m, 0.06 m or 0.3 m) per permeability for the periodic initial perturbations as they show a similar general behavior. The development of $\mu_{x^{\text{NaCl}}}^{\text{top}}$ and $\sigma_{x^{\text{NaCl}}}^{\text{top}}$ over time indicates the different phases of the formation of instabilities.

In the first phase, the initial standard deviation decreases due to the spreading of the initially applied perturbations by molecular diffusion. In Fig. 13a, the influence of the different fluxes on the resulting flux is shown for the first phase. As already mentioned in Sect. 2.2, the higher density at the location of the perturbation leads to an increased gravitational force and a slowed down convective upward flux. As we apply a constant evaporation rate a lower pressure develops at these locations. This horizontal pressure gradient induces a horizontal component to the convective flux toward the perturbation. However, in the first phase the diffusive flux dominates the convective flux in the horizontal direction, which leads to a degradation of the perturbation. In the vertical direction, the driving force of the pressure gradient outweighs the gravitational force. This results in an upward convective flux which also dominates the diffusive flux in the vertical direction. This leads to an upward transportation and accumulation of salt at the top during this phase.

The second phase starts at the time of onset, when the standard deviation reaches its minimum and the perturbations start to increase. The reason for that can be seen in Fig. 13b. The increasing salt concentration and fluid density enhances the gravitational downward forces, which in the following enhances the horizontal component of the convective flux toward the perturbation. In this phase, the convective flux dominates the diffusive flux in horizontal direction. This leads to an increased transport of salt toward the perturbation and consequently to its enhancement. The vertical direction of the resulting flux is still upward, which increases the salt concentration at the top. This is also demonstrated by the continuous increase of $\mu_{x^{\text{NaCl}}}^{\text{top}}$ during this phase.

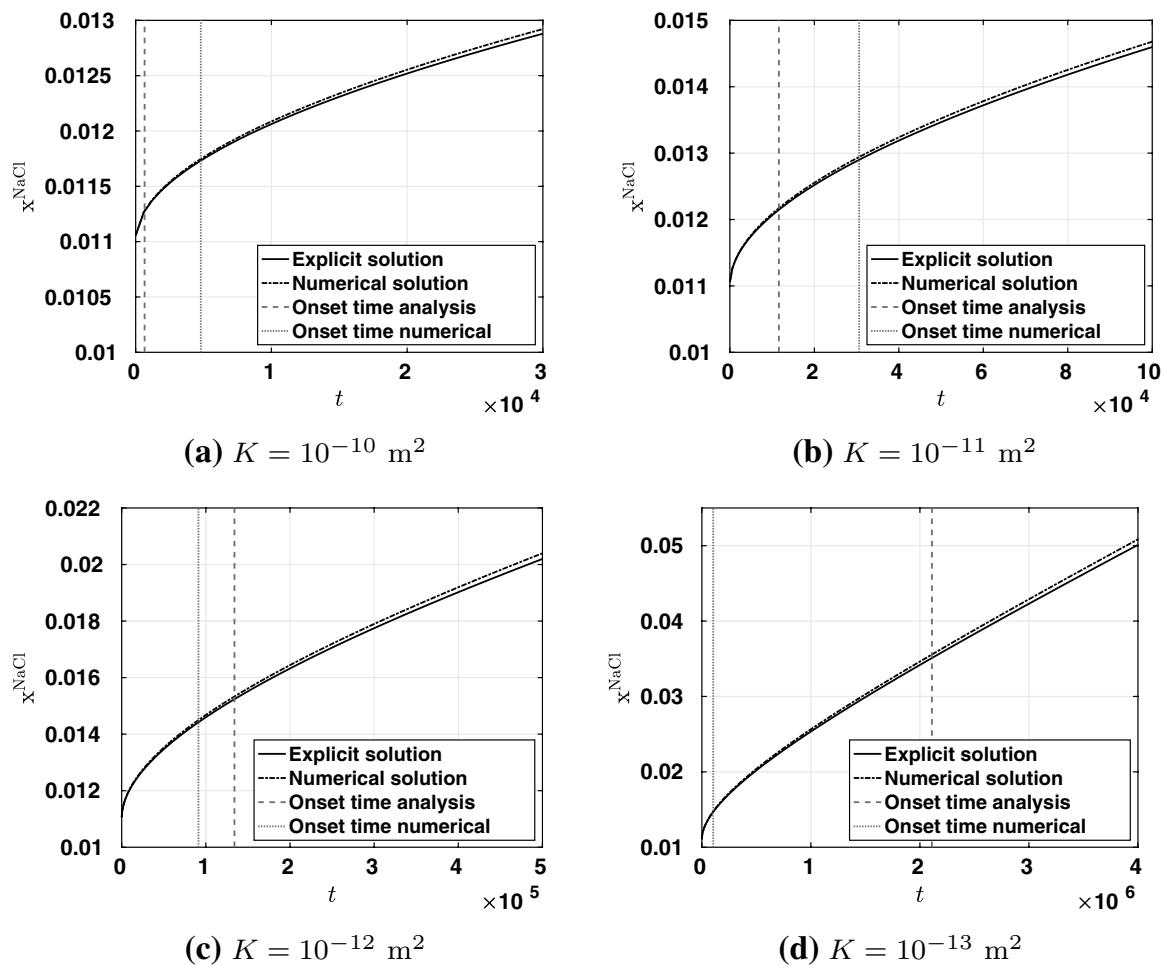


Fig. 10 Salt mole fraction $x_{\text{NaCl}}^{\text{top}}$ at top of the domain as a function of time (in seconds), for $K = 10^{-10} \text{ m}^2$ (top left), $K = 10^{-11} \text{ m}^2$ (top right), $K = 10^{-12} \text{ m}^2$ (bottom left), $K = 10^{-13} \text{ m}^2$ (bottom right), when a specific width is used. The estimated onset times are marked as vertical lines

For the higher permeabilities $K = 10^{-10} - 10^{-12} \text{ m}^2$, the third phase is characterized by a resulting downward flow and starts at the maximum value of $\mu_{x_{\text{NaCl}}^{\text{top}}}$. Until the start of the third phase, the liquid density has increased so much at the top and especially at the location of perturbations that the high gravitational force causes a convective and resulting flux downward; so-called fingers. With a lower permeability a higher density difference is needed to overcome the resistance of the porous medium, resulting in higher maximum values for $\mu_{x_{\text{NaCl}}^{\text{top}}}$. The resulting flux transports the accumulated salt at the top downward, which leads to a decrease of $\mu_{x_{\text{NaCl}}^{\text{top}}}$. Later in this phase, $\mu_{x_{\text{NaCl}}^{\text{top}}}$ stabilizes as the upward transported salt equals the amount which is transported downward with the fingers. A larger value for this stabilized salt mole fraction is observed for lower permeabilities. To match the upward flow, determined by the constant evaporation rate, the downward flow needs larger density differences for lower permeabilities. In all these cases, the solubility limit of the salt is never reached, and thus, no salt precipitation is observed in these systems. For the lowest considered permeability $K = 10^{-13} \text{ m}^2$, $\mu_{x_{\text{NaCl}}^{\text{top}}}$ reaches the solubility limit before a convective downward flow develops. Here salt precipitates and $\mu_{x_{\text{NaCl}}^{\text{top}}}$ stays constant at the solubility limit as we use an equilibrium approach to simulate the precipitation reaction (see Eq. (52)).

Note that in case of no precipitation, further phases for the instabilities can be defined. The fingers start to merge and form larger fingers with longer wavelengths. As we

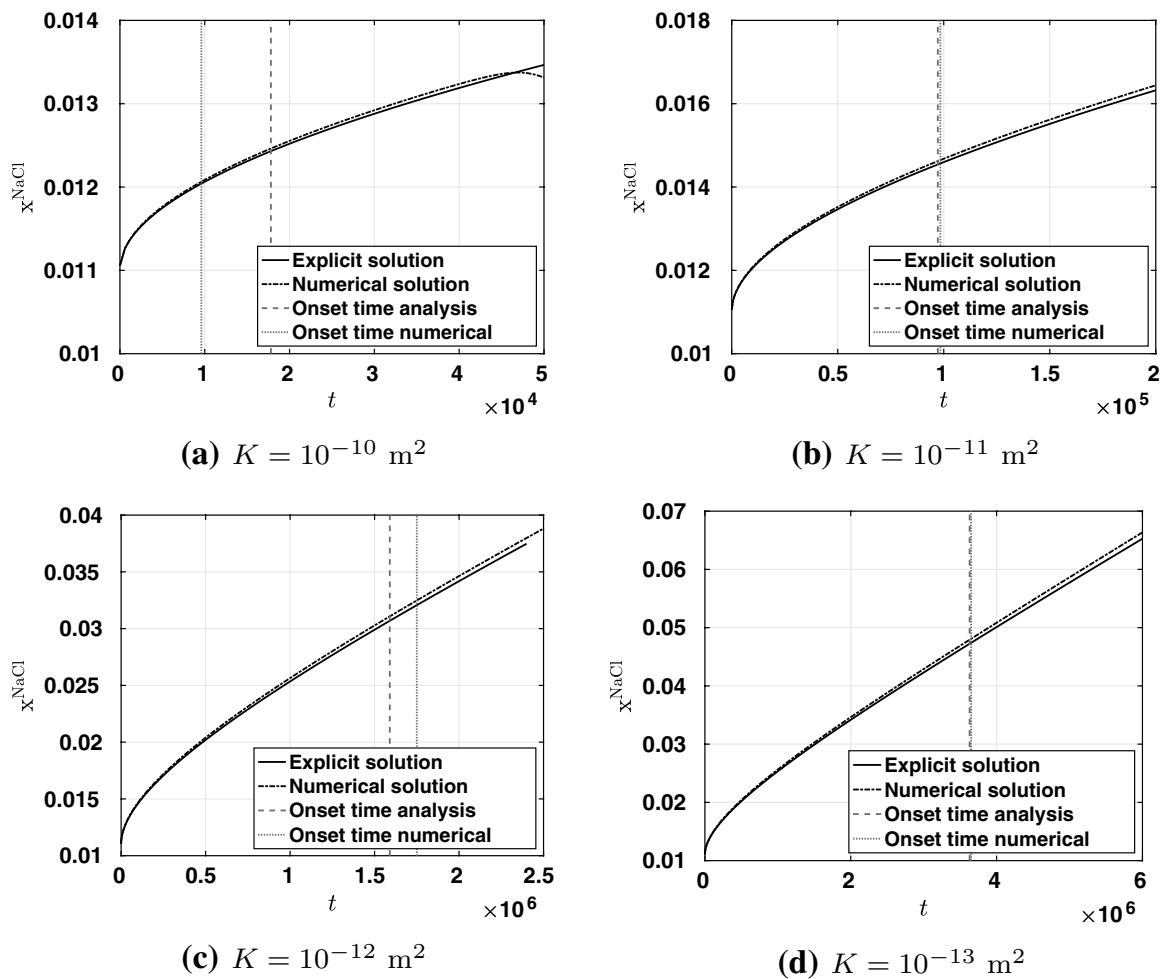


Fig. 11 Salt mole fraction x^{NaCl} at top of the domain as a function of time (in seconds), for $K = 10^{-10} \text{ m}^2$ (top left), $K = 10^{-11} \text{ m}^2$ (top right), $K = 10^{-12} \text{ m}^2$ (bottom left), $K = 10^{-13} \text{ m}^2$ (bottom right), when a specific wavelength is analyzed. The estimated onset times are marked as vertical lines. For $K = 10^{-11} \text{ m}^2$ and $K = 10^{-13} \text{ m}^2$, the vertical lines for onset are almost on top of each other

concentrate on the initial development of the instabilities, we refer to Slim (2014) for a detailed description of these merging regimes. Slim describes similar phases, although there the instabilities are not evaporation-driven.

6 Final Remarks

As water evaporates from a porous medium saturated with saline water, the accumulated salt near the top boundary will either trigger density instabilities, or precipitate in form of a salt crust, or both. In this work, we have addressed the onset of instabilities using two approaches: analytically by applying a linear stability analysis and numerically by performing simulations. The linear stability analysis simplifies the governing equations and formulates an eigenvalue problem giving conditions for whether and when instabilities can develop. The advantage of the linear stability analysis is that results for a large range of parameters can be obtained at very low costs. The numerical simulations can address the original governing equations and can time-step these to address when

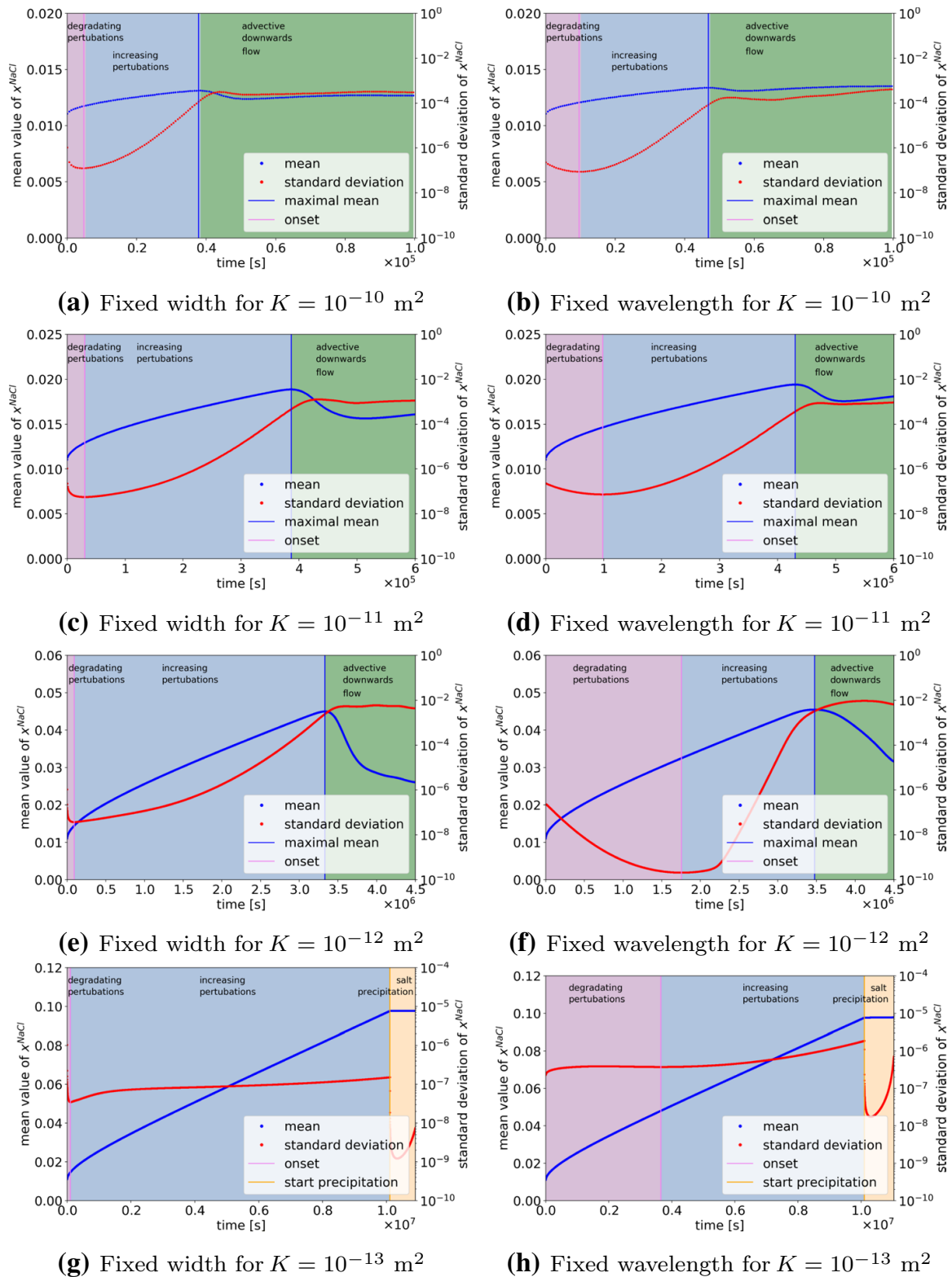
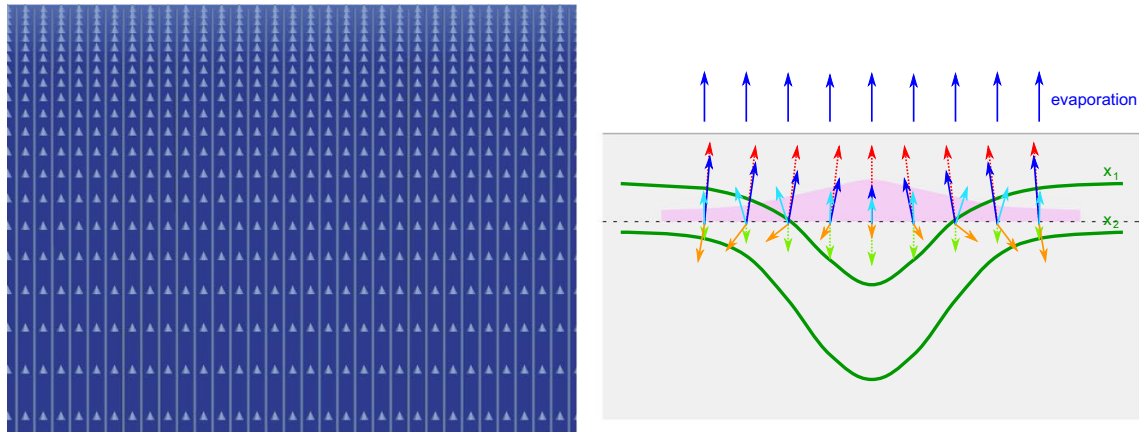
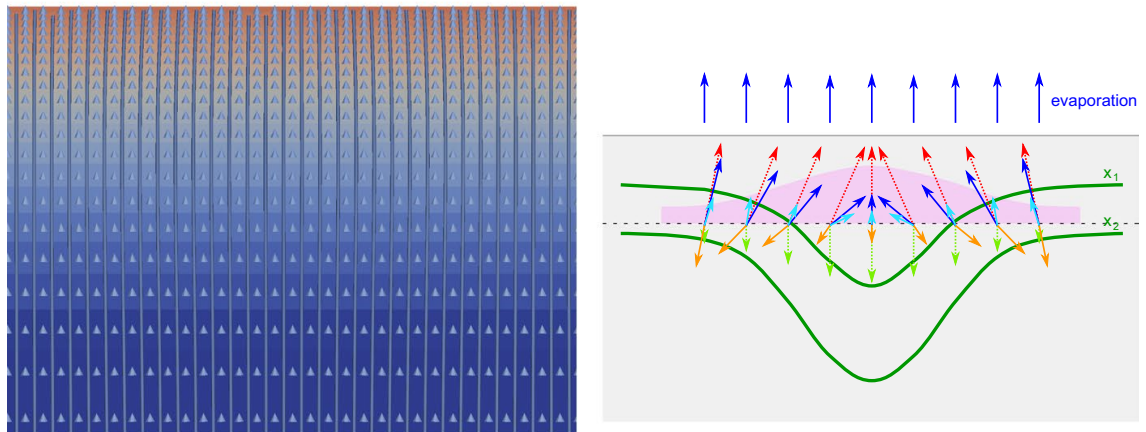


Fig. 12 Result from the numerical simulations for a domain of fixed width (left) and for fixed wavelengths (right) and the different permeabilities. For each case, the development of the mean value and standard deviation of the salt concentration is shown, as well as different phases of the development of instabilities

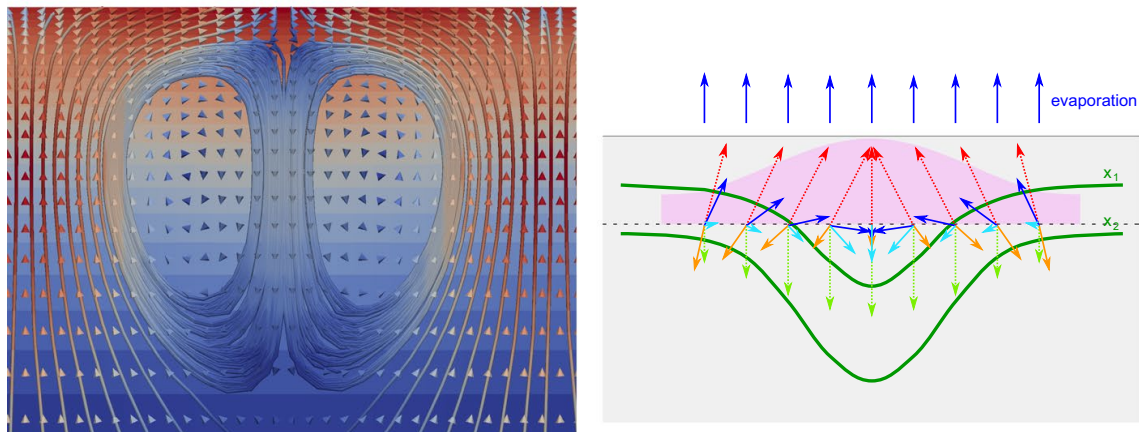
instabilities develop. The computational costs are larger, but also information for the further development after the onset of instabilities can be obtained.



(a) Phase of degrading perturbations



(b) Phase of increasing perturbations



(c) Phase of convective downwards flow

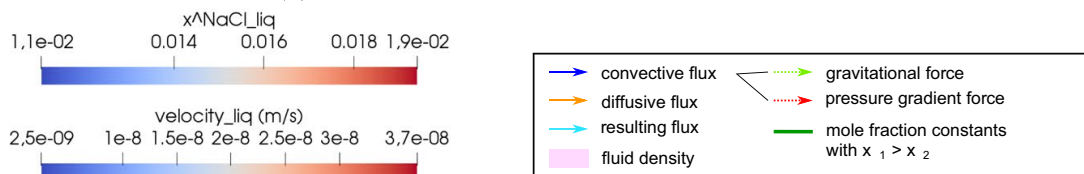


Fig. 13 Important processes and forces in the different phases of instability development. Left the convective streamlines and velocity arrows as well as the salt mole fraction in the background are shown exemplary for one perturbation for $K = 10^{-11} \text{ m}^2$ and periodic initial perturbations. Right a schematic overview of the fluxes and forces describes the formation of the resulting flux

The onset times of instabilities depend not only on the physical parameters as the medium's permeability and the strength of the evaporation rate, but also on which type of instability is considered. The boundary conditions on the sidewalls and which wavelength develops, affect the development of the instabilities. We here considered two cases; either a bounded case with no-flux boundary conditions on the sidewalls, where we tried to trigger the most unstable wavelength, or an unbounded case using periodic boundary conditions, where we tried to trigger a specific wavelength. For the first case, the onset times predicted by the two approaches deviate as the applied perturbation is different, and the two methods predict the onset of different instability modes. For the second case, the onset times largely coincide. In both cases, the development of the salt concentration up to onset of instabilities match up to the difference arising from using the Boussinesq approximation in the analytic case. This gives confidence that the two methods can correctly predict the onset of instabilities, when a specific wavelength is expected.

The numerical experiments show the development of the salt concentration also after onset of instabilities. In particular, we see how the salt concentration at the top of the domain continues to increase for some time after onset, as the instabilities are in the beginning too weak to cause a net downward transport of salt. This means that salt can still precipitate even if instabilities have been triggered.

The linear stability analysis can quickly give criteria for onset of instabilities for a large range of parameters. The numerical simulations can further give detailed information of the further development of instabilities, when applying given parameter choices. From the linear stability analysis, we see how the onset of instabilities depend strongly on parameters such the strength of the evaporation rate and of the permeability, where the latter was also investigated by the numerical simulations. The times for onset of instabilities are found to be in the range of hours to days for a realistic evaporation rate, depending on the permeability. This means that, in the lack of rainfall in that period, our findings give onset times that are realistic especially in arid regions. However, for specific implications, field-related analysis is necessary. This study shows that the current framework is suitable as analysis strategy for onset times of evaporation-induced density instabilities.

Our analysis opens also for comparison with column experiments that consider evaporation from the top of a porous column saturated with saline water having different salts, e.g., Piotrowski et al. (2020). However, the current analysis is performed under the assumption that the porous medium remains fully saturated. Hence, an extension to unsaturated porous media would give more accurate results, also in the context of relating to field observations. To accommodate such an extension, Richards equation for the evolution of the water saturation needs to be included—both in the linear stability analysis and in the numerical simulations. In this case, also capillary forces play a role for the evolution of the water saturation, giving potentially more interactions between evaporation and subsequent density instabilities. The current study remains valid for the case when the capillary pressure stays below the entry pressure, while further research is needed to address the case of varying water saturation.

A Explicit Solution of the Salt Ground State

For the (non-dimensional) ground-state salt concentration \hat{X}^0 , which is needed in Sect. 3.3, we here derive the explicit solution of

$$\begin{aligned}\partial_{\hat{t}}\hat{X}^0 &= \partial_{\hat{z}}\hat{X}^0 + \partial_{\hat{z}}^2\hat{X}^0 & \hat{z} > 0, \hat{t} > 0, \\ \hat{X}^0 + \partial_{\hat{z}}\hat{X}^0 &= 0 & \hat{z} = 0, \hat{t} > 0, \\ \hat{X}^0 &= 1 & \hat{z} > 0, \hat{t} = 0.\end{aligned}$$

We rewrite this problem in terms of the flux; $f = \hat{X}^0 + \partial_{\hat{z}}\hat{X}^0$. Since $\partial_{\hat{t}}\hat{X}^0 = \partial_{\hat{z}}f$, we have

$$\begin{aligned}\partial_{\hat{t}}f &= \partial_{\hat{t}}\hat{X}^0 + \partial_{\hat{t}}\partial_{\hat{z}}\hat{X}^0 = \partial_{\hat{z}}f + \partial_{\hat{z}}^2f & \hat{z} > 0, \hat{t} > 0, \\ f &= 0 & \hat{z} = 0, \hat{t} > 0, \\ f &= 1 & \hat{z} > 0, \hat{t} = 0.\end{aligned}$$

Writing instead in terms of $g = 1 - f$, we have

$$\begin{aligned}\partial_{\hat{t}}g &= \partial_{\hat{z}}g + \partial_{\hat{z}}^2g & \hat{z} > 0, \hat{t} > 0, \\ g &= 1 & \hat{z} = 0, \hat{t} > 0, \\ g &= 0 & \hat{z} > 0, \hat{t} = 0,\end{aligned}$$

which has a known explicit solution (Bear 1972), namely

$$g(\hat{t}, \hat{z}) = \frac{1}{2}e^{-\hat{z}}\operatorname{erfc}\left(\frac{\hat{z}-\hat{t}}{2\sqrt{\hat{t}}}\right) + \frac{1}{2}\operatorname{erfc}\left(\frac{\hat{z}+\hat{t}}{2\sqrt{\hat{t}}}\right).$$

Hence,

$$f(\hat{t}, \hat{z}) = 1 - \frac{1}{2}e^{-\hat{z}}\operatorname{erfc}\left(\frac{\hat{z}-\hat{t}}{2\sqrt{\hat{t}}}\right) - \frac{1}{2}\operatorname{erfc}\left(\frac{\hat{z}+\hat{t}}{2\sqrt{\hat{t}}}\right).$$

Using again that $\partial_{\hat{t}}\hat{X}^0 = \partial_{\hat{z}}f$, we obtain

$$\hat{X}^0(\hat{t}, \hat{z}) = 1 + \int_0^{\hat{t}} \partial_{\hat{z}}f(\theta, \hat{z}) d\theta.$$

B Derivation of and Solution Strategy for the Eigenvalue Problem

We here go detailed through the steps for deriving the eigenvalue problem (49). To investigate the stability of the ground state $\{\hat{Q}^0, \hat{X}^0, \hat{P}^0\}$ from Sect. 3.3, we write

$$\hat{Q}(\hat{t}, \hat{x}, \hat{y}, \hat{z}) = \hat{Q}^0(\hat{t}, \hat{z}) + \mathbf{q}(\hat{t}, \hat{x}, \hat{y}, \hat{z}), \quad (58)$$

$$\hat{X}(\hat{t}, \hat{x}, \hat{y}, \hat{z}) = \hat{X}^0(\hat{t}, \hat{z}) + \chi(\hat{t}, \hat{x}, \hat{y}, \hat{z}), \quad (59)$$

$$\hat{P}(\hat{t}, \hat{x}, \hat{y}, \hat{z}) = \hat{P}^0(\hat{t}, \hat{z}) + p(\hat{t}, \hat{x}, \hat{y}, \hat{z}), \quad (60)$$

where $\mathbf{q} = (u, v, w)$, χ and p are small, perturbed quantities. Since $\hat{\mathbf{Q}}$, \hat{X} and \hat{P} still need to solve the original equations and boundary conditions, we achieve equations and boundary conditions for the perturbed quantities. Inserting (58)–(60) into (26)–(28) and into (31)–(32) and linearizing, we obtain the linear perturbation equations

$$\hat{\nabla} \cdot \mathbf{q} = 0, \quad (61)$$

$$\mathbf{q} = -\hat{\nabla}p + \chi \mathbf{e}_z, \quad (62)$$

$$\partial_t \chi = \partial_z \chi - Rw \partial_z \hat{X}^0 + \hat{\nabla}^2 \chi, \quad (63)$$

with boundary conditions at the top

$$\mathbf{q}|_{\hat{z}=0} = \mathbf{0}, \quad (64)$$

$$(\chi + \partial_z \chi)|_{\hat{z}=0} = 0. \quad (65)$$

Equations (61)–(63) can be written in terms of $\{w, \chi, p\}$ only, see e.g., van Duijn et al. (2019). This results in

$$\hat{\nabla}^2 w = (\partial_{\hat{x}}^2 + \partial_{\hat{y}}^2) \chi \quad (66)$$

$$\partial_z w = (\partial_{\hat{x}}^2 + \partial_{\hat{y}}^2) p \quad (67)$$

$$\partial_t \chi = \partial_z \chi - Rw \partial_z \hat{X}^0 + \hat{\nabla}^2 \chi, \quad (68)$$

with boundary conditions

$$w|_{\hat{z}} = 0 = 0, \quad (69)$$

$$(\chi + \partial_z \chi)|_{\hat{z}=0} = 0. \quad (70)$$

We seek solutions of this system satisfying

$$w, \chi \rightarrow 0 \text{ as } \hat{z} \rightarrow \infty. \quad (71)$$

Since (66)–(71) is a linear initial-boundary problem with no coefficients depending on the spatial coordinates \hat{x} and \hat{y} , we consider solutions of the form

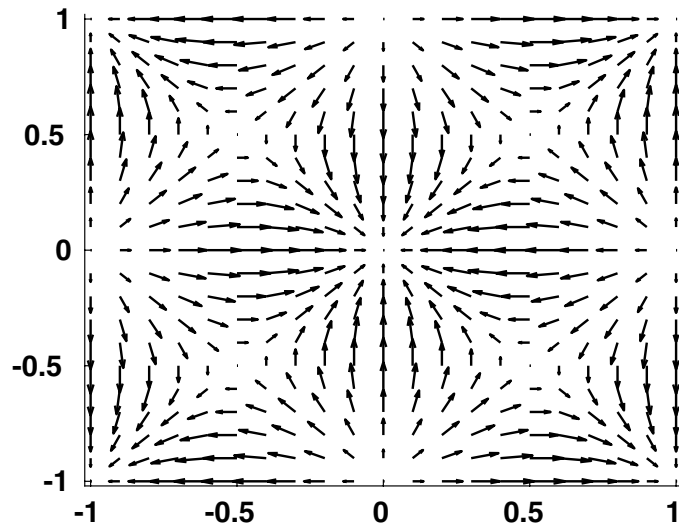
$$\{w, \chi, p\}(\hat{t}, \hat{x}, \hat{y}, \hat{z}) = \{\tilde{w}, \tilde{\chi}, \tilde{p}\}(\hat{t}, \hat{z}) \cos(\hat{a}_x \hat{x}) \cos(\hat{a}_y \hat{y}). \quad (72)$$

Here \hat{a}_x and \hat{a}_y are horizontal wavenumbers. Substituting (72) into (66)–(68) yields for the amplitudes $\{\tilde{w}, \tilde{\chi}, \tilde{p}\}$

$$\partial_z^2 \tilde{w} - \hat{a}^2 \tilde{w} = -\hat{a}^2 \tilde{\chi}, \quad (73)$$

$$\partial_z \tilde{w} = -\hat{a}^2 \tilde{p}, \quad (74)$$

Fig. 14 Horizontal discharge (u, v) seen from above for a cross section $\{(\hat{x}, \hat{y}) : |\hat{x}|, |\hat{y}| < \hat{\beta}\}$, here using $\hat{\beta} = 1$



$$\partial_{\hat{t}} \tilde{\chi} = \partial_{\hat{z}} \tilde{\chi} - R\tilde{w} \partial_{\hat{z}} \hat{X}^0 + \partial_{\hat{z}}^2 \tilde{\chi} - \hat{a}^2 \tilde{\chi}, \quad (75)$$

where $\hat{a}^2 = \hat{a}_x^2 + \hat{a}_y^2$. Expressions for the horizontal discharge components follow from Darcy's law:

$$u(\hat{t}, \hat{x}, \hat{y}, \hat{z}) = -\partial_{\hat{x}} p = -\frac{\hat{a}_x}{\hat{a}^2} \partial_{\hat{z}} \tilde{w} \sin(\hat{a}_x \hat{x}) \cos(\hat{a}_y \hat{y}), \quad (76)$$

$$v(\hat{t}, \hat{x}, \hat{y}, \hat{z}) = -\frac{\hat{a}_y}{\hat{a}^2} \partial_{\hat{z}} \tilde{w} \cos(\hat{a}_x \hat{x}) \sin(\hat{a}_y \hat{y}). \quad (77)$$

When the domain is unbounded, i.e., the half space $\{\hat{z} > 0\}$, we consider (73)–(75), subject to (69)–(70) for any $\hat{a} > 0$. In case of the bounded domain $\{(\hat{x}, \hat{y}, \hat{z}) : |\hat{x}|, |\hat{y}| < \hat{\beta}, \hat{z} > 0\}$ we need to choose \hat{a}_x and \hat{a}_y so that the boundary conditions (33) are satisfied. This requires

$$\hat{a}_x = n_x \frac{\pi}{\hat{\beta}}, \quad \hat{a}_y = n_y \frac{\pi}{\hat{\beta}}, \quad n_x, n_y = 1, 2, \dots \quad (78)$$

A sketch of a horizontal discharge field is given in Fig. 14. In this figure, we have used $\hat{\beta} = 1$ as well as $\hat{a}_x = \hat{a}_y = \pi$, corresponding to one full oscillation in both \hat{x} and \hat{y} direction.

It is clear that it suffices to consider only Eqs. (73) and (75), subject to boundary conditions (69)–(71). Once they are solved, the pressure results from (74) and the horizontal discharge from (76) to (77).

Using the linearity of (73) and (75), and assuming that the coefficients do not depend on time t , we can further separate the variables according to

$$\{\tilde{w}, \tilde{\chi}\}(\hat{t}, \hat{z}) = \{\hat{w}, \hat{\chi}\}(\hat{z}) e^{\sigma \hat{t}}, \quad (79)$$

where σ is the exponential growth rate in time, while \hat{w} and $\hat{\chi}$ describe the variability of the perturbation with \hat{z} .

Since $\hat{X}^0 = \hat{X}^0(\hat{t}, \hat{z})$, the separation of variables as proposed in (79) does not directly apply. As already explained in Sect. 3.4, we circumvent this by applying the quasi steady state approach (QSSA) or the "frozen profile" approach: For any fixed $\hat{t}_* > 0$, we consider $\hat{\tau} = \hat{t} - \hat{t}_*$ as the new time variable. Then (75) becomes

$$\partial_{\hat{t}} \tilde{\chi} = \partial_{\hat{z}} \tilde{\chi} - R\tilde{w}\partial_{\hat{z}}\hat{X}^0(\hat{t}_* + \hat{t}, \hat{z}) + \partial_{\hat{z}}^2 \tilde{\chi} - \hat{a}^2 \tilde{\chi}. \quad (80)$$

In this equation, we take \hat{t} small, $0 < \tau \ll 1$, and write $\hat{X}^0(\hat{t}_* + \hat{t}, \hat{z}) \approx \hat{X}^0(\hat{t}_*, \hat{z})$, i.e., the frozen profile. Setting now

$$\{\tilde{w}, \tilde{\chi}\}(\hat{t}, \hat{z}) = \{\hat{w}, \hat{\chi}\}(\hat{z})e^{\sigma\hat{t}}, \quad (81)$$

we obtain

$$\partial_{\hat{z}}^2 w - \hat{a}^2 \hat{w} = -\hat{a}^2 \hat{\chi} \quad (82)$$

$$\sigma \hat{\chi} = \partial_{\hat{z}} \hat{\chi} - R\hat{w}\partial_{\hat{z}}\hat{X}^0(\hat{t}_*, \hat{z}) + \partial_{\hat{z}}^2 \hat{\chi} - \hat{a}^2 \hat{\chi}, \quad (83)$$

for $0 < \hat{z} < \infty$ subject to (69)–(71).

For given $\hat{a} > 0, \hat{t}_* > 0$ and $\sigma \in \mathbb{R}$, this is an eigenvalue problem in terms of $\{\hat{w}, \hat{\chi}\}$ and R . The object is to determine the smallest positive eigenvalue $R = R_*(\hat{a}, \hat{t}_*, \sigma)$. As shown in Appendix C, there is exchange of stability; i.e.,

$$R_*(\hat{t}, \hat{t}_*, \sigma) \geq R_*(\hat{a}, \hat{t}_*, 0) \text{ if and only if } \sigma \geq 0. \quad (84)$$

This means that if the parameters of the problem are such that $R > R_*(\hat{a}, \hat{t}_*, 0)$, then at time \hat{t}_* a perturbation with wavenumber \hat{a} will emerge, implying that the ground state loses its stability at time \hat{t}_* .

Based on this observation, it suffices to analyze the eigenvalue problem for the case of neutral stability; that is, $\sigma = 0$. Thus, we need to consider the problem (dropping the asterisk in \hat{t}_* and R_*):

Given $\hat{a} > 0, \hat{t} > 0$, and $\hat{X}^0 = \hat{X}^0(\hat{t}, \hat{z})$ by (38), find the smallest $R = R(\hat{a}, \hat{t}) > 0$ such that

$$\left. \begin{array}{l} \hat{w}'' + \hat{a}^2 \hat{\chi} - \hat{a}^2 \hat{w} = 0 \quad \hat{z} > 0, \\ \hat{\chi}' - R\hat{w}\partial_{\hat{z}}\hat{X}^0 + \hat{\chi}'' - \hat{a}^2 \hat{\chi} = 0 \quad \hat{z} > 0, \\ \text{where } \hat{w} \text{ and } \hat{\chi} \text{ fulfill} \\ \hat{w} = 0, \hat{\chi} + \hat{\chi}' = 0 \quad \hat{z} = 0, \\ \hat{w} \rightarrow 0, \hat{\chi} \rightarrow 0 \quad \hat{z} \rightarrow \infty, \end{array} \right\} \quad (85)$$

has a non-trivial solution. This is the same as (49).

The eigenvalue problem (85) is solved via a Laguerre-Galerkin method. We let

$$\hat{\chi}(\hat{z}) = \sum_{n=0}^{\infty} \hat{\chi}_n \zeta_n(\hat{z}), \quad \hat{w}(\hat{z}) = \sum_{n=0}^{\infty} \hat{w}_n \eta_n(\hat{z}), \quad (86)$$

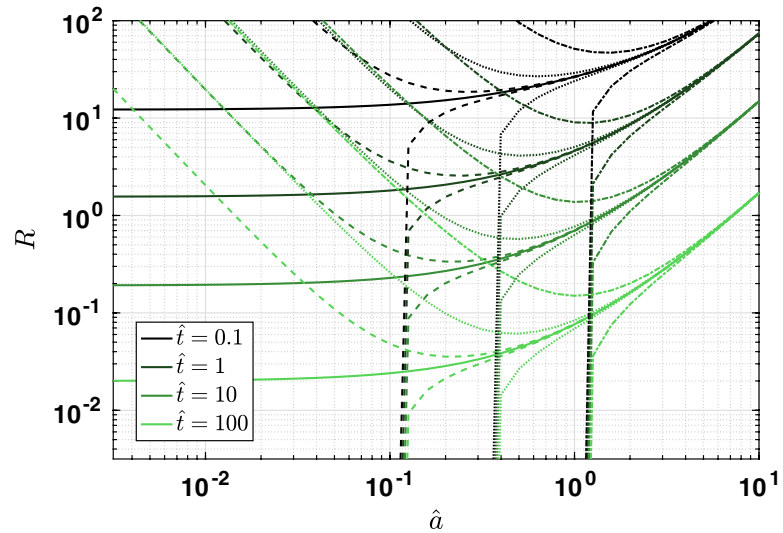
where the basis functions are given by

$$\zeta_n(\hat{z}) = e^{-\frac{\hat{z}}{2}} \left(\mathcal{L}_n(\hat{z}) + \frac{1-2n}{1+2n} \mathcal{L}_{n+1}(\hat{z}) \right) \text{ and } \eta_n(\hat{z}) = e^{-\frac{\hat{z}}{2}} \left(\mathcal{L}_n(\hat{z}) - \mathcal{L}_{n+1}(\hat{z}) \right), \quad (87)$$

and where \mathcal{L}_n is the Laguerre polynomial of degree n (Temme 1996); i.e.,

$$\mathcal{L}_n(\hat{z}) = \sum_{\ell=0}^n (-1)^\ell \binom{n}{\ell} \frac{\hat{z}^\ell}{\ell!} \text{ with } \mathcal{L}_n(0) = 1 \text{ and } \mathcal{L}'_n(0) = -n. \quad (88)$$

Fig. 15 Resulting eigenvalue R (vertical axis) as a function of wavenumber \hat{a} (horizontal axis) for various \hat{t} and σ . Solid lines correspond to $\sigma = 0$, while dashed lines correspond to $\sigma = \pm 0.01$, dotted lines to $\sigma = \pm 0.1$ and dashed-dotted to $\sigma = \pm 1$. The curves lying below the corresponding solid curve are for negative σ and the ones above the corresponding solid curve are for positive σ . Note that the eigenvalue problem degenerates when $(\hat{a}^2 + \sigma) = 0$, which is why the lines for negative σ do not extend beyond $\hat{a} = \sqrt{-\sigma}$



The special combinations in (87) are chosen so that that $\zeta_n(\hat{z})$ and $\eta_n(\hat{z})$ satisfy the boundary conditions for $\hat{\chi}$ and \hat{w} in the fourth and fifth line of (85), respectively. Inserting (87) into the first two lines of (85), multiplying with ζ_m and η_m and integrating with respect to \hat{z} yields

$$\begin{aligned} \sum_{n=0}^{\infty} \hat{w}_n \int_0^{\infty} \eta_n'' \eta_m d\hat{z} + \hat{a}^2 \sum_{n=0}^{\infty} \hat{\chi}_n \int_0^{\infty} \zeta_n \eta_m d\hat{z} - \hat{a}^2 \sum_{n=0}^{\infty} \hat{w}_n \int_0^{\infty} \eta_n \eta_m d\hat{z} &= 0, \\ \sum_{n=0}^{\infty} \hat{\chi}_n \int_0^{\infty} \zeta_n' \zeta_m d\hat{z} - R \sum_{n=0}^{\infty} \hat{w}_n \int_0^{\infty} \partial_z \hat{X}^0 \eta_n \zeta_m d\hat{z} & \\ + \sum_{n=0}^{\infty} \hat{\chi}_n \int_0^{\infty} \zeta_n'' \zeta_m d\hat{z} - \hat{a}^2 \sum_{n=0}^{\infty} \hat{\chi}_n \int_0^{\infty} \zeta_n \zeta_m d\hat{z} &= 0. \end{aligned}$$

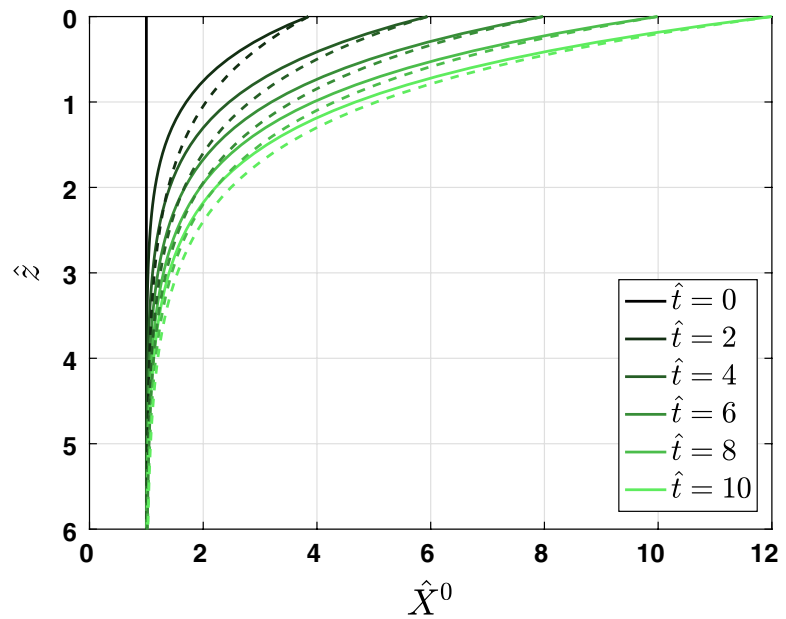
We truncate this expression at a large number $n = N$. Inspecting the convergence of the terms, we found $N = 32$ to be sufficient. The integrals can be determined analytically using the properties of Laguerre polynomials. The only exception is the integral involving $\partial_z \hat{X}^0$, which is approximated using a Gauss-Laguerre quadrature rule. This results in a system of linear equations for the weights $\hat{\chi}_n$ and \hat{w}_n , which can be expressed as a matrix multiplied with a vector containing the weights. The eigenvalues of this matrix correspond to the eigenvalues of (85).

C Investigation of Exponential Growth Rate

We here include the exponential growth rate σ as a parameter in the eigenvalue problem, as considered in Sect. 3.4 and Appendix B. As introduced in (48) and (79), $\sigma > 0$ corresponds to perturbations growing in time, while for $\sigma < 0$ perturbations decay with time. When keeping σ in the perturbed equations, we now obtain the following eigenvalue problem:

Given $\hat{a} > 0$, $\hat{t} > 0$, $\sigma \in \mathbb{R}$ and $\hat{X}^0 = \hat{X}^0(\hat{t}, \hat{z})$ by (38), find the smallest $R = R(\hat{a}, \hat{t}, \sigma) > 0$ such that

Fig. 16 Ground state solution for salt \hat{X}^0 using (38) (solid lines) and approximate solution \hat{U}^0 using (90) (dashed lines)



$$\left. \begin{aligned}
 \hat{w}'' + \hat{a}^2 \hat{\chi} - \hat{a}^2 \hat{w} &= 0 & \hat{z} > 0, \\
 \hat{\chi}' - R\hat{w}d_z\hat{X}^0 + \hat{\chi}'' - (\hat{a}^2 + \sigma)\hat{\chi} &= 0 & \hat{z} > 0, \\
 \text{where } \hat{w} \text{ and } \hat{\chi} \text{ fulfill} & & \\
 \hat{w} = 0, \hat{\chi} + \hat{\chi}' = 0 & & \hat{z} = 0, \\
 \hat{w} \rightarrow 0, \hat{\chi} \rightarrow 0 & & \hat{z} \rightarrow \infty,
 \end{aligned} \right\} \tag{89}$$

has a non-trivial solution.

For given $\hat{a}, \hat{t} > 0$ and $\sigma \in \mathbb{R}$, (89) is an eigenvalue problem where R is to be determined. We follow the same strategy as described in Sect. 3.5 to discretize and solve the eigenvalue problem. The corresponding version of Fig. 4 when including σ is shown in Fig. 15.

From Fig. 15, we observe the following: For negative σ (corresponding to perturbations decaying with time; i.e., stability), we are always below the curves corresponding to $\sigma = 0$ when looking at same \hat{t} and \hat{a} . This means, when we are below a solid curve, which means that the Rayleigh number is lower than the one on the vertical axis, we have stability since a perturbation will decay with time. Similarly, for positive σ (corresponding to perturbation growing with time), we are always above the curves corresponding to $\sigma = 0$ when looking at same \hat{t} and \hat{a} . This means, when we are above a solid curve, which means that the Rayleigh number is larger than the one on the vertical axis, a perturbation will grow exponentially with time. From this, we can conclude that investigating $\sigma = 0$ is the relevant case for the eigenvalue problem, as the eigenvalues found by using $\sigma = 0$ correspond to the shift from perturbations growing or decaying.

Note that the eigenvalue problem (89) degenerates when $\hat{a}^2 + \sigma = 0$, which is why the curves for negative σ are not extended beyond $\hat{a} = \sqrt{-\sigma}$. If one would like to investigate very small wavenumbers \hat{a} , one could overcome this by choosing a correspondingly small σ to avoid (or, more correctly, shift) the degeneracy.

D The Behavior for Small Wavenumbers \hat{a}

Figure 4 shows that for each $\hat{t} > 0$, the Rayleigh number $R(\hat{a}, \hat{t})$ has a finite value as $\hat{a} \searrow 0$. This behavior is different from other cases where $R(\hat{a}, \hat{t}) \rightarrow \infty$ as $\hat{a} \searrow 0$ and has a positive minimum at some critical wavenumber $\hat{a}_L > 0$, e.g., Riaz et al. (2006); van Duijn et al. (2002). Here we provide an explanation for an approximate eigenvalue problem. We first observe that for each $\hat{t} > 0$, the ground state solution $\hat{X}^0(\hat{t}, \hat{z})$ from (38) has its maximum at $\hat{z} = 0$ and decreases in a convex way toward $\hat{X}^0(\hat{t}, \infty) = 1$. The idea is to replace $\hat{X}^0(\hat{t}, \hat{z})$ by the expression

$$\hat{U}^0(\hat{t}, \hat{z}) = 1 + e^{-\hat{z}}(\hat{X}^0(\hat{t}, 0) - 1). \quad (90)$$

Figure 16 shows the profiles of \hat{X}^0 and \hat{U}^0 for various $\hat{t} > 0$. Note that they have the same qualitative behavior and that the relative error becomes smaller as \hat{t} increases. We propose to use $\hat{U}^0(\hat{t}, \hat{z})$ as ground state in the eigenvalue problem (49). Setting

$$R^* = (\hat{X}^0(\hat{t}, 0) - 1)R, \quad (91)$$

we obtain the neutral stability ($\sigma = 0$) eigenvalue problem:

Given $\hat{a} > 0$, find the smallest $R^* = R^*(\hat{a}) > 0$ such that

$$\left. \begin{aligned} \hat{w}'' + \hat{a}^2 \hat{\chi} - \hat{a}^2 \hat{w} &= 0 & \hat{z} > 0, \\ \hat{\chi}' + R^* e^{-\hat{z}} \hat{w} + \hat{\chi}'' - (\hat{a}^2 + \sigma) \hat{\chi} &= 0 & \hat{z} > 0, \\ \text{where } \hat{w} \text{ and } \hat{\chi} \text{ fulfill} & & \\ \hat{w} = 0, \hat{\chi} + \hat{\chi}' &= 0 & \hat{z} = 0, \\ \hat{w} \rightarrow 0, \hat{\chi} \rightarrow 0 & & \hat{z} \rightarrow \infty, \end{aligned} \right\} \quad (92)$$

has a non-trivial solution.

The equations in (92) can be combined into the fourth-order equation

$$L[w] := (D_{\hat{z}}^2 + D_{\hat{z}} - \hat{a}^2)(D_{\hat{z}}^2 - \hat{a}^2)\hat{w} = \hat{a}^2 R^* e^{-\hat{z}}, \quad (93)$$

where $D_{\hat{z}}$ denotes differentiation with respect to \hat{z} , resulting in the eigenvalue problem:

Given $\hat{a} > 0$, find the smallest $R^* = R^*(\hat{a})$ such that

$$\left. \begin{aligned} L[\hat{w}] &= \hat{a}^2 R^* e^{-\hat{z}} \hat{w} & \hat{z} > 0, \\ \text{where } \hat{w} \text{ fulfills} & & \\ \hat{w} = 0, (D_{\hat{z}}^2 - \hat{a}^2)(D_{\hat{z}} + 1)\hat{w} &= 0 & \hat{z} = 0, \\ \hat{w} \rightarrow 0 & & \hat{z} \rightarrow \infty, \end{aligned} \right\} \quad (94)$$

has a non-trivial solution.

Note that Eq. (93) also arises when studying the stability of the equilibrium state of the salt lake problem, see van Duijn et al. (2002) and references cited therein. In this study, the eigenvalue problem differs from (94) only through the second boundary condition of \hat{w} at $\hat{z} = 0$. In the salt lake problem, the second condition is $\hat{\chi}(0) = 0$, implying that $D_{\hat{z}}^2 \hat{w}(0) = 0$.

Arguing as in van Duijn et al. (2002), we treat (94) by a semi-analytical technique based on a Frobenius expansion in terms of descending exponential functions:

$$\hat{w}(\hat{z}) = \sum_{n=0}^{\infty} A_n (R^*)^n e^{(c-n)\hat{z}}, \quad (95)$$

where $c < 0$. Substituting (95) into (93) gives the indicial equation

$$(c^2 + c - \hat{a}^2)(c^2 - \hat{a}^2) = 0,$$

yielding the negative roots

$$c_1 = -\hat{a}, \quad c_2 = -\frac{1}{2} - \sqrt{\frac{1}{4} + \hat{a}^2},$$

and the recurrence relation

$$\begin{cases} \frac{A_n^{(i)}}{A_{n-1}^{(i)}} = \frac{\hat{a}^2}{f_i(n; \hat{a})} & n \geq 1, \\ A_0^{(i)} = 1, \end{cases}$$

where

$$f_i(n; \hat{a}) = ((c_i - n)^2 + (c_i - n) - \hat{a}^2)((c_i - n)^2 - \hat{a}^2), \quad n \geq 1.$$

Hence, we obtain the power series solution

$$\hat{w}(\hat{z}) = A\hat{w}_1(\hat{z}) + B\hat{w}_2(\hat{z}),$$

where

$$\hat{w}_i(\hat{z}) = \sum_{n=0}^{\infty} A_n^{(i)} (R^*)^n e^{-(c_i - n)\hat{z}}, \quad i = 1, 2, \dots$$

The boundary conditions at $\hat{z} = 0$ are satisfied if

$$\left(\sum_{n=0}^{\infty} A_n^{(1)} (R^*)^n \right) A + \left(\sum_{n=0}^{\infty} A_n^{(2)} (R^*)^n \right) B = 0 \quad (96)$$

and

$$\left(\sum_{n=0}^{\infty} A_n^{(1)} g_1(n; \hat{a}) (R^*)^n \right) A + \left(\sum_{n=0}^{\infty} A_n^{(2)} g_2(n; \hat{a}) (R^*)^n \right) B = 0, \quad (97)$$

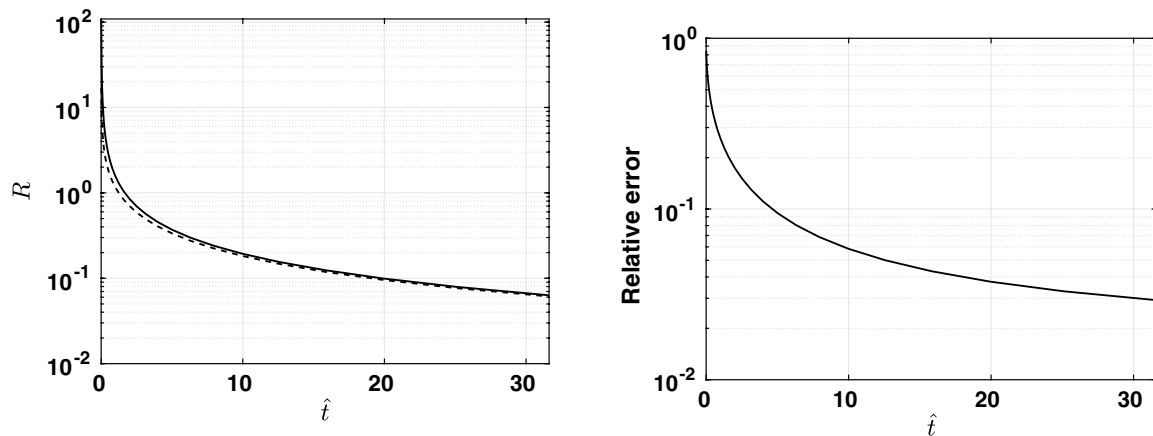
where

$$g_i(n; \hat{a}) = (c_i - n)((c_i - n)^2 + (c_i - n) - \hat{a}^2), \quad n \geq 0.$$

Writing (96) and (97) as

$$(M) \begin{pmatrix} A \\ B \end{pmatrix} = \begin{pmatrix} 0 \\ 0 \end{pmatrix},$$

we need to examine the characteristic equation $\det(M) = 0$ to find the eigenvalues of (92). For $n \leq 2$, we have



(a) Critical (solid line) and approximate Rayleigh number (dashed line).

(b) Relative error.

Fig. 17 Critical Rayleigh number from Sect. 3.5 using $\hat{a} = 10^{-4}$ and approximate Rayleigh number from (99), and the relative error between them as a function of non-dimensional time \hat{t}

$$\begin{aligned} \det(M) = & \left(1 + \frac{\hat{a}^2 R^*}{f_1(1)} + \frac{(\hat{a}^2 R^*)^2}{f_1(2)f_1(1)}\right) \left(\frac{g_2(1)}{f_2(1)} \hat{a}^2 R^* + \frac{g_2(2)}{f_2(2)f_1(1)} (\hat{a} R^*)^2\right) \\ & - \left(1 + \frac{\hat{a}^2 R^*}{f_2(1)} + \frac{(\hat{a}^2 R^*)^2}{f_2(2)f_2(1)}\right) \left(\hat{a}^2 + \frac{g_1(1)}{f_1(1)} \hat{a}^2 R^* + \frac{g_1(2)}{f_1(2)f_1(1)} (\hat{a}^2 R^*)^2\right). \end{aligned}$$

For $\hat{a} \ll 1$, we take, to leading order, $n \leq 1$ and obtain

$$\frac{g_2(1)}{f_2(1)} \hat{a}^2 R^* = \hat{a}^2 + \frac{g_1(1)}{f_1(1)} \hat{a}^2 R^*,$$

or

$$R^* \left(\frac{g_2(1)}{f_2(1)} - \frac{g_1(1)}{f_1(1)} \right) = 1.$$

Evaluating the coefficients yields

$$\frac{g_2(1)}{f_2(1)} - \frac{g_1(1)}{f_1(1)} = \frac{-4 + O(\hat{a}^2)}{8 + O(\hat{a}^2)} - \frac{-\hat{a}(1 + \hat{a})}{\hat{a}(1 + 2\hat{a})} = -\frac{1}{2} + O(\hat{a}^2) + \frac{1 + \hat{a}}{1 + 2\hat{a}} = \frac{1}{2(1 + 2\hat{a})} + O(\hat{a}^2).$$

Hence,

$$R^*(\hat{a}) = 2(1 + 2\hat{a}) + O(\hat{a}^2) \text{ as } \hat{a} \searrow 0. \quad (98)$$

That means, in the limit as \hat{a} approaches zero, we find

$$R^* = 2.$$

Using again (91), we find that

$$R = \frac{2}{\hat{X}^0(\hat{t}, 0) - 1} \quad (99)$$

approximates the critical Rayleigh number for \hat{a} approaching zero. The Rayleigh numbers using the strategy from Sect. 3.5 with $\hat{a} = 10^{-4}$ together with the approximate ones from

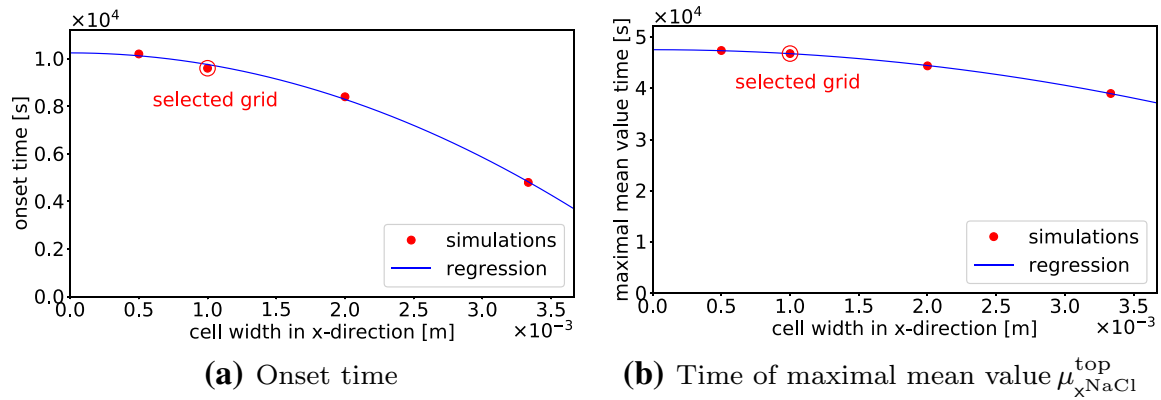


Fig. 18 Influence of the grid cell size in x -direction on the onset time and the time of maximal mean value

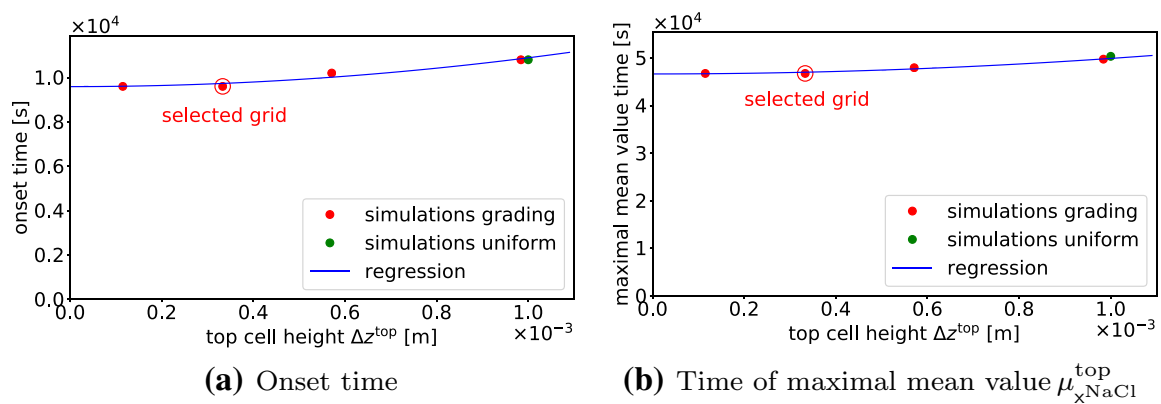


Fig. 19 Influence of the height of the top cell Δz^{top} on the onset time and the time of maximal mean value

(99) are shown in Fig. 17. The relative error between the approximate Rayleigh number and the Rayleigh number from Sect. 3.5 is larger for early times, as expected from Fig. 16 since the approximate ground state deviates more. However, the relative error is generally small, and decreases fast for later times. Hence, the approximate Rayleigh number (99) represents the behavior for low wavenumbers \hat{a} well. We also see from (98) that R^* (and hence R) decreases monotonously for low \hat{a} as \hat{a} approaches zero. This shows that $\hat{a} = 0$ corresponds to a (local) minimum for $R(\hat{a}, \hat{t})$ for given $\hat{t} > 0$.

E Grid and Time Step Convergence Study for the Numerical Simulations

A convergence study was performed to ensure that the spatial, and temporal discretization are able to capture the physical processes in sufficient detail and that the numerical diffusion has a negligible influence. The study was carried out using the same setup as described in Sect. 5 exemplary for the case with a fixed wavelength of $\lambda = 0.01$ m and a permeability of $K = 10^{-10}$ m². As this case has the lowest used wavelength and hence the lowest resolution per perturbation, the influence of the discretization should be even less for longer wavelengths. The influence of the cell width in x -direction, the discretization in z -direction and the time step size was investigated. The onset time and the time of the maximal mean value $\mu_{x,\text{NaCl}}^{\text{top}}$ are used to evaluate the influence. A quadratic regression is used

to extrapolate the values for a theoretical infinitesimal small cell width, cell height and time step.

The influence of the cell widths in x -direction on the onset time and time of the maximal mean value is shown in Fig. 18. The discretization in z -direction equals the one of the selected grid as described below. The investigated cell widths $5 \cdot 10^{-4}$ m, $1 \cdot 10^{-3}$ m, $2 \cdot 10^{-3}$ m and $3.33 \cdot 10^{-3}$ m correlate with 20, 10, 5 and 3 cells per initially applied perturbation wavelength. The selected grid uses 10 cells per perturbation wavelength. For longer wavelengths using lower permeabilities, this results in more cells per perturbation wavelength. The deviation of the selected grid from the extrapolated value is 6.3 % for the onset time and 1.6 % for the time of maximal mean value.

Figure 19 shows the investigation of the discretization in z -direction. In x -direction, the discretization equals the one of the selected grid as described above. In z -direction, a grading is used so that the top cell is the smallest, and the cell height increases toward the bottom of the domain. The same grading factor of 0.9 is used for the grids, but different numbers of cells. The different grids have 30, 35, 40 and 50 cells in z -direction, which correspond to a top cell height Δz^{top} of $9.84 \cdot 10^{-4}$ m, $5.71 \cdot 10^{-4}$ m, $3.33 \cdot 10^{-4}$ m and $1.15 \cdot 10^{-4}$ m. Additionally, a grid with uniform grid heights of $1.0 \cdot 10^{-3}$ m was simulated. It has in total 200 cells in z -direction as it discretizes the lower parts of the domain finer, whereas Δz^{top} nearly matches the coarsest graded grid. Nearly no influence could be observed from the finer discretization in the lower domain, on the time of onset and in maximal mean value. It is found that the height of the top cell has the main influence. We, therefore, look at the height of the top cell Δz^{top} of the different grids. The selected grid uses grading and deviates 0.1 % for the onset time and 0.2 % for the time of maximal mean value from the respective theoretical extrapolated value. In comparison with the cell width, the cell height has less influence on the two evaluation times.

Further, an investigation of the time step size on the evaluation times was performed. It was found that for time steps from 25 to 150 s, the evaluation is independent of the time discretization. For all simulations, we use a time step of 50 s.

Funding Open Access funding enabled and organized by Projekt DEAL. Funded by the Deutsche Forschungsgemeinschaft (DFG, German Research Foundation)—Project Number 327154368—SFB 1313.

Declarations

Conflict of interest The authors declare that they have no conflict of interest.

Data Availability The DuMu^x simulation results presented in Sect. 5 are available in <https://doi.org/10.18419/darus-2578>.

Code Availability The DuMu^x code used for the numerical simulations is available in the following git-repository: <https://git.iws.uni-stuttgart.de/dumux-pub/bringedal2021a>. The MATLAB code used for solving the eigenvalue problem is available in <https://doi.org/10.18419/darus-2577>.

Open Access This article is licensed under a Creative Commons Attribution 4.0 International License, which permits use, sharing, adaptation, distribution and reproduction in any medium or format, as long as you give appropriate credit to the original author(s) and the source, provide a link to the Creative Commons licence, and indicate if changes were made. The images or other third party material in this article are included in the article's Creative Commons licence, unless indicated otherwise in a credit line to the material. If material is not included in the article's Creative Commons licence and your intended use is not permitted by statutory regulation or exceeds the permitted use, you will need to obtain permission directly from the copyright holder. To view a copy of this licence, visit <http://creativecommons.org/licenses/by/4.0/>.

References

- Allison, G.B., Barnes, C.J.: Estimation of evaporation from the normally dry lake frome in south australia. *J. Hydrol.* **78**(3), 229–242 (1985)
- Barletta, A., Celli, M., Rees, D.A.S.: The onset of convection in a porous layer induced by viscous dissipation: A linear stability analysis. *Int. J. Heat Mass Transf.* **52**(1), 337–344 (2009)
- Bastian, P., Blatt, M., Dedner, A., Dreier, N., Engwer, C., Fritze, R., Gräser, C., Grüninger, C., Kempf, D., Klöfkorn, R., Ohlberger, M., Sander, O.: The dune framework: basic concepts and recent developments. *Comput. Math. Appl.* **81**, 75–112 (2021)
- Bear, J.: Dynamics of fluids in porous media. American Elsevier Publisher Co. (1972)
- Chandrasekhar, S.: Hydrodynamic and hydromagnetic stability. Dover Publications Inc, New York (1961)
- Chaves, M.M., Flexas, J., Pinheiro, C.: Photosynthesis under drought and salt stress: regulation mechanisms from whole plant to cell. *Ann. Bot.* **103**(4), 551–560 (2008)
- Chen, X.Y.: Evaporation from a salt encrusted sediment surface-field and laboratory studies. *Soil Res.* **30**(4), 429–442 (1992)
- Daliakopoulos, I.N., Tsanis, I.K., Koutroulis, A., Kourgialas, N.N., Varouchakis, A.E., Karatzas, G.P., Ritsema, C.J.: The threat of soil salinity: a European scale review. *Sci. Total Environ.* **573**, 727–739 (2016)
- Duffy, C.J., Al-Hassan, S.: Groundwater circulation in a closed desert basin: topographic scaling and climatic forcing. *Water Resour. Res.* **24**(10), 1675–1688 (1988)
- Elenius, M.T., Gasda, S.E.: Convective mixing driven by non-monotonic density. *Transp. Porous Media* **138**, 133–155 (2021)
- Elenius, M.T., Johannsen, K.: On the time scales of nonlinear instability in miscible displacement porous media flow. *Comput. Geosci.* **16**, 133–155 (2012)
- Elenius, M.T., Nordbotten, J.M., Kalisch, H.: Effects of a capillary transition zone on the stability of a diffusive boundary layer. *IMA J. Appl. Math.* **77**(6), 771–787 (2012)
- Geng, X., Boufadel, M.C.: Numerical modeling of water flow and salt transport in bare saline soil subjected to evaporation. *J. Hydrol.* **524**, 427–438 (2015)
- Geng, X., Boufadel, M.C.: The influence of evaporation and rainfall on supratidal groundwater dynamics and salinity structure in a sandy beach. *Water Resour. Res.* **53**(7), 6218–6238 (2017)
- Gilman, A., Bear, J.: The influence of free convection on soil salinization in arid regions. *Transp. Porous Media* **23**(3), 275–301 (1996)
- Hattori, T., Patterson, J.C., Lei, C.: On the stability of transient penetrative convection driven by internal heating coupled with a thermal boundary condition. *Int. Commun. Heat Mass Transfer* **64**, 29–33 (2015)
- Heck, K., Coltman, E., Schneider, J., Helmig, R.: Influence of radiation on evaporation rates a numerical analysis. *Water Resour. Res.* **56**(10), e2020WR027332 (2020)
- Helmig, R.: Multiphase Flow and Transport Processes in the Subsurface: A Contribution to the Modeling of Hydrosystems. Springer-Verlag (1997)
- Homsy, G.M., Sherwood, A.E.: Convective instabilities in porous media with through flow. *AIChE J.* **22**(1), 168–174 (1976)
- Jambhekar, V.A., Helmig, R., Schröder, N., Shokri, N.: Free-flow-porous-media coupling for evaporation-driven transport and precipitation of salt in soil. *Transp. Porous Media* **110**(2), 251–280, 11 (2015)
- Koch, T., Gläser, D., Weishaupt, K., Ackermann, S., Beck, M., Becker, B., Burbulla, S., Class, H., Coltman, E., Emmert, S., Fetzner, T., Grüninger, C., Heck, K., Hommel, J., Kurz, T., Lipp, M., Mohammadi, F., Scherrer, S., Schneider, M., Seitz, G., Stadler, L., Utz, M., Weinhardt, F., Flemisch, B.: DuMux 3—an open-source simulator for solving flow and transport problems in porous media with a focus on model coupling. *Comput Math Appl* (2020)
- Mejri, E., Bouhlila, R., Helmig, R.: Heterogeneity effects on evaporation-induced halite and gypsum coprecipitation in porous media. *Transp. Porous Media* **118**, 39–64 (2017)
- Mejri, E., Helmig, R., Bouhlila, R.: Modeling of evaporation-driven multiple salt precipitation in porous media with a real field application. *Geosciences* **10**, (2020)
- Nield, D.A., Bejan, A.: Convection in porous media, 5th edn. Springer, Berlin (2017)
- Piotrowski, J., Huisman, J.A., Nachshon, U., Pohlmeier, A., Vereecken, H.: Gas permeability of salt crusts formed by evaporation from porous media. *Geosciences* **10**(11), (2020)
- Pitman, M.G., Läuchli, A.: Global impact of salinity and agricultural ecosystems. In A. Läuchli and U. Lüttge, editors, *Salinity: Environment-Plants-Molecules*, pages 3–20. Springer, (2002)
- Riaz, A., Hesse, M., Tchelepi, H.A., Orr, F.M.: Onset of convection in a gravitationally unstable diffusive boundary layer in porous media. *J. Fluid Mech.* **548**, 87–111 (2006)

- Shokri, N., Lehmann, P., Or, D.: Liquid-phase continuity and solute concentration dynamics during evaporation from porous media: Pore-scale processes near vaporization surface. *Phys. Rev. E* **81**, 046308 (2010)
- Shokri-Kuehni, S.M.S., Raaijmakers, B., Kurz, T., Or, D., Helmig, R., Shokri, N.: Water table depth and soil salinization: From pore-scale processes to field-scale responses. *Water Resour. Res.* **56**(2), e2019WR026707 (2020)
- Singh, K.: Microbial and enzyme activities of saline and sodic soils. *Land Degrad. Dev.* **27**(3), 706–718 (2016)
- Slim, A.C.: Solutal-convection regimes in a two-dimensional porous medium. *J. Fluid Mech.* **741**, 461–491 (2014)
- Temme, N.M.: *Special functions: An introduction to the classical functions of mathematical physics*. Wiley, Hoboken (1996)
- van Duijn, C.J., Pieters, G.J.M., Raats, P.A.C.: On the stability of density stratified flow below a ponded surface. *Transp. Porous Media* **127**(3), 507–548 (2019)
- van Duijn, C.J., Pieters, G.J.M., Wooding, R.A., van der Ploeg, A.: Stability Criteria for the Vertical Boundary Layer Formed by Throughflow Near the Surface of a Porous Medium, pp. 155–169. American Geophysical Union (AGU) (2002)
- Vereecken, H., Burauel, P., Groeneweg, J., Klumpp, E., Mittelstaedt, W., Narres, H.-D., Pütz, T., van der Kruk, J., Vanderborght, J., Wendland, F.: Research at the agrosphere institute: from the process scale to the catchment scale. *Vadose Zone J.* **8**(3), 664–669 (2009)
- Wooding, R.A., Tyler, S.W., White, Ian: Convection in groundwater below an evaporating salt lake: 1. onset of instability. *Water Resour. Res.* **33**(6), 1199–1217 (1997)
- Wooding, R.A., Tyler, S.W., White, I., Anderson, P.A.: Convection in groundwater below an evaporating salt lake: 2. evolution of fingers or plumes. *Water Resour. Res.* **33**(6), 1219–1228 (1997)

Publisher's Note Springer Nature remains neutral with regard to jurisdictional claims in published maps and institutional affiliations.

12 Conclusion and outlook

In this habilitation thesis we have investigated how multiscale approaches can improve modeling and simulation of transport processes in porous media. This has been exemplified mainly through three types of transport processes: diffusive/conductive transport through parabolic problems, transport by two-phase flow where the two fluids interact with each other, and reactive transport where the available domain for fluid flow changes due to mineral precipitation and dissolution. These transport processes are relevant in a large variety of technical, biological and environmental applications. Especially geothermal energy production, soil salinization due to evaporation, and water management in fuel cells can be highlighted as applications where such transport processes play a role. Different multiscale approaches have been applied to address which types of models are appropriate to describe these transport phenomena at the pore scale and at the Darcy scale of a porous medium, and to construct efficient numerical schemes for these models. Through these multiscale approaches, we have found suitable modeling approaches bridging the scale gaps in porous media, and have highlighted the need to apply multiscale approaches for the considered processes and applications. In the following, the main outcomes of each of the parts and chapters are summarized, and we point to remaining open questions, in particular in terms of further development and incorporation of multiscale approaches for transport processes in porous media.

Part A focused on parabolic problems, in particular on finding effective coefficients at a larger scale for such problems. The first chapter of this part, Chapter 2, considered a non-linear parabolic problem which could represent the Richards equation for Darcy-scale unsaturated flow. In this case, the diffusion coefficient is the permeability of the porous medium. Here, an efficient numerical scheme based on mesh adaptivity and homogenization techniques was designed. Due to the mesh adaptivity, the permeability is needed at the various meshes. The permeabilities at the coarser meshes are found through solving local cell problems, which have been derived by applying homogenization. Despite the fact that homogenization relies on local periodicity, the scheme was found to work well also for non-periodic permeabilities. By applying L-scheme iterations, the non-linear solving steps were guaranteed to converge, which ensures a robust scheme. Overall, the numerical scheme was found to work well for the considered non-linear parabolic problem. It remains to apply similar approaches to problems where the non-linearities are more challenging. In particular, the permeability in this setup was constant in time and did not depend on the solution variable. Hence, the estimates of the permeability for the various meshes could therefore be decoupled from the rest of the problem. In the case of Darcy-scale two-phase flow, one has non-linear problems where the relative permeabilities depend on the saturation (as discussed in Section 1.2.2). Such relative permeability-saturation relationships are generally non-linear. It is possible to perform homogenization on such problems to find the effective permeability-saturation relationship on a larger scale (e.g. the field scale), see e.g. [45], but the adaptive algorithm from Chapter 2 would need to be adjusted to be able to estimate relative permeabilities for the coarser meshes. However, such an extension would allow for efficient and robust simulations also for Darcy-scale two-phase flow for large-scale

applications.

In Chapter 3, effective heat conductivities of a thin porous medium were investigated. Thin porous media appear in the setting of filters or can be part of a fuel cell. Here, the starting point was coupled heat transport in fluid and solid at the pore scale. By combining homogenization with ideas from transversal averaging, a dimensionally reduced Darcy-scale model for heat transport was found. The resulting cell problems for effective parameters were still three-dimensional, and depend on the boundary conditions from the top and bottom boundary of the thin porous medium. We considered here Dirichlet and Neumann boundary conditions, which represent two extremes of how the external boundaries behave. Extensions to other types of boundary conditions such as Robin boundary conditions are not straightforward as the homogenization steps depended on the type of conditions, due to the porous medium being thin. If the thin porous medium represents an interface layer between two domains, it would be beneficial to rather have an active coupling to those domains instead of applying given boundary conditions. This would result in obtaining effective transmission condition of the thin porous medium, similar as done for diffusion through membranes in [40, 41].

In Chapter 4, the final chapter of Part A, the behavior of permeability, effective solute diffusivity and effective heat conductivity was investigated. The starting point was a model derived by homogenization in [18], where Darcy-scale fluid flow, solute transport and heat transport are connected to local pore-scale cell problems for these effective parameters. The motivation of the model is to describe the influence of mineral precipitation and dissolution in a geothermal reservoir. In Chapter 4, the behavior of these effective parameters, in particular in the case when the porous medium is about to clog, was addressed. Parametrizations of these effective parameters for circular solids were found, honoring the observed changes close to clogging. These parametrizations are very useful when performing Darcy-scale simulations, as a coupled multiscale implementation is then not needed. For permeability and effective diffusivity, such parametrizations have been found for a large range of solid shapes [82, 94]. However, for heat transport, the solid is not just an obstacle, but an active part of transporting heat. Hence, extending the approaches as those found in [82, 94] to heat conductivities is possible by solving a range of cell problems, but is less generalizable than permeability and effective diffusivity, as the ratio between the heat conductivities of the fluid and solid influences the effective heat conductivity. However, this opens also for the possibility to rather apply machine learning on a selected range of heat conductivity ratios and solid shapes, and from there learn the general behavior of effective heat conductivities in porous media.

Also note that, for both Chapter 3 and Chapter 4, the cell problems for effective heat conductivity were derived under the assumptions that heat conductivities of the fluid and solid should be the same order of magnitude, and that thermal equilibrium between the fluid and solid at the pore scale applies. If the fluid and solid heat conductivities instead differ significantly or if pore-scale thermal equilibrium cannot be assumed, other effective models and other pore-scale cell problems for the effective heat transport are reached, see [9, Chapter 4]. When heat is transported by both advection and conduction, the question of which of these transport processes are dominating at the Darcy scale arises. In both Chapter 3 and Chapter 4, it was assumed that heat transport by advection and conduction were of equal importance at the Darcy scale. However, for advection-dominated processes, effective dispersion needs to be accounted for on the larger scale [6, 19]. How effective dispersion would manifest for thin porous media, remains an open question. Hence, there are many open questions on finding effective heat conductivities and understanding effective

heat transport in porous media, depending on the physical setting. However, these problems can be tackled with applying homogenization for these settings.

The main focus of Part B was on finding and understanding the effective behavior of two-phase flow. The main goal has been to incorporate the influence of the evolving fluid-fluid interface on the effective behavior. The fluid-fluid interface could in all cases evolve due to the flow itself and the interaction through surface tension between the two fluids. Three different settings were investigated, resulting in very different effective models. In Chapter 5, layered two-phase flow in a thin strip was analyzed. The thin strip represents a very simple domain for two-phase flow and is relevant for two-phase flow in a single pore or channel. By using a layer width to describe the evolution of the fluid-fluid interface and applying transversal averaging, dimensionally reduced models for the effective behavior of two-phase flow through the thin strip were derived. By considering different regimes in terms of capillary number and viscosity ratio, different effective models could be found. Such analyses highlight in particular the influence of e.g. capillary pressure and when the pressure jump between the two fluids has an influence on the effective behavior and when it does not have an impact. Since the domain is so simple, it is possible to find explicit expressions for the behavior of effective parameters. In Chapter 5, it was found that when the capillary pressure influences the effective behavior, the capillary pressure between the fluids depends on the curvature of the fluid-fluid interface and not on the saturation of one fluid, as usually assumed [48] (cf. discussion in Section 1.2.2). Numerical simulations of the original pore-scale equations showed that the dimensionally reduced models were indeed representing the average behavior well. What remains is to generalize these analyses to even further regimes (in terms of capillary number, Reynolds number, incorporating slip) to increase understanding of effective behavior for more two-phase flow settings.

Chapter 6 considered as Chapter 5 two-phase flow in a thin strip, but addressed the case where one fluid displaces the other. Here, transversal averaging could only be applied away from the fluid-fluid interface to derive a dimensionally reduced model. The region near the fluid-fluid interface was instead incorporated by matched asymptotic expansions, which hence connected the two regions at each side of the fluid-fluid interface. The resulting effective model was dimensionally reduced and incorporated also the influence of dynamic contact angle laws and slip length to the solid walls. Since the domain is rather simple, (semi-)explicit expressions for dynamic effects on the capillary pressure could be found, giving new insights to how dynamic effects influence the effective behavior. This model was later extended to axisymmetric tubes, such that effective behavior along the tube could be modeled [67]. Extending to such a domain allows the effective model to be incorporated in (dynamic) pore-network models.

Another possible extension is to combine the two approaches of Chapter 5 and Chapter 6: Instead of restricting to layered flow or one fluid displacing the other, one could consider a setting which allows for large deformations of the fluid-fluid interface by combining the modeling and averaging approaches of these two chapters. However, how to couple these two approaches where the fluid-fluid interface behaves in an “in between” form, remains an open question. An extra level of matched asymptotic expansions could allow to connect model compartments in the necessary manner. A dimensionally reduced model for this combined setting would allow for understanding the effective behavior for more general two-phase flow in thin strips or tubes. Note that a similar setup was considered in [79] (cf. plug flow in Figure 1 in [79]), but only for steady-state flow where deformation of the fluid-fluid interface was neglected. By incorporating the dynamic behavior in the effective models, a better understanding of the interactions between the two fluid phases can be

obtained.

In the last chapter of Part B, Chapter 7, two-phase flow in a periodic porous medium was investigated. By using a phase-field model for two-phase flow in a periodic pore-scale geometry and applying homogenization, a Darcy-scale model could be derived. The Darcy-scale model depends on effective parameters found through local pore-scale cell problems. Here, the influence of a varying surface tension due to a soluble surfactant was investigated. The cell problems for effective parameters depend on the phase field (which in this case corresponds to the distribution of the two fluid phases at the pore scale), which itself depends on the surface tension. The resulting two-scale model was implemented using an approach inspired by heterogeneous multiscale methods in an explicit manner. The numerical experiments highlighted the influence of the varying surface tension on the effective Darcy-scale behavior, which is relevant for example for enhanced oil recovery. For the numerical experiments, all the cell problems were solved at every time step. A more efficient algorithm could have been developed by incorporating an adaptivity criterion in terms of which cell problems have to be updated when. However, what a suitable criterion for two-phase flow would be, is not clear. The Darcy-scale model itself was derived under certain assumptions on the non-dimensional parameters for the flow rates, strength of solute diffusion and behavior of the phase field. Extending the homogenization procedure to other regimes would allow to have effective models also for more general settings of two-phase porous-medium flow.

Part C addressed modeling and simulation of reactive transport in porous media, where mineral precipitation and dissolution reactions could alter the pore-scale geometry. The first chapter of this part, Chapter 8, formulated a new phase-field model for single-phase fluid flow and solute transport, coupled with the evolving geometry due to mineral precipitation and dissolution. The motivation for formulating such a model is to describe interactions between fluid flow and geometry changes, which is relevant for geothermal energy production and soil salinization. The availability of this phase-field model allows for simpler analysis and numerical implementation of such processes, since the evolving fluid-solid interface and its boundary conditions are incorporated into the phase-field model in a smooth manner. Hence, discontinuities are avoided. The Allen-Cahn equation for the evolution of the phases is a diffusion equation with a non-linear source term, which can be implemented by most standard numerical schemes. However, as it is clear from Chapter 8, the phase-field model always includes curvature-driven motion of the fluid-solid interface, which is not necessarily physical. The curvature-driven motion became visible already from the sharp-interface limit derived by matched asymptotic expansions, and also from the numerical experiments where the model was compared to available benchmarks. There are approaches to handle the curvature-driven motion for simpler phase-field models, e.g. [1, 116], but it remains to investigate to which extent these approaches are applicable to the phase-field model developed in Chapter 8. Unlike the Cahn-Hilliard equation, the Allen-Cahn equation is not conservative. This can however be handled by including an additional non-local term, but comes with the cost that non-linear solving steps are then much more expensive [16].

By formulating the phase-field model of Chapter 8 in a periodic pore-scale geometry, an effective Darcy-scale model was found by homogenization. The derived Darcy-scale model relies on local pore-scale cell problems for effective parameters permeability and effective diffusivity, which depend on the phase field (which in this case gives the distribution of fluid and solid at the pore scale). The diffuse-interface width therefore affects the value of the effective parameters, and by comparing with solutions of corresponding sharp-interface cell

problems we found this influence to be relatively small - and decreasing when the sharp-interface width decreased. The latter opens for the question of asymptotic consistency: If one reaches the same model if first performing homogenization ($\varepsilon \rightarrow 0$) and then taking the sharp-interface limit ($\lambda \rightarrow 0$), as when one first takes the sharp-interface limit ($\lambda \rightarrow 0$) and afterwards performs homogenization ($\varepsilon \rightarrow 0$). Although the numerical solution of the cell problems indicated that one has asymptotic consistency, further analysis of the homogenized phase-field model is needed to answer this question. At least for a Cahn-Hilliard model, asymptotic consistency has recently been found in the case of transversal averaging [107].

The derived model in Chapter 8 consists of Darcy-scale and pore-scale equations, where the two scales are coupled through the reaction rate and the effective parameters. In Chapter 9, a robust and efficient scheme was constructed for this coupled two-scale model by applying a scheme from heterogeneous multiscale methods. The constructed scheme uses an iterative approach between the two scales. These two-scale iterations were in Chapter 9 proven to converge under mild restrictions on the time-step size and phase-field parameters. However, the proof was only for the case where flow was neglected. The reason for neglecting flow was the issue of bounding the variability of the permeability. This bounding could be done for the effective diffusivity by analyzing its cell problem (cf. Lemma 2 in Chapter 9). However, the cell problem for permeability has a different structure, which did not allow the same strategy to be applied. In the numerical examples, the scheme was found to converge also in the case with flow. However, a different strategy is needed to include the influence of fluid flow in the convergence proof. One possibility would be to limit the possible solid shapes in order to bound the resulting permeability variation. In this case the proof would rely on a parametrized-like expression for how permeability depends on the varying solid size, as done for a sharp-interface model in Chapter 4.

In Chapter 9, an adaptive strategy in terms of which cell problems should be updated when is applied, by extending the ideas of [85]. This turned out to give a large gain in terms of less computational effort, with only a minor loss of accuracy. The cell problems can also be solved in parallel as they do not depend on each other, allowing further speedup of the resulting numerical scheme. These strategies are relevant also for other types of applications where macro-scale equations depend on micro-scale problems for effective parameters; e.g. two-phase flow in Chapter 7, heterogeneous materials [56] and biology [98]. However, suitable adaptivity criteria are needed for each application in order to apply such a strategy.

In the last chapter of Part C, Chapter 10, modeling and numerical approaches for single-phase fluid flow with two precipitating and dissolving minerals were investigated. Interactions between the minerals were included in the sense that the dissolution of one mineral could trigger the precipitation of the other due to differences in solubility, which is a rather common setting especially for geothermal reservoirs. Such a three-phase setting is challenging to model and simulate, especially due to the movement of the fluid-solid-solid triple points. A sharp-interface model based on a modified level-set approach and a diffuse-interface model based on a ternary phase-field model were formulated, implemented, and compared against each other. Overall, both approaches were found to be able to simulate geometrical changes in a three-phase system. Numerically, the phase-field model conserved mass, while the level-set model lost up to 2% due to the approximations made for the level-set approach. In general, fewer unknowns on the same grid and fewer Newton iterations were needed for the phase-field model, highlighting its simpler numerical approach due to the diffuse nature of the model. However, the phase-field model struggled with resolving the behavior of the triple points. This was assumed to be caused by the curvature-driven

interface motion, whose presence was visible already in the sharp-interface limit. Known approaches to handle such curvature-driven motion for simpler models [1, 116] were found to not be applicable for this model. This means, further work is needed to find a suitable strategy to eliminate curvature-driven motion for this type of phase-field model. However, solving the corresponding pore-scale cell problems for the level-set and phase-field model, provided comparable values of permeability and effective diffusivity. Hence, both approaches were found to be able to predict effective parameters satisfactory if used as pore-scale models in a two-scale approach.

The last part of this thesis, Part D, addressed evaporation from a porous medium in Chapter 11. The analysis made here is motivated by soil salinization. In the model setup, water is allowed to evaporate from the top of the porous medium, while salt stays behind. There is hence a gradual accumulation of salt near the top of the porous medium, which can result in soil salinization and formation of a salt crust if the solubility of the salt is reached. Since this setting is also gravitationally unstable, instabilities in the form of fingers can develop. In this chapter, a linear stability analysis was applied to analyze the onset of instabilities. Through finding and solving a connected eigenvalue problem, onset times could be found as function of model parameters such as permeability and evaporation rate. For realistic choices of parameters, the onset times were found to be in the range of hours to days. Numerical simulations gave information about the further development of the instabilities, and their influence on the salt concentration. In particular, it was found that the instabilities gradually develop in strength and can therefore first after some time cause a net downwards transport of salt. Hence, salt can still precipitate even if density instabilities occur.

The analysis and simulations performed in Chapter 11 contributed to increased understanding of the development and importance of evaporation-induced density instabilities in porous media. However, a simplified setup was considered, which could influence the outcomes. In particular, it was assumed that the porous medium remains fully saturated during evaporation. This is the case as long the lower part of the porous medium is connected to a saturated reservoir and as long the capillary pressure remains below the entry pressure of the porous medium. However, in other cases, air would penetrate into the porous medium when there is evaporation [13]. To incorporate the possible presence of air would have required to perform the linear stability analysis and simulations with Richards equation for unsaturated flow or with Darcy-scale two-phase flow models (see Section 1.2.2). Using Richards equation introduces an additional non-linearity in the model, but linear stability analyses for Richards equation have been successfully performed for other settings [34]. In this case, potential interactions between the varying water saturation and density instabilities could be captured.

Another aspect is that the linear stability analysis and simulations in Chapter 11 considered a pure Darcy-scale approach. However, processes at the pore scale are relevant for this type of setting as well. First of all, if accounting for the presence of air in the upper parts of the porous medium due to the evaporation, there would be interactions between air and water at the pore scale. The interactions on the air-water interface are not only due to flow and surface tension, as in the pore-scale models of Part B, but also due to the mass transfer across this interface following the evaporation. In Chapter 11, the evaporation rate was applied as a given boundary condition at the top of the porous medium, while it would generally depend on temperature and vapor concentration of the air [13]. To resolve the evolving air-water interface at the pore scale, a phase-field equation could be applied. However, this phase-field equation must incorporate that the air-water interface

evolves both due to flow, surface tension and the evaporation. Secondly, when or if salt precipitates, there will be an evolving fluid-solid interface. The salt precipitation would lower the permeability, and potentially form a crust at the top of the soil [80] (see also Figure 1.4). In Chapter 11, a simple Kozeny-Carman relation was applied to model the changes of the permeability, as accurately describing the evolution of the salt precipitation was not the focus. To instead incorporate the evolving fluid-solid interface from the pore scale, a phase-field model could be applied. However, since also the influence of air should be accounted for, a ternary phase-field model for water, air and mineral would be needed. To develop such a phase-field model, the sharp-interface limit using matched asymptotic expansion could answer whether the model reduces to the expected sharp-interface physics, similar as done in Chapter 8 and Chapter 10. However, an additional analysis of the triple point would be necessary as well [20].

To incorporate the influence of the pore-scale processes on the effective behavior at the Darcy scale, homogenization could be applied. This is expected to result in a two-scale coupled model, where the Darcy-scale model equations and the pore-scale cell problems jointly depend on each other, as seen for example in Chapter 7 and Chapter 8. Performing a linear stability analysis on such a model is most likely beyond what is possible to do, due to the strong couplings within such a two-scale model. However, numerical simulations of such a model can still be performed. Then, a multiscale scheme inspired by heterogeneous multiscale methods could be applied, as seen in Chapter 9, or as simplified versions in Chapter 2 or Chapter 7. However, model development of the processes at the pore scale and homogenization strategies for such a highly coupled model is first needed to be performed. When performing the homogenization, much care must be done in choosing which regime is to be considered.

In general, since homogenization (and transversal averaging) depend on which regime is considered in terms of the size of the appearing non-dimensional numbers, the effective models derived in this thesis can be extended by considering other regimes. This is however generally not straightforward, as the coupling between the model equations can change when considering other regimes. This can make it more difficult or even impossible to derive an effective model. However, when effective models for further regimes can be found, one can use this to investigate the effective behavior of the new regime. In particular it can be useful to compare effective models for different regimes, as done in Chapter 5, as this highlights for which settings certain effects (like capillary pressure) are important and when they can be neglected at the larger scale.

To summarize, applying multiscale approaches offer great possibilities for modeling, analyzing and simulating transport processes across scales in porous media. As this thesis has highlighted, multiscale aspects are relevant for a large range of applications, as especially emphasized for subsurface applications in terms of geothermal energy production and soil salinization, and for technical applications like water management in fuel cells. In particular, the presence of interfaces - e.g. evolving fluid-fluid interfaces or fluid-solid interfaces - at the pore scale influences the effective behavior at the larger REV or field scale. For many of these porous-media applications, especially for the ones in the subsurface, a Darcy-scale model is needed in order to perform simulations efficiently. This thesis shows strategies and methods for improving such Darcy-scale models and how to still incorporate the influence of smaller-scale processes on the effective behavior. From the applications point of view, this means that we through multiscale approaches can obtain better understanding of how e.g. mineral precipitation and dissolution influence the fluid flow and heat transport through a geothermal reservoir, how the interaction between air, water and dissolved salt

influences soil salinization due to evaporation, and how the interaction between air and water inside a fuel cell affects the overall transport of water.

Bibliography

- [1] H. Abels. (Non-)Convergence of solutions of the convective Allen-Cahn equation. *Partial Differential Equations and Applications*, 3, 2022.
- [2] H. Abels, H. Garcke, and G. Grün. Thermodynamically consistent, frame indifferent diffuse interface models for incompressible two-phase flows with different densities. *Mathematical Models and Methods in Applied Sciences*, 22(03):1150013, 2012.
- [3] S. Ackermann, C. Bringedal, and R. Helmig. Multi-scale three-domain approach for coupling free flow and flow in porous media including droplet-related interface processes. *Journal of Computational Physics*, 429:109993, 2021.
- [4] M. Acosta, C. Merten, G. Eigenberger, H. Class, R. Helmig, B. Thoben, and H. Müller-Steinhagen. Modeling non-isothermal two-phase multicomponent flow in the cathode of PEM fuel cells. *Journal of Power Sources*, 159(2):1123–1141, 2006.
- [5] G. Allaire. Homogenization and two-scale convergence. *SIAM J. Math. Anal.*, 23(6):1482–1518, 1992.
- [6] G. Allaire, R. Brizzi, A. Mikelić, and A. Piatnitski. Two-scale expansion with drift approach to the Taylor dispersion for reactive transport through porous media. *Chemical Engineering Science*, 65(7):2292–2300, 2010. International Symposium on Mathematics in Chemical Kinetics and Engineering.
- [7] S. M. Allen and J. W. Cahn. A microscopic theory for antiphase boundary motion and its application to antiphase domain coarsening. *Acta Metallurgica*, 27(6):1085–1095, 1979.
- [8] R. Anderson, L. Zhang, Y. Ding, M. Blanco, X. Bi, and D. P. Wilkinson. A critical review of two-phase flow in gas flow channels of proton exchange membrane fuel cells. *Journal of Power Sources*, 195(15):4531–4553, 2010.
- [9] J.-L. Auriault, C. Boutin, and C. Geindreau. *Homogenization of coupled phenomena in heterogeneous media*, volume 149. John Wiley & Sons, 2009.
- [10] F. Barbir. *PEM fuel cells: theory and practice*. Academic press, 2012.
- [11] J. Bear. *Modeling Phenomena of Flow and Transport in Porous Media*, volume 31 of *Theory and Applications of Transport in Porous Media*. Springer, 2018.
- [12] J. Bear and Y. Bachmat. *Introduction to Modeling of Transport Phenomena in Porous Media*, volume 4. Springer Science & Business Media, 2012.
- [13] M. Bechtold, S. Haber-Pohlmeier, J. Vanderborght, A. Pohlmeier, T. P. A. Ferré, and H. Vereecken. Near-surface solute redistribution during evaporation. *Geophysical Research Letters*, 38(17), 2011.
- [14] R. Bertani. Geothermal power generation in the world 2010–2014 update report. *Geothermics*, 60:31–43, 2016.
- [15] T. D. Blake. The physics of moving wetting lines. *Journal of Colloid and Interface Science*, 299(1):1–13, 2006.

- [16] C. Bringedal. A conservative phase-field model for reactive transport. In R. Klöforn, E. Keilegavlen, F. A. Radu, and J. Fuhrmann, editors, *Finite Volumes for Complex Applications IX - Methods, Theoretical Aspects, Examples*, pages 537–545, Cham, 2020. Springer International Publishing.
- [17] C. Bringedal, I. Berre, I. S. Pop, and F. A. Radu. A model for non-isothermal flow and mineral precipitation and dissolution in a thin strip. *Journal of Computational and Applied Mathematics*, 289:346–355, 2015. Sixth International Conference on Advanced Computational Methods in Engineering (ACOMEN 2014).
- [18] C. Bringedal, I. Berre, I. S. Pop, and F. A. Radu. Upscaling of non-isothermal reactive porous media flow with changing porosity. *Transport in Porous Media*, 114(2):371–393, 2016.
- [19] C. Bringedal, I. Berre, I. S. Pop, and F. A. Radu. Upscaling of nonisothermal reactive porous media flow under dominant Péclet number: The effect of changing porosity. *Multiscale Modeling & Simulation*, 14(1):502–533, 2016.
- [20] L. Bronsard and F. Reitich. On three-phase boundary motion and the singular limit of a vector-valued ginzburg-landau equation. *Archive for Rational Mechanics and Analysis*, 124(4):355–379, 1993.
- [21] R. H. Brooks and A. T. Corey. Properties of porous media affecting fluid flow. *Journal of the Irrigation and Drainage Division*, 92(2):61–88, 1966.
- [22] G. Caginalp and P. Fife. Dynamics of layered interfaces arising from phase boundaries. *SIAM Journal on Applied Mathematics*, 48(3):506–518, 1988.
- [23] J. W. Cahn and J. E. Hilliard. Free energy of a nonuniform system. i. interfacial free energy. *The Journal of Chemical Physics*, 28(2):258–267, 1958.
- [24] P. C. Carman. Fluid flow through granular beds. *Chemical Engineering Research and Design*, 75:S32–S48, 1997.
- [25] M. M. Chaves, J. Flexas, and C. Pinheiro. Photosynthesis under drought and salt stress: regulation mechanisms from whole plant to cell. *Annals of Botany*, 103(4):551–560, 07 2008.
- [26] M. A. Christie and M. J. Blunt. Tenth SPE comparative solution project: A comparison of upscaling techniques. *SPE Reservoir Evaluation & Engineering*, 4(04):308–317, 08 2001.
- [27] D. Cioranescu and P. Donato. *An introduction to homogenization*, volume 17. Oxford university press Oxford, 1999.
- [28] H. K. Dahle and M. A. Celia. A dynamic network model for two-phase immiscible flow. *Computational Geosciences*, 3(1):1–22, 1999.
- [29] I. N. Daliakopoulos, I. K. Tsanis, A. Koutroulis, N. N. Kourgialas, A. E. Varouchakis, G. P. Karatzas, and C. J. Ritsema. The threat of soil salinity: A European scale review. *Science of The Total Environment*, 573:727 – 739, 2016.
- [30] K. Daly and T. Roose. Homogenization of two fluid flow in porous media. *Proceedings of the Royal Society A: Mathematical, Physical and Engineering Sciences*, 471(2176):20140564, 2015.
- [31] H. Darcy. *Les Fontaines publiques de la ville de Dijon. Exposition et appli cation des principes à suivre et des formules à employer dans les questions de distribution d’eau*. Victor Dalmont, 1856.

- [32] M. Dentz, T. Le Borgne, A. Englert, and B. Bijeljic. Mixing, spreading and reaction in heterogeneous media: A brief review. *Journal of Contaminant Hydrology*, 120-121:1–17, 2011. Reactive Transport in the Subsurface: Mixing, Spreading and Reaction in Heterogeneous Media.
- [33] D. A. DiCarlo. Experimental measurements of saturation overshoot on infiltration. *Water Resources Research*, 40(4), 2004.
- [34] X. Du, T. Yao, W. D. Stone, and J. M. H. Hendrickx. Stability analysis of the unsaturated water flow equation: 1. mathematical derivation. *Water Resources Research*, 37(7):1869–1874, 2001.
- [35] C. Eck. Homogenization of a phase field model for binary mixtures. *Multiscale Modeling & Simulation*, 3(1):1–27, 2005.
- [36] J. Fabricius, J. G. I. Hellström, T. S. Lundström, E. Miroshnikova, and P. Wall. Darcy’s law for flow in a periodic thin porous medium confined between two parallel plates. *Transport in Porous Media*, 115(3):473–493, 2016.
- [37] M. W. Farthing and F. L. Ogden. Numerical solution of Richards’ equation: A review of advances and challenges. *Soil Science Society of America Journal*, 81(6):1257–1269, 2017.
- [38] F. Frank, C. Liu, A. Scanziani, F. O. Alpak, and B. Riviere. An energy-based equilibrium contact angle boundary condition on jagged surfaces for phase-field methods. *Journal of Colloid and Interface Science*, 523:282–291, 2018.
- [39] I. B. Fridleifsson. Geothermal energy for the benefit of the people. *Renewable and Sustainable Energy Reviews*, 5(3):299–312, 2001.
- [40] M. Gahn, M. Neuss-Radu, and P. Knabner. Derivation of effective transmission conditions for domains separated by a membrane for different scaling of membrane diffusivity. *Discrete & Continuous Dynamical Systems - S*, 10(4):773–797, 2017.
- [41] M. Gahn, M. Neuss-Radu, and P. Knabner. Effective interface conditions for processes through thin heterogeneous layers with nonlinear transmission at the microscopic bulk-layer interface. *Networks & Heterogeneous Media*, 13(4):609–640, 2018.
- [42] H. Garcke, C. Hecht, M. Hinze, and C. Kahle. Numerical approximation of phase field based shape and topology optimization for fluids. *SIAM Journal on Scientific Computing*, 37(4):A1846–A1871, 2015.
- [43] H. Garcke, K. F. Lam, and B. Stinner. Diffuse interface modeling of soluble surfactants in two-phase flow. *Communications in Mathematical Sciences*, 12(8):1475–1522, 2014.
- [44] S. Gärttner, F. O. Alpak, A. Meier, N. Ray, and F. Frank. Estimating permeability of 3D micro-CT images by physics-informed CNNs based on DNS. *arXiv:2109.01818*, 2021.
- [45] T. Ghosh, C. Bringedal, R. Helmig, and G. P. Raja Sekhar. Upscaled equations for two-phase flow in highly heterogeneous porous media: varying permeability and porosity. *Advances in Water Resources*, 145:103716, 2020.
- [46] H. Hajibeygi and P. Jenny. Multiscale finite-volume method for parabolic problems arising from compressible multiphase flow in porous media. *Journal of Computational Physics*, 228(14):5129–5147, 2009.

- [47] T. Heister, M. F. Wheeler, and T. Wick. A primal-dual active set method and predictor-corrector mesh adaptivity for computing fracture propagation using a phase-field approach. *Computer Methods in Applied Mechanics and Engineering*, 290:466–495, 2015.
- [48] R. Helmig. *Multiphase flow and transport processes in the subsurface: a contribution to the modeling of hydrosystems*. Springer, 1997.
- [49] R. Helmig, A. Weiss, and B. I. Wohlmuth. Dynamic capillary effects in heterogeneous porous media. *Computational Geosciences*, 11(3):261–274, 2007.
- [50] J. Hommel, E. Coltman, and H. Class. Porosity–permeability relations for evolving pore space: a review with a focus on (bio-) geochemically altered porous media. *Transport in Porous Media*, 124(2):589–629, 2018.
- [51] U. Hornung, editor. *Homogenization and Porous Media*. Springer-Verlag, Berlin, Heidelberg, 1996.
- [52] C. Huh and L. Scriven. Hydrodynamic model of steady movement of a solid/liquid/fluid contact line. *Journal of Colloid and Interface Science*, 35(1):85–101, 1971.
- [53] Hydrogen Council. Path to hydrogen competitiveness: a cost perspective. *Hydrogen Knowledge Centre*, 2020.
- [54] V. A. Jambhekar, R. Helmig, N. Schröder, and N. Shokri. Free-flow–porous-media coupling for evaporation-driven transport and precipitation of salt in soil. *Transport in Porous Media*, 110(2):251–280, 11 2015.
- [55] M. Kirkesæther Brun, T. Wick, I. Berre, J. M. Nordbotten, and F. A. Radu. An iterative staggered scheme for phase field brittle fracture propagation with stabilizing parameters. *Computer Methods in Applied Mechanics and Engineering*, 361:112752, 2020.
- [56] V. Kouznetsova, W. Brekelmans, and F. Baaijens. An approach to micro-macro modeling of heterogeneous materials. *Computational mechanics*, 27(1):37–48, 2001.
- [57] J. Kozeny. Über kapillare Leitung der Wasser in Boden. *Royal Academy of Science, Vienna, Proc. Class I*, 136:271–306, 1927.
- [58] K. Kumar, T. van Noorden, and I. S. Pop. Upscaling of reactive flows in domains with moving oscillating boundaries. *Discrete & Continuous Dynamical Systems-S*, 7(1):95, 2014.
- [59] K. Kumar, T. L. van Noorden, and I. S. Pop. Effective dispersion equations for reactive flows involving free boundaries at the microscale. *Multiscale Modeling & Simulation*, 9(1):29–58, 2011.
- [60] D. Landa-Marbán, G. Bødtker, K. Kumar, I. S. Pop, and F. A. Radu. An upscaled model for permeable biofilm in a thin channel and tube. *Transport in porous media*, 132(1):83–112, 2020.
- [61] D. Landa-Marbán, F. A. Radu, and J. M. Nordbotten. Modeling and simulation of microbial enhanced oil recovery including interfacial area. *Transport in Porous Media*, 120(2):395–413, 2017.
- [62] L. D. Landau and E. M. Lifshitz. *Fluid mechanics*, volume 6 of *Course of Theoretical Physics*. Pergamon Press, 1987. Translated from the Russian by J. B. Sykes and W. H. Reid.

- [63] S. Lee and J. Yang. Modelling of effective thermal conductivity for a nonhomogeneous anisotropic porous medium. *International Journal of Heat and Mass Transfer*, 41(6):931–937, 1998.
- [64] M. Li, K. Zeng, L. Wonnell, and I. A. Bolotnov. Development of a new contact angle control algorithm for level-set method. *Journal of Fluids Engineering*, 141(6), 12 2018. 061301.
- [65] F. List and F. A. Radu. A study on iterative methods for solving Richards’ equation. *Computational Geosciences*, 20(2):341–353, 2016.
- [66] Z. Lu, S. Kandlikar, C. Rath, M. Grimm, W. Domigan, A. White, M. Hardbarger, J. Owejan, and T. Trabold. Water management studies in PEM fuel cells, Part II: Ex situ investigation of flow maldistribution, pressure drop and two-phase flow pattern in gas channels. *International Journal of Hydrogen Energy*, 34(8):3445–3456, 2009.
- [67] S. B. Lunowa, A. Mascini, C. Bringedal, T. Bultreys, V. Cnudde, and I. S. Pop. Dynamic effects during the capillary rise of fluids in cylindrical tubes. *Langmuir*, 38(5):1680–1688, 2022.
- [68] E. Mejri, R. Helmig, and R. Bouhlila. Modeling of evaporation-driven multiple salt precipitation in porous media with a real field application. *Geosciences*, 10, 2020.
- [69] S. Metzger and P. Knabner. Homogenization of two-phase flow in porous media from pore to Darcy scale: A phase-field approach. *Multiscale Modeling & Simulation*, 19(1):320–343, 2021.
- [70] C. Michalkowski, M. Veyskarami, C. Bringedal, R. Helmig, and V. Schleper. Two-phase flow dynamics at the interface between GDL and gas distributor channel using a pore-network model. *arXiv:2201.12063*, 2022.
- [71] C. Michalkowski, K. Weishaupt, V. Schleper, and R. Helmig. Modeling of two phase flow in a hydrophobic porous medium interacting with a hydrophilic structure. *arXiv:2201.13131*, 2022.
- [72] S. Molins, C. Soulaire, N. Prasianakis, A. Abbasi, P. Poncet, A. Ladd, V. Starchenko, S. Roman, D. Trebotich, H. Tchelepi, and C. Steefel. Simulation of mineral dissolution at the pore scale with evolving fluid-solid interfaces: Review of approaches and benchmark problem set. *Computational Geosciences*, 2020.
- [73] S. Molins, D. Trebotich, G. H. Miller, and C. I. Steefel. Mineralogical and transport controls on the evolution of porous media texture using direct numerical simulation. *Water Resources Research*, 53(5):3645–3661, 2017.
- [74] E. K. Mroczek, S. P. White, and D. J. Graham. Deposition of amorphous silica in porous packed beds — predicting the lifetime of reinjection aquifers. *Geothermics*, 29(6):737–757, 2000.
- [75] D. A. Nield and A. Bejan. *Convection in porous media*, volume 4. Springer, 2013.
- [76] A. Oron, S. H. Davis, and S. G. Bankoff. Long-scale evolution of thin liquid films. *Rev. Mod. Phys.*, 69:931–980, Jul 1997.
- [77] S. Osher and R. Fedkiw. *Level set methods and dynamic implicit surfaces*, volume 153. Springer Science & Business Media, 2006.

- [78] J. P. Owejan, J. J. Gagliardo, J. M. Sergi, S. G. Kandlikar, and T. A. Trabold. Water management studies in PEM fuel cells, Part I: Fuel cell design and in situ water distributions. *International Journal of Hydrogen Energy*, 34(8):3436–3444, 2009.
- [79] D. Picchi and I. Battiato. The impact of pore-scale flow regimes on upscaling of immiscible two-phase flow in porous media. *Water Resources Research*, 54(9):6683–6707, 2018.
- [80] J. Piotrowski, J. A. Huisman, U. Nachshon, A. Pohlmeier, and H. Vereecken. Gas permeability of salt crusts formed by evaporation from porous media. *Geosciences*, 10(11), 2020.
- [81] L. N. Plummer. *A computer program incorporating Pitzer’s equations for calculation of geochemical reactions in brines*, volume 88. Department of the Interior, US Geological Survey, 1988.
- [82] N. Ray, A. Rupp, R. Schulz, and P. Knabner. Old and new approaches predicting the diffusion in porous media. *Transport in Porous Media*, 124, 06 2018.
- [83] N. Ray, T. van Noorden, F. Frank, and P. Knabner. Multiscale modeling of colloid and fluid dynamics in porous media including an evolving microstructure. *Transport in Porous Media*, 95:669–696, 2012.
- [84] N. Ray, T. van Noorden, F. Radu, W. Friess, and P. Knabner. Drug release from collagen matrices including an evolving microstructure. *ZAMM - Journal of Applied Mathematics and Mechanics / Zeitschrift für Angewandte Mathematik und Mechanik*, 93(10-11):811–822, 2013.
- [85] M. Redeker and C. Eck. A fast and accurate adaptive solution strategy for two-scale models with continuous inter-scale dependencies. *Journal of Computational Physics*, 240:268–283, 2013.
- [86] M. Redeker, C. Rohde, and I. S. Pop. Upscaling of a tri-phase phase-field model for precipitation in porous media. *IMA Journal of Applied Mathematics*, 81(5):898–939, 2016.
- [87] L. A. Richards. Capillary conduction of liquids through porous mediums. *Physics*, 1(5):318–333, 1931.
- [88] N. Sannes. *Fuel cell technology: reaching towards commercialization*. Springer Science & Business Media, 2006.
- [89] R. Saye and J. Sethian. Analysis and applications of the voronoi implicit interface method. *Journal of Computational Physics*, 231(18):6051–6085, 2012.
- [90] H. Schlichting and K. Gersten. *Boundary-layer theory*. Springer Science & Business Media, 9 edition, 2017.
- [91] M. Schmuck, M. Pradas, G. A. Pavliotis, and S. Kalliadasis. Derivation of effective macroscopic Stokes–Cahn–Hilliard equations for periodic immiscible flows in porous media. *Nonlinearity*, 26(12), 2013.
- [92] R. Schofield, D. S. G. Thomas, and M. J. Kirkby. Causal processes of soil salinization in Tunisia, Spain and Hungary. *Land Degradation & Development*, 12(2):163–181, 2001.
- [93] R. Schulz and P. Knabner. Derivation and analysis of an effective model for biofilm growth in evolving porous media. *Mathematical Methods in the Applied Sciences*, 40(8):2930–2948, 2017.

- [94] R. Schulz, N. Ray, S. Zech, A. Rupp, and P. Knabner. Beyond Kozeny–Carman: Predicting the permeability in porous media. *Transport in Porous Media*, 130:487–512, 2019.
- [95] S. M. S. Shokri-Kuehni, B. Raaijmakers, T. Kurz, D. Or, R. Helmig, and N. Shokri. Water table depth and soil salinization: From pore-scale processes to field-scale responses. *Water Resources Research*, 56(2):e2019WR026707, 2020.
- [96] E. Sonnenthal, A. Ito, N. Spycher, M. Yui, J. Apps, Y. Sugita, M. Conrad, and S. Kawakami. Approaches to modeling coupled thermal, hydrological, and chemical processes in the drift scale heater test at Yucca Mountain. *International Journal of Rock Mechanics and Mining Sciences*, 42(5):698–719, 2005. Research results from the Decovalex III & Benchpar projects.
- [97] J. W. Tester, B. J. Anderson, A. S. Batchelor, D. D. Blackwell, R. DiPippo, E. M. Drake, J. Garnish, B. Livesay, M. C. Moore, K. Nichols, et al. Impact of enhanced geothermal systems on US energy supply in the twenty-first century. *Philosophical Transactions of the Royal Society A: Mathematical, Physical and Engineering Sciences*, 365(1853):1057–1094, 2007.
- [98] A. M. Uhrmacher, R. Ewald, M. John, C. Maus, M. Jeschke, and S. Biermann. Combining micro and macro-modeling in devs for computational biology. In *2007 Winter Simulation Conference*, pages 871–880, 2007.
- [99] C. J. van Duijn and I. S. Pop. Crystal dissolution and precipitation in porous media: Pore scale analysis. *Journal für die reine und angewandte Mathematik*, 2004(577):171–211, 2004.
- [100] M. van Dyke. *Perturbation methods in fluid mechanics*, volume 9 of *Applied Mathematics and Mechanics*. Academic Press, 1969.
- [101] M. T. van Genuchten. A closed-form equation for predicting the hydraulic conductivity of unsaturated soils. *Soil Science Society of America Journal*, 44(5):892–898, 1980.
- [102] T. L. van Noorden. Crystal precipitation and dissolution in a porous medium: Effective equations and numerical experiments. *Multiscale Modeling & Simulation*, 7(3):1220–1236, 2009.
- [103] T. L. van Noorden. Crystal precipitation and dissolution in a thin strip. *European Journal of Applied Mathematics*, 20(1):69–91, 2009.
- [104] T. L. van Noorden and C. Eck. Phase field approximation of a kinetic moving-boundary problem modelling dissolution and precipitation. *Interfaces and Free Boundaries*, 13(1):29–55, 2011.
- [105] T. L. van Noorden, I. S. Pop, A. Ebigbo, and R. Helmig. An upscaled model for biofilm growth in a thin strip. *Water Resources Research*, 46(6), 2010.
- [106] F. van Weert, J. van der Gun, and J. Reckman. Global overview of saline groundwater occurrence and genesis. *International Groundwater Resources Assessment Centre*, 2009. Report nr. GP 2009-1.
- [107] L. von Wolff and I. S. Pop. Upscaling of a Cahn–Hilliard Navier–Stokes model with precipitation and dissolution in a thin strip. *Journal of Fluid Mechanics*, 941:A49, 2022.
- [108] A. Wagner, E. Eggenweiler, F. Weinhardt, Z. Trivedi, D. Krach, C. Lohrmann, K. Jain, N. Karadimitriou, C. Bringedal, P. Volland, C. Holm, H. Class, H. Steeb, and I. Rybak. Permeability estimation of regular porous structures: A benchmark for comparison of methods. *Transport in Porous Media*, 138(1):1–23, 2021.

- [109] R. Wagner, M. Kühn, V. Meyn, H. Pape, U. Vath, and C. Clauser. Numerical simulation of pore space clogging in geothermal reservoirs by precipitation of anhydrite. *International Journal of Rock Mechanics and Mining Sciences*, 42(7):1070–1081, 2005. Rock Physics and Geomechanics.
- [110] Weinan E. *Principles of multiscale modeling*. Cambridge University Press, 2011.
- [111] Weinan E, B. Engquist, X. Li, W. Ren, and E. Vanden-Eijnden. Heterogeneous multiscale methods: A review. *Communications in Computational Physics*, 2, 2007.
- [112] X.-H. Wen and J. Gómez-Hernández. Upscaling hydraulic conductivities in heterogeneous media: An overview. *Journal of Hydrology*, 183(1):ix–xxxii, 1996.
- [113] S. P. White and E. K. Mroczek. Permeability changes during the evolution of a geothermal field due to the dissolution and precipitation of quartz. *Transport in porous media*, 33(1):81–101, 1998.
- [114] R. A. Wooding, S. W. Tyler, and I. White. Convection in groundwater below an evaporating salt lake: 1. onset of instability. *Water Resources Research*, 33(6):1199–1217, 1997.
- [115] R. A. Wooding, S. W. Tyler, I. White, and P. A. Anderson. Convection in groundwater below an evaporating salt lake: 2. evolution of fingers or plumes. *Water Resources Research*, 33(6):1219–1228, 1997.
- [116] Z. Xu and P. Meakin. Phase-field modeling of solute precipitation and dissolution. *The Journal of Chemical Physics*, 129(1):014705, 2008.
- [117] T. Yanaze, S. Yoo, K. Marumo, and A. Ueda. Prediction of permeability reduction due to silica scale deposition with a geochemical clogging model at Sumikawa Geothermal Power Plant. *Geothermics*, 79:114–128, 2019.
- [118] Y. Yechieli and W. W. Wood. Hydrogeologic processes in saline systems: playas, sabkhas, and saline lakes. *Earth-Science Reviews*, 58(3):343–365, 2002.
- [119] B. Zhmud, F. Tiberg, and K. Hallstenson. Dynamics of capillary rise. *Journal of Colloid and Interface Science*, 228(2):263–269, 2000.
- [120] C. Zhu, P. Lu, Z. Zheng, and J. Ganor. Coupled alkali feldspar dissolution and secondary mineral precipitation in batch systems: 4. numerical modeling of kinetic reaction paths. *Geochimica et Cosmochimica Acta*, 74(14):3963–3983, 2010.